Delivery of nanocarrier-loaded hydrophobic drugs via the airways

Zahra I. Merchant

PhD in Pharmaceutics

Supervisors:

Emeritus Professor Graham Buckton

Professor Kevin M.G. Taylor

Dr Satyanarayana Somavarapu

Thesis submitted in fulfilment of the requirements for the Doctor of Philosophy degree

UCL School of Pharmacy

Department of Pharmaceutics

2014-2017

To my dearest mom and dad,

for their incessant love and unwavering support

to my lifelong pursuit of dreams and happiness

Declaration

I, Zahra Merchant confirm that the work presented in this thesis entitled “Delivery of nanocarrier-loaded hydrophobic drugs via the airways” is my own. Where information has been derived from other sources, I confirm that this has been indicated in the thesis.

This work has been carried out at the UCL School of Pharmacy between 2014-2017 under the supervision of Professor Kevin M.G. Taylor, Emeritus Professor Graham Buckton and Dr Satyanarayana Somavarapu.

Zahra Merchant

Date- 12/09/2017

Abstract

Background and purpose: Systemic delivery of hydrophobic therapeutics represents substantial formulation challenges impeding optimal benefits due to side effects and sub-therapeutic drug levels at the target site consequently leading to progression of multi-drug resistance. This thesis describes three distinct novel nanotechnology-based strategies with desirable aerosolization characteristics for delivery via the airways, aimed at enhancing the therapeutic efficacy of hydrophobic drugs for pulmonary and neurological disorders.

Methods: The first approach involved the development of dry powder microparticles for pulmonary delivery of antifungal amphotericin B nanocomplexes, prepared by co-grinding the drug with ascorbic acid. Nanocomplexes developed were characterized for molecular interactions by FT-IR, size, zeta potential, morphology, *in vitro* aerodynamic behavior and antifungal activity. The second strategy entailed design of liposomes co-encapsulating rifampicin and ibuprofen using Design of Experiment, targeted to the mannose and/or scavenger receptors on the alveolar macrophages where TB infection resides. Spray dried microparticles were characterized for *in vitro* aerodynamic behavior and macrophage uptake using the flow cytometer in RAW 264.7 cells. The third approach involved the development of Kolliphor® HS 15 micelles incorporating neuroprotective agents CNB001 or curcumin and Kolliphor® TPGS micelles encapsulating curcumin for the treatment of neurodegeneration and neuroblastoma respectively. Nasal delivery of these micellar systems was intended for brain targeting. Micelles were characterized for size, charge, aerosol droplet size distribution, drug release, morphology and *in vitro* cellular studies on SH-SY5Y cells.

Results: Successful development of nanocarrier-based systems with a high encapsulation efficiency greater than 80% for all the systems was achieved, with particle size desirable for the end-use. Spray dried microparticles of amphotericin B nanocomplexes with L-leucine showed a high fine particle fraction of around 58% signifying likely deposition in the peripheral airways, to the areas of fungal infection. There was no loss of antifungal activity against *Candida spp* on complexation of amphotericin B. Microparticles of liposomes encapsulating antitubercular drugs showed good aerosolization, and up to 65% fine particle fraction on addition of L-leucine could be achieved. An enhanced *in vitro* cellular uptake was evident for negative-charged liposomes targeted to the scavenger receptors and the mannosylated liposomes targeted to the mannose receptors on the macrophage cell line RAW 264.7. Finally, Kolliphor® micelles encapsulating CNB001 or curcumin showed desired aerosol droplet size for delivery to the posterior nasal olfactory epithelium with median size of 42.75-54.86 µm when aerosolized by the Nasal™ Mucosal Atomization Device. The formulations intended for neuroprotection showed improved cellular viability, reduction in reactive oxygen species and nuclear morphology in the *in vitro* Parkinson's model.

Conclusion: The nanotechnology-based formulations combined with administration to or through the airways using commercially available delivery devices, represent a highly attractive formulation strategy for delivery of hydrophobic agents to the target site at a therapeutic level to combat issues of multi-drug resistance.

Research Impact Statement

The majority of failures in the development of new drug candidates from the bench-to-bedside have been attributed to poor water solubility, leading to low bioavailability and suboptimal drug concentrations at the target site. Advances in combinational chemistry have led to an increase in the development of hydrophobic drug candidates, accounting for 90% of the discovery pipeline. The study of nanotechnology or nanocarrier-based drug delivery to combat problems such as drug solubility and toxicity is increasing, with an estimated market size of $136 billion by 2021. Use of nanotechnology to combat diseases like cancer and fungal infections is not new to the market, with the development of several nanocarrier-based treatments currently undertaken.

Following systemic administration of medicaments aimed at treating airways-related diseases, tissue concentration of the drugs is often suboptimal, potentially leading to development of multi-drug resistance, in the case of infections. Hence, for diseases associated with the airways, inhalation would be an attractive approach to overcome challenges posed by systemic delivery of medicaments. The global market for inhalation therapies has been expanding rapidly and is forecast to reach $42 billion by the end of 2025. Inhalation therapies already provide essential and often life-saving remedy, with a quick onset of action, for a range of respiratory diseases, including asthma and chronic obstructive pulmonary disorder. Moreover, due to attractive properties associated with the airways, such as high vascularity and low enzymatic action, this route has been exploited for systemic delivery of medicaments for conditions such as migraine, pain control and sexual dysfunction. Furthermore, nasal inhalation is being extensively investigated for direct brain targeting, with the first two candidates namely oxytocin and monoterpene perillyl alcohol in clinical trials for the treatment of autism and malignant gliomas respectively.

The efficacy of inhalations relies greatly on the capacity of the device and formulation to deliver the correct dose of medicament to varied patient populations, with minimal dependence on patients' parameters namely inspiratory flow rate and disease conditions. Unforeseen changes in the performance of inhalation systems might pose serious implications to treatment, hence, making it necessary to understand various aerosol parameters and potential deposition behaviour that dictates aerosol performance. Research group led by Emeritus Professor Graham Buckton, Professor Kevin Taylor and Dr Satyanarayana Somavarapu at the UCL School of Pharmacy have greatly focussed for over a decade to research the performance variations of numerous inhalation systems and their potential outcomes on treatment, mostly in the form of nebulization and dry powder inhalation.

Specifically, the impact of research presented in this thesis has established three distinct and coherent strategies, demonstrating the feasibility for non-systemic delivery of hydrophobic drugs,

representing potential solutions to major delivery challenges for the pharmaceutical industry. Thus, this research demonstrates:

1. Co-grinding of amphotericin B and ascorbic acid-2-glucoside, followed by spray drying, allows pulmonary delivery of hydrophobic antifungal drug amphotericin B, at therapeutically relevant concentrations to combat lung fungal infections,

2. Co-encapsulation of hydrophobic drugs rifampicin and ibuprofen in mannosylated and anionic liposomes represent a promising formulation strategy for targeting and hence treatment of intracellularly-located TB bacilli, in the form of spray-dried microparticles,

3. Potential for treatment of Parkinson's disease and neuroblastoma by generating optimum aerosols of Kolliphor® micelles incorporating hydrophobic drugs CNB001 or curcumin, intended for brain targeting via the nasal airways.

Hence, combining the benefits of nanotechnology and inhalation would be an attractive approach, to engineer systems that may be therapeutically effective and help improve the quality of life of diseased patients.

Acknowledgments

PhD completion is truly a marathon run demanding extreme perseverance. It has been a very enjoyable journey, and would not have been possible without the support of countless people who have contributed positively and deserve to be acknowledged.

My first and most important acknowledgment goes to God for providing me the strength and patience to excel in my studies and my parents, Zaibun and Iqbal Merchant, for their love, prayers and motivation to drive me to work hard being miles away from home, I love them dearly and esteem them highly!

I would like to express my deepest gratitude to Professor Graham Buckton for the PhD Studentship and University College London for the Overseas Research Scholarship, collectively funding my PhD studies and giving me an opportunity to achieve such an accomplishment. I would also like to genuinely thank Professor Buckton for his scientific guidance and expertise to set the foundation of my PhD during the early years. Nevertheless, I wold like to thank UCL for the SLMS conference fund 2015, SLMS conference fund 2016, SOP travel fund 2015 and Yusuf Ali grant 2016 to give me an opportunity to attend numerous conferences, to meet and network with a large, diverse group of pharmaceutical scientists from around the world.

My profound appreciation and heartful gratitude to Professor Kevin M.G. Taylor for his never-falling enthusiasm, support and scientific expertise. It has been an honor and privilege to have been supervised by him. He is such a kind soul and a role model! I am very grateful to him for his contribution towards reading and editing my thesis despite his occupied schedule.

My gratitude extends to my secondary supervisor Dr Satyanarayana Somavarapu for welcoming me into his group and for the freedom to carry out research in his laboratory.

This would not have been such a wonderful PhD if it was not for my brilliant and super-supportive lab mates Norhayati Mohamed Noor, Noratiqah Mohtar, Nattika Nimmano, Acom Sornsute, and colleagues Mukrish Hanafi and Yacine Kassis. They have been an extreme support at times of ups and downs, without them I would not have enjoyed as much! They are my family away from home, and indeed with the happiness of an achievement comes a sad feeling of departing from them. Thank you to Dr Prasad Sawadkar from the UCL Division of Surgery for being an excellent friend and teaching me the basics of cell culture, without which I would not have skilled such an essential technique and for all his support scientifically.

I wish to express my sincere acknowledgment to Dr Paul Stapleton for patiently teaching me microbial studies and allowing me to access his laboratory at all times. My acknowledgment extends to Mr. David McCarthy for his support on electron microscopy as per my needs. His patience and dedication in capturing the minute details of formulations have really helped in discussing important aspects in this thesis. I am also grateful to Dr James Colin for his co-operation and help for training me on the NMR.

Furthermore, I am sincerely thankful to the supportive pharmaceutics technician team; Ms. Isabel Goncalves Cartuzzo, Mr. John Frost, Ms. Carrie Pemberton, Ms. Kate Keen, Ms. Alison Dolling and Ms. Satinder Sembi for excellent management of the Pharmaceutics department. I would like to extend my gratitude to Ms. Catherine Baumber and Mr. Victor Diran for their efficient administrative assistance.

I am grateful to Mr. Lucas Silva, Mr. Gonçalo Farias and Dr Jag Shur for welcoming me at Nanopharm Ltd to analyze aerosol droplet size distribution of my samples on the Malvern Spraytec. I would like to extend my acknowledgement to fellow lab mates Ramesh Soundararajan, Pedro Ernesto, Sarah Soares, Mina Emamzadeh and Mandana Emmzadeh for their enlightening ideas and support.

I would like to genuinely thank for his moral support my dearest friend Suleman Malik, for always helping me to cheer up when my experiments did not go as per plan, particularly during the challenging write-up phase. I would also like to acknowledge my officemates Dr Sahar Awwad and Dr Athmar Daher for all their support and cheerful office gossips, and flatmate Sanjana Marchon for being like an elder sister and teaching me the importance of assertiveness in life.

I would like to mention last but not the least a sincere gratitude to my brother Hisham Merchant, and friends Yasmin, Kumail, Rizwan, Mitesh, Dinesh, Shreya, Ajay and Saira for their love and support which has helped me overcome obstacles and hardships encountered not only through my graduate career but also in many areas of life.

My perpetual acknowledgement extends to my beautiful baby niece Khadija and nephews Ali Reza, Hasnain, Noah and Isaac for their endless love and affection, when I see them I can forget all my worries in life.

Preface

The aim of the thesis is to examine various nanocarriers encapsulating hydrophobic drugs engineered with favorable aerosol characteristics to be delivered via the airways. For this, the thesis comprises of 6 major chapters namely:

Chapter 1: Introduction

This chapter covers the literature on pulmonary and nasal delivery systems, with reference to varied types of lung infections and neurological disorders. It summarizes the limitations of current treatment options considering the biological barriers for effective drug delivery. It lastly highlights the consolidation of aerosol delivery and nanotechnology to combat these barriers and improve the therapeutic efficacy of treatment.

Chapter 2: General experimental methods

This chapter covers the basic experimental methodology that are common to the different chapters

Chapter 3: Preparation and characterization of spray-dried inhalable microparticles of co-ground and solubilized amphotericin B nanocomplexes

This chapter presents the results for nanocomplexes prepared by co-grinding amphotericin B with ascorbic acid-2-glucoside. These were characterized for size, charge, stability to ensure the complexes were stable and did not dissociate on storage, and the drug remained solubilized. The nanocomplexes intended for dry powder inhalation were spray dried and characterized for drug content, surface morphology, crystallinity, molecular interactions between amphotericin B and AA2g, *in vitro* pulmonary aerosol characteristics and *in vitro* antifungal assessment on *Candida spp* namely *Candida albicans* and *Candida tropicalis*.

Chapter 4: Preparation and characterization of spray-dried inhalable microparticles of co-encapsulated rifampicin and ibuprofen in mannosylated targeted liposomes

This chapter focuses on designing liposomal formulations targeted to the alveolar macrophages since *Mycobacterium* bacilli behaves as an intracellular pathogen, and hence its eradication is challenging, increasing tuberculosis prevalence and multi-drug resistance. Negatively-charged liposomes proposed to target to the scavenger receptors on the macrophages co-encapsulating rifampicin and ibuprofen were prepared by thin-film hydration technique, using Design of Experiment, by varying the amount of lipids DPPC: DSPG: cholesterol and drugs rifampicin: ibuprofen, to achieve maximal drug encapsulation along with desired size and charge. Moreover, negatively-charged targeted liposomes embedding mannosamine or p-amino phenyl mannopyranoside were formulated.

Mannosylated chitosan (targeting polymer) was synthesized and characterized by FT-IR and ^{1}H NMR. Negatively-charged non-targeted liposomes were coated electrostatically with mannosylated chitosan to confer a final positive charge to the liposomes with mannose on the

liposomal surface. Final formulations co-encapsulating rifampicin and ibuprofen i.e. negatively-charged DPPC: DSPG: Chol liposomes, neutral charged DPPC: Chol liposomes, positively-charged chitosan-coated DPPC: DSPG: Chol liposomes, positively-charged mannosylated chitosan-coated DPPC: DSPG: Chol liposomes and negatively-charged DPPC: DSPG: Chol mannosylated liposomes were spray dried with lyoprotectant trehalose and dispersibility enhancer L-leucine and characterized for surface morphology, *in vitro* pulmonary aerosol characteristics and *in vitro* cellular uptake studies using fluorescence qualitatively assessed on the microscope and quantitatively on the flow cytometer.

Chapter 5: Preparation and characterization of Kolliphor® micelles for nose-to-brain delivery of neuroprotective agents and cancer chemotherapeutics

Kolliphor® HS 15 (Solutol® HS 15) micelles incorporating hydrophobic neuroprotective molecules CNB001 or curcumin and Kolliphor® TPGS micelles incorporating anticancer drug curcumin were prepared by thin-film hydration technique, intended for nose-to-brain delivery. Kolliphor® HS 15 micelles were stabilized by addition of different molar ratios of cholesterol and characterized for size, morphology, aerosol droplet size distribution and *in vitro* drug release. Moreover, the biological efficacy i.e. neuroprotection, reactive oxygen species formation and nuclear morphology to assess the neuroprotection efficacy of the micellar formulations was studied on the *in vitro* cellular-based SH-SY5Y Parkinson's disease model. Kolliphor® TPGS micelles incorporating curcumin were prepared to mitochondrially target cancer cells with dequalinium. These micelles were characterized for size, charge, morphology, aerosol droplet size distribution and *in vitro* drug release. The *in vitro* anticancer efficacy of these formulations was studied on the neuroblastoma SH-SY5Y and lung adenocarcinoma A549 cell lines.

Chapter 6: General discussion and future work

Chapter 6 entails principal conclusions of the research and general discussion summarizing the major findings, relating the outcome of this thesis to present literature. Subsequently, suggestions for the future development of these systems were considered.

Table of Contents

CHAPTER 3: PREPARATION AND CHARACTERIZATION OF SPRAY-DRIED INHALABLE MICROPARTICLES OF CO-GROUND SOLUBILIZED AMPHOTERICIN B NANOCOMPLEXES

List of Figures

List of Tables

List of Abbreviations

AA2g:	Ascorbic acid-2-glucoside
ANOVA:	One-way Analysis of Variance
ABIP:	Amphotericin B inhalation powder
AD:	Alzheimer's disease
AM3:	Antibiotic medium 3
BBB:	Blood brain barrier
BBTB:	Blood brain tumour barrier
BSA:	Bovine serum albumin
CAP:	Community-associated pneumonia
CB:	Chronic bronchitis
CF:	Cystic fibrosis
CG:	Co-ground
CM:	Complete media
CNS:	Central nervous system
COPD:	Chronic obstructive pulmonary disorder
DCFH-DA:	2,7-dichlorofluorescein diacetate
DCP:	Dicetylphosphate
DLS:	Dynamic light scattering
DMEM:	Dulbecco's Modified Eagle Medium
DMSO:	Dimethyl sulfoxide
DMPG:	Dimyristoyl phosphatidylglycerol
DoE:	Design of experiment
DPIs:	Dry powder inhalers
DPPC:	Dipalmitoyl phosphatidylcholine
DSPG:	Distearoyl phosphatidylglycerol
DSPC:	Distearoyl phosphatidylcholine
ED:	Emitted dose
Egg PC:	Egg phosphatidylcholine
EM:	Electron microscopy
EPR:	Enhanced permeability and retention
FD:	Fluorescence density
FBS:	Fetal bovine serum
FPD:	Fine particle dose
FPF:	Fine particle fraction
FR:	Fraction recovered

FSC:	Forward scatter
FUS:	Focused ultrasound
FT-IR:	Fourier transform infrared spectroscopy
GSD:	Geometric standard deviation
HAP:	Hospital-associated pneumonia
HIV:	Human immunodeficiency virus
^{1}H-NMR:	Proton nuclear magnetic resonance
6-OHDA:	6-hydroxydopamine
HPLC:	High performance liquid chromatography
HSPC:	Hydrogenated soybean phosphatidylcholine
IA:	Invasive aspergillosis
IM:	Intramuscular
IN:	Intranasal
IV:	Intravenous
LOD:	Limit of detection
LOQ:	Limit of quantification
LPPs:	Large porous particles
LPNAPs:	Large porous nanoparticle aggregates
LUV:	Large unilamellar vesicles
MAD:	Nasal™ Mucosal atomization device
MAN:	Mannosamine hydrochloride
MDIs:	Metered-dose inhalers
MDR-TB:	Multi-drug-resistant tuberculosis
MEM:	Minimum Essential Medium Eagle
MIC:	Minimum inhibitory concentration
MLV:	Multi lamellar vesicles
MMAD:	Mass median aerodynamic diameter
MNTC:	Maximum non-toxic concentration
MOC:	Micro-orifice collector
MTT:	3-(4,5-dimethylthiazol-2-yl)-2,5-diphenyltetrazolium bromide assay
NGI:	Next generation impactor
NLCs:	Nanostructured lipid carriers
NSAIDs:	Non-steroidal anti-inflammatory drugs
NSD:	Nano spray dried
OD:	Optical density
PAM:	p-aminophenyl mannopyranoside
PBCA:	Polybutyl cyanoacrylate

PBS	Phosphate buffered saline
PD:	Parkinson's disease
PDI:	Polydispersity index
PIBSE:	Polyisobutylene
PLA:	Poly (lactic acid)
PLGA:	Poly (lactic-co-glycolic acid)
pMDIs:	Pressurized metered-dose inhalers
PNAPs	Porous nanoparticle aggregates
rANOVA:	Repeated Measures One-way ANOVA
RODOS:	Rotating dosing and dispersing System
ROS:	Reactive oxygen species
RPMI:	Roswell Park Memorial Institute media
RSD:	Relative standard deviation
RT:	Room temperature
SD:	Spray dried
SDS:	Sodium dodecyl sulphate
SEM:	Scanning electron microscopy
SLNs:	Solid-lipid nanoparticles
SNF:	Simulated nasal fluid
SRB:	Sulforhodamine B assay
SSC:	Side scatter
SUV:	Small unilamellar vesicles
TB:	Tuberculosis
TDR-TB:	Totally drug-resistant tuberculosis
TEM:	Transmission electron microscopy
TGA:	Thermogravimetric analysis
TIS:	Tobramycin inhalation solution
TIP:	Tobramycin inhalation powder
TPGS:	Tocopherol polyethylene glycol succinate
UATR:	Universal Attenuated Total Reflectance
VAP:	Ventilator-associated pneumonia
VMD:	Volume mean diameter
WHO:	World Health Organization
XDR-TB:	Extensively drug-resistant tuberculosis
XRPD:	X-ray powder diffraction

1

CHAPTER 1

Introduction

1.1 Background

Inhalation is one of the oldest forms of medicament delivery dating back to the ancient Egyptian civilization, where inhalation of vapors of black henbane was used to aid breathless patients to breathe [1]. Currently, this complex route is used primarily for the local treatment of respiratory diseases, such as cystic fibrosis (CF), chronic obstructive pulmonary disease (COPD), bronchiectasis, asthma, pneumonia, aspergillosis and tuberculosis (TB). Small molecules such as glucocorticoids e.g. budesonide (Pulmicort Flexhaler®, Pulmicort Turbuhaler®), fluticasone (Flovent®, Flixotide®), beclometasone (Pulvinal Beclometasone®, Qvar®); β_2-adrenoceptor agonists e.g. salbutamol (albuterol; Proventil®, Asthalin®, Salbulin®), terbutaline (Bricanyl®), salmeterol (Serevent®, Neovent®); anti-muscarinic bronchodilators e.g. ipratropium (Atrovent®), tiotropium (Spiriva HandiHaler®) and antimicrobials e.g. tobramycin (TOBI Podhaler®, TOBI TIS™, aztreonam (Caystone®), colistin (Colomycin®, Promixine®, Colobreathe®), pentamidine (Nebupent®), levofloxacin (Aeroquin™) have been, and are being successfully administered to the lungs for treatment of respiratory diseases.

Nasal inhalation is also attractive with the development and commercialization of nasal products for treatment of local diseases of the upper respiratory tract, such as allergic and non-allergic vasomotor rhinitis e.g. Azelastine (Allergodil®, Astelin®), fluticasone (Flonase®), budesonide (Rhinocort®); nasal congestion e.g. xylometazoline (Sudafed®, Afrin®) and nasal infections. Over the last few decades, nasal inhalation has also been exploited for systemic delivery of small drug molecules which require a rapid onset of action like migraine e.g. zolmitriptan (Zomig®), sumatriptan (Imigran®, Imitrex®, Onzetra® Xsail®); nicotine spray for smoking cessation (Nicorette®, Nicotrol®) and treatment of menopausal symptoms (Aerodiol®) [2]. Moreover, due to attractive properties such as high vascularity of nasal mucosa and low enzymatic action of nasal fluids the nose represents a lower physiological barrier to delivery of proteins and peptides, compared to the oral route. Hence, peptides requiring low systemic levels to be therapeutically effective e.g. desmopressin (Desmospray®), oxytocin (Syntocinon®) and calcitonin (Miacalcin®, Fortical®) are marketed as nasal sprays [2].

This introduction outlines the relevant literature vital for the reader to grasp important aspects for understanding the experimental work that follows in Chapter 3-5. It summarizes pulmonary drug delivery taking into account the pre-requisites, aerosol characteristics and delivery devices necessary for efficient aerosolization to the target site in the lungs, and briefly outlines lung infections and barriers to effective delivery of antimicrobials. Furthermore, it summarizes nasal airway drug delivery for brain targeting (nose-to-brain drug delivery) considering the pre-requisites, aerosol characteristics and delivery devices necessary for effective targeting to the central nervous system (CNS), and outlines neurogenerative diseases and brain cancer along with the barriers to treatment of neurological disorders. Finally, it describes the various nanocarrier

systems in literature and the advantages of nanotechnology for delivery to the airways (for the diseases of interest), concluding with the scope and content of the thesis.

1.2 Pulmonary drug delivery

For local rather than systemic delivery, on inhalation, the drug directly reaches the desired site of action, leading to the possibility of dose reduction as compared to oral and parenteral routes, reducing medicament costs and ensuring a higher concentration of the drug is retained at the target site [2, 3]. This reduces the possible side effects due to decreased systemic exposure and helps in achievement of a faster onset of action [3]. Numerous studies have demonstrated that antimicrobials, such as amikacin, tobramycin, rifampicin and amphotericin B used for treatment of lower respiratory tract infections caused by organisms like *Pseudomonas aeruginosa, Candida albicans* and *Mycobacterium tuberculosis* have serious adverse effects, including ototoxicity and nephrotoxicity, when administered orally or intravenously (IV), which are ameliorated by direct pulmonary delivery [4–8]. Due to the relatively low metabolic activity in the lung, pulmonary delivery is attractive for delivery of drugs which are sensitive to gastric pH, enzymes and metabolizing enzymes, particularly those associated with metabolism within the liver [9]. It is also useful for drugs belonging to Class IV of the Biopharmaceutics Classification System, such as amphotericin B, which has low water solubility and low membrane permeability, resulting in limited oral absorption and hence is administered routinely by the IV route [10–12].

Effective pulmonary drug delivery requires sophisticated aerosol formulation approaches and complex delivery devices. The drug formulation needs to be engineered with respect to size, shape, particle size distribution and density to achieve maximum therapeutic benefit from the treatment. Moreover, pulmonary delivery is a challenge due to the complex anatomy and physiology of the airways, restricting access and promoting clearance of inhaled materials [3].

1.2.1 Pre-requisites for pulmonary drug delivery: factors affecting local drug deposition

The therapeutic effect of an inhaled medicament depends largely on its deposition pattern and distribution in the lungs; hence, understanding the concepts and mechanisms of these processes is of fundamental importance to inhalation therapy. Deposition is a process by which particles come into contact with and adhere to the surface [3].

From a formulation viewpoint, the deposition profile is largely dependent on the aerosol particle characteristics, namely; aerodynamic size, particle size distribution, shape, density, electric charge, hygroscopicity and stability. Other non-formulation factors include lung morphology, clearance mechanisms (mucociliary and alveolar macrophages), type and severity of lung disease, airflow obstruction and patient factors, such as inhalation pattern, flow rate, breath-holding time and correct use of devices [14-15].

Aerosol particle deposition in the airways is governed by three principal *mechanisms* (Figure 1.1) namely: inertial impaction, gravitational sedimentation and Brownian diffusion [5]. Figure 1.1B

indicates that regional deposition in the airways is dependent on the particle diameter; pulmonary deposition is dominant for particles between 1-5 μm.

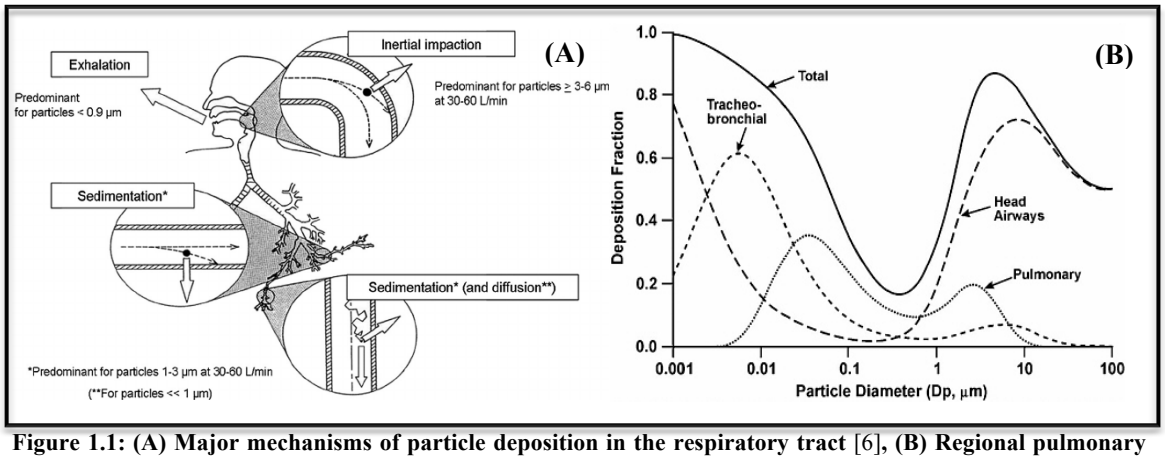

Figure 1.1: (A) Major mechanisms of particle deposition in the respiratory tract [6]**, (B) Regional pulmonary deposition of inhaled particles dependent on the particle diameter (μm)** [7]

Inertial impaction

Large particles with high momentum (i.e. the product of mass and velocity) do not follow the lung structure with the flowing air stream. These particles are deflected by the airway branching due to inertia and hence convective fluid motion leading to deposition on the airway wall [3,5,8]. This occurs mainly at bifurcations of large conducting zones of the airways, nose, mouth, pharynx, larynx and bronchial region. This is a velocity-dependent mechanism and is the main method for deposition of particles greater than 5 μm [9].

Gravitational sedimentation

This results from the gravitational force acting on particles with sufficient mass. Deposition due to gravity increases with increasing particle size, density and with longer residence time, acting when the particle velocity is low resulting in loss of balance between the gravitational force and the drag force of air leading to subsequent deposition on the lower airway surface. Gravitation sedimentation is an important mechanism of deposition for particles in the range 1-3 μm in small conducting airways, like bronchioles and alveoli where the air flow rate is low [3,5,8].

Diffusion

This mechanism of deposition predominates for particles <1 μm and is governed by random Brownian motion. Particles are displaced by random motions of air molecules and deposit on contact with the cells by sequential bombardments. Deposition by diffusion is inversely proportional to particle size and occurs in the alveoli and smaller respiratory bronchioles, where bulk airflow rate is low or absent [3,5].

1.2.2 Aerosol characteristics

Aerodynamic diameter (d_{ae}) is the most important physical property of an aerosol that governs the proportion of the dose deposited in the different parts of the airways and can be defined as the diameter of a unit density sphere that has a similar terminal settling velocity to the particle under consideration [10]. It can be mathematically described as equation 1.1 below:

$$d_{ae} = d_g \sqrt{(\rho_e/\rho_s \lambda)} \qquad \textbf{Equation 1.1}$$

where d_g is the particle geometric diameter, ρ_e and ρ_s are the effective particle density and unit particle (1 g/cm^3) density respectively and λ is the dynamic shape factor of the particle, i.e. the ratio of particle drag force to that of a sphere of equivalent volume, being 1 for a perfect sphere. Aerodynamic diameter explains the movement of aerosol particles in an air flow not only with respect to their geometric diameter but also taking into consideration their shape and density [10].

Particle shape plays an important role in the aerodynamics of dry powders. Studies have shown that the elongation ratio and shape factor of a particle dictate its trajectory in the respiratory tract. Rod-shaped particles of lactose and cromoglycic acid showed an increase in fine particle fraction compared to approximately spherical particles, due to their shape being analogous to that of asbestos fibers which have a higher susceptibility for pulmonary deposition by spatial hindering effect [11–14]. The study of the relationship between shape and surface properties is important as it can affect the aerodynamics of dry powders. With higher elongation ratios, the contact area between the particles is greater, leading to an increased cohesiveness between the particles which may ultimately affect the aerodynamic performance of the particles.

Formulation characteristics

Surface roughness of a particle impacts the aerosolization efficiency of a dry powder inhalation as it determines the interaction forces between the drug particles, and between the drug and carrier particles (if present) in a formulation. An appropriate balance between the interaction forces (during mixing/filling) and separation forces (during inhalation) of these particles is essential to ensure efficient delivery of the medicament to the peripheral lung when delivered as dry powder inhalations [13,15,16]. Studies have demonstrated that an increase in surface roughness of lactose carrier particles and sieved sorbitol particles proportionately improves the drug carrying capacity of the carrier; however, the drug particles are held tightly to the carrier particles and hence the emitted dose from the inhaler device decreases [13,15,16].

Other than size, shape and surface roughness, deposition is also governed by various other formulation parameters, such as hygroscopicity, polymorphic form, inter-particulate forces and surface charge.

1.2.3 Pulmonary drug delivery devices

Aerosols are an effective way to deliver medications to the pulmonary site. These are two-phased, stable dispersions or suspensions of solid particles or liquid droplets in a gaseous phase usually air, and can be generated by a passive breath-driven or an active single or multiple dose inhaler [17]. Therapeutic inhalation aerosols can be delivered using three broad types of devices, namely: nebulizers, pressurized metered-dose inhalers (pMDIs) and dry powder inhalers (DPIs), although other delivery means like non-pressurized metered dose inhalers have been described. The advantages and disadvantages of the different inhaler devices are outlined in Table 1.1.

Table 1.1: Advantages and disadvantages of different inhaler devices [18]

Inhaler type	Nebulizer (jet, ultrasonic, vibrating mesh)	Pressurized metered-dose inhaler (pMDI)	Dry powder inhaler (DPI)
Advantages	▪ Does not require inhalation actuation synchronization ▪ No propellant ▪ High doses can be delivered ▪ Optimal for paediatric, gaeriatric and diseased patients who cannot use other devices ▪ Present generation of vibrating mesh nebulizers can be battery operated and hence portable (e.g: Aerogen Vibronic™)	▪ Portable and compact ▪ No preparation required ▪ No contamination risks ▪ Multi-dose (approx. 200 doses) ▪ High reproducibility between doses ▪ Sealed environment prevents drug degradation ▪ Cost-effective	▪ Portable and compact ▪ Does not require inhalation actuation synchronization ▪ No propellant ▪ Ease of use ▪ Breath actuated ▪ No need for spacers
Disadvantages	▪ Expensive, wasteful ▪ Contamination risk ▪ Time consuming ▪ Different models and operating conditions lead to high-performance variability ▪ Drug formulation preparation may be necessary ▪ Nebulizer performance may decline over time ▪ Nebulization of nanocarrier-based systems can lead to instabilities of formulation like drug leak and aggregation or agglomeration of the nanocarriers	▪ Requires inhalation-actuation synchronization ▪ High oropharyngeal deposition observed ▪ Maximum dosage that can be administered is approximately 5 mg ▪ Young children require a valve-holding chamber (spacer) ▪ Propellant- based	▪ Fine particle dose dependent on inspiratory flow rate, tidal volume and breathes/cycle ▪ Fine particle dose dependent on the dry powder particle properties ▪ Moisture/electrostatic attraction may lead to powder aggregation, changing aerodynamic properties and/or causing capsule softening

1.2.3.1 Nebulizers

These were the first devices to be used for pulmonary drug delivery and are still in practise particularly by the paediatric and gaeriatric populations for delivering drugs such as salbutamol for paediatric asthma, sodium cromoglicate for inflammation, corticosteroids and bronchodilators for severe COPD and tobramycin for infections associated with CF and COPD. Nebulizers need minimum patient skills or inhalation/actuation co-ordination [19]. They deliver the drug as droplets generated from solutions or suspensions, and have an advantage of delivering large doses during tidal breathing. Nebulizers can be classified as:

Pneumatic or jet nebulizers

These operate on the Bernoulli principle by which high velocity compressed air passes through a narrow orifice creating an area of low pressure at the outlet, causing the drug solution to be drawn up from the reservoir, forming a liquid film which breaks down into liquid droplets due to surface tension. Large droplets are retained in the device and a fine mist is emitted for inhalation via a mouthpiece or a facemask [4,20].

Ultrasonic nebulizers

These contain a piezoelectric crystal which vibrates at a frequency of 1-3MHz producing waves which are transmitted to the surface of the drug solution leading to the formation of standing waves, forming a fountain of fine mist. Small droplets having a size inversely proportional to the value of crystal vibrational frequency are produced in the mist [4,20,21].

Vibrating-mesh nebulizers

These contain a piezo-element which vibrates a perforated membrane in resonant bending mode. The cross-section of the perforations is larger at the reservoir side and narrower at the droplet emergence side. The size of aerosol droplets produced can be modulated by changing the number and sizes of perforations [22].

Electrohydrodynamic atomizers (EHDA)

Also referred to as electro-spraying, these produce particles suitable for deep lung delivery by a low-shear technique. Application of electrical forces in a controlled manner can be useful in production of monodispersed droplets of size in the nanometric to micrometric range, depending on the frequency applied during particle production [23].

1.2.3.2 Pressurized metered-dose inhalers: pMDIs

These multi-dose devices consist of an aluminum canister equipped with a metering valve, which contains drug dissolved or suspended in liquid propellant(s) along with other excipients, such as surfactants, e.g. Span 85, oleic acid and soya lecithin and co-solvents, usually ethanol. Actuation of the valve leads to emission of the aerosol as a metered dose of drug dissolved or dispersed in the propellant, usually a hydrofluoroalkane [4,20,21,24].

1.2.3.3 Dry powder inhalers: DPIs

Subsequent to the development of pMDIs, dry powder inhalers (DPIs) were designed, and these received added interest in recent years since ozone-depleting chlorofluorocarbon (CFC)-based pMDIs were phased out for environmental reasons. DPIs have no propellant and in some respects are more user-friendly devices [25].

DPIs exist in many designs which need for their operation a degree of manual dexterity, although simpler DPIs are being researched [26]. DPIs dispense a metered quantity of powder in an air stream drawn through an inlet system by the patient's inspiration, directing air through the loose powder aggregates and forming a drug aerosol cloud. Hence, these are passive breath-actuated devices [21,27]. They are robust, portable and convenient in terms of formulation, processing, and stability as they are a one-phase solid system. They do not require to be sterile and avoid the formulation issues of nebulizers and pMDIs, particularly for suspension formulations, such as sedimentation, flocculation and foaming which may impact aerosol performance [28].

DPIs are receiving increasing interest due to drawbacks of the use of propellants and the requirement of inhalation-actuation synchronization when using pMDIs. The characteristics of an ideal DPI can be divided based on:

Patient acceptance [29–31]

- Simple operation
- Portable and easy to carry
- Multiple dosage reservoir
- Cost effective and/or reusable
- Dose counter, dose-ready indicator and an audiovisual indicator of doses remaining
- Patient feedback mechanism to indicate successful dosage administration

Device reliability and reproducibility with respect to dosing [29–33]

- Consistent and homogeneous dose delivery of medicament throughout the life of inhaler, at least comparable to a pMDI
- Accurate and uniform dose delivery of medicament over a wide range of inspiratory flow rates with minimal variation with respect to age, gender and disease state
- Optimum and reproducible control of respirable fractions with high fraction of particles in respirable range for deep lung delivery
- Low oropharyngeal deposition with high bronchial deposition

Efficient device [29–33]

- Good protection from environmental moisture to prevent change in powder aerosol characteristics
- In-process quality control

- Minimal adhesion between the drug and inhalation device
- Device suitable for a wide range of drugs and doses
- Environmentally accepted device

No DPI can fulfill all the requirements of an ideal inhaler; however, continuous research is being conducted to improve their performance to achieve optimal fine particle dosage of medicament, with improved patient acceptability. Patient education is of utmost importance with regards to use and storage of their DPI preparations.

Some presently marketed DPIs, nebulizers and metered-dose inhalers (MDIs, pressurized or non-pressurized) used for pulmonary delivery of medicaments are as shown in Table 1.2.

Table 1.2: Some marketed pulmonary delivery devices [4]

Cyclohaler DPI	Turbuhaler DPI	HandiHaler DPI	Diskus DPI	Easyhaler DPI
				
eFLOW nebulizer	**I-neb nebulizer**	**Compare Elite nebulizer**	**Respimat Non-pressurized MDI**	**Vannair pMDI**
				

1.2.4 Types of lung infections

Lung infections can be defined as infectious diseases of the upper or lower respiratory tract, wherein, upper respiratory tract infections include common cold, tonsillitis and acute rhinosinusitis, whereas, lower respiratory tract infections include acute bronchitis, bronchiolitis, pneumonia and tracheitis, and these pose a major health issue in many countries [34,35]. Bacterial, fungal and viral infections occur frequently and play a crucial role in the progression of chronic pulmonary diseases due to acute exacerbations leading to substantial long-term consequences, morbidity and mortality [35–37].

1.2.4.1 Bacterial infections

Bacterial pathogens can be classified based on their infection lifestyle in the host and hence can be either intracellularly or extracellularly located.

Extracellular pathogens

Most infections in CF, COPD and chronic bronchitis (CB) are caused by bacterial pathogens, such as *Staphylococcus aureus, Escherichia coli* and *Pseudomonas aeruginosa*. These organisms live extracellularly and hence are easier to eradicate than intracellular infections. Intracellular pathogens are present in special compartments, for instance, alveolar macrophages and epithelial cells, where delivery of antibiotics encounters greater barriers. Nevertheless, extracellular bacterial pathogens overcome antibiotic susceptibility by other means such as genetic modification and production of a sessile, slimy covering called a 'biofilm'. [38]. These are explained briefly in the following sections on the barriers to effective pulmonary antimicrobial therapy (section 1.2.5).

Pseudomonal infections are clinically significant and can lead to life-threatening diseases and multiple organ failure [39]. *Pseudomonas aeruginosa* is the most prevalent of this class of pathogens and has been long associated with a variety of clinical pulmonary problems. It is an opportunistic nosocomial pathogen and is a major infective organism leading to high mortality and morbidity in hospitalized patients [39,40]. It leads to sepsis in hospitalized patients and is also associated with mortality in cases of pulmonary hospital-associated pneumonia (HAP), namely ventilator-associated pneumonia (VAP) and bronchoscope-associated pneumonia [40]. This pathogen causes exacerbations of pulmonary conditions including CF and COPD, primary bacteremia in AIDS patients and pulmonary community-acquired pneumonia (CAP) [40]. *Pseudomonas aeruginosa* is also highly involved with the pathogenesis of CF [41,42].

Intracellular pathogens

Eradication of intracellular infections faces challenges due to the difficulty of access to the protective environment within cells being the major reason for multi-drug resistance to current antimicrobials. Some organisms, such as *Mycobacteria spp, Salmonella spp* and *Neisseria spp* are primarily located in phagocytic intracellular compartments, including macrophages, polymorphonuclear leukocytes and neutrophils, which recognize pathogen-associated molecular patterns (PAMPs) present on the surface of pathogens which are unique to the pathogen type. These proteins expressed on the pathogens are essential for their pathogenicity [43–47].

Mycobacterial infections: Tuberculosis, a ubiquitous and highly contagious chronic bacterial infection caused by the bacillus *Mycobacterium tuberculosis* has re-emerged dramatically since the mid-1980s, particularly since the escalation of HIV infection, which renders the host 20-30 times more susceptible to infection by *mycobacterium* [48]. According to the WHO Global Tuberculosis Report 2016, TB affected about 10.4 million people in 2015, of which 1.4 million died from TB [49,50]. Additionally, strains of *mycobacterium* which are resistant to the first-line drugs, like isoniazid and rifampicin. have a high prevalence (3.6%) amongst newly emergent TB cases worldwide [51]. Although TB can be both pulmonary and extra-pulmonary, the pulmonary

tract is a major portal of entry for *mycobacterium*, the initial site of immune response and resurgence of the disease. *Mycobacterium tuberculosis* has been shown to bind to and internalize into the alveolar macrophages, where it enhances its survival by suppression of macrophage immune responses ultimately leading to the pathogenesis of TB [45,47,52]. Furthermore, it spreads to cause extra-pulmonary TB also known as 'miliary TB' which becomes difficult to control. Treatment of such intracellular pathogens requires delivery of antibiotics to these protective compartments where the bacilli reside, making eradication and treatment particularly challenging.

1.2.4.2 Fungal infections

In the past few decades due to concurrent increases in organ transplantations, aggressive antineoplastic therapies, and immunocompromised patients; the prevalence and severity of pulmonary fungal infections have increased [53]. These infections have a lethality rate of 30-80% in immunocompromised and organ-transplant patients [54,55]. The airways being the major portal of entry of fungal spores, causing such infections, suggests direct pulmonary administration of antifungal agents to the lungs using inhaled drug delivery, could be an attractive way to treat invasive pulmonary fungal infections [53,56].

Common fungal pathogens which infect the pulmonary tract are those that cause [57]:

Invasive pulmonary aspergillosis- *Aspergillus spp*

Pulmonary candidiasis- *Candida albicans*

Pulmonary mucormycosis- *Rhizopus, Mucor* and *Rhizomucor spp*

Pulmonary cryptococcosis- *C. gattii* and *C. neoformans*

Pulmonary blastomycosis- *B. dermatitidis*

Pulmonary histoplasmosis- *H. capsulatum*

Pulmonary coccidioidomycosis- *Coccidioides immitis* and *C. posadasii* [57]

Pneumocystis pneumonia has emerged as a serious healthcare problem due to the increased incidence of HIV which causes weakening of the patients' immune systems leading to infection with opportunistic fungus *Pneumocystis jirovecii.* This infection invades the alveolar lumen in the lungs of susceptible hosts, blocking oxygenation, leading to death [58]. Current pulmonary fungal infections and their treatment strategies are considered in great detail in chapter 3.

Antimicrobial aerosols currently marketed and in clinical/preclinical trials are outlined in Table 1.3 and Table 1.4 respectively.

Table 1.3: Marketed antimicrobial aerosols [59–65]

Formulation name	Drug and indication	Device and dose	Treatment outcome(s)
TOBI® Tobramycin inhalation solution USP (TIS™) Novartis	Tobramycin Aminoglycoside antibiotic CF, COPD, CB, VAP, CAP	Nebulization PARI-LC® Plus 300 mg nebulized twice daily	Improved lung function, prevention of pulmonary exacerbations
BRAMITOB® Chiesi Farmaceutici	Tobramycin Aminoglycoside antibiotic CF, CAP	Nebulization PARI-LC® Plus 300 mg nebulized twice daily	Improved lung function, prevention of pulmonary exacerbations
TOBI® Tobramycin PulmoSphere™ inhalation powder USP (TIP) Novartis	Tobramycin Aminoglycoside antibiotic CF, COPD, CB, VAP	Podhaler 112 mg (28 mg/capsule) 4 capsules twice daily	Improved lung function, well tolerated and safe, prevention of exacerbations
CAYSTONE® Aztreonam inhalation solution (AZLI) Gilead Sciences	Aztreonam lysine Monobactam antibiotic CF	Nebulization PARI eFLOW® Altera® handset 75 mg thrice daily	Safe and efficacious in prevention of lung exacerbations, no antibiotic resistance evident, superior lung function improvement to TIS™
COLOMYCIN® Forest Laboratories	Colistimethate sodium Polymyxin antibiotic CF	Nebulization PARI eFLOW® 80-160 mg twice daily	Eradication of *P.aeruginosa*
PROMIXINE® (TADIM®) Profile Pharma	Colistimethate sodium Polymyxin antibiotic CF	Nebulization I-neb® AAD® 80-160 mg twice daily	Eradication of *P.aeruginosa*
COLOBREATHE® Forest Laboratories	Colistimethate sodium Polymyxin antibiotic CF	Turbospin inhaler device-125 mg twice daily	Safe, well tolerated, efficacy like TIS™
NEBUPENT® APP Pharmaceutical	Pentamidine isethionate Antifungal Pneumocystis carinii pneumonia	Respirgard® II nebulizer System 300 mg/4 weeks	Safer compared to parenteral delivery
AEROQUIN™ Levofloxacin inhalation solution Aptalis Pharma/ Forest laboratories	Levofloxacin Fluoroquinolone antibiotic CF, COPD	Nebulization PARI eFLOW® In study 3 dose levels-120 mg or 240 mg once daily or 240 mg twice a day	Decrease in *P.aeruginosa* density, reduced need for other anti *P.aeruginosa* antibiotic, broad spectrum activity Similar efficacy to TOBI® from Phase III clinical trial

CF- cystic fibrosis, COPD-chronic obstructive pulmonary disease, CB-chronic bronchitis, VAP-ventilator-associated pneumonia, CAP-community-acquired pneumonia

Table 1.4: Clinically studied antimicrobial aerosols [59–65]

Formulation name	Drug and indication	Device and dose	Treatment outcome(s)
ARIKAYCE™ Liposomal amikacin for inhalation Insmed Inc. (Phase III clinical trials)	Amikacin Aminoglycoside antibiotic CF, Non-tuberculous mycobacterial infections	PARI eFLOW® nebulization 560 mg once daily	Sustained release of Amikacin, well tolerable, reduction in *P. aeruginosa* density
ABELCETÂ® (Aerosolized Abelcet®) Amphotericin B lipid complex for nebulization (Phase II clinical trials)	Amphotericin B Antifungal Invasive fungal infections in paediatric patients with acute leukemia	50 mg nebulized once daily for four days	Reduction in parenteral side effects of IV Abelcet® like nausea, vomiting, disseminated fusariosis and withdrawal
CIPROINHALE Ciprofloxacin PulmoSphere™ inhalation powder (CPIP) Bayer HeathCare (Phase III clinical trials)	Ciprofloxacin Fluoroquinolone antibiotic CF, COPD	Powder inhalation In study at 2 dose levels- 32.5 mg or 48.75 mg twice daily	High concentration in the lungs, decrease in *P. aeruginosa* density

CF- cystic fibrosis, COPD-chronic obstructive pulmonary disease

1.2.5 Barriers to effective pulmonary antimicrobial therapy

1.2.5.1 Intracellular pathogens

Intracellular bacterial infections are a major cause of morbidity and mortality. Intracellular bacteria have the ability to adapt and develop to form stronger and less susceptible variants to current antibiotic treatments, as verified by a high incidence of multi-drug resistance to these. This represents a considerable public health and economic burden as these variants are difficult to eradicate and more expensive to treat. This highlights the importance of developing new and improved methods of bacterial eradication from intracellular compartments. However, development of new chemotherapy approaches to combat the rapidly growing resistant strains of bacteria is too slow, threatening our ability to treat infectious diseases in the near future [66].

1.2.5.2 Biofilms

Microbiological research focuses predominantly on planktonic state cells, i.e. bacterial cells floating in culture, to study antimicrobial activity. However, in more than 80% of microbial infections, bacteria grow as a protected structured community of sessile cells encased in a self-produced hydrated polysaccharide slimy matrix i.e. a biofilm [67–69]. Initially, a layer is formed on a surface, i.e. the foundation of the biofilm made up of organic/inorganic substances deposited and adhered to a substrate.

Planktonic bacteria from the bulk liquid are then adsorbed and start forming microcolonies by physical processes such as steric interactions, electrostatic interactions and Van der Waals forces, or by bacterial appendages such as flagella, pili and fimbriae. These then develop irreversible attachments by secretion of polysaccharide intercellular adhesion proteins and divalent cations that consolidate the surface- bacteria bond. These structures contain channels in which nutrients for the bacterial cells are circulated, and hence there is a rapid population growth of daughter sessile bacterial cells which adapt to the biofilm environment by changes in the expression of genes and in the surface properties of bacterial cells. The final stage of biofilm development is completed by quorum sensing (QS) cell signaling mechanisms, wherein stimulation of genetic expression takes places leading to the production of alginate which forms a part of the extracellular matrix of the biofilm, along with many other signal molecules that help in coordination of the biofilm bacteria. These signals govern processes such as bacterial dispersion which is essential to prevent overgrowth of the rapidly dividing bacteria, and their escape and colonization of new niches when nutrients become limited and waste products accumulate [70].

Biofilms being the refuge of *mycobacterial spp* have been reported to decrease the susceptibility of the organism up to 50 times to the common antitubercular drugs, rifampicin and isoniazid [71,72]. Moreover, *Candida spp* growing in biofilms become relatively resistant to azoles, whereas, amphotericin B formulations are completely ineffective against *Pneumocystis carinii* biofilms [73]. Numerous mechanisms are involved in the avoidance of antibiotic challenges by biofilm-associated bacteria. One mechanism is the failure, retardation or reduction in penetration

and diffusion of antibiotics into the full depth of the biofilm due to the presence of a physical polymeric barrier [67,68]. A further mechanism is a change in the microenvironment of the biofilm. Studies have shown that there are anaerobic niches in the deeper regions of the biofilms which render some antibiotics, such as those of the aminoglycoside class inactive [67,68]. Moreover, accumulation of waste products may cause a change in the pH of the biofilm niche which can directly cause inactivation or antagonism of certain antibiotics, limiting their activity [67,68]. Additionally, alteration in the osmotic environment leads to an osmotic stress response, ultimately resulting in a reduction in the permeability of bacteria to antibiotics by altering the proportion of porins in the bacterial cell wall [67,68]. A further proposed mechanism to explain reduced biofilm susceptibility is the development of slow-growing or non-growing dormant bacterial cells which become less susceptible to antibiotics, e.g. penicillin antibiotics which target cell-wall synthesis of bacteria [67,68].

1.2.5.3 Antimicrobial resistance

Multiple resistance to numerous antibiotics represents a considerable therapeutic challenge. The global report on antibiotic resistance by the WHO in 2014 revealed a serious threat worldwide and the need for urgent interventions to combat an imminent future crisis [74]. Multi-drug resistant tuberculosis (MDR-TB) has emerged swiftly, representing a global health concern, threatening TB control and treatment worldwide [75]. WHO reported a doubling in the people diagnosed with MDR-TB between 2011 and 2012, with 0.58 million new incidences of MDR-TB in 2015 [49,50]. Instances of extensively drug resistant (XRD-TB) and totally drug resistant (TDR-TB) cases have risen persistently in the past decade, posing a major challenge to the limited, time-consuming treatment options currently available to treat TB.

Bacterial resistance to antibiotics can be innate or acquired by genetic and phenotypic modifications. A speculative hypothesis explaining reduced antibiotic susceptibility is the development of resistance due to genetic chromosomal mutations of bacteria. These can result in:

(1) reduced permeability or uptake of the antibiotic; e.g. resistance to chloramphenicol antibiotics due to decreased permeability into Gram-negative bacteria, resistance to penicillin and tetracycline is evident in *Neisseria gonorrhea* due to the reduced permeability of the antibiotics [76];

(2) increased efflux of the antibiotic from the bacterial cell; e.g. in the presence of tetracycline, the *TetK* gene responsible for efflux, transcription, and translation is activated leading to an increase in the number of efflux pumps and consequently resistance to tetracycline antibiotics [77]. Moreover, up-regulation of the *norA* gene in *Staphylococcus aureus* leads to an increase in activity of efflux pumps leading to fluoroquinolone antibiotic resistance [77];

(3) enzymatic inactivation of antibiotics; e.g. β-lactamases catalyzing ring-opening of β-lactam antibiotics, aminoglycoside antibiotics are inactivated by addition of acetyl, adenyl and phosphoryl groups onto the antibiotic by aminoglycoside inactivating enzymes [78];

(4) alterations of the drug target site; e.g. alterations in the target site of DNA gyrase subunit A and B are responsible for resistance to fluoroquinolone antibiotics [79]. Moreover, resistance against rifampicin arises from mutation in the β subunit of the RNA polymerase site required by the drug to show activity and streptomycin resistance has been evident due to target site mutation on the *rrs* gene encoding 16s rRNA [80];

(5) loss of enzymes necessary for activation of the antibiotic; e.g. inactivation of the *katG* gene leads to reduced catalase activity and hence the ineffective conversion of isoniazid into its active hydrazine derivative. Moreover, inactivation of pyrazinamidase by a mutation in the *pncA* gene required for conversion of pyrazinamide to its active form pyrazinoic acid results in loss of antimycobacterial activity of the antibiotic [81,82].

Further, phenotypic modifications involve sessile bacteria in biofilms that grow as spore-like biologically programmed bacterial subpopulations which are unique and highly protected dormant phenotypes, which are resistant to antibiotics in the dormant state. Another type of phenotypic modification involves the presence of salicylates, such as aspirin which make bacteria, including *Pseudomonas spp*, *Mycobacterium tuberculosis and E.coli*, less susceptible to common antibiotics due to an increased antibiotic efflux and reduced permeability, by a reduction in the level of porin expression [83].

1.2.5.4 Sputum

Mucus in the healthy lung is 10-30 μm thick in the trachea and 2-5 μm thick in the bronchial regions [84]. This thickness allows easy diffusion of gas, nutrients, ions and proteins, and the entrapment of particulate matter which is then efficiently removed by the mucociliary clearance process. Chronic lung diseases, such as COPD, CB, asthma, TB and CF are associated with impaired mucociliary clearance and necrotic death of epithelial and inflammatory cells in the patients' lungs. This leads to bronchiectasis and deposition of thick, stationary, tenacious mucus plaques where heavy colonization of bacteria is evident, due to the availability of a nutrient-rich environment that is optimal for bacterial growth [85–87]. This viscoelastic and adhesive mucus acts as a physical and electrostatic barrier which hinders diffusion of antibiotics. Necrotic cells contribute to the excess release of a network of copolymerized polyanionic contents including DNA, mucin glycoproteins and F-actin which physically bind to polycationic antibiotics, such as tobramycin leading to their deactivation [85,87,88]. Antibiotics delivered locally for treating bacterial infections associated with these diseases needs to penetrate the sputum and distribute evenly. Drugs such as ion-channel modulators or gene therapeutics which need to reach the epithelial layer must first traverse the thick mucus layer to achieve their desired activity [89,90].

1.3 Nose-to-brain delivery: Brain targeting

Intranasally-delivered therapeutics can reach the CNS by three pathways, predominantly the olfactory neural pathway and olfactory epithelial pathway (as seen in Figure 1.2) [91]. The third pathway of delivery is via systemic absorption; however, this requires transport of systemically delivered drug molecule through the BBB to reach the CNS.

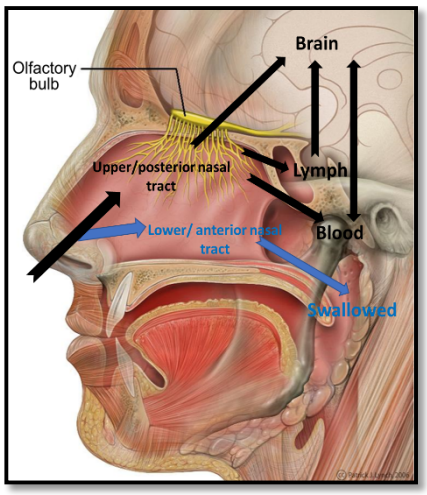

Figure 1.2: Pathways of nose-to-brain delivery

The CNS meets the outside world only at the point of the nose. The olfactory filaments or axons of the 12th cranial nerve 'olfactory nerve' penetrate the nasal mucosa on the roof, i.e. the posterior segment of the nose as seen in Figure 1.3A. Millions of neurons at this point have found usefulness in rapid delivery of medication directly to the CNS in therapeutic concentrations by intracellular, paracellular or transcellular transport as seen in Figure 1.3B. This pathway is referred to as nose-to-brain transport and has been exploited for non-invasive delivery of medicaments in numerous publications, with the first two candidates, namely, oxytocin in Phase II clinical trials for the treatment of autism OPN-300 (OptiNose US Inc.) and monoterpene perillyl alcohol in Phase I/II clinical trials for the treatment of malignant gliomas [92] (http://www.optinose.com).

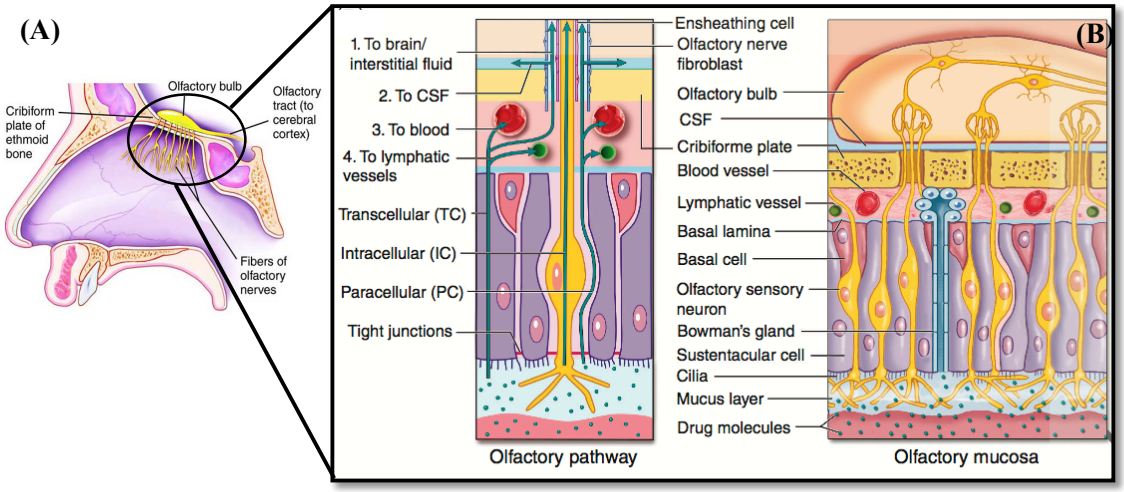

Figure 1.3: (A) Olfactory nerves innervating the nasal mucosa, the site for nose-to-brain delivery; (B) Passage of drug molecules from the nasal olfactory mucosa via the olfactory neurons into the brain. Transport of drug molecules inside the nerve axon can follow a paracellular, intracellular or transcellular pathway [93]

1.3.1 Pre-requisites for nasal inhalation: factors affecting nose-to-brain delivery

Drugs in solution

Although many different types of drugs and nanocarrier systems have shown nose-to-brain delivery efficacy, numerous studies on the direct nose-to-brain transport efficiency related to the physiochemical properties of drugs like molecular weight, logP and logD have been carried out previously, however they have been unsuccessful in identifying a correlation [94–96]. Lee et al. investigated the brain transport of 17 drugs with different physicochemical properties on intranasal administration in rats [94]. On multiple linear regression analysis, no statistically significant correlation for these was determined [94]. This was supported by Kozlovskaya et al. who studied 73 publications in the literature from 1970-2014 on direct nose-to-brain targeting of drugs in solution versus particles or gel based drug delivery systems [95].

However, contrasting findings were presented by Toshiyasu et al. who reported the dependence of lipophilicity, pH partition coefficient (ionized versus unionized form) and molecular weight of the drugs on the bioavailability in the brain on intranasal administration [97–99]. They reported that increasing the lipophilicity of drugs increased the direct transport of sulphonamides [99]. Toshiyasu et al. also reported that an increase in unionization of the drug sulfisomidine caused an increase in drug transport to the CNS by passive diffusion [98]. Furthermore, an increase in the molecular weight of fluorescent dextran increased CNS transport and suggested that drugs up to 20 kDa can successfully transport directly to the cerebrospinal fluid on intranasal delivery, with an inverse correlation between transport and molecular weight [97]. However, on the basis of these contradictory studies, conclusions on the relationship between the physiochemical properties and transport of drugs to the CNS on intranasal delivery cannot be drawn accurately. Receptor-mediated endocytosis of peptides and proteins, and chemically modified drug molecules to enhance carrier-mediated transport through nasal olfactory epithelia has shown promise in the development of CNS therapeutics [93]. The bioavailability of drugs in the brain are dictated by their affinity to efflux transporters at the apical membrane of olfactory epithelium [100]. However, human studies to determine nose-to-brain transport of drug molecules is greatly limited by ethical and practical issues decelerating the development in this field.

Drugs in nanocarriers

To overcome the issues with the passage of drug molecules across the nose to the CNS, re-engineering drug molecules by encapsulating them within nanocarriers have been extensively researched over the past few years. Passage of nanoparticles larger than 20 nm through olfactory epithelial cells has been known to involve the transcellular route [101]. Moreover, by engineering nanoparticles by means surface modification with lectin or coating with chitosan, increased mucoadhesion and hence increased bioavailability of the drugs in the CNS can be achieved. The currently investigated nanocarrier-based systems for nose-to-brain delivery of therapeutics have been outlined with more detail in section 1.4.

1.3.2 Approaches to tackle challenges posed by nose-to-brain delivery

This route poses numerous delivery challenges. Approximately 150 µL-1000 µL of liquid can be administered through the nasal tract without considerable harm to the nasal physiology, and hence nose-to-brain delivery can only be used for delivery of potent molecules [101]. Furthermore, formulations of non-potent drugs can be delivered as a powder to overcome the volume limitation of liquid aerosols [101]. Less than 1% of drug administered intranasally is transported to the brain. This is mainly due to rapid nasal clearance (12-20 min) of administered medication [101].

Hence, techniques to increase the residence of medication in the nose by means of mucoadhesion using chitosan or targeted nanoparticle engineering e.g. lectin-conjugated delivery systems with a higher affinity to the olfactory mucosa have shown promise in previous studies to improve drug bioavailability in the brain on intranasal administration (Table 1.6) [102–105]. Another approach to improve delivery to the brain on intranasal administration of medication is by proper choice of nasal delivery device. The novel breath-powered Bi-Directional™ nasal delivery device developed by OptiNose Inc. has been shown to significantly improve the amount of medication delivered to the brain via the nose [93,106–108]. Other delivery devices developed over the last few years namely the LMA® mucosal atomization device (MAD) and Kurve Inc.'s ViaNase™ have also shown promise to improve CNS bioavailability on intranasal administration, and are considered in detail in section 1.3.4. Focused ultrasound after intranasal delivery (FUS+IN) of microbubbles has been shown to significantly improve CNS delivery in an *in vivo* mice model as compared to the group where focused ultrasound did not follow intranasal microbubble delivery [109,110]. The study of fluorescence intensity of microbubble in the brain on FUS+IN and FUS+IV was not significantly different. Hence, intranasal delivery to the brain could be used as a non-invasive alternative to the invasive IV administration of drugs for neurological disorders [109]. Intranasally administered monoterpene perillyl alcohol, a Ras-protein inhibitor for the treatment of malignant gliomas has been undertaken in clinical trials in Brazil [111]. Phase I/II study on patients with recurrent malignant glioma confirmed the antitumour activity by regression of tumour size, due to tumouristatic effect and signal transduction inhibition effect of perillyl alcohol on intranasal administration, which was well tolerated [111].

1.3.3 Nasal drug delivery devices

Devices for nasal delivery depends on the dosage form of the medicament, proposed indication and patient population; wherein liquid dosage forms mostly aqueous-based systems dominate the market at present. Effective delivery of medicament to the nasal airways and beyond, and hence the use of a suitable nasal drug delivery device is highly dependent on the target site of action i.e. local nasal delivery (nasal decongestants and allergic rhinitis), delivery to the mucosal rich vascular bed of highly permeable capillaries in the respiratory region (migraine, acute pains, seizures, opioid reversal) or the olfactory mucosa and nerves for brain targeting (autism-Phase II trials, malignant gliomas- Phase I/II trials).

Instillation of liquid formulation drops with a pipette/dropper

This is the oldest form of formulation delivery to the nasal tract. Drops are instilled using a glass dropper in a head-down body position and/or extension of the neck to achieve a gravity-driven nasal deposition [2,112]. These can be single-unit pipettes/droppers or multi-unit pipettes. These have however largely been replaced by metered-dose spray pumps [2,112]. The major drawback of this conventional delivery approach is poor compliance especially in patients with rhinosinusitis who experience increased headache with head-down body positions [2,112].

Delivery of liquid formulation with rhinyle catheter or squirt tube/pipette

This involves squirting liquid formulation to the desired area under visual control by a physician by inserting the tip of a fine catheter/micropipette into the nose [2,112]. However, utmost care to prevent contact with sensitive mucosal membranes is necessary and hence self-administration using the squirt tube is not appropriate. Moreover, delivery could also be achieved by breath powered actuation technique using a rhinyle catheter which involves placing one end of the tube in the nostril and the other end in the mouth, wherein, the liquid is dispensed as a liquid drop or jet by blowing into the tube [2,112]. This is currently being used to deliver desmopressin for the treatment of diabetes insipidus and primary nocturnal enuresis [2,112]. However, use of the rhinyle catheter suffers from drawbacks of the variability of dose and cumbersomeness.

Delivery of liquid formulation filled in a squeezed bottle

Mainly used for delivery of OTC nasal decongestants is by squeezing a partially air-filled plastic bottle with a jet outlet which atomizes a certain volume of liquid [2,112]. This device, however, has a high risk of contamination due to sucking back of microorganisms and nasal fluids after formulation instillation, and difficulty in dose control as patient-to-patient pressure variation exists [2,112]. Hence, this device is not recommended to be used for instillation of vasoconstrictors in children.

Delivery of liquid formulation using metered-dose spray pumps

Metered-dose sprays at present dominate the market for the delivery of aqueous liquid solutions, suspensions and emulsions, mainly for topical decongestants, antihistamines and corticosteroids. Simple metered-dose spray pumps disperse medicaments as a spray or mist by a hand operated actuation mechanism involving replacement of emitted liquid with air. For this reason, multi-dose spray pumps require the use of preservatives [2,112]. More sophisticated pump sprays involving compensation of the emitted liquid by compressed gas, use of a collapsible bag, movable piston or aseptic air filter to filter the replacing air have been developed to allow the absence of preservatives [2,112]. However, these systems are more complex and expensive, and hence the traditional metered-dose pump sprays with preservatives are still widely used [2,112]. These devices offer high reproducibility of emitted medicament dose and plume geometry depending on the liquid formulation viscosity and surface tension, pump valve and actuator orifice [2,112].

Delivery of liquid formulation using single-dose devices

These are very valuable as preservative-free medicaments can be delivered if sterile manufacturing has been undertaken. Single-dose devices pose a reduced risk of formulation instability and hence is attractive for delivery of vaccines where aggregation in multi-dose units could cause a reduction in dose-titre [2,112]. The device consists of a vial to hold the unit dose, a piston and a swirl chamber, where the product is sprayed on hand actuation using a pressure point mechanism. Currently, marketed influenza vaccine FluMist, zolmitriptan Zomig® nasal spray and sumatriptan Imitrex® nasal spray for migraine are delivered using such single dose nasal devices [2,112].

Delivery of liquid formulation using Nasal pMDIs

Since the ban on use of CFC propellants due to ozone depletion, nasal and pulmonary pMDIs have been withdrawn from the market. Lately, however, hydrofluoroalkane-based pMDIs have been developed, like for the delivery of beclometasone dipropionate for local allergic rhinitis [2,112].

1.3.4 Nose-to-brain drug delivery devices

Although the nostril in the anterior position is only a few cm away from the olfactory epithelium, the complex labyrinth of passages ending into the slit-like olfactory cleft behind the narrow nasal valve, greatly limits the passage of medicament instilled within the nostril to the posterior region of the nose [93]. Hence traditional techniques are inadequate to deliver medicaments for nose-to-brain delivery. Specialized devices for nose-to-brain delivery of medicaments have evolved from the traditional nasal drug delivery devices.

Delivery of blue food dye with traditional nasal delivery devices e.g. pipette/dropper, spray and squirt tube was studied by Scheibe et al. [113]. Delivery using a pipette/dropper showed deposition following forces of gravity and mucociliary clearance, largely in the anterior nasal floor and nasopharynx [113]. Delivery using the nasal spray (Sprayer) evenly distributed the food dye in the nose, however, distribution was intercepted by the middle turbinate and hence did not effectively reach the olfactory cleft [113]. Other studies by means of gamma camera scanning, radiographic CT scanning, endoscopic evaluation and fluorescence dye studies on delivery using nasal sprays in healthy human volunteers have confirmed that these devices largely deposit medication to the anterior part of the nose [113–117]. Moreover, inability to reach the olfactory region using a squeeze bottle was demonstrated in a study to deposit fluorescein, evaluated by endoscopy, wherein, major deposition was seen on the septum and the inferior turbinate [118]. Using a squirt tube to deliver the drug directly into the posterior nose after decongestion by a trained physician showed olfactory epithelium deposition in most of the patients. These studies demonstrated the importance of the nasal delivery device characteristics on the area of deposition [113]. This has been confirmed by computational fluid dynamics in an MRI-based nasal airway model that has revealed that olfactory epithelium deposition is most likely when delivering

medicaments by deep nasal intubation [119]. However, use of a squirt tube/deep intubation is not a feasible technique for routine delivery of medicament at home. Hence, as delivery using traditional nasal devices is sub-optimal, alternative delivery devices to target the nasal olfactory epithelium and hence the CNS is necessary.

Powered nebulizers and atomizers

Nasal nebulizing devices use ultrasonic power, mechanical power or compressed gases (air, oxygen or nitrogen) to produce fine aerosols of liquids or suspensions. The speed of the droplets emitted from the aerosol and the aerosol droplet size (around 6 μm) has been shown to be advantageous in nebulizing an increased dose of medicament to the paranasal sinuses as compared to conventional spray nebulizers [93,112,120].

The vibrENT™ pulsating membrane nebulizer (PARI Pharma GmbH) and Aeroneb Solo® nebulizer (Aerogen, Ireland) have been routinely used in nasal delivery for treatment of chronic rhinosinusitis, the target site being the upper posterior parts of the nose. These are similar to the standard pulmonary nebulizers fitted with a nostril adapter to deliver medicament to nasal sinuses. Hence, these delivery systems can be exploited for studies where nose-to-brain targeting is intended [93,112].

Nasal atomizers are handheld battery-driven devices or highly pressurized compressed gas based systems. The Controlled Particle Dispersion® ViaNase™ atomizer (Kurve Technology Inc., USA) has been used in pre-clinical studies to administer insulin intranasally to patients with early Alzheimer's disease. The ViaNase™ is capable of generating aerosols with a narrow droplet size distributions from 3-50 μm, which can be further customized to achieve varied droplet trajectories and aerosol flow velocity; hence this device is capable of aerosolization of liquids and suspensions with varied surface tension and viscosities [93,112]. Insulin delivered using the ViaNase™ has been shown to improve memory, verbal information, attention and increased plasma beta-amyloid peptide 40 [121,122]. However, it was proposed that nasal inhalation of insulin using this device may cause significant lung deposition which could cause airway irritation and reduction in pulmonary function, as seen previously with the administration of Exubera® i.e. inhaled insulin [121,122]. Hence, longer trials of intranasal insulin therapy are necessary. Gamma camera imaging has confirmed that the ViaNase™ atomizer can target the upper roof of the nose and sinuses and hence is attractive for nose-to-brain delivery. MRI studies (Figure 1.4) have confirmed the use of ViaNase™ to saturate the nasal cavity, with distribution of ^{99m}technetium reaching the olfactory regions and sinuses was evident [121,122].

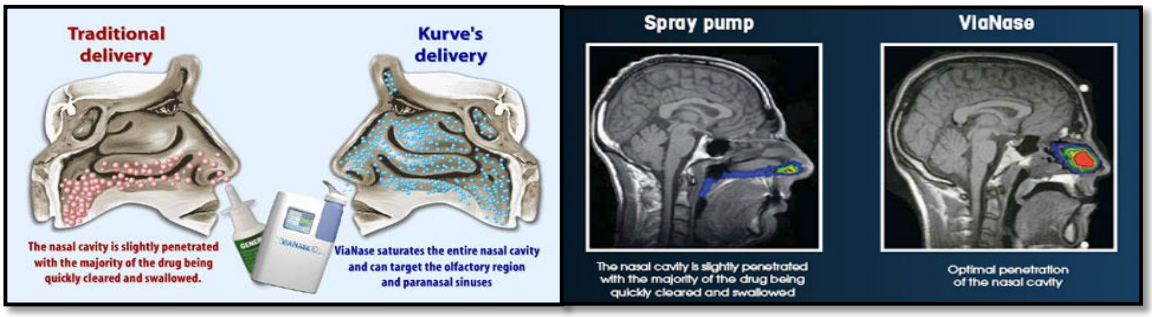

Figure 1.4: Intranasal delivery using Kurve Inc.'s ViaNase™ to target the olfactory region (left:http://www.medgadget.com/2007/06/vianase_devices_and_vortical_flow_technology_will_make_your_nose_go_round.html, right: http://www.kurvetech.com/TechnologyGamma.asp)

The use of a nitrogen-driven atomizer i.e. the Precision Olfactory Delivery™ device (POD™, Impel NeuroPharma) was intended to deliver medicament to the brain via the nose due to the narrow plume produced by the device that is directed towards the posterior nasal valve. The first human study evidence of nose-to-brain delivery was announced by Impel NeuroPharma Inc., wherein a significant increase in deposition of radiolabelled tripeptide i.e. 68.3% versus 31.7% (for conventional nasal pump) in the olfactory regions was evident by SPECT (Single-photon emission computed tomography) imaging in seven healthy volunteers (Figure 1.5), which might be attractive for brain targeting [93,123,124]. However, the reports this far are in the form of press release and poster presented at the American Association of Pharmaceutical Scientists conference, and peer-reviewed detail of trials are yet to be published.

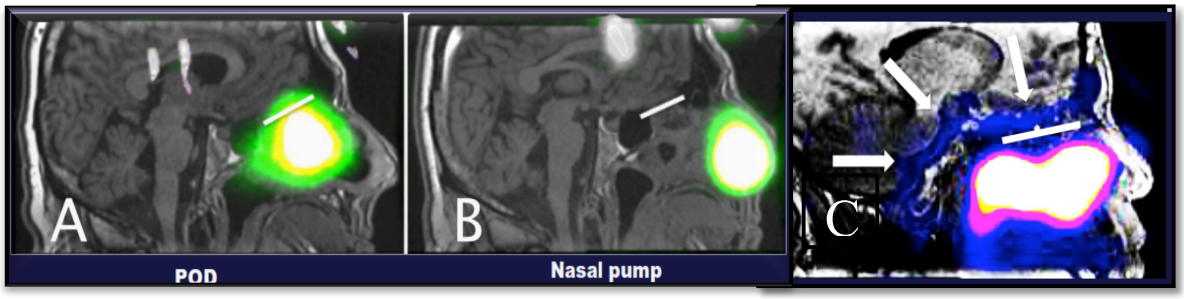

Figure 1.5: 2D SPECT image showing deposition of radiolabelled tripeptide using Impel Inc.'s Precision Olfactory Delivery (POD) device (A) versus traditional nasal pump (B). Cribriform plate that is where the nasal cavity meets the CNS is denoted by a white bar. (C) 3D SPECT image showing deposition in the olfactory bulb and cerebellum/brainstem (marked by arrows) indicating direct nose-to-brain delivery [123,124]

Breath-powered™ Bi-Directional™ technology

To overcome the medicament access problem due to complex anatomy and physiology of the airways, exploitation of natural functional aspects of the airways was undertaken to develop a novel breath-powered Bi-Directional™ nasal delivery device (OptiNose, USA, Figure 1.6) [93,112]. This device delivers medicament precisely to the upper deeper parts of the nose, by isolating the nasal tract from the rest of the respiratory system due to exhaling from the mouth into the mouthpiece of the device during nasal inhalation as seen in Figure 1.6A [93,112]. This leads to a higher oropharyngeal pressure by elevation of the soft palate and hence medicament is delivered to the upper nasal tract [93,112]. This technology has been adapted to deliver both

powder and liquid formulations, and a special nose-to-brain delivery device has also been developed by slight modification [93]. The device consists of a flexible mouthpiece that is breath powered and an optimized conical shaped sealing nosepiece that when inserted forms a mechanical seal with the flexible soft tissue at the nostril opening and expands the narrow slit of the nasal triangular valve [93,112]. The nose-to-brain variant of the device contains an elongated nosepiece tip to enable better insertion into the nostril opening [93]. This technology involves exhalation of warm and humidified air into the mouthpiece when the device is in position. This air carries the medicament posteriorly along the nasal septum and then exits through the opposite nostril after passing around the nasal septum (Bi-directional™ technology) [93,112]. The liquid variant of this device requires manual triggering during actuation by pressing on a bottle to open the valve to dispense the medicament.

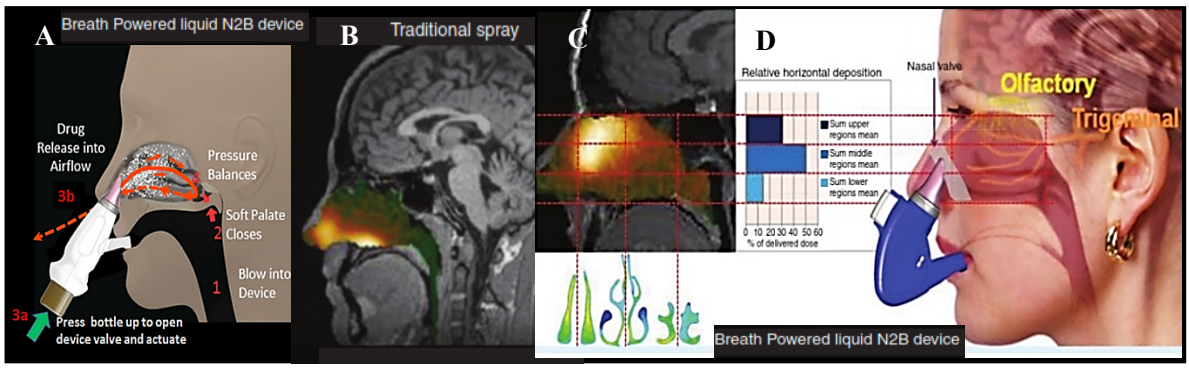

Figure 1.6: Breath-Powered™ Bi-Directional™ nose-to-brain device variant. (A) Lateral view of the nasal passages explaining the working principle of the breath-powered device; Gamma camera images superimposed using (B) traditional spray and (C) Breath-powered nose-to-brain variant device; (D) Deposition profile using the nose-to-brain variant device in seven healthy human volunteers [92,93,112]**.**

Unpublished data from OptiNose Inc. has reported that the nose-to-brain variant (Figure 1.6D) can successfully achieve higher deposition compared to the Breath-Powered™ Bi-Directional™ liquid device, which are superior to the traditional spray devices, with around 30% being deposited in the upper one-third of the nose at the olfactory mucosa and 60% in the upper two-thirds, where olfactory nerve filaments are found (Figure 1.6D) [93]. Numerous human evidence and clinical studies indicating the superiority of the breath-powered devices over conventional nasal devices for delivery to the upper and middle posterior regions of the nose have been previously published [92,107,125–127]. Delivery of oxytocin using the Breath-Powered™ Bi-Directional™ nose-to-brain variant device is currently in Phase II clinical trials for the treatment of autism spectrum disorders. Previous reports from the double-blind crossover trial studies in healthy human volunteers validated the use of the breath-powered device for targeting to the brain and significantly improving social cognition as compared to IV oxytocin [92].

Mucosal Atomization Device (MAD)

The Intranasal Mucosal Atomization Device™ (Nasal™ MAD, Figure 1.7) consists of a spray tip nosepiece that can be screwed onto a syringe with a leur lock. It is an easy to use device suitable

for self-administration and for administration to patients where IV access is difficult, allowing delivery of consistent amounts of medicament to the nasal mucosal surfaces.

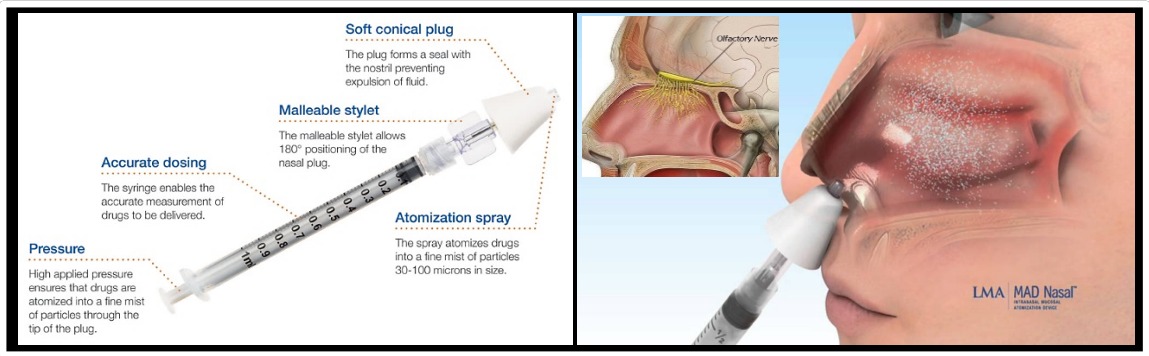

Figure 1.7: Atomized MAD Nasal™ delivering medicament to the upper posterior nasal tract towards the olfactory mucosa (http://www.lmaco.com/products/lma-mad-nasal)

It has a simple design consisting of a syringe for accurate dosing, which locks by means of a stylet into a soft conical plug that forms a seal with the nostril to prevent fluid expulsion during atomization as seen in Figure 1.7 [121]. The soft conical plug houses an atomization spray that delivers the formulation as a fine mist of aerosol droplets, in the size range of 30-100 µm on application of high pressure to the syringe plunger [121]. For efficient delivery to the posterior nasal tract, a median particle size of 30-120 µm is considered appropriate [128]. Hence, this device was used to study the aerosol droplet size of the Kolliphor® micelles formulated for nose-to-brain delivery of neuroprotective molecules and cancer chemotherapeutics (Chapter 5).

Numerous studies have highlighted that use of intranasal fentanyl opioid for paediatric acute long-bone fractures, paediatric severe painful sickle cell crises, paediatric and adult analgesia, paediatric orthopaedic trauma using the MAD Nasal™ is superior to IV/IM fentanyl/morphine, with a significant decrease in time to achieve analgesia and a reduction in pain scales/scores, hence, better pain relief especially in emergency departments [129–133]. Moreover, intranasal delivery of the antiseizure drug midazolam delivered using the MAD Nasal™ as compared to rectal/IV diazepam resulted in better seizure control in a shorter time with fewer respiratory complications and fewer hospital admissions in prehospital setups, along with better social acceptance, administration feasibility, and ease of use by caregivers [134–136]. This was concluded to be largely due to two mechanisms, one being increased absorption through the highly vascularized absorptive surface of the nasal mucosa and the drug being absorbed into the cerebrospinal fluid via the olfactory epithelium of the nasal mucosa [136]. Intranasal administration of naloxone using MAD Nasal™ during opioid overdose has been shown to prevent death due to an ease of administration using the intranasal device as compared to the other routes of administration namely IV/IM [137].

1.3.5 Central Nervous System disorders

CNS disorders encompassing neurodegenerative diseases and neuroblastoma have increasingly prevailed over the past few years, being one of the toughest economic and medical conditions to treat at present, causing considerable strain to the society and an emotional burden on patients and caregivers [138,139].

1.3.5.1 Neurodegenerative diseases

Neurodegeneration is the degeneration of the neurons in the brain and is progressive and incurable. Neurodegeneration is characterized by loss of neuronal cells, progressive cognitive decline, alterations in the motor behavior and sensory processes of patients leading to gait disturbances, postural instability and dementia [138–140]. This occurs mostly due to increased oxidative stress, mitochondrial dysfunction, and deposition of senile plaques of β-amyloid peptide and Lewy bodies [138–140]. The aging population suffers from neurodegenerative disorders like Alzheimer's and Parkinson's diseases, which are among the top 10 causes of death and disability in developed countries at present, as per the WHO [141]. Medication only improves the quality of life marginally since these pharmacological treatments do not halt the progression of the disease or address the underlying pathology, but only provide temporary symptomatic relief [138].

Alzheimer's disease (AD)

AD is the leading cause of dementia in aged people accounting for more than half the cases of dementia worldwide. Approximately 5 million people in the USA over the age of 65 have AD and this is expected to increase by 2050, wherein one million new cases are expected to develop every year i.e. one new case every 33 seconds [142]. The pathology of AD consists of different types of lesions: (1) senile plaques consisting primarily of extracellular amyloid protein deposits leading to cerebral amyloid angiopathy, (2) intracellular neurofibrillary tangles composed of hyperphosphorylated tau protein helical filaments and (3) cortical atrophy which leads to loss of cholinergic inputs [138,139,142]. There are neither diagnostic tests nor curative therapeutic treatments for AD. Present pharmacological agents serve to replace lost neurotransmitters in the CNS, consequently alleviating AD symptoms and slowing down disease progression [138,139,142]. The US FDA-approved treatments for improving cognitive manifestations in mild to moderate AD are limited to 5 drugs belonging to the class acetylcholinesterase inhibitors, i.e. rivastigmine (Exelon), donepezil (Aricept), galantamine (Razadyne, Reminyl), tacrine (Cognex) and NMDA receptor antagonist memantine (Namenda) [142]. Beyond the moderate level of AD progression, considerable loss of neurons and synapses causes patients to become unresponsive to treatment [139]. It is essential that research on discovering disease-modifying therapies targeting molecular pathway of neurodegeneration is undertaken as at present at least half of the patients are unresponsive to the current treatments [142].

Parkinson's disease (PD)

PD, the second most common neurodegenerative disorder, is characterized by loss of midbrain dopaminergic neurons in the substantia nigra pars compacta of the brain leading to aggregation of α-synuclein protein and ubiquitin i.e. Lewy bodies and Lewy neurites, and is an age-related disease [138,139,143,144]. Progressive tremor, rigidity/stiffness of limbs and trunk, bradykinesia and dementia are associated with PD due to dopamine deficiency especially evident in later stages of the disease. It is believed to advance over many years due to an interplay between environmental and genetic familial inheritance by initiation of neurotoxic factors because of inflammatory responses caused by immune activation of neuroglia. [138,139,143,144] Treatment involves an increase of dopamine in the brain by administration of L-DOPA, i.e. a metabolic precursor of dopamine, and a DOPA decarboxylase inhibitor carbidopa to increase the bioavailability of dopamine in the brain [139]. However, administered orally these drugs have a very limited bioavailability of approximately 1% in the brain and long-term treatment results in tolerance to drug and symptom resurgence [139]. There is no proper test for disease diagnosis and current pharmacological treatments only help in alleviating clinical symptoms for a short time, however, dopaminergic neuronal degeneration in the midbrain ensues [139,145]. Hence, research on treatments directed towards interfering with signaling pathways impeding the progression of consequent neuronal death is to be undertaken [145].

1.3.5.2 Brain Cancer

Prognosis of malignant gliomas accounting for approximately 80% of malignant primary brain tumour has been extremely poor due to therapeutic resistance and tumour reoccurrence [146]. Moreover, treatment is particularly challenging due to the limited permeability of most cancer drugs, like methotrexate and carboplatin through the blood-brain barrier (BBB) [139,147]. Most prominent subclass of malignant gliomas namely anaplastic gliomas (WHO III, median survival 12-15 months) and glioblastomas (WHO IV, median survival 2-5 years) are essentially incurable, hence research of novel treatment strategies are essential [138,146,148]. Other types of brain tumours have diverse etiology affecting different parts of the brain parenchyma from the intracranial tissues to the meninges; treatment and prognosis of these can be quite varied and hence challenging.

Modern pharmacological treatment modalities only provide symptomatic relief to patients marginally improving the quality of life and do not halt or reverse disease progression [138]. Moreover, lack of knowledge on the complex mechanisms involving neurological diseases is the greatest limitation to the development of efficacious treatment [138].

1.3.5.3 Barriers to effective neurological disorder therapy

Blood-brain barrier (BBB)

Pharmacologically treatment of CNS disorders like AD, PD, schizophrenia, brain tumour and meningitis faces a substantial challenge due to the presence of an interfacial structure i.e. blood-

brain barrier (BBB) which thwarts the entry of drugs into the brain and acts as a bottleneck to the development of neurotherapeutics. The BBB majorly consists of the brain capillary endothelial cells (BCECs) (Figure 1.8) which are connected with continuous tight junctions that acts like a zip resulting in a high transendothelial electrical resistance (TEER, 1500-2000 Ω cm^2) as compared to the TEER of other tissues like skin, lungs, bladder and colon (3-33 Ω cm^2). This physical barrier along with high electrical resistance prevents the paracellular and passive diffusion of molecules from the blood into the brain interstitial fluid with almost 100% macromolecules and 98% of small molecules unable to reach the CNS depending on their charge and lipid solubility [149]. Certain membrane transporters present on the BBB helps uptake, efflux, and exchange of necessary nutrients like glucose and amino acids, and waste/toxin removal [150]. Passage of chemotherapeutics through the BBB is highly restricted due to their hydrophobic nature, hydrogen bonds and size. Hydrophobic molecules like caffeine and ethanol can penetrate the CNS easily, however, hydrophilic molecules are severely limited by passage through the BBB [93]. To permeate through the BBB drug molecules must have greater lipophilicity, less positive charge and hydrogen bond donors, and size less than 400 Da [151]. Drugs with a molecular weight lower than 20 kDa, lipid soluble with less than 8 hydrogen bonds and unionized can readily pass the BBB to reach the CNS [24, 139]

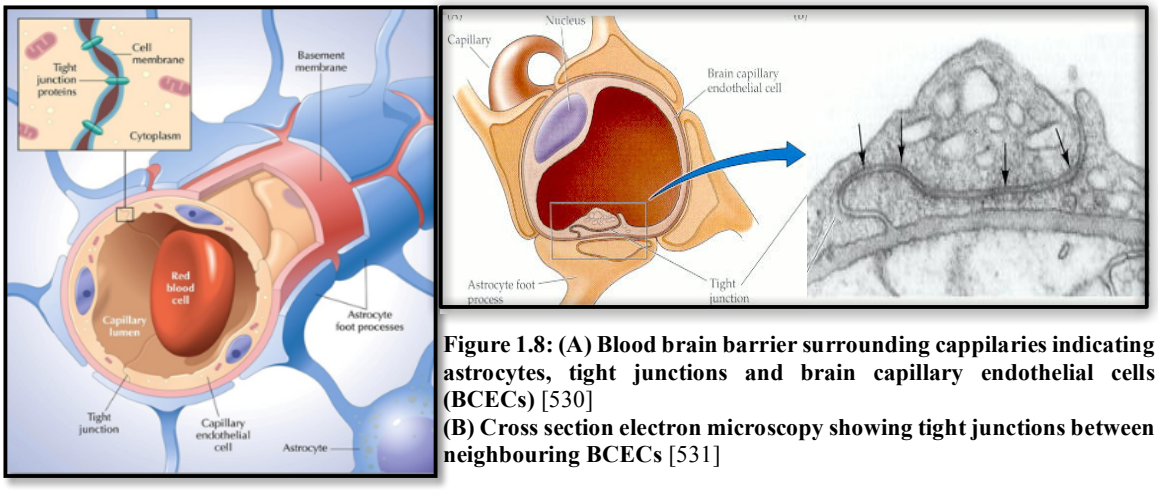

Figure 1.8: (A) Blood brain barrier surrounding cappilaries indicating astrocytes, tight junctions and brain capillary endothelial cells (BCECs) [530]
(B) Cross section electron microscopy showing tight junctions between neighbouring BCECs [531]

Blood-brain tumour barrier (BBTB)

In advanced brain tumours, drug distribution is highly restricted due to the BBTB, which exhibits a smaller pore size and overexpresses several drug efflux pumps resulting in a considerably lower concentration of chemotherapeutic agent inside the tumour than that seen in peripheral tumours, hence making treatment even more challenging [149]. With advanced brain tumours reduction in transvascular exchange of drug molecules take place due to reducing vascular surface area with increasing tumour size, leading to greater diffusional distance and depth into neoplastic cells [152]. Moreover, an increase in hydrostatic pressure in the brain parenchyma due to high tumour interstitial pressure and peri-tumoural edema is evident leading to a furthermore reduction in permeability of drugs into the neoplastic microvasculature [152]. Conventional cancer

chemotherapeutics like doxorubicin, paclitaxel, methotrexate, cisplatin and carmustin, do not cross the BBB and hence recurrence of fatal gliomas are very common [147].

Significant research has been conducted on ways to enhance drug bioavailability in the brain by means of circumventing the formidable barriers BBB and BBTB by invasive and non-invasive techniques.

Overcoming the BBB

Complex strategies have been employed to improve the bioavailability of drugs in the CNS to treat neurological disorders. The most common approach in clinical use to deliver the drug to brain lesions involves invasive administration directly into the brain by means of intrathecal or intra-arterial injections, however, these are impractical and unattractive particularly for neurological disorders requiring frequent dosing [151]. An increased systemic dose of cancer chemotherapeutic drug is administered to improve brain bioavailability, however, significant systemic drug toxicity is associated with this approach [151].

Another common approach involves transient disruption of the BBB by means of osmosis using hypertonic solutions like mannitol, ultrasound, focussed ultrasound, chemical agents like perrilyl alcohol or synthetic analog of bradykinin RMP-7 that has known to disrupt tight junctions of the BBB (studied in clinical trials), all followed by administration of chemotherapy [151]. The invasive procedure of osmotically opening the BBB has been shown to improve the tumour bioavailability of cancer chemotherapeutics from 10 to 100-fold, however, an increased risk of seizure and post-treatment neurological damage, for example, ubiquitinated neurons and deposited plaques in neuronal gap junctions and astrocytes have been associated with this invasive technique due to long treatment course [139]. Focused ultrasound a new frontier for opening the BBB has been studied at clinical set ups in the USA and its development is underway. This technique shows promise in controlling chemotherapeutic delivery to the affected part in the brain and is less invasive than other BBB opening techniques [139,153]. However, pre-clinical studies have not ruled out the prevalence of post-treatment injury and consequently permanent brain damage [139].

Nose-to-brain delivery is a non-invasive means of circumventing the BBB. This delivery approach overcomes the conventional delivery limitations and delivers drug to the CNS at therapeutic concentrations and early onset, however, it is a long way to go with only the first two candidates namely oxytocin and monoterpene perillyl alcohol in Phase II and Phase I/II clinical trials for treatment of autism and malignant gliomas respectively.

1.4 Nanotechnology for delivery of drugs to the airways

1.4.1 Choice of drug delivery systems

Researchers have made great advances in engineering new nanotechnology-based carrier systems for different airways applications. The choice of the delivery system largely depends on factors such as:

Site specificity

For different disease conditions, varied formulations are required to transport the drug to the particular site of action and impart desired pharmacological effect. Delivery of water-insoluble drugs and highly unstable drug molecules may be achieved by loading them into nanometric systems delivered directly to the site intended. Systemic delivery of insulin for the treatment of Diabetes Mellitus, dry powder microparticles have been marketed as Exubera® (Pfizer; now withdrawn) and Afrezza™ (*MannKind)* which is a Technosphere™-based inhaled insulin product. Both of these need to be deposited in the alveoli and hence require an optimized delivery device [154–156]. Moreover, local administration of antitubercular drugs needs a delivery system which not only transports the drug to the alveolar macrophages but also has the capacity of being endocytosed by these macrophages [154]. On the other hand, endocytosis of β-agonists leads to their inactivation and clearance leading to loss of efficacy, hence formulations with minimal macrophage uptake properties would be needed for such drugs [154]. Delivery of nanoparticles encapsulating antibiotics to the lung for treatment of infections associated with CF, COPD, pulmonary TB or pneumonia can present a great challenge due to the thick viscoelastic mucus barrier in the lung. To traverse this barrier, nanoparticles must have a small size and should ideally be designed with a muco-inert surface so as to prevent their adhesion to mucin fibers which are highly prevalent and pose as a severe hurdle to the delivery of antibiotics to the site of infection in these disease conditions [157].

Retainment of pharmacological effect

The formulation and preparation of the delivery system should not affect the pharmacological activity of the drug. The release profile of the drug should be optimized to achieve maximum drug efficacy and duration of activity [156].

Fate of delivery system

This important criterion needs careful consideration for inhaled nanoparticles. Varied delivery system engineering parameters, such as shape, size, materials, aggregation state, surface charge, chemical properties and formulation, may affect the toxicity profiles [158]. The small size of these new delivery systems imparts them with new physical and chemical properties different from conventional bulk drug powders [159]. It has been observed that multi-walled carbon-nanotube-

based delivery systems have the capacity to collect in the subpleural regions of the lung, leading to pulmonary fibrosis, multifocal granulomatous inflammation, diffuse histiocytic and neutrophilic inflammation and intra-alveolar lipoproteinosis [158,160]. Inhaled nanoparticles can not only cause inflammation and other exacerbations but may also interfere with the functioning of the pulmonary system. Nanoparticles fabricated of polystyrene, gold or titanium dioxide have been reported to alter the function and structure of pulmonary surfactant and hence impede its ability to decrease surface tension rapidly during a normal breathing cycle [161]. Hence, use of natural surfactants to fabricate these delivery systems would be more attractive as it would minimize the risk of interfering with natural airway functions. Clearance of nanoparticles in the alveolar region is mediated by alveolar macrophages. These recognize nanoparticles, phagocytize them, travel to the mucociliary escalator and are cleared. However, this process is very slow and the retention half-life of solid insoluble particles deposited in the alveolar region of humans can be up to 700 days. Moreover, larger particles are not easily phagocytized nor are ultrafine nanoparticles [162].

Delivery of drugs to the brain through the nasal olfactory mucosa faces substantial challenges like low bioavailability for polar drugs especially proteins and peptides which have a high molecular weight necessitating the use of transnasal absorption enhancers. Moreover, properties of the drug and the formulations like tonicity (iso, hyper or hypo), pH, temperature and viscosity alter the nasal tract mucociliary clearance and hence affect the clearance of the drugs. In general, a dominant mucociliary clearance for non-bioadhesive formulations delivered to the nose having a shelf-life of 12-20 min has been reported in earlier studies [163,164]. It is important to bear in mind the choice of material used to deliver drugs to the brain as it might be a precursor to neurological diseases. Inhaled ferrous oxide nanoparticles have been shown to predominantly deposit in the olfactory bulb, brainstem, and hippocampus and cause potential neurotoxicity [165]. Hence, the fate of the delivery system should be viewed with utmost importance during formulation development to ensure that maximum dosage reaches the intended site of action without affecting the normal functioning of the airways.

The various delivery systems which can be used to deliver medicaments to the desired site are:

1.4.2 Liposomes

Liposomes are lipid-based carrier systems which have been widely used as drug carriers for cosmeceutical and pharmaceutical applications [166,167]. Liposomes are self-assembling structures which due to intrinsic interfacial properties imparted by the phospholipids spontaneously form spherical vesicles in aqueous media. These vesicles are made up of one or more concentric phospholipid bilayers alternating with aqueous compartments [168]. Hydrophobic and amphiphilic drugs can be incorporated within the lipid bilayers, whereas, hydrophilic drugs can be encapsulated in the aqueous compartments/core. They are safe, non-toxic, biodegradable, biocompatible delivery systems for encapsulation of a wide range of drugs

having varied properties, including molecular size, charge and hydrophobicity. They interact with living cells by adsorption, endocytosis, lipid exchange and/or fusion [167,169,170].

Liposomes can be divided into categories based on their size and lamellarity; namely small unilamellar vesicles (SUV), large unilamellar vesicles (LUV) and multilamellar vesicles (MLV), or on the basis of their properties, for instance immuno-liposomes, stealth liposomes, proteoliposomes, pH-sensitive liposomes and charged liposomes [167,169,171]. Liposomes can be prepared using a number of techniques, the most frequently used of which is the thin-film method, reverse-phase evaporation, solvent injection, freeze-thaw extrusion and ultrasonication [171].

Liposome delivery to the pulmonary airways

These are an attractive delivery system to the lungs as they can be made of surfactants which are endogenous to the pulmonary tract. The first pulmonary-delivered liposomal product being Alveofact® (LyomarkPharma), instilled to the lung for treatment of respiratory distress syndrome. Deposition of liposomes, aerosolized with jet nebulizers, into the non-ciliated peripheral regions of the lung results in prolonged retention of the liposome-associated drug within the lung [172,173]. Cationic liposomes have been successful in the aerosol delivery of gene therapy [162,174,175], while liposomes conjugated with cell-penetrating peptides can act as potential carriers of macromolecules [162]. Modification of the liposome surface with O-stearyl amylopectin has been shown to increase lung tissue affinity [167], while conjugation of liposomes with octaargine or antennapedia enhanced cellular uptake in the airway cells [162]. Conjugating mannose to liposomes produces superior macrophage uptake to non-conjugated liposomes, with potential application in the treatment of diseases such as rheumatoid arthritis, TB and leishmaniasis, where the macrophages play a very important role in the disease progression [176,177].

Stability of the vesicles, vesicle delivery and the size of the aerosol cloud are major considerations when atomizing liposomes using nebulizers, and are functions of both formulation properties and the nebulizer system employed. The relationship between nebulizer performance and formulation development requires in-depth knowledge of formulation properties like lipid concentration, bilayer composition, bilayer rigidity; and the working principles of the various nebulizer types [172,178–180]. An attractive approach would be to deliver liposomes by DPIs produced by spray drying the liposomes and relying on their hydration in situ on delivery in the airways [181,182]. This could be advantageous as liposomal rupture and drug loss during aerosolization would not affect the drug dosage and hence treatment outcome, which is of major concern during nebulization of liposomal formulations.

The properties of liposomes can be easily manipulated and a variety of drugs can be incorporated within them. By encapsulating antimicrobials into liposomes, improved delivery may be achieved, for instance by targeting macrophages where infections reside, or due to their small size

they can pass through biofilms and reach peripheral sites for complete bacterial eradication [169,183]. Rifampicin, an antimycobacterial drug used for TB treatment shows a very high rate of hepatotoxicity and nephrotoxicity, along with other side effects, including thrombocytopenia, immune haemolytic anaemia and intravascular haemolysis, due to its high metabolism in these organs leading to idiosyncratic metabolites which are toxic to these organs on oral delivery [184–188]. Encapsulation of rifampicin into pulmonary-delivered liposomes improves its toxicity profile and reduces hepatotoxicity [189–191].

Liposome delivery to the nasal airways

For intranasal delivery to the brain cationic liposomal formulations encapsulating fluorescent protein showed approximately 10-fold higher retention in the brain and prolonged drug effect, assumed to be due to higher residence of liposomes in the nose due to attraction between the cationic liposomes and anionic sialic acid in nasal mucus and increased lipophilicity of protein formulation, hence leading to higher transport across the olfactory mucosa [192]. Many more reports on improved delivery of antioxidants, acetylcholinesterase inhibitors and other neuroprotective peptides encapsulated within liposomes for treatment of neurodegeneration have shown promise due to improved drug bioavailability in the brain due to effective brain targeting [193–197].

Various liposomal systems for delivery to the airways of antimicrobials and neuroprotective molecules have been described in the literature, a few of which have reached clinical trials, as summarized in Table 1.5 and Table 1.6.

Table 1.5: Liposomal therapies under investigation for antimicrobial delivery

Antimicrobial	Effective against	Treatment outcome(s)
Amikacin Aminoglycoside DPPC: Chol liposome ARIKAYCE™ Clinical trials phase III [198]	*Pseudomonas aeruginosa* (Inhalation-nebulization)	Comparison of Arikayce™ versus placebo nebulized to the lungs showed beneficial results as liposomal amikacin had susceptibility to cross mucus and biofilm present in patients suffering from CF, hence a sustained and significant improvement in lung function and reduction of pseudomonas density was obtained
Amikacin Aminoglycoside HSPC: Chol: DSPG (2:1:0.1) MiKasome® (NeXstar Pharmaceuticals, Inc) [199–201]	*Mycobacterium tuberculosis* (Intratracheal administration)	Increased uptake by the mononuclear phagocyte system showed benefits especially for multi-drug resistant *M. avium*, wherein, increased killing was evident versus free amikacin which fails to reach high intracellular levels
Tobramycin Aminoglycoside Fluidosomes (Axentis Pharma) Clinical Trial II [167,202]	*Pseudomonas aeruginosa* *Escherichia coli* *Staphylococcus aureus* (Intratracheal administration)	Improved management of pulmonary infections was seen on intratracheal administration of fluid-based liposomes encapsulated tobramycin
Amphotericin B Antifungal AmBisome® (AMBINEB) (PETHEMA foundation) Clinical Trial II [203–205]	*Aspergillosis* (Inhalation-nebulization)	Amphotericin B encapsulated liposomes nebulized as prophylaxis to 768 high-risk patients displayed an overall significantly lower incidence of invasive pulmonary aspergillosis and reduced systemic exposure
Amphotericin B Antifungal Inhalation Powder (ABIP) DSPC spray dried powder (Nektar Pharmaceuticals) [206,207]	*Aspergillosis* (Inhalation-DPI)	Minimal systemic amphotericin B was observed on inhalation of dry powders containing high doses of amphotericin B up to 25 mg in clinical human studies (amphotericin B dose 50% w/w of dry powder)
Rifampicin+ isoniazid DPPC: Chol Passively targeted [208,209]	*Mycobacterium tuberculosis* (Inhalation)	Increased therapeutic drug level found in the plasma on inhalation of a single dose in guinea pigs Drugs found to localize in the alveolar macrophages of the lungs

Table 1.5: Liposomal therapies under investigation for pulmonary delivery (continued)

Antimicrobial	Effective against	Treatment outcome(s)
Rifampicin+ isoniazid DPPC: Chol: O-stearylamylopectin: DCP: DSPC-PEG 2K Actively targeted [189,208,210]	*Mycobacterium tuberculosis* (Intravenous)	Superior efficacy of the formulations against *M. tuberculosis* with a reduction in mycobacterial colony forming units in liver, kidney and lungs. Reduction in nephrotoxicity associated with the free drug and normal lung morphology observed
Rifampicin Egg PC: Chol: O-stearyl amylopectin: DCP or Actively targeted [208,211]	*Mycobacterium tuberculosis* (Inhalation-nebulization)	The targeted liposomes showed improved lung accumulation specifically improved alveolar macrophage uptake and accumulation showing the feasibility of the inhalation for eradication of *M. tuberculosis*
No drug specified HSPC: Chol: DCP: MAN Actively targeted [208,212,213]	- (Intratracheal aerosolization MicroSprayer™)	Significantly higher internalization and selective targeting to alveolar macrophages *in vivo* with the mannose-linked liposomes compared to non-targeted liposomes
Ciprofloxacin-Fluoroquinolone or Azithromycin-Macrolide DSPG: Chol [169,214]	*Mycobacterium avium* (*In vitro* J774 cells)	43-fold greater potency was seen against *M.avium* compared to free ciprofloxacin due to increased negative charge imparted by the liposomal formulation

CF- cystic fibrosis, TB- tuberculosis, DSPG- distearoyl phosphatidylglycerol, DCP- dicetylphosphate, HSPC- hydrogenated soy phosphatidylcholine, Egg PC- egg phosphatidylcholine, EC- dioleoylethyl phosphatidylcholine, DOPC-dioleoyl phosphatidylcholine, DSPC- distearoyl phosphatidylcholine, Chol- cholesterol, MAN- mannose

Table 1.6: Liposomal therapies under investigation for nose-to-brain delivery

Drugs	Effective against	Treatment outcome(s)
H102 Peptide EPC: DSPE-PEG 2K: Chol [196]	Alzheimer's disease	IN administered liposomes encapsulating peptide showed higher brain absorption as compared to IN delivered H102 solution Spatial memory impairment was ameliorated in AD model rats
Rivastigmine Acetylcholinesterase inhibitor Soy lecithin: Chol [195]	Alzheimer's disease	Significantly higher concentration of rivastigmine (brain C_{max} 0.98 µg/mL) was observed in the brain along with sustained release of drug from liposomes when compared to IN (brain C_{max} 0.33 µg/mL) or orally (brain C_{max} 0.17 µg/mL) administered rivastigmine
Donepezil Acetylcholinesterase inhibitor DSPC: Chol: PEG [215]	Alzheimer's disease	Significantly higher concentration of donepezil (brain C_{max} 0.22 µg/mL) was observed in the brain from intranasally administered liposomes when compared to intranasally (brain C_{max} 0.15 µg/mL) or orally (brain C_{max} 0.11 µg/mL) administered free donepezil

AD- Alzheimer's disease, IN- intranasal

1.4.3 Polymeric microparticles and nanoparticles

Microparticles are in the micrometer size range and include microspheres, i.e. uniform spheres constructed of polymeric matrices, or microcapsules, i.e. a thin polymer membrane encapsulating an oily core [216]. Nanoparticles can also be used for airway delivery; however, due to their small size, they may be exhaled and hence not deposit in the airways. To overcome this drawback they can be delivered by nebulization after suspending in a suitable liquid, with deposition governed by the size characteristics of the nebulized droplets, or incorporated into larger carrier particles and delivered as dry powders [217]. Microparticles are used as an alternative to liposomes, being more readily stable on storage or in the biological fluids, and they offer the possibility of modulation of release rate [218].

Polymers are used in different fields such as pharmaceutical, biomedicine, tissue engineering and cosmeceuticals [219]. Polymeric microspheres prepared from biodegradable or biocompatible, natural or synthetic polymers have been studied as systems for airway delivery to control delivery of drugs and to protect them from enzymatic degradation. Polymer selection is critical for the success of the formulation, with appropriate control of drug release. As for all pulmonary delivery, the size of the nanoparticles and microparticles and their adequate dispersion are critical to ensure deep lung delivery [216,217]. Moreover, for nasal delivery to the brain, the residence time dictated by size and charge of the nanoparticles and microparticles is of critical importance for sufficient brain distribution.

Particulate systems have several key parameters, including morphology, size, size distribution, porosity, density, surface charge, surface energy and controlled or sustained release. These parameters are functions of many variables to be considered in formulation development, such as, polymer lengths, surfactants, use of organic solvent and preparation methods. A wide range of natural polymers, for instance, albumin, collagen and chitosan are available, however, users must consider a potential lack of purity, the presence of homogeneity and the possibility of disease transmission. Nevertheless, these natural polymers can be modified, for instance, the acylation of chitosan, to achieve favourable characteristics like release rate. Synthetic polymers, like poly(lactide-co-glycolide) (PLGA) copolymers, polyacrylates, poly(lactic) acid (PLA), poly(butyl cyanoacrylate) and poly(lactic-co-lysine) graft polymers and poly anhydrides are available and offer advantages over natural polymers as they can provide sustained/controlled release, and have high purity, homogeneity and other desirable properties [216–218,220].

Targeting can also be achieved by using ligands. For instance, lectin may be used with polymeric microspheres, as it binds to simple/complex carbohydrates on bacterial cell walls, and hence has been used against *Helicobacter pylori* infections by conjugation onto gliadin nanoparticles [220]. Lectin conjugated nanoparticles have also shown to improve nose-to-brain delivery and hence CNS bioavailability by increasing residence of nanoparticles in the nasal cavity (Table 1.8).

Polymeric nanoparticles can be prepared by various methods, namely, emulsification-solvent removal, phase coacervation, interfacial polymerization and spray drying; depending on the

desired size and properties of the microsphere to be made, and physicochemical properties of the drug [218].

Table 1.7: Polymeric nanoparticles/microparticle therapies under investigation for antimicrobial delivery

Polymer/ antimicrobial	Effective against	Treatment outcome(s)
PBCA nanoparticle Rifampicin Antimycobacterial [220,221]	*Mycobacterium avium* *Staphylococcus aureus*	2 to 3-fold superior delivery of rifampicin-loaded-PBCA to the alveolar macrophages leading to 2-fold increase in rifampicin efficacy compared to free rifampicin
PLGA nano embedded microparticles Tobramycin Aminoglycoside [222]	*Pseudomonas aeruginosa* (Inhalation-DPI)	PLGA-loaded tobramycin nanoparticles embedded in respirable lactose microparticles and consisting of helper polymers like chitosan showed greater mucin interactions and behaved as drug reservoirs to achieve sustained drug release
PLGA nanoparticles Ciprofloxacin Fluoroquinolone [198,220,223]	*Staphylococcus aureus* *Pseudomonas aeruginosa* (Inhalation-DPI)	Nano-ciprofloxacin formulations achieved sustained release of drug directly at the site of pulmonary infection and appropriate aerodynamic particle size to achieve deep lung access
PIBSA nanoparticles Ciprofloxacin Fluoroquinolone [169]	*Mycobacterium avium*	Administration of ciprofloxacin-loaded PIBSA showed greater activity due to higher uptake in alveolar macrophages compared to free ciprofloxacin

PLGA-Poly(lactide-co-glycolide), PIBSA-Polyisobutyl cyanoacrylate, PBCA-Polybutyl cyanoacrylate,

Table 1.8: Polymeric nanoparticles/microparticle therapies under investigation for nose-to-brain delivery

Polymer	Effective against	Treatment outcome(s)
Neuroprotective drugs		
Lectin (Wheat germ agglutinin) conjugated PEG-PLA NPs [103]	-	Lecithin conjugated NPs showed 2-fold higher uptake in the brain owing to binding of lecithin to sialic acid and N-acetyl-D-glucosamine found in nasal cavity, hence, increasing the residence time of the NPs and improving brain uptake
Odorranalectin conjugated PEG-PLGA NPs Urocortin peptide [104]	Parkinson's disease	Lectin conjugated NPs showed increased uptake in DiR fluorescence studies *in vivo* up to 8 h, whereas, unconjugated NPs showed an initially similar uptake (to conjugated NPs) for 2 h after which fluorescence in the brain reduced. This indicated that conjugated NPs could remain longer in the nasal mucosa and hence release for a longer duration leading to greater brain distribution Moreover, neuroprotective effects on 6-hydroxy dopamine hemiparkinsonian rats was significantly enhanced for conjugated NPs encapsulating peptide delivered intranasally
Chitosan NPs Estradiol/ didanosine/ thymoquinone [224–226]	Alzheimer's disease (estradiol/ thymoquinone) HIV (didanosine)	Approximately 2.5-fold increase in estradiol delivery, significantly higher levels of didanosine and thymoquinone were seen in the CSF and brain of rats as compared to IV delivery of the NPs. 18-fold higher concentration of thymoquinone was seen from the NP formulation as compared to simple solution and amelioration of cognition was evident. Chitosan was considered to significantly improve the delivery by increasing the residence time due to mucoadhesion
Chitosan NPs Olanzapine [227]	Schizophrenia Bipolar I disorder	Chitosan NPs encapsulating olanzapine delivered intranasally showed higher plasma concentration as compared to olanzapine solution delivered intranasally and approximately 2-fold higher absolute bioavailability as compared to IV administered olanzapine
Anticancer drugs		
Chitosan microspheres Methotrexate [227]	Primary central nervous system lymphoma	Methotrexate loaded chitosan microspheres showed a higher nose-to-brain delivery and absolute bioavailability as compared to nasally delivered methotrexate solution, whereas, IV administered methotrexate solution was not detected in the brain sections
Nano-co-Plex magnetic NPs Carmustin [228]	Glioblastoma	Significantly higher uptake and cytotoxicity of the Nano-co-Plex encapsulated carmustin in the presence of an external magnetic field was seen in *in vitro* studies on human glioblastoma cells

Nano-co-Plex-polyvinyl alcohol/polyethyleneimine/folate (Polyplex) complex coated magnetite, PEG-PLGA-poly (ethylene glycol)–poly (lactic-co-glycolic acid), NPs- nanoparticles

The mechanism of drug release from nanoparticles is governed by either homogenous (bulk) erosion or heterogeneous (surface) erosion. Bulk erosion occurs by degradation or erosion of the polymeric matrix throughout the entire system, whereas, surface erosion occurs by degradation or erosion of the polymeric matrix near the surface of the nanoparticles [229]. If the polymer matrix undergoes degradation, it releases the drug by diffusion through the channels created due to polymeric chain breakage [229]. Erosion of the polymer matrix leads to spontaneous drug release [218,219]. To date, most nanoparticles have been aerosolized using nebulizers. However, storage of colloidal preparations results in instabilities, such as polymer hydrolysis, drug loss, particle-particle interaction of nanoparticles or microparticles and particle aggregation. Previous studies have highlighted the importance of formulation development and nanoparticle size on production of aerosols with an optimum droplet size and the incorporation of particles into nebulized droplets. In addition to size, the surface properties of individual particles and their concentration play an important role in determining formulations release kinetics and the output from the nebulizer [230–232]. Dry powder formulations can be achieved by spray drying nanoparticle or microparticle dispersions, and this can be an attractive alternative ensuring long-term stability of the particles. However, redispersion on aerosolization in the airway fluid is an important criteria, and retention of the particle size in the airways post-aerosolization can be a challenge [232].

1.4.4 Lipid microparticles and nanoparticles- solid lipid nanoparticles

Lipid microspheres and nanospheres may be used as an alternative to polymeric microspheres and liposomes. Solid-lipid nanoparticles (SLNs) or nanostructured lipid carriers (NLCs) range from 50-400 nm and have attracted attention in the past 25 years due to the easy fabrication techniques. SLNs are viewed as a potential airway delivery system due to the low toxicity of phospholipid ingredients compared to polymer-based systems, higher tolerability in lungs, prolonged and controlled release properties and rapid *in vivo* degradation compared to PLGA or PLA particles [162,220]. Their composition includes fatty acids, steroids, triglycerides, partial glycerides, waxes that are solids/liquids at room temperature as well as surfactants to stabilize the SLNs. They can be prepared by simple spray drying, ultra-sonication or high-pressure homogenization and delivered as dry powders or dispersions for delivery via a nebulizer [162,220].

Lipid microparticles and nanoparticles described in the literature are summarized in Table 1.9.

Table 1.9: Solid lipid nanoparticles therapies under investigation for antimicrobials, neuroprotective molecules, and cancer chemotherapeutics

Solid lipid	Effective against	Treatment outcome(s)
Antimicrobial (For pulmonary diseases)		
Stearic acid, soya, phosphatidylcholine and sodium taurocholate Tobramycin- Aminoglycoside Ciprofloxacin- Fluoroquinolone [220]	*Pseudomonas aeruginosa*	Increased drug bioavailability and prolonged drug release
Stearic acid Rifampicin, isoniazid or pyrazinamide- Antimycobacterials [220,233]	*Mycobacterium tuberculosis*	Increased residence time, increased macrophage uptake and lymphatic system delivery achieved, decreased administration frequency due to increased bioavailability
Neuroprotective molecules (For nose-to-brain delivery)		
Stearic acid, lecithin, poloxamer 188 Astaxanthin Antioxidant [234]	Alzheimer's disease Parkinson's disease	Intranasal administration of ^{99m}Tc labeled SLNs encapsulating astaxanthin showed approximately 2-fold higher uptake as compared to IV administered formulation as confirmed by gamma scintigraphy imaging and biodistribution studies *in vivo*. *In vitro,* neuroprotection studies demonstrated protection against hydrogen peroxide induced oxidative stress
Anticancer molecules (For nose-to-brain delivery):		
Precirol, Capmul MCM, Tween 80, soya lecithin Curcumin [235]	Astrocytoma-glioblastoma	Significantly higher drug concentration of curcumin encapsulated in NLCs in the brain after intranasal administration as compared to plain drug suspension was reported

1.4.5 Micelles

Amphiphilic macromolecules having hydrophobic and hydrophilic regions tend to assemble in aqueous environments at a concentration greater than the critical micellar concentration into nano-sized micelles. These have widespread application within pharmaceutics, as hydrophobic drugs can be solubilized within the hydrophobic core of the micelles, allowing formulation at concentrations greater than their intrinsic water solubility. Moreover, these micelles can provide protection from degradation of the drug molecules and release kinetics can be manipulated by chemical alterations of the micellar surface, e.g. by cross-linking.

Micellar formulations for airway applications described in the literature are summarized in Table 1.10.

Table 1.10: Micellar therapies under investigation for antimicrobials and cancer chemotherapeutics

Polymer/lipid	Effective against	Treatment outcomes(s)
Antimicrobial (For pulmonary diseases)		
Depolymerized chitosan-stearic acid Nebulization Amphotericin B Antifungal [236]	*Candida albicans, Aspergillus spp*	Similar efficacy against all the different fungi Retention of encapsulation of amphotericin B after nebulization indicating no detrimental effect on the physical properties of the micelles on aerosolization using a jet nebulizer
Branched polyethyleneimine-stearic acid lipopolymer DPI Rifampicin Antimycobacterial [237]	*Mycobacterium smegmatis*	Higher uptake and internalization of the cationic micelles encapsulating rifampicin into phagosomal compartments of the alveolar macrophage cells THP-1 due to proton-sponge effect was observed
Anticancer molecules (For nose-to-brain delivery)		
MPEG-Polycaprolactam and MPEG-Polycaprolactam-Tat (cell penetrating peptide) targeted Camptothecin [238,239]	Intracranial Glioma Tumour	Intranasally administered MPEG-PCL-Tat encapsulated camptothecin showed higher mean survival of tumour-bearing rats compared to intranasally administered camptothecin solution due to stronger interactions of the positive Tat molecule with glioma cells

Micelles can be formed from polymers/lipids that can been synthesized to achieve specific functionalities, such as targeting [216]. Polymeric micelles have been shown to be more stable than conventional surfactant micelles, having critical micellar concentrations less than 10^{-6} M [216,240–242]. One of the most prominent reasons for resistance to current antibiotics is the downregulation of uptake receptors on the surface of microorganisms. It would be an attractive approach to encapsulate such antibiotics within self-assembling micelles which would not be recognized by the receptor surfaces and hence help in intake of antibiotics into resistant bacteria.

1.4.6 Large porous carriers

Large porous carriers referred to as 'Trojan particles' by Tsapi et al. are micrometer-sized particles for inhaled drug delivery, particularly for pulmonary infections [243]. These can be of two types namely:

1.4.6.1 Large porous particles (LPPs)

These are characterized by a geometric size greater than 4-5 μm and a mass density less than 0.1 g/cm^3, resulting in the formation of particles which have a low aerodynamic diameter [59,243,244]. LPPs are an attractive system for pulmonary delivery as they have superior aerodynamic properties as compared to conventional particles of the same physical size. 60% of the nominal dose of such particles may reach the deep lung. Moreover, they are not cleared easily

by alveolar macrophages, due to their large size. Hence they are attractive for sustained release of drug in the lungs [59,245]. The highly porous surfaces and relatively large sizes of such particles help to decrease inter-particulate cohesion and consequently disperse more easily in the presence of airflow shear forces [59,245].

Large porous capreomycin particles were manufactured by spray drying with L-leucine from a 50% aqueous ethanol solution to produce particles having a mass median aerodynamic diameter (MMAD) of 5 μm. Insufflation delivery of these particles to guinea pigs resulted in reduced bacterial burdens, decreased alveolar clearance and hence a potential to lower the dose and decrease toxic side effects [246]. Edwards et al. determined the systemic bioavailability of insulin and suppression of blood glucose levels, using large porous PLGA particles encapsulating insulin, prepared by solvent evaporation techniques [247]. Inhalation of large porous insulin particles (mean physical diameter 6.8 μm, MMAD 2.15 μm) demonstrated higher insulin bioavailability and glucose suppression for 96 h than non-porous insulin particles (mean diameter 4.4 μm, MMAD 2.15 μm) which showed lower bioavailability and glucose suppression for only 4 h. Moreover, inhalation of large porous testosterone particles (mean diameter 20.4 μm and 10.1 μm) showed a higher systemic bioavailability when compared to subcutaneous administration of these porous particles. These results were attributed to the reduction in phagocytosis by deep lung alveolar macrophages, which are inefficient in the removal of particles greater than 3 μm, leading to sustained release and greater bioavailability of drug systemically [247].

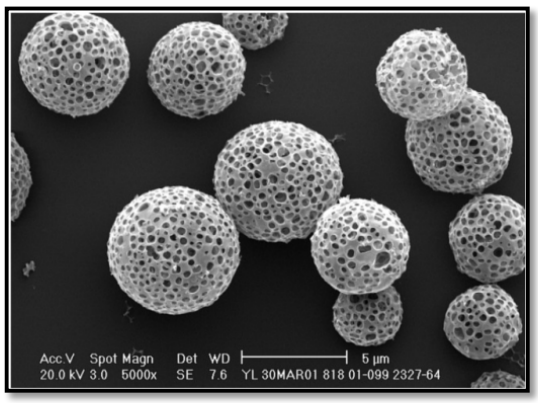

Figure 1.9: An SEM image of LPPs of tobramycin produced by PulmoSphere™ technology [59]

An established engineering technique for preparation of LPPs is the Novartis PulmoSphere™ technology. These are manufactured by emulsion-based spray drying, wherein the submicron oil in water emulsion droplets are generated by high-pressure homogenization of perfluorooctyl bromide in water. The principal lipid component of PulmoSpheres is distearoylphosphatidylcholine (DSPC). Drugs, such as tobramycin and amphotericin B are dissolved in the oil phase of the emulsion [59]. An SEM image of PulmoSphere particles of tobramycin (Novartis Pharmaceuticals Canada Inc.) is as shown in Figure 1.9.

PulmoSphere formulations of antimicrobials, namely tobramycin, amphotericin B, and ciprofloxacin have undergone at least Phase II clinical trials. Tobramycin inhalation powder-

TIP™ (TOBI® Podhaler®; Novartis Pharmaceuticals) is safe and efficacious in treating *P. aeruginosa* lung infections in CF patients, and has now been licensed and is marketed in several European countries, South America and Canada [59], [60]. A questionnaire survey of 39 patients and their parents, as well as 54 respiratory therapists, revealed that TIP™ (TOBI® Podhaler®) was considered to be more convenient and acceptable than tobramycin inhalation solution (TIS™ TOBI®) [59,248]. Ciprofloxacin PulmoSpheres (Bayer HealthCare) have also shown efficacy for the treatment of *P. aeruginosa* in CF patients [249]. This formulation was successful in Phase I clinical trials in 2013 to evaluate the potential of ciprofloxacin DPI for mild to moderate COPD. It also passed Phase II studies to evaluate safety and efficacy in patients with CF in May 2014 [64,250,251].

1.4.6.2 Large porous nanoparticle aggregates (LPNAPs)

LPNAPs comprise of micron-sized particles consisting of nanoparticles (1-100 nm) held together by Van der Waals forces or present in a matrix having components such as biopolymers, surfactants, amino acids, lipids, or proteins (Figure 1.10). LPNAPs have been made from a range of materials including silica, polystyrene, DPPC, albumin, hydroxypropyl cellulose and lactose in sizes ranging from 25 to 1000 nm. LPNAPs have similar physical and aerodynamic properties to LPPs, and once delivered to the lungs they dissociate to form individual nanoparticles [243]. LPNAPs can overcome the problems associated with the pulmonary delivery of nanoparticles, i.e. exhalation due to their small size, yet provide the advantages of nanoparticles when they are liberated in situ following deposition of the larger particles in the lungs.

Rifampicin encapsulated in PLGA nanoparticles spray dried to form LPNAPs has demonstrated sustained release of drug delivered directly as an aerosol wherein a Cmax of rifampicin above the MIC was seen in the lungs and alveolar cells for up to 8 h, whereas free unencapsulated rifampicin was not detectable in the lung tissue or bronchoalveolar lavage 8 h after dosage [252]. This delivery system has a potential therapeutic advantage for treatment of extended resident infections which are difficult to eradicate like pulmonary TB.

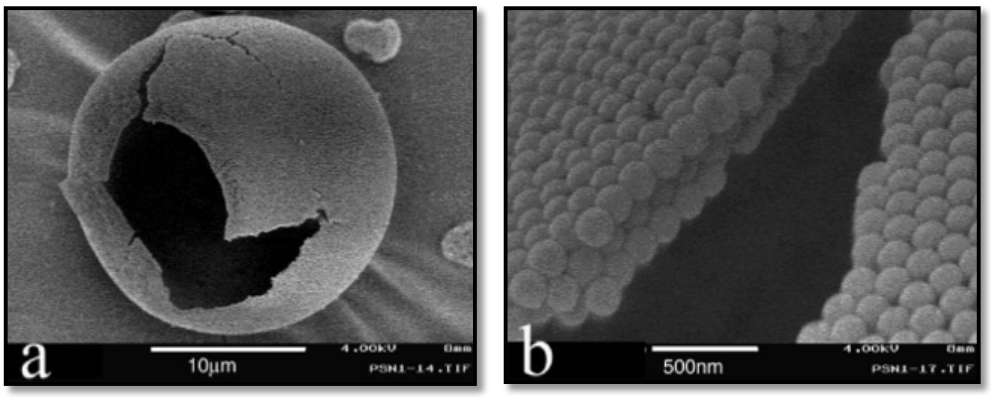

Figure 1.10: SEM images of LPNAPs, (A) hollow sphere and (B) magnified view of the particle surface [241]

1.4.7 Advantages of nanotechnology for airway delivery

1.4.7.1 Protective vesicles preventing cargo degradation

Nanocarriers can be an attractive approach for delivery of medicaments as they provide a protective environment that shields the cargo preventing degradation. Antibiotic inactivation by enzymes or interactions with other components in the biofilm matrix may reduce drug activity or cause complete resistance to it which contributes to multi-drug resistance. Human sputum being rich in polyanionic components, namely mucin, DNA, F-actin, lipopolysaccharides and lipoteichoic acid has been shown to reduce the antimicrobial properties of the cationic antibiotics, due to the formation of an electrostatic attraction complex, hampering complete eradication of the bacteria [88,253,254]. Encapsulation of these antibiotics in liposomes reduces formation of the electrostatic complex 100-fold, giving a 4-fold improved inhibition of *P. aeruginosa* colonies, suggesting a potential application in the eradication of chronic lung infections associated with CF [253,255].

1.4.7.2 Controlled release

Antimicrobial therapy is hampered by the short availability of drug at the target site, potentially limiting treatment outcomes. Currently, for chronic pulmonary infections, high doses and frequent parenteral administration are necessary to achieve the pulmonary sputum concentrations required to eradicate the chronic colonies of biofilm and macrophage-associated bacteria [256–258]. However, protracted and recurrent administration of high dose antibiotics is associated with antibiotic resistance [258–260]. Inhaled antibiotics also face considerable challenges as they are rapidly cleared from the lungs by natural clearance mechanisms, namely exhalation for small particles, phagocytosis by macrophages and dendritic cells, mucociliary clearance and enzyme degradation. This may lead to antibiotic exposure at sub-inhibitory levels, leading to incomplete eradication of bacterial colonies embedded in the protective layers of sputum and biofilms, leading to higher incidences of antibiotic resistance [87].

A logical approach to enhance the delivery of antibiotics for treating chronic infections by increasing their residence time, is to load them into appropriately sized carriers which could serve to deliver the drug to the site of infection. However, chronic administration of the carrier may lead to their accumulation in the airways. Despite the phospholipids used in the preparation of liposomes sometimes being endogenous to the lungs; their repeated administration can lead to cumulative doses of lipids in the lungs greater than the original surfactant pool, resulting in adverse effects, such as phospholipidosis [182,261,262]. Hence, excipients should be minimized, with nanocarriers designed to deliver antimicrobials encapsulated in controlled/ sustained/ extended release vesicles which release the drug over extended periods, maintaining therapeutic levels in the vicinity of the biofilm, improving patient compliance whilst reducing chances for development of resistance [87,258]. Although a number of research articles have been published on the controlled release of antibiotics given systemically or as post-operative implants, few

reports are associated with the controlled release of antibiotics following pulmonary delivery [182,263–265]. Sustained release PNAPs comprising of PLGA nanoparticles encapsulating rifampicin showed lung tissue Cmax levels above MIC for up to 8 h after aerosolization, whereas rifampicin was undetectable in the lung tissue 8 h after aerosolization of the free drug [252].

Release profiles are of utmost importance for consideration when the medicament is to be delivered to the brain via intranasal administration as mucociliary clearance is highly dominant which affects the formulation residence time. Due to the limitation of delivery volumes to the nasal tract (0.4-1 mL) a combination of mucoadhesive formulations along with sustained/ controlled release of medicaments would be optimum to improve the bioavailability in the CNS. Nimodipine encapsulated microemulsions which gel in-situ due to temperature differences showing a sustained release of nimodipine exhibited a 10-fold higher brain concentration *in vivo* in rats as compared to intranasally administered nimodipine solution [266].

These studies highlight the susceptibility of chronic bacterial infections and brain bioavailability on nasal administration to nanocarrier formulations and the importance of the formulation parameters, such as drug properties, choice of polymer, mucoadhesion, particle size and distribution, method of preparation of nanoparticles and release profile.

1.4.7.3 Non-specific/Local delivery

Pulmonary delivery

Nanoparticles can be targeted locally by selective extravasation at the site of infection, due to the increased porosity of blood vessels induced by increased inflammatory factors [38]. Eradication of intracellular organisms presents severe challenges as therapeutic concentrations of antimicrobials in intracellular compartments are difficult to achieve due to their limited penetration capacity [267,268]. Thus, many antibiotics, such as β-lactam and aminoglycoside antibiotics show low concentrations in intracellular compartments due to poor penetration along with acidic and enzymatic degradation. However, quinolone and macrolide antibiotics, such as clindamycin, levofloxacin and amphotericin B attain higher intracellular concentrations as opposed to extracellular concentrations [267–269]. *Mycobacterium tuberculosis* binds to and internalizes in the alveolar macrophages as a survival mechanism, and hence is very difficult to eradicate completely. A study of liposome-encapsulated clofazimine against TB showed that liposomal formulations were much more effective in being taken up naturally by the macrophages, where the infection prevails, improving treatment outcomes and reducing the off-target toxicity of the antitubercular drug *in vitro* and *in vivo* [270,271]. Liposomal clofazimine was more effective in the treatment of acute and chronic murine TB, giving a bactericidal effect with no re-emergence of *Mycobacterium tuberculosis* infection in mice [270,271].

The fusogenic property of liposomes makes them an attractive approach for delivering antimicrobials directly to cells, due to their potential to fuse with phospholipid cell membranes. The fluidity of the liposomes can be achieved by lowering the phase transition temperature, by

incorporation of components of the inactivated Sendai virus envelope, using lipids which have the phosphatidylethanolamine moiety, lipids with double bonds and/or asymmetry in acyl chain, or by the addition of cholesterol [255,272–276]. Antibiotics enter Gram-negative bacteria by two routes: hydrophobic drugs enter by passive transport via the lipopolysaccharide and protein-rich outer membrane; whereas hydrophilic drugs enter through the outer membrane water-filled porin channels. A reduction in antibiotic susceptibility of resistant strains of bacteria has been reported due to the acquisition of genetic factors which lead to changes in the bacterial outer membrane porin channels, which strongly impacts the influx of antibiotics and hence bacterial susceptibility [275,277–280]. Fluidosomes™-Tobramycin is being developed by Axentis Pharma (Switzerland) and has demonstrated good safety and efficacy profiles in pre-clinical and Phase II clinical trials, when compared to the present available marketed treatments for management of chronic infection caused by *Burkholderia cepacia* pathogens associated with cystic fibrosis [255].

Non-specific approaches to targeting suffer from the drawbacks of non-specific drug delivery and uptake, hence selectively targeting to the site of infection may represent an attractive approach to increase uptake, to achieve higher doses to eradicate bacteria at the appropriate site, allow a reduction in dose and potentially reduce the potential for antimicrobial resistance.

Nose-to-brain delivery

Nanoparticles have shown to improve the bioavailability and therapeutic effect of several drugs like nimodipine, diazepam and morphine when applied intranasally due to passive/non-specific brain targeting [136,266,281]. Technetium-99m-labeled PLGA encapsulated diazepam nanoparticles showing sustained release for over 24 h and 61.3% direct nose-to-brain transport as compared to 1% for technetium-99m-labeled diazepam solution, whereas, drug targeting efficiency i.e. brain uptake via the blood increased 2-fold for the nanoparticles as compared to the solution, indicating that diazepam was majorly absorbed into the blood and then delivered to the brain when intranasally administered as a solution [282]. Moreover, intranasal morphine delivered with maltodextrin nanoparticles showed faster antinociceptive activity as compared to its subcutaneous counterpart which produced higher plasma levels of morphine but lower analgesia, suggesting direct nose-to-brain passive targeting of nanoparticles when intranasally administered [281]. However, there is a lack of literature confirming the route of uptake of nanoparticles via the olfactory nerves, as these and several more studies can only demonstrate superior drug bioavailability when encapsulated within nanocarriers as opposed to simple solutions, but cannot confirm the mechanism of the passage of these nanocarriers [100].

For delivery to brain tumours, nanoparticles <100 nm have demonstrated the ability to extravasate through the fenestrations and leaky vasculature of tumours and hence locate themselves primarily at tumour sites known as the enhanced permeability and retention effect (EPR). Accumulation of imaging agents and cancer chemotherapeutics within the porous BBTB has been achieved in the past [283,284]. However, circumvention of the BBB remains a major barrier for delivery of cancer chemotherapeutics given as an IV to achieve passive targeting to the BBTB. This is because the

BBB remains largely intact at the margins of the tumour and is more distorted in the bulk [284]. Hence passive nose-to-brain delivery to circumvent the BBB after which passive targeting via the EPR effect to the BBTB can be undertaken by encapsulating cancer chemotherapeutics within nanocarriers of size <100 nm administered intranasally.

1.4.7.4 Specific targeting

Pulmonary delivery

Biofilm targeting- Understanding the generation of biofilms at the genetic and molecular levels has informed the development of drug delivery systems which may help in overcoming this physical barrier to effective antimicrobial therapy and help in improved elimination of chronic bacterial infections associated with biofilms. An attractive approach in disassembling the EPS matrix of bacterial biofilms, and hence enhancing antibiotic therapy has been studied previously [285,286]. Ciprofloxacin was loaded into PLGA nanoparticles, with and without a coating of DNAse enzyme. This enzyme has been found to be very effective in disrupting the integrity and viscoelastic nature of the DNA-rich EPS of biofilms, and greatly improves diffusion through it [285,286]. Ciprofloxacin was encapsulated in PLGA coated with DNAse by means of covalent linkage using poly-lysine on the surface of PLGA nanoparticles. These particles had improved mobility in *Pseudomonas aeruginosa* biofilms in both static and dynamic conditions, providing a platform for the treatment of biofilm-associated bacteria with biofilm disassembling and antibacterial agents [286].

Sputum targeting- Numerous studies have been conducted on the sputum expectorated from CF patients to understand the nature of the matrix microstructure, mesh spacing and its components to aid in delivering antibiotics and gene vectors through this obstacle majorly challenging the treatment of CF. Suk et al. have shown that densely packed low molecular weight PEG imparted 'muco-inertness' to the surface of polystyrene (PS) nanoparticles of different sizes. Transport of these nanoparticles through CF sputum, studied using multiple-particle-tracking analysis, showed that the uncoated PS nanoparticles with a charge on the surface due to a terminal amine group had a strongly hindered transport, whereas similarly sized nanoparticles with a muco-inert surface which showed greater movement in time-lapse studies. This was attributed to possible polyvalent adhesion interactions between the hydrophobic mucin fibers and hydrophobic core of PS nanoparticles, and electrostatic interactions of the positively-charged nanoparticles with sputum components, such as DNA and F-actin, all of which were masked when particles were densely coated with hydrophilic, uncharged PEG molecules [286]. This demonstrates the importance of nanoparticle properties such as surface charge, hydrophobicity, molecular weight and size, on the transport of particles and the encapsulated drug through the sputum [286,287].

Macrophage targeting- As highlighted above, alveolar macrophages play a major role in combating infections. However, in chronic infections, bacteria and other organisms take these over, locating themselves in the protective environment where they multiply and become difficult to eradicate with routine antibiotics. To eradicate these intracellular infections, directly targeting to the macrophages could be a highly effective strategy. Much research has been performed to study the potential of PLGA microparticles and nanoparticles to target the alveolar macrophages, as they may remain membrane bound onto the alveolar macrophages for up to 2 weeks [288–296]. Makino et al. showed the phagocytic uptake of rifampicin encapsulated in PLGA nanoparticles. 19-times higher uptake of rifampicin by the macrophage cells *in vitro* was found for PLGA-encapsulated rifampicin formulation compared to free drug in solution [293]. A similar study exploring the reasons for an increased uptake of PLGA nanoparticles into macrophage cells, concluded that 90% of PLGA nanoparticles encapsulating rifampicin were taken up and remained membrane bound onto the low pH hydrolase-rich regions of the phagolysosomes for 13 days, as shown by fluorescence and immune-electron microscopy, from where rifampicin is released over time. Further studies have confirmed that this formulation system was more efficient in the eradication of *mycobacterium bovis* infected macrophage RAW 264.7 cells compared to free rifampicin at the same concentration. Actively targeting nanoparticles to alveolar macrophages has been extensively investigated for the treatment of various infections associated with tuberculosis, visceral leishmaniasis and arthritis [297–299]. Gelatin nanoparticles encapsulating isoniazid with and without mannose conjugated to the surface of nanoparticles, required for selective delivery to macrophages, have been studied. Macrophage-uptake studies showed that mannosylated nanoparticles were taken up preferentially into macrophages compared to non-mannosylated nanoparticles. The antitubercular activity, studied by inducing TB infection in BALB/C mice, showed much lower CFU/mL of spleen when the mice were treated with mannosylated gelatin nanoparticles encapsulating isoniazid, compared to non-mannosylated nanoparticles encapsulating isoniazid and free isoniazid. This suggests the macrophage uptake of the drug encapsulated in nanoparticles is an important pre-requisite for the treatment of intracellular infections. Similar results have been observed by others, studying conjugation of mannose onto SLNs, liposomes and polypropylene imine dendrimers [300–302].

Nose-to-brain delivery

Active targeting to brain tumours and hence preferential accumulation within the tumour can be achieved by promoting drug release specifically at the tumour site by means of release from nanoparticles by microenvironmental change of pH or overexpression of protease and delivery of prodrugs active only in the tumour interstitial. Folate receptors are primarily overexpressed in cancer cells due to an increased requirement of folic acid for sustaining the rapid rate of growth and division of the cells [284]. Folic acid-conjugated nanoparticles have shown promise in the delivery of medicaments to many kinds of tumours including lungs, kidneys and brain [303].

Chlorotoxin conjugated chitosan nanoparticles have shown promise in specifically targeting to the glioma cells and hence an improved uptake in gliomas in mice [284,304], Mitochondria targeting is another strategy for treatment of neurological disorders wherein mitochondria-specific antioxidants e.g. MitoQ and SS31 have shown to mitigate oxidative stress and synaptic dysfunctions associated with AD [305]. Triphenyl phosphonium (TPP)-Ceria nanoparticles were targeted to the mitochondria by means of electrostatic attraction between the lipophilic TPP cation and anionic charge of the mitochondrial membrane potential. These targeted nanoparticles showed protection of neurons against oxidative stress studied by ROS formation, mitochondrial morphology changes and mitigation of neuronal death markers in AD model of mice [305].

1.4.7.5 Higher uptake and retention in lung tissue

Antimicrobial lung concentrations are of crucial importance, as a drug concentration above the MIC and MBIC are required to achieve successful eradication of the infecting pathogens. Liposome-encapsulated amphotericin B has long been successfully marketed under the name AmBisome for intravenous infusion for the treatment of severe systemic and deep mycosis in the lungs. Several studies have been performed delivering these liposomes and other lipid-based systems via nebulization directly to the pulmonary tract to achieve high local concentrations and reduce undesirable systemic effects [306–308]. One such study has highlighted the beneficial effects of nebulized amphotericin B encapsulated in liposomes, compared to Fungizone (sodium deoxycholate complex) using a SPAG-2 nebulizer. AmBisome showed an eight-time higher concentration in the lungs (207 µg/mg lung tissue) than Fungizone (24.4 µg/mg lung tissue) using *in vivo* in murine models infected with *Aspergillus fumigatus*. Also, with a medium infection load of 10^7 CFU/g of tissue, AmBisome produced nearly completely eradicate from the lungs (mean CFU/g of lung tissue=0.54); however, Fungizone showed no improvement in eradication compared to the control group (mean CFU/g of lung tissue=3.31 for Fungizone and 5.30 for control). This demonstrates the importance of higher lung retention achieved with nanotechnology- based vesicles and their consequent beneficial effects on eradication of bacteria. Clinical trials are on-going for nebulized AmBisome (AMBINEB) in the prophylaxis of Invasive Pulmonary Aspergillosis in patients with Acute Myeloid Leukaemia and Allogeneic Haematopoietic Progenitor Cell Transplantation. Further clinical trials are being conducted following completion of Phase II studies of prophylactic nebulization of amphotericin B-lipid complex (Albecet®) in paediatric patients with acute leukemia [306–308].

1.4.8 Disadvantages of nanotechnology for airways delivery

1.4.8.1 Formulation drawbacks

Nanoparticles present many challenges, potentially limiting their progress onto the market. Key drawbacks include:

(1) Scale up and transitional development from the laboratory bench to industrial production is a challenge due to differences in the properties of nanoparticles compared to their bulk counterparts. Smaller sizes and commensurate large surface area can lead to high chances of aggregation, hindering physical handling at an industrial level [309]

(2) Low drug encapsulation is a major limitation, and is often dependent on aqueous/lipid solubility, as exemplified by a drug's logP

(3) Stability of nanocarrier drug formulation may be problematic, for instance, leakage of drug on storage, changes in size and surface properties and, particle-particle interaction and aggregation

(4) Stability of formulation for aerosolization processes, especially by nebulization of nanocarriers dispersed in liquid may result in particle rupture and drug loss and consequently unpredictable deposition patterns within the airways

1.4.8.2 Toxicity of nanoparticles to the airways

With the advent of nanoparticle drug delivery in pharmaceutical, biomedicine and cosmeceutical areas, the field of nanotoxicology has emerged to investigate potential adverse reactions to nanoparticles [38,310]. Nanomaterial structures, due to their very small size and large surface area have a potential to be more toxic than conventionally sized bulk samples of the same materials. This is due to their deeper airway penetrations, large surface/mass ratios, aggregation capabilities and low water solubility. It has been seen that human alveolar macrophages are not capable of removing nanoparticles of size 70 nm and less, leading to their deep lung access and entrance into the bloodstream through the alveolar epithelium, and causing evident inflammation in other organs. The aggregation state is another important determinant. Aggregates of ultrafine carbon particles at concentrations of 1 μg/mL and greater impair the phagocytic function of human alveolar macrophage [38,310]. The large surface area/mass ratio enables these nanoparticles to undergo various reactions which result in toxicity and cause inflammation in animal models, whereas their counterpart larger particles have a demonstrable safety. This is due to novel surface characteristics which may contribute to reactions like generation of reactive oxygen species, i.e. free radical formation as shown for CuO and SiO_2 nanoparticles; interlukin-8 cytokine production evident following exposure to cobalt or TiO_2 nanoparticles; increase in mRNA levels of inflammatory markers shown for by yttrium and zinc oxide nanoparticles [38,310].

To study toxicity, regulatory authorities require animal studies; however, *in vivo* studies are conducted using oral, intraperitoneal or dermal routes which do not completely portray inhalation effects. *In vitro* methods have been developed to study toxic effects on airway cells (Calu-3 human cell line), alveolar epithelium (A549-human pulmonary cell line) or tissues. These are quicker, simpler and less expensive than *in vivo* tests. However, they do not completely take in account lung characteristics, such as microenvironments and inhalation effects [310].

1.5 Scope and Content of the thesis

The aim of the thesis is to examine various nanocarriers encapsulating hydrophobic drugs engineered with favorable aerosol characteristics to be delivered via the airways. To achieve the aim, the objectives of the thesis are:

- To engineer nanoparticles for the delivery of hydrophobic drugs, modulated to have desirable features to improve the efficacy of the drug formulation and to characterize these
- To develop aerosol formulations and study parameters that dictate aerosolization efficiency
- To investigate the effect of the formulation parameters on the *in vitro* biological performance of the nanoparticles

For this purpose, the thesis has been divided into 6 chapters beginning with the introduction as chapter 1 which summarizes the literature relevant to the present work, followed by the general methods in chapter 2. Chapter 3-5 embodies the experimental sections of the research work carried out concluding with chapter 6 comprising of general discussions and future work. Each chapter outlines a brief introduction, followed by aims and objectives, materials and methods, results and discussion ending with a conclusion.

2

CHAPTER 2

Experimental methodology

2.1 Determination of particle size and zeta potential (surface charge) using Malvern Zetasizer

The hydrodynamic diameter and the polydispersity index (PDI) of the nanosized formulations and the re-constituted spray dried powders were measured using dynamic light scattering (DLS) on a Malvern Zetasizer Nano ZS (Malvern Instruments Inc., UK) at a backscattering angle of 173°, calculated using the Mark-Houwinck parameter. The dispersion medium for both the studies was deionized water with a viscosity of 0.8872 cP, refractive index of 1.330 and dielectric constant 78.5.

0.5% w/v dispersion of each of the formulations were prepared in deionized water, of which 2 mL was placed in a clear disposable polystyrene sizing cuvette (DTS0012) and measurements were performed immediately after preparation/reconstitution in triplicate at 25°C. The reported size was the Z-average size (or cumulative mean) and the PDI was a width parameter calculated from the cumulative data of signal intensities.

The surface charge i.e. zeta potential was also determined using Malvern Zetasizer Nano ZS (Malvern Instruments Inc., UK), by calculating from the Smoluchowski's equation with an F(Kα) value of 1.50 using the principle of electrophoretic light scattering also known as laser Doppler velocimetry. 1 mL of the same 0.5% w/v solution was placed in a clear disposable zeta-cell (DTS1060C, Malvern Instruments Inc., UK) and measurements performed at 25°C. The results were expressed as the mean of triplicate measurements.

2.2 Fourier transform infrared (FT-IR) spectroscopy

FT-IR spectrum of the spray dried, physically mixed and co-ground powders were determined to analyze the chemical interactions between the drug and the excipients of the respective formulations (Chapter 3). FT-IR was also used to study the success of synthesis of mannosylated chitosan by analysis of the change in the fingerprint of the chemical groups on the chitosan polymer backbone (Chapter 4). A Spectrum™ 100 spectrophotometer (PerkinElmer, UK) operating in the mid-infrared region, equipped with a Universal Attenuated Total Reflectance (UATR) device was used. The UATR polarization assembly features a robust diamond crystal to study reflectance from the sample and has a 9-bounce diamond top-plate serving as a sample lens. Triplicate scans for each sample were run in the spectral region of 4000-6500 cm^{-1} with 25 scans recorded at a 4-cm resolution. Approximately 2 mg of powder was placed on the sample lens and pressed against it with the UATR device. Scans were run and the spectrum recorded using a PerkinElmer spectrum express software version 1.02.00. Before each scan, a background was run to eradicate any peaks arising from impurity on the sample lens.

2.3 X-ray powder diffraction (XRPD)

The crystallinity of individual raw materials, physically mixed powders, co-ground powders and the spray dried powders was determined at room temperature using wide angle X-ray diffraction with a 5^{th} generation Rigaku Miniflex 600 X-ray powder diffractometer equipped with a 600-watt

X-ray tube, a copper anode operating in reflectance mode at wavelength kα λ 1.5418 Å, voltage of 40 kV and current 15 mA. The instrument uses a NaI scintillator as the detector, Kβ foil filter, and a graphite monochromator. Samples to be analyzed for crystallinity were mounted perpendicular to the horizontal axis and then rotated to obtain a scanning range of 5-60° 2Θ at a step size of 0.025°/min and step rate of 2 step/min at 25°C, and hence a scanning time of 27.5 min per sample with a total of 2750 points. The relative long-range order (crystalline) versus non-order (amorphous) was assessed by comparison of the data obtained by XRPD for each sample using the PDXL version 2.7 software (Rigaku, Kent, England) linked to the diffractometer.

2.4 Morphology analysis using electron microscopy

Electron microscopy (EM) is a widely-used tool for structural analysis of particles in the nanometric and micrometric scale, which provides an insight into the morphology of particles in the liquid and solid state. Along with morphology, EM also provides some information about crystallinity, particle topography, density, surface roughness and porosity of particles which may influence the dispersibility of particles, and their aerodynamics.

2.4.1 Scanning electron microscopy (SEM)

The shape and surface morphology of the spray dried powders was examined using a FEI Quanta 200F Scanning Electron Microscope (FEI, Netherlands). The samples were prepared by placing a small amount of freshly prepared spray dried powder, with the help of a brush, onto a 12.5 mm aluminium specimen pin stub covered with a double-sided adhesive black carbon tabs (Agor Scientific, UK) and then sputter-coated with gold in a Qourum Q150R rotary-pumped sputter coater (Qourum Technologies, UK). A coating of approximately 10 nm was established under vacuum, and an argon atmosphere purge at 20 mA for 3 min to prepare the non-conducting or poorly conducting specimens' optimum for observation under SEM at 20 kV.

2.4.2 Transmission electron microscopy (TEM)

TEM micrographs for morphological examination of nanoparticles after preparation and reconstituted spray dried microparticles was carried out using an FEI CM120 BioTwin Transmission Electron Microscope (FEI/Philips, USA). 10 µL of nanoparticulate solution was placed on a Formvar/carbon coated 300-mesh copper specimen grid (F196/100:3.05 mm, Tab Labs, UK) after which excess sample was removed using a Whatman filter paper No.1, then negatively stained with 1% uranyl acetate (Sigma-Aldrich, Poole, UK) aqueous solution for 90 s and allowed to dry at room temperature. This specimen grid was then loaded onto a CM120 grid-holder which was inserted into the goniometer compustage wherein the sample was exposed to an operating voltage of 120 kV and high-resolution images were captured using a digital camera AMT XR80 (AMT Imaging, USA).

2.5 Laser diffraction particle size analysis

The particle size distribution of the co-ground and spray dried powders was determined using Sympatec HELOS particle size analyzer (Sympatec GmbH, Clausthal-Zellerfeld, Germany) based on the principle of laser diffraction following the Lorenz-Mie theory. An R2 lens was selected which measures particle size in the range 0.25 to 87.5 µm, and powders were dispersed with a RODOS i.e. 'Rotating Dosing and Dispersing System' dry powder disperser (Sympatec) at different pressures [311]. The analysis was carried out using a parallel beam from an optical system consisting of a helium-neon laser at 623.8 nm and a semicircular 180° multi-element photodetector [312]. Particle size distribution data was processed by MIEE, i.e. Mie Extended Evaluation, for spherical particles of known refractive index in the range of 0.1-8750 µm. Data obtained were expressed as the volume-weighted mean particle size using a WINDOX 5 software [313].

Measurements were performed on a RODOS/M disperser supplying a near constant mass flow of sample equipped with a micro-dosing device ASPIROS/L designed to feed small amounts of powder. A feed rate of 50 mm/s was applied and analysis performed at different pressures. An empty sample glass vial was placed into the ASPIROS and a measurement was run to be read as a reference after which approximately 5-10 mg of each sample powder was filled into the glass vial and placed back in the ASPIROS. Three replicates were performed on a single sample of powder and three batches of each powder analyzed to ensure accuracy and reproducibility of measurements. Results recorded on a HELOS system was expressed as volume weighted mean particle size namely Dv10, Dv50 and Dv90 (also known as X10, X50, X90). The Span of the volume distribution i.e. a dimensionless parameter used for quantification of volume distribution relative to the 10^{th}, 50^{th} and 90^{th} percentile of cumulative distribution was derived from equation 2.1:

$$Span = \frac{Dv90 - Dv10}{Dv50} \qquad \textbf{Equation 2.1}$$

where, Dv10, Dv50 and Dv90 stand for the particle sizes of a given percentage of particles smaller than the specified size. Span is reflective of the uniformity of distribution wherein a high Span value is an indication of a wider particle size distribution and size heterogeneity of the powders.

2.6 In *vitro* aerosol deposition and aerodynamic behavior studies using the Next Generation Impactor (NGI)

Spray dried microparticles prepared with the intention of being delivered as a dry powder inhalation were tested for their aerodynamic behavior using the Next Generation Pharmaceutical Impactor (Copley Scientific, Ph. Eur. Apparatus E, NGI) operated in specifications by the European Pharmacopoeia (Ph. Eur. 9^{th} edition, monograph 2.9.18).

In each experiment size 3 transparent gelatin capsules (Dr T & T Health, UK) were filled manually with 30 ± 0.2 mg of formulation and used for NGI. As per the European Pharmacopeia, two

factors were to be considered before performing and accepting results from the NGI. The first important factor to consider is the *mass balance* phenomenon. To ensure a valid inference, it is important to recover 100 ± 25% of the initial average dose of the active drug. *Re-entrainment* being the second factor should be prevented by coating the pans with silicone oil, glycerol or other high viscosity liquids through the evaporation of a volatile solvent. Re-entrainment was minimized in the present experiment by coating the pans of stages 1-7 of the NGI with 1% silicone oil (Sigma- Aldrich, UK) in n-hexane and leaving them aside for 20 min for n-hexane to evaporate and the pans to be evenly coated with silicone oil. A 75-mm internal filter (Copley Scientific, UK) was placed in stage 8, i.e. the micro-orifice collector (MOC), to prevent very fine particles of the formulation to exit into the pump and cause clogging. After the pans were dried, the apparatus with the assembly of pans on the bottom frame was closed by the seal body using the clamping handle (Figure 2.1).

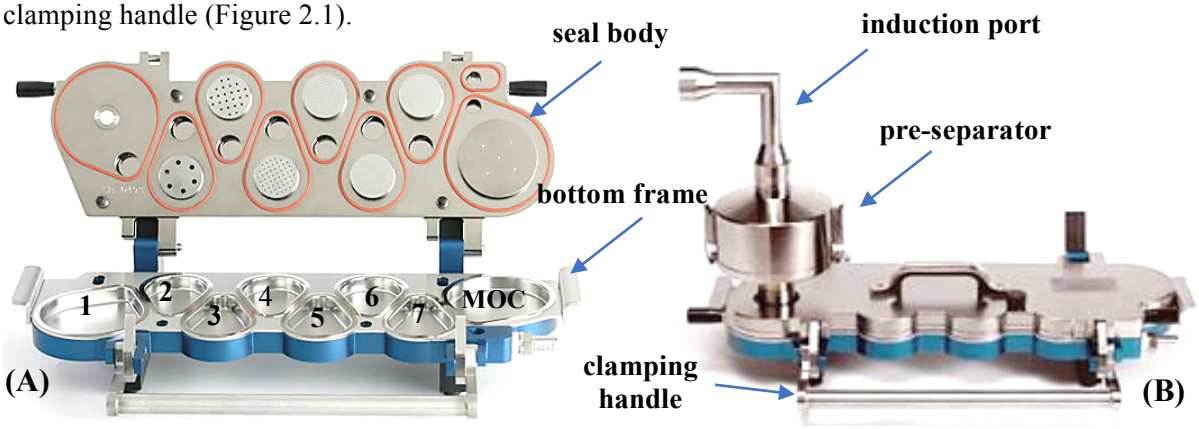

Figure 2.1: NGI in open view (A) and closed view (B) (adapted from www.copleyscientific.com)

The central cup of the pre-separator insert was filled with 15 mL of solvent used for HPLC (DMSO: methanol (1:1) for amphotericin B nanocomplexes and methanol for rifampicin and ibuprofen co-encapsulated liposomes). The pre-separator was then closed by clamping the two side clutches together and subsequently placed onto the port of the first stage as seen in Figure 2.1B. This was then connected to a stainless steel 90° induction port which was connected to the mouthpiece and inhalation device Cyclohaler®.

The vacuum pump (Model HCP5, Copley Instruments, UK) that was attached to the outlet of the NGI was switched on and was modulated to achieve an air flow of 60 L/min which was well within the accepted pharmacopoeial limits of 30-100 L/min. This flow rate was confirmed using an efficient flow meter model DFM2000 (Copley Scientific, UK). An actuation time of 4 s controlled by a timer on the critical flow controller was chosen to match the pharmacopeial standard, to achieve 4 L in a normal adult [314]. After this was set, the induction port was connected to a mouthpiece adapter and was attached to a Cyclohaler® (also known as the Aerolizer®, Pharmacemie, UK) containing filled capsules. The capsule was pierced, and without leaving the pins of the Cyclohaler® it was placed into the mouthpiece adapter. The timer was instantly put on when the pins were released and perforations on the capsule allowed discharge of the dry powder formulation during actuation.

The stage classifications and dilutions are as given in Table 2.1 below:

Table 2.1: Table showing NGI stage differentiations and cut-off diameters at 60 L/min

Stage	NGI components	Cut-off diameter (µm)	Dilutions (mL)
X	Capsules	-	10
A	Cyclohaler® + Mouthpiece adapter	-	50
B	Induction port	-	25
C	Pre-separator	-	50
1	Stage 1	8.06	10
2	Stage 2	4.46	10
3	Stage 3	2.82	10
4	Stage 4	1.66	10
5	Stage 5	0.94	10
6	Stage 6	0.55	10
7	Stage 7	0.34	10
8	Micro orifice collector +75mm filter	0.14	10

After the experiment, each stage was rinsed with the HPLC solvent (DMSO: methanol (1:1) for amphotericin B nanocomplexes and methanol for rifampicin and ibuprofen co-encapsulated liposomes), placed in separate volumetric flasks and appropriate dilutions performed (taking into consideration the Beer-Lambert linearity range for each drug, Table 2.1) to detect the concentration of drug(s) at each stage of the NGI after experimentation using HPLC.

Calculations were performed to determine the aerosol parameters as follows:

Emitted dose (ED)- expressed as a percentage; is the total mass of drug that exited the capsule and was impacted into the NGI from stage A to stage 8 over the total average mass of drug loaded into the capsules. It can be expressed as equation 2.2:

$$ED\ (\%) = \frac{Amount\ of\ drug\ recovered\ from\ stage\ A\ to\ 8}{Amount\ of\ drug\ recovered\ from\ stage\ X\ to\ 8} \times 100$$

Equation 2.2

Fraction recovered (FR)- expressed as a percentage; is the total mass of drug aerosolized and recovered from stage X to 8, versus the total average mass of drug that was initially loaded into the capsules and aerosolized. It can be expressed as equation 2.3:

$$FR\ (\%) = \frac{Amount\ of\ drug\ recovered\ from\ stage\ \ X\ to\ 8}{Amount\ of\ drug\ theroetically\ aerosolized} \times 100$$

Equation 2.3

Fine Particle Fraction (**FPF**, expressed as a percentage) and **fine particle dose** (**FPD**, expressed in mg); is the total mass of drug impacted from stage 2 to stage 8 that is having an aerodynamic

diameter below 5 µm, versus the total sum of drug recovered from impaction on stage X to stage 8 of the NGI. Stage 2 had a cut-off diameter of 4.46 µm at an operational flow rate of 60 L/min (Table 2.1). FPF can be expressed as equation 2.4:

$$FPF\ (\%) = \frac{Amount\ of\ drug\ recovered\ from\ stage\ 2\ to\ stage\ 8}{Amount\ of\ drug\ recovered\ from\ stage\ X\ to\ 8} \times 100$$

Equation 2.4

Each measurement was performed in triplicates and reported as mean ±SD.

Mass median aerodynamic diameter (MMAD)- expressed in µm; is defined as the median particle diameter i.e. diameter at which 50% of the particles are smaller and 50% are larger by mass, deposited within the NGI.

Geometric standard deviation (GSD)- measures the spread of the mass median aerodynamic particle size distribution, calculated as the square root of the aerodynamic diameter at the 84.13th percentile ($d_{84.13}$) over the 15.87th percentile ($d_{15.87}$) of the aerosol mass. It can be expressed as equation 2.5:

$$GSD = \sqrt{\frac{d_{84.13}}{d_{15.87}}}$$

Equation 2.5

The MMAD and GSD of the formulations were determined using the plot of cumulative mass distributions versus the logarithm of aerodynamic diameter, on the MMAD calculator (www.mmadcalculator.com), which follows recommendations by the ISO 27427:2013 Nebulizing Systems and Components.

2.7 High-performance liquid chromatography (HPLC)

The drug content of formulations after encapsulation and spray drying, and the amount of drug deposited at each stage of the NGI was determined with an HPLC using Agilent 1260 infinity series (Agilent Technologies UK Ltd., UK). The specific methods for drug elution and detection are outlined in the individual chapters. The analytical method development and validation were in accordance with the International Conference on Harmonisation (ICH) guideline Q2(R1): Validation of Analytical Procedures: Text and Methodology.

Analytical method validation

HPLC method developed for the determination of amphotericin B, rifampicin, ibuprofen, CNB001 or curcumin, was validated for linearity, accuracy, and precision, to ascertain that the method adopted was unbiased and without error.

Linearity: Linearity of an analytical method can be defined by the Beer-Lambert law, as a mathematical relationship where absorbance is directly proportional to the concentration of

analyte in a sample within a definite range of study [315]. Beer-Lambert law of linear regression operates over a range of diluted analytes and it should be kept in mind that deviation from linearity can be observed when the sample is too concentrated or below the limit of quantification (LOQ). Hence, the range of interest for each drug was set in accordance with the Beer-Lambert law of linear regression.

A standard curve (calibration curve) was constructed for each sample analysis in triplicate using the same method of HPLC analysis as that intended for the formulations. Peak area as an average of 5 replicates was used to derive the standard equation and correlation coefficient (R^2) of the best fit line, by least square regression method. This standard equation was then considered linear if the R^2 value was approximately 1 and used for calculation of the concentration of drug in the respective nano-formulations and for determination of the fraction of drug retained at each stage of the NGI.

Accuracy*:* Accuracy can be referred to as closeness of agreement of an individual observation or an average of a set of observations, i.e. the 'measured value' to the conventional 'true value' or an accepted reference value [316,317]. The 'true value' considered in the calculation of accuracy is the result that would be expected in an absence of error, i.e. random or systemic errors related to the test procedure and result [315]. Accuracy in intraday and inter-day analysis was determined by 9 determinations over a minimum of 3 different concentrations covering a specified range with low, medium and high concentrations of drug within the range. The accuracy obtained is represented as % bias or % relative error (i.e. error from the added theoretical concentration) and can be defined as the percentage agreement, calculated from equation 2.6, and a value of <15% for all concentrations was considered as acceptable [318,319]:

$$Relative\ error\ (\%) = \frac{True\ value - measured\ value}{True\ value} \times 100$$

Equation 2.6

Precision: Precision is the extent of variation (percent coefficient of variance) or closeness in agreement of a series of measurements obtained by multiple sampling of a single sample under similar conditions of analysis [316,320]. It helps to analyze random errors in intra and inter-day analysis. It can be subdivided into two aspects namely reproducibility and repeatability by determination of the coefficient of variance (CV) or the relative standard deviation (RSD) (from the true precision) for the analysis. The RSD or CV expressed as a percentage can be calculated using the equation 2.7:

$$RSD\ or\ CV\ (\%) = \frac{standard\ deviation}{mean} \times 100$$

Equation 2.7

2.8 Statistical analysis

The values were calculated as an average of three separate repeats and presented as mean±SD. Comparison of groups was undertaken using One-way Analysis of Variance (ANOVA) Tukey post-hoc test using the software OriginPro 8 SR0 v8.0724. Repeated Measures One-way ANOVA (rANOVA) Tukey post-hoc was used to compare different groups measured at multiple time points to see changes to the response as a whole. This was studied using the software IBM SPSS Statistics v24.0. A p value of less than 0.05 was considered significant for both the statistical tests.

3

CHAPTER 3

Preparation and characterization of spray-dried inhalable microparticles of co-ground solubilized amphotericin B nanocomplexes

3.1 Introduction

3.1.1 Pulmonary fungal infections

Pulmonary fungal infections can be categorized as endemic infections affecting both immunocompetent and immunocompromised patients, or opportunistic infections which can specifically affect immunocompromised patients. Opportunistic infections have steadily increased over the past few decades owing to ever-growing risk factors such as human immunodeficiency virus (HIV), solid organ or haematopoietic cell transplant and haematological malignancy, leading to immune suppression and increased susceptibility to fungal infections.

Invasive pulmonary aspergillosis being a highly opportunistic life-threatening infection affects immunocompromised patients the most, however, over the previous years an increase rate of infection has been seen in immunocompetent patients, patients with COPD on corticosteroid therapy and critically ill patients diagnosed with invasive pulmonary aspergillosis. Review of literature for the invasive aspergillosis infection in 1941 patients demonstrated that about 70% of infections involved the pulmonary tract, wherein, patients with malignancies and HIV were most likely to develop invasive pulmonary aspergillosis [55,321]. Pulmonary candidiasis is another serious fungal infection, which mostly challenges immunocompromised patients and has seen an increase in incidence over the past years. However, the diagnosis of pulmonary candidiasis can be difficult as normal human flora has the presence of *Candida spp*, and hence the mortality rate associated with pulmonary candidiasis is alarmingly high, especially in patients with malignancies [322–324]. Current pulmonary fungal infections and their treatment strategies have been outlined in Table 3.1, which indicates the importance of use of amphotericin B as a broad spectrum antifungal agent in clinical practice.

Table 3.1: Current treatment strategies for lung fungal infections (amphotericin B formulations in bold) [56,57,323,325,326]

Pulmonary Infection	First-line treatment	Second-line treatment
Opportunistic infections		
Aspergillosis	Voriconazole 4 mg/kg bid IV	**Lipid amphotericin B** (Abelcet® /Amphocil®/ AmBisome®) 5 mg/kg/d IV
Cryptococcosis	Severe or immunocompromised patients: **Lipid amphotericin B** (Abelcet®/Amphocil®/AmBisome®), 3-5 mg/kg/d IV + flucytosine 25 mg/kg/qid oral	**Amphotericin B deoxycholate** (Fungizone®) 0.7-1 mg/kg/d IV + flucytosine 25 mg/kg/qid oral
Candidiasis	Echinocandin caspofungin 70mg/d or Fluconazole (12 mg/kg/d) IV or oral	**Lipid amphotericin B** (Abelcet®/Amphocil®/ AmBisome®) 3-5 mg/kg/d IV
Mucormycosis	**Lipid amphotericin B** (Abelcet®/Amphocil®/AmBisome®), 5 mg/kg/d or more IV	**Amphotericin B deoxycholate** (Fungizone®) 1 mg/kg/d IV + Echinocandin
Endemic infections		
Histoplasmosis	Severe or immunocompromised patients: **Lipid amphotericin B** (Abelcet®/Amphocil®/AmBisome®) 3-5 mg/kg/d IV	**Amphotericin B deoxycholate** (Fungizone®) 0.7-1 mg/kg/d IV until stable then Itraconazole 200 mg bid oral
Blastomycosis	Severe or immunocompromised patients: **Lipid amphotericin B** (Abelcet®/Amphocil®/AmBisome®) 3-5 mg/kg/d IV	**Amphotericin B deoxycholate** (Fungizone®) 0.7-1 mg/kg/d IV until stable then Itraconazole 200 mg bid oral
Coccidioidomycosis	Severe or immunocompromised patients: **Lipid amphotericin B** (Abelcet®/Amphocil®/AmBisome®) 3-5 mg/kg/d IV	**Amphotericin B deoxycholate** (Fungizone®) 0.7-1 mg/kg/d IV until stable then Itraconazole 200 mg bid oral

3.1.2 Amphotericin B: The 'gold' standard treatment and its shortcoming

Despite the advent of other antifungal drugs, for over 50 years since its first clinical experience and approval around 1966 as a deoxycholate complex (Fungizone®), amphotericin B a macrocyclic polyene antifungal has been regarded as the 'gold standard' for the management and treatment of varied fungal infections, due its broad spectrum of activity and low rate of fungal resistance [327,328]. Fungal resistance to amphotericin B by *Candida albicans* has been reported only *in vitro*, however, no such resistance has been noted during clinical use of the drug to any fungal species [327]. Hence this polyene antibiotic is still the first choice of treatment for serious life-threatening fungal infections

Amphotericin B (Figure 3.1 and Table 3.2) a zwitterionic amphiphile, is very poorly absorbed following oral administration wherein peak serum levels of only 0.04-0.05 µg/mL were observed on administration of 1.6-5 g/day [327].

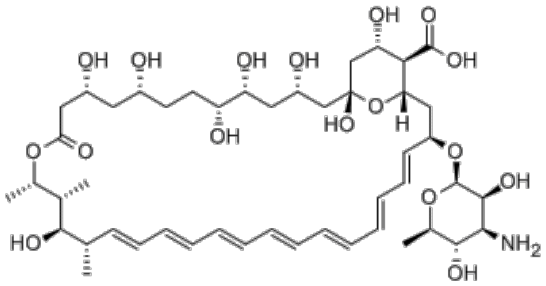

Figure 3.1: Structure of amphotericin B

Table 3.2: Physicochemical properties of amphotericin B

Molecular formula	$C_{47}H_{73}NO_{17}$
pKa	5.5
Molecular weight	924.091 g/mol
Solubility	Practically insoluble in water, ethanol, toluene and ether Soluble in dimethylformamide and DMSO

Numerous studies to alter the oral dosage regimen of amphotericin B have been carried out with no progress, and hence to date treatment of pulmonary and systemic fungal infections have been restricted to the parenteral route. Owing to its poor water and organic solvent solubility, being classified as BCS Class IV compound (low solubility and permeability), a more soluble form of amphotericin B needs to be parenterally administered, and hence Fungizone® also known as 'conventional form of amphotericin B' has been used over the years [329]. The parenteral route of administration, however, has several limitations, the most serious being life-threatening hyperkalemia, inducing arrhythmias, which has been observed with rapid amphotericin B infusion requiring slow infusion rates [330]. Goodwin et al. reported 71% patients receiving amphotericin B (Fungizone®) IV infusion developed at least one infusion-related adverse effect including

nausea, fever, chills, thrombophlebitis and arthralgia [331]. Hence, efforts are being made to progressively utilize nanomedicine and develop other soluble forms of amphotericin B which might be better tolerated than the conventional form Fungizone®.

Other than infusion-related adverse effects, administration of amphotericin B as its deoxycholate salt has been greatly challenged by the issues of dose-limiting acute or chronic organ toxicity, especially nephrotoxicity. Amphotericin B selectively binds to ergosterol in the fungal cell membrane, forming pores ultimately leading to fungal death due to rapid leakage of monovalent ions like potassium, sodium and chloride. Moreover, amphotericin B also has an affinity to cholesterol in human host cell membrane, although less than its affinity to fungal cell membrane ergosterol. This non-selective binding to human cell membrane cholesterol leads to the formation of pores and hence its lethal effects on human cells [332,333].

The currently marketed nano-formulations of amphotericin B are outlined in Table 3.3.

Table 3.3: Marketed amphotericin B nano-formulations for treatment of fungal infections [334–336]

Formulation name, type and composition	Route of administe-ration and dose	Drawback	Cost and treatment outcomes(s)
Surfactant-based nano formulation **Fungizone® (colloidal system)** 50 mg Amphotericin B: 41 mg sodium deoxycholate Lyophilized powder forms micellar dispersion on reconstitution, however, on infusion in the blood, the CMC of deoxycholate is not reached and hence forms monomeric dissociates of amphotericin B	1-1.5 mg/kg IV infusion over 2-6 h (> 1.5 mg/kg is lethal dose)	Fever, chills, nausea, hypotension, tachypnea and nephrotoxicity which is the major dose-limiting factor	£3.88/ 50 mg vial Although Fungizone® is the cheapest and oldest amphotericin B formulation approved by FDA in 1966, the toxicity profile associated with this formulation has necessitated the need for development of less toxic amphotericin B formulations
Lipid-based nano formulation **Abelcet®/ Amphocil® (lipid complex)** Amphotericin B 1:1 lipid (DMPC: DMPG 7:3) >250 nm ribbon-like structure, 1.6–11 µm **Amphotec® (colloidal lipid dispersion)** Amphotericin B 1:1 sodium cholesteryl sulphate, 122 nm x 4 nm colloidal disc-shaped particles	5 mg/kg IV infusion over 2 h (allows fast infusion) 3-4 mg/kg IV infusion at a rate of 1 mg/kg/h	Fever, chills, nausea and vomiting	£77.50/ 20 mL vial Abelcet® and £63.58/ 100 mg vial Amphotec®, FDA 1995 and 1996 respectively Targeting to the mononuclear phagocytes helps in selective transfer of the amphotericin B lipid complex to the fungal wall and hence minimal uptake in human cells
Liposomes **AmBisome® (Unilamellar liposomes)** Amphotericin B 50 mg encapsulated in hydrogenated soy PC: Chol: DSPG (2:0.8:1 molar) spherical 60-70 nm	3-5 mg/kg IV infusion over 1-2 h (allows fast infusion)	IV infusion of AmBisome® leads to fever, chills, nausea and diarrhoea	£82.19/ 50 mg vial, FDA 1997 The negative charge on the liposome helps in uptake into the mononuclear phagocytes, and hence a direct transfer onto the fungal wall leading to minimal association and toxicity with human cells. A comparative double-blind study compared to Fungizone and Abelcet® showed that AmBisome® is significantly less nephrotoxic than the other formulations

Nephrotoxicity is a major concern especially when the treatment group consists of immunocompromised patients. A study on severely immunocompromised patients treated with conventional amphotericin B for the management of suspected or proven aspergillosis, the kidney function declined indicated by the doubling of the creatinine levels for 53% of the patients. 14.5 % patients underwent dialysis, of which 76% patients died due to nephrotoxicity [337,338]. Increased renal failure and fatality due to amphotericin B nephrotoxicity have also been reported previously in other clinical studies [339,340]. Harbarth et al. evaluated the outcome of conventional amphotericin B treatment in a 9-year study involving 494 hospitalized patients. He concluded that nephrotoxicity was involved with a 2.7-fold higher fatality rate (p <0.001) [336,341]. Hence, although amphotericin B is considered a mainstay therapy for treatment of systemic fungal infections due to its broad spectrum of activity and lack of drug resistance, its clinical use is discouraged due to its low tolerability, especially in immunocompromised patients. Numerous strategies like dose reduction, alternative amphotericin dosing and intervals, saline loading and vigorous patient hydration, have been used to reduce the nephrotoxicity and infusion-related adverse effects of amphotericin B [329]. However, these did not reduce the undesirable tolerance profiles of the drug [329].

Replacement of Fungizone® with other amphotericin B formulations as shown in Table 3.3, has been found to significantly improve the tolerability of the formulation by reducing adverse effects. Comparative studies of lipid-based Abelcet® versus Fungizone® demonstrated a lower circulation amphotericin B serum concentration. It was observed that due to the large size (1.6-11 μm) of the discs, the complexes were readily uptaken by macrophages, and distributed to the liver, spleen and lung. An approximately 6.8 and 13.2-fold higher level of amphotericin B in the lungs as compared to AmBisome® and Fungizone® respectively, revealed its prospect in use for treatment of pulmonary fungal infections [336]. Moreover, the complexes were more stable in plasma when compared to Fungizone® and released amphotericin B from the lipid complexes at sites where activated host inflammatory cells or invading fungal cells released phospholipases [342]. Owing to this, free amphotericin B was not available in the bloodstream reducing the chances of toxicity to human cells. Further pharmacokinetic studies suggesting that Abelcet® acts as a depot for amphotericin B release, limiting its exposure to human cells hence improving the toxicity profile of amphotericin B [336,343,344].

Liposomal amphotericin B AmBisome® owing to the small size (60-70 nm) and high negative surface charge has been shown to establish a much higher Cmax of 83 ± 35.2 μg/mL as compared to the Cmax of Fungizone® 1.5–2.9 μg/mL or Abelcet® 1.7 μg/mL. This is due to its ability to avoid initial substantial recognition and uptake by the macrophages on infusion. Moreover, the pharmacokinetic profile of amphotericin B is altered wherein slow release from the liposomes and prevention of uncontrollable drug leakage reduces the chances of host cell interactions and hence reduces the toxicity of amphotericin B [336]. Clinical trial studies have demonstrated that liposomal amphotericin B is at least as or better tolerated than other lipid-based amphotericin B

formulations and significantly better tolerated than conventional amphotericin B [330]. Furthermore, a significantly better clinical efficacy in HIV patients infected with moderate to severe disseminated histoplasmosis owing to its lower clearance and higher Cmax, showed its superiority in treatment of systemic fungal infections [330].

However, clinical use of lipid-based amphotericin B nano-formulations are limited by the high cost of these i.e. 24-40 times more than conventional amphotericin B. This along with other reasons such as requiring patient hospitalization and still prevalent adverse effects (to a lower extend with lipid based amphotericin B formulations) has limited their widespread clinical use suggesting progressive development of nano-formulations of amphotericin B is necessary.

3.1.3 Amphotericin B aerosolization

Treatment of pulmonary fungal infections may be tackled by using direct inhalation strategies instead of IV infusion, as it could help in overcoming the nephrotoxicity and infusion-related adverse effects of amphotericin B. Delivering high concentrations at the site of infection reducing the dose, increasing residence time of antimicrobial and eventually reducing toxicity along with costs, make direct aerosolization more practical. IV administration of the amphotericin B formulations at a 5 mg/kg/day dose has been shown to be insufficient for eradication of fungus from the lungs [345]. Gavaldà et al. studied the effect of nebulized versus IV infusion of Fungizone® and AmBisome® in immunosuppressed female Wistar rats. The study highlighted that aerosolized formulations significantly improved or at least prolonged survival rate, suggesting its usefulness for treatment of invasive pulmonary Aspergillosis [345]. Numerous pilot randomized trials and clinical trials to study the effect of nebulized amphotericin B formulations have been carried out and outlined in Table 3.4.

Table 3.4: Randomized clinical trials evaluating the use of aerosolized amphotericin B nano-formulations for treatment of fungal infections

Formulation	Side effects	Conclusion
Nebulized Fungizone® as prophylaxis [65]	Well tolerated with only a few mild side effects Severe bronchospasm observed requiring for withdrawal of prophylaxis in only one patient	Minimal systemic absorption of the drug was noticed hence no amphotericin B related nephrotoxicity recorded Treatment with nebulized amphotericin B was successful in preventing invasive aspergillosis
Nebulized Fungizone® as prophylaxis [346]	Well tolerated with no apparent toxicity in a 49-day follow-up study	Nebulization of 0.6 mg/kg/day of amphotericin B, there were no cases of invasive aspergillosis reported
Nebulized Fungizone® (25mg) versus nebulized Abelcet® (50 mg) [347,348]	Discontinuation of prophylactic treatment was more evident in patients administered Fungizone® as compared to Abelcet® due to adverse effects	Clinical efficacy of both the formulations was the same however, tolerance profile of Abelcet® was much better than Fungizone®
Nebulized Fungizone® (25mg) versus nebulized AmBisome® (50 mg) [349,350]	Tolerability data for both these formulations were similar wherein 2.9% patients were withdrawn from the treatment with nebulized AmBisome® and 4.1% for Fungizone® both due to bronchospasms	Minimal systemic absorption of the drug was noticed hence averts the risk of amphotericin B related nephrotoxicity The rate of aspergillus infection in patients receiving the formulations remained similar (10.2% for Fungizone®, 7.7% for AmBisome®)
Nebulized Fungizone® as prophylaxis [351]	No discontinuation of treatment was recorded	Significantly lower rate of invasive aspergillosis (IA) (2.5%=Fungizone®, 6.6%=placebo) and higher mortality in patients diagnosed with IA (66.6%=Fungizone®, 94.1%=placebo) was evident. Moreover, a higher overall survival rate at the end of a 4.6-year period (59%=Fungizone®, 42.4%=placebo)
Amphotericin B inhalation powder (ABIP) DSPC spray dried powder [206,207]	No changes in pulmonary functional markers was observed in contrast to 20% reduction in pulmonary function on aerosolization of other amphotericin B formulations	Minimal systemic amphotericin B was observed on inhalation of dry powders containing high doses of amphotericin B up to 25 mg in clinical human studies (amphotericin B dose 50% w/w of dry powder)

3.1.4 Excipients used in study

Ascorbic acid-2-glucoside

Ascorbic acid and ascorbic acid-2-glucoside (AA2g, Figure 3.2) have been FDA approved for intravenous administration as an anti-scorbutic agent and for intradermal applications like skin lightening and UV protection. However, ascorbic acid is unstable to thermal and oxidative degradation under normal culture conditions of 37°C and in the presence of aqueous solutions. For this reason, a more stable, safe, physiologically active derivative of ascorbic acid i.e. ascorbic acid-2-glucoside was used for solubilization of the antifungal drug amphotericin B [352].

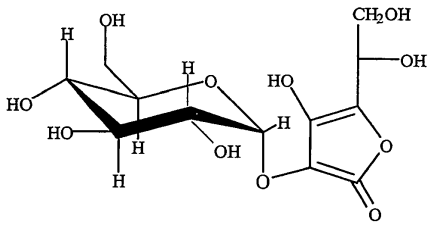

Figure 3.2: Structure of ascorbic acid-2-glucoside

Lactose

Lactose (Lactohale® LH300) is a common sugar approved by the Food and Drug Administration as an excipient to improve the aerosolization of powder as it imparts roughness to the surface of the particles when added to the feedstock prior to spray drying, leading to a reduction in adhesive forces between particles, consequently increasing aerosolization of powder [353,354]. During the process of spray drying, low product yield is a major disadvantage as the particles are sucked by the airflow and get trapped in the filter, hence are not collected [355]. This is of chief concern for expensive drugs. Moreover, an elevated temperature used during the process tends to be detrimental for temperature-sensitive drugs [355]. An attractive approach to overcome these shortcomings is to co-spray dry the drug-excipient systems with carriers such as lactose, glucose, sucrose etc. to provide protection to the drugs and improve yield [355].

L-leucine

L-leucine used as a dispersibility enhancer has been attributed to increase fine particle fraction for many drugs like salbutamol sulphate, disodium chromoglycate, dapsone and budesonide [356–361]. Incorporation of L-leucine leads to decrease in surface energy of the particles, an increase in geometric particle diameter leading to significant decrease in particle surface area and density due to the formation of hollow spheres consequently increasing aerosolization [361]. Along with dispersibility enhancement, L-leucine can also protect the spray dried powders from moisture absorption [362]. This is of advantage for amorphous spray dried microparticles which are likely to absorb atmospheric moisture, causing aggregation due to recrystallization and capillary forces [362].

3.2 Aims and Objectives

Amphotericin B is poorly soluble in all aqueous solvents and a few organic solvents because of its zwitterionic and amphiphilic nature, and asymmetrical distribution of hydrophobic and hydrophilic groups [334]. This leads to aggregation in aqueous solutions, which has been reported to be the cause of toxicity and low membrane permeability resulting in limited oral absorption of amphotericin B [236].

Hence, the aim of the study was

- To engineer nanocomplexes for the delivery of hydrophobic drug amphotericin B by co-grinding with antioxidant ascorbic acid-2-glucoside
- To design and develop dry powder aerosols and study parameters that dictate aerosolization efficiency
- To investigate the effect of the formulation parameters on the *in vitro* antifungal activity against *Candida spp* namely *Candida albicans* and *Candida tropicalis*

3.3 Materials

Amphotericin B ≥ 95% purity (HPLC grade) was purchased from Cayman chemical (Michigan, USA), ascorbic acid-2-glucoside (AA2g) was a gift from Aston chemicals (Aylesbury, UK), L-leucine ≥ 98.0% purity (TLC grade) and HPLC grade ethylenediaminetetraacetic acid disodium salt (EDTA-Na_2) were purchased from Sigma-Aldrich (Poole, UK) and lactose (Lactohale® LH300) was purchased from Friesland Foods Domo (Zwolle, Netherlands).

For the NGI, silicon oil (high temperature) was obtained from Sigma-Aldrich (Poole, UK) and 75 mm internal micro-orifice collector (MOC) filter was purchased from Copley Scientific (Nottingham, UK).

Candida albicans and *Candida tropicalis* were purchased from ATCC (England, UK) and AM3 broth was purchased from BioMérieux (Basingstoke, UK) for *in vitro* antifungal studies.

HPLC grade acetonitrile, water, n-hexane were purchased from Fisher Scientific (Loughborough, UK). Deionized water was used throughout the experiments. All other reagents used were of analytical grade.

3.4 Methods

3.4.1 Solubilization enhancement and preparation of respirable powders

3.4.1.1 Solubility enhancement of amphotericin B

Solubility enhancement of amphotericin B was studied by co-grinding at different molar ratios with AA2g in a mortar with a pestle for 10 min at room temperature (Table 3.5). 10 mL of deionized water was then added to the ground mixture to make a solution, which was passed through a 0.22 µm mixed cellulose esters syringe-driven filter (Millex MP, Ireland) to remove the unsolubilized amphotericin B. The solubility of amphotericin B at the different molar ratios to solubilization agent AA2g was investigated using the HPLC to determine the optimum stoichiometric ratio of drug and AA2g required to obtain maximum drug content of the nanocomplexes formed (section 3.4.2.2 and section 3.4.2.3). The stability of these nanocomplexes was investigated for their size and zeta potential using the Nano Zetasizer ZS (Malvern Instruments, UK) on storage at 25°C and 4-8°C on day 1, 6 and 10.

Table 3.5: Different molar ratio of drug (amphotericin B) to solubilizer (AA2g) for optimization studies

Formulation (molar ratio)	Amphotericin B (molecular weight 924.08) [mg]	AA2g (molecular weight 338.27) [mg]
Amphotericin B: AA2g **1:0.5**	46.25	8.46
Amphotericin B: AA2g **1:1**	46.31	16.91
Amphotericin B: AA2g **1:2**	46.21	33.83
Amphotericin B: AA2g **1:3**	46.27	50.74
Amphotericin B: AA2g **1:4**	46.39	67.65

The solutions were prepared based on the dosage indications of the marketed amphotericin B formulations for pulmonary aspergillosis which ranges from 0.5-0.7 mg/kg/day (35-49 mg/day) to 25-50 mg/day/twice a week as a nebulization or 25 mg/day as a dry powder inhalation (ABIP, Nektar therapeutics) for treatment of pulmonary aspergillosis, depending on the patients cardio-renal function and pathogenesis status of fungal infection [306,307,345,363,364].

3.4.1.2 Preparation of dry powders suitable for inhalation

Considering the latest application trends in the industry for pharmaceutical formulations and nanotechnology, dry powder inhalation wherein particle size in the micrometer range for effective peripheral pulmonary delivery was intended. Dry powders for inhalation were prepared by spray drying, carried out on a lab-scale Büchi B-90 Nano spray dryer (Büchi Labortechnik, Switzerland). The final optimized process parameters are given in Table 3.6.

Table 3.6: Process parameters for spray drying on the Buchi B-90 Nano spray dryer

Parameters	Value
Inlet temperature	120 °C
Outlet temperature	82-85 °C
Aspiration	100 %
Pump flow rate	20 mL/h
Gas flow rate	133 L/h
Instrument pressure	47 mbar
Nozzle mesh size	5.5 µm

The spray dryer was set up for the stated inlet temperature and neat solvent was pumped until the desired outlet temperature between 82-85°C was achieved and stabilized, after which spraying was commenced. All the solutions were spray dried individually and the instrument temperature was allowed to cool below 60°C, after which the powder was collected from the electrostatic particle chamber using a collecting brush. The yield of the

final product was determined gravimetrically and the powder was immediately transferred to a glass vial and stored in a desiccator to prevent powder crystallization due to absorption of environmental moisture.

A parallel spray drying process with different processing parameters was performed using lab-scale Büchi B-290 Mini spray dryer (Büchi Labortechnik, Switzerland) to compare the difference in yield of the microparticles obtained. The final optimized process parameters are given in Table 3.7.

Table 3.7: Process parameters for spray drying on the Buchi B-290 Mini spray dryer

Parameters	Value
Inlet temperature	120 °C
Outlet temperature	62-65 °C
Aspiration	80%
Pump flow rate	20% (6 mL/min)
Spraying gas flow rate	500 L/h (50 bar)
Drying gas flow rate	35 m^3/h
Nozzle tip diameter	0.7 mm

3.4.2 Formulation characterization

3.4.2.1 Determination of particle size and zeta potential (surface charge) using Malvern Zetasizer

The hydrodynamic diameter and the polydispersity index (PDI) of the nanocomplexes were measured by DLS and the zeta potential was measured by laser Doppler velocimetry using Malvern Zetasizer Nano ZS (Malvern Instruments Inc., UK) as described in chapter 2, section 2.1.

3.4.2.2 High-performance liquid chromatography (HPLC) and analytical method validation for determination of amphotericin B

The drug content of amphotericin B after co-grinding and spray drying, and the amount of amphotericin B deposited on each stage of the NGI was determined using HPLC on an Agilent 1260 infinity series HPLC (Agilent Technologies UK Ltd., UK), equipped with an ultrasensitive diode array UV detector, G1329A autosampler and a highly efficient quaternary pump. A number of methods for HPLC analysis of amphotericin B have been described previously [365–368]. For this experiment, a new, rapid, sensitive, precise and accurate method was developed, which gave reproducible results, separation of retention between amphotericin B and AA2g, and chromatograms with sharp peaks and a stable baseline.

Briefly, 20 µL samples were eluted with a mobile phase flow rate at 1.3 mL/min comprising 0.25 M disodium EDTA in HPLC grade water: HPLC grade acetonitrile using a gradient elution as shown in Table 3.8.

Table 3.8: Time programming of the gradient elution tested to determine amphotericin B by HPLC

Time (min)	0.25 M disodium EDTA in water (%v/v)	Acetonitrile (%v/v)
0	67	33
3.25	55	45
4.25	55	45
5.00	67	33
6.00	67	33

Elution was performed using an Agilent 15 cm×4.6 mm, 3.5 µm Eclipse Plus C_{18} column (Agilent Technologies, Chesire, UK) with UV detection wavelength of 405 nm and column compartment temperature of 40°C. The HPLC method developed for determination of amphotericin B was validated for linearity, accuracy and precision; to ascertain that the method adopted was robust and without error. The validation method based on ICH recommendations is described in Chapter 2 for HPLC analytical validation, section 2.7.

A standard curve (calibration curve) was constructed for amphotericin B before each sample analysis in triplicate using the same method of HPLC analysis as that intended for the formulations. Concentrations of amphotericin B for the standard were 1-12 µg/mL, and peak area as an average of the triplicates was used to derive the standard equation and correlation coefficient (R^2) of the best fit line by least square regression method. This standard equation was then considered linear if the R^2 value was approximately 1 and used for calculation of content of amphotericin B in the nanocomplexes and for determination of the fraction of amphotericin B retained at each stage of the NGI.

3.4.2.3 Determination of drug content of the nanoparticulate solutions

Drug content of the formulations after co-grinding was determined using HPLC, to quantify the amount of amphotericin B solubilized at the different molar ratios. Dilutions of the formulation following removal of unsolubilized drug after syringe filtration (0.22 µm mixed cellulose esters syringe-driven filter (Millex MP, Ireland)) was performed by diluting to obtain 12 µg/mL of amphotericin B, considering 100% theoretical drug content, by dilution in DMSO: methanol (1:1) to obtain a solution concentration appropriate for HPLC measurement as per the Beer-Lambert linearity concept. The solutions were filtered into HPLC vials and quantified as described (section 3.4.2.2). The peak area for amphotericin B was used for calculation of the content of drug using

the linear regression equation from calibration curve with correlation coefficient 0.9988. It was expressed as a percentage using the following equation (Equation 3.1):

$$Drug\ content\ (\%) = \frac{Practical\ amphotericin\ B\ content\ by\ HPLC\ after\ co-grinding}{Theoretical\ amphotericin\ B\ content\ initially\ weighed} \times 100$$

Equation 3.1

3.4.2.4 Stability studies

Stability studies were performed on the co-ground formulations on aqueous re-dispersion to ascertain the stability of the nanocomplexes formed, and hence consequently the solubilization of amphotericin B at definite time intervals. These were performed on co-ground syringe-filtered formulations formed at different molar ratios of amphotericin B to AA2g which were stored at room temperature 25°C and at 4-8°C, wrapped in aluminium foil protected from light. The size and charge were determined using the Zetasizer Nano ZS (Malvern Instruments Inc., UK) and drug content was determined using HPLC (Agilent technologies, Chesire, UK) on day 1, 6 and 10 by filtering the respective formulation using a 0.22 μm mixed cellulose esters syringe-filter, to ensure that any dissociated amphotericin B from the nanocomplex was entrapped in the membrane of the filter and removed prior to analysis. This helps to verify the interaction capability and the strength of association of amphotericin B with AA2g over the period of study, also serving to ascertain the molar ratio of solubilizer to drug necessary to form stable nanocomplexes.

3.4.3 Powder characterization

3.4.3.1 Determination of yield following spray drying

The yield of spray dried microparticles was determined by gravimetry and calculated as a percentage by comparing the initial amount of compounds in the feedstock of formulation to the spray dried powder obtained after the process.

3.4.3.2 Determination of drug content of spray dried powders

The drug content of the spray dried powders was analyzed using HPLC (section 3.4.2.2). A known amount of spray dried powder in mg quantities (above 5 mg to achieve consistency in weighing and minimizing manual error) was weighed to approximately obtain 12 μg/mL of amphotericin B on appropriate dilution considering a 100% theoretical drug content of amphotericin B. The powder was weighed and dissolved in 100 mL of DMSO:methanol (1:1) using a vortex mixture and was further diluted approximately 40 times to obtain a solution concentration appropriate for HPLC measurement as per the Beer-Lambert linearity concept. The solutions were filtered into HPLC vials and determination was performed with the same method as that of HPLC calibration curve for amphotericin B (section 3.4.2.2). The peak area for amphotericin B was used for calculation of the content of drug using linear regression equation from calibration curve with R^2

of 0.9988. Drug content was expressed as a percentage using the following equation (Equation 3.2):

$$Drug\ content\ (\%) = \frac{Practical\ amphotericin\ B\ content\ by\ HPLC}{Theoretical\ amphotericin\ B\ content} \times 100$$

Equation 3.2

3.4.3.3 Laser diffraction particle size analysis

The particle size distributions of all the spray dried powders were analyzed using laser diffraction with a Sympatec HELOS particle size analyzer, on a RODOS/M particle dispenser fitted with a micro-dosing device ASPIROS/L (Sympatec GmbH, Clausthal-Zellerfeld, Germany) as outlined in chapter 2, section 2.5.

3.4.3.4 Morphology analysis using electron microscopy

The method used to explore the morphology of nanocomplexes in solution using the TEM and spray dried microparticles using the SEM is outlined in chapter 2, section 2.4.

3.4.3.5 X-Ray powder diffraction (XRPD)

The order of the molecules and hence crystallinity of individual raw materials, physically mixed powders, co-ground powders and the spray dried powders were determined at room temperature using wide angle X-ray diffraction. The method used is as mentioned in chapter 2, section 2.3.

3.4.3.6 Fourier transform infrared spectroscopy (FT-IR)

FT-IR of the spray dried, physically mixed and co-ground powders were determined to analyze the chemical interactions between the drug and the excipients of the respective formulations. The procedure followed is as mentioned in chapter 2, section 2.2. The spectrum for the co-ground/ spray dried powder was compared with drug, excipient, physical mixtures and co-ground powders at the same molar ratios to characterize the interactions in the co-ground/spray dried powders which consequently affects the solubilisation of amphotericin B.

3.4.3.7 *In vitro* aerosol deposition and aerodynamic behavior studies using the Next Generation Impactor

The aerosol parameters and deposition of spray dried microparticles at the different stages of the NGI were determined using the method described in chapter 2, section 2.6. In each experiment size 3 transparent gelatin capsules (Dr. T & T Health, UK) were filled manually with 30 ± 0.2 mg of spray dried microparticles and aerosolized using the Cyclohaler®. As per literature the dose of nebulized amphotericin B was 40-50 mg, hence, approximately 45 mg amphotericin B was used per analysis of NGI for powders by adjusting the number of capsules aerosolized.

3.4.3.8 *In vitro* antifungal assessment of amphotericin B nanocomplexes by MIC studies

The minimum inhibitory/fungicidal concentration (MIC) of amphotericin B, AA2g and the co-ground and spray dried formulations were determined by the broth dilution method in 96-well

microplates (BD biosciences Falcon™, UK). Two amphotericin B sensitive strains of *Candida* were used for the experiment namely *Candida albicans* and *Candida tropicalis*.

Preparation of inoculum: *Candida spp* were grown on a recovery media i.e. Sabouraud's dextrose agar at 37°C in ambient environment for 24-36 h until the yeast grew well on the agar bed. Fungal suspensions were prepared in phosphate buffer saline (PBS) by picking up a distinct colony of about 1 mm diameter from the agar bed and vigorously mixing it in PBS and vortexing to form a stable suspension. The suspension was diluted to obtain an optical density (OD) of 0.8 at 530 nm which corresponds to $1\text{-}5\times10^6$ CFU/mL, after which a 100 times dilution with non-synthetic broth Antibiotic Medium 3 (AM3) was performed to obtain $1\text{-}5\times10^4$ CFU/mL which was the final concentration used in the determination of MIC.

Preparation of test solution of amphotericin B: A final working concentration of 64 µg/mL of amphotericin B was prepared based on the MIC shown from previous studies. However, amphotericin B being a hydrophobic drug, the original stock solution was made 100 times more concentrated than the required working concentration in absolute DMSO and then diluted 100 times with AM3 broth to obtain the test solution with minimal acceptable amount of DMSO (less than 1% DMSO in the final test sample of amphotericin B).

Preparation of test solution of amphotericin B particles: Aqueous solutions in single strength AM3 broth of spray dried and co-ground powders were prepared as per the drug loading for each formulation to obtain a concentration of 64 µg/mL of amphotericin B in each of the test solutions. All the solutions were filtered through a 0.22 µm mixed cellulose esters syringe-filter (Millex, Ireland) to ensure that they were sterile.

Microplate preparation: Broth dilutions were performed serially in a 96-well plate to obtain concentrations ranging from 64 µg/mL to 0.006 µg/mL in a final volume of 50 µL in each well. To these wells 50 µL of the respective *Candida spp* (*Candida albicans* or *Candida tropicalis*) suspensions with $1\text{-}5\times10^4$ CFU/mL in AM3 broth were added into each well reducing the working concentration of the test solutions by 50% i.e. from 32 µg/mL to 0.003 µg/mL. A control well (column 12) containing 50 µL of drug-free AM3 broth and 50 µL of the same yeast suspension was prepared as a sterility control for the media and also to ascertain that the yeast grew appropriately in the experimental setup. The plates were then incubated with shaking at 33°C.

Reading results: The MIC endpoints for all the tested materials were read at 24 h and 48 h by visual inspection where no turbidity corresponded to inhibition of growth of the organism and hence was the minimum concentration of the test formulation required for inhibition of a respective strain of *Candida spp*.

3.5 Results and discussion

3.5.1 Rationale of study and solubilization of amphotericin B

In the preliminary study, 47 mg of amphotericin B was dispersed in 10 mL of deionized water. This suspension was passed through a 0.22 µm syringe filter. The undissolved amphotericin B was trapped in the mixed cellulose esters membrane of the filter and the filtrate obtained was clear and colorless as shown in Figure 3.3. The clear colorless filtrate indicates that amphotericin B had little or no solubility in deionized water. The filtrate gave no absorbance as evident by the absence of amphotericin B peak in the HPLC chromatogram at a retention time of 4.14 min measured at 405 nm, indicative of aggregation of hydrophobic amphotericin B in deionized water.

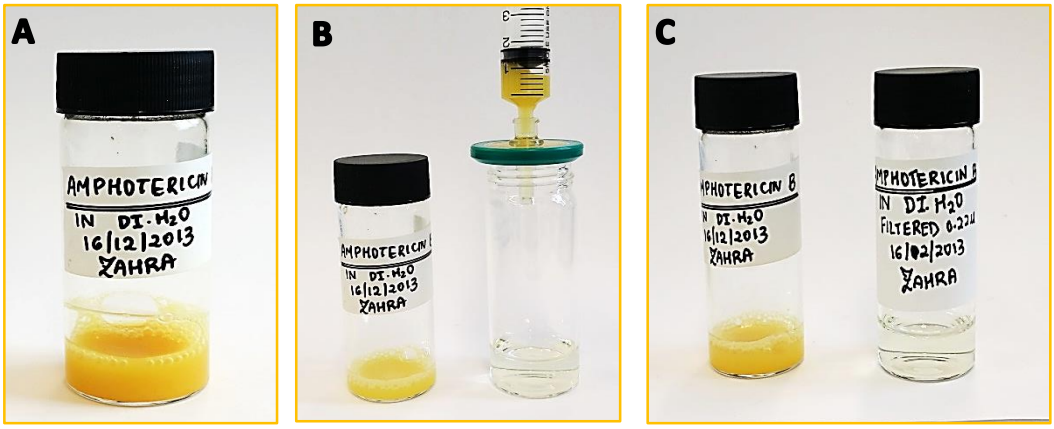

Figure 3.3: Lack of solubility of amphotericin B in deionized water
A) Dispersion of amphotericin B in deionized water
B) Dispersion of amphotericin B passing through 0.22 µm syringe filter
C) Colourless filtrate

A strategy to enhance the solubility of amphotericin B using solubilizing agent AA2g was investigated. Two different approaches were used. In the first approach, 47 mg of amphotericin B and 51 mg of AA2g were *mixed physically*, followed by vortexing the dispersion in 10 mL of deionized water. This was passed through a 0.22 µm syringe filter to obtain a clear and colorless filtrate, and absence of amphotericin B peak in the HPLC chromatogram was evident. This confirmed that physically mixing amphotericin B with solubilizing agent (AA2g) was not sufficient to improve aqueous solubility of the antifungal drug. This is as evident in Figure 3.4.

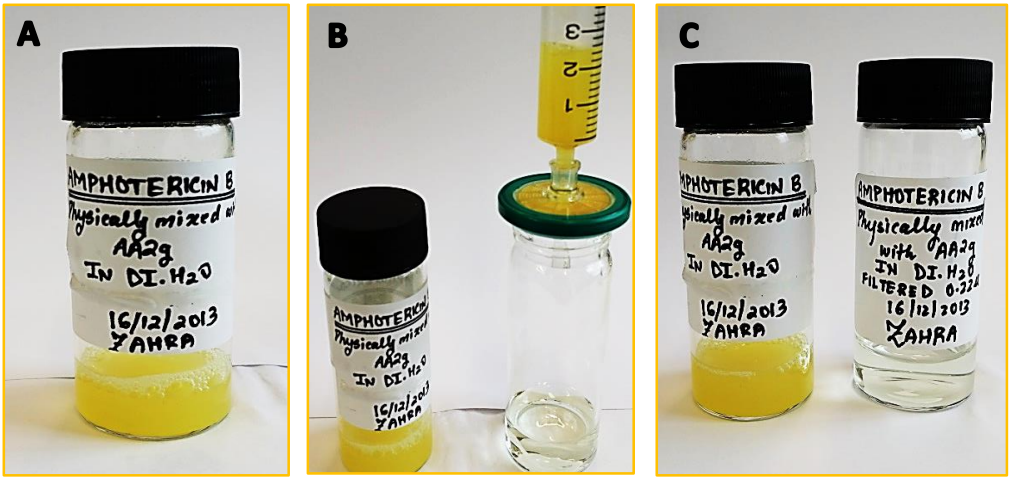

Figure 3.4: Lack of solubility of amphotericin B in deionized water when *physically mixed* with AA2g A) *Physical mixture* of amphotericin B and AA2g dispersed in deionized water
B) Dispersion of *physically mixed* amphotericin B and AA2g passing through 0.22 µm syringe filter
C) Colourless filtrate

The second strategy involved *co-grinding* together amphotericin B and AA2g. There was a difference in the appearance of the solution when the co-ground powder mixture was dispersed in water and filtered through a 0.22 µm syringe filter (Figure 3.5). The solution obtained was yellow in color and a peak corresponding to amphotericin B at 4.14 min was observed in the HPLC chromatogram. This shows that co-grinding of amphotericin B and AA2g is a crucial step to form stable nanocomplexes to achieve solubilization of the hydrophobic drug.

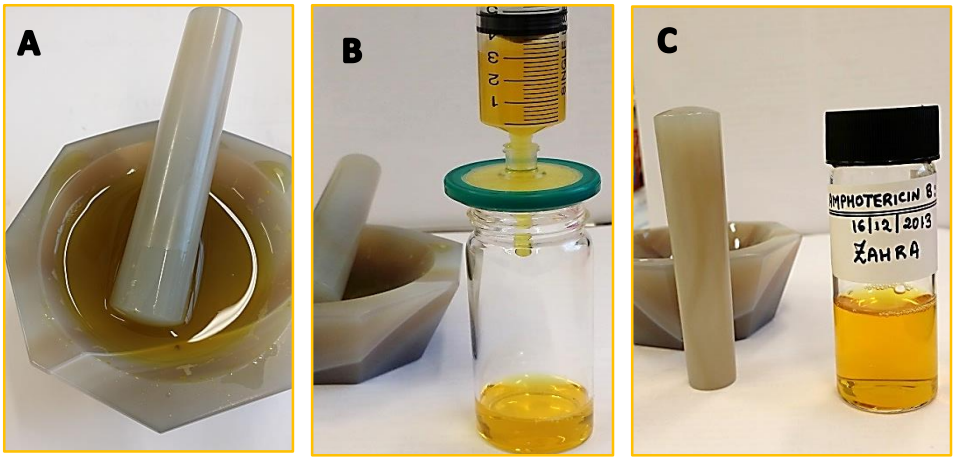

Figure 3.5: Solubilization of amphotericin B in deionized water when *co-ground* with AA2g
A) *Co-ground* mixture of amphotericin B and AA2g dispersed in deionized water
B) Dispersion of *co-ground* mixture of amphotericin B and AA2g passing through 0.22 µm syringe filter
C) Yellow coloured filtrate solution confirming the solubilization of amphotericin B

Solubilization of the hydrophobic drug clarithromycin by *co-grinding* and *physically mixing* with AA2g has been studied previously [369]. *Physically mixing* AA2g and clarithromycin at a molar ratio of 1:1 improved the wettability and solubility of clarithromycin, hence enhancing the drug solubilization by 80% [369]. On *co-grinding* with AA2g complete solubilization of clarithromycin was evident [369]. However, for solubilization of amphotericin B, *physically mixing* with AA2g was not sufficient for solubility enhancement and *co-grinding* was crucial for molecular interaction with AA2g to take place. Further studies to evaluate the interactions between amphotericin B and AA2g affecting solubilization has been explained in section 3.5.3.7.

3.5.2 Formulation characterization

3.5.2.1 Particle size and zeta potential (surface charge)

DLS was used to determine the mean hydrodynamic diameter (nm) and polydispersity index (PDI) of the nanocomplexes formed by co-grinding amphotericin B and AA2g at the different molar ratios. Figure 3.6A and Figure 3.6B shows the hydrodynamic diameter of nanocomplexes on day 1, 6 and 10 when stored at room temperature 25°C and in the fridge at 4-8°C respectively. A unimodal and sharp distribution was seen when measuring the size using DLS, indicative of a narrow distribution of nanocomplexes for all the molar ratios studied at each time interval. The hydrodynamic diameter of nanocomplexes formed on co-grinding decreases with increasing molar ratio of amphotericin B: AA2g. The lowest ratio of amphotericin B: AA2g being 1:0.5 shows mean diameters of 122±2.02 nm, whereas the highest ratio of amphotericin B: AA2g (1:4) shows a mean diameter of 110±1.82 nm on day 1, which implies that increasing the amount of AA2g for complexation of a constant amount of amphotericin B leads to formation of smaller size nanocomplexes. However, ANOVA/Tukey analysis depicts that the difference between the mean diameters of nanocomplexes on day 1 at the molar ratios 1:2, 1:3 and 1:4 is insignificant at a level of p is 0.05. Hence, from the molar ratio of 1:2 amphotericin B: AA2g onwards the nanocomplexes formed were stable with respect to mean diameter studied on day 1.

The PDI of the nanocomplexes (data not shown) were seen to increase from 0.24 to 0.33 with an increase in amount of AA2g which could be attributed to a higher loading of amphotericin B onto the complexes, wherein, the difference was only significant between ($p < 0.05$) complexes made with 1:0.5 amphotericin B: AA2g over 1:3 and 1:4 amphotericin B: AA2g. There was no significant difference ($p > 0.05$) in the PDI of the other formulations relative to each other.

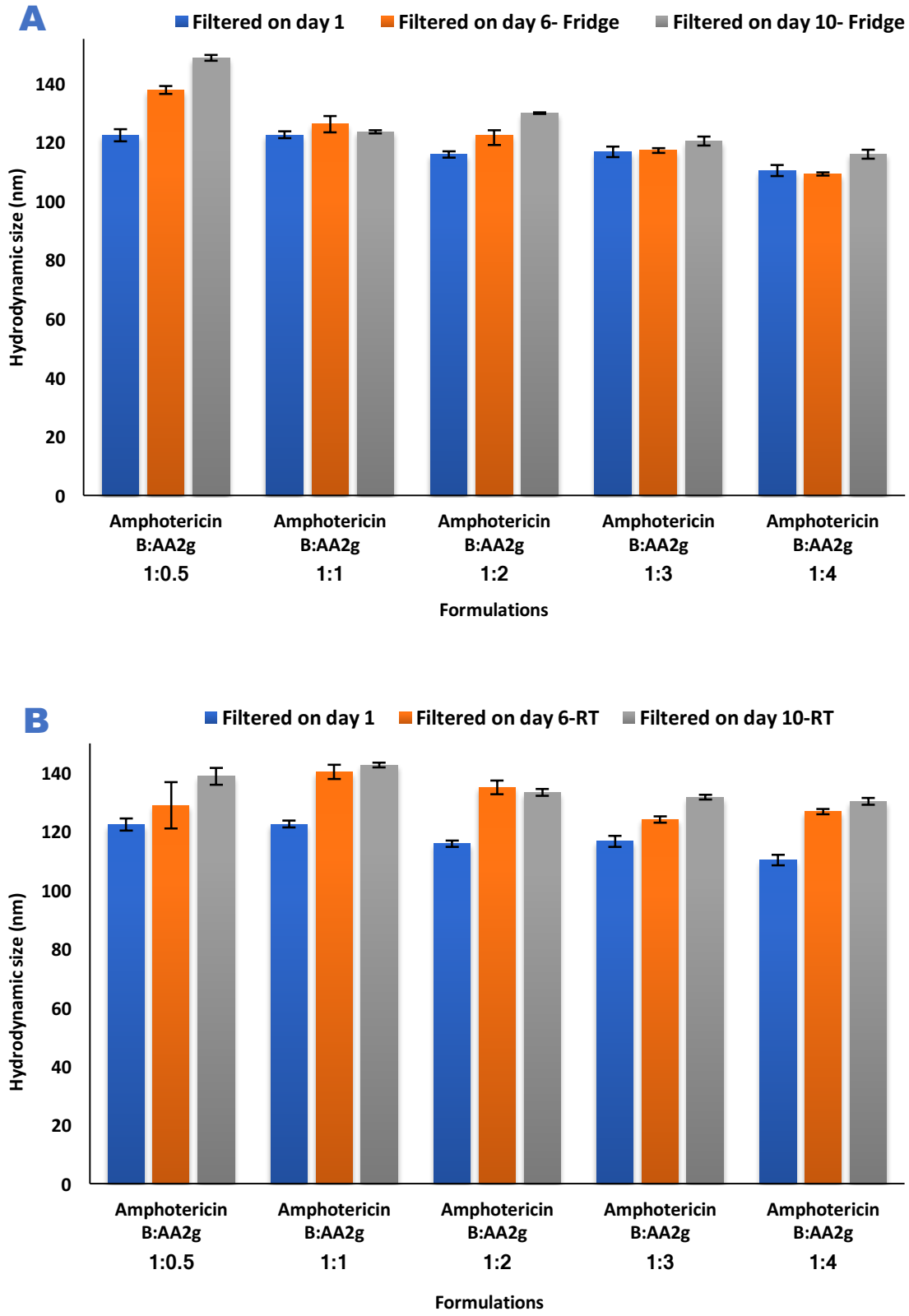

Figure 3.6: Hydrodynamic diameter (nm) of nanocomplexes formed at different molar ratios of amphotericin B: AA2g; (A) stored at 4-8°C and (B) stored at RT; (n=3, mean ± SD)

Nanocomplexes formed at a molar ratio of 1:0.5 amphotericin B: AA2g stored at 25°C and 4-8°C, and nanocomplexes formed at a molar ratio of 1:1 amphotericin B: AA2g stored at 25°C showed a significant difference ($p < 0.05$) in mean diameters on day 10 as compared to day 1. The other molar ratios namely 1:2, 1:3 and 1:4 amphotericin B: AA2g stored at 25°C and 4-8°C also showed a significant difference ($p < 0.05$) in mean diameters between the respective days under the duration of study. This suggested that storage conditions had an influence on the nanocomplex integrity with respect to mean diameter, hence, the aqueous nanocomplexes of 1:2 amphotericin B: AA2g were converted into dry powder microparticles by spray drying immediately after formulation.

Study of particle size of nanoparticles by light scattering formed by co-grinding clarithromycin and AA2g has been reported in literature. Co-grinding at a molar ratio of 2:1 clarithromycin: AA2g, the formation of nanoparticles with a size 280 nm was observed [369]. The process of co-grinding clarithromycin with AA2g was carried out in a vibration mill, whereas in the present study amphotericin B and AA2g were co-grounded manually in a mortar and pestle. Hence, the difference in the method of preparation adopted could lead to differences in mean diameter of the nanoparticles.

Zeta potential analysis of the nanocomplexes indicated a high positive surface charge of 20-30 mV on the nanoparticle surface as seen in Figure 3.7. The different molar ratios in the order of increasing AA2g showed a continuous significant ($p < 0.05$) increase in the positive charge on the nanoparticle surface, on day 1. This trend was evident due to an increase in the number of positive NH_2 groups on the amphotericin B molecule present, as a higher amount of amphotericin B was solubilized (Table 3.10) by increasing the amount of AA2g. Co-grinding clarithromycin and AA2g, a similar positive zeta potential of 25.2±1.5 mV, attributed to the positive charge on the nitrogen of dosamine of clarithromycin was evident in a previous study [369]. The electrostatic repulsion due to the high surface positive charge contributed to nanocomplex stability, which was evident by the insignificant reduction in amphotericin B drug content (Figure 3.9) on storage at 4-8°C

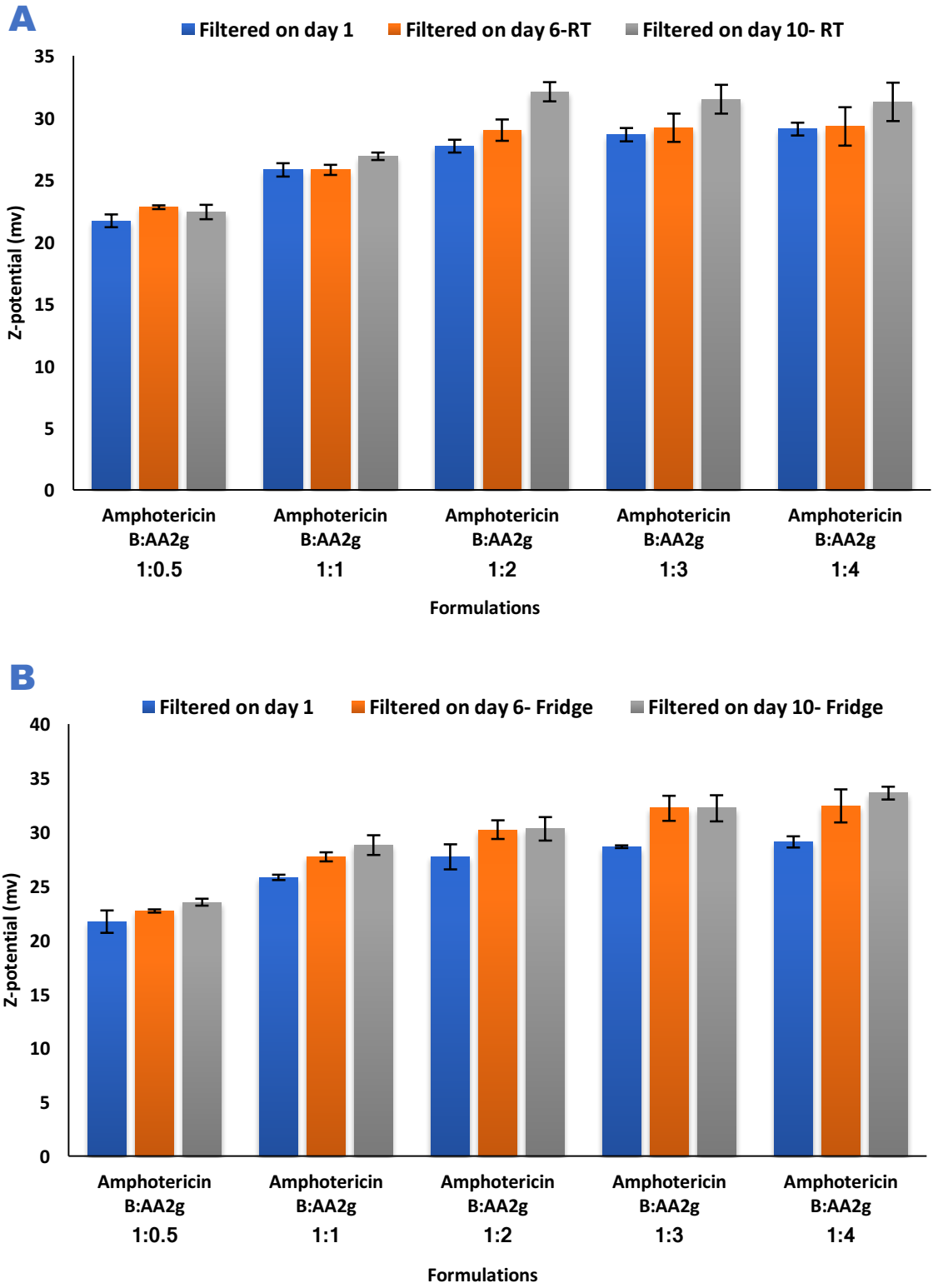

Figure 3.7: Zeta potential (mv) of nanocomplexes formed at different molar ratios of amphotericin B: AA2g; (A) stored at 25°C and (B) stored at 4-8°C; (n=3, mean ± SD)

3.5.2.2 High-performance liquid chromatography (HPLC) and analytical method validation for determination of amphotericin B

Linearity: The data for HPLC calibration curve of amphotericin B was fitted into an equation of *y=43.24x–2.859* (where x=concentration of analyte and y=area under curve), and was observed to follow linearity and hence Beer-Lambert law in the concentration range under study i.e.1-12 µg/mL as shown in Figure 3.8. A regression analysis was performed and correlation coefficient R^2 of 0.9988 indicated the existence of a linear relationship between peak area and concentration of drug analyzed.

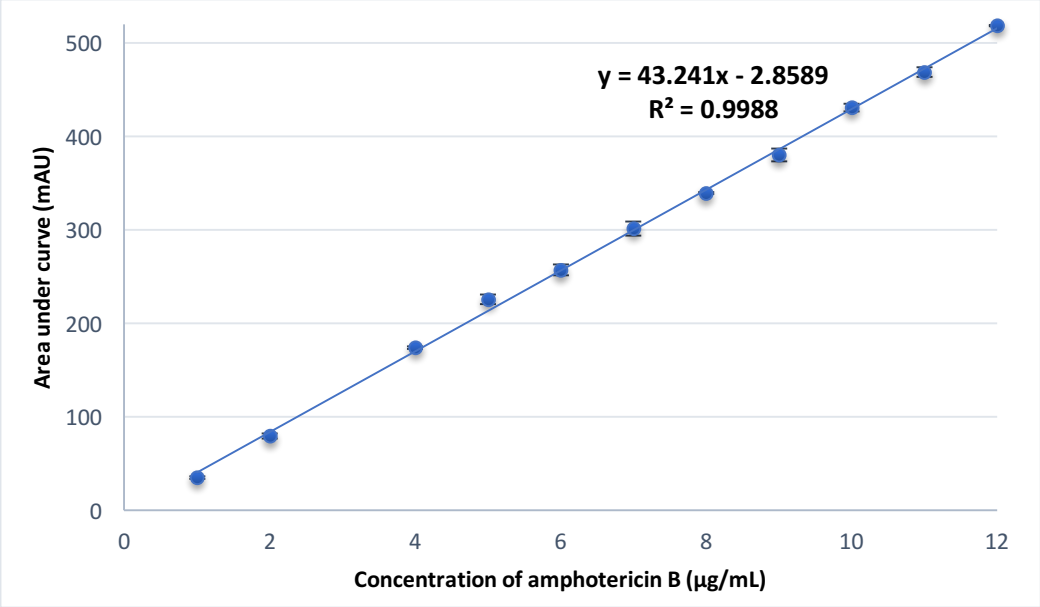

Figure 3.8: Calibration curve of amphotericin B analyzed by HPLC (mean±SD, n=5)

Parameters determining linearity from HPLC analysis for amphotericin B are shown in Table 3.9.

Table 3.9: Linearity parameters for HPLC analysis method of amphotericin B

Parameters	Results
λmax	405
Linearity range	1-12 µg/mL
Regression equation	y = 43.24x–2.859
Correlation coefficient	0.9988
Retention time	4.14 min

Representative chromatogram of amphotericin B and validation for accuracy and precision of HPLC method is as seen in Appendix 1, A1.1.

3.5.2.3 Amphotericin B drug solubilization in co-ground nanocomplexes

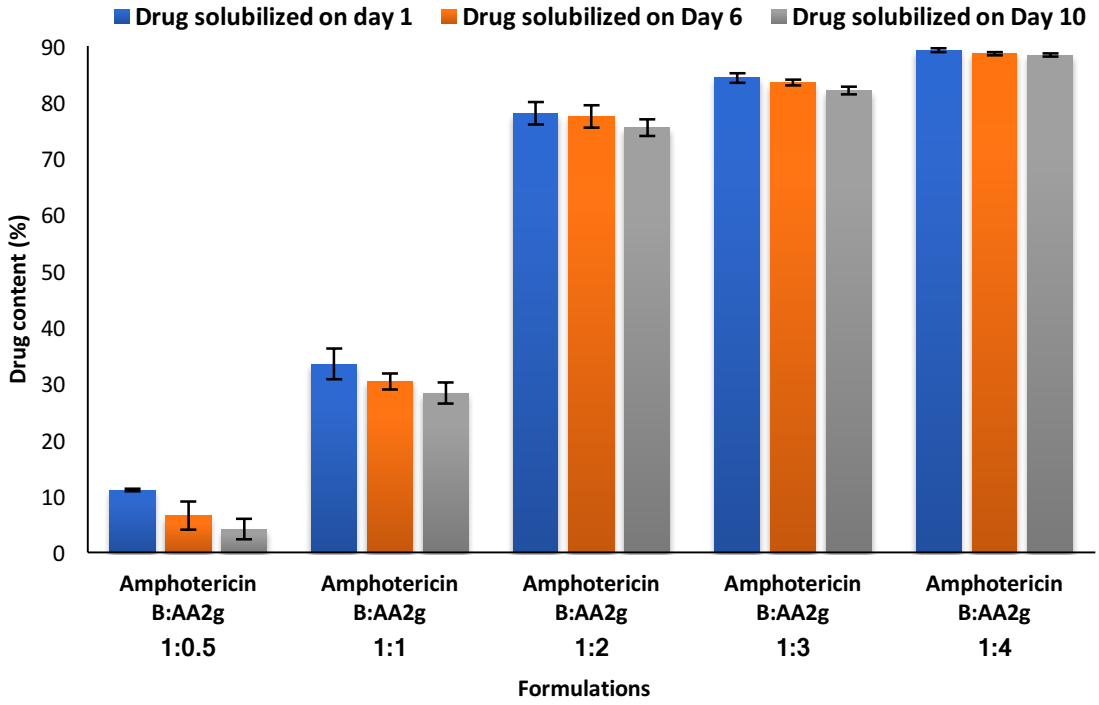

Figure 3.9: Amphotericin B drug content of co-ground formulations as determined by HPLC analysis (n=3, mean ± SD)

Stable nanocomplexes over a 10-day period of the study analyzed on storage at 4-8°C (Figure 3.9) depicted minimal loss in amphotericin B observed by HPLC analysis, showing that the complexes formed were stable. There was a significant increase ($p < 0.05$) in amphotericin B solubilization with an increasing amount of AA2g when the different molar ratios were compared on day 1, as seen in Table 3.10. On increasing the amount of AA2g to make nanocomplexes, there was an increase in OH groups of AA2g available for complexation to the NH_2 groups of amphotericin B, and consequently, a higher amount of amphotericin B was loaded in the nanocomplexes.

The drug content of amphotericin B was maximal for the nanocomplexes with molar ratio 1:2 amphotericin B: AA2g. This indicates that a molar ratio of 1:2 amphotericin B: AA2g is a perfect stoichiometry to form stable nanocomplexes and is the minimum molar ratio of amphotericin B: AA2g required to achieve high amphotericin B solubilization and content. Moreover, an increase in the stoichiometric molar ratio to 1:3 or 1:4 showed a significant decrease ($p < 0.05$) in amphotericin B content since there was an increase in the solubilization agent AA2g. Hence, a ratio of 1:2 amphotericin B: AA2g was chosen for further studies, so as to deliver more drug by reducing the amount of excipients in the formulation.

Table 3.10: Amphotericin B drug solubilization and drug content in co-ground nanocomplexes

Formulation (molar ratio)	Amphotericin B solubilization on day 1 (relative to the total amount of amphotericin B initially added, %)	Amphotericin B drug content on day 1 (relative to the total amount of amphotericin B and AA2g, %)
Amphotericin B: AA2g **1:0.5**	11.12 ± 0.20	37.81 ± 0.42
Amphotericin B: AA2g **1:1**	33.58 ± 2.72	47.86 ± 2.02
Amphotericin B: AA2g **1:2**	78.06 ± 2.00	51.60 ± 0.64
Amphotericin B: AA2g **1:3**	84.36 ± 0.89	43.48 ± 0.26
Amphotericin B: AA2g **1:4**	89.27 ± 0.33	37.97 ± 0.09

3.5.3 Powder characterization

3.5.3.1 Spray dried amphotericin B powder yields

The use of an electrostatic particle collector on the Büchi B-90 Nano spray dryer gave good yields of spray dried microparticles ranging from 69-76%. A similar experiment performed on the Büchi B-290 Mini spray dryer showed significantly lower ($p < 0.05$) yields for each of the powders with and without excipients, as shown in Table 3.11.

Table 3.11: Drug yields of spray dried microparticles (n=3; mean ± SD)

Spray dried powders	Prep weight (mg)	Weight of powders obtained after spray drying (mg)		Yield (%)	
		Büchi B-90	Büchi B-290	Büchi B-90	Büchi B-290
Amphotericin B: AA2g (1:2)	300	205.4 214.7 200.2	129.6 114.7 133.0	68.92 ± 2.45	41.92 ± 3.24
Amphotericin B: AA2g (1:2): L-Leucine	375	284.7 248.3 280.2	174.9 161.3 157.2	73.17 ± 3.76	43.85 ± 2.47
Amphotericin B: AA2g (1:2): lactose	600	444.1 467.0 453.9	388.1 353.8 397.4	75.83 ± 1.91	53.29 ± 3.82

The yield obtained on the B-290 for spray dried amphotericin B: AA2g without excipients was 41.92 ± 3.24%, of which only 10.21% was collected from the particle collector and the rest 31.71% was scraped from the cyclone walls; while it was 68.92 ± 2.45% for the B-90 collecting chamber. This could be attributed to the low density of powder formed which got lost in exhaust gases of the cyclone technology of the B-290. In the B-290 collection is dependent on the mass of the particles generated on spray drying leading to lower mass particles carried with the gas stream, and hence collected in the filter, not depositing in the collection chamber or cyclone. In

the B-90 spray drying is carried out using a piezoelectric driven droplet atomizing technology in conjunction with an electrostatic particle collector, where particles are deposited directly downwards without being dependent on mass or density. Hence, a higher yield was seen when Nano spray dryer B-90 was used for spray drying the formulations as compared to Mini spray dryer B-290.

3.5.3.2 Content of amphotericin B in spray dried powders

Table 3.12: Amphotericin B content (%) of the spray dried microparticles

Spray dried powders	Amphotericin B content before spray drying (%)	Amphotericin B content after spray drying (%)
Amphotericin B: AA2g	45.21 ± 4.13	42.80 ± 2.54
Amphotericin B: AA2g: L-leucine	35.10 ± 4.77	31.45 ± 1.73
Amphotericin B: AA2g: lactose	27.43 ± 3.20	21.04 ± 3.89

There was no significant loss ($p > 0.05$) of amphotericin B on spray drying as seen in Table 3.12.

3.5.3.3 Laser diffraction particle size analysis

Dv50 represents the volume median diameter (VMD) of particles, which corresponds to the diameter of particles where 50% distribution is above and below the said value of particle size, hence, displays average particle size taking into account the total powder volume selected randomly. A bar chart indicative of Dv50 values of all the powders studied at pressures 1, 2 and 4 bar are represented in Figure 3.10.

Figure 3.10A indicates that the size of nano spray dried amphotericin B microparticles were in the respirable range appropriate for deposition in the peripheral airways i.e. the Dv50 was in a range of 2.41-3.06 µm for spray dried microparticles of amphotericin B: AA2g (1:2) with and without excipients. *Aspergillus fumigatus* has been shown to deposit within the peripheral airways, and hence targeted delivery to the alveoli and bronchi using amphotericin B inhalation powder (ABIP, Nektar therapeutics) in clinical trials has been shown to be advantageous for treatment of invasive pulmonary aspergillosis, due to an aerodynamic size in the range of 2-5 µm [206].

The physically mixed powders of the same ratio of constituents as that of the spray dried showed significant difference ($p < 0.05$) in the size analyzed by laser diffraction, wherein the physically mixed powders were not in the respirable range of 2-5 µm. This indicates that spray drying is a crucial step required to engineer particles appropriate to deliver the drug to the peripheral airways where the fungal infection resides.

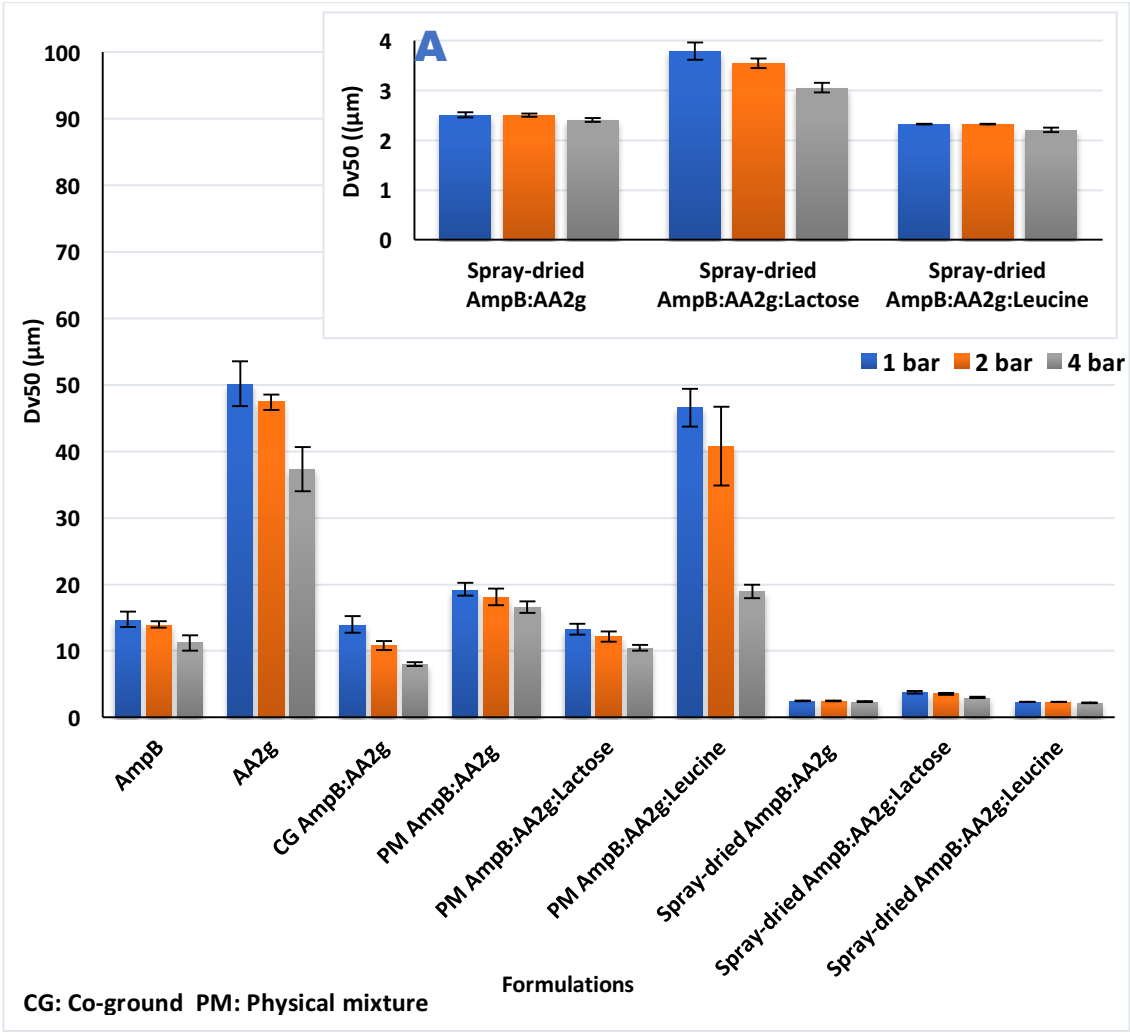

Figure 3.10: Effect of pressure on size analysis (Dv50) of spray dried, physically mixed and co-ground microparticles (Inset A: effect of pressure on size analysis of spray dried microparticles) (n=3, mean ± SD)

As seen in Figure 3.11, the particle size distribution of spray dried amphotericin B: AA2g was unimodal with particle size distribution well in the respirable range, whereas, the distribution profile of co-ground amphotericin B: AA2g was found to multimodal, with a wide size distribution of the co-ground microparticles making them sub-optimum to be delivered to the peripheral lung to target fungal infections.

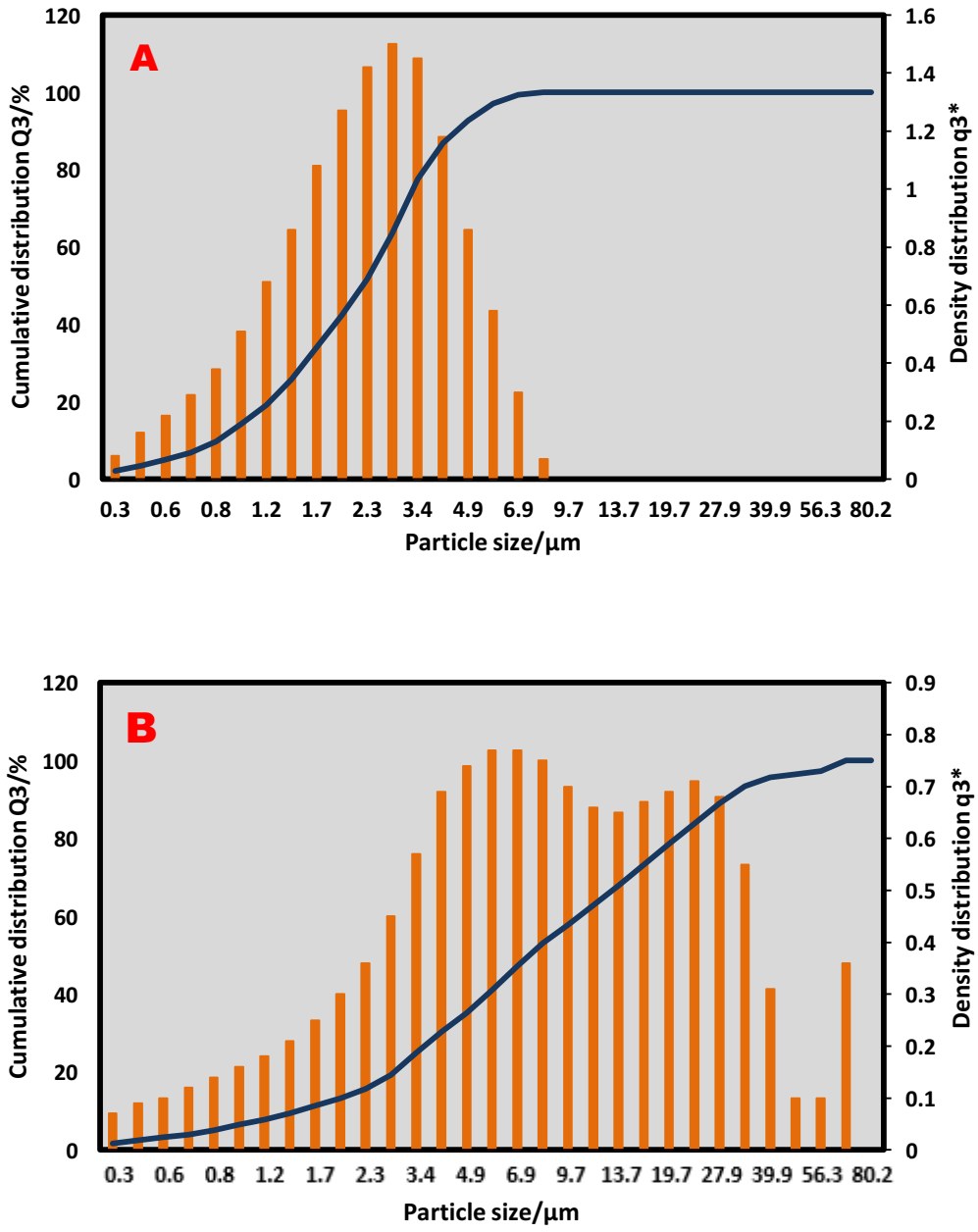

Figure 3.11: Particle size distribution of A) spray dried amphotericin B: AA2g B) co-ground amphotericin B: AA2g

As seen in Figure 3.12, the particle size distribution of spray dried amphotericin B: AA2g: L-leucine and spray dried amphotericin B: AA2g: lactose was shown to be unimodal with a particle size in the respirable range.

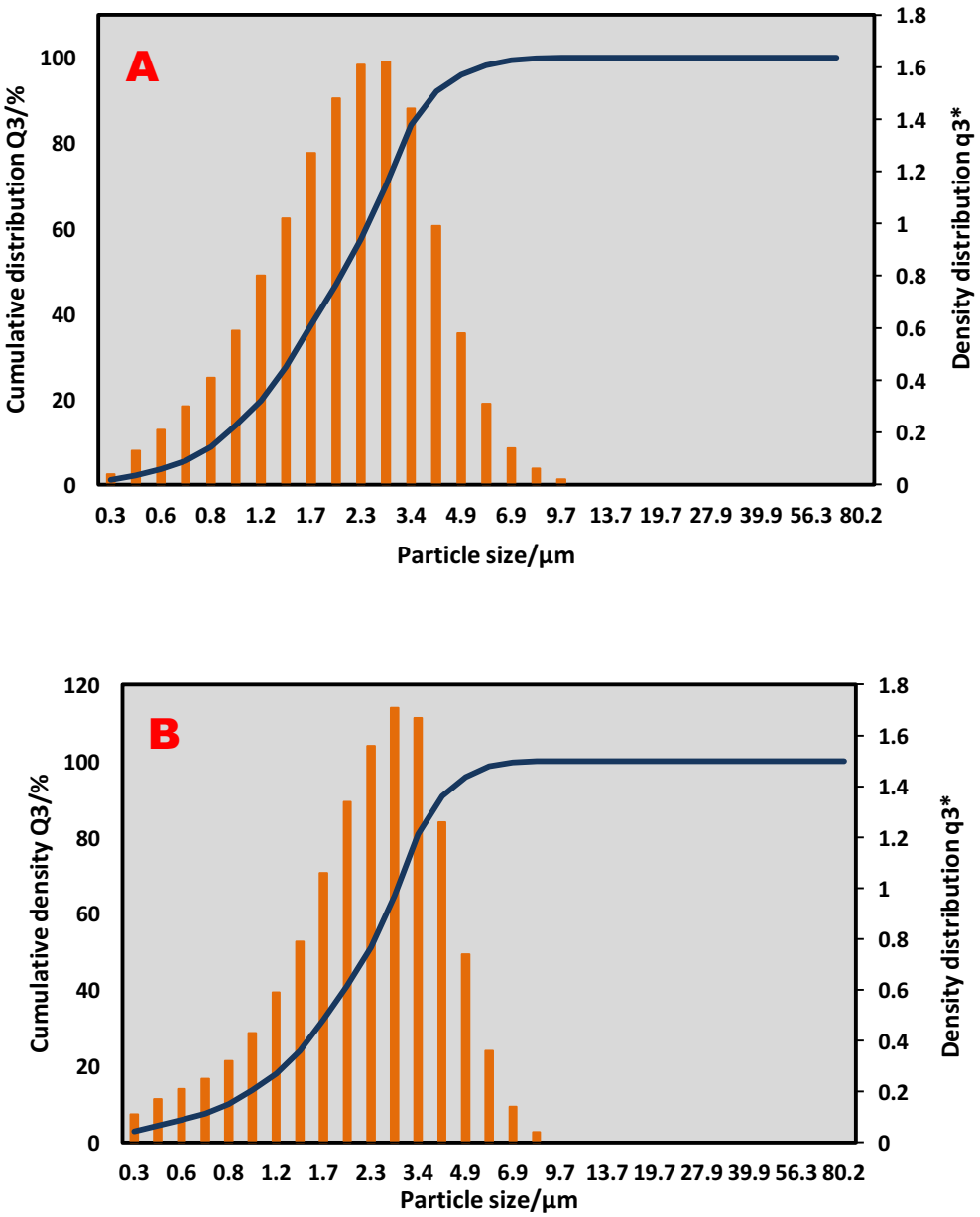

Figure 3.12: Particle size distribution of A) spray dried amphotericin B: AA2g: L-leucine B) spray dried amphotericin B: AA2g: lactose

Physically mixed powders, co-ground powders and raw materials showed a high Span value, significantly different ($p < 0.05$) when compared to the Span of spray dried microparticles, indicative of heterodisperse powders and multimodal distribution pattern as seen in Table 3.13. The data obtained are expressed in the terms of particle diameter at 10, 50 and 90% of volume distribution, as Dv10, Dv50 and Dv90 respectively.

Table 3.13: Laser particle size distribution data (Dv10, Dv50 and Dv90 are in units of µm) (n=3, mean ± SD)

Microparticles	4 bar			Span
	Dv_{10}	Dv_{50}	Dv_{90}	at 4 bar
Amphotericin B	2.32±0.67	12.03±2.07	31.4±4.90	2.42±0.06
Ascorbic acid-2-glucoside (AA2g)	5.62±2.06	36.97±2.99	79.27±0.43	2.00±0.22
Co-ground amphotericin B: AA2g	1.58±0.05	8.03±0.27	29.39±2.08	3.46±0.22
Physically mixed amphotericin B: AA2g	2.9±0.216	16.59±0.89	55.14±1.71	3.16±0.26
Spray dried amphotericin B: AA2g	0.91±0.01	2.41±0.04	4.87±0.08	1.65±0.02
Physically mixed amphotericin B: AA2g: lactose	2.35±0.06	10.52±0.43	27.9±1.93	2.43±0.08
Spray dried amphotericin B: AA2g: lactose	1.17±0.03	3.06±0.10	6.43±0.17	1.72±0.01
Physically mixed amphotericin B: AA2g: L-leucine	2.86±0.55	18.93±1.00	57.7±0.37	2.90±0.17
Spray dried amphotericin B: AA2g: L-leucine	0.93±0.02	2.21±0.04	4.22±0.09	1.49±0.01

Effect of pressure applied during measurement on the particle size distribution of spray dried, physically mixed and raw material microparticles

Choice of an optimum pressure for dispersion of particles is of crucial importance to achieve and read diffraction of primary particles from the agglomerated dry powder fed into the Sympatec. Very high pressures applied might fracture the primary particles, whereas low pressure applied may lead to inadequate segregation of the agglomerated particles, both resulting in erroneous results. For this purpose, three different pressures of 1, 2 and 4 bar were used on the Sympatec to compare the dependence of particle size analyzed on the pressure applied indicative of ease of dispersion from the inhalation device and hence a direct correlation on the patient-to-patient variation of dry powder size on inhalation. Patient to patient variation arises from the difference in age e.g. the force of inhalation for paediatric patients might be less as compared to adults; there might also be variations in the force of inhalation for diseased patients. These parameters would lead to dosage variations and hence effect end-point treatment. Hence, engineering particles that show a minimal patient-to-patient variation on inhalation and a low difference in the fine particle fraction and fine particle dose, dependent on patients' flow rate is desired.

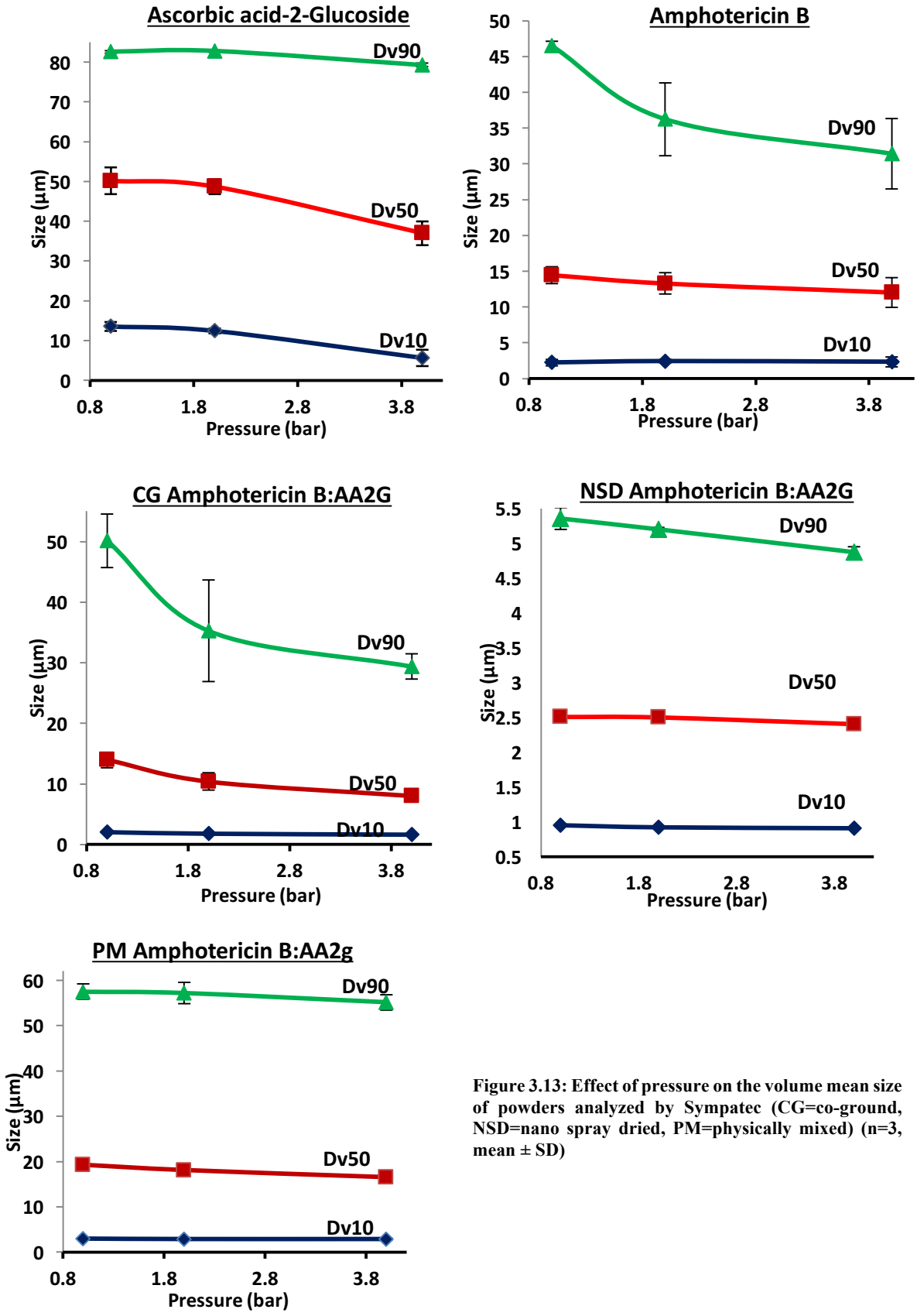

Figure 3.13: Effect of pressure on the volume mean size of powders analyzed by Sympatec (CG=co-ground, NSD=nano spray dried, PM=physically mixed) (n=3, mean ± SD)

As evident in Figure 3.13, the nano spray dried microparticles of amphotericin B: AA2g show no significant difference ($p < 0.05$) in the D10, Dv50 and Dv90 particle size at 1, 2 or 4 bar pressure, indicative of a pressure-independent analysis using laser diffraction. On the other hand, co-ground

amphotericin B: AA2g and raw materials amphotericin B and AA2g, showed a significant difference ($p < 0.05$) in particle size analyzed by laser diffraction at 1, 2 or 4 bar pressure, indicative of pressure-dependent analysis and consequently a potential patient-to-patient variation. This highlights the potential of spray dried amphotericin B: AA2g to be used as a successful dry powder aerosol to treat peripheral lung fungal infections.

However, laser diffraction results are based on the volume mean diameter i.e. the geometric diameter and not the aerodynamic diameter. It assumes that the particles are spherical when laser diffraction is applied, however, micronized co-ground, spray dried and raw material microparticles could show deviation from this spherical behavior, hence making it necessary to study the aerodynamic diameter (section 3.5.3.8) of the various powders [370].

3.5.3.4 Morphology analysis of spray dried microparticles by electron microscopy: Scanning electron microscope

SEM was performed on freshly prepared spray dried and co-ground powder samples stored in a desiccator at room temperature. The SEM micrographs were captured at different degrees of magnification to highlight the specific details of the particles.

SEM micrographs of raw material amphotericin B and AA2g (Figure 3.14) showed the presence of columnar irregular crystals stacked as blocks, with a wide size distribution. The crystallinity of the raw materials was confirmed by X-ray powder diffraction (Figure 3.19 and Figure 3.20). Particle sizes observed from these micrographs were in accordance to that obtained for the raw materials using laser diffraction (Figure 3.10). Due to an elongated flat shape, there is a larger contact area between the longitudinal surfaces of these columnar particles due to high surface energy, which is responsible for the cohesiveness and poor flowability subsequently leading to a poor aerosolization.

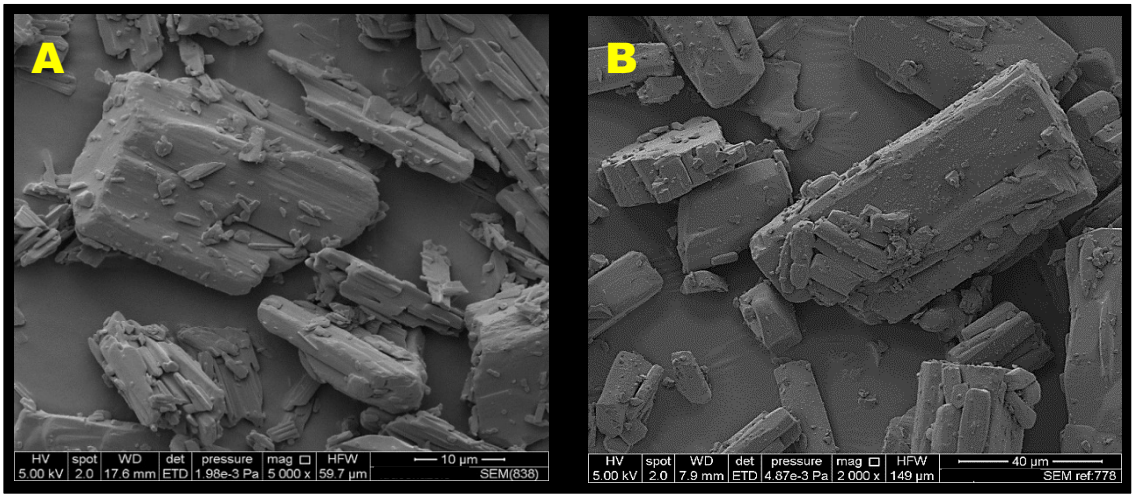

Figure 3.14: SEM micrographs of unprocessed raw materials (A) amphotericin B and (B) AA2g

SEM micrograph of co-ground and spray dried amphotericin B: AA2g- To study the effect of spray drying on microparticle morphology

As indicated in the SEM micrographs, co-ground (Figure 3.15A) and spray dried (Figure 3.15B) powders of amphotericin B: AA2g complexes differ not only in the surface morphology but also in the bulk morphology and particle size. The co-ground powder without excipients was aggregated into small clusters showing an irregular rough surface and shape (Figure 3.15A). The sheer and impact stress applied during the co-grinding process transformed the particles, and hence a change from complete crystalline columnar form of amphotericin B and AA2g to a less crystalline co-ground form confirmed by X-ray powder diffraction (Figure 3.21) was evident.

Spray drying of the amphotericin B: AA2g complexes lead to the formation of non-agglomerated and spherical microparticles (Figure 3.15B), indicative of an amorphous nature as confirmed by X-ray powder diffraction (Figure 3.22A). This spherical morphology of the microparticles decreases the contact area between the neighboring particles, decreasing interparticulate interactions, leading to greater flowability and consequently reduced cohesiveness. The SEM micrograph of spray dried amphotericin B: AA2g showed a narrow particle size distribution, with a particle size in good agreement with the size measured by laser diffraction analysis i.e. between 1-3 µm optimum for aerosolization to the peripheral lung (Figure 3.10).

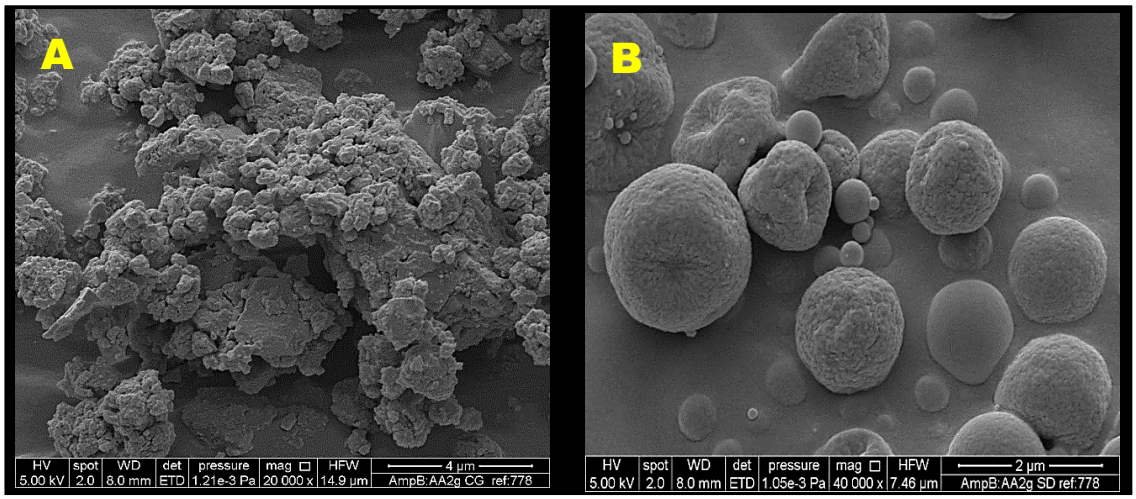

Figure 3.15: SEM micrographs of (A) co-ground amphotericin B: AA2g and (B) spray dried amphotericin B: AA2g

The slight presence of corrugations (roughness) on the particle surface of spray dried amphotericin B: AA2g can be explained examining the spray drying process. The liquid feed during the atomization phase, was sprayed through the nozzle of a 5.5 µm mesh in the form of fine droplets into the drying chamber, where it encountered hot gas at temperatures of about 90-120°C. When a co-current method is adopted, the droplets are subjected to the highest temperature in a moist state which leads to instant drying of the external surface of droplets. The temperature of the drying chamber gradually decreases due to this heat exchange needed to dry the external surface of droplet, and further drying takes place by the formation of holes to let go out the trapped

internal solvent. This leaves behind the dried solid with a size similar to the size of the atomized droplet. Previous literature has confirmed that a spray drying temperature of 110/74°C is responsible for greater degree of shrinkage and hence corrugations as compared to drying at higher temperatures [371].

SEM micrograph of spray dried amphotericin B: AA2g with excipients- To study the effect of spray drying with excipients on the particle morphology

To further increase the aerosolization and hence fine particle fraction of spray dried amphotericin B: AA2g, it was spray dried with excipients which would further decrease its cohesiveness. Numerous approaches have been implemented to engineer microparticles with improved dispersion and respirable powder performance. It was evident in literature that improvement of dispersibility and hence respirable fraction can be achieved by decreasing interparticulate interactions between the cohesive drug particles by incorporation of excipients in the spray drying feedstock [372,373].

L-leucine- Amphotericin B: AA2g was spray dried with amino acid L-leucine which has been shown to improve the aerosolization of powders as evident in previous literature [373–375]. The SEM micrographs of spray dried amphotericin B: AA2g with 25% mass fraction of L-leucine in Figure 3.16 shows the presence of fractured hollow surfaced spheres with curved plates of nanometric thickness. These have spaces which are capable of being filled and hence produce open powder structures which can encapsulate cohesive powders like amphotericin B and increase dispersibility (confirmed by NGI). This SEM micrograph was similar to that reported by various authors previously [372,373,361,376]. Incorporation of L-leucine leads to decrease in surface energy of the particles, an increase in geometric particle diameter leading to significant decrease in particle surface area and density due to the formation of hollow spheres consequently increasing aerosolization [361].

The effect of inlet temperature of the spray dryer also plays a major role in the morphology of particles containing L-leucine, wherein low temperatures of 100°C showed open structures (as evident from the micrograph) obtained by surface diffusion of L-leucine in its condensed phase and subsequent deposition on the surface of the powder at the air-water interface during spray drying. However at higher temperatures of 180- 200°C, sublimation of L-leucine occurs and gaseous L-leucine molecules directly transform into solid crystals and nucleate on the drug surface [375,357,356]. Hence, a proper control of temperature during spray drying plays a crucial role on the crystallization and consequently the aerosolization of powders containing L-leucine.

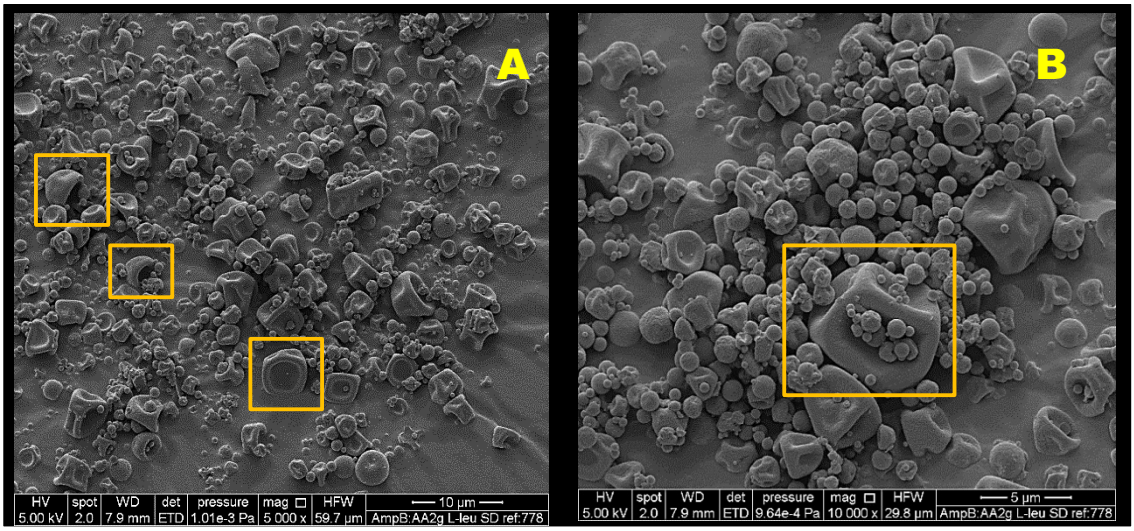

Figure 3.16: SEM micrographs of spray dried amphotericin B: AA2g with L-Leucine at different magnifications (Boxes indicate representatives of particle morphology)

Lactose- SEM micrographs of spray dried amphotericin B: AA2g with lactose (Figure 3.17) showed the formation of non-agglomerated, spherical, rough particles with a particle size in good agreement of that obtained by laser diffraction studies on the Sympatec (Figure 3.10).

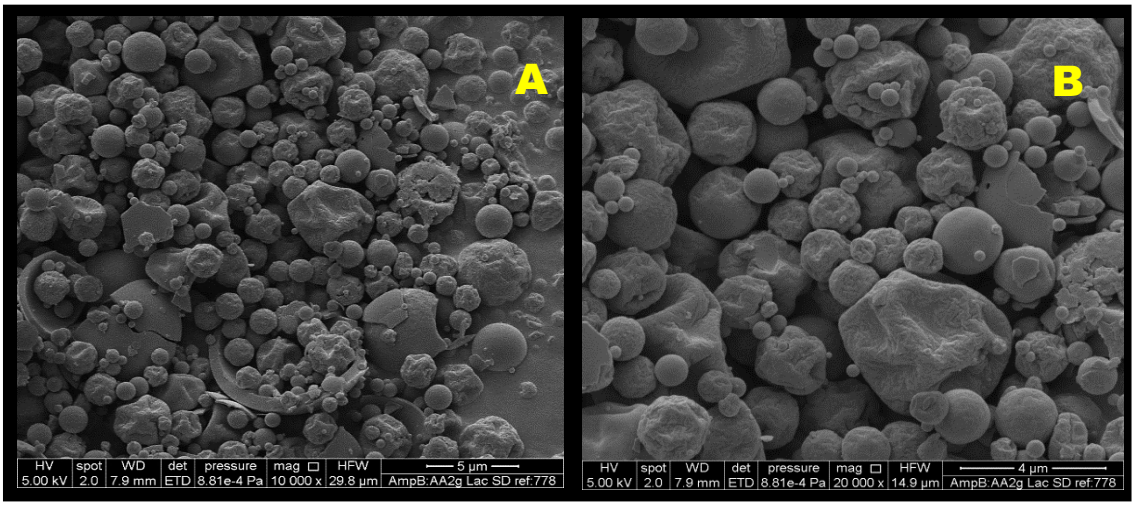

Figure 3.17: SEM micrographs of spray dried amphotericin B: AA2g with lactose at different magnifications

3.5.3.5 Morphology analysis of spray dried microparticles by electron microscopy: Transmission electron microscope

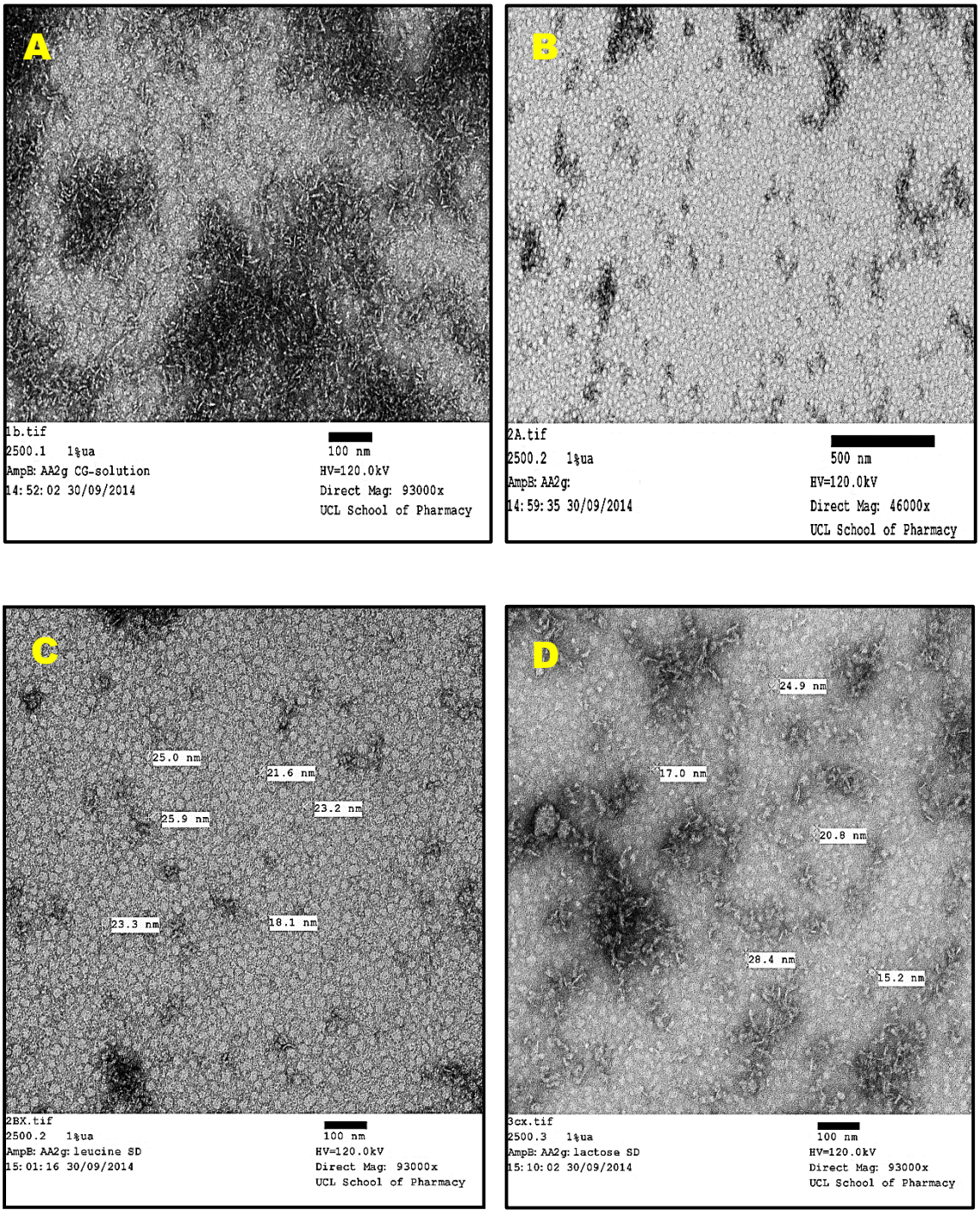

Figure 3.18: TEM micrographs of nanocomplexes; (A) co-ground amphotericin B: AA2g (1:2), (B) spray dried and re-dispersed amphotericin B: AA2g (1:2), (C) spray dried and re-dispersed amphotericin B: AA2g (1:2): L-leucine, (D) spray dried and re-dispersed amphotericin B: AA2g (1:2): lactose

The TEM micrographs for co-ground amphotericin B: AA2g nanocomplexes (Figure 3.18A), and re-dispersed spray dried amphotericin B: AA2g microparticles with and without L-leucine/lactose (Figure 3.18B, Figure 3.18C, Figure 3.18D), showed the presence of nanometric range of spherical particles. These images confirm that nanocomplexes were obtained on redispersion of

microparticles after spray drying, similar to the co-ground nanocomplexes, confirming maintenance of complexation and consequently solubilization of amphotericin B.

The particle size of the nanocomplexes as evident by the TEM micrographs was in the range of 18-25 nm, showing a unimodal and even distribution pattern. However, the particle size analyzed by laser diffraction using the Nano Zetasizer showed that the particle size was 115.86 ± 1.066 nm which was significantly ($p < 0.05$) different from that observed by electron microscopy. When nanocomplexes are analyzed by laser diffraction the size read is the hydrodynamic diameter, measured indirectly via a principle of photon correlation spectroscopy, and hence there could be a deviation between true size and hydrodynamic diameter observed. Previous literature studies have portrayed that when the nanoparticle size is very low (<30 nm) the particles have a tendency to absorb some of the laser light incident on them, instead of scattering it completely. Hence, the principle of dynamic light scattering used by the Zetasizer fails at this point and leads to a hydrodynamic diameter significantly larger than the actual size of dispersion [377]. Hence, for this reason, a more direct microscopic method like TEM would be of greater benefit to view the morphology, size and homogeneity of nanoparticles

3.5.3.6 Molecular order evaluation using X-ray powder diffraction

XRPD was performed on the raw materials amphotericin B and AA2g, co-ground amphotericin B: AA2g, physically mixed amphotericin B: AA2g and spray dried amphotericin B: AA2g with and without excipients. XRPD of crystalline compounds is detected by sharp characteristic peaks whereas those of amorphous compounds are indicated by simple halos above the baseline.

The XRPD diffractogram of marketed amphotericin B (Figure 3.19) exhibits sharp peaks at 2Θ values of 9.24, 13.85, 15.08, 17.04, 18.21 and 21.53 characteristic of untreated amphotericin B, which confirms the definite crystalline structure and identity of amphotericin B from previous literature [378,379]. The XRPD diffractogram of marketed AA2g (Figure 3.20) exhibits sharp peaks, characteristic of untreated AA2g which confirms the definite crystalline structure and identity of AA2g from previous literature studies [369].

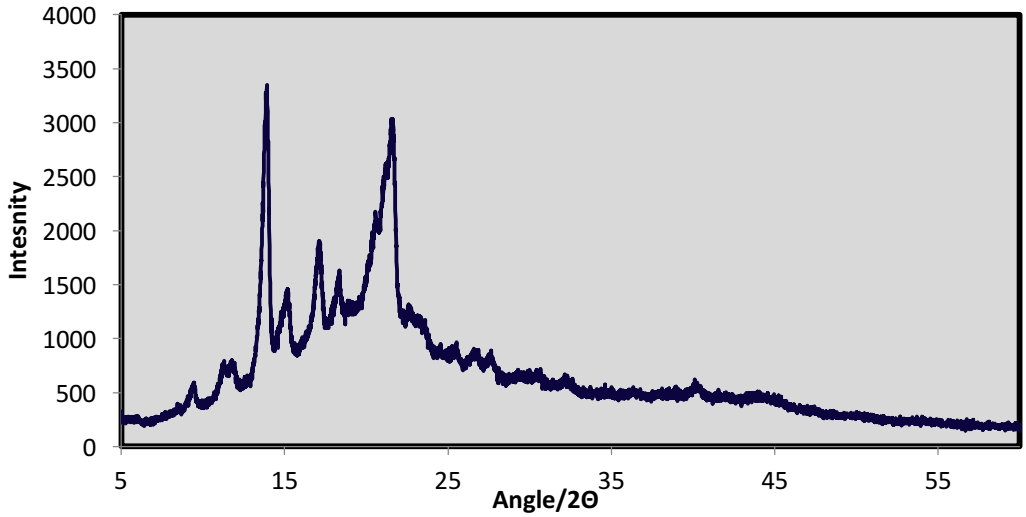

Figure 3.19: X-ray powder diffractogram of marketed amphotericin B

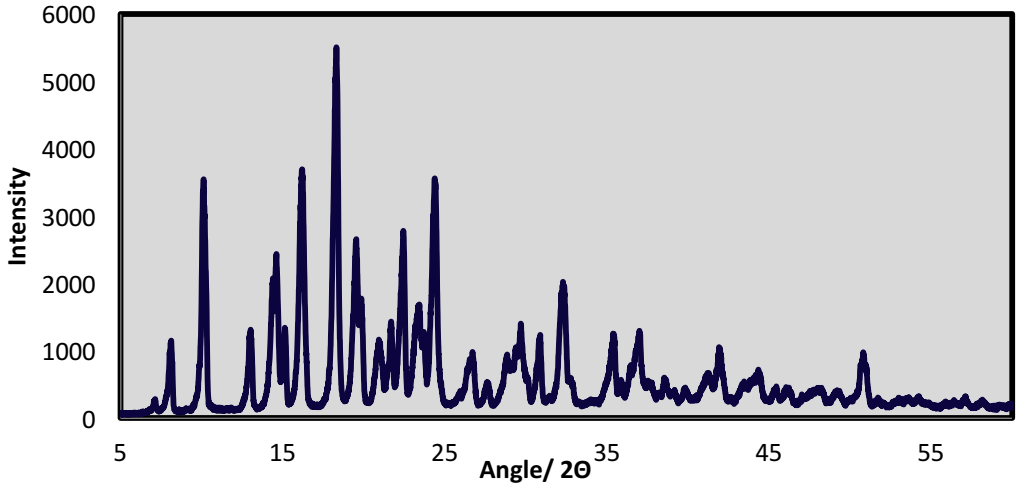

Figure 3.20: X-ray powder diffractogram of marketed AA2g

X-Ray powder diffractogram of physically mixed and co-ground powders- To study the effect of co-grinding on crystallinity of powder

The crystalline raw materials when mixed together forming the physical mixture at the molar ratio amphotericin B: AA2g 1:2 exhibited sharp crystalline deflections super-imposed on a slight halo indicative of crystalline raw materials mixed together (Figure 3.21). Co-grinding the drug with solubilizing agent AA2g at the same molar ratio for 10 min showed no significant change in the molecular order of the raw materials since diffractograms exhibited the same sharp crystalline deflections as that of the physical mixture superimposed on a halo. However, the peaks were less intense as compared to the physical mixture which could be attributed to the shear and impact forces applied during co-grinding.

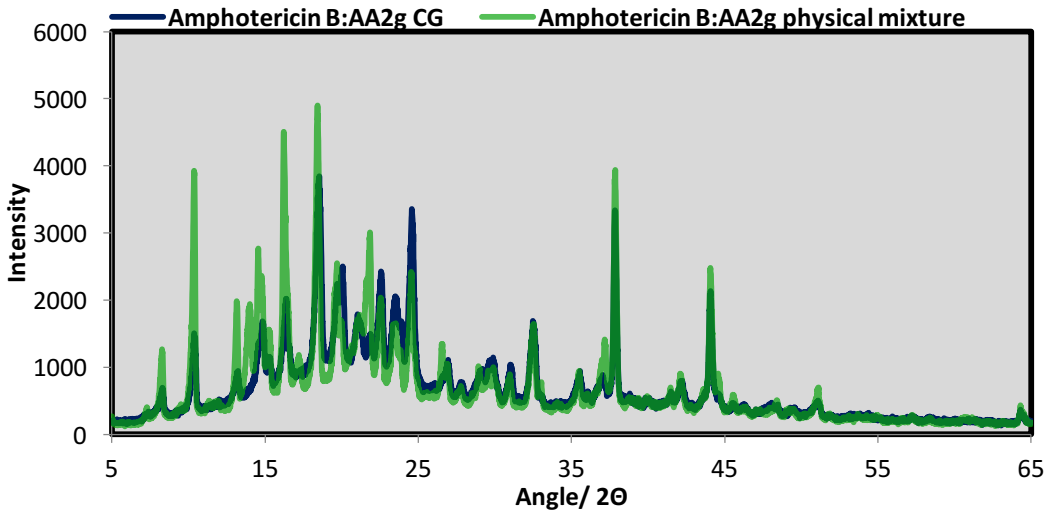

Figure 3.21: X-ray powder diffractogram of amphotericin B: AA2g co-ground (CG) and physically mixed

X-Ray powder diffractogram of physically mixed and spray dried powders with and without excipients- To study the effect of spray drying on crystallinity of powder

Spray drying the co-ground amphotericin B: AA2g formulation with and without excipients lactose/L-leucine showed a change in the XRPD diffractogram confirming an arrangement of long-range molecular disorder i.e. amorphous state (Figure 3.22). Physically mixing the respective excipients or co-grinding them showed the presence of sharp reflections indicative of long-range molecular ordered arrangement i.e. crystalline nature. On spray drying these formulations, the XRPD diffractogram showed a halo between the 2Θ of 15-25° indicative of their amorphous nature.

The molecular order of a compound is very important as it dictates dissolution rate and stability of a compound. Amorphous particles have better dissolution characteristics as compared to crystalline particles; however, they have the capability of re-crystallizing on storage in the presence of moisture and hence need to be stored well preferably in low moisture conditions. Hence, in the present study spray dried powders were stored in a desiccator at room temperature.

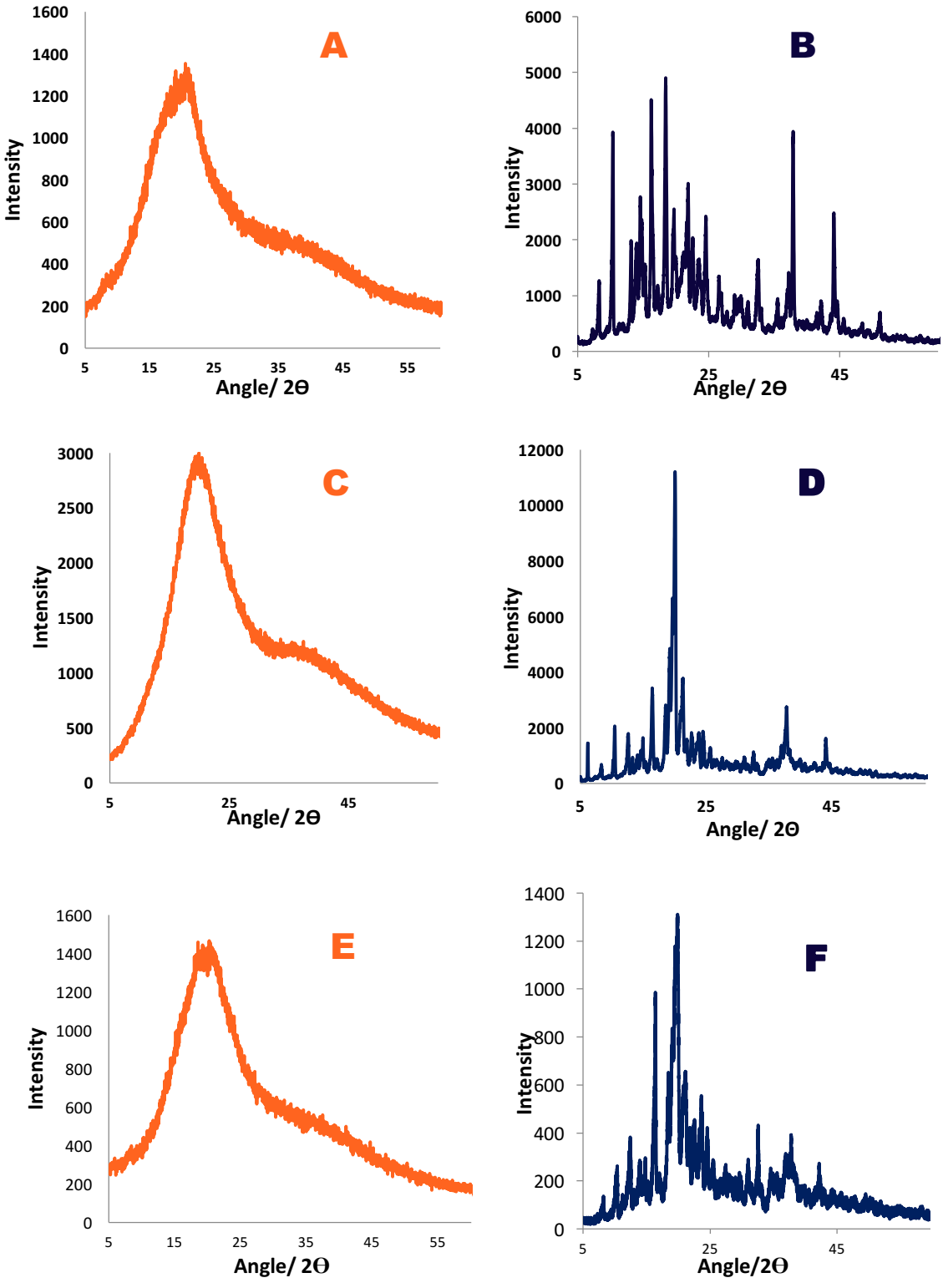

Figure 3.22: X-ray powder diffractogram of A) spray dried amphotericin B: AA2g; B) physically mixed amphotericin B: AA2g; C) spray dried amphotericin B: AA2g: lactose; D) physically mixed amphotericin B: AA2g: lactose; E) spray dried amphotericin B: AA2g: L-leucine and F) physically mixed amphotericin B: AA2g: L-leucine

3.5.3.7 Molecular interaction studies using attenuated Fourier transform infrared spectroscopy

FT-IR was performed on the spray dried and co-ground amphotericin B: AA2g to study the interactions between the functional groups of amphotericin B with AA2g, which resulted in the enhancement of amphotericin B solubilization in deionized water. FT-IR of the spray dried and co-ground microparticles were compared with that of raw materials and physically mixed powders, to observe the interactions on co-grinding. If functional groups underwent chemical or hydrogen bonding, there would be a change in FT-IR spectrum due to characteristic absorption by the newly formed bond. FT-IR of amphotericin B and AA2g shows characteristic absorption peaks as shown in Table 3.14, which are important to study the interactions between the two compounds.

Table 3.14: FT-IR spectrum absorption peaks associated with interaction and functional group representation of the raw materials

Peak absorption (cm^{-1})	Characteristic of functional group
Amphotericin B:	
3676.2	Symmetric and asymmetric stretching of amine (N-H)
3364.7	
761.28	Wagging vibration of N-H of amine
1640.1	Scissoring and bending vibration of N-H of amine
AA2g:	
1765.4	C=O stretching vibration of lactone
1700.1	C=C stretching vibration of lactone
3490	O-H vibration of OH at C_2 of lactone
3281.2	O-H vibration of OH at C_3 of lactone

In the frequency range of 1650-1800 cm^{-1} (as seen in Figure 3.25 and Figure 3.26) of the raw material AA2g, a characteristic absorption at 1769 cm^{-1} (group 1) attributed to the C=O stretching of the lactone ring was clearly evident. No such peak was observed in the spectra of amphotericin B indicative of the absence of a lactone functional group. A similar lower intensity peak around 1764 cm^{-1} was also evident in the FT-IR spectra of physically mixed amphotericin B: AA2g, attributed to no change associated with the functional groups of AA2g on physically mixing with drug amphotericin B. However, on co-grinding of amphotericin B with AA2g there was a clear shift of the peak associated with lactone C=O to a lower frequency at 1742.3 cm^{-1}. This could be attributed to an interaction between the drug and the lactone C=O of AA2g.

FT-IR of amphotericin B:

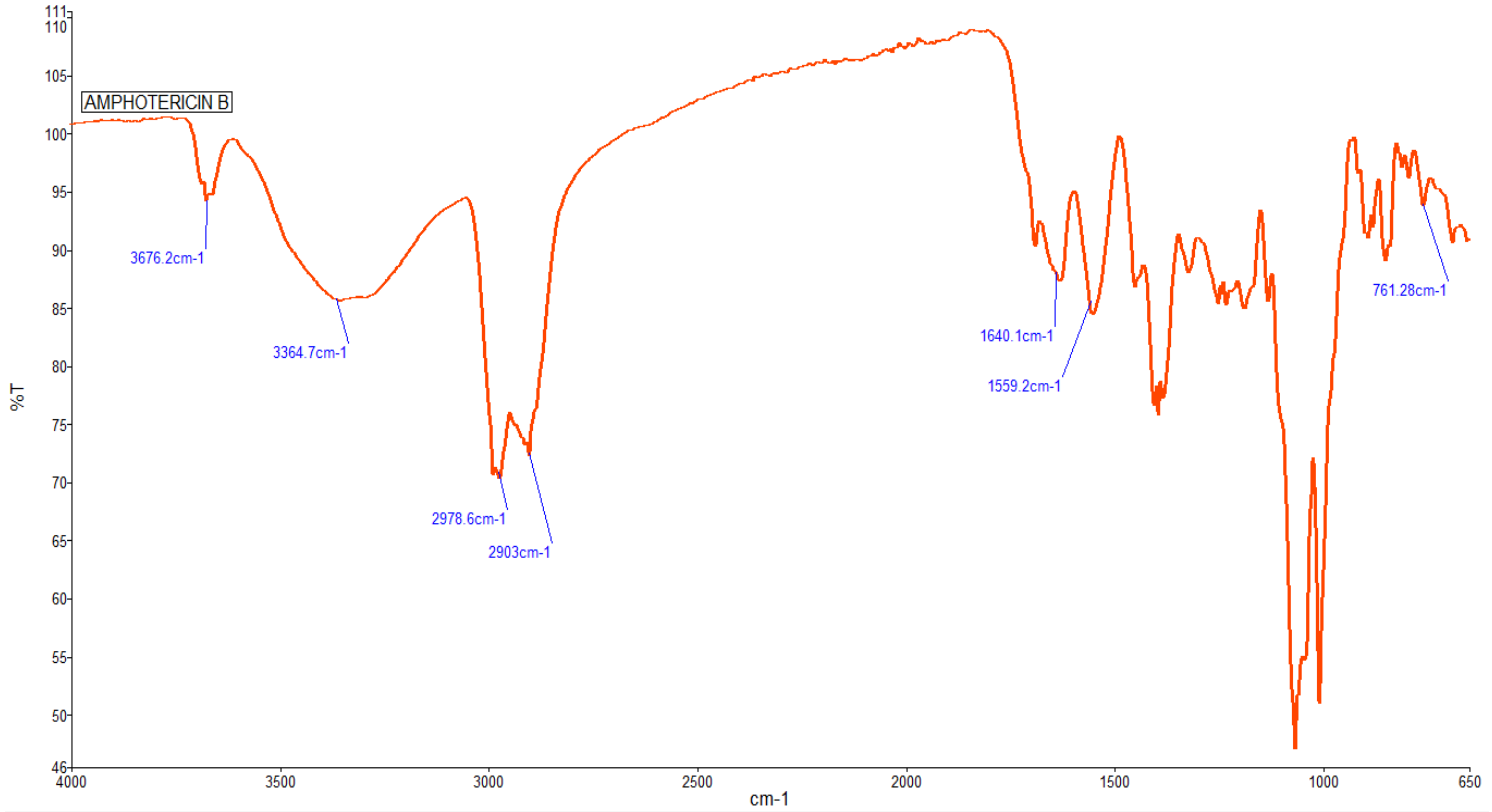

Figure 3.23: FT-IR spectrum of raw material amphotericin B

FT-IR of AA2g:

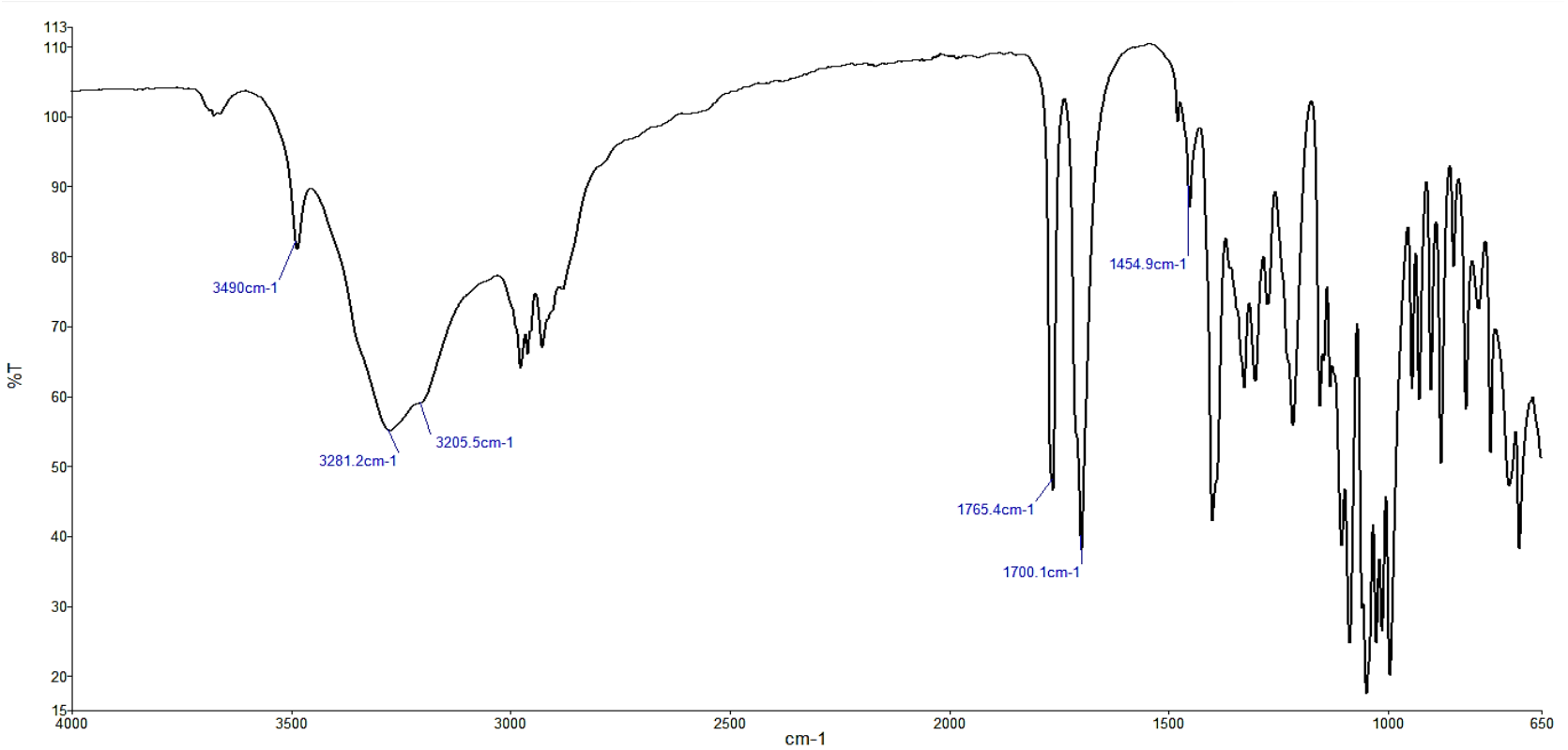

Figure 3.24: FT-IR spectrum of raw material AA2g

FT-IR of co-ground and physically mixed amphotericin B: AA2G- To study the effect of co-grinding on the interactional changes in the functional groups of the drug and solubilization agent (Group 1)

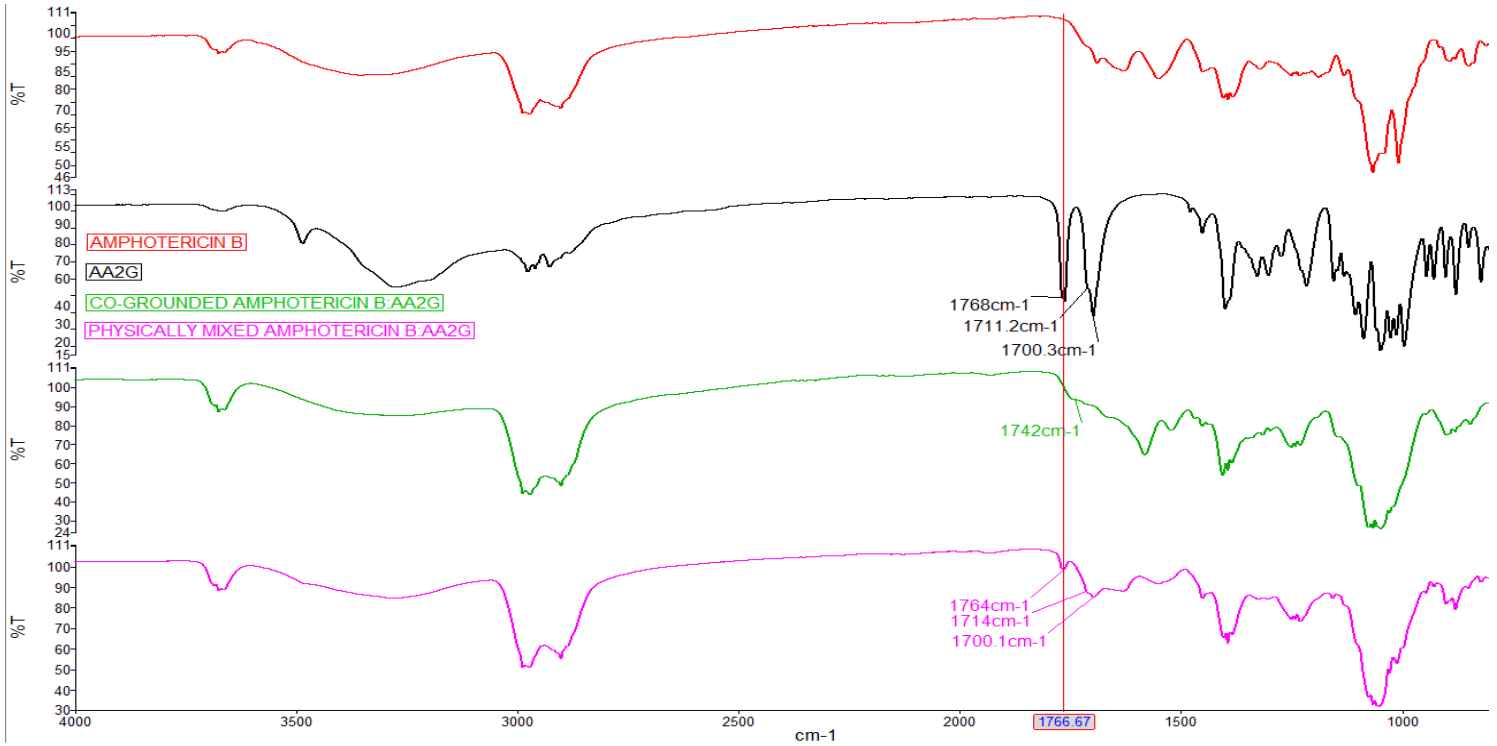

Figure 3.25: FT-IR spectrum of co-ground and physically mixed amphotericin B: AA2g (split view, group 1)

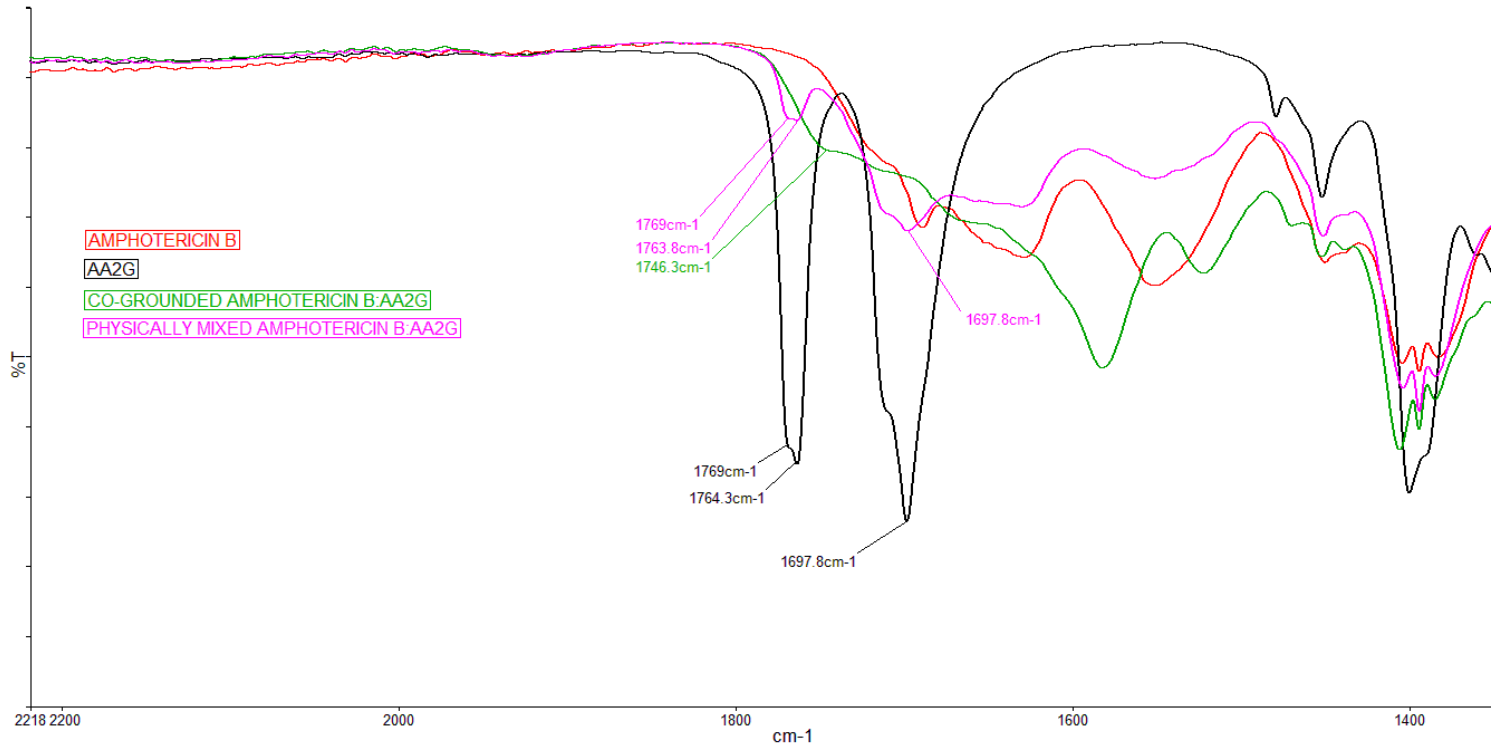

Figure 3.26: FT-IR spectrum of co-ground and physically mixed amphotericin B: AA2g from frequency range 1400-2200 cm^{-1} (overlay view, group 1)

In the frequency range of 1550-1650 cm^{-1} (Figure 3.27 and Figure 3.28) of raw material amphotericin B, a characteristic absorption at 1628.4 cm^{-1} attributed to the scissoring and bending vibration of N-H group on amphotericin B was noticeable. No such peak around the same frequency was evident in the FT-IR spectra of AA2g, confirming the absence of primary amine group on AA2g. FT-IR spectra of physically mixed amphotericin B: AA2g in this spectral region showed similar absorption peaks to amphotericin B around 1631.4 cm^{-1}, indicative of no interactions when amphotericin B and AA2g were mixed physically. On grinding together amphotericin B and AA2g, the peak attributed to scissoring and bending vibration of the primary amine group was seen to shift to a lower frequency with an increase in intensity at 1582.4 cm^{-1}. This could be attributed to interactions taking place with the amine group of amphotericin B.

In the frequency range of 3200-3500 cm^{-1} (as seen in Figure 3.29) many overlapped peaks were evident since in this spectral region there are absorptions associated with many functional groups namely amine and alcohol which are found in abundance in the molecular structure of amphotericin B and AA2g. However, around this spectral region, there is a noticeable difference between the physically mixed amphotericin B: AA2g and co-ground amphotericin B: AA2g at around 3489.4 cm^{-1} (group 3). A clear peak attributed to the O-H stretching vibration of AA2g lactone was evident in the spectra of AA2g and physically mixed amphotericin B: AA2g around this frequency range. However, this high-intensity peak was not evident in the F-IR spectra of co-ground amphotericin B: AA2g at molar ratio 1:2. This could be attributed to the interaction of the O-H bond of AA2g lactone with amphotericin B on co-grinding.

This study demonstrated that there is an interaction mostly a hydrogen bond formation which takes place between the oxygen groups namely C=O and O-H on the lactone ring of AA2g with the amine group on amphotericin B on co-grinding, resulting in increased solubilization of hydrophobic amphotericin B in deionized water. These interactions are not evident in the FT-IR spectra of physically mixed amphotericin B: AA2g at the same molar ratio, and hence no solubilization enhancement of amphotericin B is seen in aqueous solution on simple mixing with AA2g. Hence, this study clearly depicts the importance of co-grinding of amphotericin B with AA2g for enhancement of aqueous solubility of the hydrophobic antifungal.

The interactions leading to solubility enhancement of clarithromycin by co-grinding with AA2g was studied by Inoue et al. using ^{13}C NMR (carbon-13 NMR), which confirmed that hydrogen bond interaction between the ketone groups of the lactone ring of AA2g with the *N, N*-dimethyl amino groups on the desosamine sugar of clarithromycin was responsible for the enhanced solubility of the hydrophobic drug [369]. There was similar type of interaction between the amine groups of amphotericin B and lactone ketone and hydroxyl groups of AA2g, confirmed by FT-IR studies, which was responsible for the solubility of hydrophobic drug amphotericin B in deionized water.

FT-IR of co-ground and physically mixed amphotericin B: AA2g- To study the effect of co-grinding on the interactional changes in the functional groups of the drug and solubilization agent (Group 2)

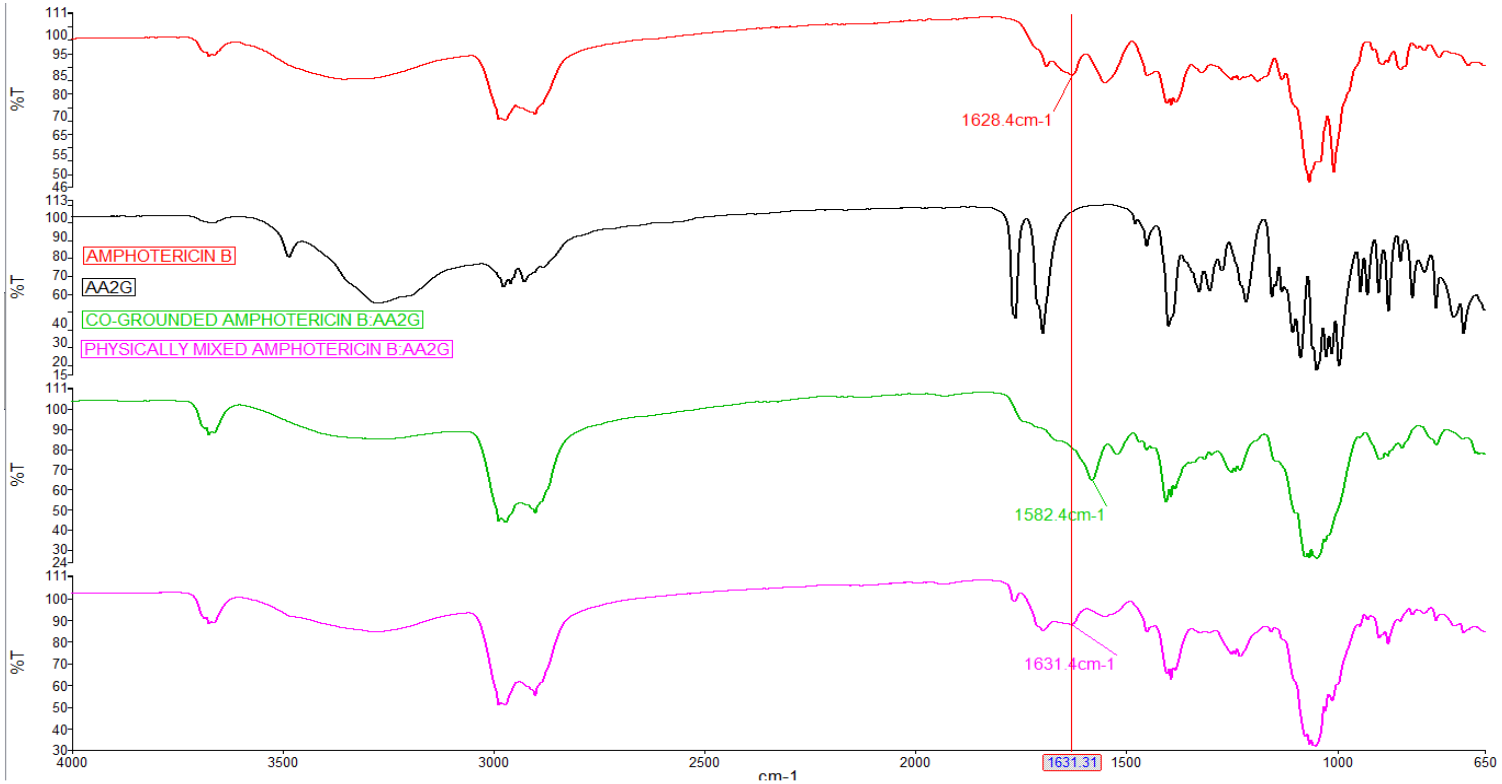

Figure 3.27: FT-IR spectrum of co-ground and physically mixed amphotericin B: AA2g from 1550-1650 cm^{-1}(split view, group 2)

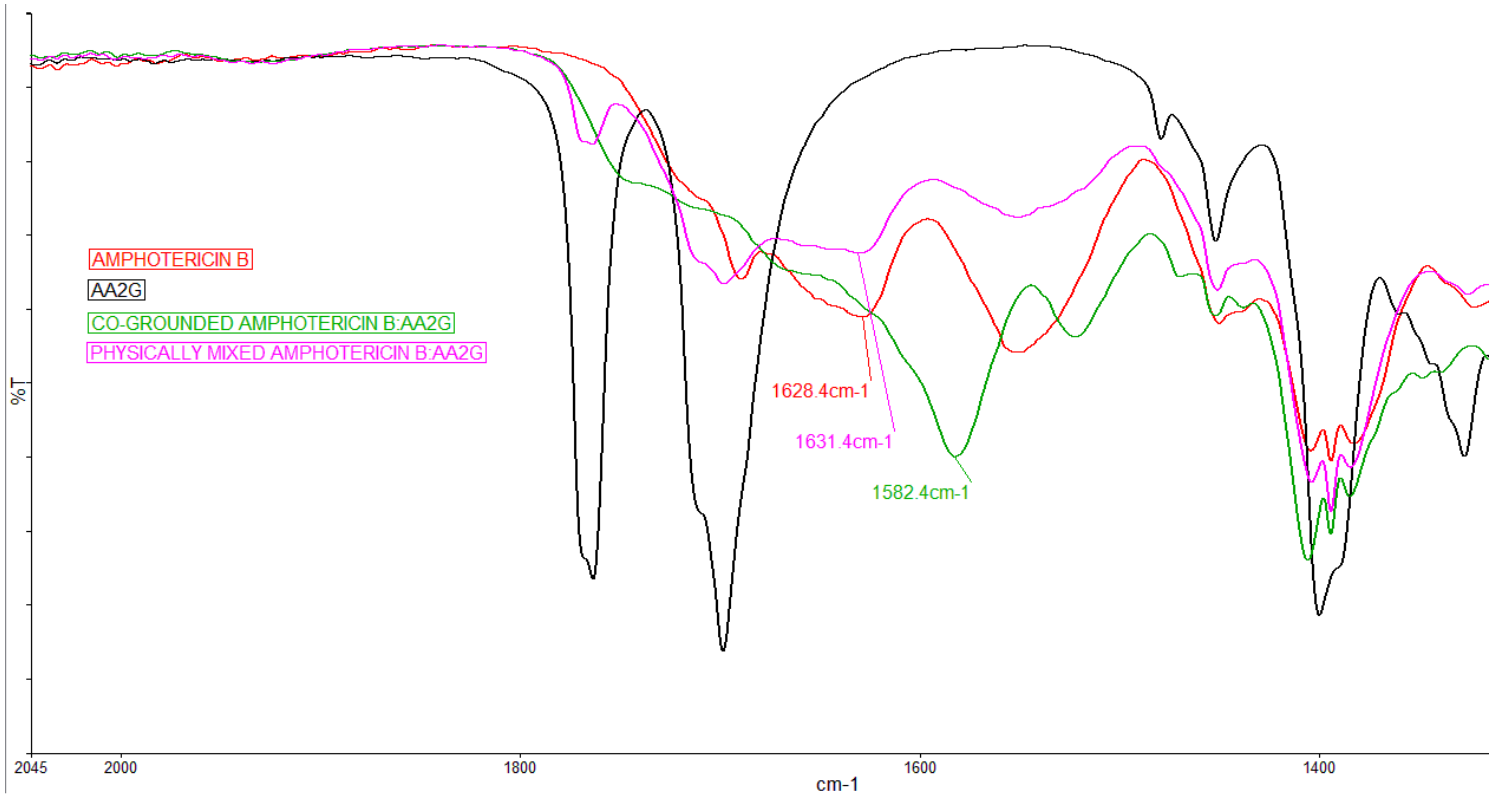

Figure 3.28: FT-IR spectrum of co-ground and physically mixed amphotericin B: AA2g from 1550-1650 cm^{-1}(overlayed view, group 2)

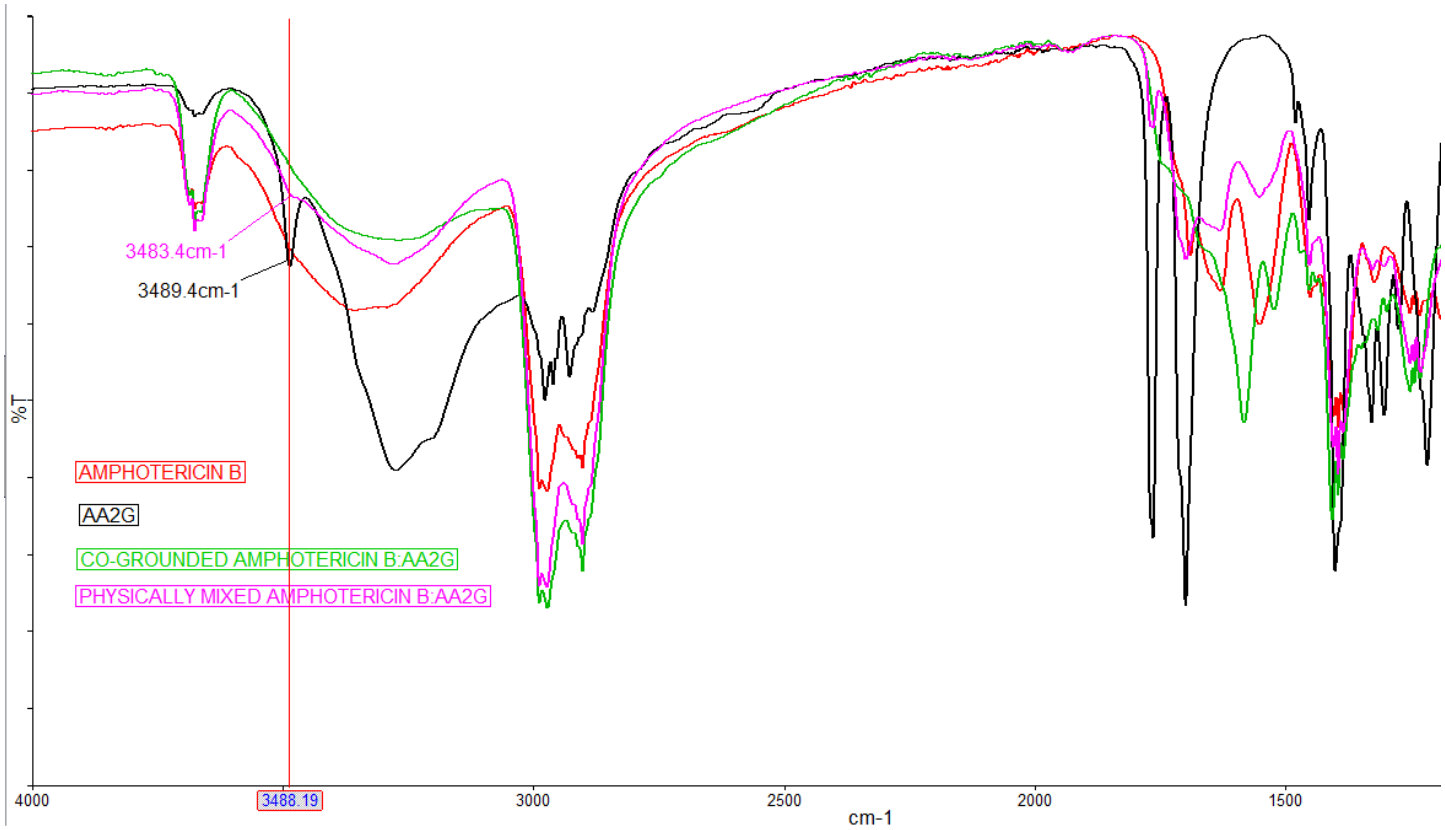

Figure 3.29: FT-IR spectrum of co-ground and physically mixed amphotericin B: AA2g from 3200-3500 cm^{-1}(overlayed view, group 3)

It is also important to ascertain if these interactions between amphotericin B and AA2g are still prevalent after spray drying, to ensure that amphotericin B is also soluble on re-dispersion of microparticles. Hence, the FT-IR spectrum of spray dried and physically mixed amphotericin B: AA2g on the addition of excipients lactose and L-leucine was studied. The spectrum (as seen in Figure 3.30 and Figure 3.32) clearly indicates that the interaction between amphotericin B and AA2g still prevails, and spray drying does not have any detrimental effect on the complexation and consequently solubilization of amphotericin B.

FT-IR of spray dried and physically mixed amphotericin B: AA2g: lactose- To study the effect of spray drying on the interactional changes in the functional groups of the drug and solubilization agent

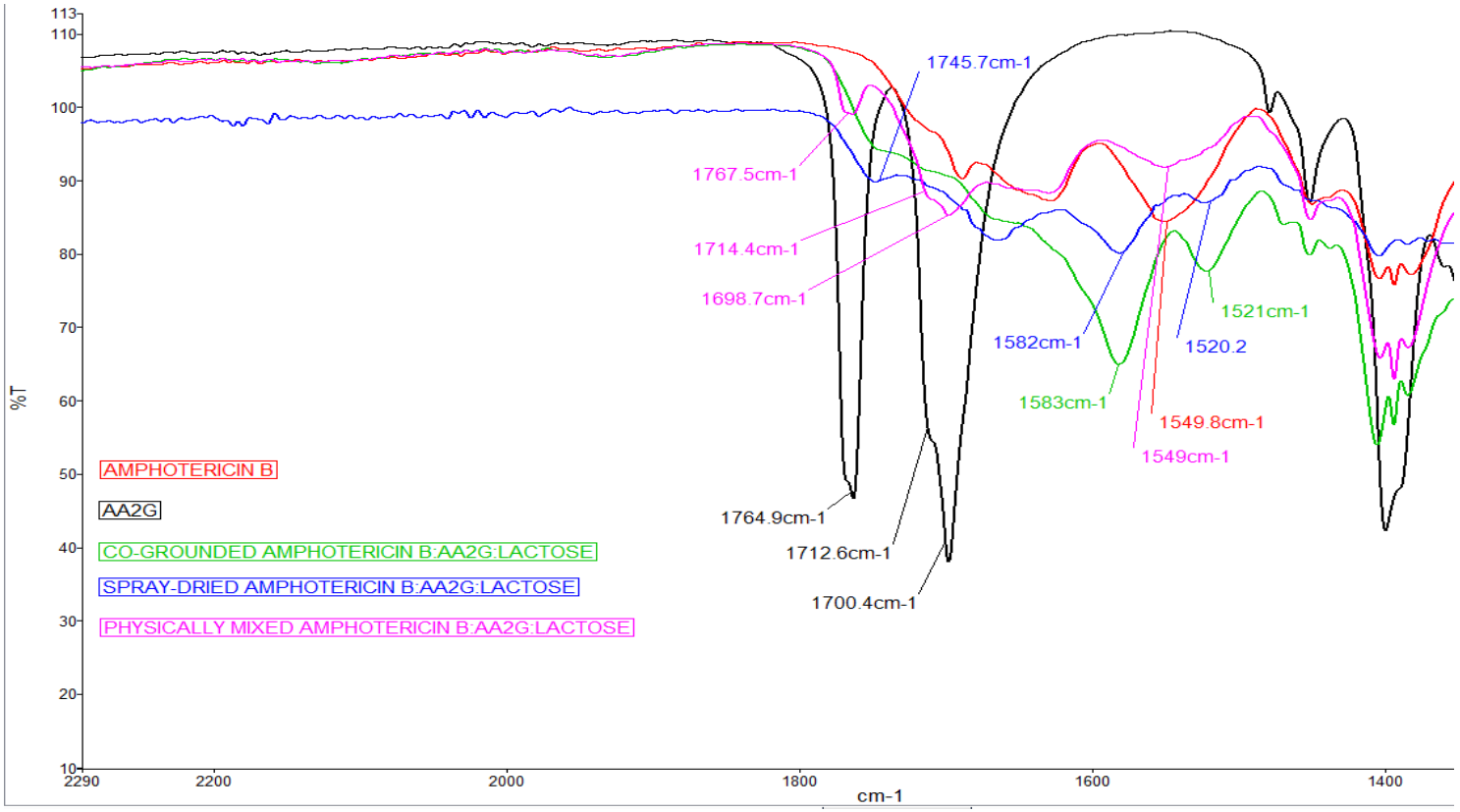

Figure 3.30: FT-IR spectrum of spray dried and physically mixed amphotericin B: AA2g: lactose (overlayed view)

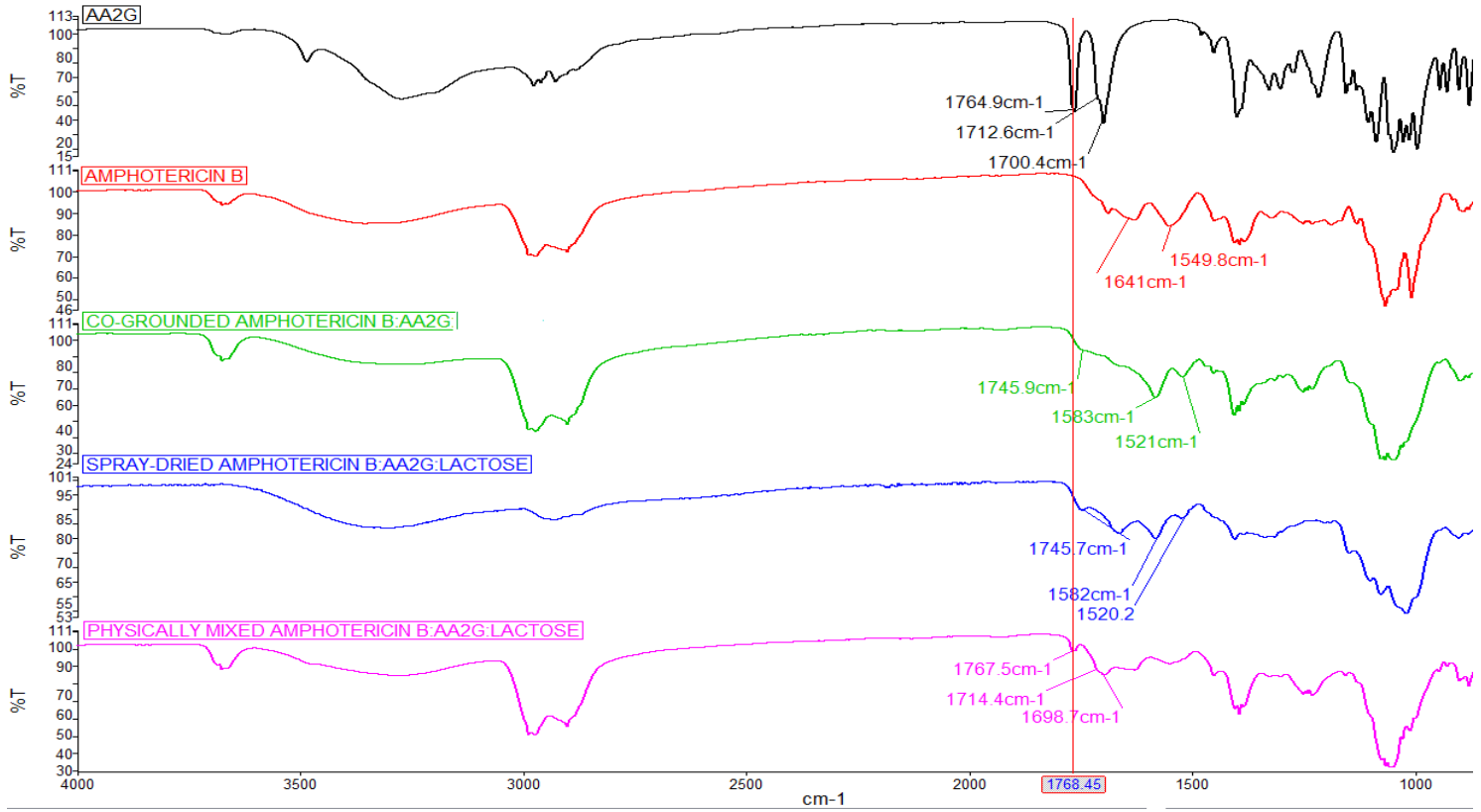

Figure 3.31: FT-IR spectrum of spray dried and physically mixed amphotericin B: AA2g: lactose (split view)

FT-IR of spray dried and physically mixed amphotericin B: AA2g: L-leucine- To study the effect of spray drying on the interactional changes in the functional groups of the drug and solubilization agent

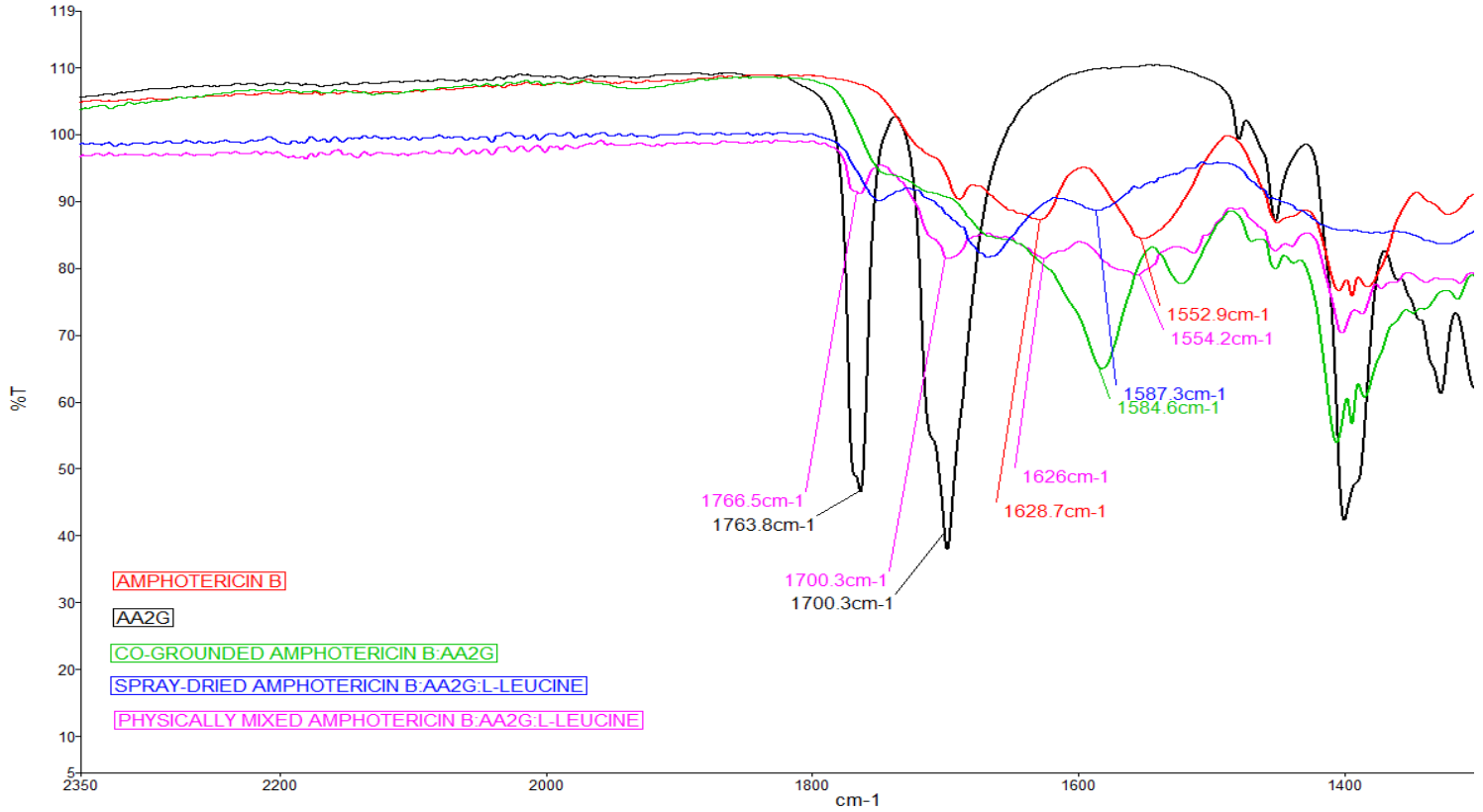

Figure 3.32: FT-IR spectrum of spray dried and physically mixed amphotericin B: AA2g: L-leucine (overlayed view)

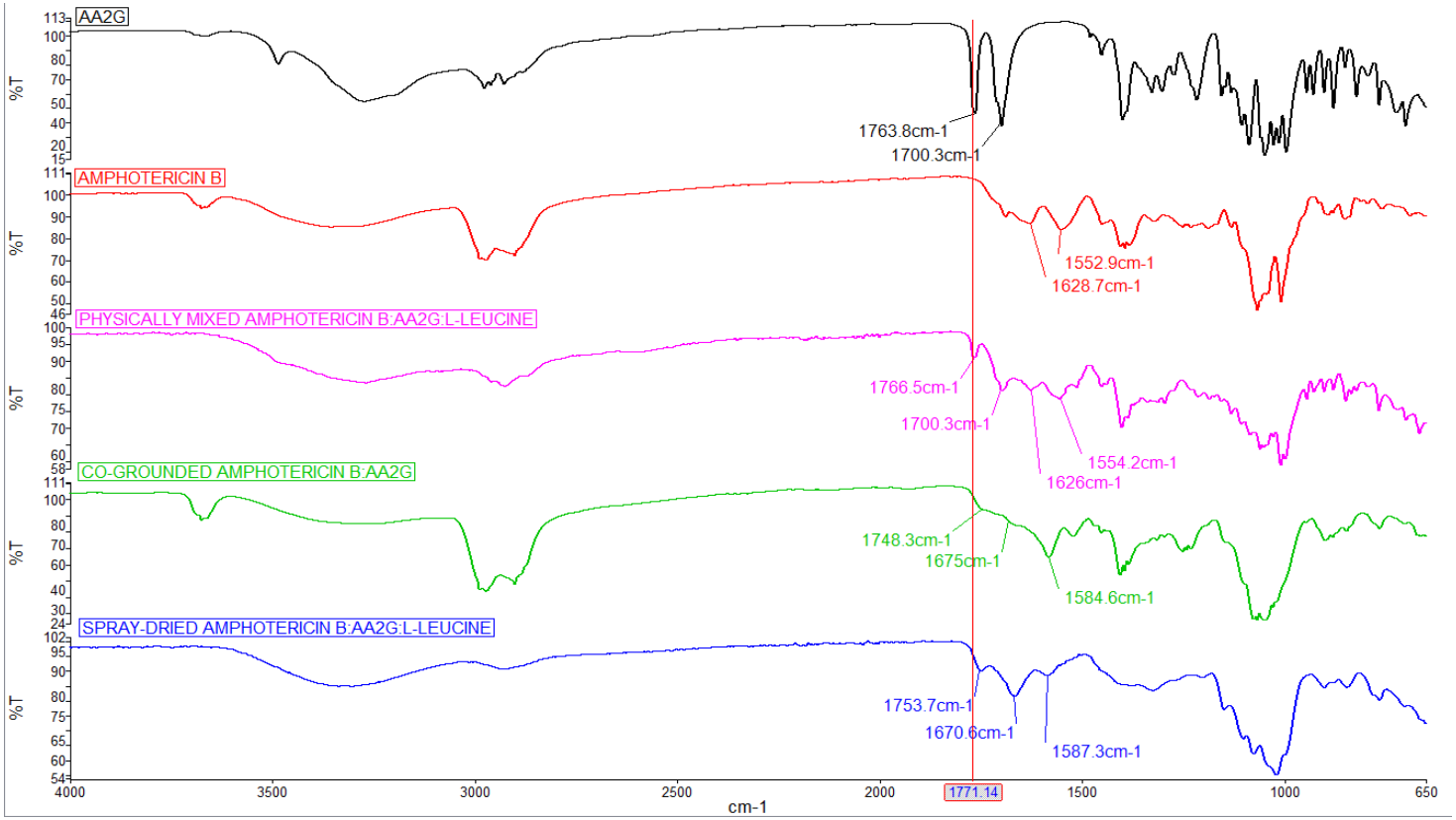

Figure 3.33: FT-IR spectrum of spray dried and physically mixed amphotericin B: AA2g: L-leucine (split view)

3.5.3.8 *In vitro* aerosol deposition and aerodynamic behavior of amphotericin B microparticles

The *in vitro* aerodynamic behavior and deposition of amphotericin B microparticles illustrated in Figure 3.34 and Figure 3.35 was studied using a Next Generation Impactor. In this study, aerosolization efficiency parameters (Table 3.15) were analyzed in triplicate for the freshly prepared spray dried and co-ground amphotericin B powders and represented as a histogram of the mean percentage of amphotericin B impacted on each stage as compared to the initial amount of amphotericin B aerosolized, ± SD.

Table 3.15: Aerosol efficiency parameters studied from the NGI (n=3, mean ± SD)

Microparticle	ED (%)	FR (%)	FPF (%)	FPD (mg)	MMAD (μm)	GSD
Co-ground amphotericin B: AA2g	57.19 ± 4.22	81.99 ± 2.31	13.87 ± 4.22	6.24 ± 1.90	3.38 ± 0.21	2.78 ± 0.17
Spray dried amphotericin B: AA2g	89.80 ± 2.86	82.69 ± 3.14	37.85 ± 2.15	17.02 ± 0.97	2.32 ± 0.15	2.02 ± 0.23
Spray dried amphotericin B: AA2g: L-leucine	99.86 ± 1.14	80.11 ± 1.97	56.75 ± 1.46	25.54 ± 0.66	2.55 ± 0.13	2.05 ± 0.15
Spray dried amphotericin B: AA2g: lactose	92.59 ± 3.62	76.84 ± 3.47	42.23 ± 3.08	19.00 ± 1.39	3.45 ± 0.29	1.45 ± 0.20
Physically mixed amphotericin B: AA2g	95.34 ± 2.71	76.06 ± 1.21	8.22 ± 1.17	3.70 ± 0.53	4.60 ± 0.67	5.44 ± 0.17

ED- emitted dose, FR- fraction recovered, FPF- fine particle fraction, FPD- fine particle dose, MMAD- mass median aerodynamic diameter, GSD- geometric standard deviation

Fraction recovered: It is very important to have a mass balance throughout the NGI [380]. A small percentage of the unrecoverable drug gets entrapped into the seal body and makes it necessary to study the mass balance of each experiment individually. A good mass balance was encountered for all the experiments with data lying between the pharmacopeial acceptable limits i.e. 76.1-82.7%. The difference in the fraction recovered of all the powders (i.e. co-ground, physically mixed and spray dried powders) was insignificant ($p > 0.05$).

Emitted dose: The ED was studied from the amount of drug left in the capsules after aerosolization and calculated as per drug content for respective formulations. High dispersibility and hence ED was exhibited by the spray dried powders with more than 86.2% contents being emitted during aerosolization for each. However, a significantly lower ($p < 0.05$) ED was evident for co-ground amphotericin B: AA2g microparticles of around 57.2%. This could be attributed to the dense property of the co-ground powder leading to poor flowability along with greater particle size (Dv50) and a significantly higher Span as compared to the spray dried microparticles when analyzed by laser diffraction (section 3.5.3.3). The spray dried microparticles containing the

dispersibility enhancer L-leucine also showed a significantly greater ($p < 0.05$) ED as compared to the spray dried microparticles without L-leucine and spray dried microparticles with lactose, indicative of the fact that incorporation of L-leucine in the feedstock before spray drying could enhance the amount of microparticles emitted from the capsules. This was evident due to the surface diffusion of L-leucine in its condensed phase and subsequent deposition on the surface of the microparticles at the air-water interface during spray drying consequently affecting aerosolization parameters [375,357,356].

MMAD and GSD: Mass median aerodynamic diameter (MMAD) refers to particle diameter as half the aerosol mass contained smaller than MMAD and half that is larger. All the spray dried powders show an MMAD of below 5 µm, wherein, the largest of 4.60 µm is achieved for physically mixed amphotericin B: AA2g and the smallest of 2.32 µm for spray dried amphotericin B: AA2g. MMAD for all the microparticles were found to be well in the respirable limits of 2-5 µm and can indicate potential deep lung deposition patterns of these microparticles. The geometric standard deviations are around 1-2 for the spray dried microparticles of amphotericin B: AA2g with and without excipients and co-ground amphotericin B: AA2G indicative of monodispersed systems and unimodal distribution of microparticles. However, the GSD of physically mixed amphotericin B: AA2g was found to be significantly ($p < 0.05$) larger i.e. 5.44 µm, indicative of the fact that simply mixing the drug and solubilizing agent together is not sufficient to obtain a well dispersible unimodal distribution of microparticles for aerosolization.

Fine particle fraction and dose: FPF and FPD are important determinants of the fraction and dosage of aerosolized drug that has potential to be deposited in the peripheral lungs and hence show therapeutic efficacy. These are explained in detail with the potential pulmonary deposition histograms.

Potential pulmonary deposition of amphotericin B microparticles

Table 3.15 and Figure 3.34, shows the effect of spray drying by comparing spray dried amphotericin B: AA2g with the physically mixed and co-ground amphotericin B: AA2g powders formulated at the same molar ratio. There was a significant increase ($p < 0.05$) in FPF and FPD of spray dried amphotericin B: AA2g as compared to the co-ground amphotericin B: AA2g and physically mixed amphotericin B: AA2g, emphasizing the importance of spray drying to produce microparticles suitable for delivery to the peripheral lung as it could offer a proper tuning of the particle size distribution, shape and density which are important parameters for a successful inhalation.

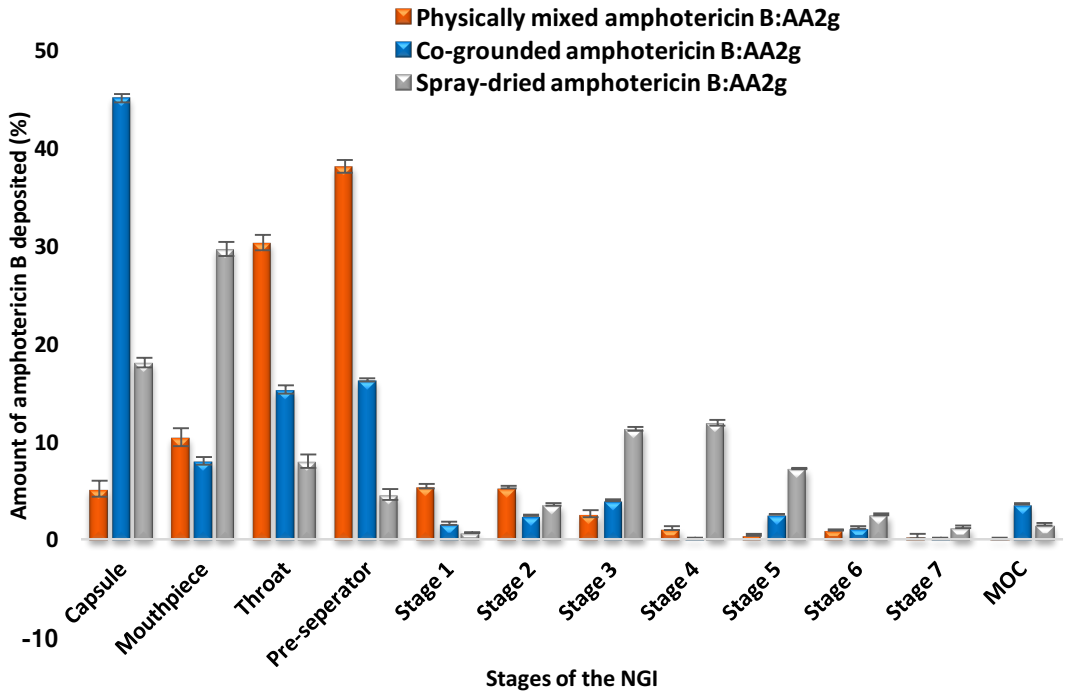

Figure 3.34: NGI deposition profile of spray dried, physically mixed and co-ground microparticles (n=3, mean ± SD)

As evident in Figure 3.34, physically mixed and co-ground amphotericin B: AA2g showed a very high deposition of amphotericin B in the throat and pre-separator stages of the NGI, indicative of higher oropharyngeal and throat deposition rather than deeper peripheral deposition in the lungs, with only 3.70±0.53 mg and 6.24±1.9 mg amphotericin B respectively reaching the lower stages of the NGI. Comparison of FPF and FPD between co-ground and physically mixed powders by one-way ANOVA at a level of p=0.05 shows that the these were significantly different. ($p < 0.05$) This depicts that co-grinding can help to improve the FPF of formulations rather than simple physical mixing.

The deposition profile obtained from the NGI indicates that simple mixing of amphotericin B with AA2g, or co-grinding amphotericin B with AA2g which helps in solubilization of the drug in aqueous solutions, is not sufficient to improve the lung deposition profile of amphotericin B, portraying the importance of spray drying. On spray drying amphotericin B: AA2g nanocomplexes a significantly ($p > 0.05$) higher FPD of 17.02 ± 0.97 mg amphotericin B as

compared to co-ground or physically mixed amphotericin B: AA2g was seen to deposit in the lower stages of the NGI. Spray drying produced spherical particles with a narrow size distribution as confirmed by SEM and laser diffraction studies, and particles were found to be amorphous as seen by the XRPD diffractograms. On the other hand, physically mixing and co-grinding retained the crystalline nature of the drug amphotericin B as seen in the XRPD diffractograms, along with wide size distribution resulted in a poor potential peripheral pulmonary deposition. This characteristic was as that reported earlier by several authors for drugs like curcumin, theophylline and terbutaline sulphate [381–383].

Furthermore, there was also a significantly higher ($p < 0.05$) FPF seen on addition of bulking agent lactose and dispersibility enhancer L-leucine which displays the importance of particle modification and reduction of interparticulate forces to consequently obtain a higher FPF.

The effect of addition of excipients in the spray drying feedstock on aerosolization and hence deposition of microparticles-

Spray dried microparticles were prepared by incorporating L-leucine in the feedstock solutions prior to spray drying. A minimum of ≥25% is required to cause a significant change in powder characteristics and subsequently aerosolization, as per published literature [361]. A significant increase ($p < 0.05$) in FPF and FPD was seen on aerosolization of amphotericin B: AA2g with dispersibility enhancer L-leucine, where 56.75% of microparticles were deposited in stages 2-8 accounting for 25.54±0.66 mg amphotericin B, indicative of potential deeper peripheral airways leading to higher dosage delivery to the areas of fungal infection and lower oropharyngeal and upper airway deposition, consequently leading to lower toxicity issues. This was evident by studying its deposition profile (Figure 3.33) which clearly portrays a higher deposition of microparticles in stages 2 to 5 as compared to the deposition profile of other microparticles formulated. As seen in the SEM micrographs (Figure 3.16), there was a change in morphology of the microparticles producing opened powdered structures on the incorporation of L-leucine at 25% weight concentration of the total constituents of the microparticles. Targeted delivery to the alveoli and bronchi using amphotericin B inhalation powder (ABIP, Nektar therapeutics) in clinical trials at a starting dose of 25 mg has been shown to be advantageous for treatment of invasive pulmonary aspergillosis, due to an aerodynamic size in the range of 2-5 μm [206]. Around 25 mg of amphotericin B was deposited in stages 2-8 of the NGI, suggesting potential peripheral lung deposition of the formulation spray dried with L-leucine for the treatment of invasive pulmonary aspergillosis.

Lactose was incorporated at a ratio of 50% of the total constituent of spray drying feedstock. However, it showed no significant difference ($p > 0.05$) in FPF and FPD as compared to the microparticles spray dried without excipients. Hence, the dose of amphotericin B delivered using microparticles spray dried with lactose would be lower as compared to the dose delivered using microparticles spray dried without excipients, indicating that incorporation of lactose did not have

a beneficial role for amphotericin B: AA2g microparticle aerosolization at a proportion of 50% weight.

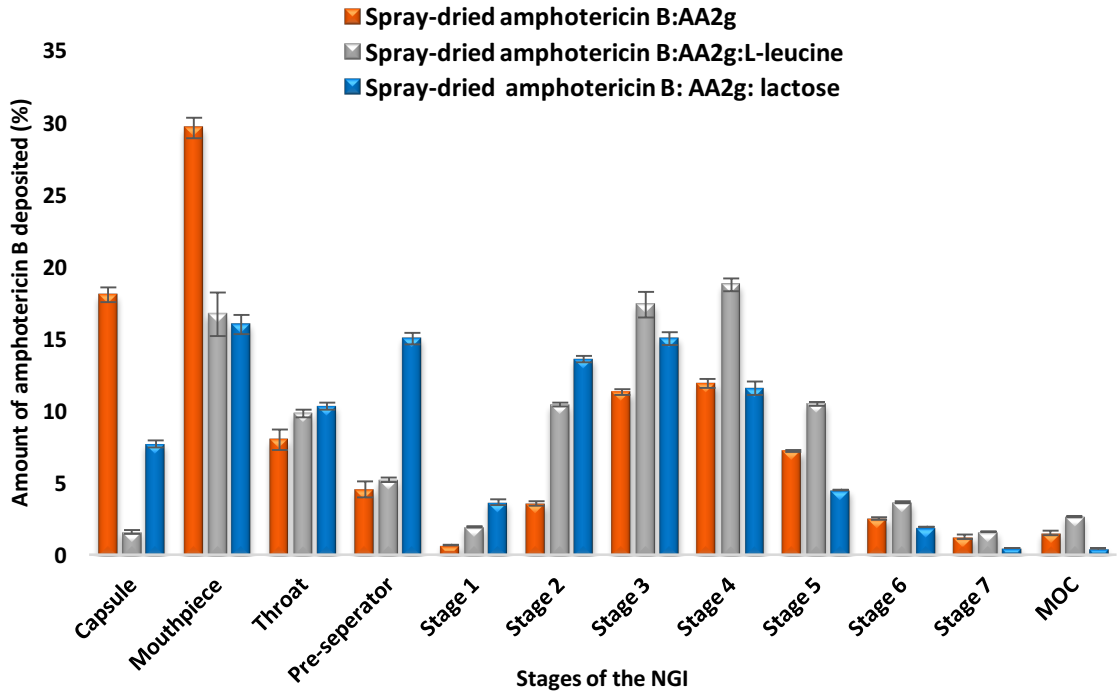

Figure 3.35: NGI deposition profile of spray dried microparticles with and without excipients (n=3, mean ± SD)

3.5.3.9 *In vitro* antifungal assessment of amphotericin B nanocomplexes against *Candida spp* by MIC studies

Optimized spray dried microparticles of amphotericin B were shown to possess *in vitro* fungicidal activity against *Candida spp* planktonic cells at varied minimum inhibitory concentration (MIC) as shown in Table 3.16.

Table 3.16: MIC (µg/mL) for various formulations against *Candida albicans* and *Candida tropicalis*

Powder	Minimum inhibitory concentration (µg/mL)			
	Candida albicans		*Candida tropicalis*	
	24 h	48 h	24 h	48 h
Amphotericin B	1.33 ± 0.58	5.33± 2.31	2	5.33± 2.31
AA2g	>64	>64	>64	>64
Co-ground amphotericin B: AA2g	1.67 ± 0.58	5.33 ± 2.31	2	8
Spray dried amphotericin B: AA2g	1.67± 0.58	5.33 ± 2.31	2	8
Spray dried amphotericin B: AA2g: L-leucine	1.33 ± 0.58	4.67± 3.055	2	4
Spray dried amphotericin B: AA2g: lactose	1.33 ± 0.58	5.33 ± 2.31	2	5.33 ± 2.31

The study was carried out against two different species of *Candida,* namely *Candida albicans* and *Candida tropicalis*. A very similar or 2- fold difference in MIC was evident for the spray dried powders as compared to raw material amphotericin B. However, the decrease was insignificant ($p > 0.05$) as analyzed by one-way ANOVA Tukey post-hoc test. This confirms that on the formation of nanocomplexes by interactions between the amine group on amphotericin B and lactone carbonyl on AA2g to enhance the solubility of amphotericin B there was no detrimental effect on the antifungal activity of the drug.

3.6 Conclusion

The aim of the chapter was to prepare nanocomplexes to solubilize hydrophobic antifungal agent amphotericin B for treatment of pulmonary fungal infections.

Based on the aforementioned results presented in this chapter, it can be concluded that:

1. Nanocomplexes were successfully formed by co-grinding at different molar ratios antioxidant solubilization agent ascorbic acid-2-glucoside (AA2g) with amphotericin B. The nanocomplexes formed at the different molar ratios between amphotericin B: AA2g were stable at 4-8°C and 25°C for 10 days with respect to hydrodynamic size, surface charge and drug content.
2. Molecular interaction between the drug and AA2g was studied to ascertain the reason for an improved amphotericin B solubilization. FT-IR studies revealed hydrogen bond interactions between the amine groups on amphotericin B and the lactone ring of AA2g on co-grinding, which was not evident on physically mixing the two compounds. This explained the improved solubilization of amphotericin B on specifically co-grinding with AA2g.
3. The most stable complexes keeping in mind the dosage requirements of amphotericin B and proper stoichiometry between the two complexing molecules i.e. amphotericin B: AA2g 1:2, (molar ratio) were taken forward for the preparation of dry powders intended for inhalation.
4. Dry powder microparticles were successfully prepared by spray drying with or without excipients to aid dispersibility and laser diffraction particle size analysis confirmed that spray dried microparticles exhibited a volume mean size lower than 5 μm, which is suitable for lower respiratory tract deposition, preferably to the alveolar regions where the infections prevail.
5. The spray dried microparticle morphology observed using SEM, displayed particles with a size in good agreement with that obtained from the laser diffraction studies. The particle morphology was summarized to be spherical, non-agglomerated and with slight corrugations on the surface.
6. The study of *in vitro* aerosol properties of amphotericin B microparticles on the NGI exhibited that an improved fine particle fraction and dose of amphotericin B on spray drying the co-ground nanocomplexes was obtained, due to the engineering microparticles with appropriate properties for aerosolization. On addition of dispersibility enhancer L-leucine to the spray drying feedstock of amphotericin B: AA2g a further improvement in fine particle fraction and dose was evident, with up to 25 mg of amphotericin B seen to deposit in the later stages of the NGI, indicative of potential peripheral pulmonary deposition.
7. *In vitro* antimicrobial assessment against *Candida spp* namely *Candida albicans* and *Candida tropicalis* by the MIC assay showed retainment of fungal activity on complexation and spray drying of amphotericin B.

4

CHAPTER 4

Preparation and characterization of spray-dried inhalable microparticles of co-encapsulated rifampicin and ibuprofen in mannosylated targeted liposomes

4.1 Introduction

Tuberculosis (TB) remains a serious healthcare issue, two decades on from the first time it was declared as a global health emergency by the World Health Organization (WHO) due to its resurgence fuelled by an increase in multi-drug resistance and coinfection due to the spread of HIV. According to the WHO, TB affected about 10.4 million people in 2015, of which 1.4 million people died as a result of it [50]. Control of the disease has become increasingly challenging because of the alarming rise of resistance in *Mycobacterium tuberculosis*, the etiological agent of TB. Multi-, extensively- and more recently, totally-drug resistant TB (MDR-, XDR-, TDR-TB) cases have increased steadily over the last decade. WHO reported 0.48 million new incidences of MDR-TB and an additional 0.1 million new cases of rifampicin-resistant TB (RR-TB) in 2015 alone [50,51]. Hence MDR-TB accounted for 3.9% of new TB cases and 21% of previously treated TB cases, of which 9.5% were XDR-TB [51]. The current portfolio of antibiotics used for anti-TB therapy is extensive but not adequate for treatment of the resistant strains of the bacteria, and hence TB remained in the top 10 leading causes of death in 2015 [50,51]. HIV and TB co-infection is presently a serious threat, as TB is the major killer of people living with HIV, accounting for about 35% of HIV deaths in 2015 [50,51].

The present study is based on the fact that TB bacilli are primarily located within alveolar macrophages in pulmonary TB hence posing a challenge to its treatment by conventional antitubercular chemotherapeutics. Previous studies have highlighted the potential of exploiting the innate property of macrophages to engulf foreign particles, hence demonstrating an improved uptake of nanocarriers encapsulating chemotherapeutics for delivery into the macrophages where the TB bacilli are primarily located (Table 4.1).

Moreover, it has been reported that receptors expressed on macrophages could be used to actively target chemotherapeutics encapsulated in varied types of nanocarriers decorated with targeting ligands for further improving the therapeutic efficacy of the drugs and hence treatment (section 4.1.5).

4.1.1 Re-purposing drugs for tackling MDR-TB

Development of new and effective drug treatment with novel and diverse mechanisms of action is of paramount importance to outpace the evolving resistance of the TB pathogen. MDR-TB occurrence has progressed due to adaption of the pathogen to combat the effects of drugs by genetic evolution. Inappropriate drug administration, sub-optimal drug concentration due to inadequate diffusion inside the lung tissue on systemic administration and patient non-compliance due to the drug regimen being extensively long, expensive, complicated in administration and toxic has hastened TB resurgence, especially in low-income countries that struggle due to excessive populations, malnutrition, poverty and HIV co-infection [384,385]. Moreover, the dormant state of the TB pathogen causes a latent TB infection that is harboured by one-third of the global population due to its resilience and coping nature to varied environments. It has the

capacity to convert to an active TB infection in 10% cases, hence requiring a lengthy drug regimen that is not only capable of eradicating the active TB, but also eliminates the dormant pathogen from the infected host [385].

New chemical entities require at least a decade to progress from the laboratory bench to clinical use and when finally administered it is not unlikely that resistance to these novel entities will develop. Repurposing drugs offer a rapid, safer and effective solution to circumvent the investment of time and other resources required for conventional drug discovery and development. For instance, sildenafil developed by Pfizer originally for the treatment of hypertension and erectile dysfunction is now being considered as a host-directed adjuvant therapy to shorten TB treatment times, as it has resulted in faster mycobacterial clearance and improved tissue resolution [386]. Forthcoming clinical trials in India are investigating repurposed Verapamil, i.e. an approved anti-hypertensive drug for its effective acceleration in clearance of mycobacterium in conjunction with other first-line treatment drugs, hence significantly reducing the treatment duration [387].

Non-steroidal anti-inflammatory drugs (NSAIDs), commonly used for pain relief have been reported to exhibit anti-TB properties both *in vitro* and *in vivo* [388–391]. Whole cell phenotypic screening has revealed the off-patent NSAID oxyphenbutazone to have antitubercular properties against actively replicating, non-replicating and drug-resistant isolates of *M. tuberculosis* [388,392]. NSAIDs ibuprofen, carprofen and other 2-aryl propanoic acid derivatives have also demonstrated antitubercular activity in whole-cell phenotypic assay [389]. Moreover, ibuprofen has demonstrated enhanced elimination of *in vivo* bacterial loads when used in combination with the antitubercular drug pyrazinamide [393]. Furthermore, NSAIDs may also facilitate healing of the lung tissue that has been damaged due to prolonged antitubercular drug regimens owing to their anti-inflammatory activity [385]. However, development of ibuprofen as an antitubercular drug for the lungs is limited by its highly acidic nature.

4.1.2 Drug delivery systems for treatment of TB

Development of drug delivery systems capable of direct administration of drugs to the lungs could represent a breakthrough in the treatment of TB. This can circumvent the requirement of high oral doses to reach optimal sputum levels for the elimination of bacillary load. High doses of anti-TB drugs like rifampicin for a protracted period causes considerable systemic toxicity, such as nephrotoxicity and hepatotoxicity, along with a serious effect on the gut microflora and a substantial contribution in developing antibiotic resistance and its transmission. Aerosolization would help target specific regions in the lungs with the aid of nanoscale drug delivery systems to administer higher doses of drug and reduce systemic toxicity. Other potential advantages would be improving the stability of the drug, the feasibility of incorporation of both hydrophilic and hydrophobic substances and controlled (sustained) drug release from the lipid/polymer matrix. Nanoparticles delivered via the pulmonary route have demonstrated potential to enable

improvement of drug bioavailability and reduce the dosing frequency, which could resolve the problem of non-adherence, one of the major roadblocks in TB control [394].

Liposomal formulations of clofazimine were much more effective in being taken up naturally by the macrophages where the infection prevails, hence improving treatment outcome [270]. Stoops et al. have reported that aerosolization of lipids/surfactants along with antitubercular drugs have the tendency to strip off the waxy trehalose dimycolate armor of mycobacterium, acting as cell permeabilizing agents, hence increasing the effectiveness of the co-administered antibiotics for the treatment of pulmonary TB [395].

Ever-mounting evidence has demonstrated that *Mycobacterium tuberculosis* and several other *mycobacterial* species have a strong propensity to grow matrix encapsulating structures 'biofilms' which induce antibiotic drug tolerance as a survival strategy in chronic infection [68,396,397]. Various studies on nano-liposomal antibiotic formulations have demonstrated successful penetration through bacterial biofilms and effective eradication of bacteria. A study of cationic liposomes encapsulating rifampin has been shown to effectively eradicate *Staphylococcus epidermidis* from biofilms, reducing the bacterial load much efficiently compared to rifampin alone [398,399].

4.1.3 TB etiology and pathogenesis: Rationale for macrophage targeting

TB is an airborne disease and infection starts with the host inhaling viable tubercle bacilli contained in droplets [208,400,401]. Tubercle bacilli are aerobic, acid-fast, gram-positive, slender rod-shaped and non-motile bacteria [401]. They have a capacity to adapt to changes in the environment including host defense mechanisms viz. nutrient deprivation, hypoxia, intraphagosomal acidification and exogenous stress from the environment, staying viable in the air for a long time [208,401]. *Mycobacterium tuberculosis* has a unique cell wall which is composed of mycolyl arabinogalactan–peptidoglycan (mAGP) complex, i.e. a complex composed of mycolic acids and peptidoglycans, along with other glycolipids, cell-wall proteins and cord factors [208,402]. This constitutes a strong diffusion barrier making mycobacteria around 100-1000 times less permeable than *E.coli* to the passage of hydrophilic molecules, resistant to digestion by phagolysosomal enzymes and pH, and the killing effects of pulmonary macrophages [208,402]. Hence the hydrophobic cell wall of the tubercle bacilli is a major determinant of its virulence due to the resistance it possesses to the entry of antibiotics.

Tuberculosis is most commonly caused by reactivation of the latent tubercle bacilli which the host carries for many years rather than by primary infection [208,400]. During the latency period of the bacilli, they are hosted in macrophages, wherein surviving bacilli remain alive and consume host lipids but do not multiply [208,400]. Alveolar macrophages act as a double-edged sword as they primarily serve to limit the growth and dissemination of bacilli into the extrapulmonary areas. This helps the bacilli to stay within the granuloma and produce large numbers of lipid-free vacuoles and lipid-containing bodies known as foamy macrophages, formed due to oxygenation

of the mycolic acids. Alveolar macrophages serve as a reservoir for preserving bacilli for a long time, hence altering their function and phenotype as immune defense cells [208,400]. These macrophages then gets surrounded by a fibrous capsule which leads to exclusion of immune lymphocytes from the bacilli, leading to active infection [208,400,403]. The bacterial foci within the macrophages break down when the host defense is weak and re-grow particularly in alveolar spaces and disseminate the infection [208,400,403]. After 3 months of active infection, numerous small foci develop in highly irrigated organs like CNS, spine, lymph nodes, liver, kidney and genitalia leading to exaggerated extrapulmonary manifestation known as miliary TB [208,400].

4.1.4 Passive macrophage targeting by liposomes on IV/pulmonary delivery

The adapted macrophages act as a formidable barrier to delivery of small molecule drugs, vaccines and diagnostic agents for the eradication of the intracellular TB bacilli. It is hence of extreme importance to understand the structure of the macrophages and generate strategies to increase the uptake of antimycobacterial agents by targeting the macrophages where the TB bacilli are protected from the host immune surveillance. Macrophages have an innate propensity to engulf foreign particles as a mean of defense, which is a highly size-dependent [208,404]. Particles 1-3 μm in size are most likely to be passively taken up by alveolar macrophages, whereas, particles <0.2 μm and >10 μm may escape phagocytic endocytosis [404]. Particles <0.2 μm undergo cytosis via pinocytosis that includes micropinocytosis (100 nm-0.2 μm), clathrin-medicated pinocytosis (~100 nm), caveolin-mediated pinocytosis (~80 nm) or clathrin and caveolin-independent pinocytosis (~50 nm) [404,405].

Moreover, the surface chemistry of particles also plays an important role in macrophage uptake. Internalization of liposomes into cells has been reported to occur by means of surface adsorption, membrane fluidization and membrane-bilayer fusion leading to diffusion and endocytosis [404]. Fluorescence microscopy of FITC-Bovine serum albumin (BSA) encapsulated liposomes and radioactivity studies of I^{131}-BSA along with liposomal membrane marker studies have suggested that liposomes are taken up intact into macrophages by phagocytosis. Exploiting this natural tendency, passive drug delivery using liposomes would seem like an attractive approach to treat intracellular pathogens like mycobacterium. Passively targeted liposomes for IV/pulmonary delivery of antitubercular drugs in literature and their treatment outcomes are outlined in Table 4.1.

Table 4.1: Passively targeted liposomes encapsulating tubercular drugs (IV/nebulization)

Antimicrobial drug	Liposomal composition	Therapeutic effect	Treatment outcome(s)
Rifabutin IV (mice) [208,406]	Liposome MLVs DPPC: DSPG (7:3 molar)	Significant accumulation of the liposomes in the spleen and liver, and hence a significant reduction in bacterial load as compared to the free drug treated group. No significant difference in bacilli load resident in the lungs between the two groups	Good to tackle extrapulmonary disseminated TB infection For pulmonary TB treatment, aerosol administration would be an interesting approach
Amikacin IV (mice) [208,407]	Liposome MLVs Soya PC: DSPG: Chol (2:0.1:1 molar)	Liposomal amikacin showed 2.4-5 fold superior activity against mycobacterium as compared to free amikacin in an acute murine TB model Liposomes showed a low clearance rate and hence prolonged residence time of the drug	An attractive approach for reducing the administration frequency and hence enhancing patient compliance
Clofazimine IV (mice) [270]	Liposome MLVs DMPC: DMPG (7:3 molar)	Liposomal clofazimine showed a reduction in toxic effects of the drug clofazimine *in vitro* and *in vivo*	Excellent approach for treatment of extrapulmonary TB and to some extent pulmonary TB Adams et al. advised that direct aerosol inhalation of the liposomal clofazimine would be attractive for treatment of pulmonary TB
Rifampicin and Isoniazid co-encapsulation Inhalation by nebulization (guinea pigs) [209]	Liposome MLVs PC: Chol (2:1.5 molar)	Sustained release of drugs from the liposomal formulations was evident and consequently a longer duration of alveolar drug stay up to 120 h with nebulized liposomal rifampicin and isoniazid as opposed to 48 h for free drugs nebulized or given IV was seen with a single dose	Reduction in the dosing frequency could be achieved with the liposomal drugs and hence better patient compliance
Rifampicin Intratracheal instillation of re-suspended freeze-dried liposomes (Wister rats) [408]	Liposome Soya lecithin: Chol (varied ratios)	Enhanced drug permeation through alveolar epithelium was evident for liposomal rifampicin in alveolar macrophages Pulmonary residence time of liposomal rifampicin was superior to the free drug	Sustained release of drug from the liposomes would be an attractive approach to reduce dosing frequency

MLVs-multilamellar vesicles, PC- phosphatidylcholine, Chol- cholesterol, DSPG- distearyl phosphatidylglycerol, DMPG- dimyristoyl phosphatidylglycerol, DPPC- dipalmitoyl phosphatidylcholine, IV- intravenous

4.1.5 Active macrophage targeting by liposomes on IV/pulmonary delivery

Binding to receptors on macrophages has shown promise in the targeting of delivery systems to internalize chemotherapeutics via receptor-mediated endocytosis for several diseases viz. rheumatoid arthritis, AIDS, leishmaniasis, TB and Gaucher disease [176]. Active targeting of antitubercular delivery systems involves modification of the carrier surface with ligands, antibodies or peptides for inducing selective affinity and interaction with the macrophages and hence uptake [409].

Carbohydrate receptors bind specifically to polysaccharides like mannose, galactose, pectin and sialic acid and have been extensively researched in previous years. Mannose receptors i.e. a trans-membrane protein receptor expresses three extracellular regions, specifically, a C-type lectin receptor with the carbohydrate-recognition domain, an amino-terminal cysteine-rich domain and a fibronectin domain [176,409]. These are highly expressed on alveolar macrophages and hence can be exploited for the treatment of intracellular tuberculosis which is primarily hosted inside alveolar macrophages [176,409].

Moreover, active targeting of delivery systems can also be achieved by exploiting the scavenger receptors present on the surface of macrophages, specifically the SR-B1 and CD36 classes of scavenger macrophage receptors which bind tightly to polyanionic molecules like. anionic phospholipids [410]. Tuftsin a naturally occurring tetrapeptide produced by enzymatic cleavage of the heavy chains of immunoglobulin G has a natural tendency to target the macrophages and lead to upregulation of macrophage-mediated phagocytosis, and hence can enhance the innate bactericidal and tumouricidal activity of macrophages [411]. This makes tuftsin an attractive ligand for attachment to the surface of nanocarriers for binding specifically to macrophages carrying intracellular pathogens. Moreover, its natural killer potentiation activity by upregulation of phagocytosis can help to improve the therapeutic efficacy of antitubercular drugs [411]. Actively targeted liposomes for IV/pulmonary delivery of antitubercular drugs in literature for macrophage targeting and their treatment outcomes are outlined in Table 4.2.

Table 4.2: Actively targeted liposomes encapsulating tubercular drugs to macrophages (Targeting moiety in bold)

Antimicrobial drug/ targeting	Liposomal composition	Therapeutic effect	Treatment outcome(s)
None Mannose receptor Inhalation with liquid Micro Sprayers (Rats) [412]	Liposome MLVs Soybean PC: Chol: DCP: **4-aminophenyl-a-D-mannopyranoside**	2.2-fold enhanced drug uptake by alveolar/peritoneal macrophages was seen both *in vitro* (NR8383 cells) and *in vivo* (rats) for the mannosylated liposomes as compared to non-mannosylated liposomes	Good approach for delivery of antitubercular drugs to the alveolar macrophages for treatment of pulmonary TB
None Mannose receptor Intratracheal instillation (Rats) [212]	Liposome DSPC, Chol, Fluorescein-DHPE: **Mannosylated cholesterol**	Alveolar macrophage uptake of mannosylated liposomes increased with an increase in surface functionalization with mannosylated cholesterol derivative	Increasing mannose residues on the surface appeared to be a good approach for delivery of antitubercular drugs to the alveolar macrophages for treatment of pulmonary TB
None Mannose Receptor Intratracheal spray (Male SD rats) [213]	Liposome Egg PC Chol: DCP: **4-aminophenyl-a-D-mannopyranoside**	An enhanced uptake of mannosylated liposomes was evident both *in vitro* (NR8383) and *in vivo* (rats) alveolar macrophages	Good approach for delivery of antitubercular drugs to the alveolar macrophages for treatment of pulmonary TB
Rifampicin Class B1 scavenger receptor Inhalation aerosol using the nose-only exposure model (Wistar Albino rats) [211,413]	Liposome MLVs PC: Chol (7:3 molar) Coated with DPPE-**MBSA (maleyated bovine serum albumin)** PC: Chol: **DCP** (7:3:0.1)	MBSA targeted anionic liposomes resulted in 39.6±3.3% lung accumulation in macrophages after 6 h of aerosolization, whereas on aerosolization of neutral liposomes there was an initial high lung accumulation which dropped to nil over 6 h, similar to the free drug. With the DCP anionic liposomes the lung accumulation was 29.7±2.9% after 6 h of aerosolization	Aerosolization of antitubercular drug encapsulated liposomes surface modified to attain an anionic charge could be useful to target to the scavenger receptors and hence deliver more payload to the lung macrophages to treat pulmonary TB

Table 4.2: Actively targeted liposomes encapsulating tubercular drugs to macrophages (Targeting moiety in bold) (continued)

Antimicrobial drug/ targeting	Liposomal composition	Therapeutic effect	Treatment outcome(s)
None Class B1 scavenger receptor [410]	Liposome ULVs Egg PC: Chol: phosphatidyl **serine** (1:1:1) Egg PC: Chol: phosphatidyl **inositol** (1:1:1)	*In vitro* uptake and receptor-binding studies showed an enhanced uptake of anionic liposomes with phosphatidyl serine or phosphatidyl inositol as compared to neutral or cationic liposomes	Passive targeting to the scavenger receptors on the macrophages could serve to enhance delivery to the macrophages in the lung for treatment of pulmonary tuberculosis
Rifampicin and Isoniazid Carbohydrate receptor using polysaccharide pectin IV (mice) [210]	Liposome MLVs Egg PC: Chol, **O-SAP (O-stearyl amylopectin)** (2:3 molar, coated with O-SAP) Egg PC: Chol: DCP, **O-SAP** (2:3:2 molar, coated with O-SAP)	1h post IV injection in tuberculosis mice lung accumulation of the O-SAP targeted liposomes was 19.0 ±2.0% as opposed to 4.70±1.06% for non-targeted liposomes due to higher recognition by the RES. Moreover, addition of DCP further enhanced drug accumulation to 23.0 ±2.0% due to targeting of the anionic liposomes by dual specificity to scavenger and carbohydrate receptors	The study suggested the possibility of enhancing lung accumulation by delivery of antitubercular drugs in liposomes with surface modified to have greater recognition by the RES and hence an attractive approach for treatment of pulmonary TB administered systemically
Rifampicin Tuftsin tetrapeptide for targeting to peptide receptors IV (Swiss Albino Mice) [208,411]	Liposome SUVs Egg PC: **Tuftsin** (7-8% of by weight of egg PC)	The efficiency of the liposomes with tuftsin was found to be better than non-targeted liposomes for a two week twice weekly administration, wherein, there was a 2000-fold reduction in *Mycobacterium tuberculosis* load and mice lung weight as compared to free drug	More effective formulation for macrophage targeting and hence treatment of pulmonary TB on administration of drug systemically

MLVs-multilamellar vesicles, SUVs- small unilamellar vesicles, ULVs- unilamellar vesicles, PC-phosphatidylcholine, DCP- dicetylphosphate, Chol- cholesterol, DSPC- distearyl phosphatidylcholine, DHPE-dihexadecanoyl phosphoethanolamine, IV-intravenous

4.1.6 Drugs and excipients used in study

In the present study, development of dry powder microparticles of liposomes co-encapsulating antitubercular drugs rifampicin and ibuprofen was aimed.

Rifampicin

Rifampicin (Figure 4.1), a first-line antitubercular drug, is one of the most potent and broad-spectrum antibiotic for the treatment of pulmonary tuberculosis.

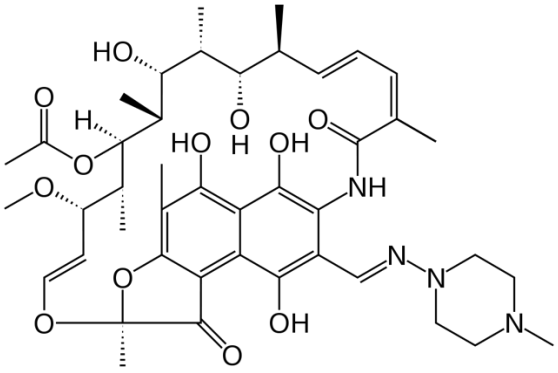

Figure 4.1: Structure of rifampicin

Table 4.3: Physicochemical properties of rifampicin

Molecular formula	$C_{43}H_{58}N_4O_{12}$
pKa	2.7
Molecular weight	822.953 g/mol
Solubility	Slightly soluble in water at pH 7.3 Soluble in dimethylformamide, methanol, chloroform, acetone and DMSO

Due to its optimum physiochemical properties (Table 4.3), it diffuses freely into intracellular compartments of living cells, tissues and bacteria and hence is useful for treatment of *Mycobacterium tuberculosis* [414]. Rifampicin binds to and inhibits DNA-dependent RNA polymerase with high affinity, hence the bacterial cells can no longer produce RNA more than 2-3 nucleotide long, ultimately failing protein transcription. Resistance against rifampicin arises from mutation in the β subunit of the RNA polymerase site required by the drug to show activity [80].

Ibuprofen

Re-purposing of NSAID ibuprofen (Figure 4.2, section 4.1.1), a 2-aryl propanoic acid derivative previously demonstrated antitubercular activity was intended.

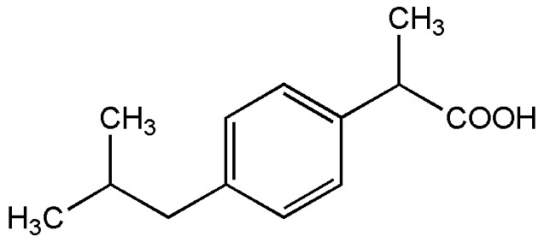

Figure 4.2: Structure of ibuprofen

Table 4.4: Physicochemical properties of ibuprofen

Molecular formula	$C_{13}H_{18}O_2$
pKa	3.97
Molecular weight	206.285 g/mol
Solubility	Insoluble in water Soluble in ethanol, methanol, chloroform and acetone

Trehalose

Dehydrating liposomes in the absence of additives may lead to reduction of head group spacing, aggregation, fusion of liposomes and leakage of the encapsulated material during rehydration of liposomes. Phosphate groups on dry DPPC liposomes exhibit an FT-IR wavenumber of 1254 cm^{-1}, whereas, phosphate groups in the hydrated form interacts with the surrounding water molecules by means of hydrogen bonding and hence exhibit a wavenumber of 1230 cm^{-1}. Phosphate groups on DPPC liposomes spray dried in the presence of trehalose or glucose have shown to exhibit a wavenumber similar to hydrated liposomes, indicating formation of hydrogen bonds between hydroxyl groups on stabilizers and phosphate groups on DPPC. Moreover, hydrogen bond formation helps to alter the packing density and increases lipid head group spacing, decreasing intermolecular Van der Waals interaction [415]. Trehalose a non-reducing sugar with a Tg of 117°C has been used as a bulking powder and stabilizer to produce powders for aerosol applications for spray dried liposomes, due to its lyoprotection action.

L-leucine

L-leucine was added as a dispersibility enhancer in the formulation before spray drying. Its role is clarified in section 3.1.4.

4.2 Aims and Objectives

The present investigation was aimed towards the development of dry powder microparticles of liposomes co-encapsulating antitubercular drugs rifampicin and ibuprofen, actively targeted to the scavenger or the mannose receptor of macrophages to enhance uptake of the formulation.

Hence, the aim of the study was

- To engineer liposomes for the co-delivery of hydrophobic drugs rifampicin and ibuprofen, prepared by thin film hydration
- To design and develop dry powder aerosols and study parameters that dictate aerosolization efficiency
- To investigate the effect of charge (neutral, anionic or cationic) and/or targeting moiety mannose on the qualitative and quantitative *in vitro* cellular uptake kinetics in RAW 264.7 murine macrophage cell line

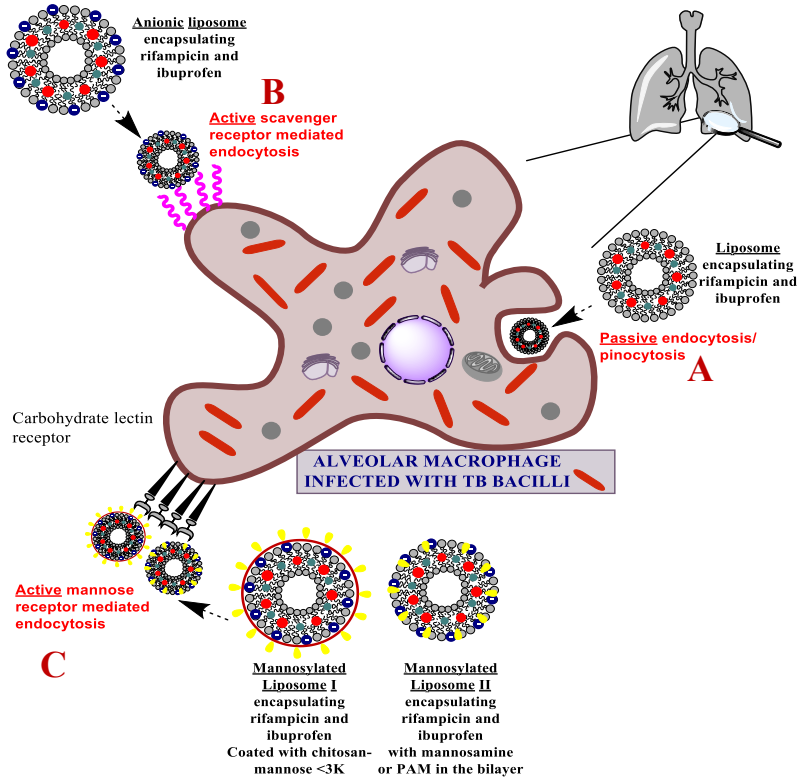

Figure 4.3: Various liposomal nanocarrier formulations designed to study macrophage uptake

The various liposomal formulations investigated in the present chapter are shown in Figure 4.3. Liposomes co-encapsulating rifampicin and ibuprofen with a neutral, positive and negative liposomal charge were formulated, to study the effect of surface charge on the uptake of liposomes by macrophages (Figure 4.3B). Negative liposomes were further mannosylated either by coating them with synthesized mannosylated chitosan imparting a final positive charge (Figure 4.3C) or by embedding mannose moieties viz. mannosamine and PAM (p-amino phenyl mannopyranoside) by interaction of the positive amine groups with the negative charge of the liposomal bilayer (Figure 4.3C).

4.3 Materials

Rifampicin ≥ 98.0% purity (HPLC grade) with molecular weight of 822.94 g/mol and 2-(4-isobutylphenyl) propanoic acid (ibuprofen) ≥ 98.0% purity (HPLC grade) with molecular weight of 206.29 g/mol were purchased from Tokyo Chemical Industry UK (Oxford, UK). Lipids 1,2-dipalmitoyl-sn-glycero-3-phosphatidylcholine (DPPC) and 1,2-dioctadecanoyl-sn-glycero-3-phospho-(1'-rac-glycerol) (sodium salt) (DSPG) were purchased from Lipoid GmbH (Ludwigshafen, Germany) and used without further purification. L-leucine ≥ 98.0% purity (TLC grade), HPLC grade di-potassium hydrogen orthophosphate, mannopyranosyl phenyl isothiocyanate, 4-aminophenyl α-D-mannopyranoside and D-mannosamine hydrochloride were purchased from Sigma-Aldrich (Poole, UK) and lactose (Lactohale® LH300) was purchased from Friesland Foods Domo (Zwolle, Netherlands). Chitosan <3K was purchased from Carbosynth Ltd. (Berkshire, UK).

For the NGI, silicon oil was obtained from Sigma-Aldrich (Poole, UK) and 75 mm internal micro-orifice filter was purchased from Copley Scientific (Nottingham, UK). For *in vitro* cell culture studies fetal bovine serum (FBS), Dulbecco's Modified Eagle Medium (DMEM), penicillin-streptomycin and PBS pH 7.4 used to evaluate qualitative and quantitative cellular uptake were purchased from ThermoFisher Scientific (Loughborough, UK). Coumarin-6 fluorescent dye was obtained from Sigma-Aldrich (Poole, UK).

HPLC grade tetrahydrofuran, water, n-hexane and isopropanol were purchased from Fisher Scientific (Loughborough, UK). Deionized water was used throughout the experiments unless specifically mentioned. All other reagents used were of analytical grade.

4.4 Methods

4.4.1 Preparation of rifampicin and ibuprofen co-encapsulated liposomes

Liposomes were prepared using the thin film hydration method as previously described [416–420]. Multilamellar vesicles (MLVs) were prepared by dissolving constitutive lipids as per the formulations in 20 mL of 1:2 v/v methanol: chloroform. A known amount of drug rifampicin and ibuprofen was then added to the lipid solution and the organic solvent was removed under vacuum using a rotary evaporator KNF RC 900 (KNF Neuberger UK, Oxfordshire, UK) at 55 °C and 200 rpm for 20 min. A dried thin and homogeneous lipid film was obtained and further dried under a stream of nitrogen gas for 20 min to ensure complete removal of residual solvent. The lipid film was then hydrated using 15 mL deionised water adjusted to pH 7.0 (3.5 mg lipid/mL) at 55 °C i.e. a temperature above the phase transition temperature of the lipids at 250 rpm for 20 min and was then left to anneal at room temperature for 1 h. The liposomes obtained were negatively-charged or had a neutral charge depending on their composition.

Macrophage-targeted liposomes were prepared by either coating liposomes with mannosylated chitosan, or by incorporating mannose moieties within the liposomal bilayers (section 4.4.3.2).

To obtain a positively-charged liposomal surface, chitosan <3K was added to the negatively-charged liposomal suspension after hydration to induce coating by electrostatic attraction. Briefly, the liposomal suspension was allowed to anneal for 1 h after hydration and then varied volumes and concentrations of chitosan (Table 4.10) was added to the suspension which was magnetically stirred at 600 rpm for 30 min at room temperature to allow interaction between the negatively-charged liposomal surface and positively-charged chitosan. Mannosylated positively-charged liposomes were prepared by coating liposomes with chitosan-mannose (section 4.4.3.1) in the same manner as described for chitosan coating.

Unentrapped amphiphilic rifampicin and uncoated chitosan <3K/ chitosan-mannose <3K (in the case of positively-charged liposomes) was removed from liposomal preparations by exhaustive dialysis using a Spectra/Por® dialysis membrane (3500 Da MW cut-off, <2 nm pore size; Spectrum Laboratories, UK) against deionized water at room temperature for 2 h (replacing water every 15 min). This allowed 'sink conditions' for the dissolution and consequent removal of the unentrapped amphiphilic rifampicin and/or uncoated chitosan <3K, and avoided the destabilization and breakage of the liposomes by osmotic swelling and vesicle fusion. The resultant liposomal dispersion was then size reduced to obtain small unilamellar vesicles (SUVs) using a probe sonicator (Soniprep 150 ultrasonic disintegrator, MSE Crowley, London, UK), using 5 cycles of 2 min each (with 1 min between the cycles, in an ice bath) for size reduction. The clear red opalescent dispersion obtained was filtered using a 0.22 μm syringe filter (Millex MP, Ireland) to remove the unentrapped hydrophobic ibuprofen and amphiphilic rifampicin. The resultant liposomal dispersion was then characterized for size and charge using the Nano Zetasizer ZS (Malvern instruments, Malvern, UK) and the encapsulation efficiency of the co-encapsulated drugs developed using HPLC (section 4.4.4.2).

4.4.2 Design of experiments (DoE) for developing optimal liposomal formulation

4.4.2.1 DoE 1- Choice of lipids

DPPC (transition temperature, Tm 41°C) was used as the major constituent of the liposome bilayer as it is the most abundant component of lung surfactant, constituting up to one-third of the total phospholipids present [421].

The traditional approach of one factor at a time experimentation commonly known as the OFAT i.e. changing one factor at a time whilst keeping the other conditions constant can suffer various limitations including more resources, time and costly experimentation, and it is not a suitable method to study the interactions between the different experimental factors. For this reason, a matrix-based multifactorial method of experimentation involving Design of Experiments (DoE) has been recognized as an important tool for understanding and rapid development of pharmaceutical processes and products. The validation of the experiments was studied using DoE and the choice of factors and responses to be investigated was largely based on a study of the literature and experience.

A randomized full factorial design was initiated using Design-Expert® 10 trial version (Stat-Ease, USA) for generation and evaluation of a statistical experimental design to study the effect of two independent factors (X) DSPG and cholesterol content on the response (Y) of the liposomal size (Y_1), zeta potential (Y_2), polydispersity index (Y_3) as well as the encapsulation of rifampicin (Y_4) and ibuprofen (Y_5).

Chitosan/chitosan-mannose coating was intended for the surface of the liposomes so as to achieve targeting to the macrophages, where tubercular infection prevails. This could be achieved by imparting a negative charge to the liposomal surface which could electrostatically bond the positive targeting ligand or the positive mannose moieties mannosamine and p-amino phenyl mannopyranoside. For this reason, the first independent variable (X_1) negative lipid DSPG was studied at 5 different levels.

The second independent variable (X_2) cholesterol was also studied at 5 different levels as cholesterol has been long known to alter the lipid bilayers membrane fluidity and ordering, and hence imparts better stability to the system. Therefore, a full factorial design of experimental trials (shown in Table 4.5) generated 25 possible experiments, each of which was repeated in triplicate.

Table 4.5: DoE factors and responses for choice of lipid

Factors (Independent variables)	**Levels**	**Factor levels used**
Amount of DSPG (µM)	5	0 10 20 30 40
Amount of cholesterol (µM)	5	0 5 10 20 30
Responses (Dependent variables)		**Method**
Size (nm)- Y_1		Section 2.1
Zeta potential (mV)- Y_2		Section 2.1
Polydispersity index- Y_3		Section 2.1
Encapsulation efficiency of rifampicin (%)- Y_4		Section 4.4.4.3
Encapsulation efficiency of ibuprofen (%)- Y_5		Section 4.4.4.3

4.4.2.2 DoE 2- Ratio of drugs

Once a stable liposomal formulation was determined, the optimum ratio of the two drugs that could be loaded within the chosen liposomal constitution and their interactions was to be studied. A full factorial design (shown in Table 4.6) incorporating two independent factors (X) namely rifampicin (X_1) and ibuprofen (X_2) at 3 levels each was developed using Design-Expert® 10. This matrix generated 9 possible experiments each of which was repeated in triplicate.

Table 4.6: DoE factors and responses for ratio of rifampicin and ibuprofen

Factors (Independent variables)	Levels	Factor levels used
Amount of rifampicin (μM)	3	12.5 25 50
Amount of ibuprofen (μM)	3	50 75 100
Responses (Dependent variables)		**Method**
Size (nm)- Y_1		Section 2.1
Zeta potential (mV)- Y_2		Section 2.1
Polydispersity index- Y_3		Section 2.1
Encapsulation efficiency of rifampicin (%)- Y_4		Section 4.4.4.3
Encapsulation efficiency of ibuprofen (%)- Y_5		Section 4.4.4.3

4.4.2.3 DoE 3- Preparation of dry powders suitable for inhalation

Critical process parameters during spray drying can affect the final product and hence the aerodynamic behaviour of the microparticles intended to be delivered using a dry powder inhalation. A two-level factorial design (shown in Table 4.7) was developed with three independent variables (X) namely amount of lyoprotectant trehalose (X_1), addition of dispersibility enhancer L-leucine (X_2) and temperature of spray drying (X_3), using Design-Expert® 6. This matrix generated 8 possible experiments each of which was repeated in triplicate.

Table 4.7: DoE factors and responses for preparation of dry powders suitable for inhalation

Factors (Independent variables)	Levels	Factor levels used	Factor codes
Amount of trehalose (with respect to total formulation)	2	0.5 (33.33% of final powder) 1.0 (50% of final powder)	A- A+
20% (w/w) L- leucine (with respect to total formulation)	2	- +	C- C+
Temperature of spray drying (°C)	2	80 120	B- B+
Responses (Dependent variables)			**Method**
Mean particle size at 50th percentile of cumulative distribution Dv50			Section 2.5
Mean particle size at 90th percentile of cumulative distribution Dv90			Section 2.5
Span- Sympatec			Section 2.5
Moisture content (%)- Thermogravimetric analysis			Section 4.4.2.3.3

An open-loop mode was used to spray dry the formulations on the Büchi B-290 Mini spray dryer (Büchi Labortechnik, Switzerland) using compressed air as drying gas. Other process parameters during spray drying, shown in Table 4.8, were kept constant for all the experiments. The spray

dryer was set up for the stated inlet temperature and neat solvent was pumped until the desired outlet temperature was achieved and stabilized, after which spraying was commenced. All the solutions were spray dried individually after which the instrument temperature was allowed to cool below 25°C. The powder was then collected from the cyclone and collector using a particle collecting brush. The powder was immediately transferred to a glass vial and stored in a desiccator to prevent powder uptake of environmental moisture.

Table 4.8: Process parameters for spray drying using the Büchi B-290 Mini spray dryer

Parameters	Value
Aspiration	100 %
Pump flow rate	20% (6 mL/min)
Spraying gas flow rate	500 L/h
Drying gas flow rate	35 m^3/h
Nozzle tip diameter	0.7 mm

The typical matrix of experiments to be investigated, developed by the software in all the above cases, was performed and results were analyzed using ANOVA statistical model to determine the significance of the model developed and the significance of each of the factors and their interactions on the responses under study, wherein a probability value $p < 0.05$ was considered significant. A 3-Dimensional plot was generated which revealed the influence of each of the independent factors and their interactions on the outcome of the responses under study.

4.4.2.3.1 Surface morphology analysis using Scanning electron microscopy (SEM)

Method used to explore the morphology of liposomes spray dried as microparticles using the SEM is outlined in chapter 2, section 2.4.1.

4.4.2.3.2 Laser diffraction particle size analysis

The particle size distributions of all the spray dried powders were analyzed using laser diffraction with a Sympatec HELOS particle size analyzer, on a RODOS/M particle dispenser fitted with a micro-dosing device ASPIROS/L (Sympatec GmbH, Clausthal-Zellerfeld, Germany) as outlined in chapter 2, section 2.5.

4.4.2.3.3 Moisture content using thermogravimetric analysis (TGA)

The determination of the residual water content of the spray dried microparticles was performed using TGA, wherein the change in mass of the powder depending on its thermal stability and solvent content is measured as a function of temperature and time, in a controlled temperature atmosphere. This was performed using Pyris 6 TGA (Perkin Elmer, UK). 7 to 9 mg samples filled in re-usable open ceramic pans were placed on the balance and heated from 20°C to 300°C at a rate of 10°C/min. Details of the method is as given in Table 4.9. The moisture content of the

formulations was determined by the percentage weight change recorded by the thermobalance between 20°C to 130 °C.

Table 4.9: TGA experimental conditions

Sample mass (mg)	7-9
Sample container	Open ceramic pans
Purge gas	nitrogen
Purge gas flow rate (mL/min)	20
Heating rate (°C/min)	10
Temperature range (°C/min)	20-300

4.4.3 Coating/incorporation of targeting polymer

Mannose, the targeting moiety chosen to actively target liposomes encapsulating antitubercular drugs to macrophages was coated onto the liposomes or incorporated into the bilayers. The effect of the position of the targeting moiety on the uptake of the liposomes was then studied using flow cytometry to ascertain whether the appearance of the mannose to the mannose receptors on the macrophages would cause differential uptake kinetics.

4.4.3.1 Coating liposomes with mannosylated chitosan

To obtain positively-charged liposomes, chitosan/chitosan-mannose which has a high positive charge (0.05% in 0.2% acetic acid +52±1.24 mV and 0.03% in 0.2% acetic acid +40±1.24 mV) was added to the negatively-charged liposomes to coat the surface via electrostatic attraction. Uncoated chitosan < 3K/chitosan-mannose < 3K was removed via exhausted dialysis using a 3500 Da MW cut-off dialysis membrane, as described in section 4.4.1.

4.4.3.1.1 Synthesis of mannosylated chitosan for coating liposomes

Mannosylation of chitosan was carried out using the method previously reported (Figure 4.4) [422]. Briefly, 500 mg chitosan <3K (Carbosynth Ltd., Berkshire, UK) was dissolved in 8 mL of water, and 25 mg of α-D-Mannopyranosyl phenyl isothiocyanate (Carbosynth Ltd., Berkshire, UK) in 2 mL DMSO was added. The reaction mixture was magnetically stirred (multi-position magnetic stirring, RO 10 power IKA WERKE, Germany) for 24 h at room temperature, after which mannosylated chitosan was precipitated out using excess isopropanol. The precipitate was then collected by centrifugation at 13,000 rpm for 10 min after which the synthesized polymer was washed with isopropanol 5 times and finally collected using centrifugation at 13,000 rpm for 10 min.

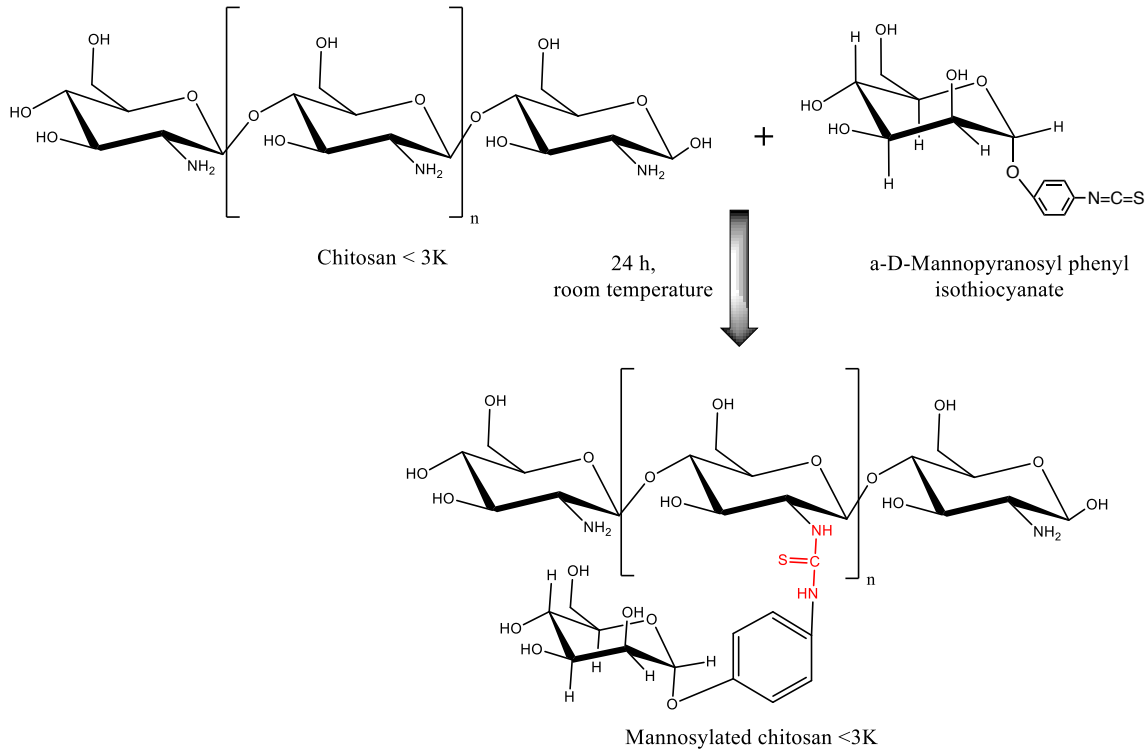

Figure 4.4: Reaction scheme for synthesis of mannosylated chitosan <3K

4.4.3.1.2 ^{1}H-NMR proton nuclear magnetic resonance

High resolution ^{1}H-NMR was conducted using a Bruker AVANCE 500 spectrometer (Bruker Corporation, Massachusetts, USA) to confirm the macromolecular structure of chitosan and mannosylated chitosan and ascertain the success of derivatization. The spectra were obtained at 298 K using 64 scans per sample at a resonance frequency of 500.13MHz for ^{1}H. The polymer solution was prepared at a concentration of 10 mg/mL in D_2O. The NMR solvent was used as an internal standard to assign chemical shifts to the particular protons in the macromolecular structures of chitosan and synthesized chitosan derivative.

4.4.3.1.3 Fourier transform infrared spectroscopy

FT-IR spectrum of chitosan and mannosylated chitosan were determined to analyze the success of mannosylation. A Spectrum™ 100 spectrophotometer (PerkinElmer, UK) operating in the mid-infrared region equipped with a UATR device was used. The procedure followed was as described in chapter 2, section 2.2.

An appropriate ratio of cationic and anionic charges is necessary to achieve an interaction leading to formation of a homogeneous dispersion. After a certain range of electroneutrality between the positive and negative charges, complexes formed might aggregate and precipitate in solution. Preliminary experiments were performed and then different volume and concentration of chitosan solutions were investigated to obtain homogeneous chitosan-coated liposomal dispersions (shown in Table 4.10) in triplicate.

Table 4.10: Conditions for coating liposomal dispersions with targeting polymer

Type of polymer	2	Chitosan <3K Chitosan-mannose <3K
Concentration of chitosan (%) in 0.2% acidified water	2	0.03 0.05
Volume of chitosan solution (per 15 mL formulation) (mL)	3	2.5 5 7.5

4.4.3.2 Incorporation of mannose within liposomal bilayers

20 mg of D-mannosamine hydrochloride (36.75% mole) or 10 mg p-aminophenyl mannopyranoside (18.78% mole) were added to the organic phase in the preparation of liposomes before solvent evaporation, as seen in section 4.4.1. This helped in incorporating these mannose moieties within the bilayer since hydration at pH 7.0 (i.e. HPLC grade water was adjusted to pH 7) the NH_2 group of these mannosylated derivatives are protonated to a positive charge and would electrostatically embed in the negatively-charged headgroup region of the liposomes.

4.4.4 Formulation/powder characterization

4.4.4.1 Determination of particle size and zeta potential (surface charge) using Malvern Zetasizer

The hydrodynamic diameter and the polydispersity index (PDI) of the liposomal formulations were measured by DLS and the zeta potential was measured by laser Doppler velocimetry using Malvern Zetasizer Nano ZS (Malvern Instruments Inc., UK) as described in chapter 2, section 2.1.

4.4.4.2 High-performance liquid chromatography (HPLC) and analytical method validation for simultaneous determination of rifampicin and ibuprofen

The encapsulation efficiency of rifampicin and ibuprofen in liposomes and the amount of these drugs deposited in each stage of the NGI (section 4.4.4.6) was determined using HPLC using an Agilent 1260 infinity series HPLC (Agilent Technologies UK Ltd., UK), equipped with an ultrasensitive diode array UV detector, G1329A auto sampler and a highly efficient quaternary pump. A number of methods for HPLC analysis of both rifampicin and ibuprofen have been described [423–427]. However, for this study a new, rapid, sensitive, precise and accurate method was developed, which gave reproducible results, separation of the retentions between the two drugs, and chromatograms with sharp peaks and a stable baseline.

Briefly, 10 µL samples were eluted with the mobile phase comprising of a ratio of 60:40 50 µM phosphate buffer at pH 7.4 in HPLC grade water: HPLC grade tetrahydrofuran at a flow rate of 1 mL/min using an isocratic elution method. Separation was performed using an Agilent 15 cm×4.6 mm, 3.5 µm Eclipse Plus C8 column (Agilent Technologies, Cheshire, UK) with a bimodal UV detection wavelength of 335 nm for the first 5 min i.e. at the λmax of rifampicin and 220 nm for

the following 10 min of elution i.e. at the λmax of ibuprofen, using a column compartment temperature of 40°C. The HPLC method developed for simultaneous determination of rifampicin and ibuprofen was validated for linearity, accuracy and precision; to ascertain that the method adapted was robust and without error. The validation method based on ICH recommendations is described in Chapter 2 for HPLC analytical validation, section 2.7.

A standard curve (calibration curve) was constructed individually for ibuprofen and rifampicin before each sample analysis in triplicate using the same method of HPLC analysis as that intended for the formulations. Concentrations of rifampicin and ibuprofen for the standard were 2.5, 5, 10, 20, 30, 40, 50, 60, 70, 80, 90 and 100 µg/mL and peak area as an average of the triplicates was used to derive the standard equation and correlation coefficient (R^2) of the best fit line, by least square regression method. This standard equation was then considered linear if the R^2 value was approximately 1 and used for calculation of concentration of rifampicin and ibuprofen encapsulated in the liposomes and for determination of the fraction of rifampicin and ibuprofen retained at each stage of the NGI.

4.4.4.3 Determination of drug encapsulation efficiency of the liposomal preparations

Encapsulation efficiency of the formulations after preparation was determined using HPLC to quantify rifampicin and ibuprofen solubilized in the liposomal formulations. Dilutions of the formulation following removal of unsolubilized drugs by dialysis (Spectra/Por® dialysis membrane, 3500 Da MW cut-off, <2 nm pore size; Spectrum Laboratories, UK) and filtration (0.22 µm mixed cellulose esters syringe-driven filter (Millex MP, Ireland)) was performed by diluting approximately 50 times in methanol to obtain a solution concentration appropriate for HPLC measurement as per the Beer-Lambert law. The solutions were filtered into HPLC vials and quantified as described (section 4.4.4.2). The peak areas for rifampicin and ibuprofen from the formulations were used for calculation of the encapsulation efficiency of drug, using linear regression equation from calibration curve with correlation coefficients of 0.9997 and 0.9999 for rifampicin and ibuprofen respectively. Encapsulation efficiency was expressed as a percentage using the equation 4.1:

$$Encapsulation\ efficiency(\%) = \frac{Practically\ determined\ amount\ of\ drug\ \ in\ formulation}{Amount\ of\ drug\ initially\ weighed} \times 100$$

Equation 4.1

4.4.4.4 Determination of particle size and zeta potential (surface charge) on rehydration of spray dried liposomes in deionized water using Malvern Zetasizer

5 mg of spray dried powder was dispersed in 2 mL of deionized water previously heated to 37°C (to mimic body temperature) and bath sonicated for 2 min. The hydrodynamic diameter and the polydispersity index (PDI) of the resulting re-dispersed spray dried liposomes were measured by DLS and the zeta potential was measured by laser Doppler velocimetry using Malvern Zetasizer Nano ZS (Malvern Instruments Inc., UK) at 37°C.

4.4.4.5 Morphology analysis of liposomes using Transmission electron microscopy

TEM micrographs for morphological examination of liposomal preparations was carried out using the method outlined in chapter 2, section 2.4.2.

4.4.4.6 *In vitro* aerosol deposition and aerodynamic behaviour studies using the Next Generation Pharmaceutical Impactor

The aerosol parameters and deposition of spray dried microparticles at the different stages of the NGI were determined using the method described in chapter 2, section 2.6. In each experiment five size 3 transparent gelatin capsules were filled manually with 30±0.2 mg of spray dried microparticles and aerosolized using the Cyclohaler® (Pharmacemie, UK).

4.4.4.7 Quantitative assessment of cellular uptake kinetics using flow cytometry and qualitative assessment using fluorescent microscopy

Flow cytometry was used to examine the cellular uptake kinetics of various liposomal formulations, encapsulating fluorescent dye coumarin-6 to study the effect of the liposomal charge and the targeting moiety on the interaction and uptake in the murine macrophage cell line RAW 264.7, at different time points. Specifically, $2x10^5$ RAW 264.7 cells/well (cells were routinely passaged at 80-85% confluency using cell scrapers, passage no. 9-15 used for experiment) were seeded in 12-well plates in Dulbecco's Modified Eagle medium (DMEM) supplemented with 10% fetal bovine serum and 1% penicillin-streptomycin (complete media) and grown at 37°C and 5% carbon dioxide for 36 h. The medium was then carefully aspirated and the cells were washed with PBS pH 7.4, to remove any dead/suspension cells. The cells were then treated with liposomes diluted in complete media at a final concentration of coumarin-6 of 1 µg/well and incubated for 0.25, 0.5, 2, 4 or 8 h. At the specific time points, the cells were washed 3 times with ice-cold PBS pH 7.4 to remove any liposomes adhered to the cells and to stop uptake. The cells were then suspended in warm PBS pH 7.4 using cell scrapers and transferred into Falcon™ round bottom polystyrene tubes (Fischer Scientific, UK). The fluorescence intensity of coumarin-6 at each time point for each liposomal formulation was analyzed using MACSQuant® Analyzer 10 (Miltenyi Biotech, Surrey, UK) Flow Cytometer in the FL B-2 channel excitation emission. Prior to the experiment, blank RAW 264.7 cells were used to set up the voltage of the forward scatter (FSC), side scatter (SSC) and FL B-2 channel to ensure that all the cells under study were accommodated into the window of analysis. The region 'P1' then selected was such so as to exclude dead cells, cell debris and clumped cells and to study specifically living cells, which accounted for around 83-86% for all the samples analyzed.

For visualizing the coumarin-6 uptake at the different time points for the various liposomal formulations, $1x10^5$ cells were seeded in 12-well plates in complete media and grown at 37 °C and 5% carbon dioxide for 36 h. The medium was then carefully aspirated and the cells were washed with PBS pH 7.4, to remove any dead/suspension cells. The cells were then treated with liposomes diluted in complete media at a final concentration of coumarin-6 of 0.2 µg/well and

incubated for 0.25, 0.5, 2, 4 or 8 hours. At the specific time points, the cells were washed 3 times with ice-cold PBS pH 7.4, to remove any liposomes adhered to the cells and stop uptake and then imaged under EVOS™ Fluorescence Cell Imaging System using the GFP filter (470 nm excitation, 525 nm emission) under 20X magnification and phase contrast annuli 4/10 condenser.

4.5 Results and Discussion

4.5.1 High-performance liquid chromatography (HPLC) and analytical method validation of simultaneous determination of rifampicin and ibuprofen

Linearity: The data for HPLC calibration curve of rifampicin and ibuprofen was fitted into a linear equation of *y=17.947x–6.8517* and *y=26.385x+1.4183* respectively (where x=concentration of analyte and y=area under curve), and was observed to follow linearity and hence Beer-Lambert law in the concentration range under study i.e.2.5-100 µg/mL, as shown in Figure 4.5 and Figure 4.6. A regression analysis was performed and correlation coefficient R^2 of 0.9997 and 0.9999 (for rifampicin and ibuprofen respectively) indicated the existence of a linear relationship between peak area and concentration of drug analyzed. Parameters determining linearity from HPLC analysis for rifampicin and ibuprofen are shown in Table 4.11.

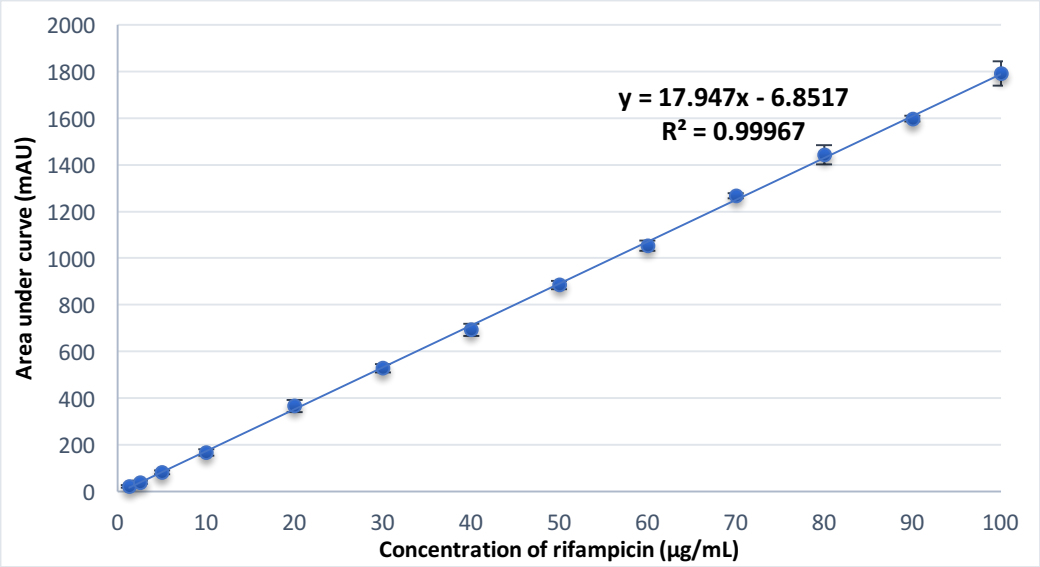

Figure 4.5: Calibration curve of rifampicin analyzed by HPLC (mean±SD, n=5)

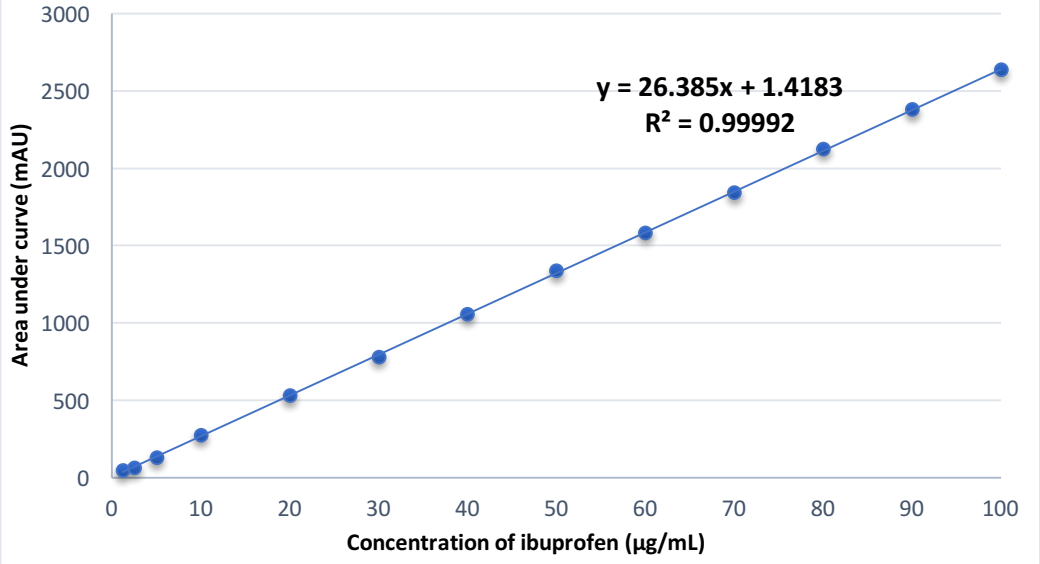

Figure 4.6: Calibration curve of ibuprofen analyzed by HPLC (mean±SD, n=5)

Table 4.11: Linearity parameters for HPLC analysis method of simultaneous determination on rifampicin and ibuprofen

Parameters	Results (Rifampicin)	Results (Ibuprofen)
λmax	335	220
Linearity range	2.5-100 µg/mL	2.5-100 µg/mL
Regression equation	y=17.947x–6.8517	y=26.385x+1.4183
Correlation coefficient	0.9997	0.9999
Retention time	2.78 min	9.10 min
Limit of detection (LOD)	0.89 µg/mL	0.44 µg/mL
Limit of quantification (LOQ)	2.47 µg/mL	1.48 µg/mL

Representative chromatogram of rifampicin and ibuprofen and validation for accuracy and precision of HPLC method is as seen in Appendix 1, A1.2.

4.5.2 Design of Experiment (DoE)

4.5.2.1 DoE 1- Choice of lipids

ANOVA studies for effect of factors DSPG (X_1) and cholesterol (X_2) on all the responses (Y) (Table 4.5) generated a statistically significant ($p < 0.0001$) factorial model, which could be used to determine the best choice of lipids to formulate a stable liposomal dispersion. Lack of fit test (F-test) and diagnostic plot of normal percentage probability of studentized residuals (Appendix 2) were used to validate the model statistics, which was in good correlation with the ANOVA studies performed for the factorial model. In the normal percentage probability plot the spread of data points was approximately along a straight line depictive of a good correlation between the model predicted and model fitted, confirming that the model fitted was normal and could be used to study the effect of the different factors on the various responses [428].

The response of zeta potential (Y_2) (**Figure 4.**7A) demonstrates a significant decrease in the value of zeta potential with an increase in content of negative lipid DSPG (X_1, $p < 0.0001$). Cholesterol also showed a significant (X_2, $p = 0.0015$) effect on the value of zeta potential. Point-based ANOVA (OriginPro v8.0724) studies demonstrated that the addition of cholesterol produced a statistically significant reduction ($p < 0.05$) in the value of zeta potential when added to neutral DPPC liposomes. This was in good correlation to previously reported studies, where addition of cholesterol decreased the zeta potential of neutral DPPC and DSPC liposomes to negative values [429,430]. Strong hydrogen bond interactions between the choline methyl groups of PC lipids and the hydroxyl groups of cholesterol which increases the state of order by lipid chain conformational changes to prevent rapid release of the drugs from the liposomes, which is responsible for the reduction in the zeta potential values [430–432]. However, the effect of cholesterol on the value of zeta potential in the highly negatively-charged liposome bilayer containing DPPC: DSPG (all ratios) was probably shielded and hence showed no significant difference ($p > 0.05$) of addition of cholesterol on zeta potential for negative liposomes.

ANOVA studies of the developed factorial model showed a significant influence of the factors DSPG (X_1, $p < 0.0001$) and cholesterol (X_1, $p < 0.0001$) on the mean size (hydrodynamic diameter) of the liposomes (**Figure 4.**7B). Moreover, a significant interaction was seen between the two factors X_1X_2, $p < 0.0001$, wherein a decrease in size was seen with increasing DSPG with a more gradual effect in DPPC liposomes with a high percentage of cholesterol. An increase in liposomal size was evident with increasing cholesterol, wherein the effect was more evident in DPPC liposomes with a lower percentage of negative lipid DSPG.

Study of polydispersity index of the liposomes demonstrated a significant effect of DSPG (X_1, $p < 0.0001$, **Figure 4.**7C) was seen on the PDI of the liposomes. Cholesterol however did not have a significant (X_1, $p = 0.1192$) effect on the PDI; a higher PDI was evident for neutral DPPC liposomes (DPPC liposomes without DSPG) (0.30-0.50). Addition of negative lipid DSPG reduced the PDI to around 0.21-0.25 for most of the formulations.

The model developed to study the effect of factors X_1 (DSPG) and X_2 (Cholesterol) on the response of co-encapsulation efficiency of the drug rifampicin (Y_4) demonstrated a significant ($p < 0.0001$, Figure 4.8A) effect of addition of DSPG and cholesterol. Addition of 10-20 micromolar DSPG caused a reduction in rifampicin encapsulation for the formulations with higher cholesterol content (20-30 micromolar), which may be due to the improper bilayer formation leading to an increased leakage of drug at the particular ratio of components. With an increase in DSPG (30-40 micromolar) this effect was nullified. Maximum loading of rifampicin was observed for DPPC: DSPG: Chol 100:40:0, 100:40:20 and 100:40:30.

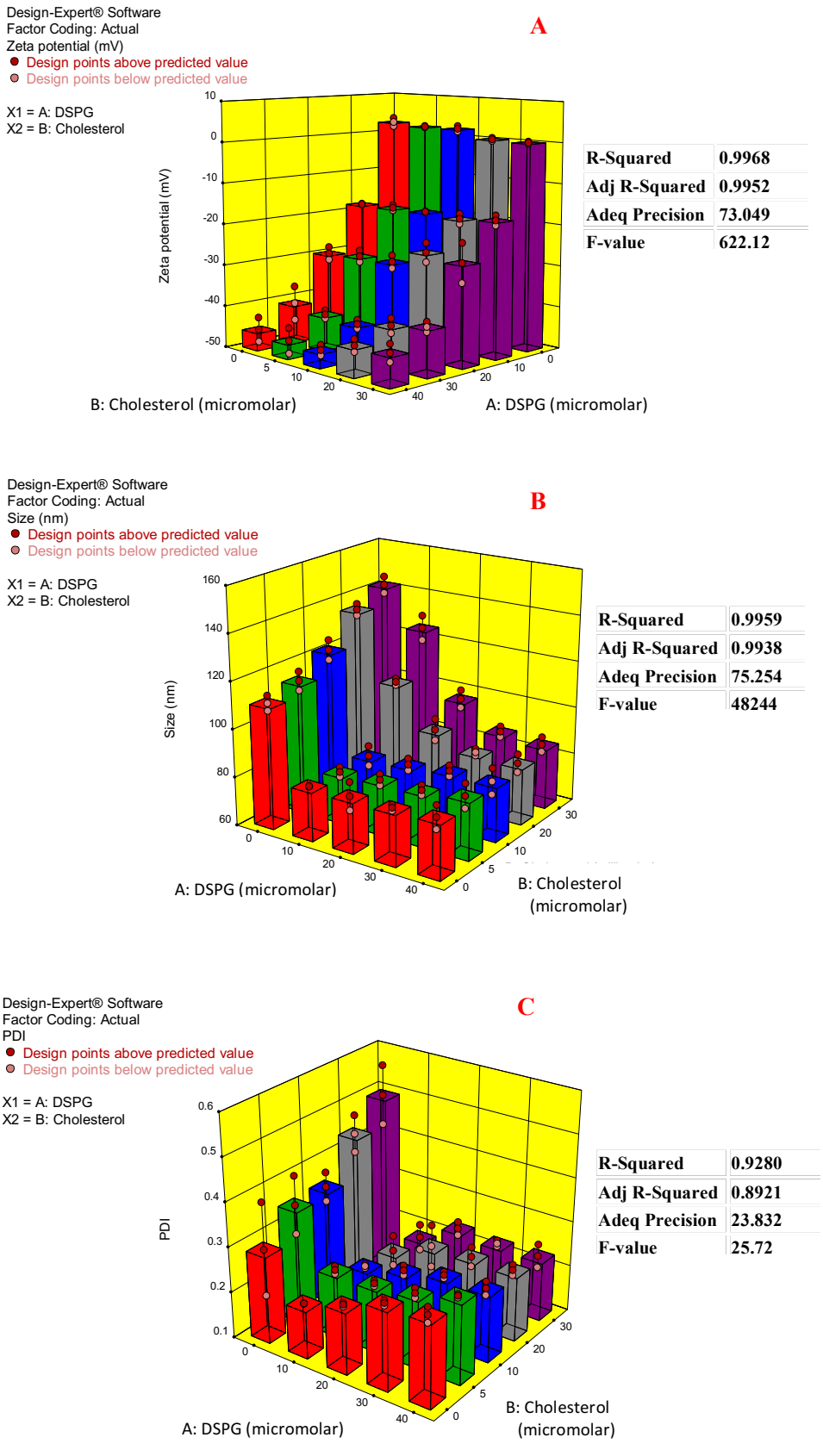

Figure 4.7: DoE 1- Choice of lipids, the effect of factors DSPG and cholesterol on responses zeta potential (A), mean size (B) and PDI (C) (mean±SD, n=3, 3D surface plot Design-Expert® 10 (Stat-Ease, Inc.))

Moreover, the model developed to study the effect of factors X_1 (DSPG) and X_2 (Cholesterol) on the co-encapsulation efficiency of drug ibuprofen (Y_5) depicted a significant ($p < 0.0001$, Figure 4.8B) effect of addition of DSPG on the encapsulation of ibuprofen, however, addition of cholesterol did not significantly affect its encapsulation. A pattern similar to encapsulation of rifampicin was observed, wherein, addition of 10-20 micromolar DSPG caused a reduction in ibuprofen encapsulation with a gradual increase in encapsulation of ibuprofen with greater amounts of DSPG (30-40 micromolar), indicating that for proper bilayer formation approximately 23% mole of DSPG to total lipids is required to co-encapsulate rifampicin and ibuprofen.

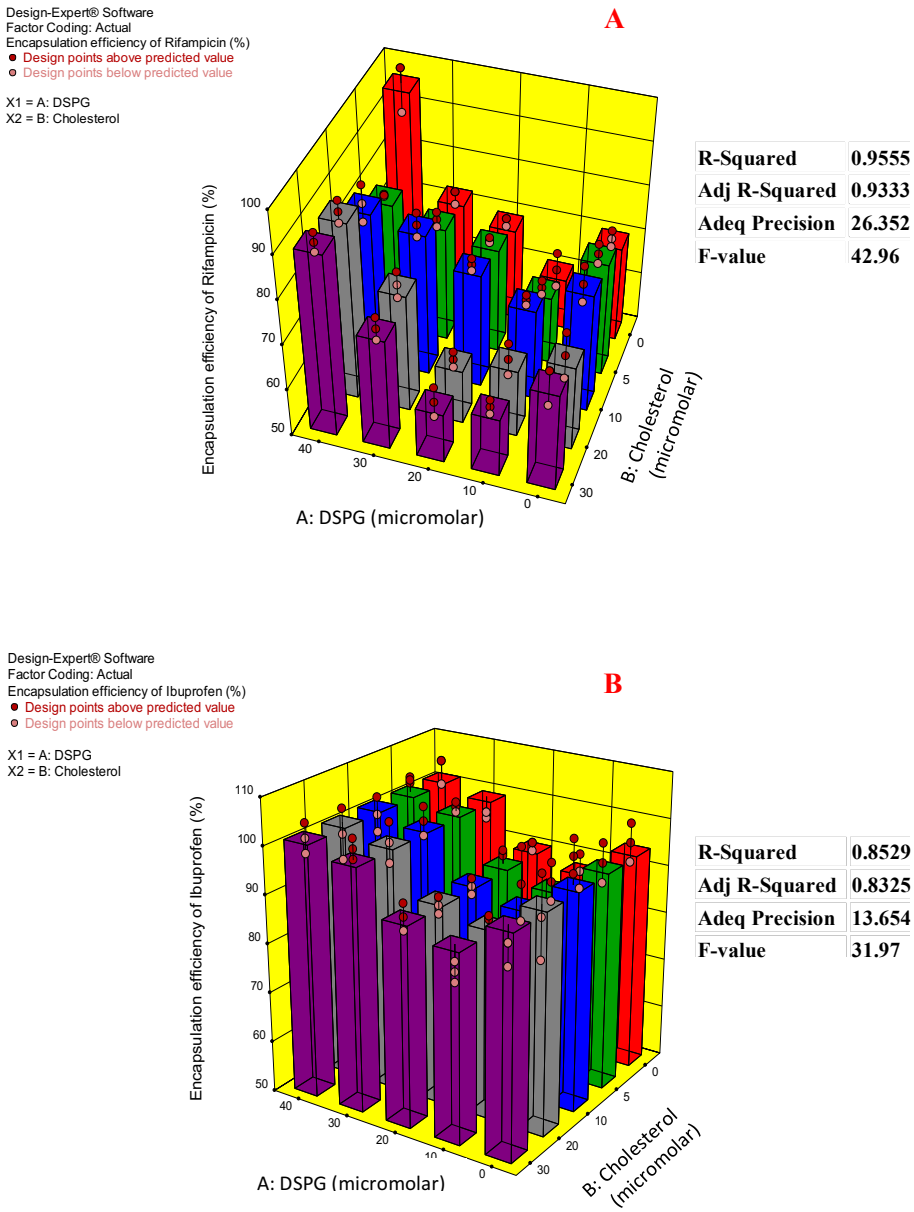

Figure 4.8: DoE 1- Choice of lipids, the effect of factors DSPG and cholesterol on responses encapsulation efficiency of rifampicin (A) and encapsulation efficiency of ibuprofen (B) (mean±SD, n=3, 3D surface plot Design-Expert® 10 (Stat-Ease, Inc.))

Previous literature using 28% and 35% mole of DSPG to phosphatidylcholine has been shown to successfully encapsulate hydrophobic drug cisplatin and hydrophilic drug sodium selenite [433,434]. There was a more drastic effect of lipid composition evident on the encapsulation efficiency of rifampicin (Figure 4.8B) which ranged from 57.51-92.91%, as compared to the encapsulation efficiency of ibuprofen (Figure 4.8B) which ranged from 80.82-105.19%. This was due to the bulky size of rifampicin which required optimal packing of the bilayer for improved rifampicin incorporation, in good correlation with previous studies [191].

On analyzing the responses observed in the above factorial model a maximum co-loading of drugs was desired with small size and high negative zeta potential for an optimum and stable formulation. Keeping in mind the encapsulation profile of rifampicin and ibuprofen, 40 micromolar negative lipid DSPG (28.57% mole of total lipids) was chosen. Moreover, there was no significant difference ($p > 0.05$) in all the responses for DPPC: DSPG (100:40) formulations at 20 micromolar (14.29% mole cholesterol to lipids) and 30 micromolar (21.43% mole of cholesterol to lipids) cholesterol, hence DPPC: DSPG: Chol 100:40:20 was chosen as the optimum composition of lipids.

4.5.2.2 DoE 2- Ratio of drugs

Maximum loading of antitubercular drugs is desirable to reduce the amount of formulation to be administered to the patient. Moreover, earlier studies have reported the importance of hydrophobicity of drug on the stability of DPPC liposomes, wherein destabilization of liposomes and hence a greater dye leakage was evident on storage when hydrophobic rhodamine was encapsulated as compared to hydrophilic fluorescein [435]. This was due to an increased expulsion of the hydrophobic dye from the liposomal bilayer on movement of the phospholipid tail on storage, as opposed to the cargo of hydrophilic dye inside the liposomal core [435]. Furthermore, complexity of the liposomal system increases when different drugs are co-encapsulated making it important to study the interaction of one drug on the encapsulation of the other and vice versa, to be able to determine an optimum ratio for maximum encapsulation of both the drugs. The matrix developed using DoE® 10.1 was evaluated with experimentation and the responses obtained have been highlighted in Figure 4.9 and Figure 4.10.

It was evident that a statistically significant model explaining the effect of amount of rifampicin (X_1) and amount of ibuprofen (X_2) was developed for responses zeta potential (Y_2) and encapsulation efficiencies of rifampicin (Y_4) and ibuprofen (Y_5). Mean size (hydrodynamic diameter, Y_1) and PDI (Y_3) of the liposomes did not change on alteration of the amount of drugs encapsulated and hence the model developed was insignificant and could not be used to study the significance of the individual terms and their interactions with respect to these responses. Point-based ANOVA Tukey post-hoc analysis using OriginPro v8.0724 was hence performed, which confirmed that there was no significant difference in mean size and PDI ($p > 0.05$, $p > 0.005$) for the different formulations under experimentation.

Lack of fit test (F-test) and diagnostic plot of normal percentage probability of studentized residual (Appendix 2) were used to validate the model statistics, which were in good correlation with the ANOVA studies performed indicating that the factorial model was well fitted to study the effect of factors (amount of rifampicin and ibuprofen) on the statistically significant responses (Y_2, Y_4 and Y_5).

ANOVA study of the response of zeta potential (Y_2, Figure 4.9C) indicated that there was a significant effect of amount of rifampicin (X_1, $p < 0.0001$) and ibuprofen (X_2, $p = 0.0039$) on the value of zeta potential of the liposomes. However, the interaction between the two factors rifampicin and ibuprofen (X_1X_2, $p = 0.0761$) was not significant on the change of zeta potential.

The results explaining the response of encapsulation of rifampicin (Figure 4.10A) and ibuprofen (Figure 4.10B) demonstrated that the individual factors X_1 and X_2 had a significant effect ($p < 0.0001$) on the encapsulation efficiency of rifampicin as well as ibuprofen.

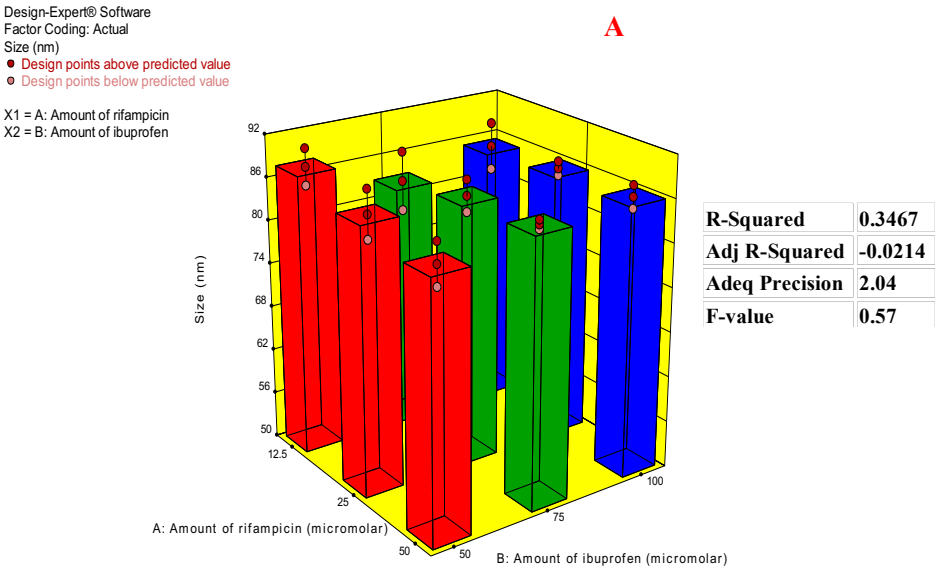

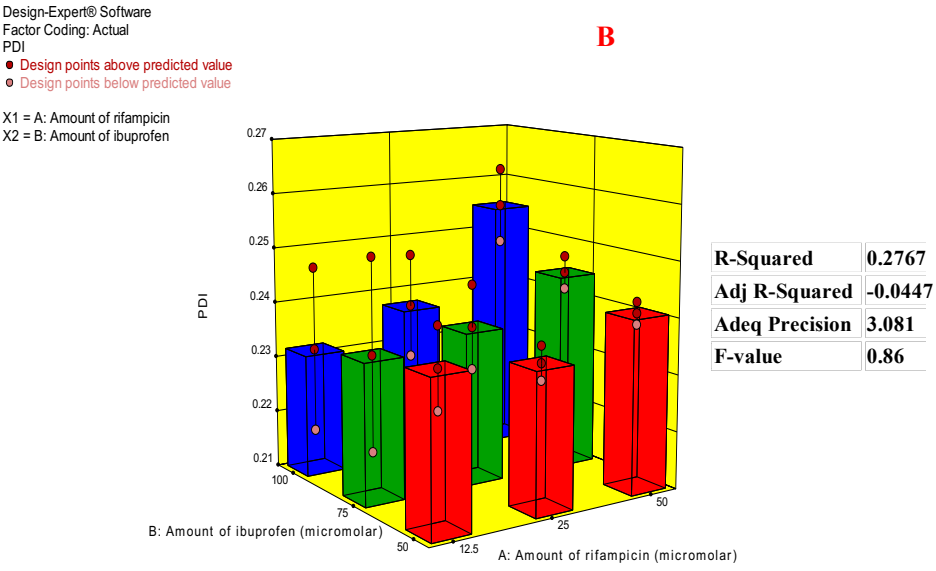

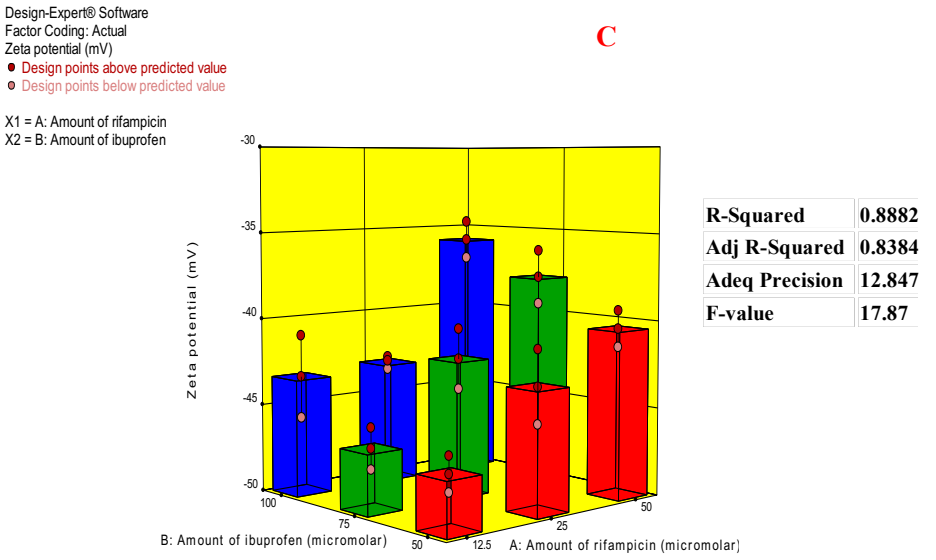

Figure 4.9: DoE 2- Ratio of antitubercular drugs, the effect of factors amount of rifampicin and amount of ibuprofen on responses mean size (A), PDI (B) and zeta potential (C) (mean±SD, n=3, 3D surface plot Design-Expert® 10 (Stat-Ease, Inc.))

Moreover, there was an interaction between the two factors X_1X_2, wherein, an increase in ibuprofen caused a significant reduction ($p < 0.0001$) in amount of rifampicin encapsulated. An increase in the amount of rifampicin similarly caused a reduction in amount of ibuprofen, indicating a significant ($p = 0.0458$) interaction between X1 and X2. Rifampicin and ibuprofen are incorporated within liposomal bilayers due to their hydrophobic nature [191,436]. Moreover, due to the bulky size of rifampicin molecules, displacement of cholesterol from bilayers of DPPC liposomes have been previously reported [191,437]. Hence, it was evident that increase in the amount of one drug reduced the encapsulation of the other, due to a competition between these to be incorporated within the liposomal bilayer.

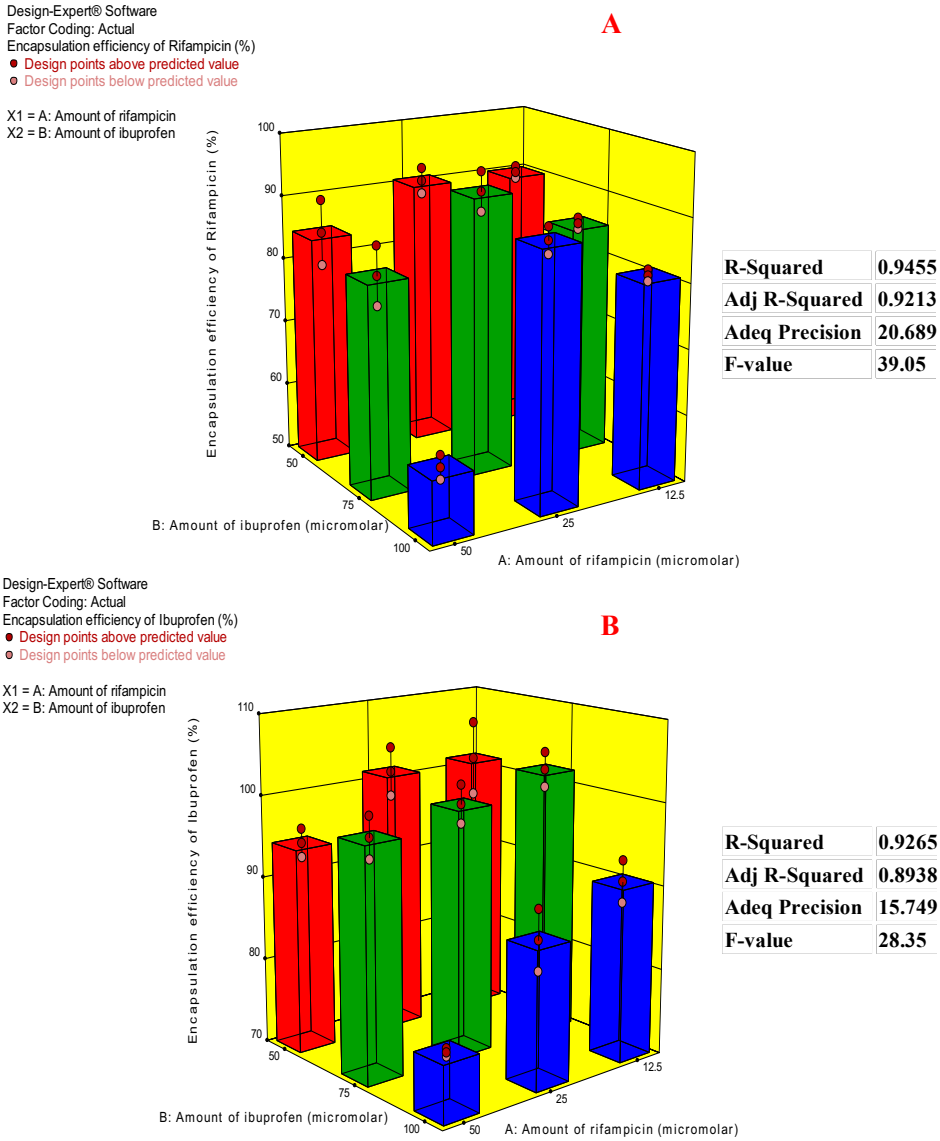

Figure 4.10: DoE 2- Ratio of antitubercular drugs, the effect of factors amount of rifampicin and amount of ibuprofen on responses encapsulation efficiency of rifampicin (A) and encapsulation efficiency of ibuprofen (B) (mean±SD, n=3, 3D surface plot Design-Expert® 10 (Stat-Ease, Inc.))

As maximum encapsulation is attractive to design therapeutically relevant formulations, the factorial model developed gave a good understanding of the interactions of the two drugs co-

encapsulated within the liposomes. Formulations with 75 micromolar versus 50 micromolar of ibuprofen did not show any significant difference ($p > 0.05$) on encapsulation of rifampicin, in point-based ANOVA studies, when compared keeping the amount of rifampicin constant in the formulation. However, there was a significant difference ($p < 0.05$) in encapsulation of rifampicin in formulations with 75 micromolar versus 100 micromolar ibuprofen. Moreover, there was a significant ($p < 0.05$) difference in the encapsulation efficiency of ibuprofen in formulations with 25 micromolar versus 50 micromolar rifampicin, when ibuprofen was kept constant, and no significant difference ($p > 0.05$) in encapsulation of ibuprofen in formulations with 25 micromolar versus 12.5 micromolar rifampicin. Hence 25 micromolar rifampicin and 75 micromolar ibuprofen was chosen for the preparation of liposomes to be converted into dry powder aerosols.

4.5.2.3 DoE 3- Preparation of dry powders suitable for inhalation

Effects of spray drying inlet and outlet temperature, amount of lyoprotectant trehalose and dispersibility enhancer L-leucine on the powder properties like crystallinity, morphology, roughness, density and stickiness are evident, making these a critical process parameters to study. These powder properties directly affect its aerosolization and hence the fine particle dose reaching the site of infection. Rifampicin is stable in a solid form at temperatures up to 70°C and hence the inlet temperature for spray drying was chosen so as to achieve an outlet temperature of lower than 70°C [438].

Trehalose a non-reducing sugar with a Tg of 117°C has been used as a bulking powder and stabilizer to produce powders for aerosol applications for spray dried liposomes, due to its lyoprotection action. Previous studies have shown that high concentration of trehalose i.e. >50% w/w may result in particle agglomeration due to the adhesive nature of the non-reducing sugar [439]. Hence, in the present study 33.33% (factor level 0.5 i.e. 0.5 times trehalose to final formulation) and 50% (factor level 1.0 i.e. 1.0 time trehalose to final formulation) was studied to ascertain the effect of stabilizer addition on the aerosolization of the dry powder. 20% w/w L-leucine has been shown to produce hollow-surfaced spheres and hence an open powder structure with good dispersion in previous literature [373]. This concentration of L-leucine in the feedstock spray dried at 100°C has been shown to improve aerosolization by means of surface diffusion of L-leucine in its condensed phase and subsequent deposition on the surface of the microparticles during spray drying [375,357,356].

A statistically significant model explaining the effect of factors amount of trehalose (X_1), addition of 20% (w/w) L-leucine (X_2) and temperature of spray drying (°C) (X_3), on the responses, volume mean particle size at 90th percentile of cumulative distribution DV90 (Y_2, $p = 0.0165$), Span (Y_3, $p = 0.0058$) and moisture content (%) (Y_4, $p = 0.0255$) was developed. Volume mean particle size at 50th percentile of cumulative distribution VMD (DV50, Y_1, $p = 0.3528$) of the spray dried liposomal microparticles did not undergo change on alteration of the factors and hence the model

developed was insignificant and could not be used to study the significance of the individual factors and their interactions.

Lack of fit test (F-test) were used to validate the model statistics which was in good correlation with the ANOVA studies performed for the factorial model indicating that the model was well fitted to study the effect of factors on the statistically significant responses (Y_2, Y_3 and Y_4). This study generated 3D cubic graphs for each response, where the vertices of the cube represents a point which reflects the value of the particular response (DV50, DV90, Span or moisture content) based on the three factors under study along the X, Y and Z-axis. For factor codes refer to Table 4.7.

ANOVA study of the response of mean particle size at 90th percentile of cumulative distribution DV90 (Y_2, Figure 4.11B) with the various experimental trials developed a significant factorial model which indicated that there was a significant effect of amount of trehalose (X_1, p =0.0267), addition of 20% (w/w) L-leucine (X_2, p =0.0105) and inlet temperature of spray drying (X_3, p = 0.0086) on the DV90 of the spray dried microparticles. Moreover, there was a significant interaction between the amount of trehalose and addition of 20% w/w L-leucine (X_1X_3, p = 0.0350), and amount of trehalose and temperature of spray drying (X_2X_3, p = 0.0116) on the DV90 of the spray dried microparticles.

Study of Span (Y_3) of the spray dried microparticles as depicted in Figure 4.11C, demonstrated a significant effect of amount of trehalose (X_1, p = 0.0110), addition of 20% (w/w) L-leucine (X_2, p = 0.0041) and temperature of spray drying (X_3, p = 0.0030) on the Span of the spray dried microparticles. Similar interaction as that of DV90 i.e. X_1X_2, p = 0.0110 and X_1X_3, p = 0.0039 was seen for the Span of microparticles.

These studies are explained in more detail with respect to the microparticle morphology and volume particle size distribution in section 4.5.2.3.1.

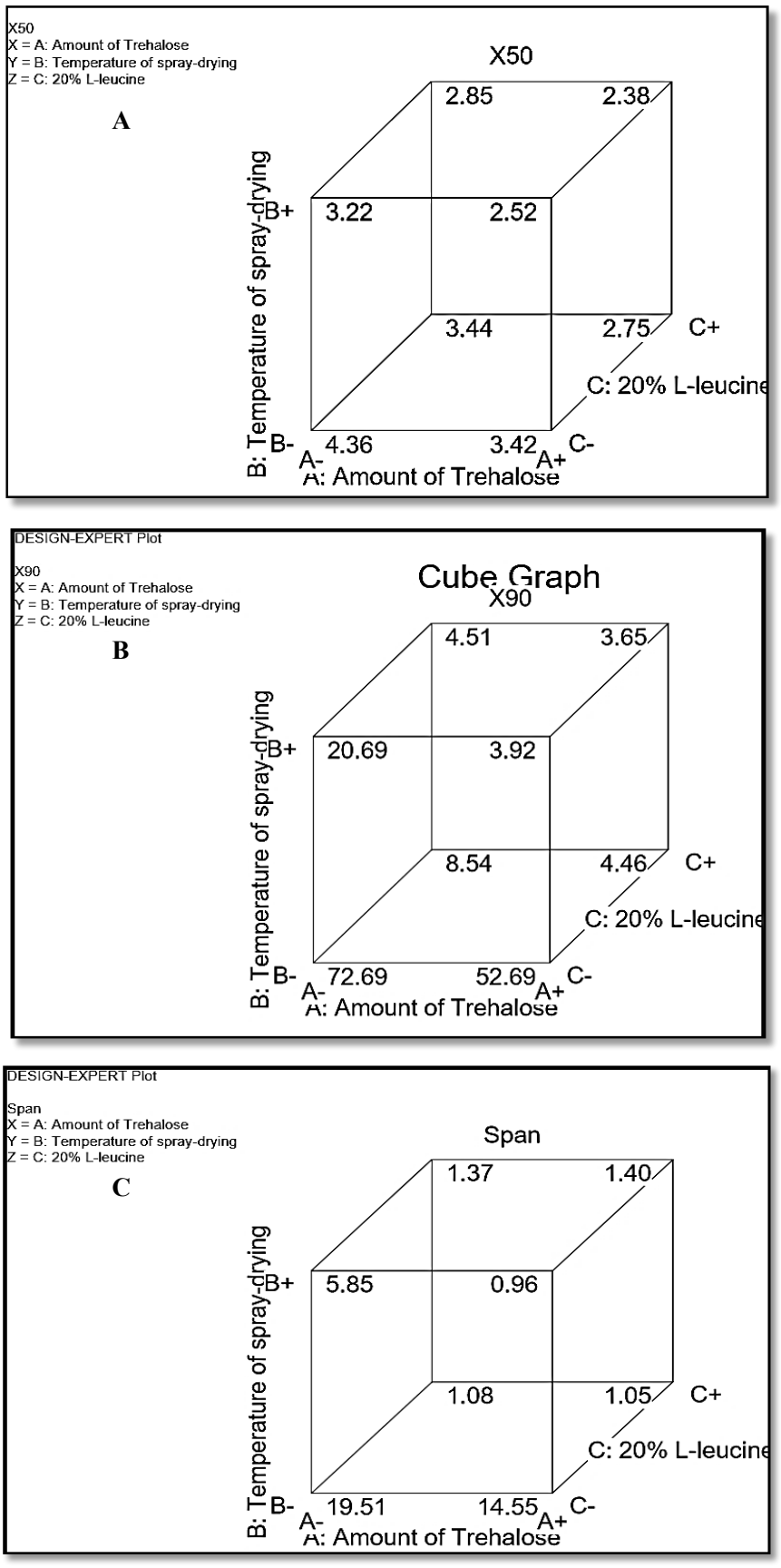

Figure 4.11: DoE 3- Preparation of dry powders suitable for inhalation, the effect of factors on responses DV50 (or X50) (A). DV90 (or X90) (B) and Span (C) (mean±SD, n=3, 3D cube plot Design-Expert® 6 (Stat-Ease, Inc.)) (For factor codes refer to Table 4.7)

4.5.2.3.1 Scanning electron microscopy and laser diffraction analysis

Dehydrating liposomes using spray drying involves the use of high temperature and shear stress of atomization, which could lead to a detrimental impact on the liposomes structure, like disruption of the liposomal bilayer structure and degradation of the lipid components during the process [415]. Hence it was important to carefully adjust the additives used for spray drying, their concentration versus the concentration of the lipid and the spay drying process parameters. SEM micrographs served as a visual means to screen various microparticulate formulations to be spray dried using the matrix of DoE experiments. RODOS/M was used to disperse the particles to analyze the volume mean particle size (DV50, VMD), and particle size distribution of the spray dried powders using the HELOS laser diffraction technique on the Sympatec.

SEM micrographs of spay dried microparticles with low amount of lyoprotectant trehalose (0.5 times trehalose with respect to liposomal formulation) sprayed at 80 °C as seen in Figure 4.12A, showed partially fused and agglomerated particles with no proper particle formation. These micrographs were supported by the particle size distribution histograms obtained from laser diffraction (Sympatec) studies, wherein an DV90 of 72.47 µm and VMD of 6.54 µm (Span 19.53) were observed. On addition of 20% w/w L-leucine (Figure 4.12B), SEM micrographs of spray dried microparticles with low amount of lyoprotectant trehalose, sprayed at 80 °C showed agglomerated spherical particles with better separation as compared to powders without L-leucine (Figure 4.12A). Moreover, an improved laser diffraction particle size distribution was also evident with an DV90 of 20.91 µm and VMD of 4.67 µm (Span 5.83). To obtain aerosolization and an improved dispersion of respirable microparticles the particle size of the spray dried dry powder should be less than 5 µm with a unimodal distribution depicted by a Span value close to 1.

Spray drying at 80 °C with a higher amount of lyoprotectant trehalose (1.0 times trehalose with respect to liposomal formulation) without L-leucine (Figure 4.13A) showed the presence of spherical particles clumped together and dry powder laser diffraction particle size DV90 of 52.91 µm and VMD of 3.54 µm (Span 14.53). However, addition of 20% w/w L-leucine to the above formulation (Figure 4.13B) improved the dry powder microparticle morphology, wherein, particles with wrinkled surface spheres, with an DV90 value of 4.24 and VMD of 2.50 µm (Span 1.07) were evident.

80ºC: 0.5X trehalose

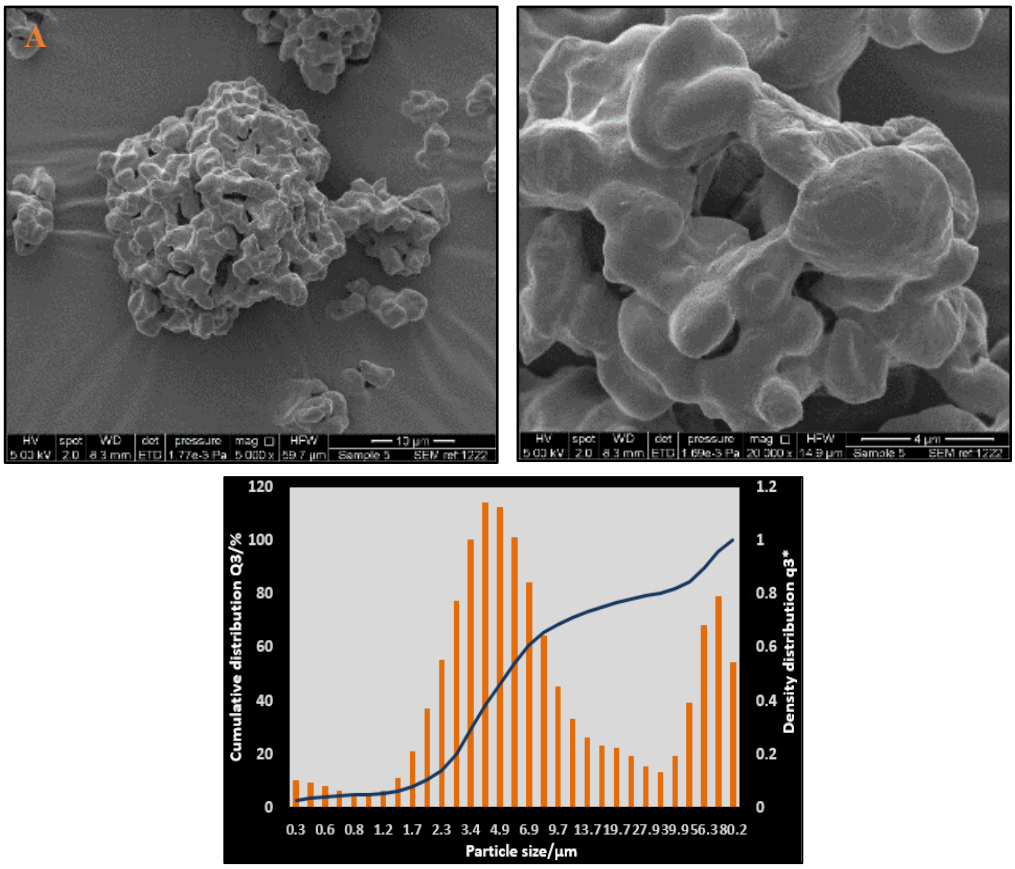

80ºC: 0.5X trehalose: 20% w/w L-leucine

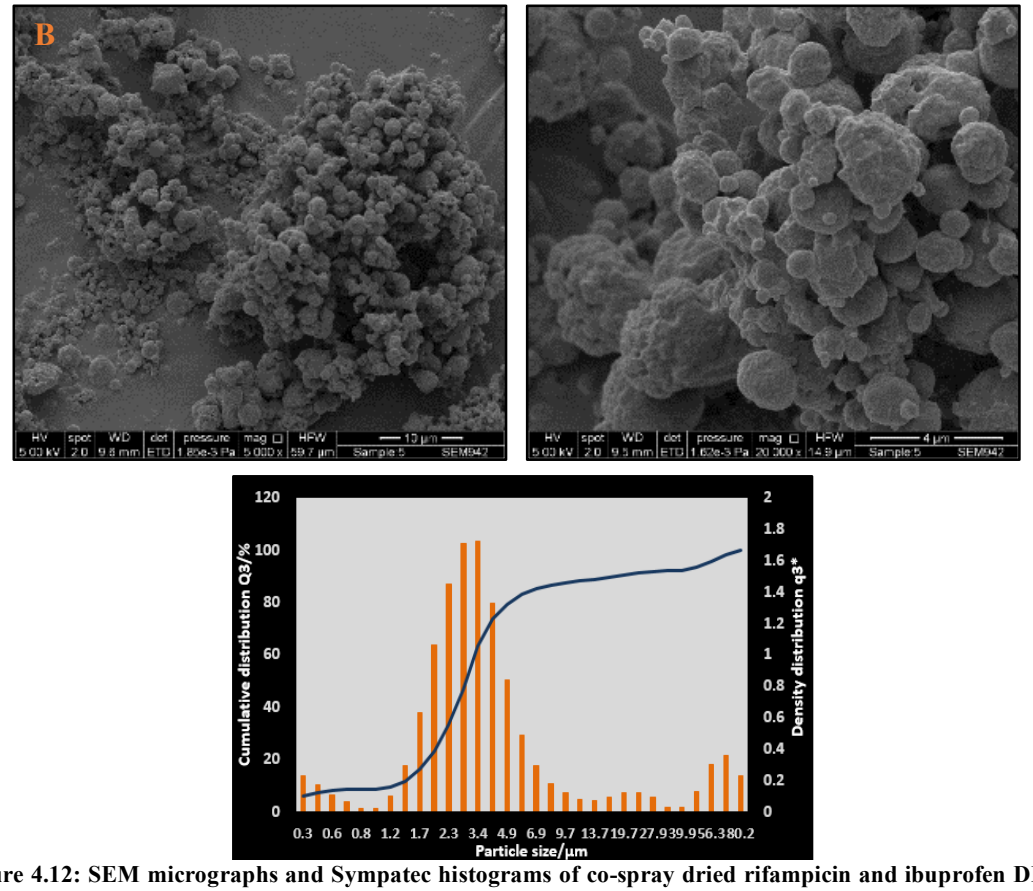

Figure 4.12: SEM micrographs and Sympatec histograms of co-spray dried rifampicin and ibuprofen DPPC: DSPG: Chol 100:40:20 liposomes at 80ºC (inlet temperature) and low lyoprotectant trehalose concentration (0.5 times trehalose with respect to liposomal formulation)
A: without 20% w/w L-leucine, B: with 20% w/w l-leucine

80ºC: 1.0X trehalose

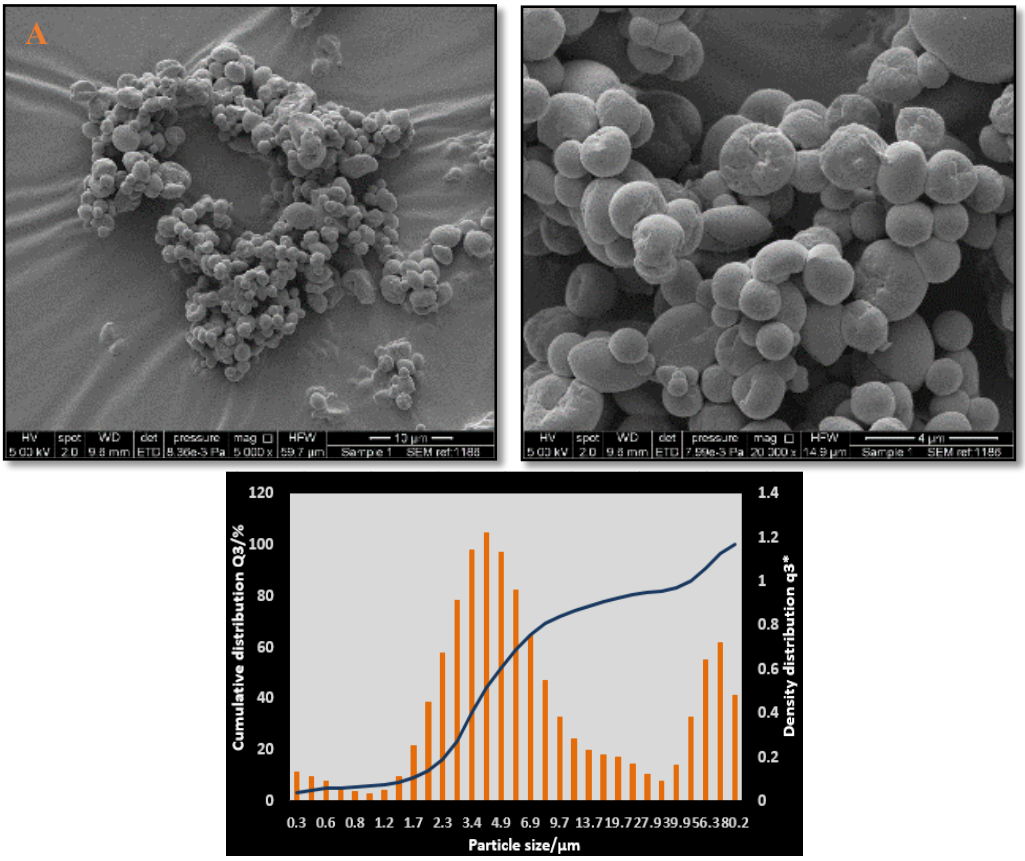

80ºC: 1.0X trehalose: 20% w/w L-leucine

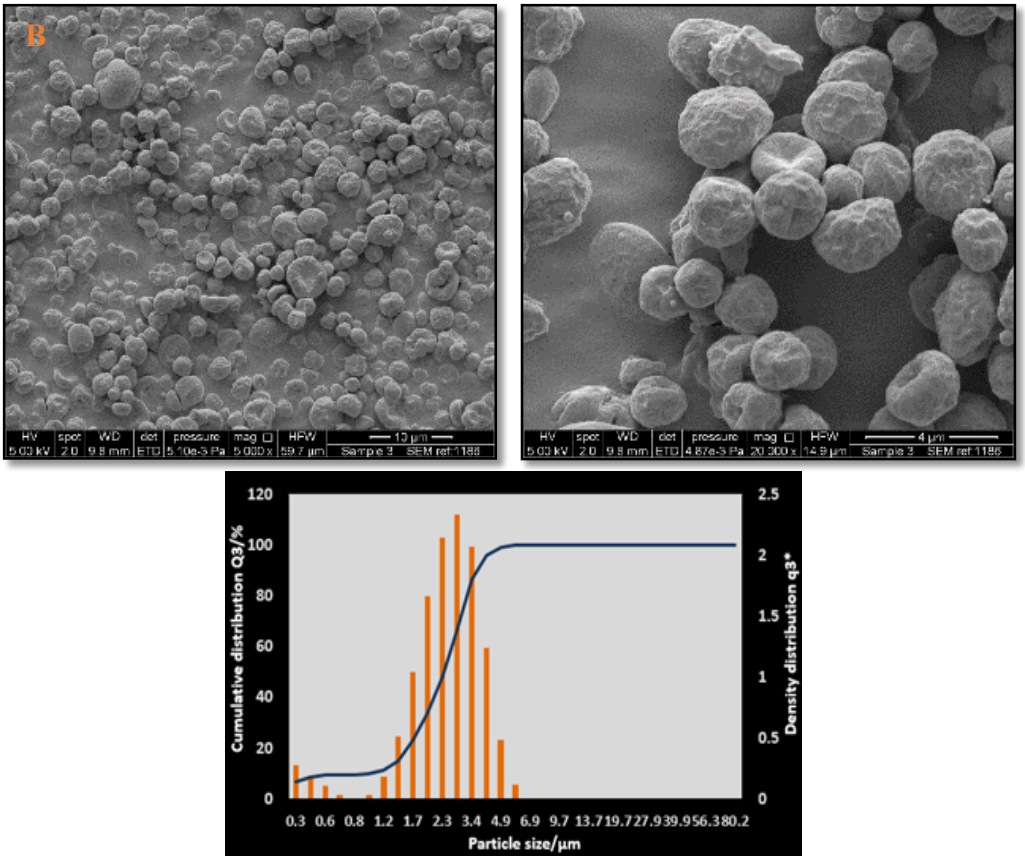

Figure 4.13: SEM micrographs and Sympatec histograms of co-spray dried rifampicin and ibuprofen DPPC: DSPG: Chol 100:40:20 liposomes at 80ºC (inlet temperature) and high lyoprotectant trehalose concentration (1.0 time trehalose with respect to liposomal formulation)
A: without 20% w/w L-leucine, B: with 20% w/w l-leucine

Spray drying to form dry powder microparticles at 120°C with low amount of lyoprotectant trehalose (0.5 times trehalose with respect to liposomal formulation) without L-leucine is as shown in Figure 4.14A. SEM micrographs of spray dried microparticles at the above conditions showed the presence of partially formed spherical particles with a wide range of size distribution, having a laser diffraction size DV90 of 8.76 μm and VMD of 3.34 μm (Span 2.47). Spray drying with L-leucine (Figure 4.14B) improved the particle morphology resulting in formation of wrinkled hollow sphere structures formed as curved plates with an DV90 of 4.29 μm and VMD of 2.73 μm (Span 1.39). This morphology has been reported in earlier literature to be responsible for producing an open powder structure and hence reduce particle density subsequently improving dispersion of aerosols [373].

Moreover, microparticles produced by spray drying at a higher temperature i.e. 120ºC showed slight corrugations (roughness) on the particle surface. The liquid feed during the atomization phase was sprayed through a nozzle with a tip diameter of 0.7 mm, in the form of fine droplets into the drying chamber, where it encountered hot gas at temperatures of about 90-120°C. The droplets are subjected to the highest temperature in a moist state which leads to instant drying of the external surface of droplets. The temperature of the drying chamber gradually decreases due to this heat exchange needed to dry the external surface of droplet, and further drying takes place by the formation of holes to let go out the trapped internal solvent. This leaves behind the dried solid with a size similar to the size of the atomized droplet. Previous literature has confirmed that a spray drying temperature of 110/74°C is responsible for shrinkage and hence corrugations [371].

SEM micrographs and laser diffraction studies of dry powder microparticles spray dried at 120°C in the presence of high amount of lyoprotectant trehalose (1.0 time trehalose with respect to liposomal formulation) without L-leucine (Figure 4.15A) showed the presence of wrinkled surfaced spherical microparticles, with an DV90 of 3.7 and VMD of 2.40 μm (Span 0.98). Addition of L-leucine (Figure 4.15B) to the above formulation resulted in change of morphology to form hollower wrinkled spherical microparticles with an DV90 of 3.87 and VMD of 2.63 μm (Span 1.38), however, a more prominent curved plate hollow microparticle structure was evident in formulations spray dried at 120°C (Figure 4.14B) containing lower lyoprotectant concentration (0.5 times trehalose). This is attributed to the difference in the weight ratios of trehalose: L-leucine in both the formulations and hence a more prominent role of L-leucine where the trehalose concentration was less.

120ºC: 0.5X trehalose

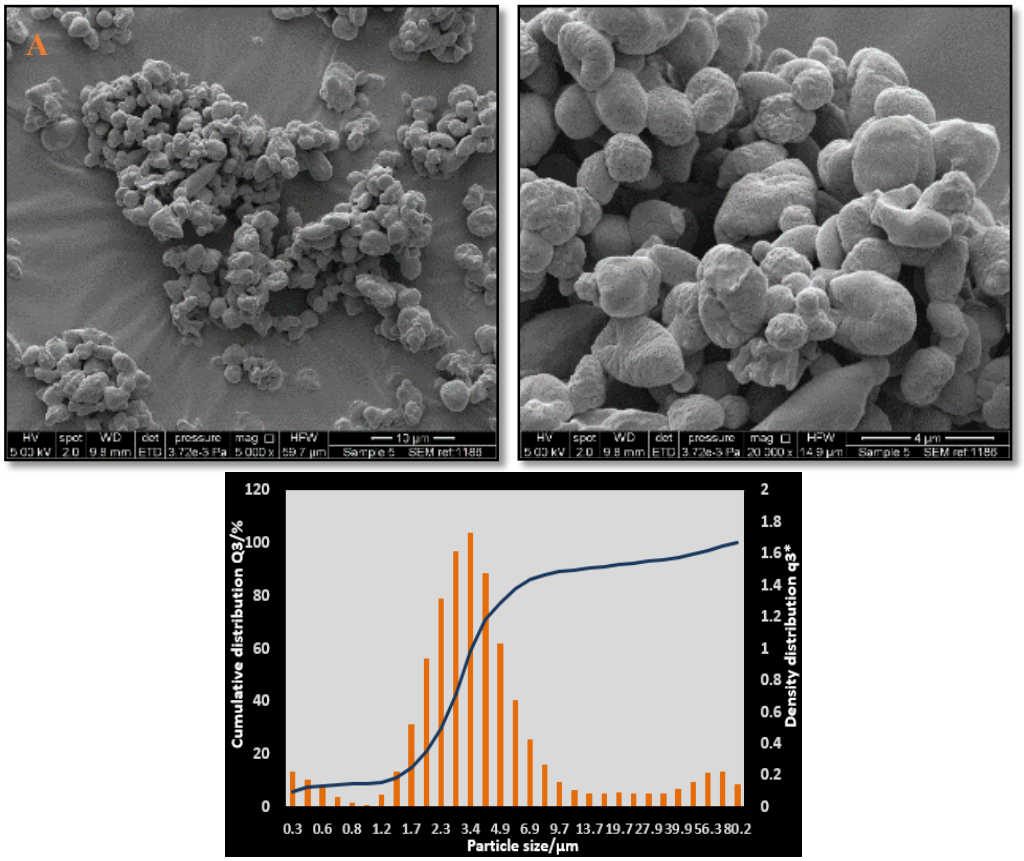

120ºC: 0.5X trehalose: 20% w/w L-leucine

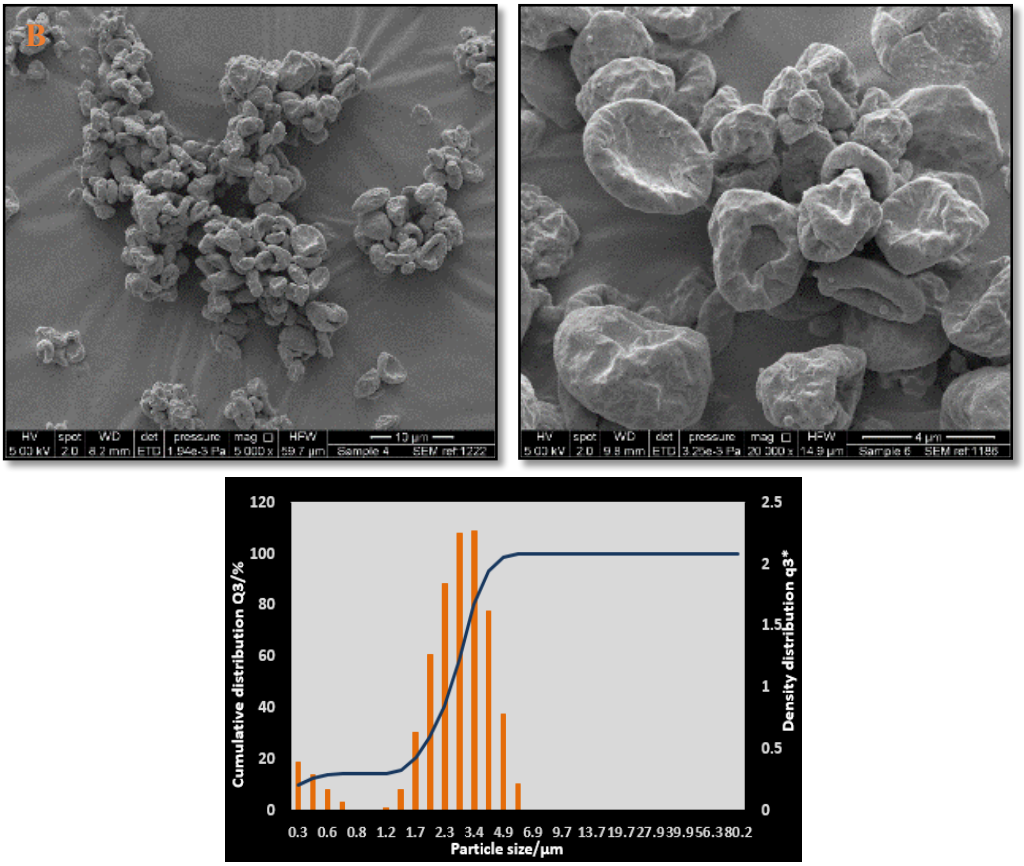

Figure 4.14: SEM micrographs and Sympatec histograms of co-spray dried rifampicin and ibuprofen DPPC: DSPG: Chol 100: 40: 20 liposomes at 120ºC (inlet temperature) and low lyoprotectant trehalose concentration (0.5 times trehalose with respect to liposomal formulation)
A: without 20% w/w L-leucine, B: with 20% w/w l-leucine

120°C: 1.0X trehalose

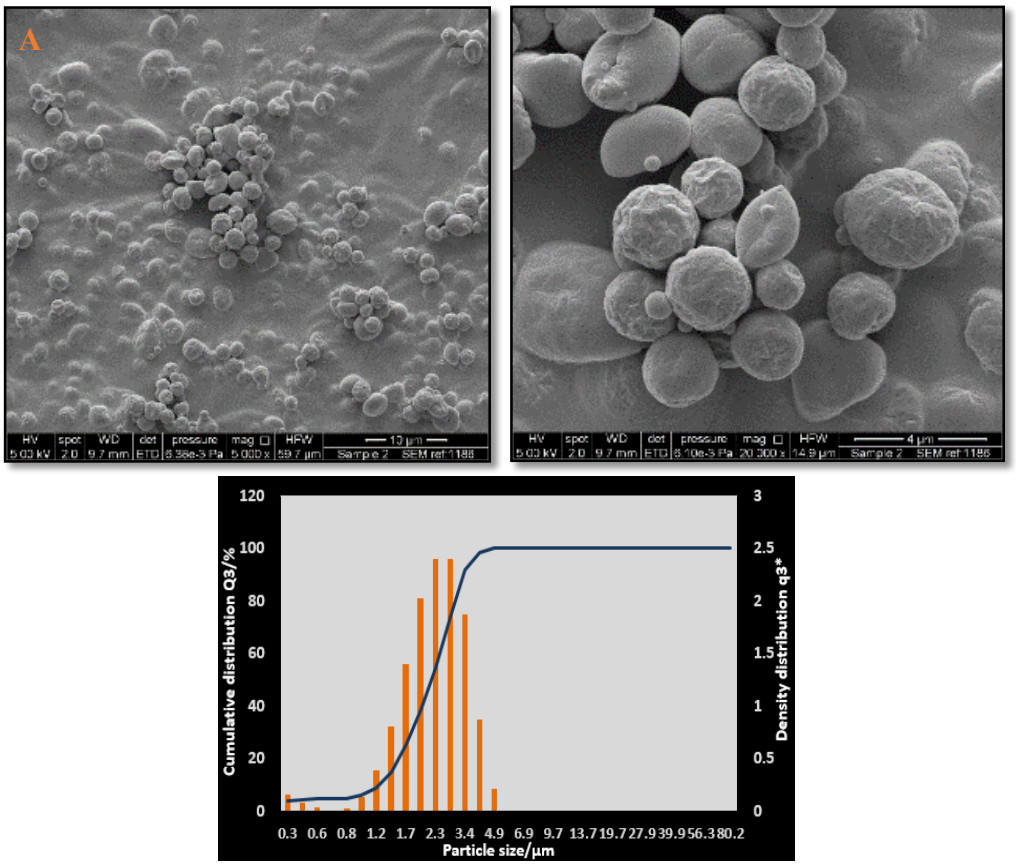

120°C: 1.0X trehalose: 20% w/w L-leucine

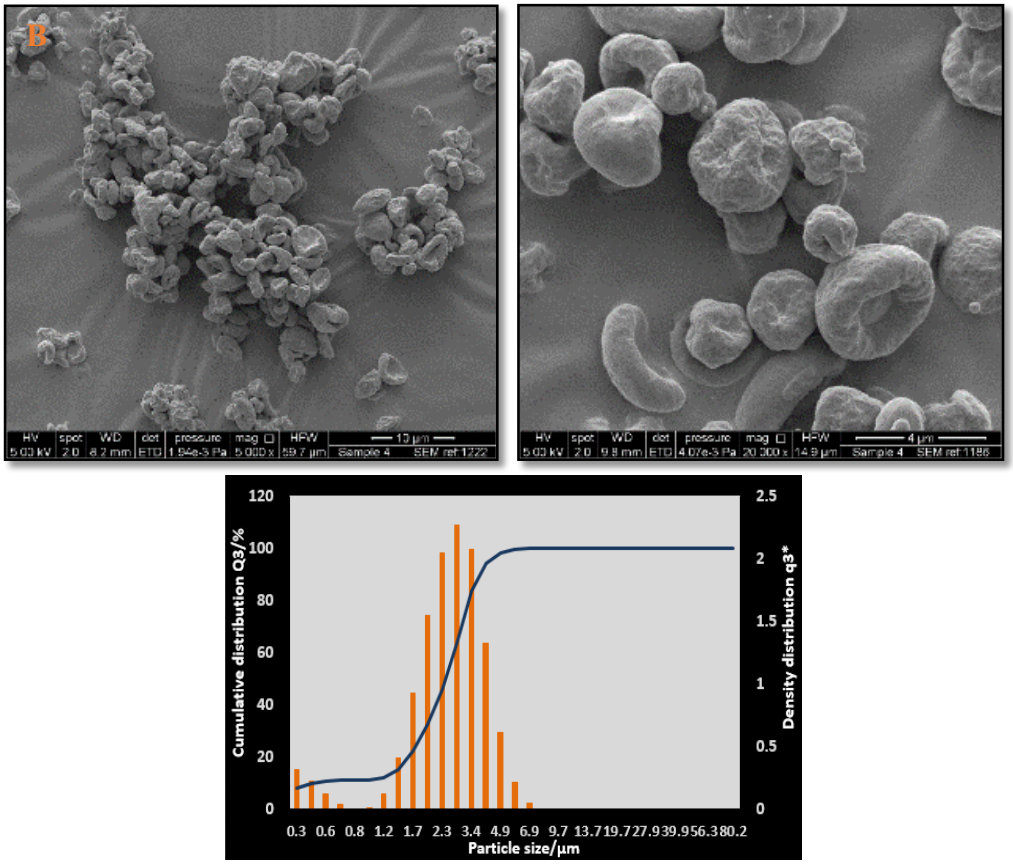

Figure 4.15: SEM micrographs and Sympatec histograms of co-spray dried rifampicin and ibuprofen DPPC: DSPG: Chol 100:40:20 liposomes at 120°C (inlet temperature) and high lyoprotectant trehalose concentration (1.0 times trehalose with respect to liposomal formulation) A: without 20% w/w L-leucine, B: with 20% w/w l-leucine

Laser diffraction studies at different pressures on the Sympatec for the spray dried microparticles (Figure 4.16) gave a further insight into the dependence of pressure applied on the measured volume mean particle size, indicative of ease of dispersion. This is of importance when considering patient-to-patient variation in the force of inhalation due to age and disease condition and the ease of dispersion of powders from devices during aerosolization.

Effect of pressure applied during measurement on the size of spray dried, physically mixed and raw material microparticles:

Microparticles showing minimal differences in the size at different pressures would be attractive as the fine particle fraction and dose would be independent of the patient's inspiratory flow rate. Spray drying liposomes at 80°C with or without 20% w/w leucine at a low trehalose concentration (0.5 times trehalose) showed significant differences ($p < 0.05$) in the volume mean particle size i.e. DV50 mean particle size at the different pressures of dispersion (Figure 4.16). Spray drying these at the same temperature with a higher trehalose concentration (1.0 times trehalose) was seen to improve the particle size profile between the different pressures.

On the other hand, spray drying liposomes at 120°C with 20% leucine at low and high trehalose concentration and spray drying liposomes at 120°C without 20% leucine at high trehalose concentration showed no significant difference ($p > 0.05$) in volume mean particle size analyzed by laser diffraction at 1, 2, 3, 4 or 5 bar pressure, indicative of pressure-independent analysis and consequently no potential patient-to-patient variation.

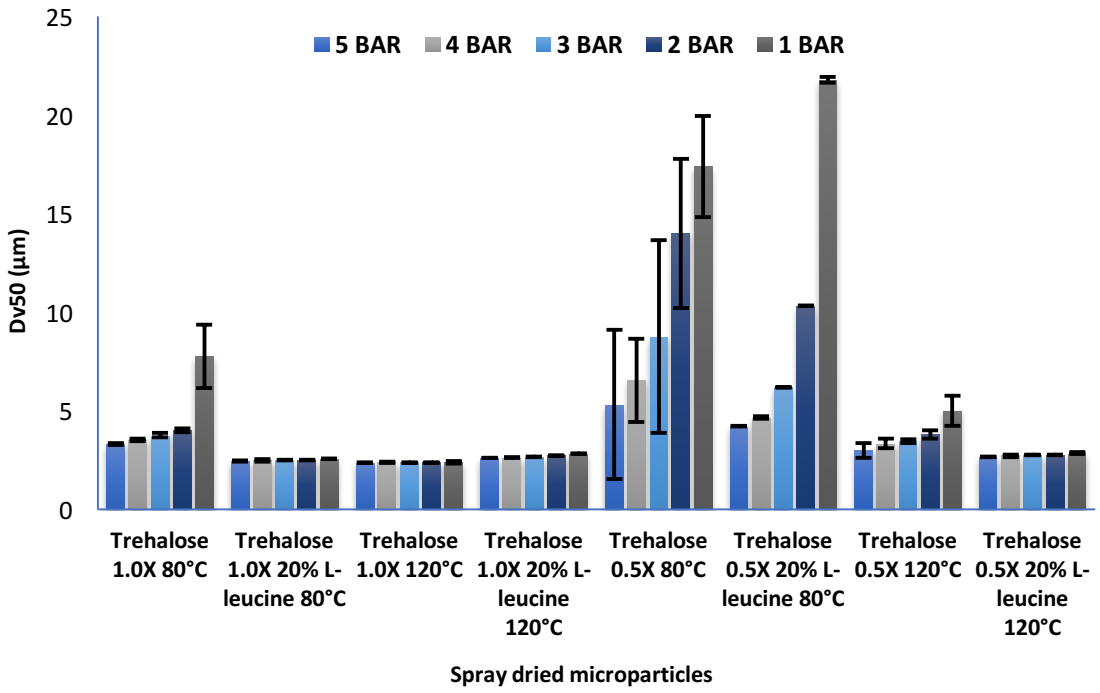

Figure 4.16: Effect of pressure on size analysis (Dv50) of spray dried microparticles of co-encapsulated DPPC: DSPG: Chol 100: 40: 20 liposomes (mean±SD, n=3)

4.5.2.3.2 Moisture content analysis by TGA

Spray drying often leads to formation of amorphous microparticles due to the process adopted, wherein, the initial feedstock solution/dispersion droplet formed encounters hot drying gas in the drying chamber, which dehydrates the droplet from the outer surface to the inner droplet core, leaving behind a stable, homogenous amorphous powder with a size similar to the size of the initial droplet formed [371]. However, this increases the tendency of water sorption and recrystallization of microparticles on storage. Hence, it was important to study the content of moisture that is sorbed to the microparticle.

The response of moisture content (%) (Y_4) (Figure 4.17) clearly demonstrates than a significant increase in moisture of microparticles was seen with an increase in the amount of trehalose (X_1, $p = 0.0088$). The other factors i.e. temperature of spray drying and addition of 20% w/w L-leucine had no significant effect on the moisture content of the microparticles.

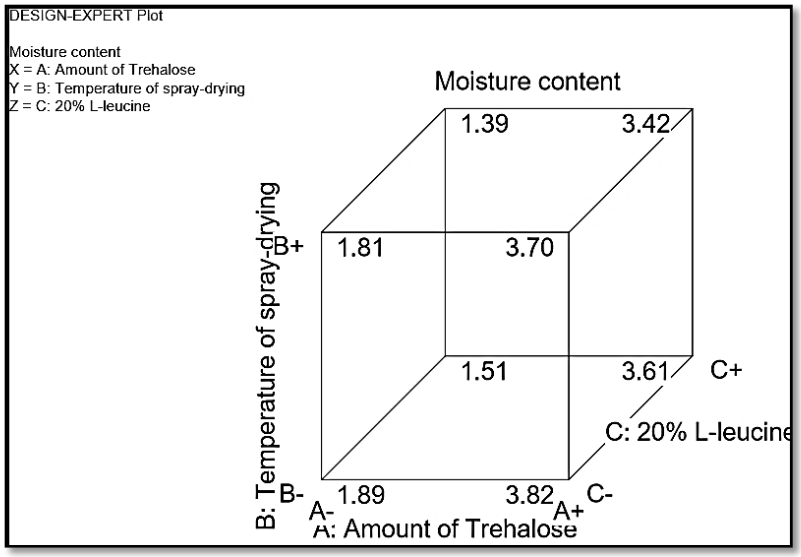

Figure 4.17: DoE 3- Preparation of dry powders suitable for inhalation, the effect of factors on response moisture content (%) (mean±SD, n=3, 3D cube plot Design-Expert® 6 (Stat-Ease, Inc.)) (For factor codes refer to Table 4.7)

On analyzing the responses observed in the above factorial model DoE 3 for preparation of dry powders suitable for inhalation, it was evident that temperature of spray drying had a significant effect on the DV90 and Span, hence, the potential aerosol properties of the microparticles especially when low amount of trehalose was used. SEM morphology and laser diffraction volume size distribution were useful to select 4 formulations (1 formulation with 0.5 times trehalose and 3 formulations of 1.0 time trehalose relative to final formulation) out of the matrix of 8 initially designed for spray drying that. These powders had DV50 and DV90 below 5 µm and a Span close to 1, necessary for a good dispersion to enhance delivery to the lungs. A decrease in drug content of the dry powder and an increase in moisture content were evident with an increase in trehalose from 33.33% (0.5 times trehalose) to 50% (1.0 time trehalose), and hence dry powders for further analysis were selected with lower amount of trehalose (0.5 times) and 20% w/w L-leucine spray dried at an inlet temperature of 120°C (outlet temperature of 62°C).

4.5.3 Polymer coating

4.5.3.1 ^{1}H-NMR proton nuclear magnetic resonance

The ^{1}H-NMR of commercial chitosan is shown in Figure 4.18. The internal standard used for assigning the chemical shifts of protons was D_2O. The chemical shifts of internal standard appeared at 4.75 ppm.

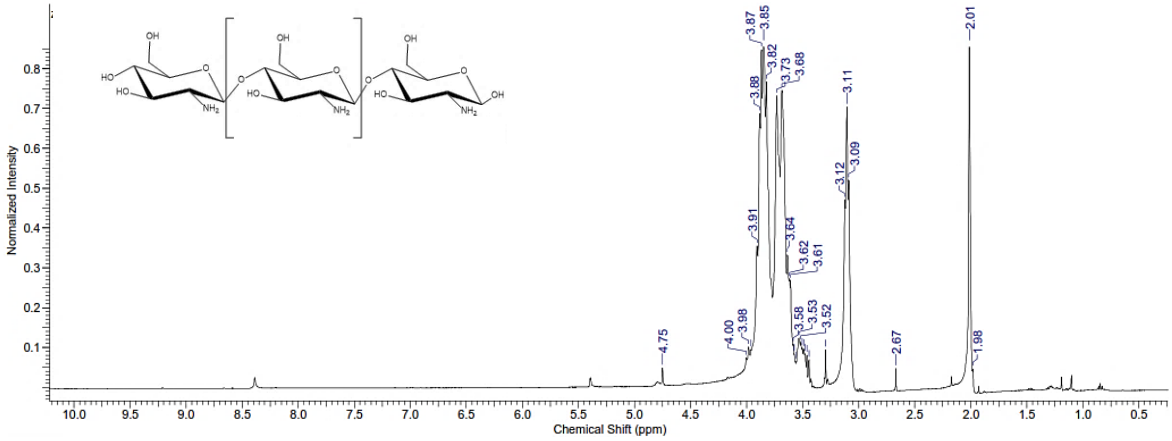

Figure 4.18: ^{1}H-NMR spectrum of commercial chitosan < 3K

The chemical shift at 2.0-2.1 ppm represents three protons (-NH-CO-C<u>H</u>$_3$) of N-acetyl glucosamine (GlcNAc). The chemical shifts of the non-anomeric protons connected to ring skeleton of glucosyl residue having similar electron densities show a partially overlapping behaviour to produce a broad signal around 3.5-4.0 ppm. The –C<u>H</u>-OH, HOHC-C<u>H</u>-CH$_2$ and –C<u>H</u>$_2$-OH protons appear at around 3.73 ppm, whereas, the chemical shifts of –C<u>H</u>-CH$_2$ and C<u>H</u>$_2$*OH appears at 3.64 ppm. The anomeric proton due to their neighbouring glycosidic and ring oxygen appear at higher chemical shifts as compared to non-anomeric protons i.e. at 3.09 ppm. The –C<u>H</u>-NH$_2$ proton appears at a chemical shift of 3.11 ppm [373]. The ^{1}H-NMR of mannosylated chitosan shown in Figure 4.19 contains similar peaks to commercial chitosan confirming the backbone of chitosan. However, a new peak at 7.19-7.22 ppm assigned to phenyl group with four hydrogen atoms from the phenyl isothiocyanate attached to mannopyranoside confirmed the successful reaction of mannosylated chitosan as seen in previous literature [422].

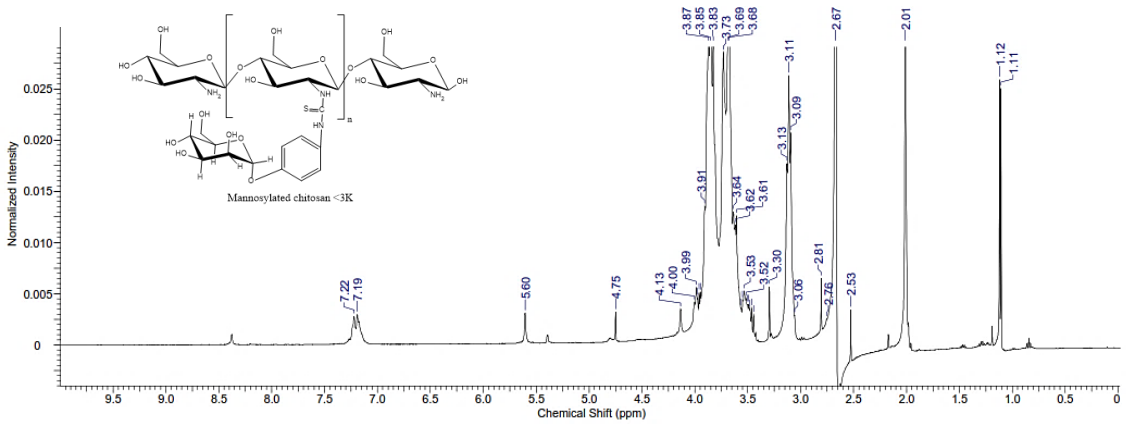

Figure 4.19: ^{1}H-NMR spectrum of mannosylated chitosan < 3K

4.5.3.2 Fourier transform infrared spectroscopy (FT-IR)

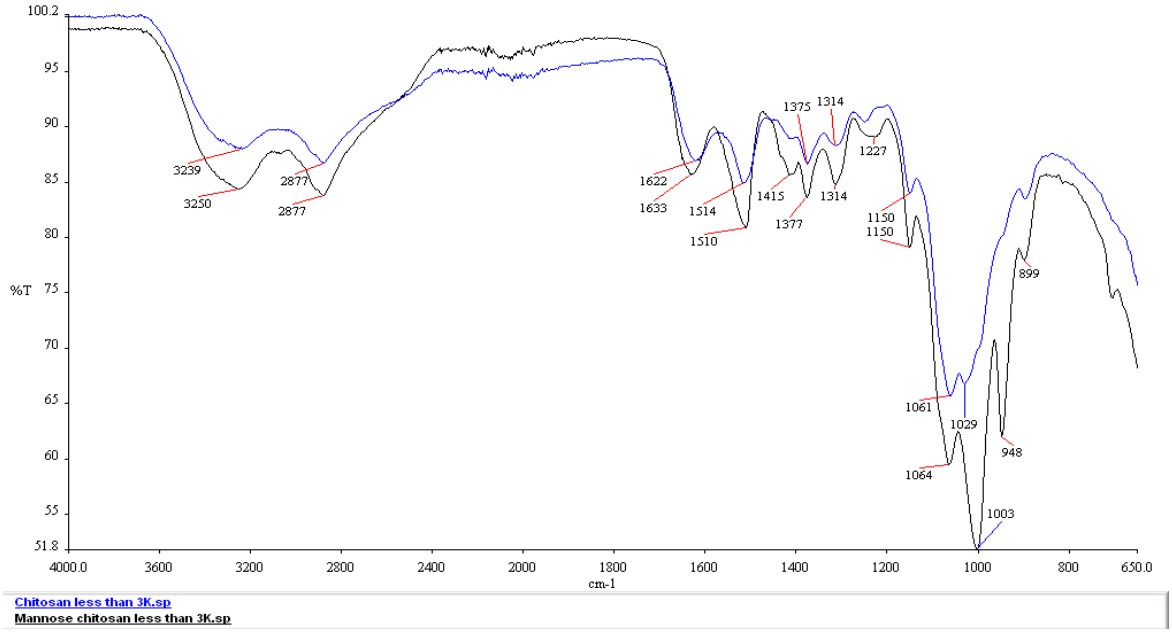

Figure 4.20: Overlay of FT-IR spectra of chitosan<3K and mannosylated chitosan <3K

FT-IR spectra of chitosan is as that reported previously by various authors. Spectrum (Figure 4.20) shows characteristic absorption peaks at 3239 cm^{-1} indicative of amino N-H bend absorption of $-NH_2$ functional group overlapping with N-H stretch of amide at 3100 cm^{-1} hence giving a broad peak. Absorption peak at 2877 cm^{-1} corresponds to aliphatic –CH and $–CH_2$ stretching, whereas, double peaks of absorption occurring at 1622 cm^{-1} and 1514 cm^{-1} corresponding to C=O absorption and N-H group bending vibration respectively of N-acetamido group are evident. C=O absorption normally takes place roughly at a frequency of 1700 cm^{-1} or greater, however, due to resonance stabilization there is a 'back-donating' effect leading to transfer of unpaired electrons of nitrogen resulting in increased single bond C-O absorption and lowering of double bond C=O absorption. The bands appearing at frequencies 1061 cm^{-1} and 1029 cm^{-1} corresponds to stretching of C-O group, whereas, band at 1375 cm^{-1} corresponds to stretching of C-O-N group. Lastly, the absorption bands occurring at a frequency of 899 cm^{-1} and 1150 cm^{-1} can be attributed to glycosidic bonding i.e. β (1→4) stretching of chitosan sugar backbone. These characteristic absorption bands confirm the presence of chitosan [373].

FT-IR spectrum of mannosylated chitosan exhibited characteristic band of mannose at 899 cm^{-1} and 948 cm^{-1}. Moreover, there was a shift and increase in intensity at 1510 cm^{-1} which is attributed to the contribution by the phenyl group of mannopyranoside isothiocyanate and reaction at the amine of chitosan leading to changes in the N-H bending also confirmed by shift in the peak at 1622 cm^{-1} to 1633 cm^{-1} affecting the N-H bending of chitosan amine [422]. Previous literature has also shown that disappearance of peak of isothiocyanate group from mannopyranoside phenyl isothiocyanate at 2125 cm^{-1} is indicative of reaction of these groups with polymer backbone [440].

4.5.4 Final formulations selected for spray drying

Based on the DoE experiments, different formulations (Table 4.12) were selected as final formulations to be spray dried. These formulations were also used to study the *in vitro* cellular uptake by encapsulation of 0.25 mg fluorescent dye coumarin-6 instead of the drugs rifampicin and ibuprofen. The concentration of coumarin-6 used for the study was to obtain a 100% encapsulation for all the formulations and a similar hydrodynamic size so as to prevent difference in uptake kinetics due to these parameters. The difference in zeta potential between the different formulations was however necessary to study the effect of charge on the surface of the liposomes and incorporation of targeting moieties on the uptake in macrophage RAW 264.7 cells.

Table 4.12: Characterization of the final formulations selected for aerosolization and uptake studies

Formulation (lipid concentration in molar)	Drug/ Fluorescent dye	Hydrodynamic diameter (nm)	Zeta-potential (mV)	Encapsulation efficiency (%)
Negative liposomes (DPPC: DSPG: Chol 100:40:20)	Rifampicin and Ibuprofen	84.09 ± 3.89	-43.5 ± 1.50	**RIF**-89.75 ± 2.40 **IBU**-99.0 ± 2.20
	Coumarin-6	103.18 ± 5.41	-45.00 ± 0.75	104.31 ± 2.12
Negative liposomes PAM (DPPC: DSPG: Chol 100:40:20)	Rifampicin and Ibuprofen	93.12 ± 3.11	-41.21 ± 2.15	**RIF-** 87.14 ± 1.28 **IBU**-91.21 ± 2.07
	Coumarin-6	129.73 ± 1.62	-42.77 ± 3.07	104.67 ± 3.87
Negative liposomes MAN (DPPC: DSPG: Chol 100:40:20)	Rifampicin and Ibuprofen	85.94 ± 2.63	-43.67 1.84	**RIF**-93.59 ± 3.14 **IBU**-97.84 ± 2.74
	Coumarin-6	103.13 ± 4.26	-43.10 ± 2.62	94.68 ± 0.23
Positive liposomes chitosan-coated (DPPC: DSPG: Chol 100:20:20)	Rifampicin and Ibuprofen	145.34 ± 2.12	37.21 1.89	**RIF**-63.12 ± 1.06 **IBU**-92.51 ± 2.0
	Coumarin-6	130.43 ± 3.37	37.73 ± 1.79	95.56 ± 1.63
Positive liposomes chitosan-mannose coated (DPPC: DSPG: Chol 100:20:20)	Rifampicin and Ibuprofen	141.67 ± 3.68	35.33 2.70	**RIF**-62.22 ± 1.79 **IBU**-89.33 ± 1.69
	Coumarin-6	122.33 ± 1.05	35.63 ± 1.03	97.67 ± 0.98
Neutral liposomes (DPPC: Chol 100:20)	Rifampicin and Ibuprofen	135.91 ± 2.52	0.23 ± 0.36	**RIF**-69.14 ± 5.21 **IBU**-92.04 ± 4.33
	Coumarin-6	130.8 ± 4.08	4.03 ± 0.33	100.93 ± 3.12

DPPC- dipalmitoyl phosphatidylcholine, DSPG- distearyl phosphatidylglycerol, Chol- cholesterol, MAN- mannosamine hydrochloride, PAM- p-aminophenyl α-D-mannopyranoside

4.5.4.1 Re-hydration of spray dried liposomes

Critical process parameters were carefully considered for dehydration of liposomes to ensure that they would re-disperse on aerosolization in the airway fluid, without considerable loss of formulation integrity and retention of particle size post-aerosolization. It is important to study the size of liposomes following spray drying on re-hydration in water or buffer, as the liposomes can suffer from disruption or aggregation and hence drug leakage during dehydration.

There was no significant difference ($p > 0.05$) in the hydrodynamic diameter and zeta-potential of liposomes studied post dehydration, when the spray dried powders were redispersed in deionized water, indicative of optimal spray drying conditions for the liposomal formulation under study (Table 4.13).

Table 4.13: Characterization of the formulations on rehydration of spray dried liposomes in deionized water

Formulation (lipid concentration in molar)	Hydrodynamic diameter (nm) before spray drying	Zeta-potential (mV) before spray drying	Hydrodynamic diameter (nm) on rehydration in deionized water	Zeta-potential (mV) on rehydration in deionized water
Negative liposomes (DPPC: DSPG: Chol 100:40:20)	84.09 ± 3.89	-43.5 ± 1.50	77.25 ± 4.83	-42.7 ± 1.18
Negative liposomes PAM (DPPC: DSPG: Chol 100:40:20)	93.12 ± 3.11	-41.21 ± 2.15	96.30 ± 2.17	-39.3 ± 1.34
Negative liposomes MAN (DPPC: DSPG: Chol 100:40:20)	85.94 ± 2.63	-43.67 ± 1.84	89.11 ± 2.96	-46.2 ± 2.63
Positive liposomes chitosan-coated (DPPC: DSPG: Chol 100:20:20)	145.34 ± 2.12	37.21 ± 1.89	149.7 ± 3.04	39.92 ± 0.98
Positive liposomes chitosan-mannose coated (DPPC: DSPG: Chol 100:20:20)	141.67 ± 3.68	35.33 ± 2.70	147.9 ± 2.11	37.11 ± 0.52
Neutral liposomes (DPPC: Chol 100:20)	135.91 ± 2.52	0.23 ± 0.36	140.12 ± 5.21	-0.11 ± 1.01

DPPC- dipalmitoyl phosphatidylcholine, DSPG- distearyl phosphatidylglycerol, Chol- cholesterol, MAN- mannosamine hydrochloride, PAM- p-aminophenyl α-D-mannopyranoside

4.5.4.2 Transmission electron microscopy

Charge of the liposomal surface has an effect on the negative staining process since it affects the binding of the contrasting agent uranyl, the electron scattering pattern and eventually the TEM micrograph. Moreover, negative stain EM for liposomes suffers from various drawbacks of sample preparation which might cause liposomal fusion, aggregation or rouleau formation [441,442]. For this reason an optimized staining protocol as previously published was followed for improving the contrast of the micrographs [442].

Negative liposomes (DPPC: DSPG: Chol 100:40:20)

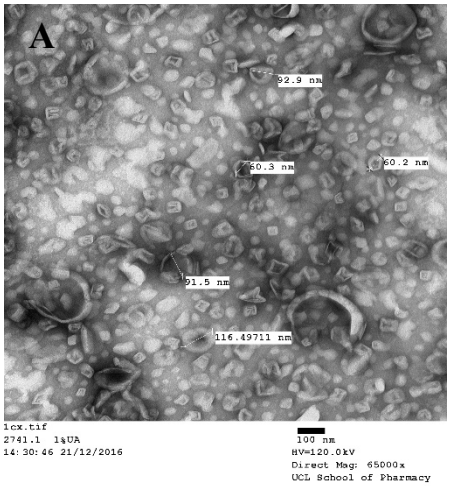

Neutral liposomes (DPPC: Chol 100:20)

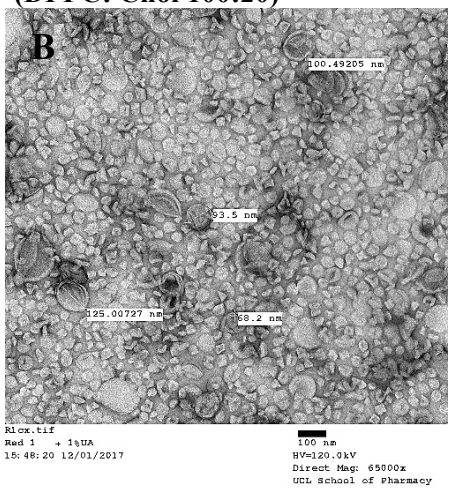

Negative liposomes PAM (DPPC: DSPG: Chol 100:40:20)

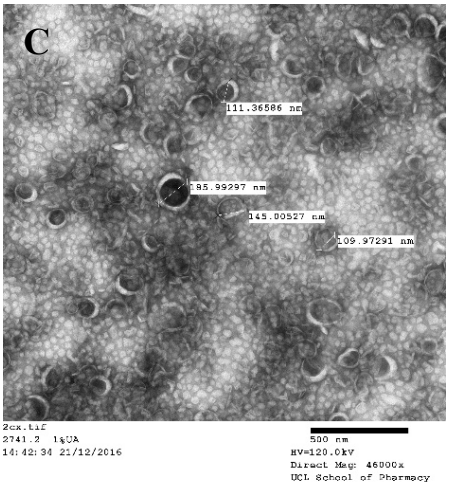

Positive liposomes chitosan-coated (DPPC: DSPG: Chol 100:20:20)

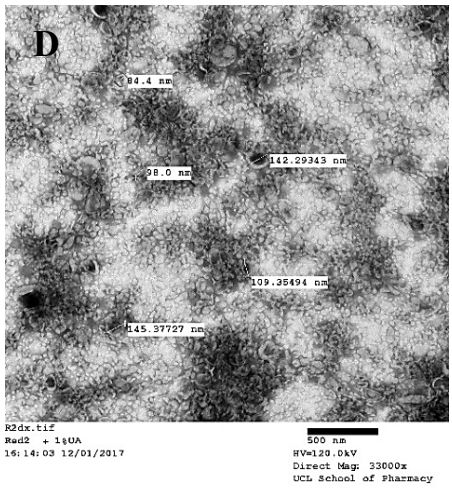

Negative liposomes MAN (DPPC: DSPG: Chol 100:40:20)

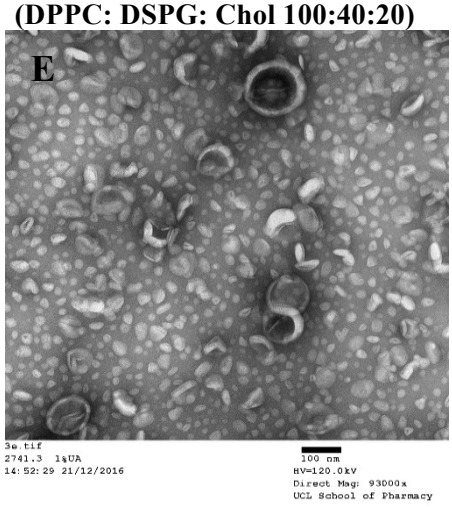

Positive liposomes chitosan-mannose coated (DPPC: DSPG: Chol 100:20:20)

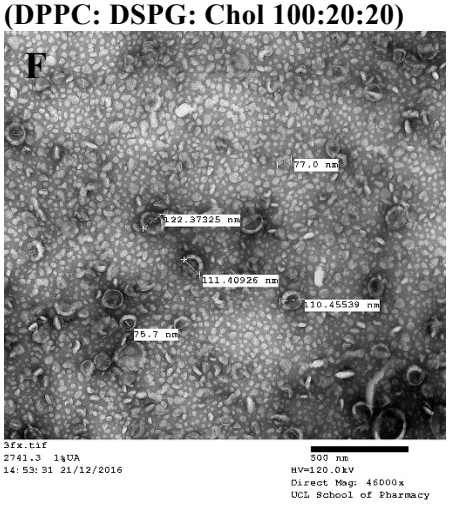

Figure 4.21: TEM micrographs of liposomes co-encapsulating rifampicin and ibuprofen, (A) DPPC:DSPG:Chol 100:40:20 liposomes, (B) DPPC:Chol 100:20 liposomes, (C) DPPC:DSPG:Chol 100:40:20-PAM liposomes, (D) chitosan-coated DPPC: DSPG: Chol 100:20:10 liposomes, (E) DPPC:DSPG:Chol 100:40:20 MAN liposomes, (F) mannosylated chitosan-coated DPPC: DSPG: Chol 100:20:10 liposomes

The TEM micrographs for liposomes as captured in Figure 4.21 showed the presence of nanometric range of spherical particles with a smooth surface. Particle size was in good correlation with that obtained from the DLS analysis using the Zetasizer ZS (Table 4.12).

4.5.4.3 Scanning electron microscopy and laser diffraction analysis

SEM was performed on freshly prepared spray dried samples (chosen from the final formulations) stored under a desiccator at room temperature. It was performed to analyze the morphological and surface behaviour associated with the different compositional powders and to study their particle size. The SEM micrographs were captured at different degrees of magnification to highlight the details of the particles.

Spray drying to form dry powder microparticles of negatively-charged non-targeted and targeted liposomes at 120°C with lower lyoprotectant trehalose concentration (0.5 times) and L-leucine is as depicted in Figure 4.22. SEM micrographs of spray dried microparticles of negatively-charged liposomes (Figure 4.22A) at the above conditions with L-leucine resulted in formation of wrinkled hollow sphere structures formed as curved plates with an DV90 of 4.29 μm and VMD of 2.73 μm (Span 1.39). This morphology has been reported in earlier literature to be responsible for producing an open powder structure and hence reduce particle density subsequently improving dispersion [373].

Moreover, negatively-charged liposomes containing p-amino phenyl mannopyranoside (PAM, Figure 4.22B) and mannosamine hydrochloride (MAN, Figure 4.22C) embedded in the bilayer spray dried at the same conditions also showed the presence of wrinkled hollow sphere structures formed as curved plates with an DV90 of 4.71 μm (VMD 2.24 μm, Span 1.73) and DV90 4.75 μm (VMD 1.91 μm, Span 1.55) respectively.

DPPC: DSPG: Chol (100:40:20) liposomes

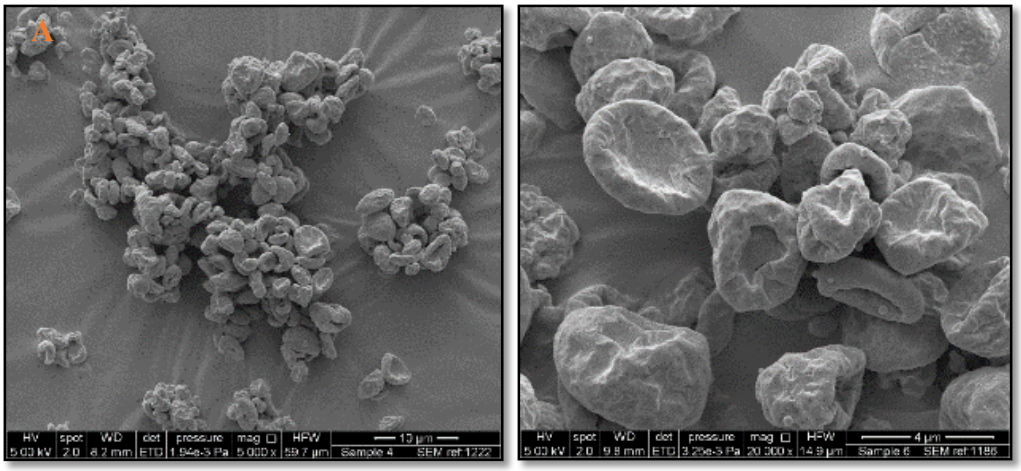

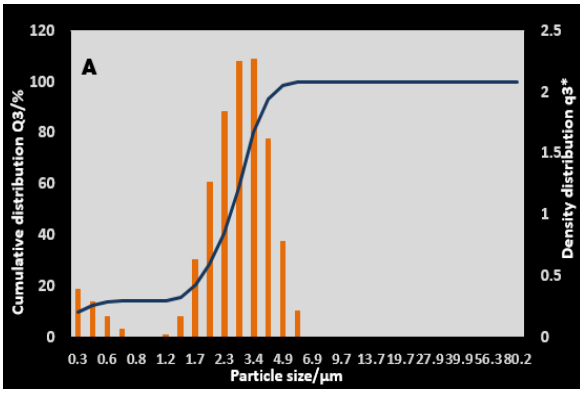

DPPC: DSPG: Chol (100:40:20) PAM liposomes

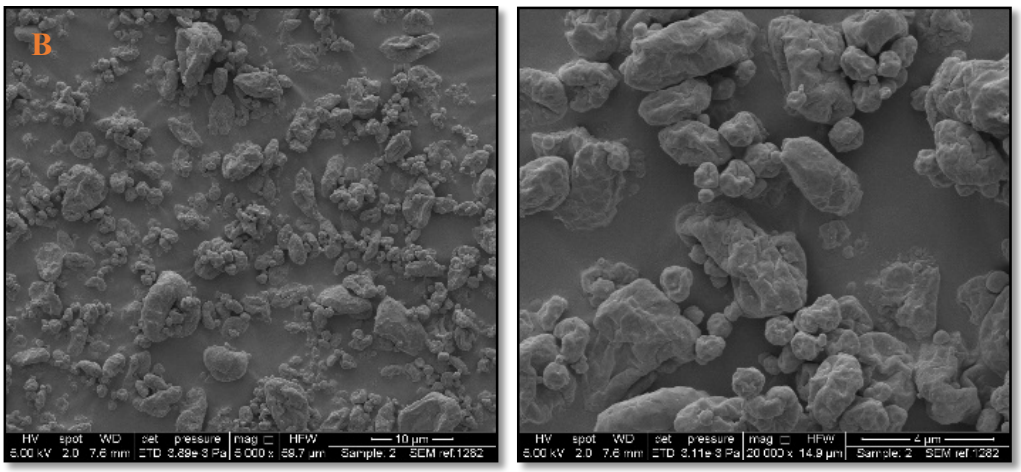

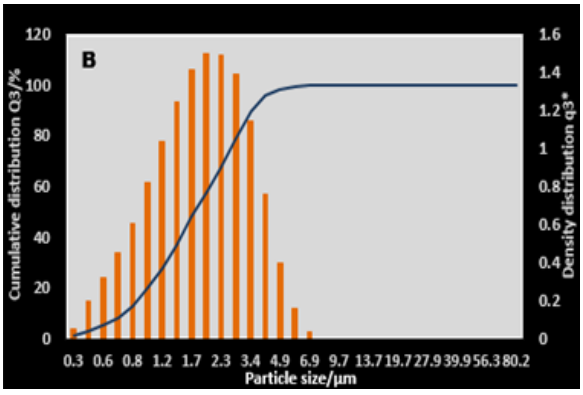

DPPC: DSPG: Chol (100:40:20) MAN liposomes

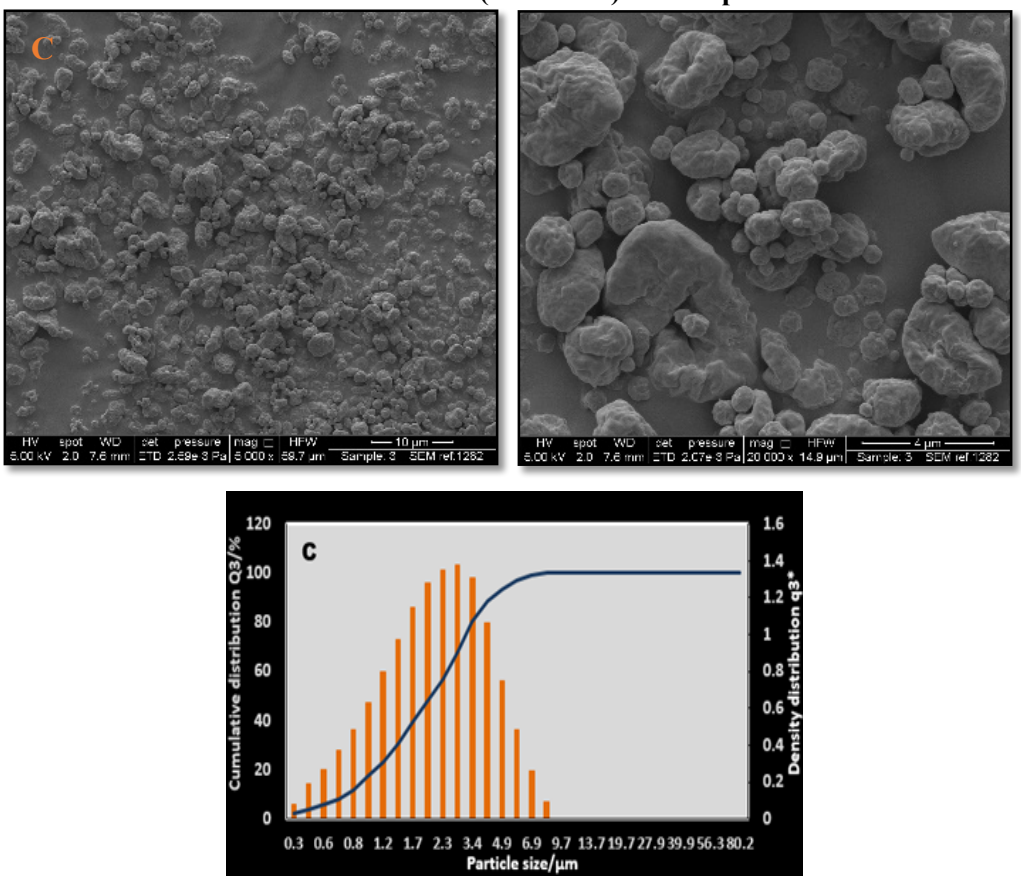

Figure 4.22: SEM micrographs and Sympatec histograms of co-spray dried rifampicin and ibuprofen DPPC: DSPG: Chol 100:40:20 negative liposomes at 120ºC (inlet temperature), low lyoprotectant concentration (0.5 times trehalose with respect to liposomal formulation) and 20% w/w L-leucine
A: Negative liposomes, B: Negative PAM liposomes, C: Negative MAN liposomes

Spray drying to form dry powder microparticles of positively-charged chitosan-coated and mannosylated chitosan-coated liposomes at 120°C with lower lyoprotectant trehalose concentration (0.5 times) and L-leucine is as depicted in **Figure 4.**23. SEM micrographs of positively-charged chitosan-coated liposomes spray dried as microparticles (**Figure 4.**23A) at the above conditions with L-leucine resulted in formation of spherical microparticles with an DV90 of 4.44 µm (VMD 2.55 µm, Span 1.20). Moreover, positively-charged mannosylated chitosan-coated liposomes (**Figure 4.**23B) showed the presence of similar spherical structures with an DV90 of 4.54 µm (VMD 2.70 µm, Span 1.17).

All the above microparticles were spray dried under the same conditions with 33.33% trehalose and 20% w/w L-leucine showed desirable DV50, DV90, Span and morphology to obtain an aerosol for potential peripheral pulmonary deposition to the site of infection. These spray dried microparticles were evaluated for their *in vitro* aerosol efficiency parameters and pulmonary deposition pattern using the NGI.

Chitosan-coated DPPC: DSPG: Chol (100:20:20) liposomes

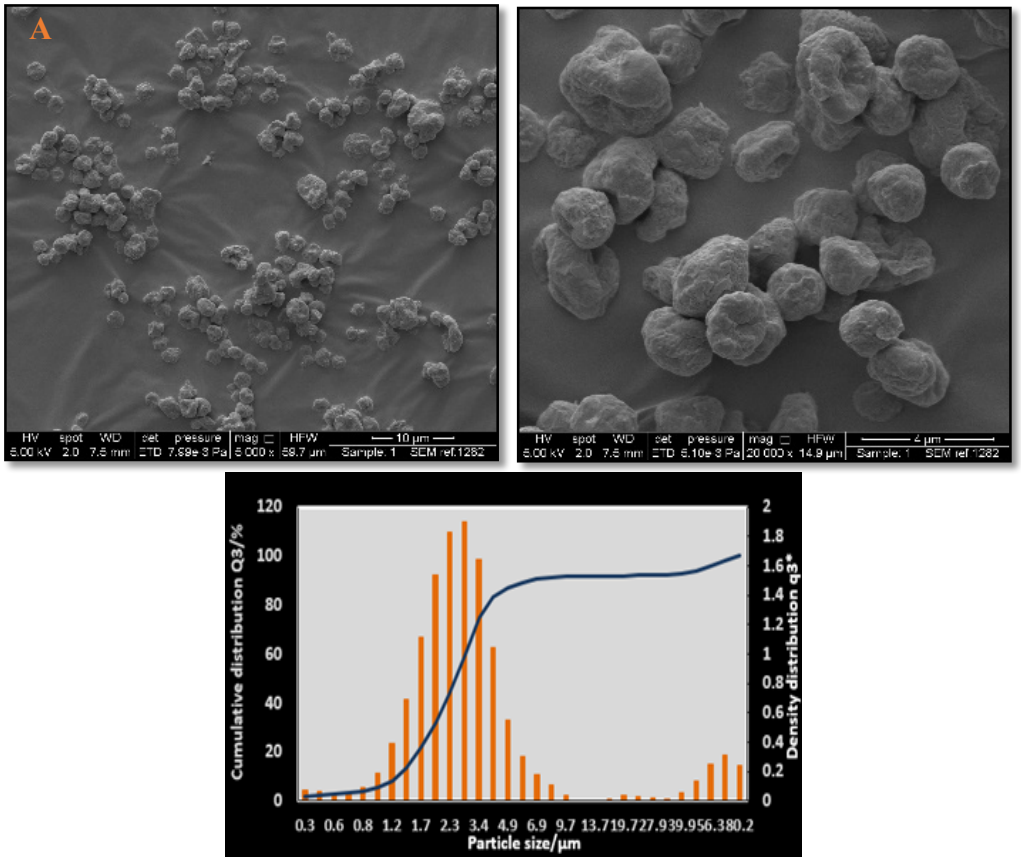

Mannosylated chitosan-coated DPPC: DSPG: Chol (100:20:20) liposomes

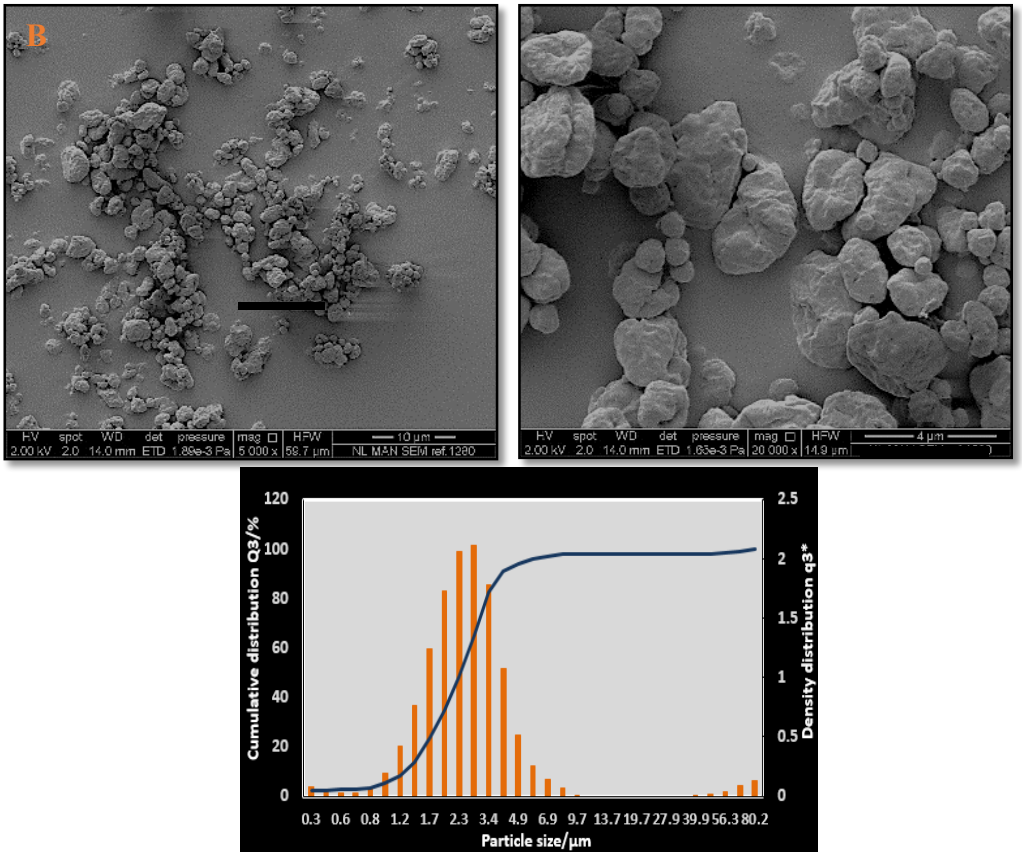

Figure 4.23: SEM micrographs and Sympatec histograms of co-spray dried rifampicin and ibuprofen chitosan-coated DPPC: DSPG: Chol 100:20:20 negative liposomes at 120°C (inlet temperature), low lyoprotectant concentration (0.5 times trehalose with respect to liposomal formulation) and 20% w/w L-leucine
A: Positive chitosan-coated liposomes, B: Positive mannosylated chitosan-coated liposomes

4.5.5 *In vitro* aerosol deposition and aerodynamic behaviour studies of rifampicin and ibuprofen liposomal microparticles

The *in vitro* aerodynamic behaviour and deposition of the liposomal rifampicin and ibuprofen microparticles illustrated in Figure 4.24 and Figure 4.25 was studied using a Next Generation Impactor. In this study, aerosolization efficiency parameters (Table 4.14) were analyzed in triplicate for the freshly prepared spray dried powders and represented as a histogram of the mean percentage of rifampicin or ibuprofen impacted on each stage as compared to the initial amount of drugs aerosolized, ±SD.

Table 4.14: Aerosol parameters studied using the NGI

Microparticle	Drug	ED (%)	FR (%)	FPF (%)	FPD (mg)	MMAD (µm)	GSD
Negative liposomes (DPPC: DSPG: Chol 100:40:20)	Rifampicin	91.15 ± 3.59	88.23 ± 5.45	62.83 ± 4.06	6.33 ± 0.41	2.95 ± 0.20	1.70 ± 0.04
	Ibuprofen	91.47 ± 3.02	90.04 ± 4.72	63.28 ± 4.05	5.32 ± 0.34	2.87 ± 0.17	1.72 ± 0.06
Negative liposomes PAM (DPPC: DSPG: Chol 100:40:20)	Rifampicin	93.80 ± 0.82	93.03 ± 2.29	61.68 ± 2.02	6.22± 0.20	2.85 ± 0.13	1.67 ± 0.09
	Ibuprofen	93.59 ± 1.09	93.02 ± 2.12	58.99± 2.09	4.51 ± 0.16	2.82 ± 0.26	1.7 ± 0.11
Negative liposomes MAN (DPPC: DSPG: Chol 100:40:20)	Rifampicin	94.69 ± 1.23	91.30 ± 3.2	61.69 ± 2.25	6.42 ± 0.20	2.47 ± 0.15	1.82 ± 0.07
	Ibuprofen	93.92 ± 0.88	83.42 ± 3.93	61.46 ± 1.03	5.16 ± 0.09	2.47 ± 0.09	1.84 ± 0.05
Positive liposomes chitosan-coated (DPPC: DSPG: Chol 100:20:20)	Rifampicin	96.99 ± 2.64	81.08 ± 1.78	62.82 ± 1.12	4.51 ± 0.08	3.16 ± 0.33	1.55 ± 0.21
	Ibuprofen	96.87 ± 3.92	82.88 ± 0.94	64.79 ± 3.34	5.03 ± 0.26	3.03 ± 0.35	1.58 ± 0.19
Positive liposomes chitosan-mannose coated (DPPC: DSPG: Chol 100:20:20)	Rifampicin	96.54 ± 1.37	83.21 ± 2.41	60.50 ± 2.01	4.22 ± 0.14	3.14 ± 0.41	1.54 ± 0.24
	Ibuprofen	96.22 ± 2.47	82.64 ± 1.44	62.09 ± 1.39	4.76 ± 0.10	3.09 ± 0.32	1.61 ± 0.26
Neutral liposomes (DPPC: Chol 100:20)	Rifampicin	92.11 ± 1.14	89.32± 1.07	61.96 ± 0.97	4.79 ± 0.08	3.27 ± 0.24	1.79 ± 0.14
	Ibuprofen	93.24 ± 1.07	88.14± 0.91	62.41 ± 0.84	4.83 ± 0.07	3.15 ± 0.31	1.84 ± 0.18

PAM- p-aminophenyl α-D-mannopyranoside, MAN- mannosamine hydrochloride, ED- emitted dose, FR- fraction recovered, FPF- fine particle fraction, FPD- fine particle dose, MMAD- mass median aerodynamic diameter, GSD- geometric standard deviation

Fraction recovered: It is very important to have a mass balance throughout the NGI, wherein, a total mass balance of active substance recovered should not be less than 75% nor more than 125% of average delivered dose as per the European Pharmacopeia [380]. A small percentage of unrecoverable drug gets entrapped into the seal body and makes it necessary to study the mass balance of each experiment individually. A good mass balance was encountered for all the spray dried with data lying between the limits of 81.08-93.03%.

Emitted dose: The ED was studied from the amount of drug left in the capsules after aerosolization and calculated as per drug loading for respective formulations. High dispersibility and hence ED was evident for the spray dried powders with more than 91.15% contents being emitted during aerosolization for each, indicative of low adhesion to the inhaler. The study of dependence of pressure on the volume mean particle size and hence dispersion of spray dried microparticles (section 4.5.2.3.1) studied by laser diffraction, was well correlated with the high dispersion seen in the *in vitro* aerosolization studies.

It was evident that the emitted dose for all the powders of the different liposomal formulations compared for the individual drugs was insignificant ($p > 0.05$). The spray drying conditions derived from Design of Experiment (DoE 3, section 4.5.2.3) i.e. inlet temperature, amount of lyoprotectant trehalose and addition of 20% w/w/ L-leucine, were used for spray drying these liposomal formulations, and hence there was no difference in aerosolization of the different microparticles.

MMAD and GSD: Mass median aerodynamic diameter (MMAD) refers to particle diameter as half the aerosol mass contained smaller than MMAD and half that is larger. All the spray dried powders show an MMAD of below 5µm, wherein, the largest of 3.27 µm was achieved for the spray dried neutral DPPC: Chol liposomes and the smallest of 2.47 µm for spray dried negative DPPC: DSPG: Chol liposomes incorporating targeting agent mannosamine hydrochloride. MMAD for all the microparticles were found to be well in the respirable limits of 2-5 µm and indicates potential deep lung deposition patterns of these microparticles. The geometric standard deviation for the spray dried microparticles was around 1-2 indicative of monodispersed systems and unimodal distribution of microparticles.

Fine particle fraction and dose: FPF and FPD are important determinants of the fraction and dosage of aerosolized drug that has potential to be deposited in the peripheral airways and hence show therapeutic efficacy. Fine particle fraction of the different liposomal microparticles for both rifampicin and ibuprofen was not significantly different ($p > 0.05$). Moreover, the FPF of rifampicin and ibuprofen obtained for each spray dried microparticle formulation was similar indicating that the microparticles constituted and dispersed both the drugs homogenously on aerosolization. Chougule et al. reported a similar, high FPF of 62.8 ± 2.8% on aerosolization of

spray-dried DPPC: Chol liposomes encapsulating dapsone, formulated with lactose, and delivered from a DPI Brev I. S. F. device into an Andersen Cascade Impactor [360].

The FPD of rifampicin and ibuprofen co-encapsulated in negative DPPC: DSPG: Chol liposomes non-targeted and targeted with mannose moieties was significantly greater ($p < 0.05$) than the neutral DPPC: Chol and positively-charged chitosan-coated DPPC: DSPG: Chol liposomes, owing to differences in the encapsulation efficiency of the drugs within the different liposomal formulations (Table 4.12).

Potential pulmonary deposition of rifampicin and ibuprofen microparticles

Figure 4.24 and **Figure 4.**25 demonstrates the potential pulmonary deposition profile for all the microparticles spray dried from the different liposomal feedstocks, indicating that the conditions used for spray drying were optimum to produce microparticles suitable for delivery to the peripheral lung. Spray drying offers a proper tuning of the particle size, shape and density which are important parameters for successful inhalation of DPIs.

All the spray dried microparticles showed low deposition in the throat and pre-separator stages of the NGI (<20%), indicative of low oropharyngeal and throat deposition and hence a deeper peripheral deposition in the lungs as depicted by increased deposition (>60%) in the stages 2-7 and MOC (stage 8) of the NGI. Negatively-charged DPPC: DSPG: Chol liposomal microparticles non-targeted and targeted (**Figure 4.**24), displayed predominant deposition in stages 2-5 of the NGI, especially in stage 3 and stage 4 having cut-off dimeter 2.82 µm and 1.66 µm respectively.

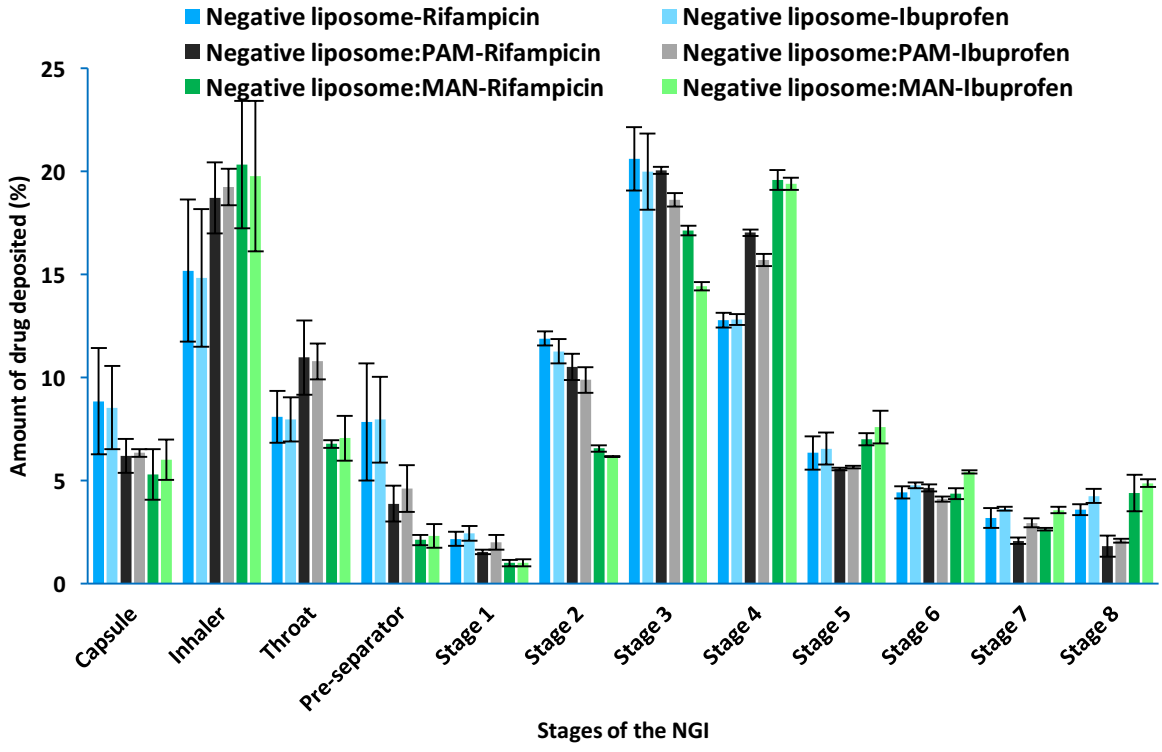

Figure 4.24: NGI deposition profile of spray dried negatively-charged DPPC: DSPG: Chol liposomal microparticles (mean±SD, n=3)

Positively-charged chitosan-coated DPPC: DSPG: Chol liposomal microparticles non-targeted and targeted and neutral-charged DPPC: Chol liposomal microparticles (**Figure 4.**25), displayed predominant deposition in stages 2-5 of the NGI, especially in stage 2 and stage 3 having cut-off dimeter 4.46 µm and 2.82 µm respectively. Therefore, the overall MMAD of the positively-charged liposomal microparticles was greater than the negatively-charged liposomal microparticles.

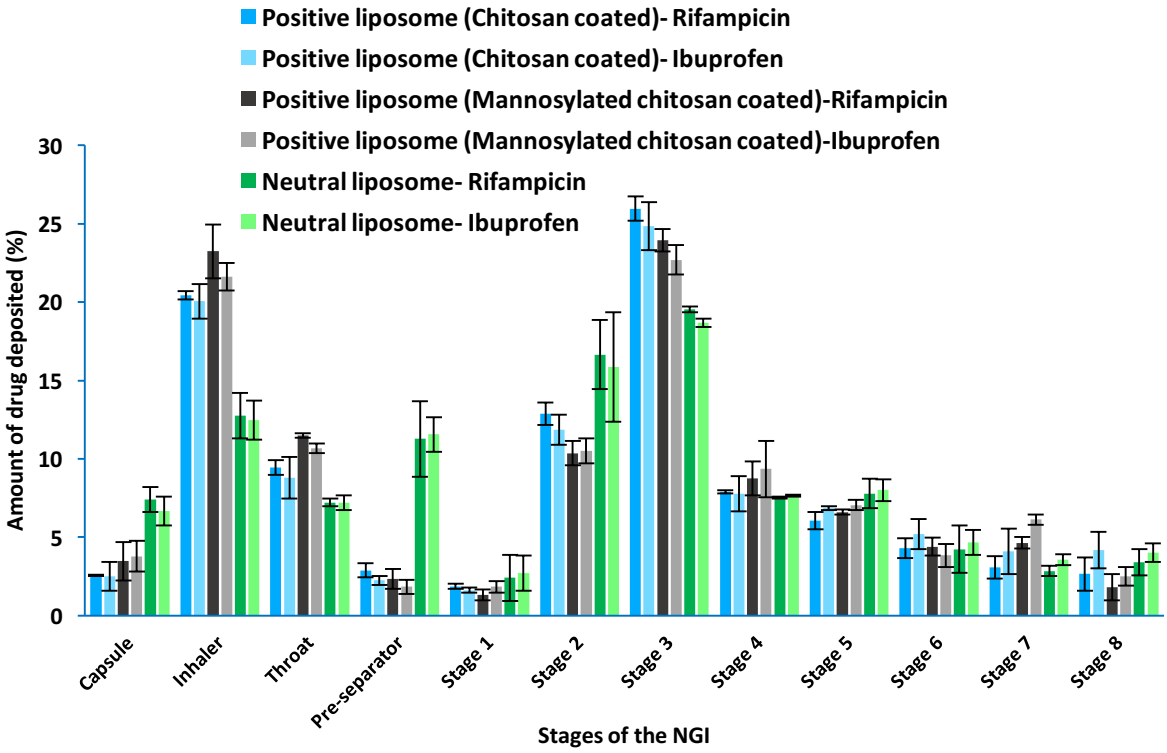

Figure 4.25: NGI deposition profile of spray dried positively-charged chitosan-coated DPPC: DSPG: Chol and neutrally-charged DPPC: Chol liposomal microparticles (mean±SD, n=3)

4.5.6 Cellular uptake studies

The cellular uptake kinetics of the various formulations encapsulating fluorescent dye coumarin-6 using flow cytometry and fluorescence microscopy was assessed on the macrophage RAW 264.7 cells at numerous time points until saturation of uptake into the cells was observed. Uptake kinetics is dependent on the liposomal charge, particle size, surface chemistry and shape [443]. In the present study, the mean size of all the formulations was around 110-130 nm (Table 4.12) for coumarin-6 encapsulated liposomes, hence, the difference in uptake would be specifically due to the differences in surface charge and chemistry of the liposomes. The comparison of mean fluorescence intensity of the different liposomal formulations at varied time points is as shown in Figure 4.26.

The uptake of all the liposomes was linear at 37 °C for about 4 hours after which it levelled off due to saturation of the capacity of RAW 264.7 cells. Repeated Measures One-way ANOVA (rANOVA) using Tukey post-hoc analysis was performed to compare the different groups

considering 'time' as an independent variable, wherein p at a level of 0.05 i.e. $p < 0.05$ was a significant difference. When the model was analyzed a p value of 0.275 was obtained, confirming that the model was valid to be studied using Ranova, as it did not violate Mauchly's Test of Sphericity and that the variances of difference between the different subject groups (formulations) at all levels were equal.

Comparison of the uptake of neutral-charged DPPC: Chol liposomes with the negatively-charged DPPC: DSPG: Chol liposomes and the positively-charged chitosan-coated DPPC: DSPG: Chol showed a significantly slower uptake (rANOVA, $p < 0.05$), reaching saturation between 4-8 hrs.

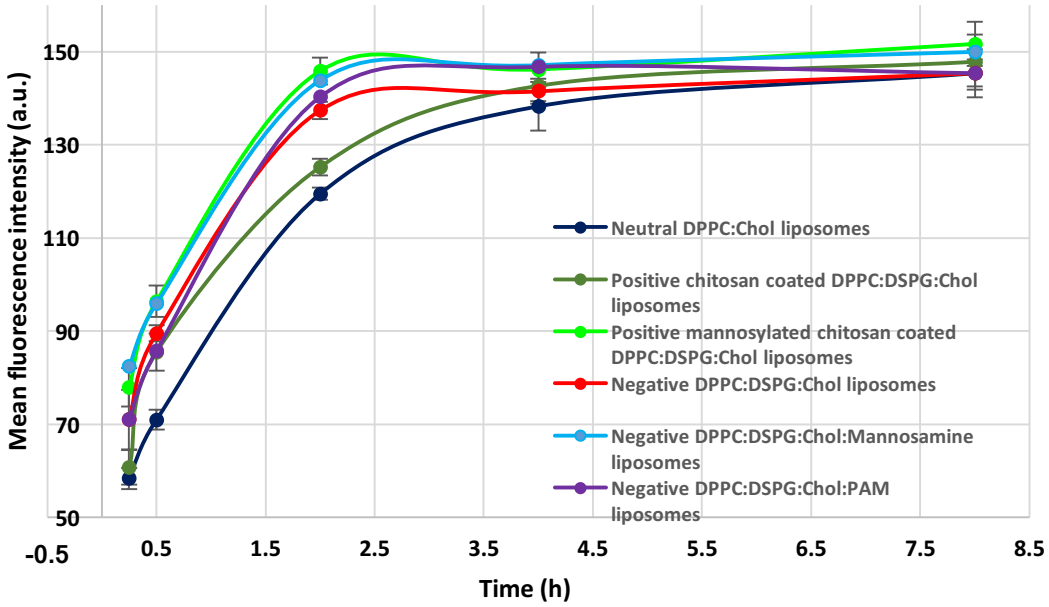

Figure 4.26: Mean fluorescence intensity (arbitrary units) showing quantitative cellular uptake kinetics as measured by the flow cytometer (mean±SD, n=3)

Figure 4.27 shows the uptake kinetics of neutral liposomes qualitatively and quantitatively over a period of 8 h. An increase in fluorescence intensity was evident with increasing time (Figure 4.27A-E) depicting increased uptake of neutral-charged DPPC: Chol liposomes. The flow cytometry histogram (Figure 4.27F) for the region selected for study 'P1', shows the x-axis as the fluorescence intensity and y-axis as cell count. The results support the qualitative fluorescence microscopy images that the uptake of neutral-charged DPPC: Chol liposomes increased up to 4 h, after which an overlap of histograms for 4 h and 8 h was evident (light blue and black histograms) suggesting saturation of uptake after 4 h, also confirmed by the mean fluorescence intensity shown in Figure 4.26.

Negatively-charged DPPC: DSPG: Chol liposomes showed a significantly higher (rANOVA, $p = 0$) uptake as compared to neutral-charged DPPC: Chol liposomes and positively-charged chitosan-coated DPPC: DSPG: Chol liposomes (rANOVA, $p = 0.019$), as evident by the mean fluorescence intensity kinetics in Figure 4.26. An increase in the fluorescence intensity was seen with increasing time (Figure 4.28A-E), wherein, at the 2 h time-point more fluorescence was evident for the negatively-charged liposome treated cells as compared to the neutral-charged

liposome treated cells. This was supported by the mean fluorescence intensity value and shift in histogram at 2 h (dark blue), wherein, an overlap between the histograms at 2 h (dark blue), 4 h (light blue) and 8 h (black) was seen. These results proposed that negatively-charged DPPC: DSPG: Chol (Figure 4.28F) liposomes were taken up more quickly as compared to neutral liposomes, suggesting an active scavenger receptor mediated endocytosis of the anionic liposomes as seen earlier by Rigotti et al. [410].

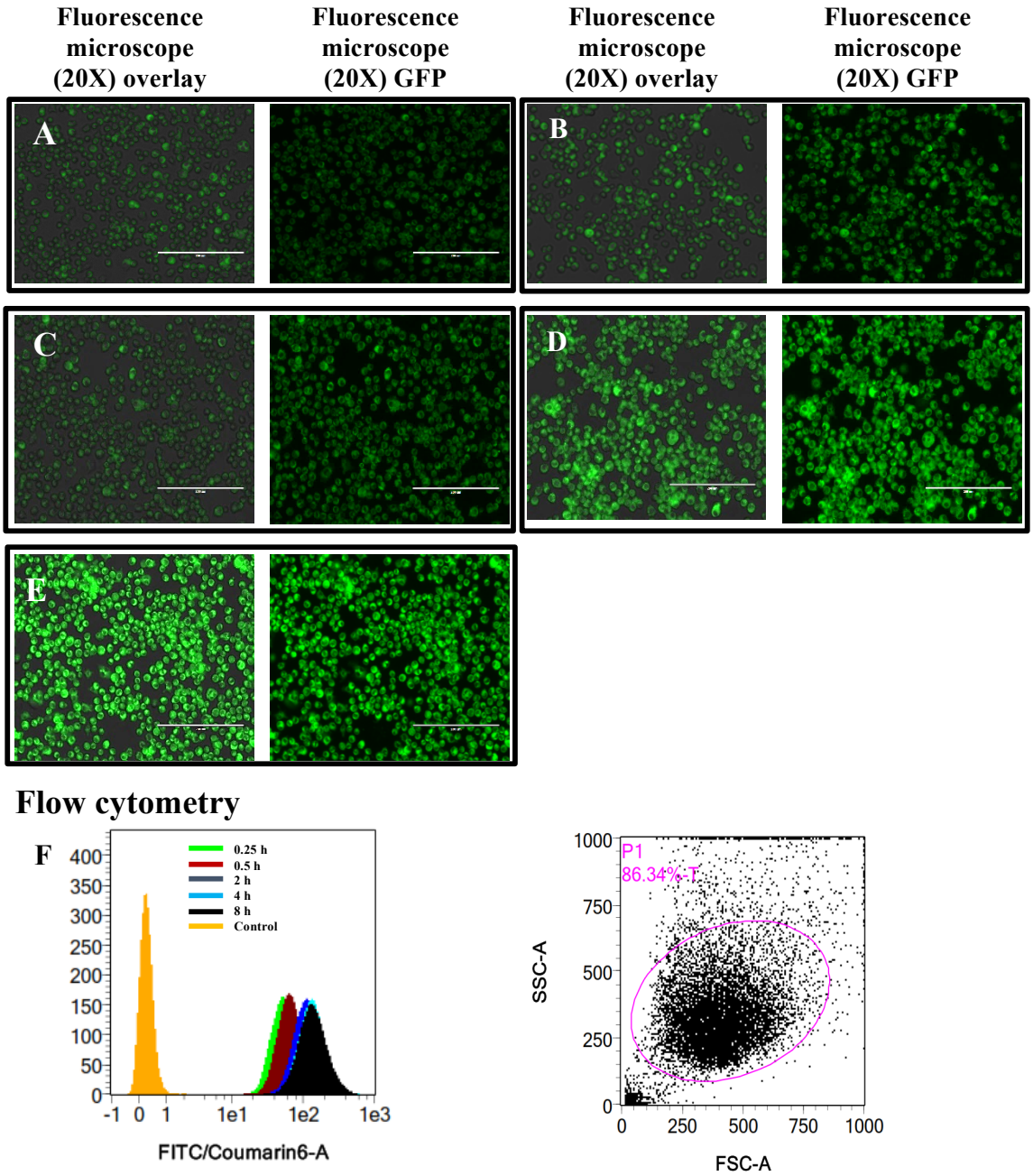

Figure 4.27: Time-dependent qualitative uptake of neutrally-charged DPPC: Chol liposomes monitored using fluorescence microscopy at (A) 0.25 h, (B) 0.5 h, (C) 2 h, (D) 4 h and (E) 8 h
(F) Time-dependent quantitative uptake of neutrally-charged DPPC: Chol liposomes studied using flow cytometry (P1 is the region chosen for the study)

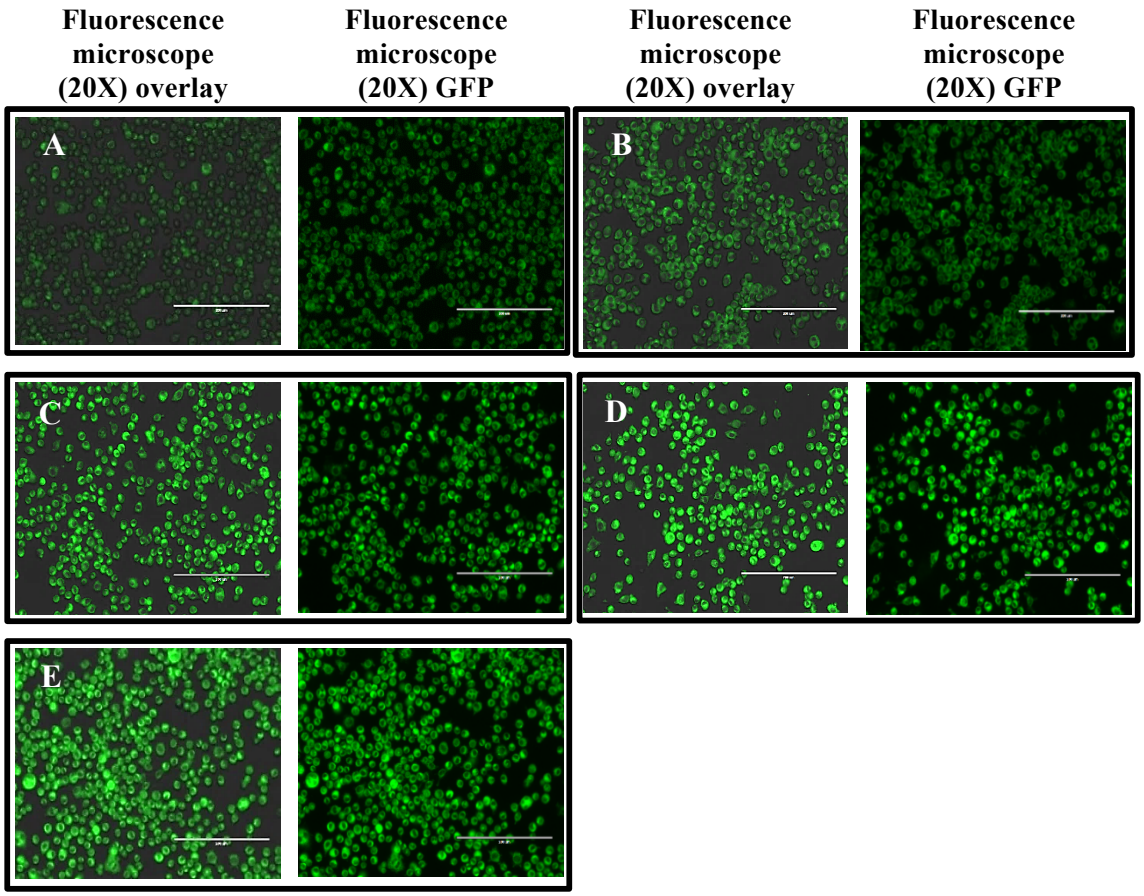

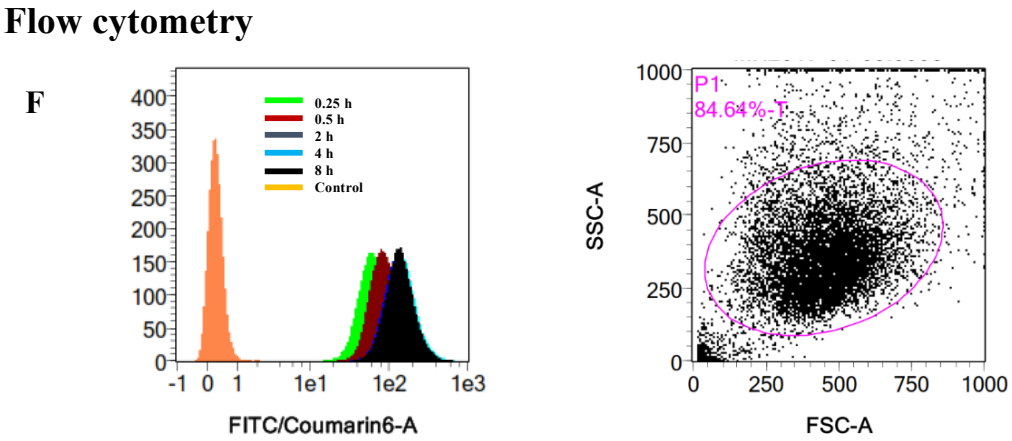

Figure 4.28: Time-dependent qualitative uptake of negatively-charged DPPC: DSPG: Chol liposomes monitored using fluorescence microscopy at (A) 0.25 h, (B) 0.5 h, (C) 2 h, (D) 4 h and (E) 8 h
(F) Time-dependent quantitative uptake of negatively-charged DPPC: DSPG: Chol liposomes studied using flow cytometry (P1 is the region chosen for the study)

To further improve uptake of negatively-charged DPPC: DSPG: Chol liposomes targeting moiety mannosamine was incorporated into the bilayer by interaction of the positive amino groups of mannosamine with the negatively-charged liposomal bilayer induced by phosphatidylglycerol at pH 7. Negatively-charged mannosylated liposomes incorporating mannosamine or p-aminophenyl mannopyranoside have previously been shown to improve uptake *in vivo* and *in vitro* in epithelial cells and alveolar macrophages [213,444,445].

Negatively-charged mannosamine incorporated DPPC: DSPG: Chol liposomes showed an improved uptake kinetics as compared to both neutral-charged DPPC: Chol liposomes (rANOVA,

p = 0) and negatively-charged DPPC: DSPG: Chol liposomes (rANOVA, p = 0.009) as seen in Figure 4.29. An increase in uptake of negatively-charged DPPC: DSPG: Chol mannosamine liposomes was seen in the fluorescence microscopy images (Figure 4.29A-E) with increasing time. The flow cytometry histograms (Figure 4.29F) for the selected region also showed a quicker uptake, wherein, an overlap of histograms for the initial 0.25 h (green) and 0.5 h (brown) time point was seen indicating a quicker uptake, due to an increased initial interaction obtained by active targeting to both the scavenger and mannose receptors on the macrophage cell membrane.

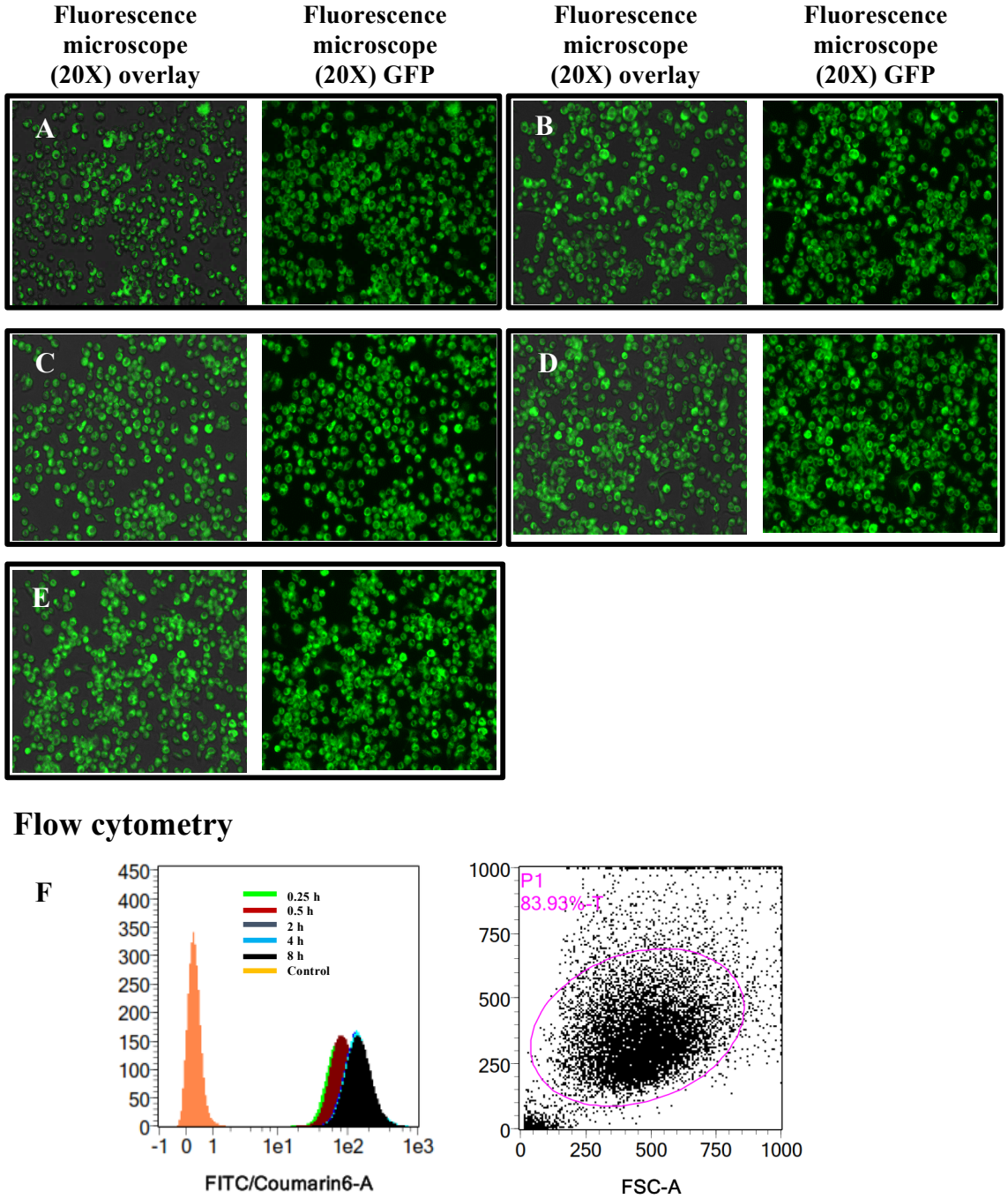

Figure 4.29: Time-dependent qualitative uptake of negatively-charged DPPC: DSPG: Chol mannosamine liposomes monitored using fluorescence microscopy at (A) 0.25 h, (B) 0.5 h, (C) 2 h, (D) 4 h and (E) 8 h (F) Time-dependent quantitative uptake of negatively-charged DPPC: DSPG: Chol mannosamine liposomes studied using flow cytometry (P1 is the region chosen for the study)

Maximal uptake was seen within 2 h apparent by the overlap of the fluorescence intensity histograms for uptake at 2 h (dark blue), 4 h (light blue) and 8 h (black). Chono et al. reported a similar enhanced drug uptake by alveolar/peritoneal macrophages *in vitro* (NR8383 cells) and in *vivo* (rats) when inhaled from a liquid Micro Sprayer device, for the mannosylated negatively-charged PC: Chol liposomes as compared to non-mannosylated negatively-charged liposomes [412]. Youngren et al. also reported an enhanced uptake of mannosamine targeted DPPC: DSPG: Chol liposomes *in vitro* in MH-S mouse alveolar cells [433].

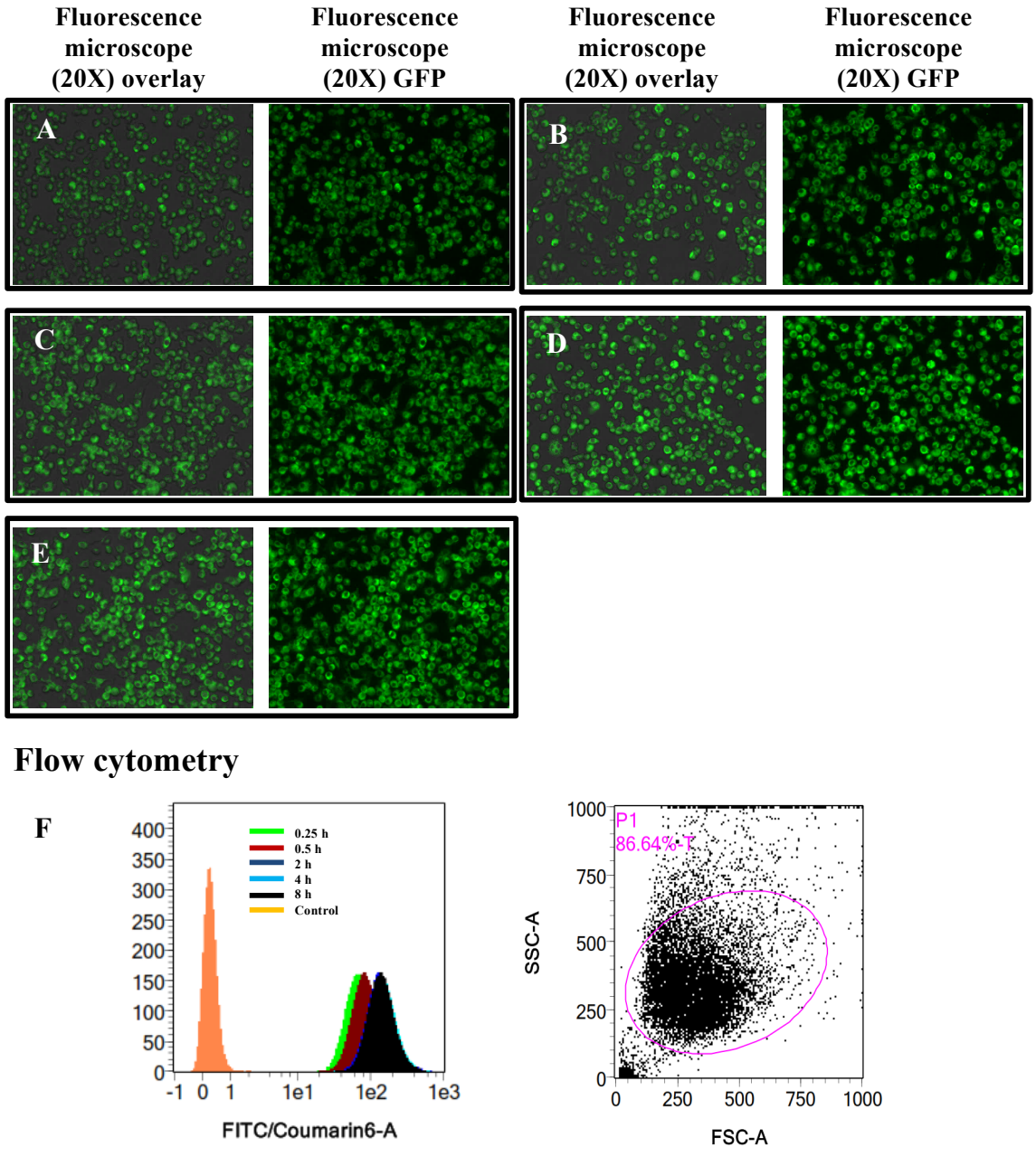

Figure 4.30: Time-dependent qualitative uptake of negatively-charged DPPC: DSPG: Chol p-aminophenyl mannopyranoside liposomes monitored using fluorescence microscopy at (A) 0.25 h, (B) 0.5 h, (C) 2 h, (D) 4 h and (E) 8 h
(F) Time-dependent quantitative uptake of negatively-charged DPPC: DSPG: Chol p-aminophenyl mannopyranoside liposomes studied using flow cytometry (P1 is the region chosen for the study)

Another strategy to improve the uptake of negatively-charged DPPC: DSPG: Chol liposomes into macrophages was by incorporation of p-aminophenyl mannopyranoside (PAM) by means of attraction of the amino group on PAM with the negatively-charged liposomal bilayer. There was a significantly improved (rANOVA, $p = 0$) uptake of negatively-charged DPPC: DSPG: Chol PAM liposomes as compared to the neutral-charged DPPC: Chol liposomes, however, uptake was not significantly improved (rANOVA, $p = 1$) as compared to the negatively-charged DPPC: DSPG: Chol liposomes. This is due to insufficient PAM incorporated within the liposomal bilayers used in the study.

There was a time-dependent increase in fluorescence intensity of thes negatively-charged DPPC: DSPG: Chol PAM liposomes (Figure 4.30A-E), levelling off at around 2 h evident by the overlay in fluorescence intensity histograms (Figure 4.30F) at 2 h (dark blue), 4 h (light blue) and 8 h (black), similar to the negatively-charged DPPC: DSPG: Chol liposomes.

Positively-charged chitosan-coated DPPC: DSPG: Chol liposomes showed a significantly higher uptake (rANOVA, $p = 0.008$, Figure 4.26) as compared to the neutral-charged DPPC: Chol liposomes, which is attributed to a higher extent of interaction between the positively-charged liposomal surface and negatively-charged cell membrane, hence, bringing the liposomes closer to the cells consequently improving uptake by endocytosis. However, uptake was significantly lower than actively targeted negatively-charged DPPC: DSPG: Chol liposomes (rANOVA, $p = 0.019$) and mannosylated negatively-charged DPPC: DSPG: Chol liposomes (rANOVA, $p = 0$ negatively-charged mannosamine liposomes, $p = 0.016$ negatively-charged PAM liposomes). The fluorescence intensity was seen to increase with time (Figure 4.31A-E). The flow cytometry histograms (Figure 4.31F) for the selected region ‘P1’ also showed an increased uptake levelling off at 4 h depicted by the overlay between the florescence intensity histogram at 4 h (light blue) and 8 h (black).

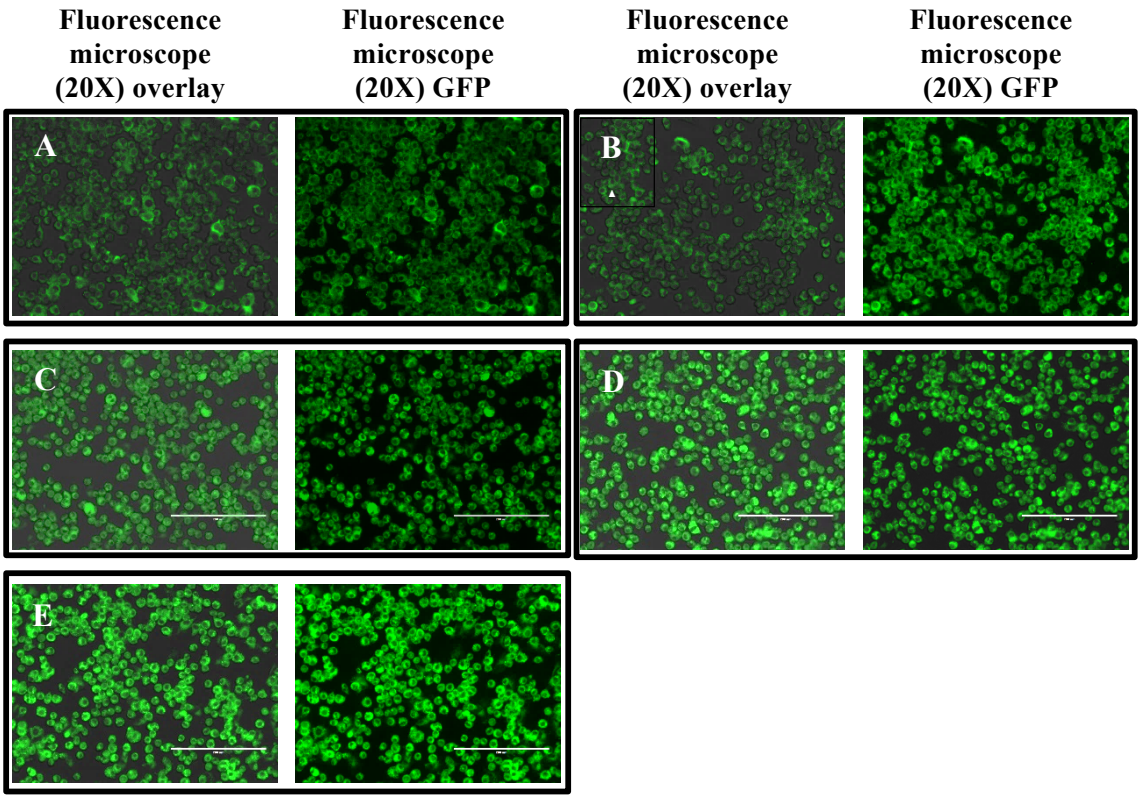

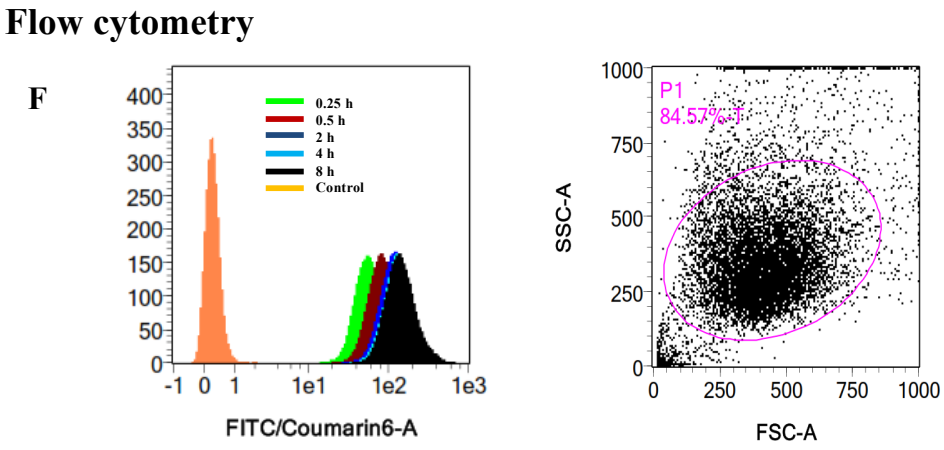

Figure 4.31: Time-dependent qualitative uptake of positively-charged chitosan-coated DPPC: DSPG: Chol liposomes monitored using fluorescence microscopy at (A) 0.25 h, (B) 0.5 h, (C) 2 h, (D) 4 h and (E) 8 h (F) Time-dependent quantitative uptake of positively-charged chitosan-coated DPPC: DSPG: Chol liposomes studied using flow cytometry (P1 is the region chosen for the study)

To further improve the uptake of positively-charged DPPC: DSPG: Chol liposomes into macrophages they were coated with mannosylated chitosan to achieve active targeting using mannose receptors on the macrophage cell membrane. A significantly higher uptake (rANOVA, $p = 0$, Figure 4.26) was seen for the mannosylated chitosan-coated DPPC: DSPG: Chol liposomes as compared to the neutral-charged DPPC: Chol liposomes. Moreover, mannosylated chitosan-coated liposomes also showed a higher uptake when compared to positively-charged chitosan-coated liposomes (rANOVA, $p = 0$), negatively-charged liposomes targeted to scavenger receptors (rANOVA, $p = 0.009$) and negatively-charged PAM liposomes (rANOVA, $p = 0.011$). However, the uptake kinetics of mannosylated chitosan-coated liposomes studied using mean

fluorescence intensity at the various time points was not significantly different (rANOVA, $p = 1$, Figure 4.26) when compared to the negatively-charged mannosamine liposomes, depicting that both the formulations had an improved uptake due to efficient targeting to the mannose receptors.

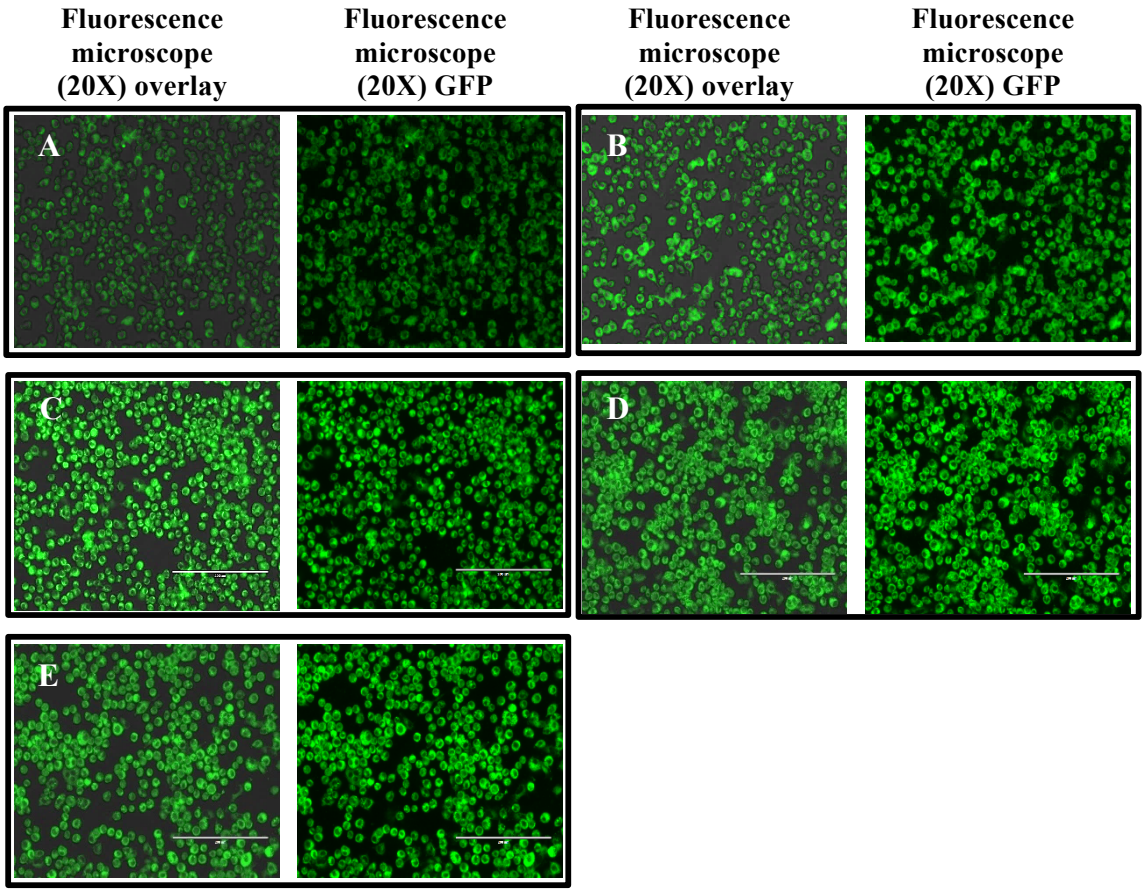

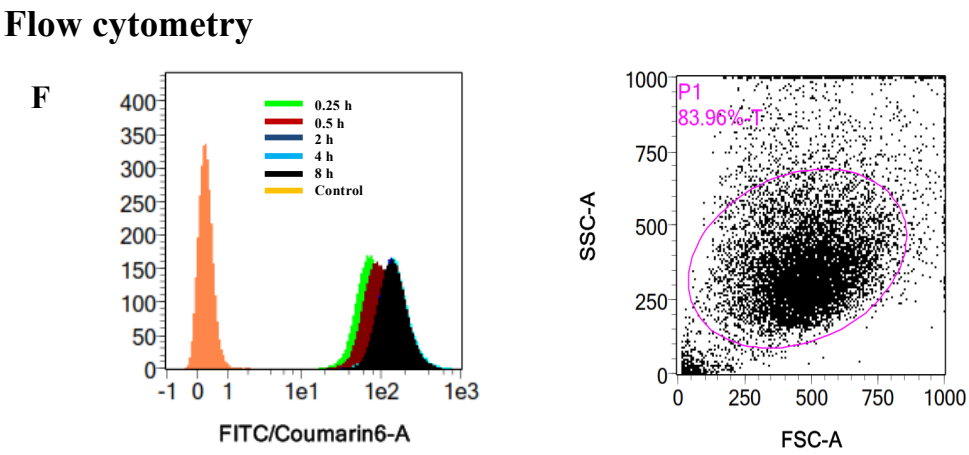

Figure 4.32: Time-dependent qualitative uptake of positively-charged mannosylated chitosan-coated DPPC: DSPG: Chol liposomes monitored using fluorescence microscopy at (A) 0.25 h, (B) 0.5 h, (C) 2 h, (D) 4 h and (E) 8 h
(F) Time-dependent quantitative uptake of positively-charged mannosylated chitosan-coated DPPC: DSPG: Chol liposomes studied using flow cytometry (P1 is the region chosen for the study)

There was a time-dependent increase in the fluorescence intensity of mannosylated chitosan-coated positively-charged liposomes as confirmed by the fluorescence microscopy images and flow cytometry histograms as seen in Figure 4.32. The fluorescence intensity histograms (Figure 4.32F) showed levelling off uptake in 2 h indicated by the overlay of the histograms for uptake at 2 h (dark blue), 4 h (light blue) and 8 h (black) and the mean fluorescence intensities in Figure 4.26.

In conclusion, changing the surface charge of liposomes from neutral to negative or positive showed a significant improvement (rANOVA, $p < 0.05$) in uptake by means of endocytosis by targeting the scavenger receptors (negative liposomes) or by simple attraction of the positively-liposomes to the negatively-charged cell membrane. Moreover, mannosylation of the negatively or positively-charged liposomes showed a significantly higher uptake (rANOVA, $p < 0.05$) as compared to their charged counterparts or neutral-charged liposomes. Hence, macrophage cellular uptake of liposomes may be improved by not only passive targeting of formulations directly to the lung by means of DPIs, but also improving uptake into the macrophages where the intracellular TB infection resides by means of actively targeting the scavenger or mannose receptors once the liposomes are dispersed in the lung fluid.

4.6 Conclusion

The aim of this chapter was to not only utilize the art of preparation of liposomes to aid in solubilization of hydrophobic drugs to be delivered to the lungs, but also alter the surface chemistry of the liposomes to obtain active targeting when infections are intracellularly-located within deep compartments of the lungs.

Based on the aforementioned results presented in this chapter, it can be concluded that:

1. Liposomes co-encapsulating antitubercular drugs rifampicin and ibuprofen were successfully formulated with the help of Design of Experiment, by developing a factorial design for studying the effect of choice of lipids DPPC: DSPG: Chol and their constitution on the mean size, zeta potential, PDI of the liposomes and encapsulation efficiencies of rifampicin and ibuprofen. The lipid constitution of 100: 40: 20 DPPC: DSPG: Chol was selected to form stable liposomes with encapsulation efficiency of 89.75±2.40% and 99.00±2.20% for rifampicin (25 micromolar) and ibuprofen (50 micromolar) respectively, with a mean size of 84.09±3.89 nm and surface zeta potential of -43.5±1.5 mV.
2. Co-encapsulation of antitubercular drugs into one liposomal system can be complex due to interaction between the drugs. A second factorial design was successfully developed to study the interaction of rifampicin and ibuprofen in the liposomal system chosen from the first study.
3. To further enhance uptake by targeting actively to the scavenger and the mannose receptors, negatively-charged DPPC: DSPG: Chol liposomes were further successfully modified with mannose moieties mannosamine hydrochloride and p-aminophenyl mannopyranoside, by means of embedding these within the negatively-charged liposomal bilayer by electrostatic attraction with the positively-charged amino groups on these mannose moieties at pH 7.
4. Positively-charged liposomes were prepared by coating the negative surface of DPPC: DSPG: Chol (100: 20: 20) liposomes with chitosan by means of electrostatic attraction. The liposomes so formed showed an encapsulation efficiency of 63.12±1.06% and 92.50±2.00% for rifampicin and ibuprofen respectively, with a mean size of 145.34±2.12 nm and surface charge of +37.21±1.89 mV.
5. To further enhance cellular uptake by targeting the positively-charged liposomes to the mannose receptors, coating with mannosylated chitosan was carried out in a similar way to that of chitosan. Mannosylated chitosan was successfully synthesized and its structure was confirmed using ^{1}H-NMR and FT-IR.
6. A full factorial design was set up to gain an insight and understanding on the formulation of inhalable microparticles of the above liposomal formulations, by studying the effects of amount of lyoprotectant trehalose, dispersibility enhancer L-leucine and inlet temperature of spray drying on dry powder particle size distribution, Span and moisture content. Microparticles obtained by spray drying at 120°C in the presence of 33.33% of lyoprotectant

trehalose and 20% dispersibility enhancer L-leucine had dry powder particle size in respirable range of 2-5 µm, along with low moisture content. These process parameters were also used to spray dry the targeted negative liposomes, non-targeted and targeted positive liposomes.

7. *In vitro* potential pulmonary deposition studies for the microparticles sprayed from the different liposomal constitutions co-encapsulating rifampicin and ibuprofen showed a low deposition in the throat and pre-separator stages of the NGI (<20%), and an increased deposition (>60%) in the stages 2-7 and MOC of the NGI, wherein a fine particle fraction of 58.99-64.79% was evident for all the microparticles, indicative of potential peripheral pulmonary deposition.
8. *In vitro* cellular uptake was performed qualitatively using the fluorescence microscope and quantitatively using the flow cytometer on murine macrophage RAW 264.7 cells by replacing the drugs with fluorescent dye coumarin-6. Neutral DPPC: Chol liposomes showed the slowest uptake kinetics. Changing the surface charge of liposomes to negative i.e. DPPC: DSPG: Chol liposomes or positive chitosan-coated DPPC: DSPG: Chol liposomes significantly improved uptake (rANOVA, $p < 0.05$) when compared to neutral DPPC: Chol liposomes. Moreover, embedding mannosamine in the negatively-charged DPPC: DSPG: Chol bilayer or coating with mannosylated chitosan to confer a final positive charge to liposomal surface) facilitated uptake as compared to both neutral liposomes and negatively-charged non-targeted liposomes. Hence, cellular uptake studies validated the hypothesis of using actively targeted nanocarrier systems for delivering tubercular drugs directly to the alveolar macrophages, where the TB bacilli infects and resides.

5

CHAPTER 5

Preparation and characterization of Kolliphor® micelles for nose-to-brain delivery of neuroprotective agents and cancer chemotherapeutics

5.1 Introduction

5.1.1 Neurological effects of curcumin

Curcumin (Figure 5.1) is a naturally occurring polyphenol extracted from the dried ground rhizome of Curcuma longa commonly known as turmeric.

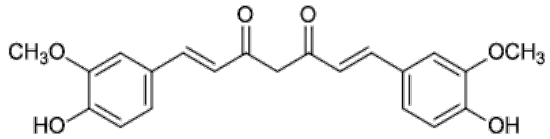

Figure 5.1: Structure of curcumin

Table 5.1: Physicochemical properties of curcumin

Molecular formula	$C_{21}H_{20}O_6$
pKa	8.54
Molecular weight	368.385 g/mol
Solubility	Insoluble in water and ether Soluble in ethanol, acetone and chloroform

Pharmacological and therapeutic benefits of curcumin are restricted due to its pharmacokinetic properties (Table 5.1) especially its hydrophobic nature, leading to delivery issues of low oral absorption and poor bioavailability, extensive metabolism and rapid elimination [446]. Hence, to overcome these and increase its bioavailability its entrapment within nanocarriers such as liposomes, cyclodextrins and polymeric nanoparticles has been researched extensively [446]. Moreover, encapsulation of curcumin can protect the drug from degradation and metabolism along with improving drug efficacy, specificity, tolerability and therapeutic index [446]. Furthermore, drug targeting to the site of interest can be achieved by passive targeting of curcumin encapsulated nanocarriers e.g. enhanced permeability and retention (EPR) effect in cancer or active targeting to the upregulated receptors by means of ligands e.g. folic acid/CD44 receptor targeting in cancer and mannose receptors on macrophages for tuberculosis and rheumatoid arthritis.

Curcumin and brain cancer

Curcumin has diverse pharmacological effects such as anti-inflammatory, antimicrobial, neuroprotection, antioxidant and anticancer, hence, has diverse therapeutic application for diseases like diabetes, Alzheimer's disease, Parkinson's disease, stroke, inflammatory bowel conditions, arthritis, glioblastoma and lung cancer. The underlying mechanisms of these effects are dependent on the regulation of multiple targets. Curcumin has the ability to intervene in molecular and biochemical cascades by directly binding and modulating receptor activity by means of upregulation or downregulation, or indirectly regulating receptor function [446–448].

Its cancer growth prevention and tumor growth suppression properties has been attributed to its strong free radical scavenging and anti-inflammatory effects. Specifically, curcumin supresses nuclear factor kappa B (NF-κB) and activates extracellular-signal-regulated kinase pathways ultimately leading to suppression of cancer [449]. It has the ability to completely block the activation of NF-κB by blocking the IκK-mediated phosphorylation and degradation of IκBα in the cytoplasm. As a consequence, binding between NF-κB and IκBα is altered and thus NF-κB is not able to enter the nucleus to activate RNA transcription [449].

The numerous molecular targets of curcumin conferring its anticancer properties in brain cancer has been outlined in Figure 5.2.

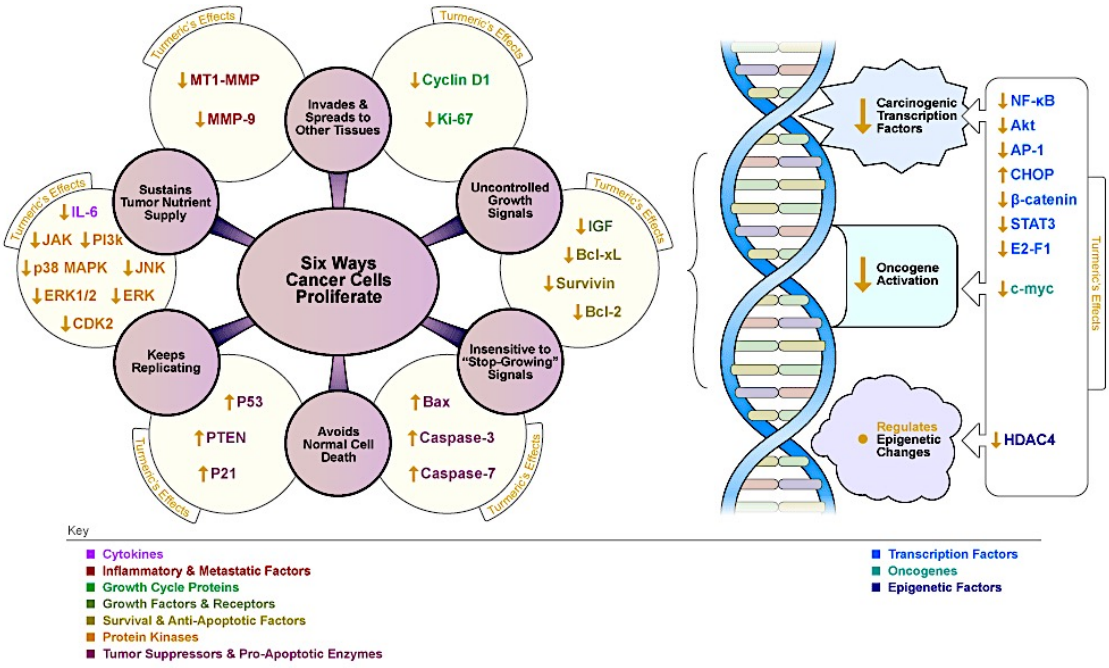

Figure 5.2: Molecular targets of curcumin (turmeric) in brain cancer [450]

5.1.2 Neurological effects of CNB001

CNB001 (Figure 5.3) i.e. 4-((1E)-2-(5-(4-hydroxy-3-methoxystyryl-)-1-phenyl-1H-pyrazoyl-3-yl) vinyl)-2-methoxy-phenol, a novel pyrazole derivative of curcumin was synthesized by Salk Institute for Biological Sciences (California, USA). This molecule is a hybrid of two neuroprotective drugs namely, curcumin and cyclohexyl bisphenol A, and has improved CNS bioavailability, demonstrating neuroprotection superior to curcumin *in vivo* in diseased models of Alzheimer's and Parkinson's disease [451,452].

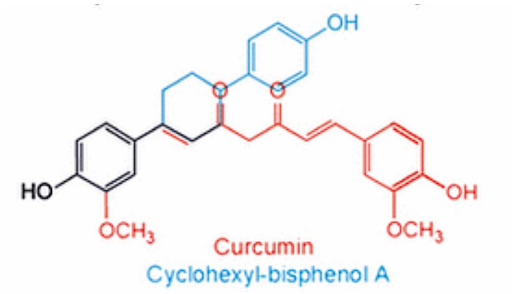

Figure 5.3: Structure of CNB001

Table 5.2: Physicochemical properties of CNB001

Molecular formula	$C_{27}H_{24}N_2O_4$
pKa	Not reported (hydrophobic)
Molecular weight	440.49 g/mol
Solubility	Insoluble in water Soluble in DMSO

Curcumin has shown to exhibit excellent neuroprotection of dopaminergic neurons *in vitro* due to its potential effects on ROS formation, ATP production and mitochondrial membrane potential [451,452]. However, due to low bioavailability in the CNS on parenteral administration, owing to reduced passage through the BBB, it fails to inhibit excitation of neurons and consequently apoptosis [451,452]. CNB001 shows superior neuroprotection to parent molecules *in vitro* and *in vivo*, due to superior inflammatory properties of CNB001 by suppression of interlukin-6, interlukin-13, TNF-α and serine peptidase inhibitor clade E (SERPINE1) studied on normal human bronchial epithelial cells [453]. *In vitro* CNB001 has lower EC50 for tropic factor withdrawal, glucose starvation, oxidative stress, excitotoxicity, intracellular and extracellular amyloid inhibition and hence superior neuroprotective effect [454].

Since, bioavailability of curcumin and CNB001 would largely be dictated by the transport of molecules across the nasal olfactory epithelium in the present study and not by the passage through the BBB on parenteral administration, both curcumin and CNB001 were used as neuroprotective molecules.

5.1.3 Nanotechnology and curcumin

CNB001 has not been previously delivered in a nanocarrier-based system *in vitro* or *in vivo*, however, nanocarrier-based curcumin has been extensively researched. Nanocarrier encapsulated curcumin for treatment of neurological disorders like brain cancer and neuroprotection are outline in Table 5.3.

Table 5.3: Nanocarrier therapies under investigation for delivery of curcumin for treatment of neurological disorders

Formulation	Effective against	Treatment outcome(s)
Solid lipid nanoparticles Precirol, Capmul MCM, Tween 80, soya lecithin Curcumin [235]	Astrocytoma-glioblastoma	Significantly higher drug concentration of curcumin encapsulated in NLCs in the brain after intranasal administration as compared to plain drug suspension was reported
Dendrosomes Curcumin [455]	Glioblastoma	Significantly inhibits glioblastoma proliferation Synergistic delivery of dendrisome curcumin with p53 overexpression enhanced apoptotic cells by 90% as opposed to 38% for dendrisome curcumin alone
Lactoferrin nanoparticles Curcumin [456]	Neuroprotection	Greater intracellular uptake, sustained retention and superior neuroprotection *in vitro* as compared to curcumin alone
Polymeric nanoparticles NanoCurc™ N-isopropylacrylamide, vinylpyrrolidone and acrylic acid Curcumin [457]	Neuroprotection-Alzheimer's disease	NanoCurc™ protects and rescues SK-N-SH cells from reactive oxygen species- hydrogen peroxide insult
PLGA nanoparticles Curcumin [458]	Neuroprotection-Alzheimer's disease	Inhibits amyloid aggregates and reactive oxygen species, responsible for neuroprotection *in vitro* in glioma cells

5.2 Aims and Objectives

The present investigation was aimed towards the development of non-ionic surfactant micelles for incorporation of drugs curcumin and CNB001 to be targeted to the brain via the nose, to enhance therapeutic efficacy of the drugs by by-passing the blood brain barrier (BBB).

Hence, the aim of the study was

- To engineer Kolliphor® micelles for the delivery of hydrophobic drugs curcumin or CNB001, prepared by thin film hydration
- To design and develop aerosol formulations and study parameters that dictate aerosolization efficiency
- To investigate the effect of formulation development of Kolliphor® TPGS micelles incorporating curcumin targeted to the mitochondria, on the quantitative *in vitro* cellular cancer growth inhibition in the neuroblastoma SH-SY5Y and lung adenocarcinoma A549 cell lines
- To investigate the effect of formulation development of Solutol® HS 15 (Kolliphor® HS 15) micelles incorporating CNB001 or curcumin, on the quantitative and qualitative *in vitro* cellular Parkinson's disease model insulted with neurotoxin 6-hydroxydopamine, developed on the neuroblastoma SH-SY5Y cell line

The various nanocarrier formulations investigated in the present chapter are shown below:

(A) Solutol® HS 15 (Kolliphor® HS 15) micelles incorporating hydrophobic neuroprotective agent's curcumin or CNB001

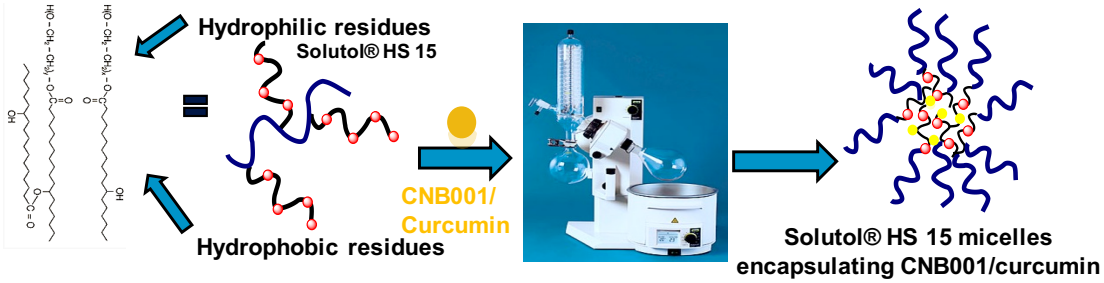

Solutol® HS 15 (Polyethylene glycol (15)-hydroxystearate, Kolliphor® HS 15) has been shown to be neuroprotective in rat models of cerebral ischemia, and hence its use in preparation of micelles incorporating hydrophobic potentially neuroprotective molecules was investigated [459].

(B) Kolliphor® TPGS micelles incorporating hydrophobic cancer chemotherapeutic curcumin targeted to the mitochondria

Kolliphor® TPGS (D-α-tocopherol polyethylene glycol 1000 succinate) has been shown to induce apoptosis in cancer cell lines as well as to reverse multi-drug resistance in lung cancer, and hence was chosen as the surfactant of choice for preparation of micelles incorporating cancer drugs [460,461]. Targeting of the formulations to the mitochondria was intended to further improve the

delivery of the curcumin to the cancer cell mitochondria by incorporating dequalinium, a cationic mitochondrial targeting agent [462].

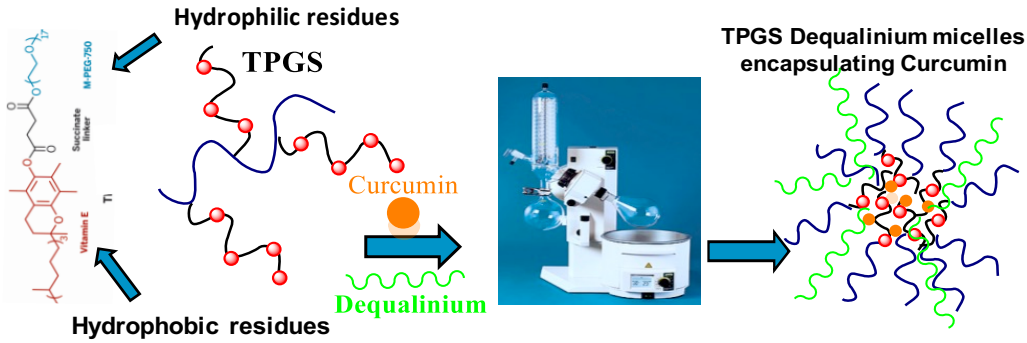

.

5.3 Materials

Curcumin ≥ 95.0% curcuminoid content (from Tumeric rhizome) with molecular weight of 368.39 g/mol was purchased from Alfa Aesar UK (Lancashire, UK). CNB001 with molecular weight of 440.49 g/mol was purchased from Salk Institute for Biological Sciences (California, USA). Non-ionic surfactants Kolliphor® HS 15 (also known as Solutol® HS 15, Polyethylene glycol (15)-hydroxystearate) and Kolliphor® TPGS (D-α-tocopherol polyethylene glycol 1000 succinate) were purchased from BASF (Cheshire, UK) and used without further purification. Cholesterol, sodium dodecyl sulphate (SDS), acetic acid, sodium chloride, potassium chloride, calcium chloride dihydrate were purchased from Sigma-Aldrich (Poole, UK).

For *in vitro* cell culture studies fetal bovine serum (FBS), Roswell Park Memorial Institute (RPMI) 1640, Minimum Essential Medium Eagle (MEM), Ham's F12 Nutrient Mixture, penicillin-streptomycin, L-glutamine, non-essential amino acids and PBS pH 7.4 were purchased from ThermoFisher Scientific (Loughborough, UK). 6-hydroxydopamine, 2′,7′-dichlorofluorescin diacetate, bisBenzimide H 33258 (Hoechst) ≥98%, (3-(4,5-dimethylthiazol-2-yl)-2,5-diphenyltetrazolium bromide (MTT reagent), sulforhodamine B sodium salt, Trizma® (TRIS base) and trichloroacetic acid were purchased from Sigma-Aldrich (Poole, UK).

HPLC grade water, acetonitrile and dimethyl sulfoxide (DMSO) were purchased from Fisher Scientific (Loughborough, UK). Deionized water was used throughout the experiments unless specifically mentioned. All other reagents used were of analytical grade.

5.4 Methods

5.4.1 Preparation of CNB001 or curcumin incorporated Kolliphor® micelles

The surfactant/polymer was selected for each study to achieve a good encapsulation of the hydrophobic drug along and based on the end-use of the formulation i.e. Kolliphor® TPGS for cancer formulations and Solutol® HS 15 for neuroprotection formulations.

50 mg of non-ionic surfactant (Kolliphor® TPGS or Solutol® HS 15) and 5 mg of drug (CNB001 or curcumin) were dissolved in 20 mL methanol:chloroform 1:1. For preparation of stable Solutol® HS 15 micelles, cholesterol at different molar ratios was added at this stage. Moreover, for Kolliphor® TPGS micelles intended for delivery of cancer chemotherapeutics, the mitochondrial targeting moiety dequalinium chloride was added at different molar ratios in organic solvent. The organic solvent was removed under vacuum using a rotary evaporator KNF RC 900 (KNF Neuberger UK, Oxfordshire, UK) at 60 °C and 200 rpm for 20 min. A dried thin and homogeneous film was obtained and was further dried under a stream of nitrogen gas for 20 min to ensure complete removal of residual solvent. The film was then hydrated using 20 mL of acidified deionised water (0.2% glacial acetic acid, pH 3.14) at 60 °C and 250 rpm for 20 min, and was finally bath sonicated (Clifton M-14 ultrasonic bath sonicator, Progen Scientific, London) for 15 min.

5.4.2 Formulation characterization

5.4.2.1 Determination of particle size and zeta potential (surface charge) using Malvern Zetasizer

The hydrodynamic diameter and the polydispersity index (PDI) of the micellar formulations were measured by DLS and the zeta potential was measured by laser Doppler velocimetry using Malvern Zetasizer Nano ZS (Malvern Instruments Inc., UK) as described in chapter 2, section 2.1.

5.4.2.2 High-performance liquid chromatography (HPLC) and analytical method validation for determination of CNB001 and curcumin

The encapsulation efficiency of CNB001 or curcumin in Solutol® HS 15 micelles and encapsulation efficiency of curcumin in Kolliphor® TPGS, was determined with HPLC using an Agilent 1260 infinity series HPLC (Agilent Technologies UK Ltd., UK), equipped with an ultrasensitive diode array UV detector, G1329A auto sampler and a highly efficient quaternary pump. For this study a new, rapid, sensitive, precise and accurate method was developed, which gave reproducible results and chromatograms with sharp peaks and a stable baseline.

10 µL curcumin samples were eluted with the mobile phase comprising of 50:50 0.1% trifluoroacetic acid in HPLC grade water: HPLC grade acetonitrile at a flow rate of 1 mL/min using an isocratic elution method. Separation was performed using a Phenomenex 250 mm×4.6 mm, 4 µm Synergi Polar-RP C18 column (Phenomenex Inc., Cheshire, UK) with a UV detection wavelength of 420 nm, using a column compartment temperature of 40°C.

For CNB001, 10 µL samples were eluted with the mobile phase comprising of 40:60 0.1% trifluoroacetic acid in HPLC grade water: HPLC grade acetonitrile at a flow rate of 1 mL/min using an isocratic elution method. Separation was performed using a Phenomenex 250 mm×4.6 mm, 4 µm Synergi Polar-RP C18 column (Phenomenex Inc., Cheshire, UK) with a UV detection wavelength of 326 nm, using a column compartment temperature of 40°C.

The HPLC method developed for curcumin and CNB001 was validated for linearity, accuracy and precision; to ascertain that the method adapted was robust and without error. The validation method based on ICH recommendations is described in Chapter 2 for HPLC analytical validation, section 2.7.

A standard curve (calibration curve) was constructed individually for curcumin and CNB001 before each sample analysis in triplicate using the same method of HPLC analysis as that intended for the formulations. Concentrations of the standard tested were 1.0-50 µg/mL for curcumin and 1.25-30 µg/mL for CNB001, and peak area as an average of the triplicates was used to derive the standard equation and correlation coefficient (R^2) of the line of best fit by least square regression method. The equation was then considered linear if the R^2 value was approximately 1 and used for calculation of concentration of curcumin or CNB001 encapsulated in the micelles.

5.4.2.3 Determination of drug encapsulation efficiency of the micellar formulations

Encapsulation efficiency of the formulations after preparation was determined using HPLC to quantify curcumin or CNB001 solubilized in the micellar formulations. Dilutions of the formulation following removal of unsolubilized drugs by filtration (0.22 μm mixed cellulose esters syringe-driven filter (Millex MP, Ireland)) was performed by diluting approximately 50 times in methanol to obtain a solution concentration appropriate for HPLC measurement as per the Beer-Lambert law. The solutions were filtered into HPLC vials and quantified as described (section 5.4.2.2). The peak areas for curcumin or CNB001 from the formulations were used for calculation of the encapsulation efficiency of drug using linear regression equations from calibration curve with correlation coefficients of 0.9999 and 1.0000 for curcumin and CNB001 respectively. Encapsulation efficiency was expressed as a percentage using equation 5.1:

$$Encapsulation\ efficiency(\%) = \frac{Practically\ determined\ amount\ of\ drug\ \ in\ formulation}{Amount\ of\ drug\ initially\ weighed} \times 100$$

Equation 5.1

5.4.2.4 Laser diffraction aerosol droplet size analysis

Nasal spray droplet measurement size was performed by laser diffraction studies using a Malvern Spraytec® (Malvern Instruments Inc., UK) with RT Sizer software in an open bench configuration. The Nasal™ Mucosal Atomization Device (Nasal™ MAD) was used as it has the capability to aerosolize medicament to the posterior mucosal surfaces of the nose and hence target the brain. The method employed was modified from earlier studies to suit the Spratyec®, device and nano-formulations under study, as this combination has not been studied before [463,464]. Prior to measurement initiation, the device was primed by firing 3 actuations to waste. 0.4 mL of nano-formulations were withdrawn into a 1 mL syringe and leur-locked onto the atomization spray plug of the device (Figure 1.7). This was then mounted at a 3 cm distance from the laser beam (He-Ne Laser, 632.8nm) at an angle of 45° to allow firing in an upward self-administration fashion. Droplet size distribution was studied at 25°C by laser diffracted using 6 actuations per formulation and plotted as a volume weighted average distribution from which Dv10, Dv50 and Dv90 (10%, 50% and 90% of the cumulative volume undersize) were calculated. Span was calculated using equation 5.2:

$$\text{Span} = \frac{Dv90 - Dv10}{Dv50}$$

Equation 5.2

To ascertain the effect of aerosolization on the size of micelles incorporating drug, change in particle size using laser diffraction studies on the Malvern Zetasizer was studied before and after the formulation was aerosolized using the Nasal™ MAD in to glass vials.

5.4.2.5 *In vitro* drug release from micelles

The release of curcumin from the Solutol® HS 15 or Kolliphor® TPGS micelles and CNB001 from the Solutol® HS 15 micelles was determined using Franz diffusion cells (PermeGear, PA,

USA) with a surface area of 0.64 cm^2 and a receptor chamber volume of 5 mL mounted with mixed cellulose acetate/cellulose nitrate membrane (Merck Millipore, England, UK). The receptor compartment was filled with simulated nasal electrolyte fluid at pH 6.5 containing potassium, calcium and sodium at biological human nasal fluid concentrations [465]. 2% SDS was added to obtain 'sink conditions' to enhance the solubility of the hydrophobic curcumin or CNB001 released from the micelles into dissolution medium. 250 µL of micelles were placed in the donor compartment and drug release was studied at 37 °C under magnetic stirring at 300 rpm. At predetermined time points (0, 1, 2, 4, 6, 8, 10, 12, 24, 30, 36 h), 200 µL aliquots was taken from the receptor arm and replaced with an equivalent amount of fresh release medium. The aliquots were assayed for the drug using HPLC and studies were replicated four times to obtain the drug release plots of cumulative release with respect to time as a mean ± SD.
The kinetics of drug release from the polymeric micelles was studied by fitting the data to the following mathematical models.

Zero-order model: This model assumes that drug release from the nano-formulations is independent of concentration or time, and hence follows a steady state kinetics [466–468], described by equation 5.3:

$$Q_t = k_o \times t \qquad \textbf{Equation 5.3}$$

where Q_t is the cumulative amount of drug released (%) at time t and K_0 is the zero-order rate constant of drug release expressed in units of concentration/time. A plot of cumulative drug release (%) versus time was plotted and the regression coefficient was calculated.

First-order model: This model assumes that drug release from the nano-formulations is dependent on the initial concentration of drug present and time, and hence follows an exponential reduction within the system [466–468], described by equation 5.4:

$$Ln\left(\frac{100 - Qt}{100}\right) = k_1 \times t \qquad \textbf{Equation 5.4}$$

where K_1 is the first-order rate constant at time t. A plot of log cumulative drug remaining (%) versus time was plotted and the regression coefficient was calculated.

5.4.2.6 *In vitro* cytotoxicity studies for neuroprotective and cancer formulations

Cytotoxicity of CNB001 and curcumin when encapsulated within Solutol® HS 15 micelles was determined to ascertain the maximum non-toxic concentration (MNTC) of the respective formulations after 24 and 48 h incubation, using the sulforhodamine B (SRB) assay [469]. The MNTC or the maximum tolerable dose i.e. the Ec80 is the maximum dose at which the encapsulated neuroprotective molecules would show neuroprotection without false negative outcomes of toxicity (since the cell line used is a neuroblastoma cell line SH-SY5Y and curcumin or CNB001 also possess cancer activity).

Further, cytotoxicity of curcumin encapsulated within Kolliphor® TPGS micelles was determined to ascertain the Ic50 i.e. drug concentration at which 50% cell death was evident using the 3-(4,5-dimethylthiazol-2-yl)-2,5-diphenyltetrazolium bromide (MTT) assay. Since the Kolliphor® TPGS formulations incorporating curcumin were intended to be targeted to the mitochondria, MTT assay would be appropriate as it directly reads the mitochondrial dehydrogenase activity.

SH-SY5Y cells: Complete media composition for SH-SY5Y cells was basal medium 1:1 MEM: Ham's F-12 supplemented with 10% FBS, 1% penicillin-streptomycin, 1% non-essential amino acids and 1% L-glutamine. For both the SRB and MTT assay, dopaminergic like human neuroblastoma SH-SY5Y cells were seeded at a density of $1x10^5$ cells in 96-well plates and cultured till 80 % confluency for 48 h at 37°C, 5% CO_2. The media was then replaced with the different serially diluted treatments in complete media (curcumin and CNB001 dissolved in 0.1% DMSO in complete media) with 0.1% DMSO in complete media as a blank, and further incubated for 24 and 48 h.

A549 cells: For studying the anticancer activity of the formulations, the human lung adenocarcinoma cell line A549 was used (to validate the anticancer activity and hence effectiveness of the formulations on more than one cell line). Complete media composition for A549 cells was basal medium RPMI-1640 supplemented with 10% FBS, 1% penicillin-streptomycin and 1% L-glutamine. A549 cells were seeded at a density of $1.25x10^5$ cells in 96-well plates and cultured till 80% confluency for 24 h. The media was then replaced with the different serially diluted treatments in complete media (curcumin dissolved in 0.1% DMSO in complete media) with 0.1% DMSO in complete media as a blank, and further incubated for 48 h.

For the SRB assay (neuroprotection), at the end of the incubated period, cell fixation was carried out by addition of 50 µL of 40% trichloroacetic acid to each well supernatant for 1 h at 4°C. The plates were then washed with deionized water four times and were allowed to air-dry at 25 °C overnight. Cell staining was carried out by addition of 100 µL of 0.057% of SRB solution and left at room temperature for 1 h. The plates were washed with 1% acetic acid solution to remove the unstained SRB reagent four times and allowed to air-dry. 200 µL of 10 mM Tris base (pH 10.5) was added to solubilize the protein bound SRB dye and optical density (OD) was measured by spectroscopy (SpectraMAX Plus 384, Molecular Devices, Berkshire, UK) at 510 nm after shaking the plates mechanically for 5 min.

For the MTT assay (cancer), at the end of the incubation period the treatments from all the wells were removed carefully and 50 µg/mL MTT solution (stock of 5 mg/mL MTT salt in PBS, pH 7.4) diluted in complete media was added to each well. After further incubation of 2 h in a humidified atmosphere (37°C, 5% CO_2), the medium was carefully removed and any formazan crystals generated were solubilized with 100 µL of DMSO. Thereafter, the OD was measured

using spectroscopy (SpectraMAX Plus 384, Molecular Devices, Berkshire, UK) at 570 nm after shaking the plates mechanically for 2 min.

The relative cell viability (%) was calculated using equation 5.5 as follows:

$$Cell\ viability\ (\%) = \frac{OD\ of\ test\ well}{OD\ of\ reference\ well} \times 100 \qquad \textbf{Equation 5.5}$$

The cell viability was presented as percentage of control cells and a dose-response curve of cell viability vs log (concentration) was plotted for accurate determination of Ec80/Ic50 for each treatment.

5.4.2.7 *In vitro* Parkinson's disease model development

Neurotoxin 6-hydroxydopamine-insulted dopaminergic-like human neuroblastoma SH-SY5Y cells have been shown to be a suitable experimental model to study *in vitro* Parkinson's disease (PD) in previous studies [470,471]. To determine the neuroprotection potential of CNB001 or curcumin encapsulated Solutol® HS 15 micelles, a PD model was developed.

SH-SY5Y cells were seeded at a density of $1x10^5$ cells in 96-well plates and cultured till 80% confluency for 48 h. Thereafter media was carefully removed and serially diluted neurotoxin 6-hydroxydopamine (stock prepared in PBS pH 7.4, 2 mg/mL, 11822 µM) in complete media was added to insult the neuroblastoma cells. After 24 h, cell viability at the different concentrations was determined using the SRB assay as in section 5.4.2.6 and the Ic50 of 6-hydroxydopamine insult, i.e. the concentration that reduced viability of cells to about 50% was determined by plotting a dose-response curve of cell viability versus log (concentration of neurotoxin). This concentration of neurotoxin 6-hydroxydopamine was used further for the neuroprotection assays.

5.4.2.8 Protective effects of Solutol® HS 15 micelles incorporating curcumin and CNB001 on *in vitro* PD model: Neuroprotection assay

SH-SY5Y cells were seeded at a density of $1x10^5$ cells in 96-well plates and cultured till 80% confluency for 48 h. Thereafter media was carefully removed and 100 µL of serially diluted micellar formulations below the maximum non-toxic concentration of the drugs, i.e. 18 µM of curcumin or CNB001, were added to the cells, taking into consideration the critical micellar concentration of the formulations. The cells were incubated at 37°C, 5% CO_2 for 2 h, after which the cells were insulted with 100 µL of 30 µM neurotoxin 6-hydroxydopamine (added on top of the formulations already present) for 24 h. Negative controls comprised cells only treated with formulations and not insulted with neurotoxin thereafter. The concentration of the formulations and neurotoxin was adjusted taking into consideration the final volume of the well on addition of all reagents. After 24 h, the SRB assay (section 5.4.2.6) was performed to determine the cell viability to ascertain the effect of formulations on protection of insulted neuroblastoma cells. Cell viability of cells insulted and/or treated was calculated as a percentage of the viability of control cells in the reference well.

5.4.2.9 Protective effects of Solutol® HS 15 micelles incorporating curcumin and CNB001 on *in vitro* PD model: ROS formation assay

For determination of cellular reactive oxygen species (ROS), a fluorescent-based assay was carried out in black plates and under dark conditions throughout. SH-SY5Y cells were seeded at a density of $1x10^5$ cells in 96-well plates and cultured till 80% confluency for 48 h. Thereafter media was carefully removed and 100 µL of serially diluted micellar formulations below the MNTC of the drugs, were added. The cells were incubated at 37°C, 5% CO_2 for 2 h, after which the cells were insulted with 100 µL of 30 µM neurotoxin 6-hydroxydopamine (added on top of the formulations already present) for 1 h. Thereafter, 50 µL of probe 10 µM 2,7-dichlorofluorescein diacetate (DCFH-DA) was added and the cells were further incubated. In the presence of an oxidant like ROS, DCFH-DA is taken up by the cells and is converted to a highly fluorescent molecule dichlorofluorescein which can be measured quantitatively on the fluorescence plate reader. A kinetic experiment was performed wherein ROS production was read at intervals of 4, 6, 8, 12, 16, 20 and 24 h, incubating the plates in the dark in between. At each time-point, fluorescence was measured spectrometrically on a fluorescence microplate reader (SpectraMAX Plus 384, Molecular Devices, Berkshire, UK) at excitation and emission wavelengths of 485 nm and 520 nm respectively. Each experiment was performed five independent times and results for the ROS production on treatments were expressed as:

$$\text{ROS production}(\%) = \frac{[\text{FD of treated \& insulted cells} - (\text{FD of treated cells} + \text{FD of CM})] - \text{FD of reference well}}{\text{FD of reference well}} \times 100$$

Equation 5.6

where CM is complete media and FD is fluorescence density.

The FD of treated cells without insult was taken into consideration as curcumin is a naturally fluorescent molecule and hence would result in false negative results due to the higher intensity contributed by the innate fluorescence of curcumin. FD of complete media was considered so as to eliminate any interaction in fluorescence intensity from the media.

The FD of insulted cells without treatment was expressed as:

$$\text{ROS production } (\%) = \frac{[\text{FD of insulted cells} - \text{FD of CM}] - [\text{FD of reference well}]}{\text{FD of reference well}} \times 100$$

Equation 5.7

5.4.2.10 Nuclear staining for assessment of apoptosis: Hoechst staining

The nuclear morphology of the apoptotic cells was investigated by staining with chromatin-specific dye; Hoechst 33258.The SH-SY5Y cells were seeded on Nunc™ Lab-Tek™ II Chamber Slides™ (ThermoFisher Scientific, Paisley, UK) and cultured till 80% confluency for 24 h at

37°C, 5% CO_2. The media was then replaced with 18 µM of the neuroprotective drugs or drugs encapsulated in Solutol® HS 15 micelles and incubated for 2 h. These treated cells were then insulted by addition of 30 µM of neurotoxin 6-hydroxydopamine (added on top of the formulations already present) for 24 h. The media was removed after 24 h and the cells were fixed for 10 min with 4% paraformaldehyde in PBS at room temperature. The cells where then rinsed with PBS, pH 7.4 three times and subsequently stained with 10 µg/mL Hoechst 33258 in PBS, pH 7.4 for 10 min at 37°C. The stain was rinsed off with PBS three times and the mounted slides were visualized under EVOS™ Fluorescence Cell Imaging System using the DAPI filter (360 nm excitation, 447 nm emission) under 20X magnification and phase contrast annuli 4/10 condenser. To semi-quantify the fluorescence intensity of cells to distinguish between apoptotic cells and non-apoptotic cells, image processing program ImageJ v1.48 (National Institute of Health, USA) was used.

5.5 Results and Discussion

5.5.1 Formulation characterization

5.5.1.1 High-performance liquid chromatography (HPLC) and analytical method validation for determination of CNB001 and curcumin

Linearity: The data for HPLC calibration curves of curcumin and CNB001 fitted into the linear equations *y=60.117x–4.3765* and *y=73.653x-10.2370* respectively (where x=concentration of analyte and y=area under curve) and being in the concentration range under study i.e. 1.0-50 µg/mL and 1.25-30 µg/mL for curcumin and CNB001 respectively, as shown in Figure 5.4 and Figure 5.5. A regression analysis was performed and correlation coefficient R^2 of 0.9999 and 1.00 (for curcumin and CNB001 respectively) indicated linear relationship between peak area and concentration of drug analyzed.

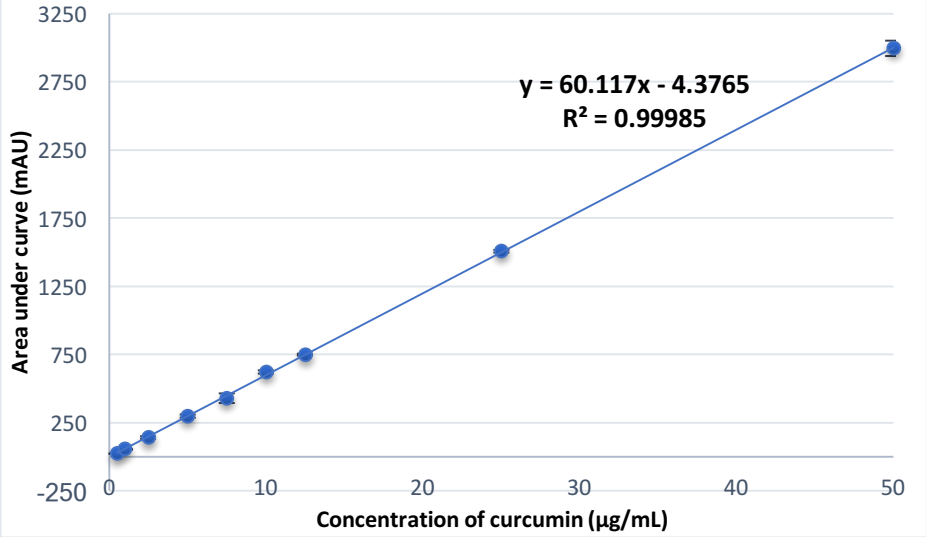

Figure 5.4: Calibration curve of curcumin analyzed by HPLC (n=5, mean ± SD)

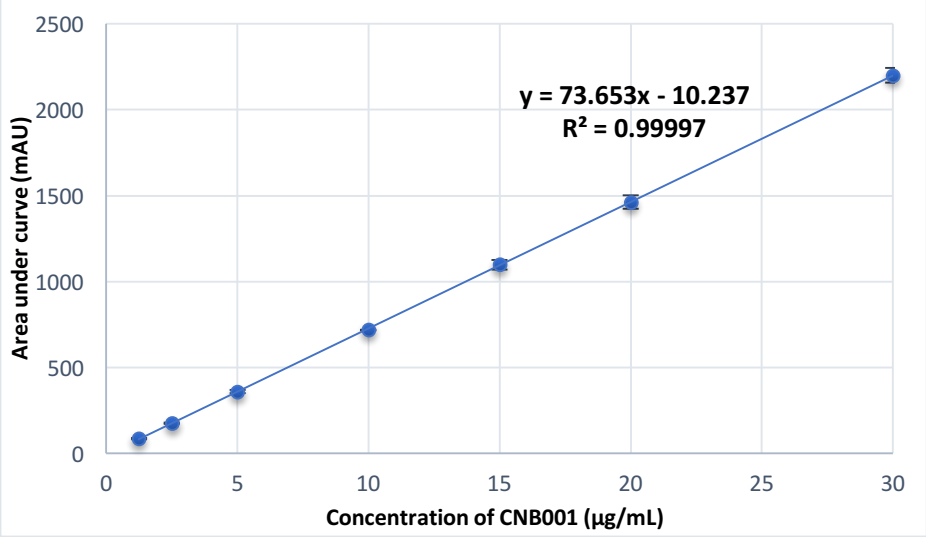

Figure 5.5: Calibration curve of CNB001 analyzed by HPLC (n=5, mean ± SD)

Parameters determining linearity from HPLC analysis are shown in Table 5.4.

Table 5.4: Linearity parameters for HPLC analysis method of curcumin and CNB001

Parameters	Results (Curcumin)	Results (CNB001)
λmax	420	326
Linearity range	1.0-50 µg/mL	1.25-30 µg/mL
Regression equation	*y=60.117x–4.3765*	*y=73.653x-10.2370*
Correlation coefficient	0.9999	1.00
Retention time	10.49 min	7.25 min
Limit of detection (LOD)	0.27 µg/mL	0.11 µg/mL
Limit of quantification (LOQ)	0.89 µg/mL	0.38 µg/mL

Representative chromatograms of curcumin and CNB001, and validation for accuracy and precision of HPLC method is as seen in Appendix 1, A1.3

5.5.1.2 Solutol® HS 15 micelles incorporating curcumin or CNB001

5.5.1.2.1 Morphology investigation and particle size analysis

Solutol® HS 15 micelles, with and without cholesterol, incorporating curcumin/CNB001 were formed within the size range of 15-100 nm (Figure 5.6). The size of CNB001 or curcumin encapsulated Solutol® HS 15 micelles without cholesterol were in good correlation with the size of Solutol® HS 15 micelles developed in previous studies [472,473].

With an increase in cholesterol content in the Solutol® HS 15 micelles there was an increase in mean size as evident by the intensity size distribution Z-average seen in Figure 5.6.

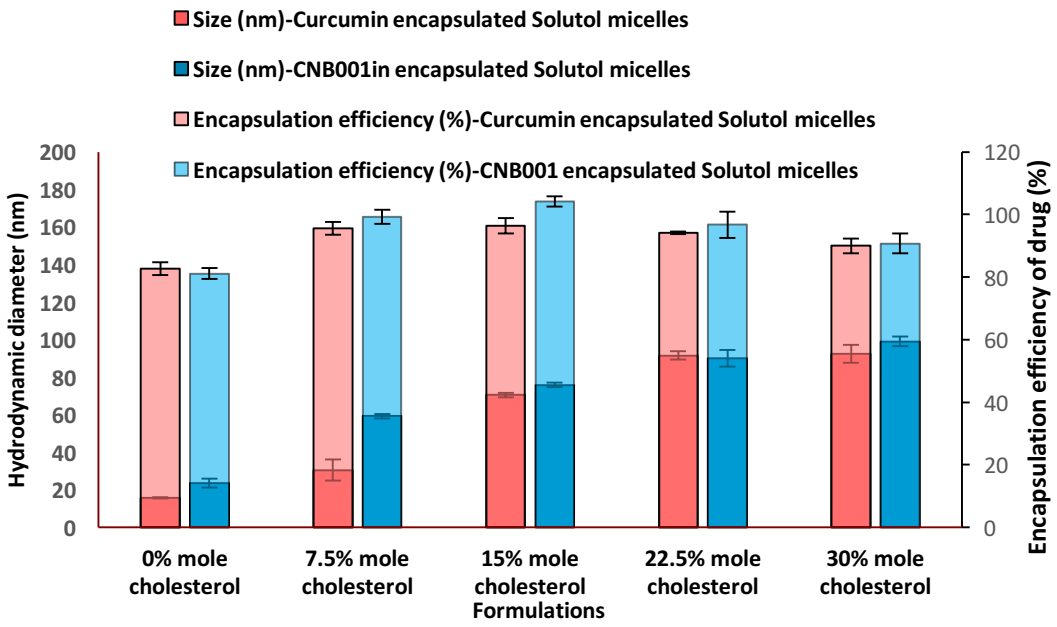

Figure 5.6: Size and encapsulation efficiency for the Solutol® HS 15 micelles with varying concentrations of cholesterol prepared by thin-film hydration, at a concentration of 2.5 mg/mL polymer. (n=3, mean ± SD)

The structure and physical properties of a non-ionic surfactant vesicles has been shown to be influenced by addition of cholesterol, as these can form niosomes i.e. bilayered vesicles as

opposed to micelles [474]. It modulates their fluidity, rigidity, mechanical strength and cohesion, consequently their permeability to water [474]. At a particular molar ratio of cholesterol: non-ionic surfactant micelles start to convert into niosomes However, preparation of niosomes requires higher amount of cholesterol relative to non-ionic surfactant as previously reported to be 1:1-1:2 molar ratio surfactant: cholesterol [475–477].

Addition of cholesterol in general, has resulted in an increased encapsulation efficiency of primaquine phosphate and pregabalin in Span 60 vesicles due to hydrogen bond interactions as seen in Figure 5.7 [474,478]. Similarities in structure of Span 60 with Solutol® HS 15 suggests that cholesterol could stabilize the micelles and improve the encapsulation of neuroprotective molecules by forming hydrogen bond interactions with the oxoethylene bridge of Solutol® HS 15.

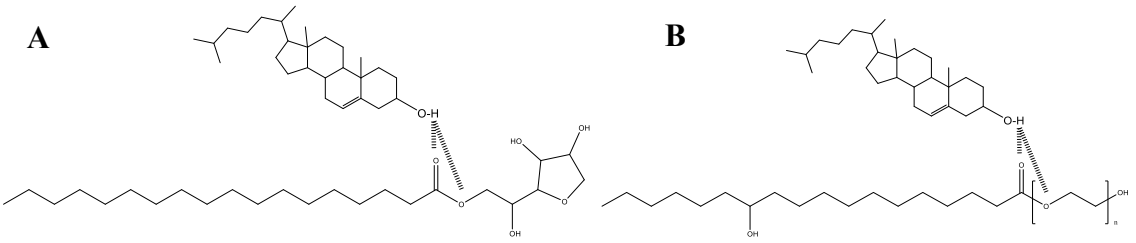

Figure 5.7: Structural interaction between cholesterol and oxoethylene bridge of (A) Span 60, (B) Solutol® HS 15

As HLB of surfactant increases above 10, cholesterol is required to stabilize the micelles by interactions with the larger head groups [474,479]. Brij et al. studied the effect of presence of cholesterol on the stability of non-ionic surfactants incorporating insulin with varied HLB 4.9-16.9 [479]. Vesicles with higher HLB values 15.7 and 16.9 could not spontaneously form without cholesterol due to a mismatch between the volume of hydrophilic and hydrophobic chains [479]. Addition of cholesterol to higher HLB vesicles prepared by thin film hydration method showed a better encapsulation of insulin and stability. Moreover, there was no significant increase in entrapment of drug with increasing cholesterol prepared with lower HLB (4.9 and 5.3) non-ionic surfactants. Since, the HLB of Solutol® HS 15 is 15.2, cholesterol was added to improve the stability of the micelles and study the effect of increasing molar concentration of cholesterol on encapsulation of hydrophobic drugs curcumin and CNB001.

TEM images were studied to evaluate the morphology of the micelles, and to gain a better understanding into the vesicle system generated on addition of cholesterol. For the Solutol® HS 15 micelles without cholesterol incorporating curcumin or CNB001, the micelles were spherical, well dispersed and size was in good correlation to the peak of hydrodynamic diameter obtained using the DLS of around 16-18 nm as seen in Figure 5.8 and Figure 5.9.

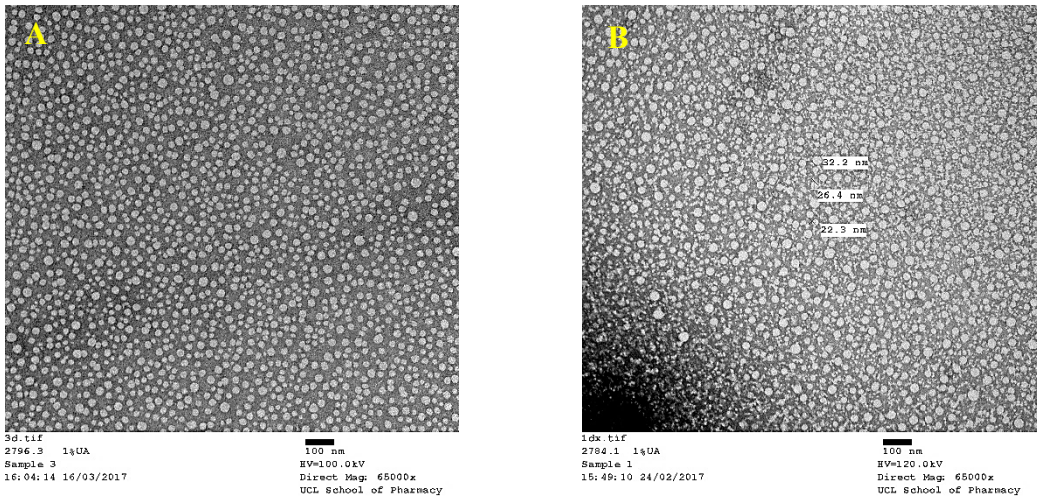

Figure 5.8: TEM images of curcumin encapsulated Solutol® HS 15 micelles cholesterol (A) and CNB001 encapsulated Solutol® HS 15 micelles without cholesterol (B)

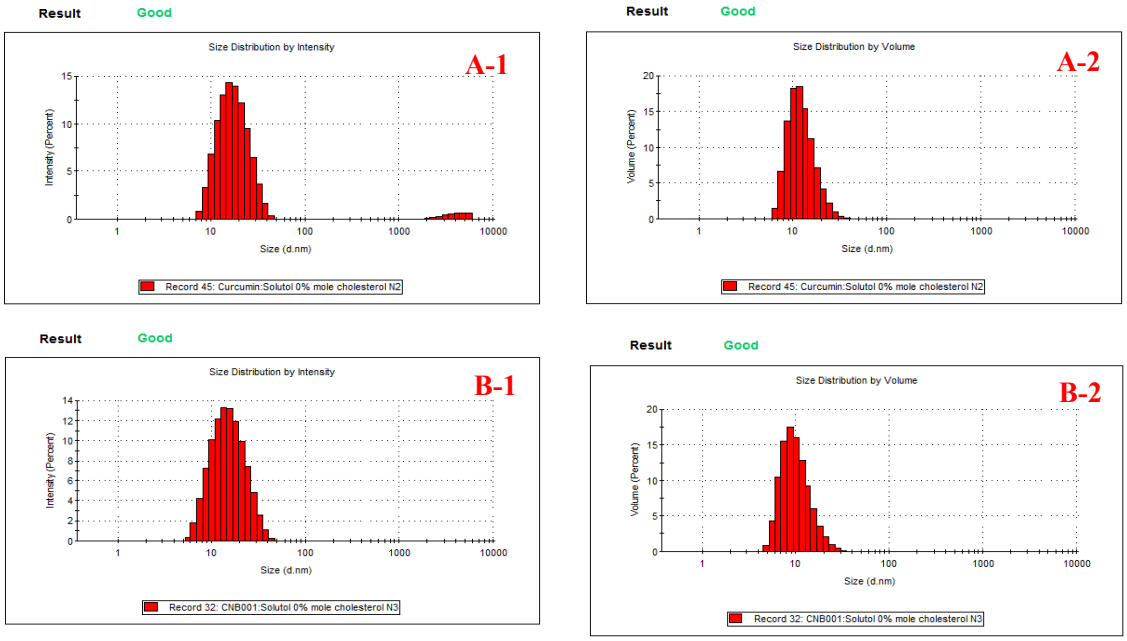

Figure 5.9: Size distribution by intensity (1) and volume (2), of Solutol® HS 15 micelles without cholesterol incorporating (A) curcumin and (B) CNB001

For the Solutol® HS 15 micelles with 15% mole cholesterol incorporating neuroprotective drugs curcumin and CNB001, the micelles were spherical and well dispersed (Figure 5.10). Size distribution by intensity as analyzed by the DLS shows the presence of 2 peaks at around 110-140 and 15-23 nm (Figure 5.11A-1 and Figure 5.11B-1). Two-sized vesicles with a similar size can also be seen in the TEM images (Figure 5.10). Addition of cholesterol to non-ionic surfactants has been proposed to prepare niosomes, i.e. bilayered vesicles that have greater particle size and stability like liposomes, but are low cost and easy to prepare [476]. Niosomes incorporating curcumin were prepared by addition of cholesterol at a 50% molar concentration to Tween 20 (HLB=16.7) [476]. The size of the niosomes were around 100 nm as measured by DLS and

showed improved stability to temperature due to hydrogen bond interactions between the oxoethylene units on the Tween-20 headgroup and the curcumin hydroxyl groups [476].

Intensity distribution measurement by DLS is naturally weighted as per the scattering of each particle and hence larger particle species can dominate the distribution profile in the presence of smaller particle species. Thus, conversion of intensity distribution that describes the scattering capability of the species to volume distribution describing the volume of each species was undertaken. Size distribution by volume (Figure 5.11A-2 and Figure 5.11B-2) shows that smaller particles around 14-20 nm dominated (85%) the volume distribution histogram which was in good correlation with the sizes observed on the TEM. The larger particles around 100 nm were likely bilayered vesicles niosomes that were present in lower amount (volume) compared to the micelles, since the maximum amount of cholesterol relative to the non-ionic surfactant was 30% mole. As previously mentioned, preparation of niosomes requires higher amount of cholesterol relative to non-ionic surfactant as previously reported to be 1:1-1:2 molar ratio surfactant: cholesterol [475–477].

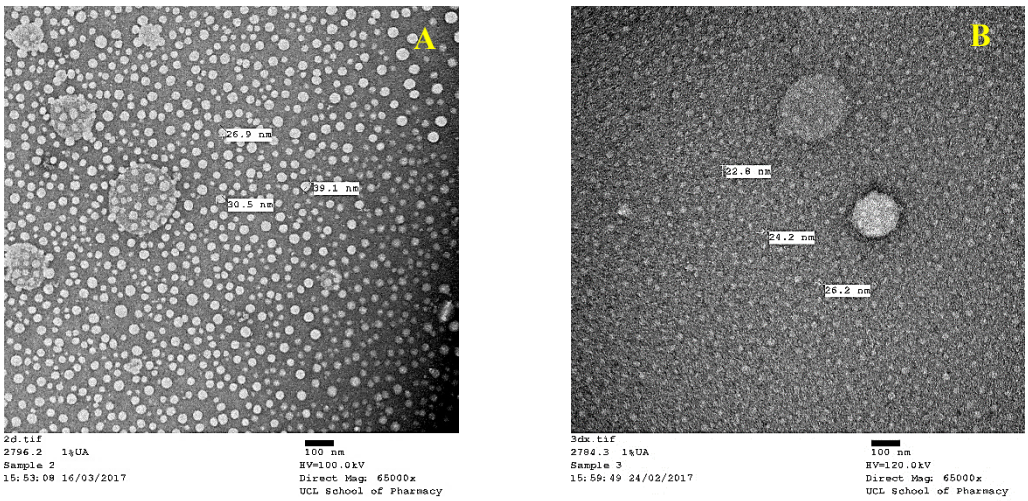

Figure 5.10: TEM images Solutol® HS 15 micelles with 15% mole cholesterol incorporating curcumin (A) and CNB001 (B)

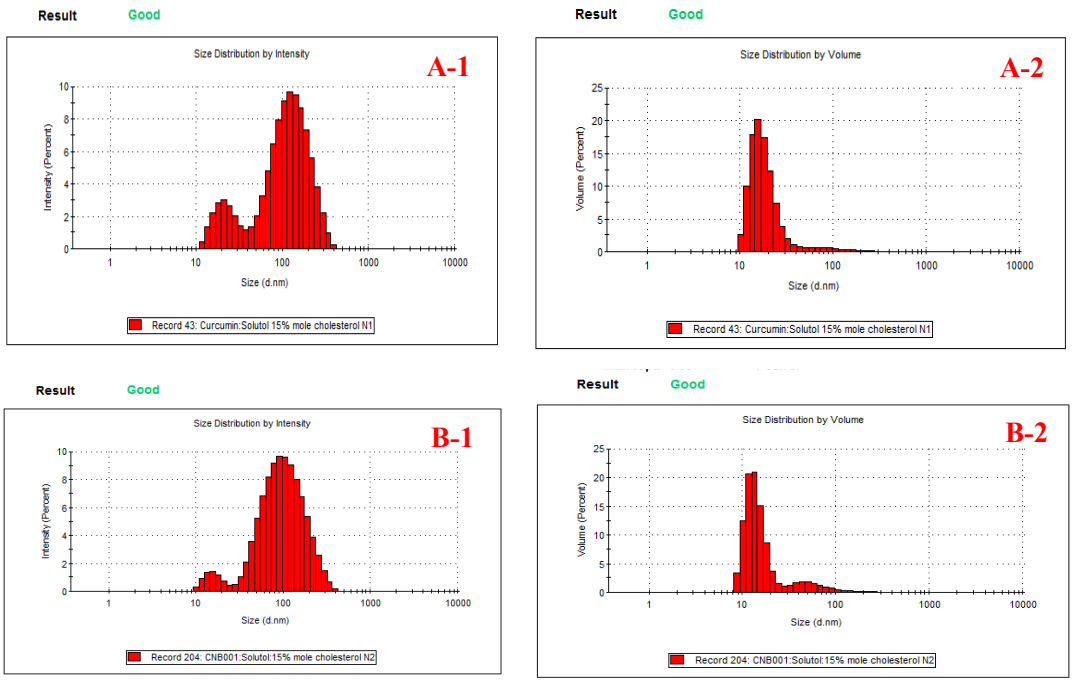

Figure 5.11: Size distribution by intensity (1) and volume (2), of Solutol® HS 15 micelles with 15% mole cholesterol incorporating (A) curcumin and (B) CNB001

For the Solutol® HS 15 micelles with 30% mole cholesterol incorporating CNB001, the micelles were spherical and well dispersed as seen in Figure 5.12. Size distribution by intensity as analyzed by the DLS shows the presence of 2 peaks at around 140-170 and 19-25 nm (Figure 5.13A-1 and Figure 5.13B-1). Two-sized vesicles with a similar size can also be seen in the TEM images. Size distribution by volume (Figure 5.13A-2 and Figure 5.13B-2) exhibited that smaller particles around 16-22 nm dominated (90%) the volume distribution histogram which was in good correlation with the sizes observed on the TEM.

Hence, Solutol® HS 15 incorporating curcumin or CNB001, in the presence of cholesterol produced two-sized vesicular systems dominated by micelles, as evident from the volume size distribution and TEM images, hence, the system will be referred to as micelles hereafter.

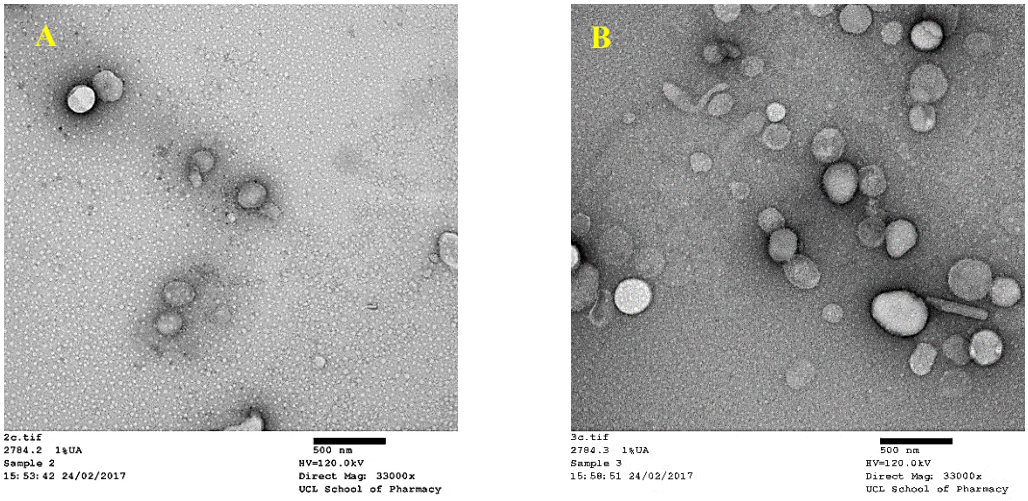

Figure 5.12: TEM images Solutol® HS 15 micelles with 30% mole cholesterol incorporating curcumin (A) and CNB001 (B)

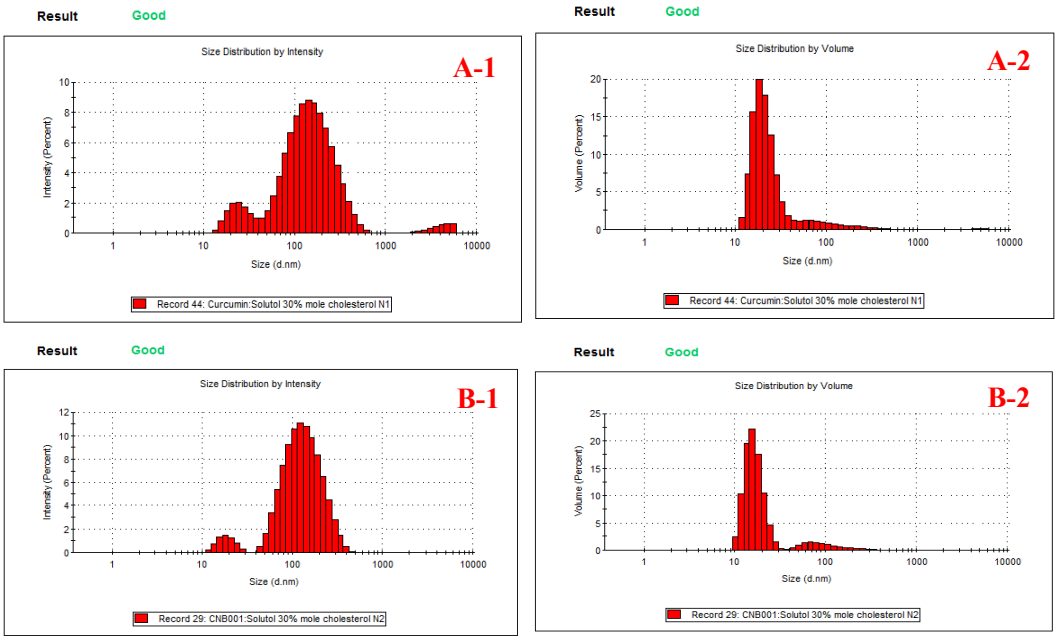

Figure 5.13: Size distribution by intensity (1) and volume (2), of Solutol® HS 15 micelles with 30% mole cholesterol encapsulating (A) curcumin and (B) CNB001

5.5.1.2.2 Curcumin or CNB001 encapsulation efficiency in Solutol® HS 15 micelles

An increase in encapsulation efficiency of CNB001 or curcumin was evident with increasing cholesterol, with maximum encapsulation for the Solutol® HS 15 micelles with 15% mole cholesterol, as seen in Figure 5.6. An encapsulation efficiency of around 80% was obtained for both curcumin and CNB001 in Solutol® HS 15 micelles without cholesterol. The addition of 15% mole cholesterol, improved the encapsulation to approximately 100% for curcumin and CNB001. This is likely due to the hydrogen bond interaction between the oxyethylene of Solutol® HS 15 and hydroxyl group of cholesterol. As previously demonstrated, non-ionic surfactants with higher HLB cannot spontaneously form stable vesicles, due to a mismatch between the hydrophilic and hydrophobic chains [479]. Incorporating cholesterol would improve the stability of the vesicles, however, stability studies would be helpful to give a better insight to this.

5.5.1.3 Kolliphor® TPGS micelles incorporating curcumin

5.5.1.3.1 Particle size analysis and zeta potential (surface charge)

Kolliphor® TPGS micelles, with and without dequalinium, incorporating curcumin were formed within the size range of 12.51-14.44 nm with no significant difference ($p > 0.05$) between the various formulations (Figure 5.14). This was in good correlation with the size of Kolliphor® TPGS micelles described in previous studies [480–482]. It was important to ensure that the targeting moiety dequalinium was incorporated into the Kolliphor® TPGS micellar layer rather than forming DQAsomes incorporating curcumin separately. The size distributions by intensity for curcumin encapsulated in Kolliphor® TPGS:30% mole dequalinium and Kolliphor® TPGS:0% mole dequalinium are seen in Figure 5.15A-1 and Figure 5.15B-1. Size distribution by volume

(Figure 5.15A-2 and Figure 5.15B-2) confirmed that 100% micelles were of size 8.91±0.57 nm for curcumin encapsulated in Kolliphor® TPGS:30% mole dequalinium. Curcumin encapsulated DQAsomes prepared by thin-film hydration have been studied in literature to have size ranging from 170-225 nm depending on the ratio of dequalinium and curcumin [462]. Since there was no peak evident in the size distribution data in this range, it is apparent that a mixed micellar structure contributed majorly by Kolliphor® TPGS, incorporating dequalinium was achieved.

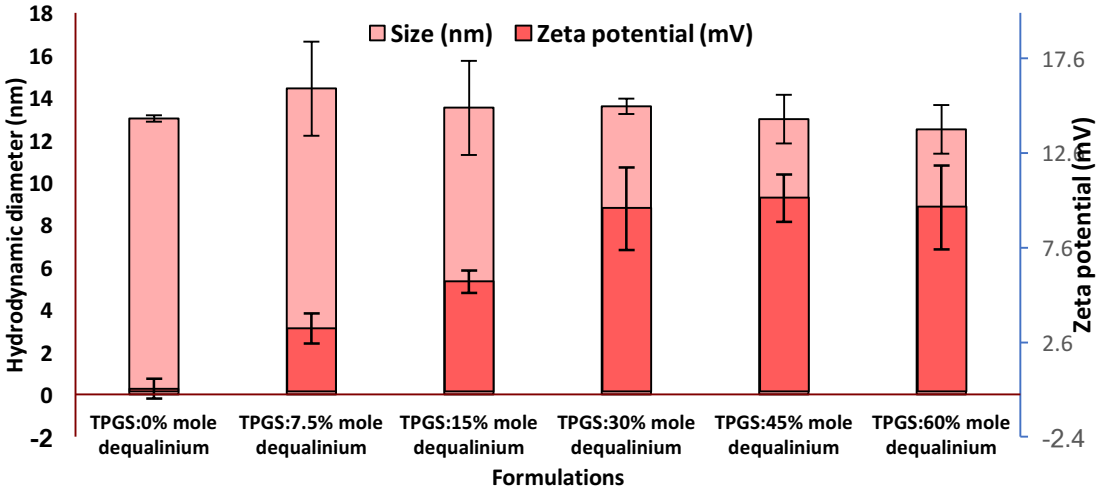

Figure 5.14: Mean hydrodynamic diameter and zeta potential for the non-targeted and targeted Kolliphor® TPGS micelles prepared by thin-film hydration, at a concentration of 2.5 mg/mL polymer. Data are mean ± SD (n=3)

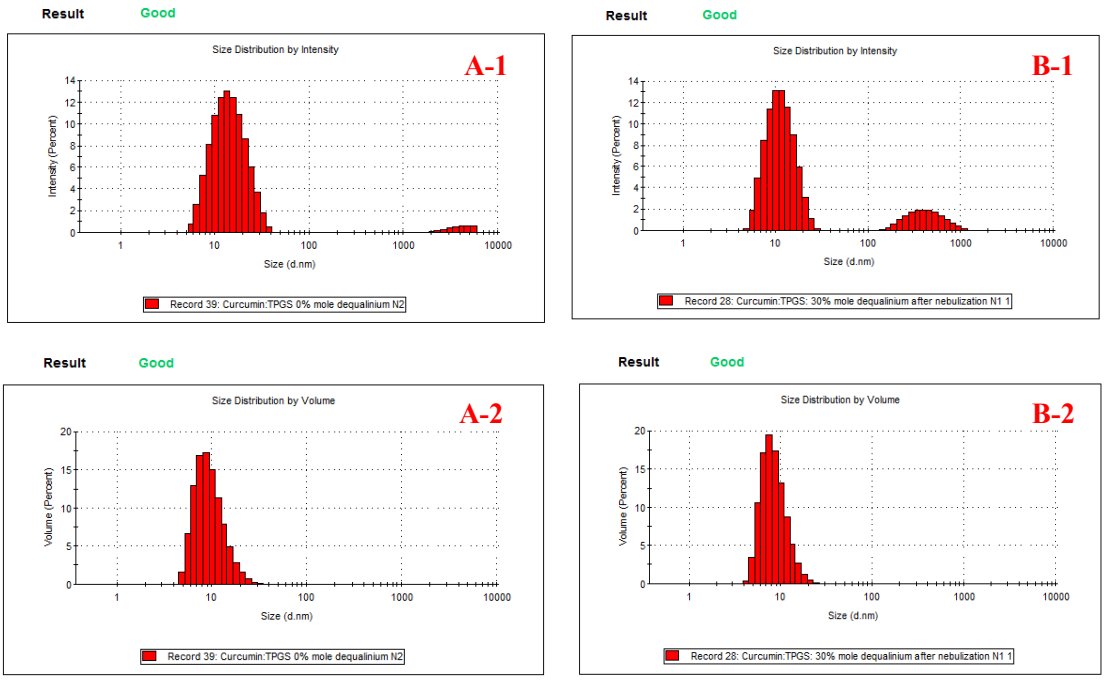

Figure 5.15: Size distribution by intensity (1) and volume (2), of Kolliphor® TPGS nanocarriers A) without dequalinium and B) with 30% mole dequalinium

Cationic peptide nanoparticles stable on intravenous administration reported in literature had a CMC value of 0.031 mg/mL (10.1 µM) [483]. Since, the CMC value of Kolliphor® TPGS has

been previously reported to be around 0.2 mg/mL (132.2 μM), it is unstable for intravenous injection, as the micelles can easily dissociate on excessive dilution in plasma [484]. There are several published reports on preparation of mixed micelles of Kolliphor® TPGS with lipids and polymers such as DSPE-PEG 2000, Pluronic® P105, Pluronic® P123 and Soluplus®, intended for intravenous administration [484–487]. However, administration of the curcumin encapsulated Kolliphor® TPGS micelles prepared in this study is proposed for nose-to-brain delivery for the treatment of glioma/neuroblastoma, hence these micelles should be relatively stable and not dissociate in the low volume nasal fluid.

The zeta potential is as reported in Figure 5.14. The surface charge was neutral for curcumin encapsulated Kolliphor® TPGS micelles without dequalinium. On addition of targeting moiety dequalinium there was a significant increase ($p < 0.05$) in positive charge up to 30% mole of dequalinium to Kolliphor® TPGS, after which addition of dequalinium did not result in any significant increase ($p > 0.05$) in zeta potential. This suggests that at a 30% mole dequalinium, the Kolliphor® TPGS micelles could no longer incorporate dequalinium into the structure and have reached a saturation point; hence any increase would have no more dequalinium incorporated and hence no further effect on the charge. The increase in positive charge was due to the presence of amine groups in the structure of dequalinium which was now incorporated within the neutral Kolliphor® TPGS micellar layer. Therefore, the formulation of curcumin encapsulated Kolliphor® TPGS:30% mole dequalinium was taken forward for further studies.

There was no significant difference evident ($p > 0.05$) in the mean polydispersity index of the various Kolliphor® TPGS micellar formulations, with and without dequalinium, which ranged from 0.24-0.28.

5.5.1.3.2 Curcumin encapsulation efficiency in Kolliphor® TPGS micelles

Kolliphor® TPGS micelles with and without dequalinium had a high encapsulation efficiency of around 100% (Figure 5.16). Compared with Kolliphor® TPGS micelles in previous studies, levels of 75-85% have been reported, depending on the drug encapsulated [480,481]. Nonetheless, the high encapsulation suggests a strong interaction between curcumin and the hydrophobic core of vitamin E within the Kolliphor® TPGS micelles. Furthermore, incorporation of targeting moiety dequalinium in the micellar structure did not significantly influence ($p > 0.05$) the drug loading. There was no change in mean size of the micelles, as seen in Figure 5.14, due to a similar amount of curcumin encapsulated within the micelles for each formulation.

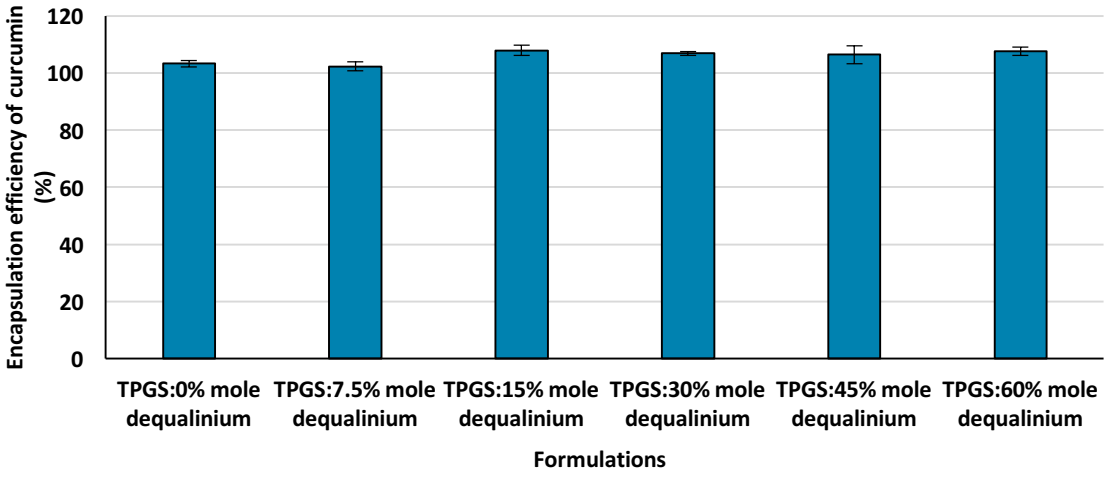

Figure 5.16: Encapsulation efficiency of curcumin in Kolliphor® TPGS micelles with increasing molar ratio of dequalinium. Data are mean±SD (n=3)

5.5.1.3.3 Transmission electron microscopy

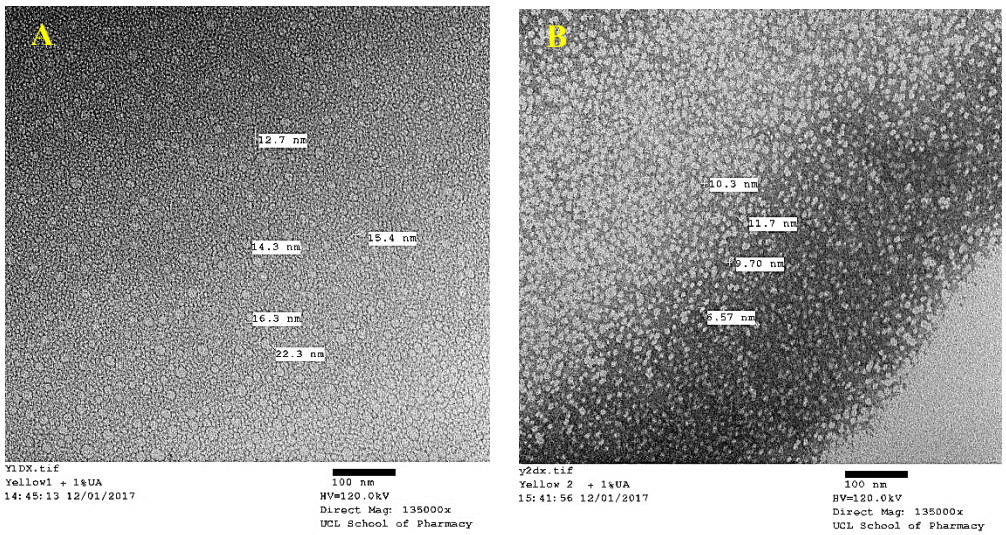

Figure 5.17: TEM images of curcumin encapsulated Kolliphor® TPGS micelles without dequalinium (A) and with 30% mole dequalinium (B)

TEM images for curcumin encapsulated Kolliphor® TPGS micelles is shown in Figure 5.17. Both formulations showed Kolliphor® TPGS micelles that were spherical, well dispersed and the sizes were in good correlation to the DLS results.

5.5.1.4 Laser diffraction aerosol droplet size analysis

The FDA requires the use of laser diffraction or cascade impactors for determination of droplet size distribution of nasal aerosols [128,464]. Formulation properties such as viscosity and surface tension, device design and actuation properties greatly affect the measured aerosol droplet size distribution [464]. Average weighted scatter graphs of time-history transmission (%) against time (h:m:s) was obtained by the software wherein 3 regions were allocated as shown in Figure 5.18. The time-history plots were studied from aerosol droplet formation to final aerosol dissipation where drastic fluctuations for laser transmission, Dv10 and Dv50 were evident in region 1 and 3

with a prominently stable region 2. Post-actuation of aerosol from the device, there was a fall in transmission evident due to rapidly rising aerosol droplet concentration known as the 'formation phase'. The 'fully developed phase' which followed had a stable droplet flow value and hence transmission, indicating stable aerosol particle size and concentration. Thus region 2 was chosen to study the droplet size distribution for comparative analysis, as recommended by the FDA. As the dose was delivered and the device was emptied droplet concentration and flow rate dropped to zero and laser transmission increased giving rise to the 'dissipation phase'.

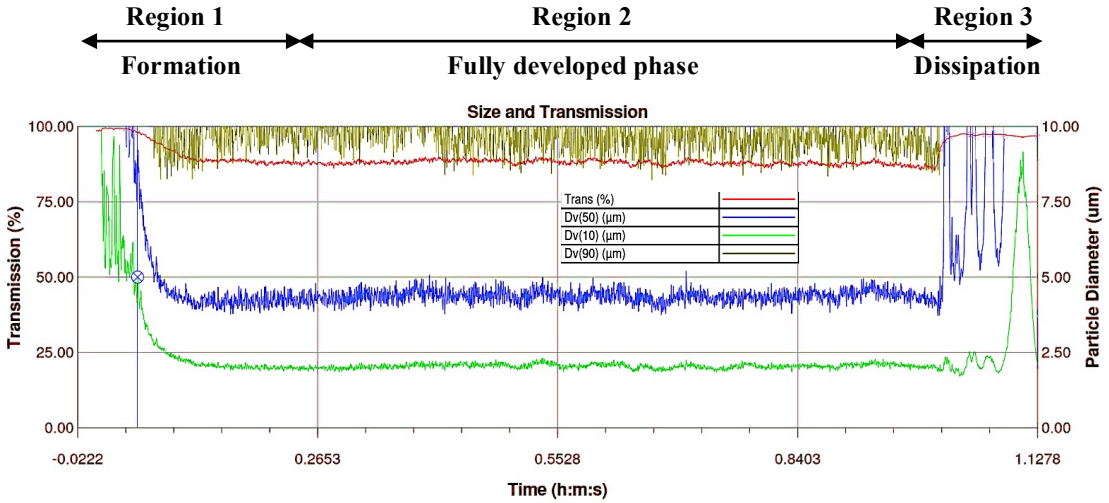

Figure 5.18: Time-history plots showing changes in transmission (%) and droplet size distribution i.e. Dv10, Dv50 and Dv90 (µm) on actuation with respect to time (h:m:s, ranging from 0-1.1278 min)

Aerosol droplet particle size distribution and volume particle diameter measured as Dv10, Dv50 and Dv90 by laser diffraction, measured in region 2, of the time-history plots of the Solutol® HS 15 and Kolliphor® TPGS micellar formulations, is shown in Figure 5.19.

Curcumin: Solutol® HS 15 formulations:

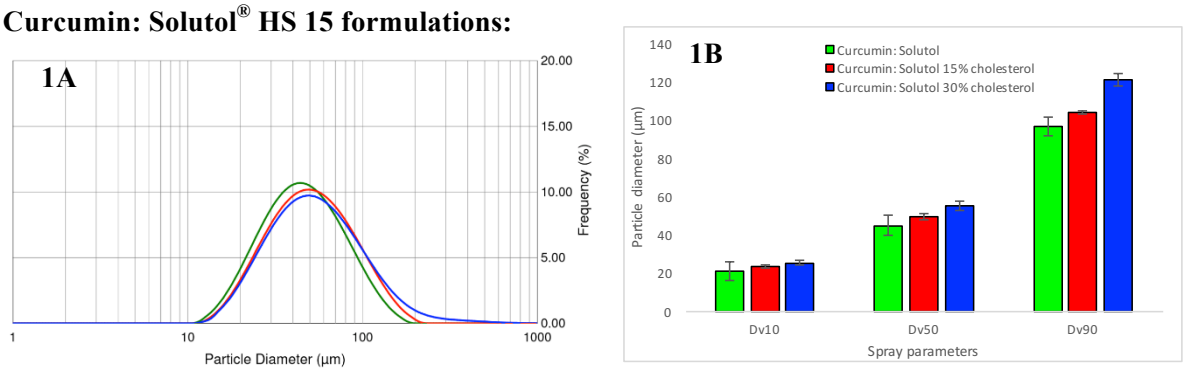

CNB001: Solutol® HS 15 formulations:

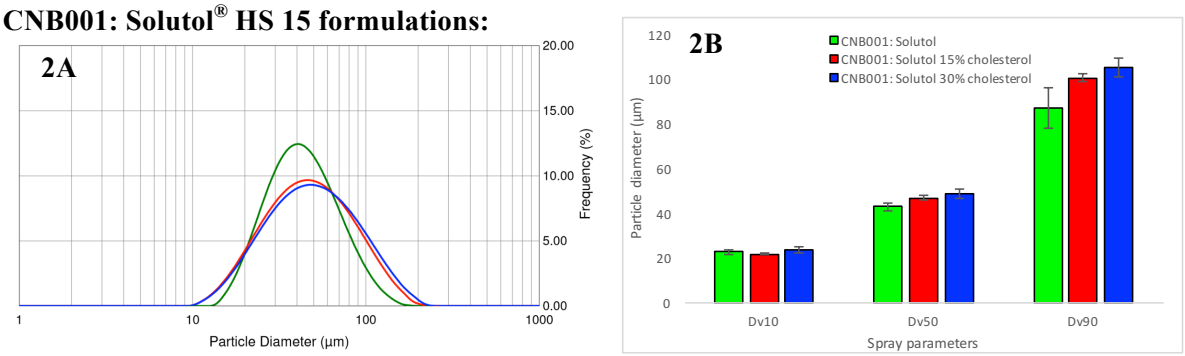

Curcumin: Kolliphor® TPGS formulations:

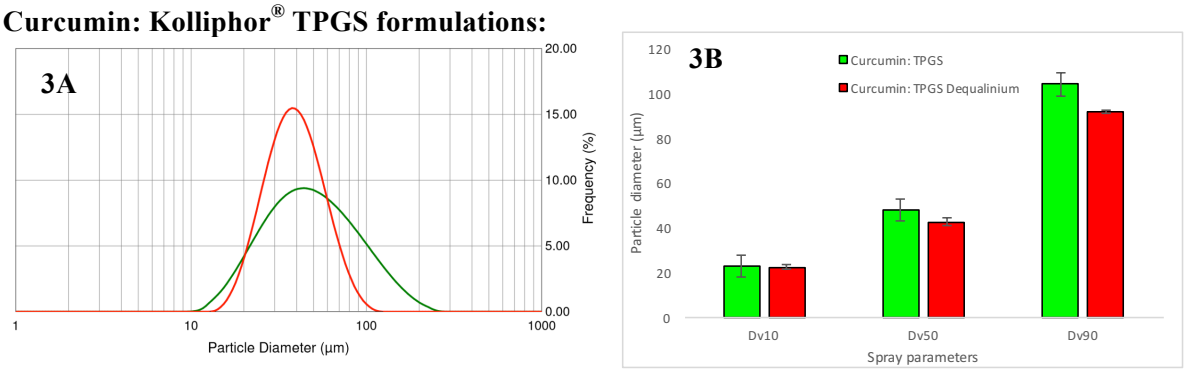

Figure 5.19: (A) Aerosol frequency particle size distribution (%) and (B) Particle diameter (µm) at 10, 50 and 90th percentile for the various micellar formulations as measured by laser diffraction on the Spraytec®, n=3, mean± SD

For efficient delivery to the posterior nasal tract a median particle size of 30-120 µm is considered appropriate [128]. Particle size greater than 120 µm have the tendency to deposit in the anterior nose. The Nasal™ MAD produces a broad aerosol spray of 30-100 µm droplet size which covers a wide mucosal area on delivery (http://www.lmaco.com/products/lma-mad-nasal). Formulation factors can affect the final spray parameters consequently affecting the deposition site and medicament efficiency, hence it was important to study the aerosol droplet size of the micelles especially since this device has not been investigated previously for delivery of nanocarrier formulations.

All the micellar formulations of Solutol® HS 15 and Kolliphor ® TPGS showed mean Dv50 between 42.75-54.86 µm. There was a significant increase ($p < 0.05$) in the Dv50 of formulations with increasing cholesterol content for curcumin encapsulated Solutol® HS 15 micelles from 44.86±1.27 µm (0% mole cholesterol) to 49.55±1.62 µm (15% mole cholesterol) and 54.86±2.46

µm (30% mole cholesterol). A similar significant increase ($p < 0.05$) was observed for CNB001 encapsulated Solutol® HS 15 micelles from 42.75±1.60 µm (0% mole cholesterol) to 46.82±0.83 µM (15% mole cholesterol) and 49.67±1.20 µm (30% mole cholesterol). With increased cholesterol content the distribution curve was skewed towards the larger particle size and hence a more prominent effect of addition of cholesterol on the 90th percentile particle size was seen (Figure 5.19).

FDA requires the measurement of Span as a measure of the quality of the aerosol generated, with smaller Span values representing narrow droplet size distribution [464]. Studies have shown that aerosols with the same droplet size but different Span have different deposition profiles [464]. With increasing concentration of cholesterol, there was an increase in the Span for Solutol® HS 15 micelles incorporating curcumin and CNB001. Curcumin encapsulated Solutol® HS 15 micelles showed Span values of 1.52±0.13 (0% mole cholesterol), 1.62±0.05 (15% mole cholesterol) and 1.75±0.18 (30% mole cholesterol). A similar trend was evident for CNB001 encapsulated Solutol® HS 15 micelles with Span values of 1.50±0.17 (0% mole cholesterol), 1.68±0.01 (15% mole cholesterol) and 1.70±0.08 (30% mole cholesterol). However, the difference was not significant at a level of 0.05 as analyzed by One-way ANOVA. The Span values for Kolliphor ® TPGS incorporating curcumin micelles with and without dequalinium were 1.70±0.11 and 1.63±0.16 respectively, however the difference was not significant ($p > 0.05$).

There was no significant difference ($p > 0.05$) in the size of the micelles before and after aerosolization (Figure 5.20), indicating that aerosolization using this device does not cause micellar rupture. Hence, due to favourable aerosol droplet size, Span and micellar stability; the Nasal™ Mucosal Atomization Device could be used to effectively deliver nanocarrier-based formulations to the posterior nasal tract for brain targeting.

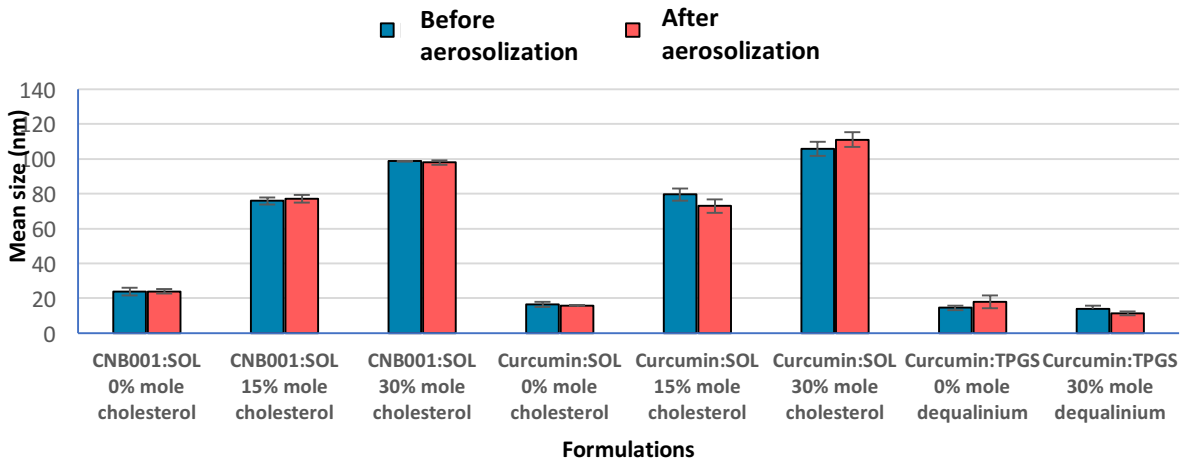

Figure 5.20: Mean hydrodynamic diameter for the micelles incorporating CNB001 or curcumin before and after spraying through the Nasal™ MAD, at a concentration of 2.5 mg/mL polymer, n=3, mean±SD

5.5.1.5 *In vitro* drug release

CNB001 and curcumin release from Solutol® HS 15 micelles is as shown in Figure 5.21. CNB001 exhibited release in a sustained manner over 36 h, whereas, curcumin was released in a burst

manner in the first 10 h and then a slower release for the remainder of the study up to 36 h. The log P values reported in literature for CNB001 and curcumin is 5.7 and 3.29 respectively; CNB001 being more hydrophobic than curcumin. Differences in the hydrophobicity of the drugs may affect their interactions with the hydrophobic micellar core and hence contribute to *in vitro* release profile differences. Increased hydrophobicity would result in increased interaction of the drug with the hydrophobic hydroxystearate chains of the Solutol® HS 15 micelles and hence a slower release profile as seen for CNB001 in comparison to curcumin.

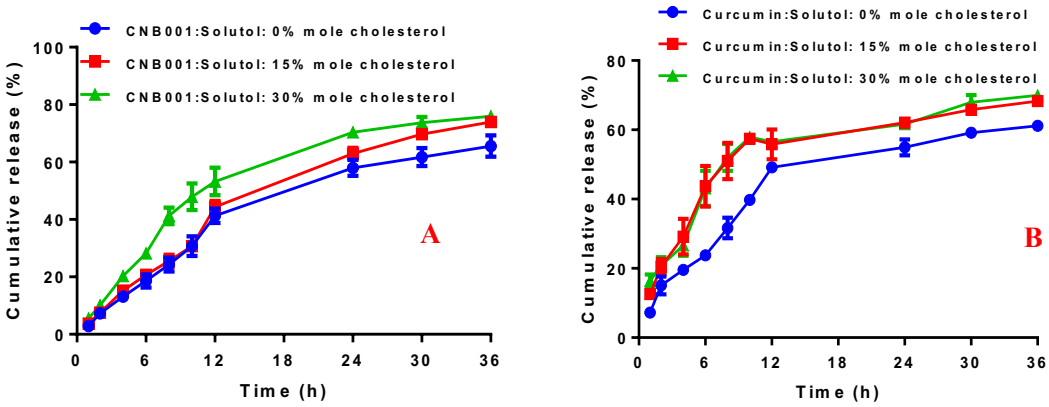

Figure 5.21: ***In vitro*** **cumulative drug release profiles of (A) CNB001 and (B) Curcumin from Solutol® HS 15 micelles into simulated nasal fluid (SNF), 2% SDS and 0.05% sodium azide from the various formulations. Data are mean ± SD (n=4)**

There was a significant increase ($p < 0.05$) in cumulative release of CNB001 with increase in mole % of cholesterol from 0% to 15% mole and 30% mole as analyzed by repeated measures ANOVA (rANOVA). Moreover, release profiles of curcumin from Solutol® HS 15 micelles showed a significant ($p < 0.05$, rANOVA) increase in cumulative release on addition of cholesterol up to 15% mole. However, there was no significant ($p > 0.05$, rANOVA) difference in release of curcumin when 30% mole cholesterol was added. Addition of cholesterol to non-ionic surfactant micelles/niosomes of different HLB values has been shown to alter micellar mechanical strength, permeability to water and hence drug release [474,488]. Hence, results suggest that with an increase in mole % of cholesterol in Solutol® HS 15 micelles there was an increase in drug release rate as compared to Solutol® HS 15 micelles without cholesterol due to alterations in drug-surfactant interactions on cholesterol incorporation. Increased hydrogen bonding between cholesterol hydroxyl groups and the Solutol® HS 15 oxoethylene bridge, may lead to possible reductions in available oxoethylene molecules to form hydrogen bonds with curcumin or CNB001, resulting in an increased cumulative drug release with respect to Solutol® HS 15 micelles without cholesterol.

Curcumin release from Kolliphor® TPGS micelles into simulated nasal fluid is shown in Figure 5.22. There was no significant difference ($p > 0.05$, rANOVA) between the release profile of curcumin from Kolliphor® TPGS micelles with or without dequalinium, wherein, a sustained release was evident for 48 h with approximately 40% curcumin being released. Drug release

profiles from Kolliphor® TPGS micelles are dependent on the log p and drug content due to differences in interaction with polymer core. Docetaxel (log p=2.83) has been shown to demonstrate significantly different release profiles on variation of the surfactant: drug content, with a slower drug release kinetics from 87% to 40% with reducing drug content due to stronger interaction of the drug with TPGS [480,481].

Moreover, release profiles of curcumin from Solutol® HS 15 (Figure 5.21B) and Kolliphor® TPGS (Figure 5.22) micelles were significantly different ($p < 0.05$, rANOVA). This may be attributed to the differences in the HLB values of the two polymers; 15.2 and 13 for Solutol® HS 15 and Kolliphor® TPGS respectively. With a decrease in HLB value of surfactants an increase in hydrophobicity is evident. Kolliphor® TPGS having a more hydrophobic core would seem to interact more strongly with hydrophobic drug curcumin and hence impedes its release.

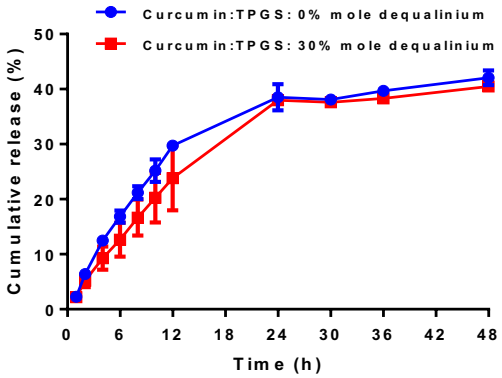

Figure 5.22: *In vitro* cumulative drug release profiles of curcumin from Kolliphor® TPGS micelles into simulated nasal fluid (SNF), 2% SDS and 0.05% sodium azide from the formulations with and without dequalinium. Data are mean ± SD (n=4)

Release kinetics of the drugs from the different surfactants were fitted into various kinetic models and the regression coefficient R^2 used to ascertain the best fit model. These kinetic models are shown in Appendix 3 and the calculated R^2 are shown in Table 5.5.

For CNB001 release from Solutol® HS 15 micelles with 0% mole cholesterol and 15% mole cholesterol, a regression coefficient for first-order kinetics was lower than that of zero-order kinetics indicating that CNB001 release was independent of CNB001 concentration. However, with increase in cholesterol to 30% mole of Solutol® HS 15 first-order release kinetics of CNB001 was evident wherein release was dependent on the concentration of CNB001. These differences were likely to be due to the varied interactions of the drug with the surfactant on addition of cholesterol.

For curcumin release from Solutol® HS 15 micelles with 0% mole cholesterol, a regression coefficient for first order kinetics was lower than that of zero order kinetics indicating that Curcumin release from Solutol® HS 15 micelles without cholesterol was independent of drug concentration, following a zero-order kinetics. However, with an increase in cholesterol to 15 and 30% mole of Solutol® HS 15 first-order release kinetics of curcumin was evident wherein release was dependent on the concentration of the drug. A similar drug release kinetics was evident for

Kolliphor® TPGS micelles with and without dequalinium incorporating curcumin, wherein release followed a first-order kinetics and hence was dependent on concentration of curcumin. This was in good correlation to the release of docetaxel from TPGS micelles, which followed a drug concentration-dependent first-order kinetics.

Table 5.5: Release kinetics of *in vitro* drug release from various polymers in simulated nasal fluid

Formulations	Zero order R^2	First order R^2
CNB001: Solutol® HS 15: 0% mole cholesterol:	0.9911	0.9738
CNB001: Solutol® HS 15: 15% mole cholesterol:	0.9843	0.9625
CNB001: Solutol® HS 15: 30% mole cholesterol:	0.9917	0.9937
Curcumin: Solutol® HS 15: 0% mole cholesterol:	0.9619	0.9478
Curcumin: Solutol® HS 15: 15% mole cholesterol:	0.9690	0.9708
Curcumin: Solutol® HS 15: 30% mole cholesterol:	0.9205	0.9631
Curcumin: Kolliphor® TPGS: 0% mole dequalinium	0.9915	0.9974
Curcumin: Kolliphor® TPGS: 30% mole dequalinium	0.9965	0.9989

5.5.2 *In vitro* cellular assays for anticancer activity

5.5.2.1 Assessment of cellular viability by MTT assay

MTT assay ((3-(4,5-dimethylthiazol-2-yl)-2,5-diphenyltetrazolium bromide) tetrazolium reduction assay) was used to study the Ic50, i.e. maximal concentration of drug/formulations required to cause 50% inhibition in the biological activity of cancer cells. Dequalinium was used to mitochondrially target the micelles incorporating curcumin and hence the MTT assay that involves measurement of the mitochondrial activity of the cancer cells was used to study and compare the activity of the formulations as potential cancer chemotherapeutics. The Ic50 values (μM, concentration of drug incorporated) of the various formulations are shown in Table 5.6 and their respective dose-response curves on the A549 and SH-SY5Y cancer cell lines are shown in Figure 5.23, Figure 5.24, Figure 5.25 and Figure 5.26.

Table 5.6: Ic50 (µM, concentration of drug incorporated) values derived from the dose-response curve of the various formulations on the SH-SY5Y and A549 cancer cell lines using the MTT assay (* $p < 0.05$ as compared to blank micelles and # $p < 0.05$ as compared to curcumin alone)

Formulations	Ic50 best-fit value SH-SY5Y	Ic50 95% confidence SH-SY5Y	R^2 SH-SY5Y	Ic50 best-fit value A549	Ic50 95% confidence A549	R^2 A549
Curcumin	29.99	26.63 to 33.76	0.9770	70.59	62.76-96.5	0.9899
Blank: Kolliphor® TPGS	4.514#	4.10-4.63	0.9941	8.765#	8.20-9.37	0.9929
Curcumin: Kolliphor® TPGS	4.355#	4.34-4.69	0.9976	6.526* #	6.09-7.00	0.9895
Blank: Kolliphor® TPGS: 30% mole dequalinium	2.364#	1.74-1.99	0.9960	7.966#	7.31-8.69	0.9875
Curcumin: Kolliphor® TPGS: 30% mole dequalinium	1.862#	2.23-2.50	0.9969	4.283* #	3.98-4.61	0.9907

There was a significant difference ($^{\#}p < 0.05$) between the Ic50 values of curcumin incorporated Kolliphor® TPGS micelles with or without dequalinium when compared to curcumin alone in both the SH-SY5Y and A549 cells. This was due to the anticancer activity of Kolliphor® TPGS as confirmed by the Ic50 of the blank Kolliphor® TPGS micelles (Table 5.6).

The blank Kolliphor® TPGS micelles with and without dequalinium did not show a significant difference ($p > 0.05$) in the Ic50 values on the A549 cell line, probably since 30% mole of dequalinium was not sufficient to exhibit anticancer activity. However, there was a significant difference ($p < 0.05$) in the Ic50 values of curcumin encapsulated Kolliphor® TPGS micelles with and without dequalinium. This could be due to an enhanced delivery of curcumin to the mitochondria of the A549 cells and hence an increased anticancer activity of the drug. There was a significant difference (* $p < 0.05$, Table 5.6) between similar formulations of micelles incorporating and not incorporating curcumin. The transform of dose-response curves (change in x-axis to logarithmic concentration to obtain a sigmoid-shaped curve) for the blank and curcumin encapsulated formulations on the A549 cell line are shown in Figure 5.23 and Figure 5.24.

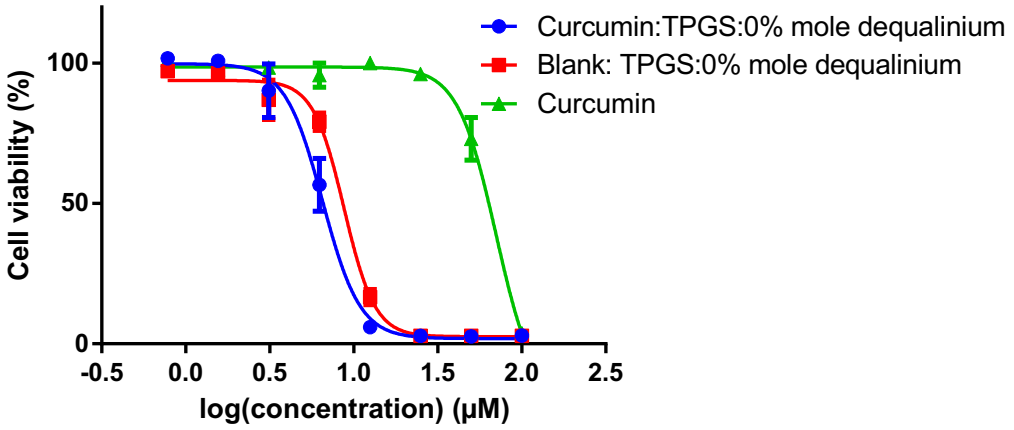

Figure 5.23: Dose-response curves with mean values ± SD (n=3) indicating the cell viability at the different micellar concentrations of Kolliphor® TPGS formulations as analyzed by the MTT assay on A549 cells

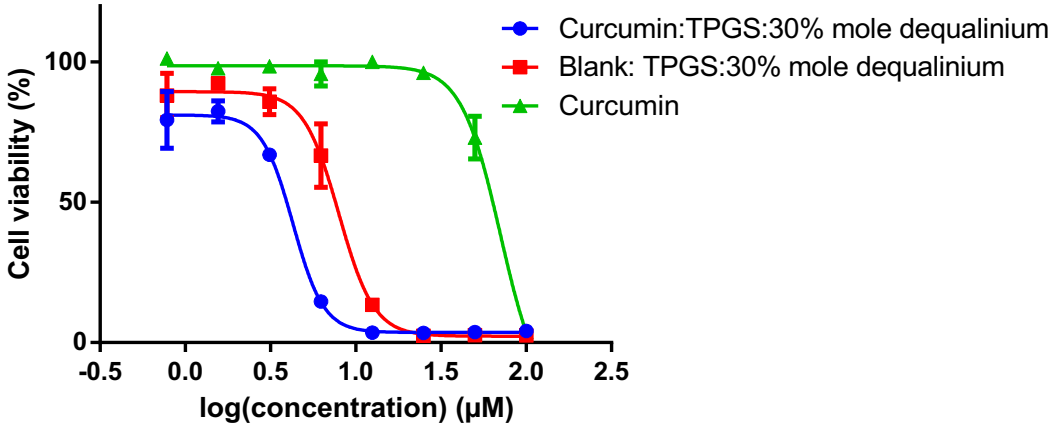

Figure 5.24: Dose-response curves with mean values ± SD (n=3) indicating the cell viability at the different micellar concentrations of Kolliphor® TPGS: dequalinium formulations as analyzed by the MTT assay on A549 cells

Blank and curcumin encapsulated Kolliphor® TPGS micelles with and without dequalinium, showed a significant difference ($p < 0.05$) in the Ic50 values on the SH-SY5Y cell line. The transform of dose-response curves (change in x-axis to logarithmic concentration to obtain a sigmoid-shaped curve) for the blank and curcumin encapsulated formulations on the SH-SY5Y cell line are shown in Figure 5.25 and Figure 5.26 respectively.

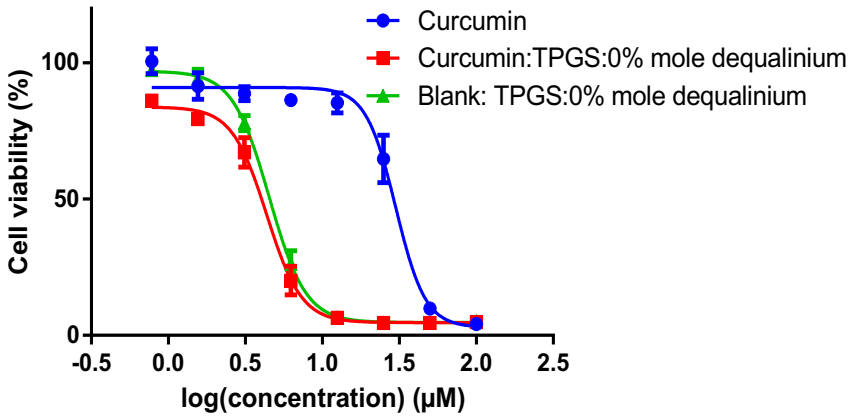

Figure 5.25: Dose-response curves with mean values ± SD (n=3) indicating the cell viability at the different micellar concentrations of Kolliphor® TPGS formulations as analyzed by the MTT assay on SH-SY5Y cells

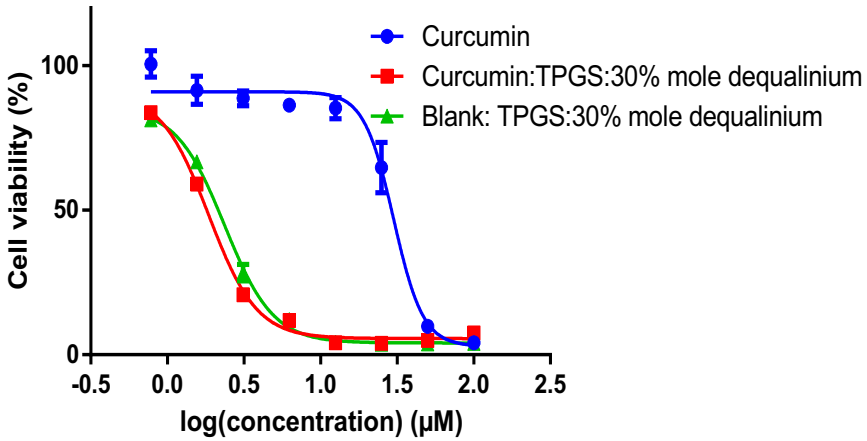

Figure 5.26: Dose response curves with mean values ± SD (n=3) indicating the cell viability at the different micellar concentrations of Kolliphor® TPGS: dequalinium formulations as analyzed by the MTT assay on SH-SY5Y cells

Kolliphor® TPGS cisplatin prodrug micelles have shown to have an enhanced uptake efficiency and anticancer activity in SH-SY5Y cells as compared to cisplatin-PEG prodrug micelles and cisplatin alone [489]. Moreover, enhanced uptake of Kolliphor® TPGS cancer therapeutic micelles has been validated on other cells lines such as MCF-7 breast cancer and C-6 brain glioma cells wherein a greater intracellular uptake and distribution was evident for the Kolliphor® TPGS micelles, which showed a lower Ic50 compared to drug alone (doxorubicin) and hence enhanced anticancer activity [490,491]. Mixed micelles of phosphatidylethanolamine-PEG/ Kolliphor® TPGS incorporating camptothecin has also shown a remarkably enhanced anticancer activity against lung, rectal, melanoma and breast/mammary cancer cells [492,493]. These results of enhanced anticancer activity are in correlation with the results obtained for Kolliphor® TPGS micelles incorporating anticancer drug previously. Hence, Kolliphor® TPGS micelles targeted to the mitochondria with dequalinium could help in enhancement of delivery of cancer chemotherapeutics. Curcumin being used as a model hydrophobic anticancer drug in the present study could be replaced with more effective anticancer drug like paclitaxel, avastin amd

vincristine, currently used for the treatment of malignant brain tumours. Cellular uptake studies would give a better insight into the targeting efficacy of the Kolliphor® TPGS formulations with dequalinium.

5.5.3 *In vitro* cellular assays for neuroprotective activity

5.5.3.1 Assessment of cellular viability and MNTC by Sulphorhodamine-B (SRB) assay

The SRB assay was used to determine the MNTC, i.e. EC80 of the formulations by determining the protein content and hence the cell density of the cells on treatment with the various formulations of potentially neuroprotective molecules. A drug concentration range of 100 µM to 3.125 µM for CNB001 and curcumin incorporating micelles (serially diluted micelles, concentration in µM of active CNB001 or curcumin considering encapsulation efficiency) and a similar concentration of blank Solutol® HS 15 micelles were analyzed. The Ec80 results are shown in Table 5.7 and transform of dose-response curves (change in x-axis to logarithmic concentration to obtain a sigmoid-shaped curve) are shown in Figure 5.27.

Table 5.7: Maximum non-toxic concentration (Ec80, µM) of active curcumin or CNB001 incorporated in micelles as studied by SRB assay

Formulation	Ec80 (µM of active curcumin or CNB001) 24 h	Ec80 (µM of active curcumin or CNB001) 48 h
Curcumin: Sol:0% mole Chol	29.63 ± 6.35	21.52 ± 1.05
Curcumin: Sol:15% mole Chol	27.97 ± 2.02	20.42 ± 0.079
Curcumin: Sol:30% mole Chol	24.14 ± 1.347	21.54 ± 3.27
Curcumin (drug alone)	23.34 ± 2.38	22.02 ± 1.05
CNB001: Sol:0% mole Chol	37.98 ± 5.49	21.73 ± 2.33
CNB001: Sol:15% mole Chol	29.59 ± 6.22	27.91 ± 2.94
CNB001: Sol:30% mole Chol	24.74 ± 0.75	20.76 ± 5.77
CNB001 (drug alone)	23.89 ± 0.51	18.17 ± 1.61
Empty Sol:0% mole Chol	95.26 ±5.50	62.06 ±4.52
Empty Sol:15% mole Chol	77.04 ±6.85	46.75 ±3.18
Empty Sol:30% mole Chol	57.83 ±6.01	22.99 ±5.48

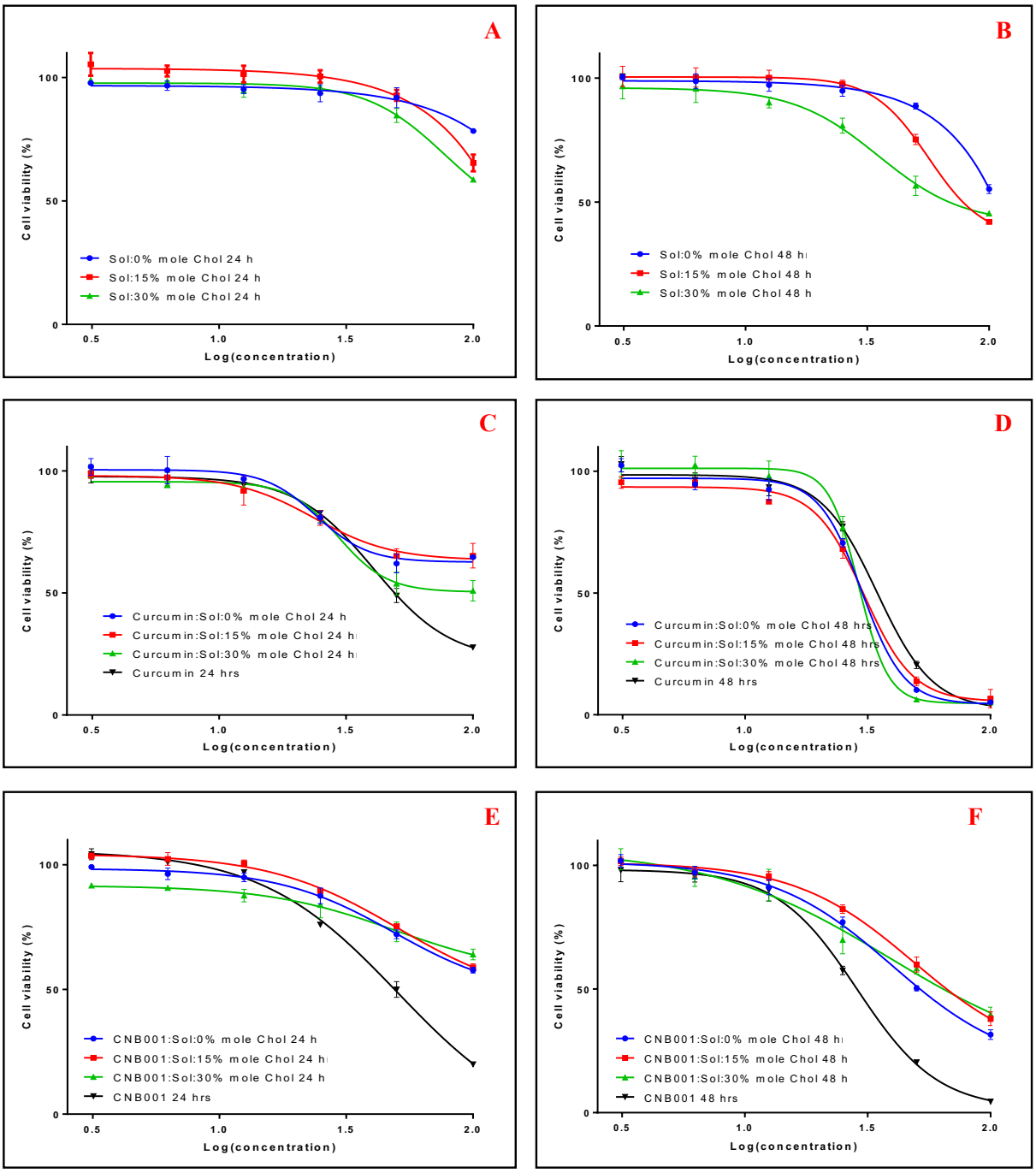

Figure 5.27: Dose-response curves with mean values ± SD (n=3) indicating the cell viability of the different micellar formulations (concentrations of active curcumin or CNB001) (A) empty Solutol® HS 15 micelles after 24 h, (B) empty Solutol® HS 15 micelles after 48 h, (C) curcumin incorporated Solutol® HS 15 micelles after 24 h, (D) curcumin incorporated Solutol® HS 15 micelles after 48 h, (E) CNB001 incorporated Solutol® HS 15 micelles after 24 h and (F) CNB001 incorporated Solutol® HS 15 micelles after 48 h, as analyzed by the SRB assay

Cytotoxicity analysis of curcumin and its formulations showed no significant difference ($p > 0.05$) in Ec80 of the drug alone compared to curcumin incorporated in Solutol® HS 15 micelles with varying amounts of cholesterol over 24 and 48 h. However, cytotoxicity studies of CNB001 encapsulated in micelles showed a significantly higher Ec80 ($p < 0.05$) (and hence less toxicity) when encapsulated in Solutol® HS 15 micelles (without cholesterol) as compared to drug alone at 24 h. This could be attributed to the release of CNB001 from the micelles which was slower as compared to the other formulations (Figure 5.21), hence, the drug not being immediately available

leading to lower toxicity and higher non-toxic concentration of this formulation. Moreover, the other formulations of CNB001 with varying concentration of cholesterol at 24 and 48 h and CNB001 encapsulated in Solutol® HS 15 micelles (without cholesterol) showed no significant difference ($p > 0.05$) in Ec80 as compared to drug alone, since the release rate of these was relatively faster (Figure 5.21). Empty micelles of Solutol® HS 15 showed a significantly higher ($p < 0.05$) cytotoxicity with increasing amount of cholesterol incorporated in the micelles.

To compare similar concentration of formulations for neuroprotection assays, a maximum non-toxic concentration of 18 µM downwards, of active curcumin or CNB001 incorporated within micelles (based on the encapsulation efficiency of each formulation) was chosen. Previous studies have reported a MNTC of 20 µM for curcumin on the SH-SY5Y cells, which was in good agreement with our studies, however, the MNTC of CNB001 has not been studied previously on this cell line [494].

5.5.3.2 *In vitro* Parkinson's disease (PD) model development: 6 hydroxydopamine-insulted SH-SY5Y cells

It was important to access the effect of the concentration of neurotoxin 6-hydroxydopamine insult on the viability of SH-SY5Y cells *in vitro*. With increasing concentration of the neurotoxin there was a dose-dependent reduction in cell viability in both the 24 h and 48 h studies (Figure 5.28).

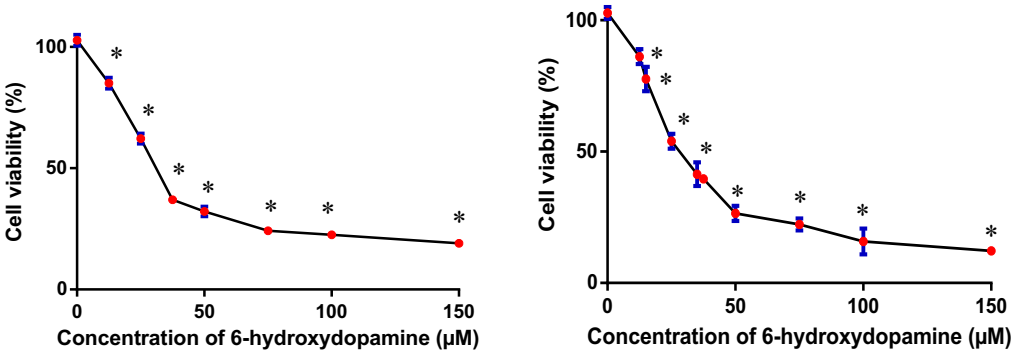

Figure 5.28: Effect of various concentrations of neurotoxin 6-hydroxydopamine for (A) 24 h and (B) 48 h on viability of SH-SY5Y cells (* $p < 0.05$ as compared with control, n=3, mean±SD)

6-hydroxydopamine at a concentration of 29.73 µM and 33.47 µM for 24 and 48 h respectively decreased the cell viability to approximately 50% of control (Ic50), hence a concentration of 30 µM was selected for further neuroprotection experiments. The results obtained were in good agreement with studies which have previously reported that a concentration of 25-30 µM 6-hydroxydopamine decreases SH-SY5Y cell viability by approximately 50% [494,495]. Moreover, there was no significant difference seen in the Ic50 values of neurotoxin dose-response for 24 h and 48 h studies when 95% confidence intervals were considered. Hence, further *in vitro* neuroprotection studies were performed over a 24 h time-period.

5.5.3.3 Protective effects of Solutol® HS 15 micelles incorporating curcumin and CNB001 on *in vitro* PD model: Neuroprotection assay

Pre-treatment with curcumin and CNB001 and the Solutol® HS 15 formulations incorporating curcumin or CNB001, at 18, 14, 9 and 7 µM (concentrations of active curcumin or CNB001, below the MNTC of the drugs) prior to insulting with neurotoxin 6-OHDA (30 µM) showed significant protection ($p < 0.05$, denoted by *) of the neuroblastoma cells, as seen by an increase in the cellular viability (Figure 5.29 and Figure 5.30). A cellular viability of 56.46±3.59% was evident for the 6-OHDA (30 µM) insulted SH-SY5Y cells that were not treated with curcumin or CNB001, representing significant toxicity ($p < 0.05$, denoted by #) as compared to control cells (not insulted, not treated).

At 18 and 14 µM pre-treatment, cell viability was not significantly different ($p > 0.05$) from the control cells with a viability of 97.83±4.55% and 93.66±2.50% respectively seen on pre-treatment with curcumin. Solutol® HS 15 formulations incorporating curcumin (concentration of active drug curcumin 18 and 14 µM) with different concentrations of cholesterol (0%, 15% and 30% mole), showed a similar trend to curcumin alone, hence encapsulation of curcumin within micelles did not reduce its neuroprotection capability.

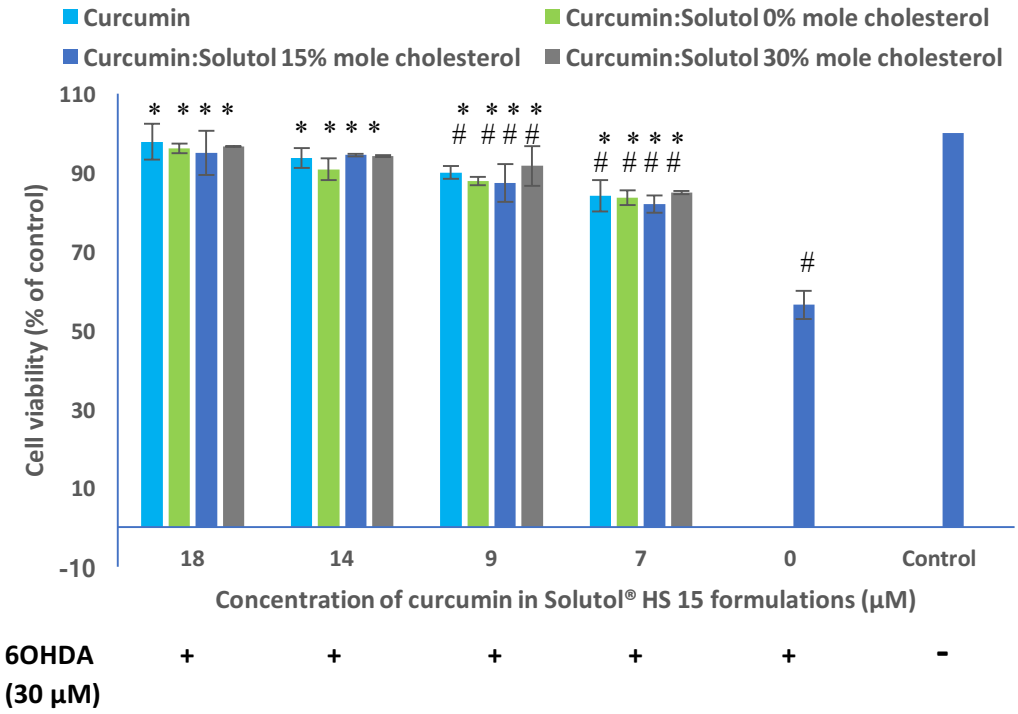

Figure 5.29: Neuroprotective effects of curcumin incorporating Solutol® HS 15 formulations on cell viability of SH-SY5Y cells insulted with 6-hydroxydopamine (6-OHDA). Cells were treated with the various formulations 2 h prior to insulting with neurotoxin 6-OHDA. * $p < 0.05$ as compared to not treated insulted cells and # $p < 0.05$ as compared to control cells (not insulted, not treated), n=3, mean±SD

Previous reports have demonstrated the neuroprotective effects of curcumin on 6-OHDA induced neuronal death at a concentration of 20 µM and 10 µM with a viability of 96.6 ± 4.6% and 86.2 ± 2.6% reported, which was similar to that obtained in the present investigation [494].

The different concentrations, i.e. 18, 14, 9 and 7 µM of CNB001 and the Solutol® HS 15 formulations incorporating CNB001 showed a significant increase ($p < 0.05$, denoted by *) in cellular viability of 6-OHDA insulted neuroblastoma cells (Figure 5.30). At 18 µM pre-treatment with CNB001, cell viability was not significantly different ($p > 0.05$) from the control cells with a viability of 103.5±5.12 % seen on pre-treatment with CNB001, hence, CNB001 can protect the cells from neurotoxin 6-OHDA insult. Solutol® HS 15 formulations incorporating CNB001 (concentration of active drug CNB001 18 µM) with different concentrations of cholesterol (0%, 15% and 30% mole) showed a similar trend to CNB001 alone, hence encapsulation of CNB001 within micelles did not reduce its neuroprotection capability. Neuroprotection of CNB001 has not been studied previously *in vitro* on 6-OHDA insulted neuronal cells, however, earlier reports of rotenone insulted neuron-like SK-N-SH cells representing Parkinson's disease model have demonstrated an increase in cellular viability on pre-treatment with 2 µM CNB001 [451].

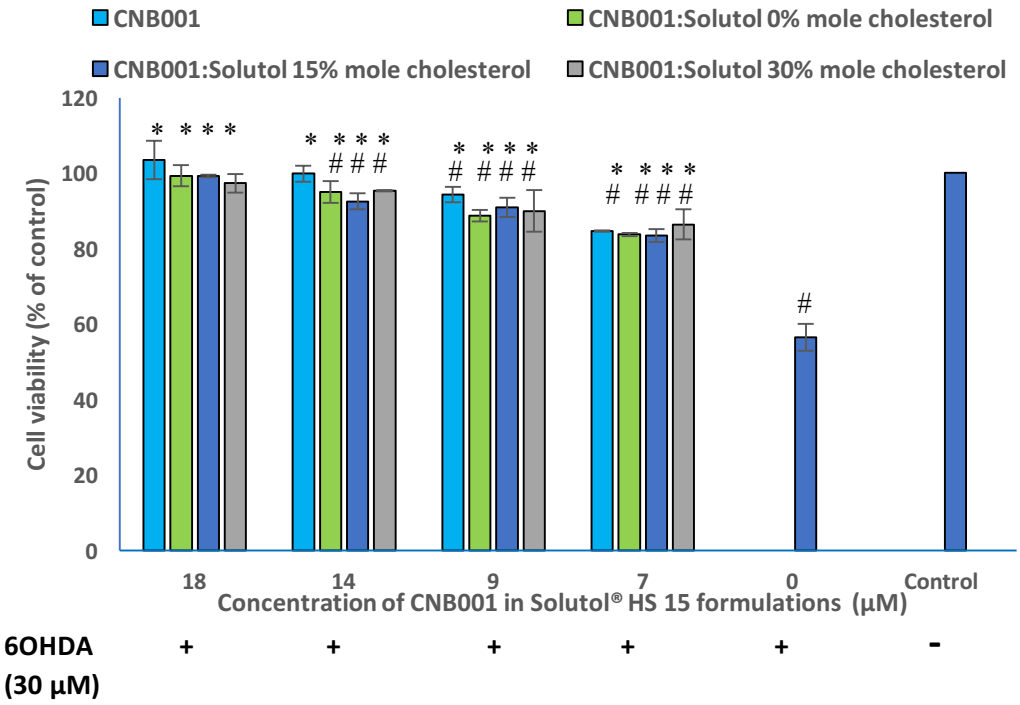

Figure 5.30: Neuroprotective effects of CNB001 incorporating Solutol® HS 15 formulations on cell viability of SH-SY5Y cells insulted with 6-hydroxydopamine (6-OHDA). Cells were treated with the various formulations 2 h prior to insulting with neurotoxin 6-OHDA. * $p < 0.05$ as compared to not treated insulted cells and # $p < 0.05$ as compared to control cells (not insulted, not treated), n=3, mean±SD

5.5.3.4 Protective effects of Solutol® HS 15 micelles incorporating curcumin and CNB001 on *in vitro* PD model: ROS formation assay

Elevation of ROS and hence oxidative stress is evident when cells are not treated before insulting with 6-hydroxydopamine, in the *in vitro* Parkinson's disease model. A time-based study was performed to compare the various formulations and to understand the ROS formation of the cells on neurotoxin insult *in vitro*. Solutol® HS 15 micelles incorporating curcumin or CNB001, at different cholesterol contents (0%, 15% and 30% mole) did not show any significant difference ($p > 0.05$) in neuroprotection, hence, Solutol® HS 15 micelles without cholesterol was chosen for further studies.

Elevation of ROS was around 45-50% (0% for control cells without treatment and insult) after 24 h of neurotoxin insult, as seen in Figure 5.31. This was in agreement with previous studies, wherein, neurotoxin 6-hydroxydopamine on SH-SY5Y cells caused an elevation of ROS from 1 (for control cells) to 1.5-fold of control for insulted non-treated cells i.e. elevation by 50% of control [494].

Time-dependent studies revealed that initially there was an elevated amount of ROS generated on insult (no treatment), which was then shown to stabilize and level off at around 12 h, up to 24 h, since there was no significant difference ($p > 0.05$) in ROS production after 12 h (Figure 5.31A rightmost bar cluster). A similar pattern of levelling off ROS production at 12 h was evident for the curcumin alone/curcumin incorporated Solutol® HS 15 micelles at various concentrations as evident from Figure 5.31. This reduction in ROS formation in the initial hours of the experiment would be due to an increased consumption of the oxidative species to cause cellular apoptosis and hence an imbalance between ROS production and consumption which was seen to stabilize after 12 h. Hence comparison of the different formulations was made at a 24 h time-point after the level of ROS was stable for the particular treatment/no treatment after insult.

Pre-treatment with curcumin drug alone (dissolved in complete media with 0.1% DMSO) (Figure 5.31A) at 7, 9, 14 and 18 µM for 2 h before exposure to 6-hydroxydopamine for 24 h, significantly reduced ($p < 0.05$) the levels of ROS produced in a concentration-dependent manner to 32.63± 3.51%, 26.32±4.24%, 8.90±5.74% and -13.43±0.16% from 52.12±2.61% (non-treated insulted cells) ROS respectively. This was in good correlation with results obtained in previous studies, wherein, curcumin at a level of 5 µM and 10 µM reduced production of ROS relative to control to 30% ± 4% and 20%±3% from 50±7% ROS for non-treated insulted cells [494].

Solutol® HS 15 incorporated curcumin micelles showed a similar trend of increased ROS initially which levelled off after around 12 h, as seen in Figure 5.31B. Pre-treatment with curcumin incorporated Solutol® HS 15 micelles at 7, 9, 14 and 18 µM curcumin for 2 h before exposure to 6-hydroxydopamine for 24 h, significantly reduced ($p < 0.05$) the levels of ROS produced in a concentration-dependent manner to 28.22±1.70%, 18.60±1.24%, -4.92±4.76% and -24.73± 2.62% respectively from 50.00±2.32% ROS (for non-treated insulted cells), confirming that curcumin incorporated in the micelles caused a reduction in oxidative stress to a basal level in the *in vitro* Parkinson's disease model. There was no significant difference ($p > 0.05$) in the production of ROS between the treatments of curcumin alone and incorporated within Solutol® HS 15 micelles, hence, encapsulation of curcumin had no effect on the antioxidant activity of curcumin, which is majorly responsible for its neuroprotection effect.

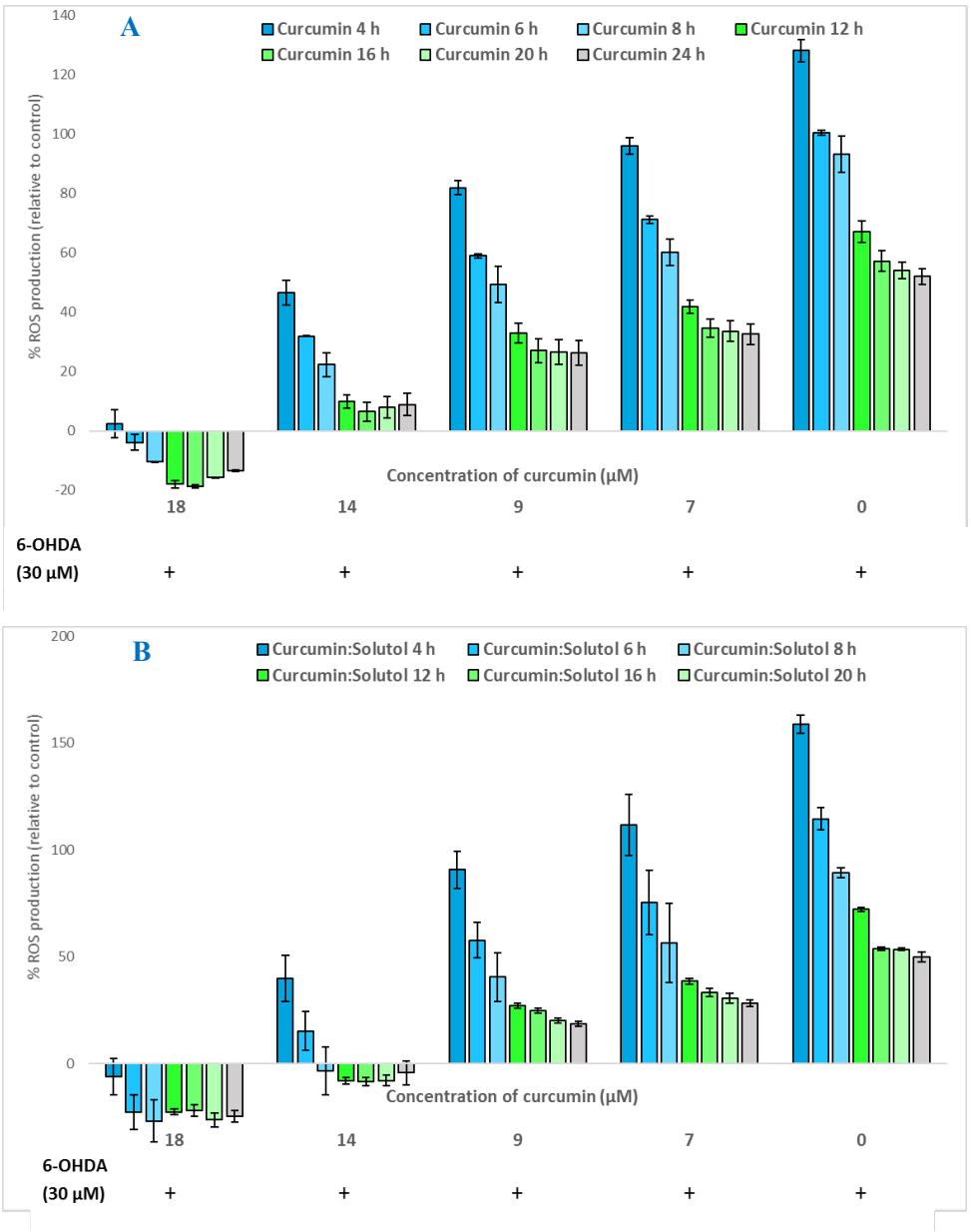

Figure 5.31: Neuroprotective effects of curcumin formulations on ROS formation by SH-SY5Y cells insulted with 6-hydroxydopamine (6-OHDA). Cells were treated with the (A) Curcumin and (B) Solutol® HS 15: Curcumin, 2 h prior to insulting with neurotoxin 6-OHDA, n=5, mean±SD

Pre-treatment with CNB001 drug alone (Figure 5.32A) at 7, 9, 14 and 18 µM for 2 h before exposure to 6-hydroxydopamine for 24 h, significantly reduced ($p < 0.05$) the levels of ROS produced in a concentration-dependent manner to 33.76±1.79%, 28.69±2.40%, 25.49±1.95% and 20.33±2.12% respectively from 50.90±2.62% ROS (non-treated insulted cells). Previous studies have shown that CNB001 can protect dopaminergic SK-N-SH cells against rotenone induced oxidative stress, that represents Parkinson's disease [451,452]. Moreover, CNB001 has been shown to protect HT-22 cells against glutamate oxidative stress representative of Alzheimer's disease [454].

Solutol® HS 15 incorporated CNB001 micelles showed a similar trend of increased ROS initially which levelled off after around 12 h, as seen in Figure 5.32B. Pre-treatment with CNB001 encapsulated in Solutol® HS 15 micelles at 7, 9, 14 and 18 µM of CNB001 for 2 h before exposure

to 6-hydroxydopamine for 24 h, significantly reduced ($p < 0.05$) the levels of ROS produced in a concentration-dependent manner to 32.03±1.92%, 29.25±0.72%, 24.84±1.18% and 18.14± 0.94% respectively from 49.76±0.34% ROS (non-treated insulted cells), confirming that CNB001 caused a 60% reduction in oxidative stress in the *in vitro* Parkinson's disease model. There was no significant difference ($p > 0.05$) in the production of ROS between the treatments of CNB001 alone and incorporated within Solutol® HS 15 micelles, hence, encapsulation of CNB001 had no effect on the antioxidant activity of CNB001, which is responsible for its neuroprotection effect.

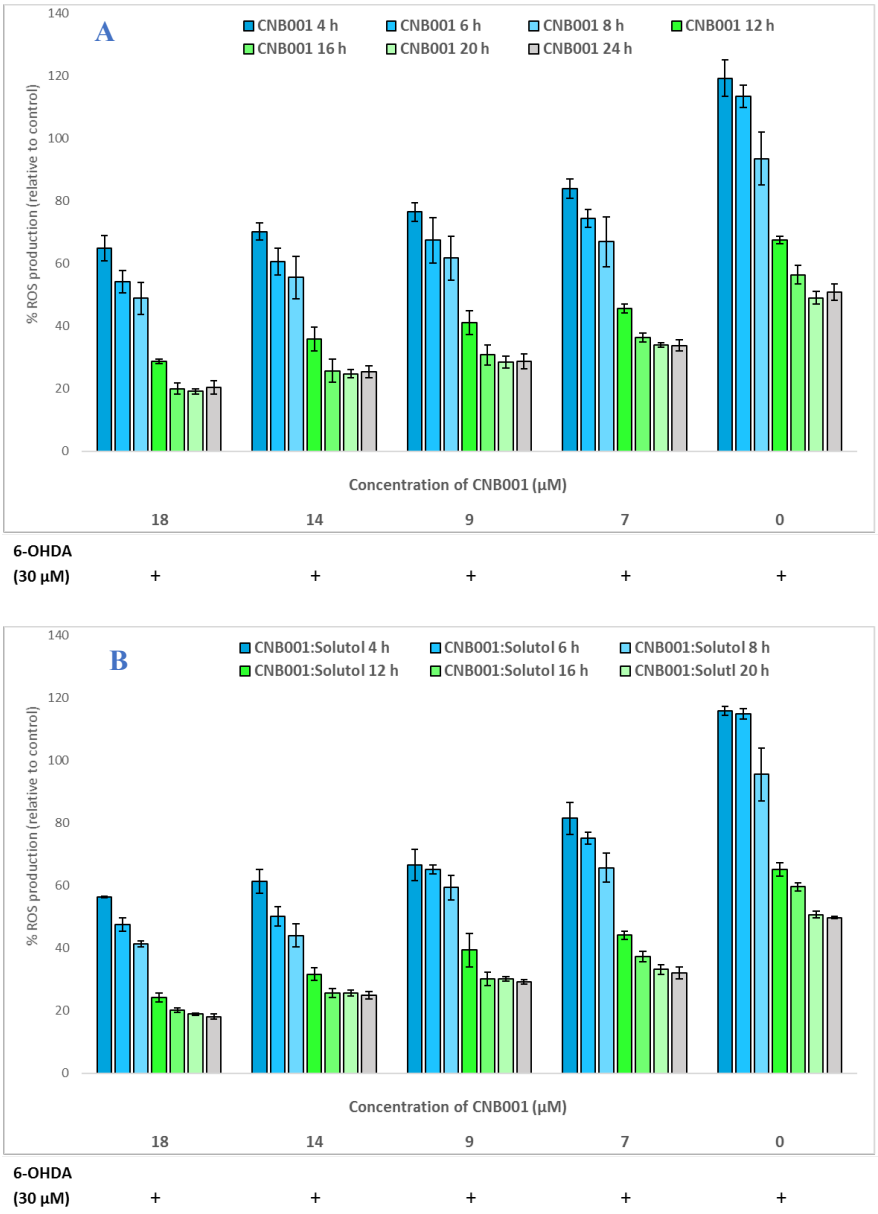

Figure 5.32: Neuroprotective effects of CNB001 formulations on ROS formation by SH-SY5Y cells insulted with 6-hydroxydopamine (6-OHDA). Cells were treated with (A) CNB001 and (B) Solutol® HS 15: CNB001, 2 h prior to insulting with neurotoxin 6-OHDA, n=5, mean±SD

5.5.3.5 Protective effect of the Solutol® HS 15 micelles incorporating curcumin or CNB001 on 6-OHDA induced cellular apoptosis: Hoechst staining

Neuronal apoptosis, evident by changes in nuclear morphology of SH-SY5Y cells on insulting with 6-OHDA, was studied on staining with DNA-binding Hoechst 33258 dye. Nuclear condensation and fragmentation, evident by brightly fluorescent rounded nuclei, and cell density reduced significantly when neuronal cells were insulted for 24 h with 30 µM 6-OHDA as seen in Figure 5.33B. On the other hand, control cells (non-treated, non-insulted) showed pallid blue nuclei as seen in Figure 5.33A.

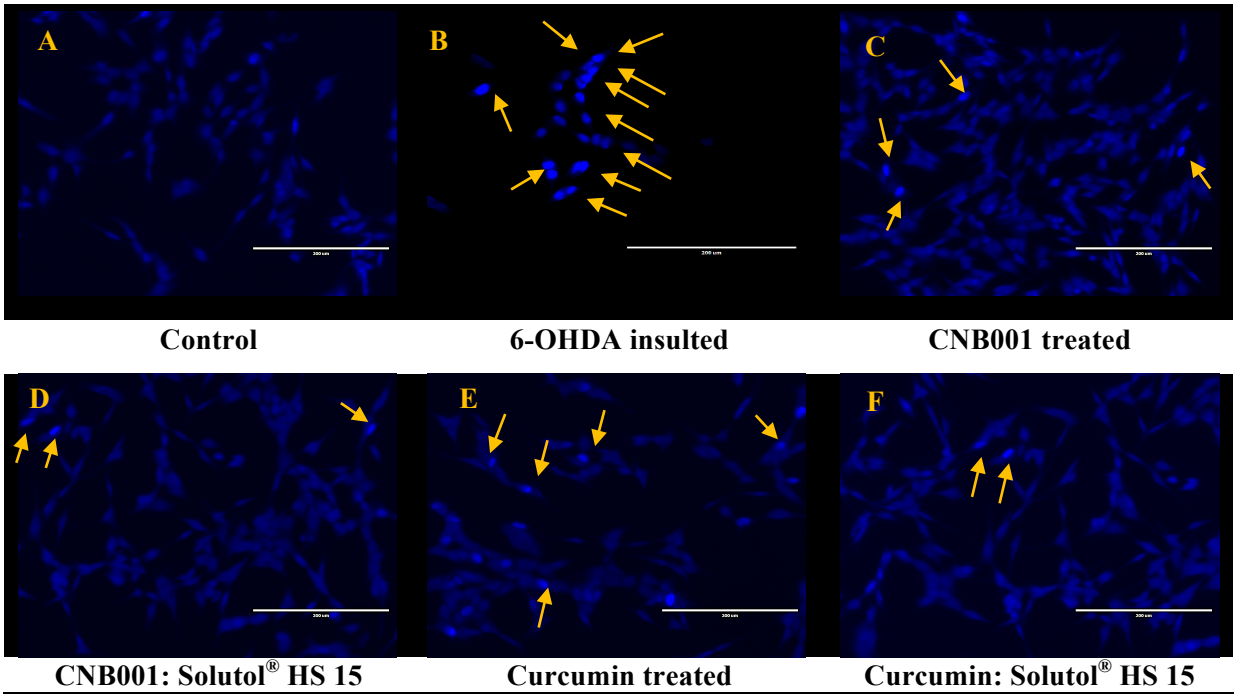

Figure 5.33: Fluorescence microscopic analysis to study the effect of curcumin and CNB001 and their Solutol® HS 15 formulations on 6-OHDA-induced neuronal SH-SY5Y cell apoptosis, as studied by nuclei observation on staining with DNA-binding fluorochrome Hoechst 33258. Yellow arrows denote apoptotic cells representing condensed or fragmented nuclei with bright stain. (A) Control cells (not insulted and not treated), (B) 6-OHDA insulted cells (not treated), (C) 18 µM CNB001 treated 6-OHDA insulted cells, (D) 18 µM CNB001: Solutol® HS 15 treated 6-OHDA insulted cells, (E) 18 µM curcumin treated 6-OHDA insulted cells, (F) 18 µM curcumin: Solutol® HS 15 treated 6-OHDA insulted cells

Pre-treatment with 18 µM CNB001 and curcumin and their Solutol® HS 15 formulations showed an improvement in the nuclear morphology of insulted cells, wherein, the number of apoptotic nuclei was lower than that observed with untreated insulted cells. Morphological changes studied using Hoechst staining due to 6-OHDA neurotoxin insult in SH-SY5Y cells has been previously reported [496–498].

ImageJ was used to semi-quantify the fluorescence intensity of the cells, so as to be able to compare different formulations. Mean fluorescence intensity was measured at the centre of the cell nucleus and an example of processed 6-OHDA-insult rescued CNB001 SH-SY5Y cells is as shown in Figure 5.34.

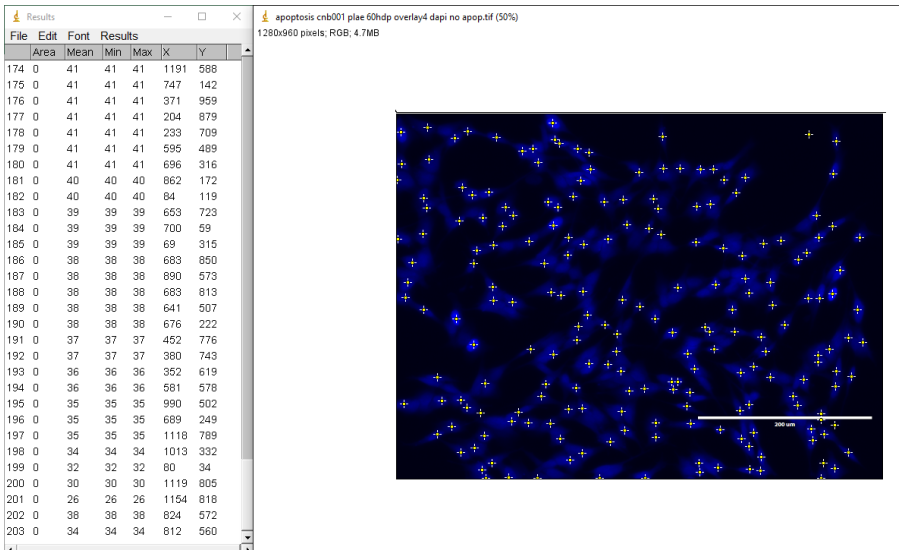

Figure 5.34: Measurement of mean fluorescence intensity of SH-SY5Y cells after staining with Hoeschst using ImageJ

There was a significant neuroprotective ($p < 0.05$) effect of curcumin and CNB001, and their Solutol® HS 15 formulations as seen by a decrease in cellular Hoechst fluorescence, on 6-OHDA insulted neuronal cells that represent the *in vitro* Parkinson's model (Figure 5.35). This demonstrates the ability of the Solutol® HS 15 micelles incorporating neuroprotective molecules to protect cells from dopamine toxicity.

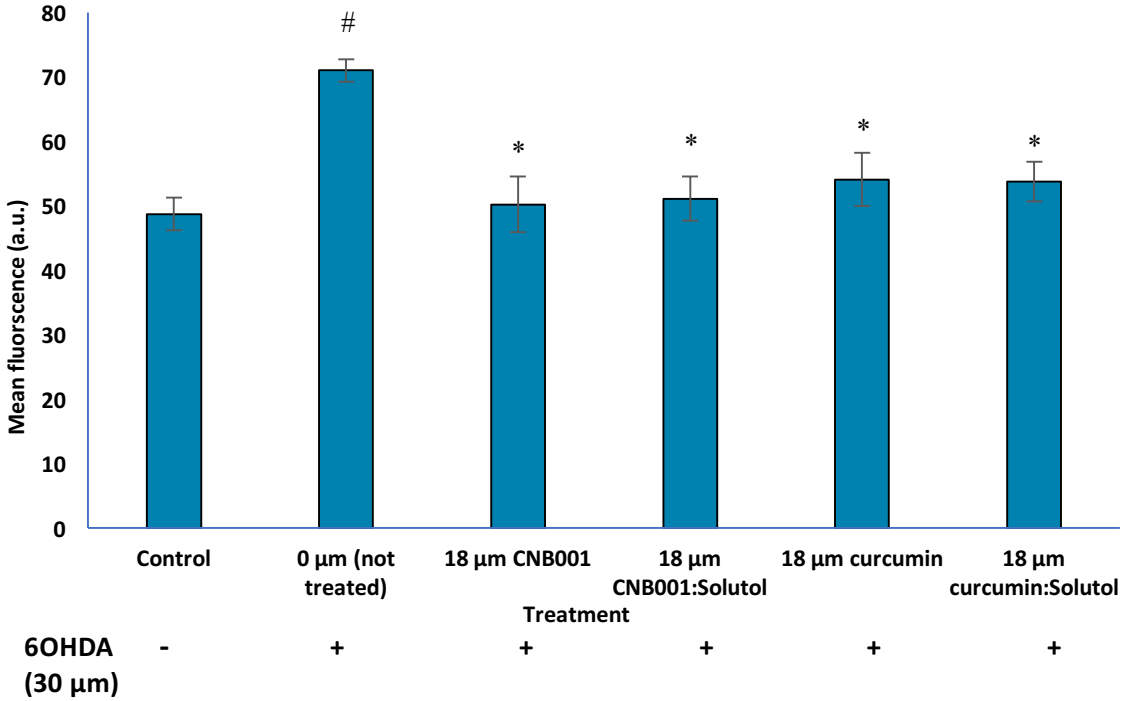

Figure 5.35: Mean fluorescence intensity as measured using ImageJ on 10 images per group. For the treatment groups, cells were treated with the various curcumin or CNB001 formulations 2 h prior to insulting with neurotoxin 6-OHDA. * $p < 0.05$ as compared to not treated insulted cells and # $p < 0.05$ as compared to control cells (not insulted, not treated)

5.6 Conclusion

The aim of the chapter was to prepare Kolliphor® TPGS and Kolliphor® HS 15 (Solutol® HS 15) micelles incorporating hydrophobic drugs CNB001 or curcumin, intended for brain targeting on delivery via the nasal airways.

Based on the aforementioned results presented in this chapter, it can be concluded that:

1. Kolliphor® TPGS micelles incorporating anticancer curcumin were successfully prepared with varying amount of mitochondrial targeting agent dequalinium, by the thin-film hydration technique. Kolliphor® TPGS has previously demonstrated apoptosis in cancer cell lines due to the active vitamin E (tocopherol) chain of the non-ionic surfactant [461].
2. Solutol® HS 15 micelles incorporating neuroprotective molecules CNB001 or curcumin were successfully prepared by the thin-film hydration technique, with varying amount of cholesterol to confer stability to the micelles. The FDA approved non-ionic surfactant Solutol® HS 15 currently used as an injectable, has been shown to possess neuroprotection in rat models of cerebral ischemia/stroke [459].
3. Aerosolization of the micellar solutions (Kolliphor® TPGS or Solutol® HS 15) was studied using the Nasal™ Mucosal Atomization Device that has previously shown promise for brain targeting via the nasal airways, as it directs medication to the posterior epithelium i.e. the site for nose-to-brain delivery. All the micellar formulations displayed a volume mean aerosol droplet size Dv50 between 42.75-54.86 μM, that was in good agreement with the manufacturers specifications for delivery of medicament to the posterior nasal mucosal surface.
4. Kolliphor® TPGS encapsulating curcumin with and without dequalinium, showed a superior *in vitro* anticancer activity as compared to curcumin alone, in the neuroblastoma SH-SY5Y and lung adenocarcinoma A549 cell lines. This was due to the anticancer potential of Kolliphor® TPGS and mitochondrial targeting by dequalinium, however, further cellular uptake studies using flow cytometry would be necessary to confirm this.
5. Solutol® HS 15 encapsulated CNB001 or curcumin, showed neuroprotection on the *in vitro* Parkinson's disease model i.e. 6-hydroxydopamine-insulted neuroblastoma SH-SY5Y cells at 18 and 14 μM (concentration of active in the micelles) pre-treatment. Moreover, pre-treatment confirmed reduction in the reactive oxygen species formation by the Parkinson's disease model and reduction in apoptotic nuclei evident by DNA-binding fluorochrome Hoechst 33258 staining, demonstrating the neuroprotective activity of the formulations. However, there was no significant difference ($p > 0.05$) in the neuroprotection activity of the micellar formulations as compared to the drugs alone, indicating that Solutol® HS 15 is not neuroprotective in Parkinson's disease models, at the concentration and time of study.

6

CHAPTER 6

General discussion and future perspectives

General discussion and future perspectives

Systemic delivery of hydrophobic therapeutics presents substantial formulation challenges, which may impede optimal benefits due to side effects and sub-therapeutic drug levels at the target site. The majority of failures in the development of new drug candidates have been attributed to poor water solubility, leading to low bioavailability and suboptimal drug concentrations [499]. Advances in combinatorial chemistry have led to an increase in the development of hydrophobic drug candidates, accounting for 90% of the discovery pipeline [499]. Moreover, hydrophobic drugs belonging to BCS Class IV, such as amphotericin B and paclitaxel, exhibit low water solubility and low or variable gastric permeability, hence requiring delivery via the invasive IV route [500]. Hydrophobic drugs delivered directly to the airways get trapped within the overall hydrophilic mucus, particularly the thick viscoelastic mucus of diseased patients; this is the rate limiting factor of diffusion to the site of action [501]. These interactions are governed by hydrophobic bonds between the drug and hydrophobic naked protein core of mucin, impeding diffusion to the site of action, leading to clearance via the mucociliary escalator [502]. Formulation development of hydrophobic drugs can be achieved by [500]:

1) particle size reduction using mechanical micronization by milling or homogenization,
2) particle engineering by crystallization or spray drying/ spray freeze drying,
3) nanocarriers encapsulating hydrophobic drugs, e.g. liposomes, nanoparticles, nanocomplexes, polymeric micelles and self-emulsifying systems.

Aerosol delivery aimed at enhancing the therapeutic efficacy of hydrophobic drugs by delivering a high drug payload at the target site with reduced systemic toxicity would be an attractive approach for combating local diseases. This thesis described three distinct novel nanotechnology-based formulation approached yielding carriers with desirable aerosolization characteristics to be delivered to and via the airways for combating pulmonary and neurological disorders.

6.1 Dry powder microparticles of amphotericin B nanocomplexes

The studies in chapter 3 describe the development of nanocomplexes of antifungal amphotericin B with antioxidant ascorbic acid-2-glucoside (AA2g) for improved drug solubilization.

Ascorbic acid readily photodecomposes in aqueous media, hence the glucoside derivative of ascorbic acid, AA2g, was selected as it has previously shown improved stability to thermal and oxidative degradation [503]. An increased solubilization of amphotericin B was evident on increasing solubilizing agent AA2g from 1:0.5 molar amphotericin B: AA2g until 1:2 molar amphotericin B: AA2g, when the two molecules were co-ground. Further increasing the stoichiometric molar ratio to 1:3 or 1:4 molar amphotericin B: AA2g gave no significant increase ($p > 0.05$) in relative amphotericin B content. Hence, a molar ratio of 1:2 amphotericin B: AA2g was chosen for further studies, for delivery of a high dose of amphotericin B with minimal excipient. Approximately 80% of the initially added amphotericin B was solubilized in the 1:2 molar co-ground formulation.

Nanocomplexes formed by co-grinding amphotericin B and AA2g (before spray drying) showed minimal loss of amphotericin B from the complex, studied over a 10-day period when stored at 4-8°C.

Synthesized amphiphilic derivatives of antioxidant ascorbic acid, such as ascorbyl–decanoate and octanoyl-6-O-ascorbic acid, have previously been reported to form self-assembled micellar solutions enhancing the solubility of hydrophobic drugs such as phenacetin, danthron, retinoic acid, griseofulvin and dithranol [504,505]. Inoue et al. reported solubilization of clarithromycin on physically mixing and co-grinding with hydrophilic AA2g at a 1:1 molar ratio, due to molecular interactions between N, N-dimethyl group on clarithromycin with the hydroxyl group of AA2g, which was stable over a 7-day period [369]. 100% solubilization was evident on co-grinding clarithromycin with AA2g; with up to 80% solubilization on physically mixing clarithromycin with AA2g [369]. Physically mixing amphotericin B with AA2g did not show solubility enhancement and co-grinding seems essential for inducing molecular interactions between the drug and excipient. FT-IR studies confirmed molecular interactions via hydrogen bond formation between the amine groups on amphotericin B and the lactone ring carboxyl and hydroxyl of AA2g on co-grinding. These interactions were not evident on physically mixing the two molecules. Zeta potential analysis of the nanocomplexes showed a high positive charge on the nanoparticle surface of around +27.7 mV for a 1:2 molar ratio, contributing to good nanoparticle stability on storage. This was in good agreement with the zeta potential of around +25.2 mV for co-ground clarithromycin: AA2g 1:1 molar ratio [369]. The mean hydrodynamic diameter of the nanocomplexes was around 100-120 nm, and increasing the amount of AA2g for complexation of a constant amount of amphotericin B, led to the formation of smaller size nanocomplexes.

Dry powder microparticles for aerosol delivery as a dry powder were prepared by spray drying the co-ground amphotericin B: AA2g nanocomplexes using the Büchi Nano spray dryer B-90, with or without excipients lactose and L-leucine to aid dispersibility. Laser diffraction particle size analysis of spray dried microparticles, with and without excipients, showed a mean geometric size at 4 bar pressure of 2.21-3.06 µm, which is suitable for lower respiratory tract deposition, including the alveolar regions where pulmonary fungal infections prevail. However, the mean size of co-ground microparticles was 8.03 µm. This showed the importance of spray drying for engineering dry powders suitable for potential peripheral pulmonary deposition. This was further highlighted in the study of *in vitro* aerosolization efficiency using the Next Generation Impactor (NGI), whereby, a significantly lower ($p < 0.05$) fine particle fraction of 16.95± 4.22% (fine particle dose of 6.24±1.9 mg amphotericin B) was achieved for the co-ground amphotericin B: AA2g microparticles, as opposed to 37.85±2.15% (fine particle dose of 17.02±0.97 mg amphotericin B) for the spray dried amphotericin B: AA2g particles. µmization using techniques like mechanical jet milling and grinding often lead to highly cohesive compacted powders which have a high surface energy and consequently poor flowability and aerosolization [506]. On the

other hand, spray drying can improve aerosol performance due to the production of spherical, porous/wrinkled microparticles with more uniform surface energy distributions and significantly lower dispersive, specific and total surface energy as compared to jet-milled particles [506]. Bulk compacted morphology was evident under the SEM for the co-ground microparticles, whereas, spherical, non-agglomerated particle morphology with slight corrugations was evident for spray dried microparticles.

The addition of L-leucine has been shown to reduce the surface energy of microparticles due to its surfactant-like properties on migration to particle surfaces during spray drying [373,507]. This effect was seen in the present studies, wherein addition of L-leucine significantly increased ($p < 0.05$) the fine particle fraction of spray dried microparticles to 56.75±1.46 % (fine particle dose of 25.54±0.66 mg amphotericin B), even though the MMAD of microparticles was similar i.e. 2.05 ± 0.15 μm to spray dried microparticles without L-leucine i.e. 2.02 ± 0.23 μm. SEM micrographs showed an open powder structure with wrinkled hollow spheres formed as curved plates, in good agreement with previous SEM micrographs of spray dried microparticles with L-leucine [373]. Changes in pressure used to disperse the spray dried microparticles gave no significant differences ($p > 0.05$) in the mean sizes at pressures of 1, 2 and 4 bar for the Sympatec; indicative of ease of dispersion and consequently a potentially reduced inter-patient variability in deposition on inhalation.

In vitro antimicrobial assessment of preparations against *Candida spp* namely *Candida albicans* and Candida *tropicalis* by the MIC assay showed retainment of the fungal activity of the drug on complexation and spray drying, hence signifying the feasibility of using amphotericin B: AA2g nanocomplexes, engineered into microparticles suitable for dry powder inhalation, for effective therapy of pulmonary fungal infections.

Amphotericin B inhalation powder (NKTR-024, Nektar Therapeutics, CA, USA) has been developed and studied as a spray dried microparticle system with distearoylphosphatidylcholine and amphotericin B at 1:1 weight ratio (25 mg amphotericin B) [206]. The aerosol following delivery from a DPI device has a mean particle size of 2-5 μm, considered favourable to achieve deep lung penetration to target *Aspergillus fumigatus* that has a similar size of 2-5 μm and has been shown to deposit deep in the airways, making its eradication challenging [206]. In human studies, a dose of 25 mg amphotericin B has been shown to be safe, with minimal systemic amphotericin B absorption and no change in pulmonary functional markers. In the present study, around 25 mg of amphotericin B was deposited in stages 2-8 of the NGI, suggesting potential peripheral lung deposition of amphotericin B: AA2g: L-leucine microparticles for the treatment of invasive pulmonary aspergillosis. Spray dried microparticles of amphotericin B nanocomplexes with antioxidant AA2g would be an extremely valuable and cost-effective option (compared to phospholipid-based systems) for the prophylactic therapy of pulmonary fungal infections in immunocompromised patients.

Future work: Ascorbic acid is an FDA-approved injectable as an antiscorbutic. It helps in improved collagen synthesis, resistance to infections and tissue repair due to its involvement in tyrosine metabolism, carbohydrate metabolism, iron metabolism, conversion of folic acid to active form folinic acid and improved cellular respiration [508]. Moreover, it has also been studied as a topical cosmeceutical agent for treatment of UV-induced photodamage and wound healing [509,510]. However, the toxicity of ascorbic acid to the lungs delivered as an aerosol needs to be considered.

Several studies have highlighted the major shortcoming of amphotericin B following IV administration, being associated with serious side-effects particularly nephrotoxicity. In contrast, Alsaadi et al. have shown that nebulization of amphotericin B for treatment of pulmonary aspergillosis showed low apparent toxicity in mice [511]. Other studies have yielded similar results, with little or no amphotericin B found in organs other than the lungs, including the kidneys, following pulmonary administration, suggesting benefit in this approach for combating nephrotoxicity-related mortality in patients treated with conventional amphotericin B formulations [511–515].

Amphotericin B has cellular toxicity by means of its interaction with mammalian cell wall cholesterol. Strong oxidative bursting of the fungus leads to an increase in reactive oxidative species (ROS), subsequently leading to toxicity in the surrounding cells as previously reported [516].

Ascorbic acid is a powerful oxidative scavenger that reacts directly with aqueous ROS by inhibition of lipid peroxidation-associated cellular toxicity [517,518]. Therefore, it is important to determine the toxicity profile of the amphotericin B formulations under study using a pulmonary cell line, such as A549 or Calu-3, to ensure that minimal toxicity is observed to host lung cells on airways' deposition, and to compare the efficacy and toxicity of formulations containing ascorbic acid or with the drug alone. This study would also be useful to determine the maximum dosage of amphotericin B/amphotericin B formulations associated with minimal toxicity to the pulmonary cell line.

6.2 Dry powder microparticles of co-encapsulated rifampicin and ibuprofen liposomes targeted to the macrophages

Pulmonary infections are difficult to eradicate particularly when the pathogen lifestyle includes intracellular infection. In Chapter 4, the liposomes co-encapsulating rifampicin and ibuprofen as antitubercular agents targeted to the macrophages where pulmonary tubercle bacilli reside were studied. Rifampicin, a common first-line antitubercular drug was chosen. However, multi-drug resistant TB is increasing, with WHO reporting 0.48 million new incidences of MDR-TB and an additional 0.1 million new cases of rifampicin-resistant TB (RR-TB) in 2015 [50,51]. Re-purposing of the non-steroidal anti-inflammatory ibuprofen has been proposed as it has demonstrated antitubercular activity in whole-cell phenotypic assay [389]. Moreover, ibuprofen

has demonstrated enhanced elimination of *in vivo* bacterial loads when used in combination with the antitubercular drug pyrazinamide. Co-delivery of ibuprofen may also facilitate healing of the lung tissue that has been damaged due to prolonged antitubercular drug regimens owing to its anti-inflammatory activity [385,393]. Current TB therapy consists of systemic delivery of multiple drugs for long periods. However, macrophage-resident TB bacilli do not respond entirely due to insufficient drug diffusion into the pulmonary tissue and hence to the alveolar macrophages. Increasing the dosage leads to systemic toxicity and bacteria persistent during the treatment develop resistance. Hence, delivery of multiple drugs encapsulated within a nanocarrier system aerosolized directly to the pulmonary tract, ideally targeted to the macrophages would be a potentially valuable approach for eradication of intracellular TB.

Design of Experiments (DoE) was used to generate a factorial design of possible experiments to study the amount of negative lipid distearoyl phosphatidylglycerol (DSPG) and cholesterol for the formulation of stable negatively-charged liposomes encapsulating rifampicin and ibuprofen. Bilayer formation was evident at concentrations of approximately 30% mole and more of DSPG to dipalmitoyl phosphatidylcholine (DPPC) required to co-encapsulate maximal rifampicin and ibuprofen. This was in correlation to previous literature where 28% and 35% mole of DSPG to phosphatidylcholine has been shown to successfully encapsulate the hydrophobic drug cisplatin and the hydrophilic drug sodium selenite respectively [433,434]. Based on requirements of maximum co-loading of drugs with small size and high negative zeta potential, the formulation DPPC: DSPG: Chol 100:40:20 was chosen. This formulation had mean size and mean zeta potential of 84.09±3.89 nm 43.5±1.5 mV respectively and an encapsulation efficiency of 89.75±2.40% and 99.00±2.20% for rifampicin and ibuprofen respectively. Previous studies on the addition of DSPG to PC has been reported for encapsulation of drugs such as sodium selenite, amphotericin B (marketed formulation AmBisome®) and cisplatin [433,434,519]. The zeta potential of these liposomal formulations ranged from -23.4±1.58 mV to −54.5±1.1 mV, depending on the content of DSPG to PC (range 26 to 40 mole%) and the buffer used for hydration [433,434,519]. AmBisome® has shown minimal association and hence toxicity with human cells, due to an improved uptake into mononuclear phagocytes owing to its negative surface charge [308,520]. Liposomal particle sizes ranging from 120.3±1.5 nm to 154.8±23.0 nm was seen for the different PC: DSPG: Chol systems, being highly dependent on the method chosen for size reduction of the initially prepared multilamellar vesicles [433,519]. Imparting negative surface charge to the liposomes was intended to achieve active targeting to the scavenger receptors on the macrophage cell membrane and hence facilitate endocytosis as seen in previous studies [410].

Co-encapsulation of antitubercular drugs into one liposomal system can be complex due to the interaction between the drugs which may affect their encapsulation and stability within the nanocarrier. DoE was used to determine an optimum ratio wherein maximum co-loading of both the drugs in the above liposomal system can be achieved. There was an interaction evident

between the two drugs due to their hydrophobic nature and hence competition for accommodation into the lipid bilayer, whereby an increase in ibuprofen caused a significant reduction ($p < 0.05$) in the amount of rifampicin incorporated, and similarly an increase in rifampicin caused a significant reduction ($p < 0.05$) in the amount of ibuprofen incorporated. Hence, based on results, 25 micromolar rifampicin and 75 micromolar ibuprofen were chosen for the preparation of liposomes to be converted into dry powders for aerosolization. *In vitro* cellular uptake was performed qualitatively using the fluorescence microscope and quantitatively using the flow cytometer for murine macrophage RAW 264.7 cells by replacing the drugs with fluorescent dye coumarin-6. Negative non-mannosylated liposomes showed a significantly higher ($p < 0.05$) uptake when compared to neutral liposomes.

Negatively-charged mannosylated liposomes incorporating mannosamine or p-aminophenyl mannopyranoside have previously been shown to improve uptake *in vivo* and *in vitro* in epithelial cells and alveolar macrophages [213,444,445]. In this study, mannose moieties mannosamine hydrochloride (36.75% mole) or p-amino phenyl mannopyranoside (18.78% mole) were embedded within the negatively-charged liposomal bilayer by electrostatic attraction with the positive charge of the amine on the mannose moieties at pH 7. As seen in the *in vitro* cellular uptake studies, association of mannosamine with the negatively-charged bilayer facilitated uptake compared to both neutral liposomes ($p < 0.05$) and negatively-charged liposomes ($p < 0.05$).

Positively-charged non-targeted and targeted liposomes were prepared by coating the negative surface of liposomes with positive chitosan or mannosylated chitosan. Chitosan coating the liposomes formulated with 100:40:20 molar DPPC: DSPG: Chol encapsulating rifampicin and ibuprofen resulted in immediate precipitation. Consequently, liposomes with a lower amount of DSPG and hence lower surface charge of -25.1±2.31 mV (DPPC: DSPG: Chol; 100:20:20) were coated with 0.05% chitosan solution (1 mL of liposomal suspension: 0.5 mL chitosan solution). The liposomes so formed showed an encapsulation efficiency of 63.12±1.06% and 92.50±2.00% for rifampicin and ibuprofen respectively, with a mean size of 145.34±2.12 nm and surface charge of +37.21±1.89 mV. The positive charge on the liposomal surface would be expected to interact with the macrophage cells by means of attraction to the negatively-charged cell membrane, hence facilitating uptake. To further enhance cellular uptake by targeting the positive liposomes to the mannose receptors, coating with mannosylated chitosan was carried out in a similar way to that of chitosan. Mannosylated chitosan was synthesized and its structure confirmed using ^{1}H-NMR and FT-IR. Positively-charged chitosan-coated liposomes showed improved uptake as compared to neutral liposomes ($p < 0.05$) due to an attraction of the positively-charged liposomes to the negatively-charged cell membrane, hence improving the endocytosis kinetics as studied by the *in vitro* qualitative and quantitative cellular uptake. Moreover, mannosylation of the surface of positive liposomes by means of coating with mannosylated chitosan facilitated uptake ($p < 0.05$) due to active mannose receptor-mediated endocytosis. Hence, cellular uptake studies validated the hypothesis of using actively targeted nanocarrier systems for delivering tubercular drugs

directly into the alveolar macrophages where the TB bacilli reside. Mannosylated chitosan-coated liposomes have not been studied previously for their potential for macrophage targeting, however, nanoparticles made of mannosylated chitosan encapsulating curcumin or rifampicin prepared by ionic gelation have been studied [298]. Approximately 2.31-fold higher uptake was evident for mannosylated chitosan nanoparticles encapsulating rifampicin in *ex vivo* macrophage uptake studies [298]. *In vitro* uptake of curcumin-loaded mannosylated chitosan nanoparticles showed a significant qualitative and quantitative uptake in infected macrophage J774A.1 cells, and hence a significantly lower effective dose i.e. 0.430 ± 0.03 mg/L compared to free curcumin 2.1 ± 0.02 mg/L was required for treatment of intracellular visceral leishmaniasis [521]. Ciprofloxacin-loaded mannosylated liposomes showed improved uptake *in vitro* in the NR8383 macrophage cell line, and an improved uptake *in vivo* in rat alveolar macrophages and epithelial lining fluid when aerosolized using a liquid MicroSprayer™, as compared to ciprofloxacin-loaded non-mannosylated liposomes and ciprofloxacin solution [445]. Moreover, the time and concentration above MIC were studied following pulmonary administration in animal models of various intracellular organisms. Mannosylated ciprofloxacin liposomes showed a significantly improved antibacterial profile particularly against *M. tuberculosis*, *C. pneumoniae*, *L. pneumophilia* and *L. monoytogenes*, at 1/50th of oral clinical dose, highlighting the possibility of dose reduction and effective eradication of pulmonary intracellular pathogens [445]. Furthermore, the risk of mutant appearance on administration of liposomal ciprofloxacin (mannosylated and non-mannosylated) against *M. tuberculosis* and *M. avium* was ideal, with a 0% chance of mutant selection as contrast to 17% and 34% for ciprofloxacin solution against *M. tuberculosi*s and *M. avium* respectively [445].

Spray drying liposomes to produce a powder suitable for inhalation is a critical step: process parameters during spay-drying can affect the properties of the final product and hence the aerodynamic behavior of the microparticles intended to be delivered to the lung using a dry powder inhalation device. Hence, DoE was employed varying the independent factors: trehalose content, L-leucine content and temperature of spray drying. The dependent variables studied, i.e. particle size distribution (by laser diffraction) and moisture content (by thermogravimetric analysis) informed the selection of the optimal spray drying parameters. Drying liposomal dispersions could lead to disruption of the bilayer structure and degradation of lipids, due to stresses of high temperature and force applied during the process [415]. Previous studies have shown that hydrogen bond interactions between the hydroxyl group of lyoprotectant trehalose and phosphate groups of DPPC liposomes have conferred stability to the liposomal bilayers on drying [522,523]. Microparticles obtained by spray drying at 120 °C (inlet temperature) in the presence of 33.33% w/w trehalose and 20% w/w L-leucine yielded product with particle size in respirable range with a mean size of 2.73 μm and 90 percentile particle size of 4.21 μm, and a Span of 1.39 with low moisture content compared to other spray dried formulations. Moreover, the SEM micrographs showed an open powder structure with wrinkled hollow spheres formed as curved

plates, which was in good agreement with the SEM micrographs of spray dried microparticles with L-leucine from previous literature [373]. The study of the dependence of pressure used in the Sympatec to disperse the microparticles showed no significant difference ($p > 0.05$) in mean size at pressures in the range of 1-5 bar, indicating ready dispersibility. These drying process parameters were used to spray dry the mannosylated (mannosamine or p-aminophenyl mannopyranoside incorporated) DPPC: DSPG: Chol liposomes, chitosan-coated DPPC: DSPG: Chol liposomes and mannosylated chitosan-coated DPPC: DSPG: Chol liposomes to study the *in vitro* aerosol parameters using the NGI, aerosolized from the commercial DPI Cyclohaler®.

In vitro studies for the microparticles sprayed from the different liposomal constitutions co-encapsulating rifampicin and ibuprofen showed a low deposition in the throat and pre-separator stages of the NGI (<20%), indicative of low oropharyngeal and throat deposition, and hence a deeper peripheral deposition in the lungs as depicted by increased deposition (>60%) in the stages 2-7 and MOC of the NGI, with fine particle fractions of 58.99-64.79% for all the microparticles. Spray dried negatively-charged DPPC: DSPG: Chol liposomes with and without mannose moieties, showed predominant deposition in stage 3 and 4 of the NGI, with stage cut-off diameters of 2.82 μm and 1.66 μm respectively, whereas, spray dried positively-charged chitosan or mannosylated chitosan-coated DPPC: DSPG: Chol liposomes, showed predominant deposition in stages 2 and 3 of the NGI, with stage cut-off diameters of 4.46 μm and 2.82 μm respectively

Future work: Previous studies have demonstrated the efficacy of mannosylated nanocarriers against mycobacterial strains *in vitro* and *in vivo* [298,300,433,445,521]. Delivery of mannosylated nanocarriers encapsulating antibiotics has shown a significantly improved intracellular bacterial eradication from infected macrophages as compared to free drug/non-mannosylated nanocarriers.

Present qualitative *in vitro* uptake studies using flow cytometry have confirmed the improved uptake of charged (positive and negative) and mannosylated liposomal formulations encapsulating fluorescent dye coumarin-6. Consequently, it would be valuable to elucidate the efficacy of the various co-encapsulated rifampicin and ibuprofen liposomes against mycobacterial-infected macrophages along with the drug residence time within the macrophage compartments. This would help to ascertain the time of drug concentration above the MIC of the organism, and consequently the appropriate dosing concentration and regimen.

In the present study, the ratio of rifampicin: ibuprofen chosen was based on the liposomal formulation design, however, it would also be useful to study the drug combination dose ratio of free drugs and their efficacy against mycobacterium *in vitro*, since the combination of rifampicin and ibuprofen for tuberculosis has not been studied previously. The most effective combination ratio could be co-encapsulated within targeted liposomes and studied for macrophage uptake and tubercular eradication.

6.3 Aerosols of Kolliphor® and Solutol® micelles for nose-to-brain delivery

Kolliphor® TPGS and Solutol® HS 15 (Kolliphor® HS 15) micelles incorporating the hydrophobic drugs CNB001 or curcumin were successfully prepared by the thin-film hydration method.

Kolliphor® TPGS was used as the non-ionic surfactant to prepare micelles incorporating curcumin, as this surfactant has shown promise in reversal of multi-drug resistance lung and breast cancer, and can induce apoptosis due to the presence of vitamin E (tocopherol), the hydrophobic head group of the amphiphilic polymer chain [460,524]. These micelles were adapted for potential targeting to the mitochondria for better efficacy of the anticancer system, by inclusion of cationic dequalinium chloride as described in previous studies [462]. Kolliphor® TPGS micelles incorporating curcumin, with and without dequalinium, were in the size range 13-16 nm, with an encapsulation efficiency of ~100%. The zeta potential of the non-targeted micelles was approximately neutral. A significant increase ($p < 0.05$) in the zeta potential to approximately +10 mV was evident on incorporation of cationic dequalinium. TEM images showed spherical, well dispersed micelles with size correlating to that obtained from intensity and volume distribution by DLS.

Solutol® HS 15 was used as the non-ionic surfactant to prepare micelles incorporating the neuroprotective drugs CNB001 or curcumin, as this FDA-approved surfactant, currently used in injectable products has shown neuroprotection in rat models of cerebral ischemia. To improve the stability of Solutol® HS 15 micelles, cholesterol was added in increasing molar ratios from 7.5% to 30%. There was a cholesterol concentration-dependent increase in mean size from ~20 nm to ~95 nm, based on the intensity size distribution profile. However, the volume size distribution profile suggested that the predominant vesicles in the formulations incorporating hydrophobic neuroprotective drugs were micelles with mean volume size ~20 nm. Increasing the amount of cholesterol led to an increase (5-15% by volume distribution) in the presence of larger vesicles, known as niosomes, with mean size around 100 nm. Non-ionic surfactant based microemulsions of nimodipine with an average size of 25-35 nm administered intranasally, showed a significantly increased concentration of nimodipine in the brain as compared to IV administration of the formulation or the intranasal administration of nimodipine solution, highlighting the importance of formulation propertied for brain targeting via the nasal tract [525]. Moreover, the choice of surfactant and percentage of components impacts nasal ciliotoxicity, such that emulsions of Labrafil M 1944 showed no evident toxicity as compared to emulsions of Maisine 35-1 and isopropyl myristate which exhibited moderate ciliotoxicity. Furthermore, risperidone nanoemulsions with globule size 14-17 nm, showed increased direct nose-to-brain transport and drug targeting efficiency compared to intranasal risperidone alone, as studied by gamma scintigraphy and quantitatively measured by radiochemical biodistribution studies *in vivo* [526]. Moreover, on the administration of nanoemulsion formulations an improved locomotor count and hindlimb retraction time were evident, indicating superior activity of risperidone due to greater transport to the brain on nasal administration [526]. Taki et al. delivered the anticancer drug

camptothecin in mPEG/PCL-Tat micelles with a mean size of 26-50 nm; Tat a cell penetrating peptide promotes brain delivery on intranasal administration [238,239]. An improved median survival of rats bearing intracranial C6 tumours was achieved, believed to be due to improved uptake of the formulation from the nasal tract to the brain as compared to intranasal camptothecin alone [238,239].

Aerosolization of the micellar solutions was achieved in this study using the Nasal™ Mucosal Atomization Device that has previously shown promise for brain targeting via the nasal airways. For posterior nasal tract delivery, a droplet size of 30-120 μm using this device is considered appropriate [128]. All the micellar formulations of Solutol® HS 15 and Kolliphor® TPGS produced aerosols with a volume mean aerosol droplet size Dv50 between 42.75 and 54.86 μm, which is in good agreement with the manufacturer's specifications for delivery of medicament to the posterior nasal mucosal surface. There was no effect ($p > 0.05$) of aerosolization using the atomization device on the particle size distribution of the micelles, hence indicating that this device could be used to effectively deliver these nanocarrier based formulations to the posterior nasal tract for brain targeting.

In vitro cellular viability assays on SH-SY5Y and A549 cancer cells to study the effect of Kolliphor® TPGS formulations incorporating curcumin, containing and not containing dequalinium, demonstrated improved efficacy ($p < 0.05$) of the micellar system. This was probably due to the anticancer potential of Kolliphor® TPGS and mitochondrial targeting by dequalinium, however, further cellular uptake studies using flow cytometry would be a useful study to confirm this.

The neuroprotection assay for the *in vitro* Parkinson's disease model, i.e. 6-hydroxydopamine insulted neuroblastoma SH-SY5Y cells, confirmed the neuroprotection profile of Solutol® HS 15 encapsulated CNB001 or curcumin. A cellular viability of 56.46 ± 3.59% was evident for the 6-OHDA (30 μM) insulted SH-SY5Y cells that were not treated with curcumin or CNB001, representing significant toxicity ($p < 0.05$) compared to control cells. At 18 and 14 μM pre-treatment before insult with curcumin or curcumin encapsulated Solutol® HS 15 micelles, cell viability was not different ($p > 0.05$) from the control cells, with viabilities of ~97% and 94% respectively. Moreover, at 18 μM pre-treatment with CNB001 or CNB001 encapsulated Solutol® HS 15 micelles, cell viability was not significantly different ($p > 0.05$) from the control cells, with a viability of ~100 % seen on pre-treatment. Solutol® HS 15 incorporating drugs did not show any significant difference ($p > 0.05$) from the drug alone, hence the surfactant on its own did not have a neuroprotection effect at the concentration, model and time tested. Encapsulation of CNB001 or curcumin within surfactant micelles did not reduce its neuroprotection capability.

The ROS formation assay in the *in vitro* Parkinson's disease model, confirmed the antioxidant profile of Solutol® HS 15 encapsulated CNB001 or curcumin. Elevation of ROS was around 45-50% (considering 0% ROS for control SH-SY5Y cells without insult) after 24 h of neurotoxin

insult. Pre-treatment with curcumin or curcumin encapsulated Solutol® HS 15 micelles at 7, 9, 14 and 18 μM significantly reduced ($p < 0.05$) the levels of ROS produced in a concentration-dependent manner to ~30 %, 20 %, ~0% and -15% from ~51 % ROS of control for non-treated insulted cells. Moreover, pre-treatment with CNB001 or CNB001 encapsulated Solutol® HS 15 micelles at 7, 9, 14 and 18 μM significantly reduced ($p < 0.05$) the levels of ROS produced in a concentration-dependent manner to ~32 %, 28 %, 24 % and 19% from ~50 % ROS of control for non-treated insulted cells.

There was a significant neuroprotective effect ($p < 0.05$) of curcumin or CNB001 and their Solutol® HS 15 formulations, demonstrated by a decrease in cellular fluorescence and morphology, using nuclei observation on staining with DNA-binding fluorochrome Hoechst 33258, on 6-OHDA insulted neuronal cells, clearly demonstrating the ability of the CNB001 or curcumin Solutol® HS 15 micelles to protect the neuronal cells in Parkinson's disease.

Hence, Kolliphor® TPGS micelles incorporating hydrophobic anticancer agent curcumin, non-targeted or mitochondrially targeted with dequalinium, is an attractive nanocarrier formulation for nasal aerosol delivery as a potential treatment of neuroblastoma, as confirmed by the *in vitro* cellular studies. In addition, this study has demonstrated that Solutol® HS 15 micelles would be a valuable delivery system for neuroprotective agents' curcumin or CNB001 intended for potential nose-to-brain targeting in the treatment of neurodegeneration, as confirmed *in vitro* in the Parkinson's cellular model.

Future work: Mixed micelles of DSPE-PEG 2K/ Kolliphor® TPGS incorporating paclitaxel and/or parthenolide has been shown to enhance the anticancer activity on A549 and taxol resistant A549-T24 cell lines [461]. Kolliphor® TPGS is known to overcome drug resistance by inhibiting P-glycoprotein efflux pumps and hence sensitize multi-drug resistant tumours to cancer chemotherapeutics like paclitaxel, doxorubicin and vinblastine [461]. Hence, study of the anticancer activity of Kolliphor® TPGS micelles incorporating curcumin with and without targeting moiety dequalinium in resistant cell lines would be of great interest. Moreover, qualitative and quantitative *in vitro* cellular uptake studies using fluorescence microscopy and flow cytometry respectively, would give a better outlook of the potential mitochondrial targeting capacity of these formulations on the SH-SY5Y cell line.

The neuroprotective efficacy of CNB001 drug has not been studied previously on the 6-hydroxydopamine insulted SH-SY5Y neuroblastoma cells that represents an *in vitro* Parkinson's disease model. In the present thesis, neuroprotection with respect to ROS formation and apoptotic nuclei has been studied. It would be valuable to study the effect of the drug and its formulations on other pathways of neuroprotection, namely, mitochondrial membrane potential and DNA fragmentation.

Solutol® HS 15 has been shown to neuroprotective in focal and cerebral ischemia rat models due to structural similarity to stearic acid methyl ester which has previously shown to be

neuroprotective in similar models [459]. CNB001 has shown potential as a neuroprotective agent to treat stroke previously [527]. It would be interesting to study the efficacy and neuroprotection activity of the Soluto[l®] HS 15 micelles incorporating CNB001 in oxygen-glucose depleted *in vitro* models of SH-SY5Y cells that represent ischemia/stroke.

Passage of nanocarriers from the nasal tract via the olfactory epithelium to the brain and toxicity to the nasal mucosa are dependent on the size and surface characteristics of the nanocarrier systems, along with its residence time in the nasal tract, as studied previously [238,266,525,526]. It would be informative to study the *in vitro* permeation and toxicity of the Kolliphor® micelles using three-dimensional human-derived tracheal/bronchial epithelial cell cultures (EpiAirway™, MatTek Corporation, USA) that have been previously validated as a reliable *in vitro* model to screen compounds intended for delivery via the nasal mucosa for brain targeting [528,529].

7

CHAPTER 7

References

[1] Sanders, M., 2011. Pulmonary drug delivery: an historical overview, in *Controlled Pulmonary Drug Delivery*, Symth, H.D.C., Hickey A.J. (editors), Springer, New York, pp.51-73.

[2] Illum, L., 2012. Nasal drug delivery—recent developments and future prospects. *Journal of Controlled Release*, 161(2), 254-263.

[3] Hussain, M., Madl, P. and Khan, A., 2011. Lung deposition predictions of airborne particles and the emergence of contemporary diseases, Part-I. *Health*, 2(2), 51-59.

[4] Dolovich, M.B. and Dhand, R., 2011. Aerosol drug delivery: developments in device design and clinical use. *Lance*t, 377(9770), 1032-1045.

[5] Stuart, B.O., 1984. Deposition and clearance of inhaled particles. *Environmental Health Perspectives*, 55, 369-390.

[6] Demoly, P., Hagedoorn, P., de Boer, A.H. and Frijlink, H.W., 2014. The clinical relevance of dry powder inhaler performance for drug delivery. *Respiratory Medicine*, 108(8), 1195-1203.

[7] National Research Council, 2006. Overcoming challenges to develop countermeasures against aerosolized bioterrorism agents: appropriate use of animal models. *National Academies Pres*s, doi:10.17226/11640.

[8] Hickey, A.J. (editor), 2007. *Inhalation aerosols: Physical and Biological Basis for Therapy*. 2nd edition, Informa Healthcare, New York.

[9] Darquenne, C. and Prisk, G.K., 2004. Aerosol deposition in the human respiratory tract breathing air and 80: 20 heliox. *Journal of Aerosol Medicin*e, 17(3), 278-285.

[10] Hassan, M.S. and Lau, R.W.M., 2009. Effect of particle shape on dry particle inhalation: study of flowability, aerosolization, and deposition properties. *AAPS PharmSciTech*, 10(4), 1252-1262.

[11] Chan, H.K. and Gonda, I., 1989. Aerodynamic properties of elongated particles of cromoglycic acid. *Journal of Aerosol Science*, 20(2), 157-168.

[12] Zeng, X.M., Martin, G.P., Marriott, C. and Pritchard, J., 2000. The influence of carrier morphology on drug delivery by dry powder inhalers. *International Journal of Pharmaceutics*, 200(1), 93-106.

[13] Hamishehkar, H., Emami, J., Najafabadi, A.R., Gilani, K., Minaiyan, M., Mahdavi, H. and Nokhodchi, A., 2010. Effect of carrier morphology and surface characteristics on the development of respirable PLGA microcapsules for sustained-release pulmonary delivery of insulin. *International Journal of Pharmaceutic*s, 389(1), 74-85.

[14] Scheuch, G. and Heyder, J., 1990. Dynamic shape factor of nonspherical aerosol particles in the diffusion regime. *Aerosol Science and Technology*, 12(2), 270-277.

[15] Russo, P., Santoro, A., Prota, L., Stigliani, M., and Aquino, R.P., (2012). Development and investigation of dry powder inhalers for cystic fibrosis, in *Recent Advances in Novel Drug Carrier Systems*, Sezer, A.D. (editor), InTech.

[16] Kawashima, Y., Serigano, T., Hino, T., Yamamoto, H. and Takeuchi, H., 1998. Effect of surface morphology of carrier lactose on dry powder inhalation property of pranlukast hydrate. *International Journal of Pharmaceutics*, 172(1), 179-188.

[17] Ghilzai, N.K., Pulmonary drug delivery: A review [Internet]. Available from: http://www.drugdel.com/Pulm_review.pdf (accessed on 27 March 2017).

[18] Merchant, Z., Buckton, G., Taylor, K.M.G., Stapleton, P., Saleem, I.Y., Zariwala, M.G. and Somavarapu, S., 2016. A new era of pulmonary delivery of nano-antimicrobial therapeutics to treat chronic pulmonary infections. *Current Pharmaceutical Design*, 22(17), 2577-2598.

[19] Welch, M.J., 2008. Nebulization therapy for asthma: a practical guide for the busy pediatrician. *Clinical Pediatrics*, 47(8), 744-756.

[20] Labiris, N.R. and Dolovich, M.B., 2003. Pulmonary drug delivery. Part II: the role of inhalant delivery devices and drug formulations in therapeutic effectiveness of aerosolized medications. *British Journal of Clinical Pharmacology*, 56(6), 600-612.

[21] Bailey, M.M. and Berkland, C.J., 2009. Nanoparticle formulations in pulmonary drug delivery. *Medicinal Research Reviews*, 29(1), 196-212.

[22] Patil, J.S. and Sarasija, S., 2012. Pulmonary drug delivery strategies: A concise, systematic review. *Lung Indi*a, 29(1), 44-49.

[23] Yurteri, C.U., Hartman, R.P. and Marijnissen, J.C., 2010. Producing pharmaceutical particles via electrospraying with an emphasis on nano and nano structured particles-A review. *KONA Powder and Particle Journal*, 28, 91-115.

[24] Pilcer, G. and Amighi, K., 2010. Formulation strategy and use of excipients in pulmonary drug delivery. *International Journal of Pharmaceutics*, 392(1), 1-19.

[25] Smith, I.J. and Parry-Billings, M., 2003. The inhalers of the future? A review of dry powder devices on the market today. *Pulmonary Pharmacology & Therapeutics*, 16(2), 79-95.

[26] Prime, D., Atkins, P.J., Slater, A. and Sumby, B., 1997. Review of dry powder inhalers. *Advanced Drug Delivery Reviews*, 26(1), 51-58.

[27] Yianneskis, M., Martin, G.P., Marriott, C., Suen, K.O., Lee, K.L.C., Ganderton, D. and Timsina, M., King's College London, 1999. Dry powder inhalers. *U.S. Patent 5975076*.

[28] Minne, A., Boireau, H., Horta, M.J. and Vanbever, R., 2008. Optimization of the aerosolization properties of an inhalation dry powder based on selection of excipients. *European Journal of Pharmaceutics and Biopharmaceutics*, 70(3), 839-844.

[29] Newman, S.P., 2004. Dry powder inhalers for optimal drug delivery. *Expert Opinion on Biological Therapy*, 4(1), 23-33.

[30] Ashurst, I., Malton, A., Prime, D. and Sumby, B., 2000. Latest advances in the development of dry powder inhalers. *Pharmaceutical Science and Technology Today*, 3(7), 246-256.

[31] Islam, N. and Gladki, E., 2008. Dry powder inhalers (DPIs)—a review of device reliability and innovation. *International Journal of Pharmaceutics*, 360(1), 1-11.

[32] Ganderton, D., 1999. Targeted delivery of inhaled drugs: current challenges and future goals. *Journal of Aerosol Medicine*, *12*(s1), S3-S8.

[33] O'Connor, B.J., 2004. The ideal inhaler: design and characteristics to improve outcomes. *Respiratory Medicine*, 98, S10-S16.

[34] National Institute for Clinical Excellence, 2008. Respiratory tract infections–antibiotic prescribing. Prescribing of antibiotics for self-limiting respiratory tract infections in adults and children in primary care. Available at: http://publications.nice.org.uk/respiratory-tract-infections-antibiotic-prescribing-cg69, *NICE clinical guideline*, 69 (accessed on 27 March 2017).

[35] Chang, A.B., Chang, C.C., O'Grady, K. and Torzillo, P.J., 2009. Lower respiratory tract infections. *Paediatric Clinics of North America*, 56(6), 1303-1321.

[36] Pison, U., Welte, T., Giersig, M. and Groneberg, D.A., 2006. Nanomedicine for respiratory diseases. *European Journal of Pharmacology*, 533(1), 341-350.

[37] Murphy, T.F., 2008. The many faces of Pseudomonas aeruginosa in chronic obstructive pulmonary disease. *Clinical Infectious Diseases*, 47(12), 1534-1536.

[38] Salouti, M. and Ahangari, A., 2014. Nanoparticle based drug delivery systems for treatment of infectious diseases, in *Application of Nanotechnology in Drug Delivery*, Sezer, A.D. (editor), InTech.

[39] Mutlu, G.M. and Wunderink, R.G., 2006. Severe pseudomonal infections. *Current Opinion in Critical Care*, 12(5), 458-463.

[40] Garau, J. and Gomez, L., 2003. Pseudomonas aeruginosa pneumonia. *Current Opinion in Infectious Diseases*, 16(2), 135-143.

[41] Gibson, R.L., Burns, J.L. and Ramsey, B.W., 2003. Pathophysiology and management of pulmonary infections in cystic fibrosis. *American Journal of Respiratory and Critical Care Medicine*, 168(8), 918-951.

[42] Lyczak, J.B., Cannon, C.L. and Pier, G.B., 2002. Lung infections associated with cystic fibrosis. *Clinical Microbiology Reviews*, 15(2), 194-222.

[43] Ernst, J.D., 1998. Macrophage receptors for Mycobacterium tuberculosis. *Infection and Immunity*, 66(4), 1277-1281.

[44] Krutzik, S.R. and Modlin, R.L., 2004. The role of Toll-like receptors in combating mycobacteria, in *Seminars in Immunology*, 16(1), Academic Press, 35-41.

[45] Stafford, J.L., Neumann, N.F. and Belosevic, M., 2002. Macrophage-mediated innate host defense against protozoan parasites. *Critical Reviews in Microbiology*, 28(3), 187-248.

[46] Labiris, N.R. and Dolovich, M.B., 2003. Pulmonary drug delivery. Part I: physiological factors affecting therapeutic effectiveness of aerosolized medications. *British Journal of Clinical Pharmacology*, 56(6), 588-599.

[47] Rajaram, M.V., Brooks, M.N., Morris, J.D., Torrelles, J.B., Azad, A.K. and Schlesinger, L.S., 2010. Mycobacterium tuberculosis activates human macrophage peroxisome proliferator-activated receptor γ linking mannose receptor recognition to regulation of immune responses. *The Journal of Immunology*, 185(2), 929-942.

[48] Davies, P.D., 2003. The world-wide increase in tuberculosis: how demographic changes, HIV infection and increasing numbers in poverty are increasing tuberculosis. *Annals of Medicine*, 35(4), 235-243.

[49] World Health Organization, 2013. Global tuberculosis report 2013 [Internet]. *World Health Organization*. Available at http://apps.who.int/iris/bitstream/10665/91355/1/9789241564656 eng.pdf (accessed on 27 March 2017).

[50] World Health Organization, 2016. Global tuberculosis report 2016 [Internet]. *World Health Organization*. Available at http://www.who.int/tb/publications/global_report/en/ (accessed on 27 March 2017).

[51] World Health Organization, 2016. Multidrug-resistant TB (MDR-TB): 2016 Update Internet]. *World Health Organization*. Available from http://www.who.int/tb/challenges/mdr/mdr_tb_factsheet.pdf (accessed on 27 March 2017).

[52] Van Crevel, R., Ottenhoff, T.H. and Van der Meer, J.W., 2002. Innate immunity to Mycobacterium tuberculosis. *Clinical Microbiology Reviews*, 15(2), 294-309.

[53] Limper, A.H., Knox, K.S., Sarosi, G.A., Ampel, N.M., Bennett, J.E., Catanzaro, A., Davies, S.F., Dismukes, W.E., Hage, C.A., Marr, K.A. and Mody, C.H., 2011. An official american thoracic society statement: treatment of fungal infections in adult pulmonary and critical care patients. *American Journal of Respiratory and Critical Care Medicine*, 183(1), 96-128.

[54] Tortorano, A.M., Peman, J., Bernhardt, H., Klingspor, L., Kibbler, C.C., Faure, O., Biraghi, E., Canton, E., Zimmermann, K., Seaton, S. and Grillot, R., 2004. Epidemiology of candidaemia in Europe: results of 28-month European Confederation of Medical Mycology (ECMM) hospital-based surveillance study. *European Journal of Clinical Microbiology and Infectious Diseases*, 23(4), 317-322.

[55] Lin, S.J., Schranz, J. and Teutsch, S.M., 2001. Aspergillosis case-fatality rate: systematic review of the literature. *Clinical Infectious Diseases*, 32(3), 358-366.

[56] Wheat, L.J., Freifeld, A.G., Kleiman, M.B., Baddley, J.W., McKinsey, D.S., Loyd, J.E. and Kauffman, C.A., 2007. Clinical practice guidelines for the management of patients with histoplasmosis: 2007 update by the Infectious Diseases Society of America. *Clinical Infectious Diseases*, 45(7), 807-825.

[57] Smith, J.A. and Kauffman, C.A., 2012. Pulmonary fungal infections. *Respirology*, 17(6), 913-926.

[58] Porollo, A., Meller, J., Joshi, Y., Jaiswal, V., George Smulian, A. and T Cushion, M., 2012. Analysis of current antifungal agents and their targets within the Pneumocystis carinii genome. *Current Drug Targets*, 13(12), 1575-1585.

[59] Geller, D.E., Weers, J. and Heuerding, S., 2011. Development of an inhaled dry-powder formulation of tobramycin using PulmoSphere™ technology. *Journal of Aerosol Medicine and Pulmonary Drug Delivery*, 24(4), 175-182.

[60] Döring, G., Flume, P., Heijerman, H., Elborn, J.S. and Consensus Study Group, 2012. Treatment of lung infection in patients with cystic fibrosis: current and future strategies. *Journal of Cystic Fibrosis*, 11(6), 461-479.

[61] Ehsan, Z. and Clancy, J., 2015. T100: nebulized-concentrated tobramycin formulation for treatment of Pseudomonas aeruginosa infection in cystic fibrosis patients. *Expert Opinion on Orphan Drugs*, 3(8), 933-943.

[62] Anastasi, J.K. and Thomas, F., 1994. Dealing with HIV-related pulmonary infections. *Nursing*, 24(11), 60-65.

[63] Forest Laboratories, 2011. Trial of Aeroquin versus Tobramycin Inhalation Solution (TIS) in cystic fibrosis (CF) patients, ClinicalTrials.gov [Internet]. Available from: https://clinicaltrials.gov/ct2/show/NCT01270347 (accessed on 27 February 2016).

[64] Bayer, 2008. Study to evaluate the safety and efficacy of ciprofloxacin (inhaled) in patients with cystic fibrosis, ClinicalTrials.gov [Internet]. Available from: https://clinicaltrials.gov/ct2/show/NCT00645788 (accessed on 27 February 2016).

[65] Monforte, V., Roman, A., Gavalda, J., Bravo, C., Tenorio, L., Ferrer, A., Maestre, J. and Morell, F., 2001. Nebulized amphotericin B prophylaxis for Aspergillus infection in lung transplantation: study of risk factors. *Journal of Heart and Lung Transplantation*, 20(12), 1274-1281.

[66] Sharma, A., Kumar Arya, D., Dua, M., Chhatwal, G.S. and Johri, A.K., 2012. Nano-technology for targeted drug delivery to combat antibiotic resistance. *Expert Opinion Drug Delivery*, 9, 1325–1332.

[67] Beyth, N., Houri-Haddad, Y., Domb, A., Khan, W. and Hazan, R., 2015. Alternative antimicrobial approach: nano-antimicrobial materials. *Evidence-Based Complementary and Alternative Medicine*, 1-16.

[68] Stewart, P.S. and Costerton, J.W., 2001. Antibiotic resistance of bacteria in biofilms. *Lancet*, 358(9276), 135-138.

[69] Costerton, J.W., Stewart, P.S. and Greenberg, E.P., 1999. Bacterial biofilms: a common cause of persistent infections. *Science*, 284(5418), 1318-1322.

[70] Solano, C., Echeverz, M. and Lasa, I., 2014. Biofilm dispersion and quorum sensing. *Current Opinion in Microbiology*, 18, 96-104.

[71] Kulka, K., Hatfull, G. and Ojha, A.K., 2012. Growth of Mycobacterium tuberculosis biofilms. *JoVE (Journal of Visualized Experiments*), 60, e3820-e3820.

[72] Molloy, S., 2008. Biofilms: New hide-out for TB? *Nature Reviews Microbiology*, 6(7), 500.

[73] Fanning, S. and Mitchell, A.P., 2012. Fungal biofilms. *PLoS Pathogens*, 8(4), p.e1002585, 1-4.

[74] World Health Organization, 2014, April. WHO's first global report on antibiotic resistance reveals serious, worldwide threat to public health. In antimicrobial resistance–global surveillance report. *Virtual Press Conference* (Vol. 30).

[75] Smith, J.P., 2011. Nanoparticle delivery of anti-tuberculosis chemotherapy as a potential mediator against drug-resistant tuberculosis. *Yale Journal of Biology and Medicine*, 84(4), 361-369.

[76] Shafer, W.M. and Folster, J.P., 2006. Towards an understanding of chromosomally mediated penicillin resistance in Neisseria gonorrhoeae: evidence for a porin-efflux pump collaboration. *Journal of Bacteriology*, 188(7), 2297-2299.

[77] Speer, B.S., Shoemaker, N.B. and Salyers, A.A., 1992. Bacterial resistance to tetracycline: mechanisms, transfer, and clinical significance. *Clinical Microbiology Reviews*, 5(4), 387-399.

[78] Kong, K.F., Schneper, L. and Mathee, K., 2010. Beta-lactam antibiotics: from antibiosis to resistance and bacteriology. *Acta Pathologica, Microbiologica et Immunologica Scandinavica (APMIS)*, 118(1), 1-36.

[79] Jacoby, G.A., 2005. Mechanisms of resistance to quinolones. *Clinical Infectious Diseases*, 41(Supplement 2), S120-S126.

[80] Springer, B., Kidan, Y.G., Prammananan, T., Ellrott, K., Böttger, E.C. and Sander, P., 2001. Mechanisms of streptomycin resistance: selection of mutations in the 16S rRNA gene conferring resistance. *Antimicrobial Agents and Chemotherapy*, 45(10), 2877-2884.

[81] Wei, C.J., Lei, B., Musser, J.M. and Tu, S.C., 2003. Isoniazid activation defects in recombinant Mycobacterium tuberculosis catalase-peroxidase (KatG) mutants evident in InhA inhibitor production. *Antimicrobial Agents and Chemotherapy*, 47(2), 670-675.

[82] Ahmad, S. and Mokaddas, E., 2009. Recent advances in the diagnosis and treatment of multidrug-resistant tuberculosis. *Respiratory Medicine*, 103(12), 1777-1790.

[83] Fernández, L. and Hancock, R.E., 2012. Adaptive and mutational resistance: role of porins and efflux pumps in drug resistance. *Clinical Microbiology Reviews*, 25(4), 661-681.

[84] Murgia, X., De Souza Carvalho, C. and Lehr, C.M., 2014. Overcoming the pulmonary barrier: new insights to improve the efficiency of inhaled therapeutics. E*uropean Journal of Nanomedicine*, 6(3), 157-169.

[85] Kater, A., Henke, M.O. and Rubin, B.K., 2007. The role of DNA and actin polymers on the polymer structure and rheology of cystic fibrosis sputum and depolymerization by gelsolin or thymosin beta 4. *Annals of the New York Academy of Sciences*, 1112(1), 140-153.

[86] O'Donnell, A.E., 2008. Bronchiectasis. *Chest*, 134(4), 815-823.

[87] Hadinoto, K. and Cheow, W.S., 2014. Nano-antibiotics in chronic lung infection therapy against Pseudomonas aeruginosa. *Colloids and Surfaces B: Biointerfaces*, 116, 772-785.

[88] Hunt, B.E., Weber, A., Berger, A., Ramsey, B. and Smith, A.L., 1995. Macromolecular mechanisms of sputum inhibition of tobramycin activity. *Antimicrobial Agents and Chemotherapy*, 39(1), 34-39.

[89] Ibrahim, B.M., Tsifansky, M.D., Yang, Y. and Yeo, Y., 2011. Challenges and advances in the development of inhalable drug formulations for cystic fibrosis lung disease. *Expert Opinion on Drug Delivery*, 8(4), 451-466.

[90] Danahay, H. and Jackson, A.D., 2005. Epithelial mucus-hypersecretion and respiratory disease. *Current Drug Targets-Inflammation & Allergy*, 4(6), 651-664.

[91] Mistry, A., Stolnik, S. and Illum, L., 2015. Nose-to-brain delivery: investigation of the transport of nanoparticles with different surface characteristics and sizes in excised porcine olfactory epithelium. *Molecular Pharmaceutics*, 12(8), 2755-2766.

[92] Quintana, D.S., Westlye, L.T., Rustan, Ø.G., Tesli, N., Poppy, C.L., Smevik, H., Tesli, M., Røine, M., Mahmoud, R.A., Smerud, K.T. and Djupesland, P.G., 2015. Low-dose oxytocin delivered intranasally with Breath Powered device affects social-cognitive behavior: a randomized four-way crossover trial with nasal cavity dimension assessment. *Translational Psychiatry*, 5(7), p.e602, 1-9.

[93] Djupesland, P.G., Messina, J.C. and Mahmoud, R.A., 2014. The nasal approach to delivering treatment for brain diseases: an anatomic, physiologic, and delivery technology overview. *Therapeutic Delivery*, 5(6), 709-733.

[94] Kyeong-Ryoon, L.E., Maeng, H.J., Jung-Byung, C.H., Chong, S., Dae-Duk, K.I., Chang-Koo, S.H. and Chung, S.J., 2010. Lack of a primary physicochemical determinant in the direct transport of drugs to the brain after nasal administration in rats: potential

involvement of transporters in the pathway. *Drug Metabolism and Pharmacokinetics*, 25(5), 430-441.

[95] Kozlovskaya, L., Abou-Kaoud, M. and Stepensky, D., 2014. Quantitative analysis of drug delivery to the brain via nasal route. *Journal of Controlled Release*, 189, 133-140.

[96] Ruigrok, M.J. and de Lange, E.C., 2015. Emerging insights for translational pharmacokinetic and pharmacokinetic-pharmacodynamic studies: towards prediction of nose-to-brain transport in humans. *AAPS*, 17(3), 493-505.

[97] Sakane, T., Akizuki, M., Taki, Y., Yamashita, S., Sezaki, H. and Nadai, T., 1995. Direct drug transport from the rat nasal cavity to the cerebrospinal fluid: the relation to the molecular weight of drugs. *Journal of Pharmacy and Pharmacology*, 47(5), 379-381.

[98] Sakane, T., Akizuki, M., Yamashita, S., Sezaki, H. and Nadai, T., 1994. Direct drug transport from the rat nasal cavity to the cerebrospinal fluid: the relation to the dissociation of the drug. *Journal of Pharmacy and Pharmacology*, 46(5), 378-379.

[99] Sakane, T., Akizuki, M., Yamashita, S., Nadai, T., Hashida, M. and Sezaki, H., 1991. The transport of a drug to the cerebrospinal fluid directly from the nasal cavity: the relation to the lipophilicity of the drug. *Chemical and Pharmaceutical Bulletin*, 39(9), 2456-2458.

[100] Mistry, A., Stolnik, S. and Illum, L., 2009. Nanoparticles for direct nose-to-brain delivery of drugs. *International Journal of Pharmaceutics*, 379(1), 146-157.

[101] Van Woensel, M., Wauthoz, N., Rosière, R., Amighi, K., Mathieu, V., Lefranc, F., Van Gool, S.W. and De Vleeschouwer, S., 2013. Formulations for intranasal delivery of pharmacological agents to combat brain disease: a new opportunity to tackle GBM? *Cancers*, 5(3), 1020-1048.

[102] Malhotra, M., Tomaro-Duchesneau, C., Saha, S. and Prakash, S., 2014. Intranasal delivery of chitosan–siRNA nanoparticle formulation to the brain. *Drug Delivery System*, 233-247.

[103] Gao, X., Tao, W., Lu, W., Zhang, Q., Zhang, Y., Jiang, X. and Fu, S., 2006. Lectin-conjugated PEG–PLA nanoparticles: preparation and brain delivery after intranasal administration. *Biomaterials*, 27(18), 3482-3490.

[104] Wen, Z., Yan, Z., Hu, K., Pang, Z., Cheng, X., Guo, L., Zhang, Q., Jiang, X., Fang, L. and Lai, R., 2011. Odorranalectin-conjugated nanoparticles: preparation, brain delivery and pharmacodynamic study on Parkinson's disease following intranasal administration. *Journal of Controlled Release*, 151(2), 131-138.

[105] Wu, H., Hu, K. and Jiang, X., 2008. From nose to brain: understanding transport capacity and transport rate of drugs. *Expert Opinion on Drug Delivery*, 5(10), 1159-1168.

[106] Djupesland, P.G. and Skretting, A., 2012. Nasal deposition and clearance in man: comparison of a bidirectional powder device and a traditional liquid spray pump. *Journal of Aerosol Medicine and Pulmonary Drug Delivery*, 25(5), 280-289.

[107] Djupesland, P.G., Skretting, A., Winderen, M. and Holand, T., 2006. Breath actuated device improves delivery to target sites beyond the nasal valve. *Laryngoscope*, 116(3), 466-472.

[108] Tepper, S.J., Cady, R.K., Silberstein, S., Messina, J., Mahmoud, R.A., Djupesland, P.G., Shin, P. and Siffert, J., 2015. AVP-825 Breath-Powered intranasal delivery system containing 22 mg sumatriptan powder vs 100 mg oral sumatriptan in the acute treatment

of migraines (the COMPASS study): a comparative randomized clinical trial across multiple attacks headache. *Journal of Head and Face Pain*, 55(5), 621-635.

[109] Chen, H., Chen, C.C., Acosta, C., Wu, S.Y., Sun, T. and Konofagou, E.E., 2014. A new brain drug delivery strategy: focused ultrasound-enhanced intranasal drug delivery. *PloS One*, 9(10), p.e108880, 1-8.

[110] Chen, H., Yang, G.Z.X., Getachew, H., Acosta, C., Sánchez, C.S. and Konofagou, E.E., 2016. Focused ultrasound-enhanced intranasal brain delivery of brain-derived neurotrophic factor. *Scientific Reports*, 6, 1-8.

[111] Da Fonseca, C.O., Schwartsmann, G., Fischer, J., Nagel, J., Futuro, D., Quirico-Santos, T. and Gattass, C.R., 2008. Preliminary results from a phase I/II study of perillyl alcohol intranasal administration in adults with recurrent malignant gliomas. *Surgical Neurology*, 70(3), 259-266.

[112] Djupesland, P.G., 2013. Nasal drug delivery devices: characteristics and performance in a clinical perspective—a review. *Drug Delivery and Translational Research*, 3(1), 42-62.

[113] Scheibe, M., Bethge, C., Witt, M. and Hummel, T., 2008. Intranasal administration of drugs. *Archives of Otolaryngology–Head & Neck Surgery*, 134(6), 643-646.

[114] Weber, R., Keerl, R., Radziwill, R., Schick, B., Jaspersen, D., Dshambazov, K., Mlynski, G. and Draf, W., 1999. Videoendoscopic analysis of nasal steroid distribution. *Rhinology*, 37, 69-73.

[115] Bateman, N.D., Whymark, A.D., Clifton, N.J. and Woolford, T.J., 2002. A study of intranasal distribution of azelastine hydrochloride aqueous nasal spray with different spray techniques. *Clinical Otolaryngology & Allied Sciences*, 27(5), 327-330.

[116] Newman, S.P., Moren, F. and Clarke, S.W., 1987. Deposition pattern from a nasal pump spray. *Rhinology*, 25(2), 77-82.

[117] Rudman, K.L., O'Brien, E.K. and Leopold, D.A., 2011. Radiographic distribution of drops and sprays within the sinonasal cavities. *American Journal of Rhinology & Allergy*, 25(2), 94-97.

[118] Bleier, B.S., Debnath, I., Harvey, R.J. and Schlosser, R.J., 2011. Temporospatial quantification of fluorescein-labeled sinonasal irrigation delivery. *International Forum of Allergy & Rhinology*, 1(5), 361-365.

[119] Si, X.A., Xi, J., Kim, J., Zhou, Y. and Zhong, H., 2013. Modeling of release position and ventilation effects on olfactory aerosol drug delivery. *Respiratory Physiology & Neurobiology*, 186(1), 22-32.

[120] Suman, J.D., Laube, B.L. and Dalby, R., 1999. Comparison of nasal deposition and clearance of aerosol generated by a nebulizer and an aqueous spray pump. *Pharmaceutical Research*, 16(10), 1648-1652.

[121] Pardeshi, C.V., Vanjari, Y.H. and Kulkarni, A.D., 2015. Novel nasal devices for the efficient drug delivery: a systemic review. *Indian Journal of Novel Drug Delivery,* 7(1), 1-9.

[122] Craft, S., Baker, L.D., Montine, T.J., Minoshima, S., Watson, G.S., Claxton, A., Arbuckle, M., Callaghan, M., Tsai, E., Plymate, S.R. and Green, P.S., 2012. Intranasal

insulin therapy for Alzheimer disease and amnestic mild cognitive impairment: a pilot clinical trial. *Archives of Neurology*, 69(1), 29-38.

[123] Hoekman, J., Brunelle, A., Hite, M., Kim, M. and Fuller, C, 2013. SPECT imaging of direct nose-to-brain transfer of MAG-3 in Man. Poster presentation at *AAPS (American Association of Pharmaceutical Sciences)*. Available from http://impelnp.com/wp-content/uploads/2016/03/SPECT-imaging-of-direct-nose-brain-transfer-of-MAG-3-in-Man.pdf (accessed on 27 March 2017).

[124] Majgainya, S., Soni, S. and Bhat, P. Novel approach for nose-to-brain drug delivery bypassing blood brain barrier, 2015. *Journal of Applied Pharmaceutical Science*, 7(3), 148–163.

[125] Djupesland, P.G., Messina, J.C. and Mahmoud, R.A., 2013. Breath powered nasal delivery: a new route to rapid headache relief. Headache: *The Journal of Head and Face Pain*, 53(S2), 72-84.

[126] Cady, R.K., McAllister, P.J., Spierings, E.L., Messina, J., Carothers, J., Djupesland, P.G. and Mahmoud, R.A., 2015. A randomized, double-blind, placebo-controlled study of breath powered nasal delivery of sumatriptan powder (AVP-825) in the treatment of acute migraine (the TARGET study). *Headache: The Journal of Head and Face Pain*, 55(1), 88-100.

[127] Dale, O., Nilsen, T., Loftsson, T., Tønnesen, H.H., Klepstad, P., Kaasa, S., Holand, T. and Djupesland, P.G., 2006. Intranasal midazolam: a comparison of two delivery devices in human volunteers. *Journal of Pharmacy and Pharmacology*, 58(10), 1311-1318.

[128] Copley, M. and Kippax, P., 2012. From actuation to deposition: Particle sizing techniques for characterizing nasal drug delivery systems, *Inhalation*, 12-16.

[129] Borland, M.L., Clark, L.J. and Esson, A., 2008. Comparative review of the clinical use of intranasal fentanyl versus morphine in a paediatric emergency department. *Emergency Medicine Australasia*, 20(6), 515-520.

[130] Rickard, C., O'Meara, P., McGrail, M., Garner, D., McLean, A. and Le Lievre, P., 2007. A randomized controlled trial of intranasal fentanyl vs intravenous morphine for analgesia in the prehospital setting. *The American Journal of Emergency Medicine*, 25(8), 911-917.

[131] Saunders, M., Adelgais, K. and Nelson, D., 2010. Use of intranasal fentanyl for the relief of paediatric orthopedic trauma pain. *Academic Emergency Medicine*, 17(11), 1155-1161.

[132] Barrett, M.J., Cronin, J., Murphy, A., McCoy, S., Hayden, J., an Fhailí, S., Grant, T., Wakai, A., McMahon, C., Walsh, S. and O'Sullivan, R., 2012. Intranasal fentanyl versus intravenous morphine in the emergency department treatment of severe painful sickle cell crises in children: study protocol for a randomised controlled trial. *Trials*, 13(1), 74-80.

[133] Borland, M., Jacobs, I., King, B. and O'brien, D., 2007. A randomized controlled trial comparing intranasal fentanyl to intravenous morphine for managing acute pain in children in the emergency department. *Annals of Emergency Medicine*, 49(3), 335-340.

[134] Holsti, M., Sill, B.L., Firth, S.D., Filloux, F.M., Joyce, S.M. and Furnival, R.A., 2007. Prehospital intranasal midazolam for the treatment of paediatric seizures. *Paediatric Emergency Care*, 23(3), 148-153.

[135] Lahat, E., Goldman, M., Barr, J., Bistritzer, T. and Berkovitch, M., 2000. Comparison of intranasal midazolam with intravenous diazepam for treating febrile seizures in children: prospective randomised study. *British Medical Journal*, 321(7253), 83-86.

[136] Inokuchi, R., Ohashi-Fukuda, N., Nakamura, K., Wada, T., Gunshin, M., Kitsuta, Y., Nakajima, S. and Yahagi, N., 2015. Comparison of intranasal and intravenous diazepam on status epilepticus in stroke patients: a retrospective cohort study. *Medicine*, 94(7), e555, 1-4.

[137] Doe-Simkins, M., Walley, A.Y., Epstein, A. and Moyer, P., 2009. Saved by the nose: bystander-administered intranasal naloxone hydrochloride for opioid overdose. *American Journal of Public Health*, 99(5), 788-791.

[138] Domínguez, A., Álvarez, A., Hilario, E., Suarez-Merino, B. and Goñi-de-Cerio, F., 2013. Central nervous system diseases and the role of the blood-brain barrier in their treatment. *Neuroscience Discovery*, 1(1), 1-11.

[139] VanGilder, R.L., Rosen, C.L., Barr, T.L. and Huber, J.D., 2011. Targeting the neurovascular unit for treatment of neurological disorders. *Pharmacology & Therapeutics*, 130(3), 239-247.

[140] Lin, M.T. and Beal, M.F., 2006. Mitochondrial dysfunction and oxidative stress in neurodegenerative diseases. *Nature*, 443(7113), 787-795.

[141] World Health Organization, 2015. The top 10 causes of death [Internet], *World Health Organization*. Available from http://www.who.int/mediacentre/factsheets/fs310/en/ (accessed March 29, 2017).

[142] Kumar, A. and Singh, A., 2015. A review on Alzheimer's disease pathophysiology and its management: an update. *Pharmacological Reports*, 67(2), 195-203.

[143] Kalia, L.V. and Lang, A.E., 2015. Parkinson's disease. *Lancet*, 386(9996), 896–912.

[144] Di Carlo, M., Giacomazza, D., Picone, P., Nuzzo, D. and San Biagio, P.L., 2012. Are oxidative stress and mitochondrial dysfunction the key players in the neurodegenerative diseases? *Free Radical Research*, 46(11), 1327-1338.

[145] Linazasoro, G., 2009. A global view of Parkinson's disease pathogenesis: Implications for natural history and neuroprotection. *Parkinsonism and Related Disorders*, 15(6), 401-405.

[146] Wang, H., Xu, T., Jiang, Y., Xu, H., Yan, Y., Fu, D. and Chen, J., 2015. The challenges and the promise of molecular targeted therapy in malignant gliomas. *Neoplasia*, 17(3), 239-255.

[147] Juillerat-Jeanneret, L., 2008. The targeted delivery of cancer drugs across the blood–brain barrier: chemical modifications of drugs or drug-nanoparticles? *Drug Discovery Today*, 13(23), 1099-1106.

[148] National Cancer Intelligence Network, 2013. Astrocytic brain tumours: survival rates in England. Available from http://www.ncin.org.uk/publications/data_briefings/astrocytic_brain_tumours_survival_rates_in_england (accessed February 24, 2017).

[149] Gao, H., 2016. Progress and perspectives on targeting nanoparticles for brain drug delivery. *Acta Pharmaceutica Sinica B*, 6(4), 268-286.

[150] Abbott, N.J., 2013. Blood–brain barrier structure and function and the challenges for CNS drug delivery. *Journal of Inherited Metabolic Disease*, 36(3), 437-449.

[151] Deeken, J.F. and Löscher, W., 2007. The blood-brain barrier and cancer: transporters, treatment, and Trojan horses. *Clinical Cancer Research*, 13(6), 1663-1674.

[152] Misra, A., Ganesh, S., Shahiwala, A. and Shah, S.P., 2003. Drug delivery to the central nervous system: a review. *Journal of Pharmacy & Pharmaceutical Sciences*, 6(2), 252-273.

[153] Yang, F.Y., Lin, Y.S., Kang, K.H. and Chao, T.K., 2011. Reversible blood–brain barrier disruption by repeated transcranial focused ultrasound allows enhanced extravasation. *Journal of Controlled Release*, 150(1), 111-116.

[154] Marianecci, C., Di Marzio, L., Rinaldi, F., Carafa, M. and Alhaique, F., 2011. Pulmonary delivery: innovative approaches and perspectives. *Journal of Biomaterials and Nanobiotechnology*, 2(5), 567-575.

[155] Pandey, S., Choudhary, A., Patel, B., Mahalaxmi, R., Devmurari, V. and Jivani, N.P., 2009. Pulmonary delivery as a route for insulin. *International Journal of PharmTech Research*, 1(4), 1190-1197.

[156] Madhav, S., Dwivedi, G. Pulmonary drug delivery: a review, PharmaTutor [Internet]. Available from http://www.pharmatutor.org/articles/pulmonary-drug-delivery-a-review? (accessed March 10, 2017).

[157] Lai, S.K., Wang, Y.Y. and Hanes, J., 2009. Mucus-penetrating nanoparticles for drug and gene delivery to mucosal tissues. *Advanced Drug Delivery Reviews*, 61(2), 158-171.

[158] Ferreira, A.J., Cemlyn-Jones, J. and Cordeiro, C.R., 2013. Nanoparticles, nanotechnology and pulmonary nanotoxicology. *Revista Portuguesa de Pneumologia (English Edition)*, 19(1), 28-37.

[159] Andujar, P., Lanone, S., Brochard, P. and Boczkowski, J., 2011. Respiratory effects of manufactured nanoparticles. *Revue des Maladies Respiratoires*, 28(8), e66-e75.

[160] Li, J.J.E., Muralikrishnan, S., Ng, C.T., Yung, L.Y.L. and Bay, B.H., 2010. Nanoparticle-induced pulmonary toxicity. *Experimental Biology and Medicine*, 235(9), 1025-1033.

[161] Beck-Broichsitter, M., Ruppert, C., Schmehl, T., Guenther, A., Betz, T., Bakowsky, U., Seeger, W., Kissel, T. and Gessler, T., 2011. Biophysical investigation of pulmonary surfactant surface properties upon contact with polymeric nanoparticles in vitro. *Nanomedicine: Nanotechnology, Biology and Medicine*, 7(3), 341-350.

[162] Mansour, H.M., Rhee, Y.S. and Wu, X., 2009. Nanomedicine in pulmonary delivery. *International Journal of Nanomedicine*, 4, 299-319.

[163] Marttin, E., Schipper, N.G., Verhoef, J.C. and Merkus, F.W., 1998. Nasal mucociliary clearance as a factor in nasal drug delivery. *Advanced Drug Delivery Reviews*, 29(1), 13-38.

[164] Gizurarson, S., 2015. The effect of cilia and the mucociliary clearance on successful drug delivery. *Biological and Pharmaceutical Bulletin*, 38(4), 497-506.

[165] Wang, B., Feng, W.Y., Wang, M., Shi, J.W., Zhang, F., Ouyang, H., Zhao, Y.L., Chai, Z.F., Huang, Y.Y., Xie, Y.N. and Wang, H.F., 2007. Transport of intranasally instilled fine Fe2O3 particles into the brain: micro-distribution, chemical states, and histopathological observation. *Biological Trace Element Research*, 118(3), 233-243.

[166] Puri, A., Loomis, K., Smith, B., Lee, J.H., Yavlovich, A., Heldman, E. and Blumenthal, R., 2009. Lipid-based nanoparticles as pharmaceutical drug carriers: from concepts to

clinic, in *Critical Reviews™ in Therapeutic Drug Carrier Systems*, Sachdeva, M. (editor), 26(6), pp.523-580.

[167] Drulis-Kawa, Z. and Dorotkiewicz-Jach, A., 2010. Liposomes as delivery systems for antibiotics. *International Journal of Pharmaceutics*, 387(1), 187-198.

[168] Sercombe, L., Veerati, T., Moheimani, F., Wu, S.Y., Sood, A.K. and Hua, S., 2015. Advances and challenges of liposome assisted drug delivery. *Frontiers in Pharmacology*, 6(286), 1-13.

[169] Pinto-Alphandary, H., Andremont, A. and Couvreur, P., 2000. Targeted delivery of antibiotics using liposomes and nanoparticles: research and applications. *International Journal of Antimicrobial Agents*, 13(3), 155-168.

[170] Omri, A., Suntres, Z.E. and Shek, P.N., 2002. Enhanced activity of liposomal polymyxin B against Pseudomonas aeruginosa in a rat model of lung infection. *Biochemical Pharmacology*, 64(9), 1407-1413.

[171] Vyas, S.P. and Khar, R.K., 2004. *Targeted & Controlled Drug Delivery: Novel Carrier Systems*. CBS publishers & distributors, New Delhi.

[172] Bridges, P.A. and Taylor, K.M.G., 1998. Nebulisers for the generation of liposomal aerosols. *International Journal of Pharmaceutics*, 173(1), 117-125.

[173] Farr, S.J., Kellaway, I.W., Parry-Jones, D.R. and Woolfrey, S.G., 1985. 99m-Technetium as a marker of liposomal deposition and clearance in the human lung. *International Journal of Pharmaceutics*, 26(3), 303-316.

[174] Deshpande, D., Blanchard, J., Srinivasan, S., Fairbanks, D., Fujimoto, J., Sawa, T., Wiener-Kronish, J., Schreier, H. and Gonda, I., 2002. Aerosolization of lipoplexes using AERx® pulmonary delivery system. *The AAPS Journal*, 4(3), 12-21.

[175] McLachlan, G., Baker, A., Tennant, P., Gordon, C., Vrettou, C., Renwick, L., Blundell, R., Cheng, S.H., Scheule, R.K., Davies, L. and Painter, H., 2007. Optimizing aerosol gene delivery and expression in the ovine lung. *Molecular Therapy*, 15(2), 348-354.

[176] Jain, N.K., Mishra, V. and Mehra, N.K., 2013. Targeted drug delivery to macrophages. *Expert Opinion on Drug Delivery*, 10(3), 353-367.

[177] Svenson, S. and Prud'homme, R.K. (editors), 2012. *Multifunctional Nanoparticles for Drug Delivery Applications: imaging, targeting, and delivery*. Springer Science & Business Media, New York.

[178] Bridges, P.A. and Taylor, K.M.G., 2000. An investigation of some of the factors influencing the jet nebulisation of liposomes. *International Journal of Pharmaceutics*, 204(1), 69-79.

[179] Chattopadhyay, S., Ehrman, S.H., Bellare, J. and Venkataraman, C., 2012. Morphology and bilayer integrity of small liposomes during aerosol generation by air-jet nebulisation. *Journal of Nanoparticle Research,* 14(4), 779-794.

[180] Kleemann, E., Schmehl, T., Gessler, T., Bakowsky, U., Kissel, T. and Seeger, W., 2007. Iloprost-containing liposomes for aerosol application in pulmonary arterial hypertension: formulation aspects and stability. *Pharmaceutical Research*, 24(2), 277-287.

[181] Radhakrishnan, R., Mihalko, P.J. and Abra, R.M., Liposome Technology, Inc., 1990. Method and apparatus for administering dehydrated liposomes by inhalation. *U.S. Patent 4,895,719*.

[182] Taylor, K.M. and Newton, J.M., 1992. Liposomes for controlled delivery of drugs to the lung. *Thorax*, 47(4), 257-259.

[183] Taylor, E. and Webster, T.J., 2011. Reducing infections through nanotechnology and nanoparticles. *International Journal of Nanomedicine*, 6, 1463-1473.

[184] Salih, S., Kharal, M., Qahtani, M., Dahneem, L. and Nohair, S., 2008. Acute interstitial nephritis induced by intermittent use of rifampicin in patient with brucellosis. *Saudi Journal of Kidney Diseases and Transplantation*, 19(3), 450-450.

[185] Prakash, J., Kumar, N.S., Saxena, R.K. and Verma, U., 2001. Acute renal failure complicating rifampicin therapy. *The Journal of the Association of Physicians of India*, 49, 877-880.

[186] Covic, A., Goldsmith, D.J., Segall, L., Stoicescu, C., Lungu, S., Volovat, C. and Covic, M., 1998. Rifampicin-induced acute renal failure: a series of 60 patients. *Nephrology Dialysis Transplantation*, 13(4), 924-929.

[187] Kunimoto, D., Warman, A., Beckon, A., Doering, D. and Melenka, L., 2003. Severe hepatotoxicity associated with rifampin-pyrazinamide preventative therapy requiring transplantation in an individual at low risk for hepatotoxicity. *Clinical Infectious Diseases,* 36(12), e158-e161.

[188] Min, H.K., Kim, E.O., Lee, S.J., Chang, Y.K., Suh, K.S., Yang, C.W., Kim, S.Y. and Hwang, H.S., 2013. Rifampin-associated tubulointersititial nephritis and Fanconi syndrome presenting as hypokalemic paralysis. *BMC Nephrology*, 14(1), 13-17.

[189] Deol, P., Khuller, G.K. and Joshi, K., 1997. Therapeutic efficacies of isoniazid and rifampin encapsulated in lung-specific stealth liposomes against Mycobacterium tuberculosis infection induced in mice. *Antimicrobial Agents and Chemotherapy*, 41(6), 1211-1214.

[190] Changsan, N., Nilkaeo, A., Pungrassami, P. and Srichana, T., 2009. Monitoring safety of liposomes containing rifampicin on respiratory cell lines and in vitro efficacy against Mycobacterium bovis in alveolar macrophages. *Journal of Drug Targeting*, 17(10), 751-762.

[191] Manca, M.L., Sinico, C., Maccioni, A.M., Diez, O., Fadda, A.M. and Manconi, M., 2012. Composition influence on pulmonary delivery of rifampicin liposomes. *Pharmaceutics*, 4(4), 590-606.

[192] Migliore, M.M., Vyas, T.K., Campbell, R.B., Amiji, M.M. and Waszczak, B.L., 2010. Brain delivery of proteins by the intranasal route of administration: a comparison of cationic liposomes versus aqueous solution formulations. *Journal of Pharmaceutical Sciences*, 99(4), 1745-1761.

[193] Vieira, D.B. and Gamarra, L.F., 2016. Getting into the brain: liposome-based strategies for effective drug delivery across the blood–brain barrier. *International Journal of Nanomedicine*, 11, 5381-5414.

[194] Li, W., Zhou, Y., Zhao, N., Hao, B., Wang, X. and Kong, P., 2012. Pharmacokinetic behavior and efficiency of acetylcholinesterase inhibition in rat brain after intranasal administration of galanthamine hydrobromide loaded flexible liposomes. *Environmental Toxicology and Pharmacology*, 34(2), 272-279.

[195] Arumugam, K., Subramanian, G., Mallayasamy, S., Averineni, R., Reddy, M. and Udupa, N., 2008. A study of rivastigmine liposomes for delivery into the brain through intranasal route. *Acta Pharmaceutica*, 58(3), 287-297.

[196] Zheng, X., Shao, X., Zhang, C., Tan, Y., Liu, Q., Wan, X., Zhang, Q., Xu, S. and Jiang, X., 2015. Intranasal H102 peptide-loaded liposomes for brain delivery to treat Alzheimer's disease. *Pharmaceutical Research*, 32(12), 3837-3849.

[197] Spuch, C. and Navarro, C., 2011. Liposomes for targeted delivery of active agents against neurodegenerative diseases (Alzheimer's disease and Parkinson's disease). *Journal of Drug Delivery*, 1-11.

[198] Traini, D. and Young, P.M., 2009. Delivery of antibiotics to the respiratory tract: an update. *Expert Opinion on Drug Delivery*, 6(9), 897-905.

[199] Lasic, D.D. and Papahadjopoulos, D. (editors), 1998. *Medical Applications of Liposomes*, Elsevier Science, Amsterdam.

[200] Donald, P.R., Sirgel, F.A., Venter, A., Smit, E., Parkin, D.P., Van de Wal, B.W. and Mitchison, D.A., 2001. The early bactericidal activity of a low-clearance liposomal amikacin in pulmonary tuberculosis. *Journal of Antimicrobial Chemotherapy*, 48(6), 877-880.

[201] Schiffelers, R., Storm, G. and Bakker-Woudenberg, I., 2001. Liposome-encapsulated aminoglycosides in pre-clinical and clinical studies. *Journal of Antimicrobial Chemotherapy*, 48(3), 333-344.

[202] Beaulac, C., Clement-Major, S., Hawari, J. and Lagacé, J., 1996. Eradication of mucoid Pseudomonas aeruginosa with fluid liposome-encapsulated tobramycin in an animal model of chronic pulmonary infection. *Antimicrobial Agents and Chemotherapy*, 40(3), 665-669.

[203] Xia, D., Sun, W.K., Tan, M.M., Zhang, M., Ding, Y., Liu, Z.C., Su, X. and Shi, Y., 2015. Aerosolized amphotericin B as prophylaxis for invasive pulmonary aspergillosis: a meta-analysis. *International Journal of Infectious Diseases*, 30, 78-84.

[204] Stone, N.R., Bicanic, T., Salim, R. and Hope, W., 2016. Liposomal Amphotericin B (AmBisome®): A review of the pharmacokinetics, pharmacodynamics, clinical experience and future directions. *Drugs*, 76(4), 485-500.

[205] Monforte, V., Ussetti, P., López, R., Gavaldà, J., Bravo, C., de Pablo, A., Pou, L., Pahissa, A., Morell, F. and Román, A., 2009. Nebulized liposomal amphotericin B prophylaxis for Aspergillus infection in lung transplantation: pharmacokinetics and safety. *Journal of Heart and Lung Transplantation*, 28(2), 170-175.

[206] Kirkpatrick, W.R., Najvar, L.K., Vallor, A.C., Wiederhold, N.P., Bocanegra, R., Pfeiffer, J., Perkins, K., Kugler, A.R., Sweeney, T.D. and Patterson, T.F., 2012. Prophylactic efficacy of single dose pulmonary administration of amphotericin B inhalation powder in a guinea pig model of invasive pulmonary aspergillosis. *Journal of Antimicrobial Chemotherapy*, 67(4), 970-976.

[207] Malcolmson, R.J., Sweeney, T.D., Miller, D.P., Kugler, A.R., Washco, K., Han, D., Gadiraju, R. and Nakhjiri, F., Novartis Pharma, 2006. Compositions Comprising Amphotericin B. *U.S. Patent Application 12/087,142*.

[208] Pinheiro, M., Lúcio, M., Lima, J.L. and Reis, S., 2011. Liposomes as drug delivery systems for the treatment of TB. *Nanomedicine*, 6(8), 1413-1428.

[209] Pandey, R., Sharma, S. and Khuller, G.K., 2004. Nebulization of liposome encapsulated antitubercular drugs in guinea pigs. *International Journal of Antimicrobial Agents*, 24(1), 93-94.

[210] Deol, P. and Khuller, G.K., 1997. Lung specific stealth liposomes: stability, biodistribution and toxicity of liposomal antitubercular drugs in mice. B*iochimica et Biophysica Acta (BBA)-General Subjects*, 1334(2), 161-172.

[211] Vyas, S.P., Kannan, M.E., Jain, S., Mishra, V. and Singh, P., 2004. Design of liposomal aerosols for improved delivery of rifampicin to alveolar macrophages. *International Journal of Pharmaceutics*, 269(1), 37-49.

[212] Wijagkanalan, W., Kawakami, S., Takenaga, M., Igarashi, R., Yamashita, F. and Hashida, M., 2008. Efficient targeting to alveolar macrophages by intratracheal administration of mannosylated liposomes in rats. *Journal of Controlled Release*, 125(2), 121-130.

[213] Chono, S., Kaneko, K., Yamamoto, E., Togami, K. and Morimoto, K., 2010. Effect of surface-mannose modification on aerosolized liposomal delivery to alveolar macrophages. *Drug Development and Industrial Pharmacy*, 36(1), 102-107.

[214] Oh, Y.K., Nix, D.E. and Straubinger, R.M., 1995. Formulation and efficacy of liposome-encapsulated antibiotics for therapy of intracellular Mycobacterium avium infection. *Antimicrobial Agents and Chemotherapy*, 39(9), 2104-2111.

[215] Al Asmari, A.K., Ullah, Z., Tariq, M. and Fatani, A., 2015. Preparation, characterization, and *in vivo* evaluation of intranasally administered liposomal formulation of donepezil. *Drug Design, Development and Therapy*, 10, 205-215.

[216] Smola, M., Vandamme, T. and Sokolowski, A., 2007. Nanocarriers as pulmonary drug delivery systems to treat and to diagnose respiratory and non-respiratory diseases. *International Journal of Nanomedicine*, 3(1), 1-19.

[217] Rytting, E., Nguyen, J., Wang, X. and Kissel, T., 2008. Biodegradable polymeric nanocarriers for pulmonary drug delivery. *Expert Opinion on Drug Delivery*, 5(6), 629-639.

[218] Imbuluzqueta, E., Gamazo, C., Ariza, J. and Blanco-Prieto, M.J., 2009. Drug delivery systems for potential treatment of intracellular bacterial infections. *Frontiers in Bioscience*, 15, 397-417.

[219] Vilos, C. and Velasquez, L.A., 2012. Therapeutic strategies based on polymeric microparticles. *BioMed Research International*, 672760.

[220] Zhang, L., Pornpattananangkul, D., Hu, C.M. and Huang, C.M., 2010. Development of nanoparticles for antimicrobial drug delivery. *Current Medicinal Chemistry*, 17(6), 585-594.

[221] Skidan, I.N., Gel'perina, S.E., Severin, S.E. and Guliaev, A.E., 2002. Enhanced activity of rifampicin loaded with polybutyl cyanoacrylate nanoparticles in relation to intracellularly localized bacteria. *Antibiotics and Chemoterapy*, 48(1), 23-26.

[222] Ungaro, F., d'Angelo, I., Coletta, C., di Villa Bianca, R.D.E., Sorrentino, R., Perfetto, B., Tufano, M.A., Miro, A., La Rotonda, M.I. and Quaglia, F., 2012. Dry powders based on PLGA nanoparticles for pulmonary delivery of antibiotics: modulation of encapsulation efficiency, release rate and lung deposition pattern by hydrophilic polymers. *Journal of Controlled Release*, 157(1), 149-159.

[223] Arnold, M.M., Gorman, E.M., Schieber, L.J., Munson, E.J. and Berkland, C., 2007. NanoCipro encapsulation in monodisperse large porous PLGA microparticles. *Journal of Controlled Release*, 121(1), 100-109.

[224] Al-Ghananeem, A.M., Saeed, H., Florence, R., Yokel, R.A. and Malkawi, A.H., 2010. Intranasal drug delivery of didanosine-loaded chitosan nanoparticles for brain targeting; an attractive route against infections caused by AIDS viruses. *Journal of Drug Targeting*, 18(5), 381-388.

[225] Wang, X., Chi, N. and Tang, X., 2008. Preparation of estradiol chitosan nanoparticles for improving nasal absorption and brain targeting. *European Journal of Pharmaceutics and Biopharmaceutics*, 70(3), 735-740.

[226] Alam, S., Khan, Z.I., Mustafa, G., Kumar, M., Islam, F., Bhatnagar, A. and Ahmad, F.J., 2012. Development and evaluation of thymoquinone-encapsulated chitosan nanoparticles for nose-to-brain targeting: a pharmacoscintigraphic study. *International Journal of Nanomedicine*, 7, 5705-5718.

[227] Baltzley, S., Mohammad, A., Malkawi, A.H. and Al-Ghananeem, A.M., 2014. Intranasal drug delivery of olanzapine-loaded chitosan nanoparticles. *AAPS PharmSciTech*, 15(6), 1598-1602.

[228] Akilo, O.D., Choonara, Y.E., Strydom, A.M., Du Toit, L.C., Kumar, P., Modi, G. and Pillay, V., 2016. An in vitro evaluation of a carmustine-loaded Nano-co-plex for potential magnetic-targeted intranasal delivery to the brain. *International Journal of Pharmaceutics*, 500(1-2), 196-209.

[229] Lyu, S., Sparer, R. and Untereker, D., 2005. Analytical solutions to mathematical models of the surface and bulk erosion of solid polymers. *Journal of Polymer Science Part B: Polymer Physics*, 43(4), 383-397.

[230] Mc Callion, O.N., Taylor, K.M., Thomas, M. and Taylor, A.J., 1996. Nebulisation of monodisperse latex sphere suspensions in air jet and ultrasonic nebulisers. *International Journal of Pharmaceutics*, 133(1-2), 203-214.

[231] Dailey, L.A., Schmehl, T., Gessler, T., Wittmar, M., Grimminger, F., Seeger, W. and Kissel, T., 2003. Nebulization of biodegradable nanoparticles: impact of nebulizer technology and nanoparticle characteristics on aerosol features. *Journal of Controlled Release*, 86(1), 131-144.

[232] Sung, J.C., Pulliam, B.L. and Edwards, D.A., 2007. Nanoparticles for drug delivery to the lungs. *Trends in Biotechnology*, 25(12), 563-570.

[233] Pandey, R. and Khuller, G.K., 2005. Solid lipid particle-based inhalable sustained drug delivery system against experimental tuberculosis. *Tuberculosis*, 85(4), 227-234.

[234] Bhatt, P.C., Srivastava, P., Pandey, P., Khan, W. and Panda, B.P., 2016. Nose to brain delivery of astaxanthin-loaded solid lipid nanoparticles: fabrication, radio labeling, optimization and biological studies. *RSC Advances*, 6(12), 10001-10010.

[235] Madane, R.G. and Mahajan, H.S., 2016. Curcumin-loaded nanostructured lipid carriers (NLCs) for nasal administration: design, characterization, and *in vivo* study. *Drug Delivery*, 23(4), 1326-1334.

[236] Gilani, K., Moazeni, E., Ramezanli, T., Amini, M., Fazeli, M.R. and Jamalifar, H., 2011. Development of respirable nanomicelle carriers for delivery of amphotericin B by jet nebulization. *Journal of Pharmaceutical Sciences*, 100(1), 252-259.

[237] Vadakkan, M.V., Annapoorna, K., Sivakumar, K.C., Mundayoor, S. and Kumar, G.S., 2012. Dry powder cationic lipopolymeric nanomicelle inhalation for targeted delivery of antitubercular drug to alveolar macrophage. *International Journal of Nanomedicine*, 8, 2871-2885.

[238] Taki, H., Kanazawa, T., Akiyama, F., Takashima, Y. and Okada, H., 2012. Intranasal delivery of camptothecin-loaded Tat-modified nanomicelles for treatment of intracranial brain tumours. *Pharmaceuticals*, 5(10), 1092-1102.

[239] Kanazawa, T., Taki, H., Tanaka, K., Takashima, Y. and Okada, H., 2011. Cell-penetrating peptide-modified block copolymer micelles promote direct brain delivery via intranasal administration. *Pharmaceutical Research*, 28(9), 2130-2139.

[240] Kabanov, A.V., Batrakova, E.V. and Alakhov, V.Y., 2002. Pluronic® block copolymers as novel polymer therapeutics for drug and gene delivery. *Journal of Controlled Release*, 82(2), 189-212.

[241] La, S.B., Okano, T. and Kataoka, K., 1996. Preparation and characterization of the micelle-forming polymeric drug indomethacin-incorporated poly (ethylene oxide)–poly (β-benzyl L-aspartate) block copolymer micelles. *Journal of Pharmaceutical Sciences*, 85(1), 85-90.

[242] Sahib, M.N., Abdulameer, S.A., Darwis, Y., Peh, K.K. and Tan, Y.T., 2012. Solubilization of beclometasone dipropionate in sterically stabilized phospholipid nanomicelles (SSMs): physicochemical and in vitro evaluations. *Drug Design, Development and Therapy,* 6, 29-42.

[243] Tsapis, N., Bennett, D., Jackson, B., Weitz, D.A. and Edwards, D.A., 2002. Trojan particles: large porous carriers of nanoparticles for drug delivery. *Proceedings of the National Academy of Sciences*, 99(19), 12001-12005.

[244] Edwards, D.A., Ben-Jebria, A. and Langer, R., 1998. Recent advances in pulmonary drug delivery using large, porous inhaled particles. *Journal of Applied Physiology*, 85(2), 379-385.

[245] Garcia-Contreras, L., Fiegel, J., Telko, M.J., Elbert, K., Hawi, A., Thomas, M., VerBerkmoes, J., Germishuizen, W.A., Fourie, P.B., Hickey, A.J. and Edwards, D., 2007. Inhaled large porous particles of capreomycin for treatment of tuberculosis in a guinea pig model. *Antimicrobial Agents and Chemotherapy*, 51(8), 2830-2836.

[246] Suarez, S., O'hara, P., Kazantseva, M., Newcomer, C.E., Hopfer, R., McMurray, D.N. and Hickey, A.J., 2001. Respirable PLGA microspheres containing rifampicin for the treatment of tuberculosis: screening in an infectious disease model. *Pharmaceutical Research*, 18(9), 1315-1319.

[247] Edwards, D.A., Hanes, J., Caponetti, G., Hrkach, J., Ben-Jebria, A., Eskew, M.L., Mintzes, J., Deaver, D., Lotan, N. and Langer, R., 1997. Large porous particles for pulmonary drug delivery. *Science*, 276(5320), 1868-1872.

[248] Lester, M.K., Flume, P.A., Gray, S.L., Anderson, D. and Bowman, C.M., 2004. Nebulizer use and maintenance by cystic fibrosis patients: a survey study. *Respiratory Care*, 49(12), 1504-1508.

[249] Stass, H., Nagelschmitz, J., Willmann, S., Delesen, H., Gupta, A. and Baumann, S., 2013. Inhalation of a dry powder ciprofloxacin formulation in healthy subjects: a phase I study. *Clinical Drug Investigation*, 33(6), 419-427.

[250] Bayer, 2009. Study to evaluate the safety and pharmacokinetics of inhaled ciprofloxacin in patients with moderate to severe chronic obstructive pulmonary disease (COPD), ClinicalTrials.gov [Internet]. Available from: https://clinicaltrials.gov/ct2/show/NCT00961038 (accessed on 27 February 2016).

[251] Aradigm Corporation, 2009. Safety and efficacy study of ciprofloxacin for inhalation in patients with non-cystic fibrosis bronchiectasis "ORBIT-1", ClinicalTrials.gov [Internet]. Available from: https://clinicaltrials.gov/ct2/show/NCT00889967 (accessed on 27 February 2016).

[252] Sung, J.C., Padilla, D.J., Garcia-Contreras, L., VerBerkmoes, J.L., Durbin, D., Peloquin, C.A., Elbert, K.J., Hickey, A.J. and Edwards, D.A., 2009. Formulation and pharmacokinetics of self-assembled rifampicin nanoparticle systems for pulmonary delivery. *Pharmaceutical Research*, 26(8), 1847-1855.

[253] Alipour, M., Suntres, Z.E., Halwani, M., Azghani, A.O. and Omri, A., 2009. Activity and interactions of liposomal antibiotics in presence of polyanions and sputum of patients with cystic fibrosis. *PLoS One*, 4(5), e5724, 1-9.

[254] Ramphal, R., Lhermitte, M., Filliat, M. and Roussel, P., 1988. The binding of anti-pseudomonal antibiotics to macromolecules from cystic fibrosis sputum. *Journal of Antimicrobial Chemotherapy*, 22(4), 483-490.

[255] Forier, K., Raemdonck, K., De Smedt, S.C., Demeester, J., Coenye, T. and Braeckmans, K., 2014. Lipid and polymer nanoparticles for drug delivery to bacterial biofilms. *Journal of Controlled Release*, 190, 607-623.

[256] Pedersen, S.S., Koch, C., Heiby, N. and Rosendal, K., 1986. An epidemic spread of multiresistant Pseudomonas aeruginosa in a cystic fibrosis centre. *Journal of Antimicrobial Chemotherapy*, 17(4), 505-516.

[257] Hutabarat, R.M., Unadkat, J.D., Kushmerick, P., Aitken, M.L., Slattery, J.T. and Smith, A.L., 1991. Disposition of drugs in cystic fibrosis. III. Acetaminophen. *Clinical Pharmacology and Therapeutics*, 50(6), 695-701.

[258] Adi, H., Young, P.M., Chan, H.K., Salama, R. and Traini, D., 2010. Controlled release antibiotics for dry powder lung delivery. *Drug Development and Industrial Pharmacy*, 36(1), 119-126.

[259] Lam, J., Chan, R., Lam, K. and Costerton, J.W., 1980. Production of mucoid microcolonies by Pseudomonas aeruginosa within infected lungs in cystic fibrosis. *Infection and Immunity*, 28(2), 546-556.

[260] Omri, A., Beaulac, C., Bouhajib, M., Montplaisir, S., Sharkawi, M. and Lagace, J., 1994. Pulmonary retention of free and liposome-encapsulated tobramycin after intratracheal administration in uninfected rats and rats infected with Pseudomonas aeruginosa. *Antimicrobial Agents and Chemotherapy*, 38(5), 1090-1095.

[261] Smith, B.R. and LeFrock, J.L., 1983. Bronchial tree penetration of antibiotics. *CHEST*, 83(6), 904-908.

[262] Thomas, D.A., Myers, M.A., Wichert, B., Schreier, H. and Gonzalez-Rothi, R.J., 1991. Acute effects of liposome aerosol inhalation on pulmonary function in healthy human volunteers. *CHEST*, 99(5), 1268-1270.

[263] Mathur, V., Mudnaik, R., Barde, L., Roy, A., Shivhare, U. and Bhusari, K., 2010. Formulation and evaluation of controlled release antibiotic biodegradable implants for post operative site delivery. *Acta Pharmaceutica*, 60(1), 111-117.

[264] Fulzele, S.V., Satturwar, P.M. and Dorle, A.K., 2007. Novel biopolymers as implant matrix for the delivery of ciprofloxacin: biocompatibility, degradation, and in vitro antibiotic release. *Journal of Pharmaceutical Sciences*, 96(1), 132-144.

[265] Ramchandani, M. and Robinson, D., 1998. In vitro and *in vivo* release of ciprofloxacin from PLGA 50: 50 implants. *Journal of Controlled Release*, 54(2), 167-175.

[266] Pathak, R., Dash, R.P., Misra, M. and Nivsarkar, M., 2014. Role of mucoadhesive polymers in enhancing delivery of nimodipine microemulsion to brain via intranasal route. *Acta Pharmaceutica Sinica B*, 4(2), 151-160.

[267] Briones, E., Colino, C.I. and Lanao, J.M., 2008. Delivery systems to increase the selectivity of antibiotics in phagocytic cells. *Journal of Controlled Release*, 125(3), 210-227.

[268] Hand, W.L., King-Thompson, N.E. and Holman, J.W., 1987. Entry of roxithromycin (RU 965), imipenem, cefotaxime, trimethoprim, and metronidazole into human polymorphonuclear leukocytes. *Antimicrobial Agents and Chemotherapy*, 31(10), 1553-1557.

[269] Maurin, M. and Raoult, D., 2001. Use of aminoglycosides in treatment of infections due to intracellular bacteria. *Antimicrobial Agents and Chemotherapy*, 45(11), 2977-2986.

[270] Adams, L.B., Sinha, I., Franzblau, S.G., Krahenbuhl, J.L. and Mehta, R.T., 1999. Effective treatment of acute and chronic murine tuberculosis with liposome-encapsulated clofazimine. *Antimicrobial Agents and Chemotherapy*, 43(7), 1638-1643.

[271] Mehta, R.T., 1996. Liposome encapsulation of clofazimine reduces toxicity in vitro and *in vivo* and improves therapeutic efficacy in the beige mouse model of disseminated Mycobacterium avium-M. intracellulare complex infection. *Antimicrobial Agents and Chemotherapy*, 40(8), 1893-1902.

[272] DzAu, V.J., Mann, M.J., Morishita, R. and Kaneda, Y., 1996. Fusigenic viral liposome for gene therapy in cardiovascular diseases. *Proceedings of the National Academy of Sciences*, 93(21), 11421-11425.

[273] Cevc, G., 1991. How membrane chain-melting phase-transition temperature is affected by the lipid chain asymmetry and degree of unsaturation: an effective chain-length model. *Biochemistry*, 30(29), 7186-7193.

[274] Vidal, M. and Hoekstra, D., 1995. In vitro fusion of reticulocyte endocytic vesicles with liposomes. *Journal of Biological Chemistry*, 270(30), 17823-17829.

[275] Nicolosi, D., Scalia, M., Nicolosi, V.M. and Pignatello, R., 2010. Encapsulation in fusogenic liposomes broadens the spectrum of action of vancomycin against Gram-negative bacteria. *International Journal of Antimicrobial Agents*, 35(6), 553-558.

[276] Chong, P.L. and Choate, D., 1989. Calorimetric studies of the effects of cholesterol on the phase transition of C (18): C (10) phosphatidylcholine. *Biophysical Journal*, 55(3), 551-556.

[277] Pagès, J.M., James, C.E. and Winterhalter, M., 2008. The porin and the permeating antibiotic: a selective diffusion barrier in Gram-negative bacteria. *Nature Reviews Microbiology*, 6(12), 893-903.

[278] Hancock, R.E., 1998. Resistance mechanisms in Pseudomonas aeruginosa and other nonfermentative gram-negative bacteria. *Clinical Infectious Diseases*, 27(1), S93-S99.

[279] Hancock, R.E. and Brinkman, F.S., 2002. Function of Pseudomonas porins in uptake and efflux. *Annual Reviews in Microbiology*, 56(1), 17-38.

[280] Vila, J., Martí, S. and Sánchez-Céspedes, J., 2007. Porins, efflux pumps and multidrug resistance in Acinetobacter baumannii. *Journal of Antimicrobial Chemotherapy*, 59(6), 1210-1215.

[281] Betbeder, D., Spérandio, S., Latapie, J.P., de Nadaí, J., Etienne, A., Zajac, J.M. and Francés, B., 2000. Biovector™ nanoparticles improve antinociceptive efficacy of nasal morphine. *Pharmaceutical Research*, 17(6), 743-748.

[282] Sharma, D., Sharma, R.K., Sharma, N., Gabrani, R., Sharma, S.K., Ali, J. and Dang, S., 2015. Nose-to-brain delivery of PLGA-diazepam nanoparticles. *AAPS PharmSciTech*, 16(5), 1108-1121.

[283] Chertok, B., Moffat, B.A., David, A.E., Yu, F., Bergemann, C., Ross, B.D. and Yang, V.C., 2008. Iron oxide nanoparticles as a drug delivery vehicle for MRI monitored magnetic targeting of brain tumours. *Biomaterials*, 29(4), 487-496.

[284] Tzeng, S.Y. and Green, J.J., 2013. Therapeutic nanomedicine for brain cancer. *Therapeutic Delivery*, 4(6), 687-704.

[285] Messiaen, A.S., Forier, K., Nelis, H., Braeckmans, K. and Coenye, T., 2013. Transport of nanoparticles and tobramycin-loaded liposomes in Burkholderia cepacia complex biofilms. *PLoS One*, 8(11), p.e79220, 1-8.

[286] Suk, J.S., Lai, S.K., Wang, Y.Y., Ensign, L.M., Zeitlin, P.L., Boyle, M.P. and Hanes, J., 2009. The penetration of fresh undiluted sputum expectorated by cystic fibrosis patients by non-adhesive polymer nanoparticles. *Biomaterials*, 30(13), 2591-2597.

[287] Tang, B.C., Dawson, M., Lai, S.K., Wang, Y.Y., Suk, J.S., Yang, M., Zeitlin, P., Boyle, M.P., Fu, J. and Hanes, J., 2009. Biodegradable polymer nanoparticles that rapidly penetrate the human mucus barrier. *Proceedings of the National Academy of Sciences*, 106(46), 19268-19273.

[288] Sosnik, A., Carcaboso, Á.M., Glisoni, R.J., Moretton, M.A. and Chiappetta, D.A., 2010. New old challenges in tuberculosis: potentially effective nanotechnologies in drug delivery. *Advanced Drug Delivery Reviews,* 62(4), 547-559.

[289] Sharma, R., Saxena, D., Dwivedi, A.K. and Misra, A., 2001. Inhalable microparticles containing drug combinations to target alveolar macrophages for treatment of pulmonary tuberculosis. *Pharmaceutical Research*, 18(10), 1405-1410.

[290] Quenelle, D.C., Winchester, G.A., Staas, J.K., Barrow, E.L. and Barrow, W.W., 2001. Treatment of tuberculosis using a combination of sustained-release rifampin-loaded microspheres and oral dosing with isoniazid. *Antimicrobial Agents and Chemotherapy*, 45(6), 1637-1644.

[291] Kalluru, R., Fenaroli, F., Westmoreland, D., Ulanova, L., Maleki, A., Roos, N., Paulsen, M.M., Koster, G., Egge-Jacobsen, W., Wilson, S. and Roberg-Larsen, H., 2013. Poly

(lactide-co-glycolide)-rifampicin nanoparticles efficiently clear Mycobacterium bovis BCG infection in macrophages and remain membrane-bound in phago-lysosomes. *Journal of Cell Science*, 126(14), 3043-3054.

[292] Panyam, J. and Labhasetwar, V., 2003. Dynamics of endocytosis and exocytosis of poly (D, L-lactide-co-glycolide) nanoparticles in vascular smooth muscle cells. *Pharmaceutical Research*, 20(2), 212-220.

[293] Makino, K., Nakajima, T., Shikamura, M., Ito, F., Ando, S., Kochi, C., Inagawa, H., Soma, G.I. and Terada, H., 2004. Efficient intracellular delivery of rifampicin to alveolar macrophages using rifampicin-loaded PLGA microspheres: effects of molecular weight and composition of PLGA on release of rifampicin. *Colloids and Surfaces B: Biointerfaces*, 36(1), 35-42.

[294] Hirota, K., Hasegawa, T., Nakajima, T., Inagawa, H., Kohchi, C., Soma, G.I., Makino, K. and Terada, H., 2010. Delivery of rifampicin–PLGA microspheres into alveolar macrophages is promising for treatment of tuberculosis. *Journal of Controlled Release*, 142(3), 339-346.

[295] Barrow, E.L., Winchester, G.A., Staas, J.K., Quenelle, D.C. and Barrow, W.W., 1998. Use of microsphere technology for targeted delivery of rifampin to Mycobacterium tuberculosis-infected macrophages. A*ntimicrobial Agents and Chemotherapy*, 42(10), 2682-2689.

[296] Anisimova, Y.V., Gelperina, S.I., Peloquin, C.A. and Heifets, L.B., 2000. Nanoparticles as antituberculosis drugs carriers: effect on activity against Mycobacterium tuberculosis in human monocyte-derived macrophages. *Journal of Nanoparticle Research*, 2(2), 165-171.

[297] Cui, Z., Hsu, C.H. and Mumper, R.J., 2003. Physical characterization and macrophage cell uptake of mannan-coated nanoparticles. *Drug Development and Industrial Pharmacy*, 29(6), 689-700.

[298] Chaubey, P. and Mishra, B., 2014. Mannose-conjugated chitosan nanoparticles loaded with rifampicin for the treatment of visceral leishmaniasis. *Carbohydrate Polymers*, 101, 1101-1108.

[299] Jiang, H.L., Kang, M.L., Quan, J.S., Kang, S.G., Akaike, T., Yoo, H.S. and Cho, C.S., 2008. The potential of mannosylated chitosan microspheres to target macrophage mannose receptors in an adjuvant-delivery system for intranasal immunization. *Biomaterials*, 29(12), 1931-1939.

[300] Kumar, P.V., Asthana, A., Dutta, T. and Jain, N.K., 2006. Intracellular macrophage uptake of rifampicin loaded mannosylated dendrimers. *Journal of Drug Targeting*, 14(8), 546-556.

[301] Nimje, N., Agarwal, A., Saraogi, G.K., Lariya, N., Rai, G., Agrawal, H. and Agrawal, G.P., 2009. Mannosylated nanoparticulate carriers of rifabutin for alveolar targeting. *Journal of Drug Targeting*, 17(10), 777-787.

[302] Saraogi, G.K., Sharma, B., Joshi, B., Gupta, P., Gupta, U.D., Jain, N.K. and Agrawal, G.P., 2011. Mannosylated gelatin nanoparticles bearing isoniazid for effective management of tuberculosis. *Journal of Drug Targeting*, 19(3), 219-227.

[303] Zwicke, G.L., Mansoori, G.A. and Jeffery, C.J., 2011. Utilizing the folate receptor for active targeting of cancer nanotherapeutics. *Nano Reviews*, 3(1), 18496, 1-11.

[304] Lyons, S.A., O'Neal, J. and Sontheimer, H., 2002. Chlorotoxin, a scorpion-derived peptide, specifically binds to gliomas and tumours of neuroectodermal origin. *Glia*, 39(2), 162-173.

[305] Kwon, H.J., Cha, M.Y., Kim, D., Kim, D.K., Soh, M., Shin, K., Hyeon, T. and Mook-Jung, I., 2016. Mitochondria-targeting ceria nanoparticles as antioxidants for alzheimer's disease. *ACS Nano*, 10(2), 2860-2870.

[306] PETHEMA Foundation, Nebulized Liposomal Amphotericin B AmBisome for Prophylaxis of Invasive Pulmonary Aspergillosis, ClinicalTrials.gov. (2004). Available from http://clinicaltrials.goversushow/NCT00391014 (accessed on 27 February 2016).

[307] Fundació Sant Joan de Déu, 2012. Nebulized amphotericin B lipid complex in invasive pulmonary aspergillosis in paediatric patients with acute leukaemia, ClinicalTrials.gov [Internet]. Available from: https://clinicaltrials.gov/ct2/show/NCT01615809 (accessed on 27 February 2016).

[308] Allen, S.D., Sorensen, K.N., Neial, M.J., Durrant, C. and Proffit, R.T., 1994. Prophylactic efficacy of aerosolized liposomal (AmBisome) and non-lipsomal (Fungizone) amphotericin B in murine pulmonary aspergillosis. *Journal of Antimicrobial Chemotherapy*, 34(6), 1001-1013.

[309] Wilczewska, A.Z., Niemirowicz, K., Markiewicz, K.H. and Car, H., 2012. Nanoparticles as drug delivery systems. *Pharmacological Reports*, 64(5), 1020-1037.

[310] Bakand, S., Hayes, A. and Dechsakulthorn, F., 2012. Nanoparticles: a review of particle toxicology following inhalation exposure. *Inhalation Toxicology*, 24(2), 125-135.

[311] Respiratory therapy equipment- Part 1: Nebulizing systems and their components, British Standard EN13544-1:2007+A1:2009, 3 (accessed September 10, 2015).

[312] International Standard ISO 13320:2009 (BS ISO 13320:2009). 2009. Particle size analysis-Laser diffraction methods. Geneva: International Organization for Standardization (ISO).

[313] Sympatec GmbH, Sympatec's Laser Diffraction Sensor HELOS [Internet]. Available from http://www.sympatec.com/EN/LaserDiffraction/HELOS.html, (accessed on 05 February 2015).

[314] Lindert, S., Below, A. and Breitkreutz, J., 2014. Performance of dry powder inhalers with single dosed capsules in preschool children and adults using improved upper airway models. *Pharmaceutics*, 6(1), 36-51.

[315] Hubert, P., Nguyen-Huu, J.J., Boulanger, B., Chapuzet, E., Chiap, P., Cohen, N., Compagnon, P.A., Dewé, W., Feinberg, M., Lallier, M. and Laurentie, M., 2003. Validation des procédures analytiques quantitatives Harmonisation des démarches. *STP Pharma Pratiques*, 13(3), 101-138.

[316] Bolton, S. and Bon, C., 2009. *Pharmaceutical Statistics: Practical and Clinical Applications*. CRC Press, Fifth edition, Informa Healthcare, New York.

[317] Hubert, P., Nguyen-Huu, J.J., Boulanger, B., Chapuzet, E., Chiap, P., Cohen, N., Compagnon, P.A., Dewé, W., Feinberg, M., Lallier, M. and Laurentie, M., 2004. Harmonization of strategies for the validation of quantitative analytical procedures: a SFSTP proposal—part I. *Journal of pharmaceutical and biomedical analysis*, 36(3), 579-586.

[318] Jenke, D.R., 1996. Chromatographic method validation: A review of current practices and procedures. II. guidelines for primary validation parameters. *Journal of Liquid Chromatography & Related Technologies*, 19(5), 737-757.

[319] Merodio, M., Campanero, M.A., Mirshahi, T., Mirshahi, M. and Irache, J.M., 2000. Development of a sensitive method for the determination of ganciclovir by reversed-phase high-performance liquid chromatography. *Journal of Chromatography*, 870(1), 159-167.

[320] Halde, S., Mungantiwar, A. and Chintamaneni, M., 2011. Simple, precise and accurate HPLC method of analysis for nevirapine suspension from human plasma. *Indian Journal of Pharmaceutical Sciences*, 73(4), 416-421.

[321] Kousha, M., Tadi, R. and Soubani, A.O., 2011. Pulmonary aspergillosis: a clinical review. *European Respiratory Review*, 20(121), 156-174.

[322] Barkauskas, C.E. and Perfect, J.R., 2009. Candida pneumonia: what we know and what we don't. *Current Fungal Infection Reports*, 3(1), 21-31.

[323] Pappas, P.G., Kauffman, C.A., Andes, D.R., Clancy, C.J., Marr, K.A., Ostrosky-Zeichner, L., Reboli, A.C., Schuster, M.G., Vazquez, J.A., Walsh, T.J. and Zaoutis, T.E., 2016. Clinical practice guideline for the management of candidiasis: 2016 update by the Infectious Diseases Society of America. *Clinical Infectious Diseases*, 62(4), 409-417.

[324] Low, C.Y. and Rotstein, C., 2010. Emerging fungal infections in immunocompromised patients. *F1000 Medicine Reports*, 3, 14-22.

[325] Zmeili, O.S. and Soubani, A.O., 2007. Pulmonary aspergillosis: a clinical update. *QJM*, 100(6), 317-334.

[326] Chapman, S.W., Dismukes, W.E., Proia, L.A., Bradsher, R.W., Pappas, P.G., Threlkeld, M.G. and Kauffman, C.A., 2008. Clinical practice guidelines for the management of blastomycosis: 2008 update by the Infectious Diseases Society of America. *Clinical Infectious Diseases*, 46(12), 1801-1812.

[327] Gallis, H.A., Drew, R.H. and Pickard, W.W., 1990. Amphotericin B: 30 years of clinical experience. *Review of Infectious Diseases*, 12(2), 308-329.

[328] Saravolatz, L.D., Ostrosky-Zeichner, L., Marr, K.A., Rex, J.H. and Cohen, S.H., 2003. Amphotericin B: time for a new "gold standard". *Clinical Infectious Diseases*, 37(3), 415-425.

[329] AL-Quadeib, B.T., Radwan, M.A., Siller, L., Horrocks, B. and Wright, M.C., 2015. Stealth Amphotericin B nanoparticles for oral drug delivery: In vitro optimization. *Saudi Pharmaceutical Journal*, 23(3), 290-302.

[330] Moen, M.D., Lyseng-Williamson, K.A. and Scott, L.J., 2009. Liposomal amphotericin B. *Drugs*, 69(3), 361-392.

[331] Goodwin, S.D., Cleary, J.D., Walawander, C.A., Taylor, J.W. and Grasela, T.H., 1995. Pretreatment regimens for adverse events related to infusion of amphotericin B. *Clinical Infectious Diseases*, 20(4), 755-761.

[332] Vertut-Croquin, A., Bolard, J., Chabbert, M. and Gary-Bobo, C., 1983. Differences in the interaction of the polyene antibiotic amphotericin B with cholesterol-or ergosterol-containing phospholipid vesicles. A circular dichroism and permeability study. *Biochemistry*, 22(12), 2939-2944.

[333] Laniado-Laborín, R. and Cabrales-Vargas, M.N., 2009. Amphotericin B: side effects and toxicity. *Revista Iberoamericana de Micología*, 26(4), 223-227.

[334] Torrado, J.J., Espada, R., Ballesteros, M.P. and Torrado-Santiago, S., 2008. Amphotericin B formulations and drug targeting. *Journal of Pharmaceutical Sciences*, 97(7), 2405-2425.

[335] Veerareddy, P.R. and Vobalaboina, V., 2004. Lipid-based formulations of amphotericin B. *Drugs of Today*, 40(2), 133-146.

[336] Hamill, R.J., 2013. Amphotericin B formulations: a comparative review of efficacy and toxicity. *Drugs*, 73(9), 919-934.

[337] Wingard, J.R., Kubilis, P., Lee, L., Yee, G., White, M., Louise, W., Bowden, R., Anaissie, E., Hiemenz, J. and Lister, J., 1999. Clinical significance of nephrotoxicity in patients treated with amphotericin B for suspected or proven aspergillosis. *Clinical Infectious Diseases*, 29(6), 1402-1407.

[338] Mayer, J., Doubek, M., Doubek, J., Horký, D., Scheer, P. and Štěpánek, M., 2002. Reduced nephrotoxicity of conventional amphotericin B therapy after minimal nephroprotective measures: animal experiments and clinical study. *Journal of Infectious Diseases*, 186(3), 379-388.

[339] Bates, D.W., Su, L., Yu, D.T., Chertow, G.M., Seger, D.L., Gomes, D.R.J., Dasbach, E.J. and Platt, R., 2001. Mortality and costs of acute renal failure associated with amphotericin B therapy. *Clinical Infectious Diseases*, 32(5), 686-693.

[340] Zager, R.A., O'quigley, J., Zager, B.K., Alpers, C.E., Shulman, H.M., Gamelin, L.M., Stewart, P. and Thomas, E.D., 1989. Acute renal failure following bone marrow transplantation: a retrospective study of 272 patients. *American Journal of Kidney Diseases*, 13(3), 210-216.

[341] Harbarth, S., Burke, J.P., Lloyd, J.F., Evans, R.S., Pestotnik, S.L. and Samore, M.H., 2002. Clinical and economic outcomes of conventional amphotericin B-associated nephrotoxicity. *Clinical Infectious Diseases*, 35(12), e120-e127.

[342] Swenson, C.E., Perkins, W.R., Roberts, P., Ahmad, I., Stevens, R., Stevens, D.A. and Janoff, A.S., 1998. In vitro and *in vivo* antifungal activity of amphotericin B lipid complex: are phospholipases important? *Antimicrobial Agents and Chemotherapy*, 42(4), 767-771.

[343] Adedoyin, A., Swenson, C.E., Bolcsak, L.E., Hellmann, A., Radowska, D., Horwith, G., Janoff, A.S. and Branch, R.A., 2000. A pharmacokinetic study of amphotericin B lipid complex injection (ABELCET) in patients with definite or probable systemic fungal infections. *Antimicrobial Agents and Chemotherapy*, 44(10), 2900-2902.

[344] Adedoyin, A., Bernardo, J.F., Swenson, C.E., Bolsack, L.E., Horwith, G., DeWit, S., Kelly, E., Klasterksy, J., Sculier, J.P., DeValeriola, D. and Anaissie, E., 1997. Pharmacokinetic profile of ABELCET (amphotericin B lipid complex injection): combined experience from phase I and phase II studies. *Antimicrobial Agents and Chemotherapy*, 41(10), 2201-2208.

[345] Gavaldà, J., Martín, M.T., López, P., Gomis, X., Ramírez, J.L., Rodríguez, D., Len, O., Puigfel, Y., Ruíz, I. and Pahissa, A., 2005. Efficacy of nebulized liposomal amphotericin B in treatment of experimental pulmonary aspergillosis. *Antimicrobial Agents and Chemotherapy*, 49(7), 3028-3030.

[346] Calvo, V., Borro, J.M., Morales, P., Morcillo, A., Vicente, R., Tarrazona, V. and Paris, F., 1999. Antifungal prophylaxis during the early postoperative period of lung transplantation. *CHEST*, 115(5), 1301-1304.

[347] Corcoran, T.E., Venkataramanan, R., Mihelc, K.M., Marcinkowski, A.L., Ou, J., McCook, B.M., Weber, L., Carey, M.E., Paterson, D.L., Pilewski, J.M. and McCurry, K.R., 2006. Aerosol Deposition of Lipid Complex Amphotericin-B (ABELCET) in Lung Transplant Recipients. *American Journal of Transplantation*, 6(11), 2765-2773.

[348] Drew, R.H., Ashley, E.D., Benjamin Jr, D.K., Davis, R.D., Palmer, S.M. and Perfect, J.R., 2004. Comparative safety of amphotericin B lipid complex and amphotericin B deoxycholate as aerosolized antifungal prophylaxis in lung-transplant recipients. *Transplantation*, 77(2), 232-237.

[349] Monforte, V., Ussetti, P., Gavaldà, J., Bravo, C., Laporta, R., Len, O., García-Gallo, C.L., Tenorio, L., Solé, J. and Román, A., 2010. Feasibility, tolerability, and outcomes of nebulized liposomal amphotericin B for Aspergillus infection prevention in lung transplantation. The *Journal of Heart and Lung Transplantation*, 29(5), 523-530.

[350] Quon, B.S., Goss, C.H. and Ramsey, B.W., 2014. Inhaled antibiotics for lower airway infections. *Annals of the American Thoracic Society*, 11(3), 425-434.

[351] Nihtinen, A., Anttila, V.J., Ruutu, T., Juvonen, E. and Volin, L., 2012. Low incidence of invasive aspergillosis in allogeneic stem cell transplant recipients receiving amphotericin B inhalation prophylaxis. *Transplant Infectious Disease*, 14(1), 24-32.

[352] Kumano, Y., Sakamoto, T., Egawa, M., Tanaka, M. and Yamamoto, I., 1998. Enhancing effect of 2-O-α-D-glucopyranosyl-L-ascorbic acid, a stable ascorbic acid derivative, on collagen synthesis. *Biological and Pharmaceutical Bulletin*, 21(7), 662-666.

[353] Pillay, V., Kumar, P., Choonara, Y.E., Modi, G., Naidoo, D., and du Toit, L.C., 2012. Processing and templating of bioactive-loaded polymeric neural architectures: challenges and innovative strategies. In *Recent Advances in Novel Drug Carrier Systems*, Ali Demir Sezer (editor), InTech.

[354] Rahimpour, Y. and Hamishehkar, H., 2012. Lactose engineering for better performance in dry powder inhalers. *Advanced Pharmaceutical Bulletin*, 2(2), 183-187.

[355] Wu, L., Miao, X., Shan, Z., Huang, Y., Li, L., Pan, X., Yao, Q., Li, G. and Wu, C., 2014. Studies on the spray dried lactose as carrier for dry powder inhalation. *Asian Journal of Pharmaceutical Sciences*, 9(6), 336-341.

[356] Raula, J., Kuivanen, A., Lähde, A. and Kauppinen, E.I., 2008. Gas-phase synthesis of L-leucine-coated micrometer-sized salbutamol sulphate and sodium chloride particles. *Powder Technology*, 187(3), 289-297.

[357] Raula, J., Lähde, A. and Kauppinen, E.I., 2009. Aerosolization behavior of carrier-free L-leucine coated salbutamol sulphate powders. *International Journal of Pharmaceutics*, 365(1), 18-25.

[358] Boraey, M.A., Hoe, S., Sharif, H., Miller, D.P., Lechuga-Ballesteros, D. and Vehring, R., 2013. Improvement of the dispersibility of spray dried budesonide powders using leucine in an ethanol–water cosolvent system. *Powder Technology*, 236, 171-178.

[359] Najafabadi, A.R., Gilani, K., Barghi, M. and Rafiee-Tehrani, M., 2004. The effect of vehicle on physical properties and aerosolisation behaviour of disodium cromoglycate

microparticles spray dried alone or with L-leucine. *International Journal of Pharmaceutics*, 285(1), 97-108.

[360] Chougule, M., Padhi, B. and Misra, A., 2008. Development of spray dried liposomal dry powder inhaler of dapsone. *AAPS Pharmscitech*, 9(1), 47-53.

[361] Feng, A.L., Boraey, M.A., Gwin, M.A., Finlay, P.R., Kuehl, P.J. and Vehring, R., 2011. Mechanistic models facilitate efficient development of leucine containing microparticles for pulmonary drug delivery. *International Journal of Pharmaceutics*, 409(1), 156-163.

[362] Li, L., Sun, S., Parumasivam, T., Denman, J.A., Gengenbach, T., Tang, P., Mao, S. and Chan, H.K., 2016. l-Leucine as an excipient against moisture on in vitro aerosolization performances of highly hygroscopic spray-dried powders. *European Journal of Pharmaceutics and Biopharmaceutics*, 102, 132-141.

[363] Chishimba, L., Langridge, P., Powell, G., Niven, R.M. and Denning, D.W., 2015. Efficacy and safety of nebulised amphotericin B (NAB) in severe asthma with fungal sensitisation (SAFS) and allergic bronchopulmonary aspergillosis (ABPA). *Journal of Asthma*, 52(3), 289-295.

[364] United Bristol Healthcare NHS trust, 2003. BCH Nebuliser Protocol [Internet]. Available at http://www.bristolpaedresp.org.uk/BCHNebuliserProtocol18.11.2003.pdf. (accessed on 27 March 2017).

[365] Kintzel, P.E. and Kennedy, P.E., 1991. Stability of amphotericin B in 5% dextrose injection at concentrations used for administration through a central venous line. *American Journal of Health-System Pharmacy*, 48(2), 283-285.

[366] Lopez, R.M., Ayestaran, A., Pou, L., Montoro, J.B., Hernandez, M. and Caragol, I., 1996. Stability of amphotericin B in an extemporaneously prepared iv fat emulsion. *American Journal of Health-System Pharmacy*, 53(22), 2724-2727.

[367] Wiest, D.B., Maish, W.A., Garner, S.S. and El-Chaar, G.M., 1991. Stability of amphotericin B in four concentrations of dextrose injection. *American Journal of Health-System Pharmacy*, 48(11), 2430-2433.

[368] Wilkinson, J.M., McDonald, C., Parkin, J.E. and Sunderland, V.B., 1998. A high-performance liquid-chromatographic assay for amphotericin B in a hydrophilic colloidal paste base. *Journal of Pharmaceutical and Biomedical Analysis*, 17(4), 751-755.

[369] Inoue, Y., Yoshimura, S., Tozuka, Y., Moribe, K., Kumamoto, T., Ishikawa, T. and Yamamoto, K., 2007. Application of ascorbic acid 2-glucoside as a solubilizing agent for clarithromycin: solubilization and nanoparticle formation. *International Journal of Pharmaceutics*, 331(1), 38-45.

[370] Pilcer, G., Vanderbist, F. and Amighi, K., 2008. Correlations between cascade impactor analysis and laser diffraction techniques for the determination of the particle size of aerosolised powder formulations. *International Journal of Pharmaceutics*, 358(1), 75-81.

[371] Alamilla-Beltran, L., Chanona-Perez, J.J., Jimenez-Aparicio, A.R. and Gutierrez-Lopez, G.F., 2005. Description of morphological changes of particles along spray drying. *Journal of Food Engineering*, 67(1), 179-184.

[372] Vehring, R., 2008. Pharmaceutical particle engineering via spray drying. *Pharmaceutical Research*, 25(5), 999-1022.

[373] Merchant, Z., Taylor, K.M., Stapleton, P., Razak, S.A., Kunda, N., Alfagih, I., Sheikh, K., Saleem, I.Y. and Somavarapu, S., 2014. Engineering hydrophobically modified chitosan for enhancing the dispersion of respirable microparticles of levofloxacin. *European Journal of Pharmaceutics and Biopharmaceutics*, 88(3), 816-829.

[374] Rattanupatam, T. and Srichana, T., 2014. Budesonide dry powder for inhalation: effects of leucine and mannitol on the efficiency of delivery. *Drug delivery*, 21(6), 397-405.

[375] Raula, J., Thielmann, F., Naderi, M., Lehto, V.P. and Kauppinen, E.I., 2010. Investigations on particle surface characteristics vs. dispersion behaviour of l-leucine coated carrier-free inhalable powders. *International Journal of Pharmaceutics*, 385(1), 79-85.

[376] Lucas, P., Anderson, K., Potter, U.J. and Staniforth, J.N., 1999. Enhancement of small particle size dry powder aerosol formulations using an ultra low-density additive. *Pharmaceutical Research*, 16(10), 1643-1647.

[377] NanoComposix, 2012. Guidelines for DLS measurements and analysis. Available at: http://50.87.149.212/sites/default/files/nanoComposix Guidelines for DLS Measurements and Analysis.pdf. (accessed on 27 March 2017).

[378] Schwartzman, G., Asher, I., Folen, V., Brannon, W. and Taylor, J., 1978. Ambiguities in IR and X-ray characterization of amphotericin B. *Journal of Pharmaceutical Sciences*, 67(3), 398-400.

[379] Choi, K.C., Bang, J.Y., Kim, P.I., Kim, C. and Song, C.E., 2008. Amphotericin B-incorporated polymeric micelles composed of poly (d, l-lactide-co-glycolide)/dextran graft copolymer. *International Journal of Pharmaceutics*, 355(1), 224-230.

[380] British Pharmacopoeia, 2012. Appendix XII C 7 Aerodynamic assessment of fine particles-fine particle dose and particle size distribution. Available at: http://bp2012.infostar.com.cn/Bp2012.aspx?a=display&id=901 (accessed on 27 March 2017).

[381] Asada, M., Takahashi, H., Okamoto, H., Tanino, H. and Danjo, K., 2004. Theophylline particle design using chitosan by the spray drying. *International Journal of Pharmaceutics*, 270(1), 167-174.

[382] Paradkar, A., Ambike, A.A., Jadhav, B.K. and Mahadik, K.R., 2004. Characterization of curcumin–PVP solid dispersion obtained by spray drying. *International Journal of Pharmaceutics*, 271(1), 281-286.

[383] Thi, T.H.H., Danède, F., Descamps, M. and Flament, M.P., 2008. Comparison of physical and inhalation properties of spray dried and µmized terbutaline sulphate. *European Journal of Pharmaceutics and Biopharmaceutics*, 70(1), 380-388.

[384] Fauci, A.S. and NIAID Tuberculosis Working Group, 2008. Multidrug-resistant and extensively drug-resistant tuberculosis: The National Institute of Allergy and Infectious Diseases Research agenda and recommendations for priority research. *Journal of Infectious Diseases*, 197(11), 1493-1498.

[385] Maitra, A., Bates, S., Kolvekar, T., Devarajan, P.V., Guzman, J.D. and Bhakta, S., 2015. Repurposing—a ray of hope in tackling extensively drug resistance in tuberculosis. *International Journal of Infectious Diseases*, 32, 50-55.

[386] Maiga, M., Agarwal, N., Ammerman, N.C., Gupta, R., Guo, H., Maiga, M.C., Lun, S. and Bishai, W.R., 2012. Successful shortening of tuberculosis treatment using adjuvant host-directed therapy with FDA-approved phosphodiesterase inhibitors in the mouse model. *PLoS One*, 7(2), 30749.

[387] Wellcome Trust, 2014. Fighting TB on Many Fronts-Verapamil Trials, India — Wellcome Trust - Cambridge Centre for Global Health Research [Internet]. Available at: http://wt-globalhealth.cam.ac.uk/programme-areas/infectious-diseases/pathogen-evolution-and-antimicrobial-resistance/Anti-microbial-Resistance/TBResearch (accessed November 2, 2016).

[388] Gold, B., Pingle, M., Brickner, S.J., Shah, N., Roberts, J., Rundell, M., Bracken, W.C., Warrier, T., Somersan, S., Venugopal, A. and Darby, C., 2012. Nonsteroidal anti-inflammatory drug sensitizes Mycobacterium tuberculosis to endogenous and exogenous antimicrobials. *Proceedings of the National Academy of Sciences*, 109(40), pp.16004-16011.

[389] Guzman, J.D., Evangelopoulos, D., Gupta, A., Birchall, K., Mwaigwisya, S., Saxty, B., McHugh, T.D., Gibbons, S., Malkinson, J. and Bhakta, S., 2013. Antitubercular specific activity of ibuprofen and the other 2-arylpropanoic acids using the HT-SPOTi whole-cell phenotypic assay. *BMJ open*, 3(6), p.e002672.

[390] Vilaplana, C., Marzo, E., Tapia, G., Diaz, J., Garcia, V. and Cardona, P.J., 2013. Ibuprofen therapy resulted in significantly decreased tissue bacillary loads and increased survival in a new murine experimental model of active tuberculosis. *Journal of Infectious Diseases*, 208(2), 199-202.

[391] Yin, Z., Wang, Y., Whittell, L.R., Jergic, S., Liu, M., Harry, E., Dixon, N.E., Kelso, M.J., Beck, J.L. and Oakley, A.J., 2014. DNA replication is the target for the antibacterial effects of nonsteroidal anti-inflammatory drugs. *Chemistry & biology*, 21(4), 481-487.

[392] Hoffmann, K. and Onöz, E., 1969. Inhibitory effect of oxyphenbutazone against Mycobacterium tuberculosis in vitro. *Arzneimittel-Forschung*, 19(2), 241-242.

[393] Byrne, S.T., Denkin, S.M. and Zhang, Y., 2007. Aspirin and ibuprofen enhance pyrazinamide treatment of murine tuberculosis. *Journal of Antimicrobial Chemotherapy*, 59(2), 313-316.

[394] Gelperina, S., Kisich, K., Iseman, M.D. and Heifets, L., 2005. The potential advantages of nanoparticle drug delivery systems in chemotherapy of tuberculosis. *American Journal of Respiratory and Critical Care Medicine*, 172(12), 1487-1490.

[395] Stoops, J.K., Arora, R., Armitage, L., Wanger, A., Song, L., Blackburn, M.R., Krueger, G.R. and Risin, S.A., 2010. Certain surfactants show promise in the therapy of pulmonary tuberculosis. *In Vivo*, 24(5), 687-694.

[396] Fux, C.A., Costerton, J.W., Stewart, P.S. and Stoodley, P., 2005. Survival strategies of infectious biofilms. *Trends in Microbiology*, 13(1), 34-40.

[397] Islam, M.S., Richards, J.P. and Ojha, A.K., 2012. Targeting drug tolerance in mycobacteria: a perspective from mycobacterial biofilms. *Expert Review of Anti-Infective Therapy*, 10(9), 1055-1066.

[398] Rumbaugh, K.P. and Ahmad, I., 2014. *Antibiofilm Agents: From Diagnosis to Treatment and Prevention*. Volume 8, Springer Science & Business Media, London.

[399] Moghadas-Sharif, N., Fazly Bazzaz, B.S., Khameneh, B. and Malaekeh-Nikouei, B., 2015. The effect of nanoliposomal formulations on Staphylococcus epidermidis biofilm. *Drug Development and Industrial Pharmacy*, 41(3), 445-450.

[400] Pham, D.D., Fattal, E. and Tsapis, N., 2015. Pulmonary drug delivery systems for tuberculosis treatment. *International Journal of Pharmaceutics*, 478(2), 517-529.

[401] Shegokar, R., Al Shaal, L. and Mitri, K., 2011. Present status of nanoparticle research for treatment of tuberculosis. *Journal of Pharmacy and Pharmaceutical Sciences*, 14(1), 100-116.

[402] Brennan, P.J., 2003. Structure, function, and biogenesis of the cell wall of Mycobacterium tuberculosis. *Tuberculosis*, 83(1), 91-97.

[403] Russell, D.G., Cardona, P.J., Kim, M.J., Allain, S. and Altare, F., 2009. Foamy macrophages and the progression of the human tuberculosis granuloma. *Nature Immunology*, 10(9), 943-948.

[404] Lee, W.H., Loo, C.Y., Traini, D. and Young, P.M., 2015. Nano-and micro-based inhaled drug delivery systems for targeting alveolar macrophages. *Expert Opinion on Drug Delivery*, 12(6), 1009-1026.

[405] Hirota, K., Terada, H., 2012. Endocytosis of particle formulations by macrophages and its application to clinical treatment, 413-428. In *Molecular Regulation of Endocytosis,* Ceresa, B. (editor). InTech, Rijeka, Croatia.

[406] Gaspar, M.M., Cruz, A., Penha, A.F., Reymao, J., Sousa, A.C., Eleutério, C.V., Domingues, S.A., Fraga, A.G., Longatto Filho, A., Cruz, M.E.M. and Pedrosa, J., 2008. Rifabutin encapsulated in liposomes exhibits increased therapeutic activity in a model of disseminated tuberculosis. *International Journal of Antimicrobial Agents*, 31(1), 37-45.

[407] Dhillon, J., Fielding, R., Adler-Moore, J., Goodall, R.L. and Mitchison, D., 2001. The activity of low-clearance liposomal amikacin in experimental murine tuberculosis. *Journal of Antimicrobial Chemotherapy*, 48(6), 869-876.

[408] Patil, J.S., Devi, V.K., Devi, K. and Sarasija, S., 2015. A novel approach for lung delivery of rifampicin-loaded liposomes in dry powder form for the treatment of tuberculosis. *Lung India: Official Organ of Indian Chest Society*, 32(4), 331-338.

[409] Jain, S., Amiji, M., 2012. Macrophage-targeted nanoparticle delivery systems, 48-55. In: *Multifunctional Nanoparticles for Drug Delivery Applications: Imaging, Targeting, and Delivery,* Svenson, S., Prud'homme, R. (editors). Springer, New York.

[410] Rigotti, A., Acton, S.L. and Krieger, M., 1995. The class B scavenger receptors SR-BI and CD36 are receptors for anionic phospholipids. *Journal of Biological Chemistry*, 270(27), 16221-16224.

[411] Agarwal, A., Kandpal, H., Gupta, H.P., Singh, N.B. and Gupta, C.M., 1994. Tuftsin-bearing liposomes as rifampin vehicles in treatment of tuberculosis in mice. *Antimicrobial Agents and Chemotherapy*, 38(3), 588-593.

[412] Chono, S., Tanino, T., Seki, T. and Morimoto, K., 2007. Uptake characteristics of liposomes by rat alveolar macrophages: influence of particle size and surface mannose modification. *Journal of Pharmacy and Pharmacology*, 59(1), 75-80.

[413] Kelly, C., Jefferies, C. and Cryan, S.A., 2011. Targeted liposomal drug delivery to monocytes and macrophages. *Journal of Drug Delivery*, 727241, 1-11.

[414] Campbell, E.A., Korzheva, N., Mustaev, A., Murakami, K., Nair, S., Goldfarb, A. and Darst, S.A., 2001. Structural mechanism for rifampicin inhibition of bacterial RNA polymerase. *Cell*, 104(6), 901-912.

[415] Ingvarsson, P.T., Yang, M., Nielsen, H.M., Rantanen, J. and Foged, C., 2011. Stabilization of liposomes during drying. *Expert Opinion on Drug Delivery*, 8(3), 375-388.

[416] Aditya, N.P., Patankar, S., Madhusudhan, B., Murthy, R.S.R. and Souto, E.B., 2010. Arthemeter-loaded lipid nanoparticles produced by modified thin-film hydration: Pharmacokinetics, toxicological and in vivo anti-malarial activity. *European Journal of Pharmaceutical Sciences*, 40(5), 448-455.

[417] Laouini, A., Jaafar-Maalej, C., Limayem-Blouza, I., Sfar, S., Charcosset, C. and Fessi, H., 2012. Preparation, characterization and applications of liposomes: state of the art. *Journal of Colloid Science and Biotechnology*, 1(2), 147-168.

[418] Gürsoy, A., Kut, E. and Özkırımlı, S., 2004. Co-encapsulation of isoniazid and rifampicin in liposomes and characterization of liposomes by derivative spectroscopy. *International Journal of Pharmaceutics*, 271(1), 115-123.

[419] Chen, J., Cheng, D., Li, J., Wang, Y., Guo, J.X., Chen, Z.P., Cai, B.C. and Yang, T., 2013. Influence of lipid composition on the phase transition temperature of liposomes composed of both DPPC and HSPC. *Drug Development and Industrial Pharmacy*, 39(2), 197-204.

[420] Ai, X., Zhong, L., Niu, H. and He, Z., 2014. Thin-film hydration preparation method and stability test of DOX-loaded disulfide-linked polyethylene glycol 5000-lysine-di-tocopherol succinate nanomicelles. *Asian Journal of Pharmaceutical Sciences*, 9(5), pp. 244-250.

[421] Notter RH, 2000. *Lung Surfactants: Basic Science and Clinical Applications,* Lenfant, C. (editor), Marcel Dekker Inc., New York, 207-247.

[422] Asthana, G.S., Asthana, A., Kohli, D.V. and Vyas, S.P., 2014. Mannosylated chitosan nanoparticles for delivery of antisense oligonucleotides for macrophage targeting. *BioMed Research International*, 526391, 1-17.

[423] Muralidharan, S. and Meyyanathan, S.N., 2011. Development and validation of a HPLC and an UV spectrophotometric methods for determination of dexibuprofen in pharmaceutical preparations. *ISRN Pharmaceutics*, 948314.

[424] Rifai, N., Sakamoto, M., Law, T., Galpchian, V., Harris, N. and Colin, A.A., 1996. Use of a rapid HPLC assay for determination of pharmacokinetic parameters of ibuprofen in patients with cystic fibrosis. *Clinical Chemistry*, 42(11), 1812-1816.

[425] Haikala, V.E., Heimonen, I.K. and Vuorela, H.J., 1991. Determination of ibuprofen in ointments by reversed-phase liquid chromatography. *Journal of Pharmaceutical Sciences*, 80(5), 456-458.

[426] Smith, P.J., Van Dyk, J. and Fredericks, A., 1999. Determination of rifampicin, isoniazid and pyrazinamide by high performance liquid chromatography after their simultaneous extraction from plasma. *The International Journal of Tuberculosis and Lung Disease*, 3(11), S325-S328.

[427] Kumar, A.H., Chandra, I., Geetha, R., Chelvi, K.S., Lalitha, V. and Prema, G., 2004. A validated high-performance liquid chromatography method for the determination of rifampicin and desacetyl rifampicin in plasma and urine. *Indian Journal of Pharmacology*, 36(4), 231-233.

[428] Singh, S., Singla, Y. P. and Arora, S., 2015. Statistical, diagnostic and response surface analysis of nefopam hydrochloride nanospheres using 35 box-behnken design. *International Journal of Pharmacy and Pharmaceutical Sciences*, 7(10), 89-101.

[429] Magarkar, A., Dhawan, V., Kallinteri, P., Viitala, T., Elmowafy, M., Róg, T. and Bunker, A., 2014. Cholesterol level affects surface charge of lipid membranes in saline solution. *Scientific Reports*, 4, 5005, 1-5.

[430] Szcześ, A., 2013. Effects of DPPC/Cholesterol liposomes on the properties of freshly precipitated calcium carbonate. *Colloids and Surfaces B: Biointerfaces*, 101, 44-48.

[431] Pandit, S.A., Bostick, D. and Berkowitz, M.L., 2004. Complexation of phosphatidylcholine lipids with cholesterol. *Biophysical Journal*, 86(3), 1345-1356.

[432] Briuglia, M.L., Rotella, C., McFarlane, A. and Lamprou, D.A., 2015. Influence of cholesterol on liposome stability and on in vitro drug release. *Drug Delivery and Translational Research*, 5(3), 231-242.

[433] Youngren, S.R., Mulik, R., Jun, B., Hoffmann, P.R., Morris, K.R. and Chougule, M.B., 2013. Freeze-dried targeted mannosylated selenium-loaded nanoliposomes: development and evaluation. *AAPS PharmSciTech*, 14(3), 1012-1024.

[434] Zisman, N., Santos, N.D., Johnstone, S., Tsang, A., Bermudes, D., Mayer, L., and Tardi, P., 2011. Optimizing Liposomal Cisplatin Efficacy through Membrane Composition Manipulations. *Chemotherapy Research and Practice*, 2011, 213848, 7 pages.

[435] Khan, D.R., Rezler, E.M., Lauer-Fields, J. and Fields, G.B., 2008. Effects of drug hydrophobicity on liposomal stability. *Chemical Biology & Drug Design*, 71(1), 3-7.

[436] Khajeh, A. and Modarress, H., 2014. The influence of cholesterol on interactions and dynamics of ibuprofen in a lipid bilayer. *Biochimica et Biophysica Acta (BBA)-Biomembranes*, 1838(10), 2431-2438.

[437] Zaru, M., Mourtas, S., Klepetsanis, P., Fadda, A.M. and Antimisiaris, S.G., 2007. Liposomes for drug delivery to the lungs by nebulization. *European Journal of Pharmaceutics and Biopharmaceutics*, 67(3), 655-666.

[438] Gallo, G.G. and Radaelli, P., 1976. Rifampin. *Analytical Profiles of Drug Substances*, 5, 467-513.

[439] Sou, T., Morton, D.A., Williamson, M., Meeusen, E.N., Kaminskas, L.M. and McIntosh, M.P., 2015. Spray-dried influenza antigen with trehalose and leucine produces an aerosolizable powder vaccine formulation that induces strong systemic and mucosal immunity after pulmonary administration. *Journal of Aerosol Medicine and Pulmonary Drug Delivery*, 28(5), 361-371.

[440] Hu, Y., Xu, B.H., Xu, J.J., Shou, D. and Gao, J.Q., 2014. Synthesis of Mannosylated Polyethylenimine and Its Potential Application as Cell-Targeting Non-Viral Vector for Gene Therapy. *Polymers*, 6(10), 2573-2587.

[441] Torchilin, V. P., Weissig, V., Martin, F. J. and Heath. T. D, 2003. Torchilin, V. P. & Weissig, V. (editors) *Liposomes: Practical Approach*, pp. 193–229, Oxford University Press, Oxford.

[442] Zhang, L., Song, J., Cavigiolio, G., Ishida, B.Y., Zhang, S., Kane, J.P., Weisgraber, K.H., Oda, M.N., Rye, K.A., Pownall, H.J. and Ren, G., 2011. Morphology and structure of lipoproteins revealed by an optimized negative-staining protocol of electron microscopy. *Journal of Lipid Research*, 52(1), 175-184.

[443] Lee, S.S., Lee, Y.B. and Oh, I.J., 2015. Cellular uptake of poly (dl-lactide-co-glycolide) nanoparticles: effects of drugs and surface characteristics of nanoparticles. *Journal of Pharmaceutical Investigation*, 45(7), 659-667.

[444] Pukanud, P., Peungvicha, P. and Sarisuta, N., 2009. Development of mannosylated liposomes for bioadhesive oral drug delivery via M cells of Peyer's patches. *Drug Delivery*, 16(5), 289-294.

[445] Chono, S., Tanino, T., Seki, T. and Morimoto, K., 2008. Efficient drug targeting to rat alveolar macrophages by pulmonary administration of ciprofloxacin incorporated into mannosylated liposomes for treatment of respiratory intracellular parasitic infections. *Journal of Controlled Release*, 127(1), 50-58.

[446] Khalil, N.M., do Nascimento, T., Casa, D., Dalmolin, L., de Mattos, A., Hoss, I., Romano, M. and Mainardes, R., 2013. Pharmacokinetics of curcumin-loaded PLGA and PLGA–PEG blend nanoparticles after oral administration in rats. *Colloids and Surfaces B: Biointerfaces*, 101, 353-360.

[447] Kumar, A., Ahuja, A., Ali, J. and Baboota, S., 2016. Curcumin-loaded lipid nanocarrier for improving bioavailability, stability and cytotoxicity against malignant glioma cells. *Drug Delivery*, 23(1), 214-229.

[448] Sordillo, L.A., Sordillo, P.P. and Helson, L., 2015. Curcumin for the Treatment of Glioblastoma. *Anticancer Research*, 35(12), 6373-6378.

[449] Wilken, R., Veena, M.S., Wang, M.B. and Srivatsan, E.S., 2011. Curcumin: A review of anti-cancer properties and therapeutic activity in head and neck squamous cell carcinoma. *Molecular Cancer*, 10(1), 12-31.

[450] Turmeric compounds fight brain cancer | Turmeric.com. Available at: https://www.turmeric.com/cancer/turmeric-compounds-fight-brain-cancer (accessed August 2, 2017).

[451] Jayaraj, R.L., Tamilselvam, K., Manivasagam, T. and Elangovan, N., 2013. Neuroprotective effect of CNB-001, a novel pyrazole derivative of curcumin on biochemical and apoptotic markers against rotenone-induced SK-N-SH cellular model of Parkinson's disease. *Journal of Molecular Neuroscience*, 51(3), 863-870.

[452] Jayaraj, R.L., Elangovan, N., Manigandan, K., Singh, S. and Shukla, S., 2013. CNB-001 a novel curcumin derivative, guards dopamine neurons in MPTP model of Parkinson's disease. *BioMed Research International*, 2014, 236182, 11 pages.

[453] Lin, H.W., Saul, I., Gresia, V.L., Neumann, J.T., Dave, K.R. and Perez-Pinzon, M.A., 2014. Fatty acid methyl esters and Solutol HS 15 confer neuroprotection after focal and global cerebral ischemia. *Translational Stroke Research*, 5(1), 109-117.

[454] Liu, Y., Dargusch, R., Maher, P. and Schubert, D., 2008. A broadly neuroprotective derivative of curcumin. *Journal of Neurochemistry*, 105(4), 1336-1345.

[455] Keshavarz, R., Bakhshinejad, B., Babashah, S., Baghi, N. and Sadeghizadeh, M., 2016. Dendrosomal nanocurcumin and p53 overexpression synergistically trigger apoptosis in glioblastoma cells. *Iranian journal of basic medical sciences*, 19(12), 1353.

[456] Bollimpelli, V.S., Kumar, P., Kumari, S. and Kondapi, A.K., 2016. Neuroprotective effect of curcumin-loaded lactoferrin nano particles against rotenone induced neurotoxicity. *Neurochemistry international*, 95, 37-45.

[457] Ray, B., Bisht, S., Maitra, A., Maitra, A. and Lahiri, D.K., 2011. Neuroprotective and neurorescue effects of a novel polymeric nanoparticle formulation of curcumin (NanoCurc™) in the neuronal cell culture and animal model: implications for Alzheimer's disease. *Journal of Alzheimer's disease*, 23(1), 61-77.

[458] Mathew, A., Fukuda, T., Nagaoka, Y., Hasumura, T., Morimoto, H., Yoshida, Y., Maekawa, T., Venugopal, K. and Kumar, D.S., 2012. Curcumin loaded-PLGA nanoparticles conjugated with Tet-1 peptide for potential use in Alzheimer's disease. *PLoS one*, 7(3), p.e32616.

[459] Lin, H.W., Saul, I., Gresia, V.L., Neumann, J.T., Dave, K.R. and Perez-Pinzon, M.A., 2014. Fatty acid methyl esters and Solutol HS 15 confer neuroprotection after focal and global cerebral ischemia. *Translational Stroke Research*, 5(1), 109-117.

[460] Li, P.Y., Lai, P.S., Lin, C.C., 2009. Reversal of multidrug resistance using poly(L-lactide)-Vitamin E TPGS micelles in breast cancer cell, in 2009 *International Conference on Biomedical and Pharmaceutical Engineering*. 239–243.

[461] Gill, K.K., Kaddoumi, A. and Nazzal, S., 2012. Mixed micelles of PEG 2000-DSPE and vitamin-E TPGS for concurrent delivery of paclitaxel and parthenolide: Enhanced chemosenstization and antitumour efficacy against non-small cell lung cancer (NSCLC) cell lines. *European Journal of Pharmaceutical Sciences*, 46(1), 64-71.

[462] Zupančič, S., Kocbek, P., Zariwala, M.G., Renshaw, D., Gul, M.O., Elsaid, Z., Taylor, K.M. and Somavarapu, S., 2014. Design and development of novel mitochondrial targeted nanocarriers, DQAsomes for curcumin inhalation. *Molecular Pharmaceutics*, 11(7), 2334-2345.

[463] Jayachandra Babu, R., Dayal, P.P., Pawar, K. and Singh, M., 2011. Nose-to-brain transport of melatonin from polymer gel suspensions: a microdialysis study in rats. *Journal of Drug Targeting*, 19(9), 731-740.

[464] Dayal, P., Shaik, M.S. and Singh, M., 2004. Evaluation of different parameters that affect droplet-size distribution from nasal sprays using the Malvern Spraytec®. *Journal of Pharmaceutical Sciences*, 93(7), 1725-1742.

[465] Clementino, A., Batger, M., Garrastazu, G., Pozzoli, M., Del Favero, E., Rondelli, V., Gutfilen, B., Barboza, T., Sukkar, M.B., Souza, S.A. and Cantù, L., 2016. The nasal delivery of nanoencapsulated statins–an approach for brain delivery. *International Journal of Nanomedicine*, 11, 6575-6590.

[466] Nguyen, A.T.B., Winckler, P., Loison, P., Wache, Y. and Chambin, O., 2014. Physico-chemical state influences in vitro release profile of curcumin from pectin beads. *Colloids and Surfaces B: Biointerfaces*, 121, 290-298.

[467] Butt, A.M., Iqbal, M.C., Amin, M. and Katas, H., 2015. Synergistic effect of pH-responsive folate-functionalized poloxamer 407-TPGS-mixed micelles on targeted delivery of anticancer drugs. *International Journal of Nanomedicine*, 10, 1321-1334.

[468] Gibaldi, M. and Feldman, S., 1967. Establishment of sink conditions in dissolution rate determinations. Theoretical considerations and application to nondisintegrating dosage forms. *Journal of Pharmaceutical Sciences*, 56(10), 1238-1242.

[469] Vichai, V. and Kirtikara, K., 2006. Sulforhodamine B colorimetric assay for cytotoxicity screening. *Nature Protocols*, 1(3), 1112-1116.

[470] Lopes, F.M., Schröder, R., da Frota Júnior, M.L.C., Zanotto-Filho, A., Müller, C.B., Pires, A.S., Meurer, R.T., Colpo, G.D., Gelain, D.P., Kapczinski, F. and Moreira, J.C.F., 2010. Comparison between proliferative and neuron-like SH-SY5Y cells as an in vitro model for Parkinson disease studies. *Brain Research*, 1337, 85-94.

[471] Cheung, Y.T., Lau, W.K.W., Yu, M.S., Lai, C.S.W., Yeung, S.C., So, K.F. and Chang, R.C.C., 2009. Effects of all-trans-retinoic acid on human SH-SY5Y neuroblastoma as in vitro model in neurotoxicity research. *Neurotoxicology*, 30(1), 127-135.

[472] Yan, H., Zhang, Z., Jia, X. and Song, J., 2016. d-α-Tocopheryl polyethylene glycol succinate/Solutol HS 15 mixed micelles for the delivery of baohuoside I against non-small-cell lung cancer: optimization and in vitro, in vivo evaluation. *International Journal of Nanomedicine*, 11, 4563-4571.

[473] Hou, J., Wang, J., Sun, E., Yang, L., Yan, H.M., Jia, X.B. and Zhang, Z.H., 2016. Preparation and evaluation of icariside II-loaded binary mixed micelles using Solutol HS15 and Pluronic F127 as carriers. *Drug Delivery*, 23(9), 3248-3256.

[474] Kumar, G.P. and Rajeshwarrao, P., 2011. Nonionic surfactant vesicular systems for effective drug delivery—an overview. *Acta Pharmaceutica Sinica B*, 1(4), 208-219.

[475] Shinde, U.A. and Kanojiya, S.S., 2013. Serratiopeptidase Niosomal Gel with Potential in Topical Delivery. *Journal of Pharmaceutics*, 2014, 382959.

[476] Mandal, S., Banerjee, C., Ghosh, S., Kuchlyan, J. and Sarkar, N., 2013. Modulation of the photophysical properties of curcumin in nonionic surfactant (Tween-20) forming micelles and niosomes: a comparative study of different microenvironments. *The Journal of Physical Chemistry B*, 117(23), 6957-6968.

[477] Arafa, M.G. and Ayoub, B.M., 2017. DOE Optimization of Nano-based Carrier of Pregabalin as Hydrogel: New Therapeutic & Chemometric Approaches for Controlled Drug Delivery Systems. *Scientific Reports*, 7, 41503, 15 pages.

[478] Agarwal, S., Bakshi, V., Vitta, P., Raghuram, A.P. and Udupa, N., 2004. Effect of cholesterol content and surfactant HLB on vesicle properties of niosomes. *Indian Journal of Pharmaceutical Sciences*, 66(1), 121-123.

[479] Pardakhty, A., Varshosaz, J. and Rouholamini, A., 2007. In vitro study of polyoxyethylene alkyl ether niosomes for delivery of insulin. *International Journal of Pharmaceutics*, 328(2), 130-141.

[480] Sonali, Agrawal, P., Singh, R.P., Rajesh, C.V., Singh, S., Vijayakumar, M.R., Pandey, B.L. and Muthu, M.S., 2016. Transferrin receptor-targeted vitamin E TPGS micelles for brain cancer therapy: preparation, characterization and brain distribution in rats. *Drug Delivery*, 23(5), 1788-1798.

[481] Muthu, M.S., Kulkarni, S.A., Liu, Y. and Feng, S.S., 2012. Development of docetaxel-loaded vitamin E TPGS micelles: formulation optimization, effects on brain cancer cells and biodistribution in rats. *Nanomedicine*, 7(3), 353-364.

[482] Wang, J., Sun, J., Chen, Q., Gao, Y., Li, L., Li, H., Leng, D., Wang, Y., Sun, Y., Jing, Y. and Wang, S., 2012. Star-shape copolymer of lysine-linked di-tocopherol polyethylene glycol 2000 succinate for doxorubicin delivery with reversal of multidrug resistance. *Biomaterials*, 33(28), 6877-6888.

[483] Liu, L., Xu, K., Wang, H., Tan, P.J., Fan, W., Venkatraman, S.S., Li, L. and Yang, Y.Y., 2009. Self-assembled cationic peptide nanoparticles as an efficient antimicrobial agent. *Nature Nanotechnology*, 4(7), 457-463.

[484] Zhang, Y., Huang, Y. and Li, S., 2014. Polymeric micelles: nanocarriers for cancer-targeted drug delivery. *AAPS PharmSciTech*, 15(4), 862-871.

[485] Bernabeu, E., Gonzalez, L., Cagel, M., Gergic, E.P., Moretton, M.A. and Chiappetta, D.A., 2016. Novel Soluplus®—TPGS mixed micelles for encapsulation of paclitaxel with enhanced in vitro cytotoxicity on breast and ovarian cancer cell lines. *Colloids and Surfaces B: Biointerfaces*, 140, 403-411.

[486] Gao, Y., Li, L.B. and Zhai, G., 2008. Preparation and characterization of Pluronic/TPGS mixed micelles for solubilization of camptothecin. *Colloids and Surfaces B: Biointerfaces*, 64(2), 194-199.

[487] Zhao, L., Shi, Y., Zou, S., Sun, M., Li, L. and Zhai, G., 2011. Formulation and in vitro evaluation of quercetin loaded polymeric micelles composed of pluronic P123 and Da-tocopheryl polyethylene glycol succinate. *Journal of Biomedical Nanotechnology*, 7(3), 358-365.

[488] Nasseri, B., 2005. Effect of cholesterol and temperature on the elastic properties of niosomal membranes. *International Journal of Pharmaceutics*, 300(1), 95-101.

[489] Mi, Y., Zhao, J. and Feng, S.S., 2012. Vitamin E TPGS prodrug micelles for hydrophilic drug delivery with neuroprotective effects. *International Journal of Pharmaceutics*, 438(1), 98-106.

[490] Cao, N. and Feng, S.S., 2008. Doxorubicin conjugated to d-α-tocopheryl polyethylene glycol 1000 succinate (TPGS): Conjugation chemistry, characterization, in vitro and in vivo evaluation. *Biomaterials*, 29(28), 3856-3865.

[491] Anbharasi, V., Cao, N. and Feng, S.S., 2010. Doxorubicin conjugated to D-α-tocopheryl polyethylene glycol succinate and folic acid as a prodrug for targeted chemotherapy. *Journal of Biomedical Materials Research Part A*, 94(3), 730-743.

[492] Sawant, R.R., Sawant, R.M. and Torchilin, V.P., 2008. Mixed PEG–PE/vitamin E tumour-targeted immunomicelles as carriers for poorly soluble anti-cancer drugs: improved drug solubilization and enhanced in vitro cytotoxicity. *European Journal of Pharmaceutics and Biopharmaceutics*, 70(1), 51-57.

[493] Mu, L., Elbayoumi, T.A. and Torchilin, V.P., 2005. Mixed micelles made of poly (ethylene glycol)–phosphatidylethanolamine conjugate and d-α-tocopheryl polyethylene glycol 1000 succinate as pharmaceutical nanocarriers for camptothecin. *International Journal of Pharmaceutics*, 306(1), 142-149.

[494] Jaisin, Y., Thampithak, A., Meesarapee, B., Ratanachamnong, P., Suksamrarn, A., Phivthong-ngam, L., Phumala-Morales, N., Chongthammakun, S., Govitrapong, P. and

Sanvarinda, Y., 2011. Curcumin I protects the dopaminergic cell line SH-SY5Y from 6-hydroxydopamine-induced neurotoxicity through attenuation of p53-mediated apoptosis. *Neuroscience Letters*, 489(3), 192-196.

[495] Liang, Z., Shi, F., Wang, Y., Lu, L., Zhang, Z., Wang, X. and Wang, X., 2011. Neuroprotective effects of tenuigenin in a SH-SY5Y cell model with 6-OHDA-induced injury. *Neuroscience Letters*, 497(2), 104-109.

[496] Shi, X.R., Hong, Z.Y., Liu, H.R., Zhang, Y.C. and Zhu, Y.Z., 2011. Neuroprotective effects of SCM198 on 6-hydroxydopamine-induced behavioral deficit in rats and cytotoxicity in neuronal SH-SY5Y cells. *Neurochemistry International*, 58(8), 851-860.

[497] Lin, Y.C., Uang, H.W., Lin, R.J., Chen, J. and Lo, Y.C., 2007. Neuroprotective effects of glyceryl nonivamide against microglia-like cells and 6-hydroxydopamine-induced neurotoxicity in SH-SY5Y human dopaminergic neuroblastoma cells. *Journal of Pharmacology and Experimental Therapeutics*, 323(3), 877-887.

[498] Lee, M.K., Kang, S.J., Poncz, M., Song, K.J. and Park, K.S., 2007. Resveratrol protects SH-SY5Y neuroblastoma cells from apoptosis induced by dopamine. *Experimental & Molecular Medicine*, 39(3), 376-384.

[499] Kalepu, S. and Nekkanti, V., 2015. Insoluble drug delivery strategies: review of recent advances and business prospects. *Acta Pharmaceutica Sinica B*, 5(5), 442-453.

[500] Khadka, P., Ro, J., Kim, H., Kim, I., Kim, J.T., Kim, H., Cho, J.M., Yun, G. and Lee, J., 2014. Pharmaceutical particle technologies: an approach to improve drug solubility, dissolution and bioavailability. *Asian Journal of Pharmaceutical Sciences*, 9(6), 304-316.

[501] Lee, W.H., Loo, C.Y., Traini, D. and Young, P.M., 2015. Inhalation of nanoparticle-based drug for lung cancer treatment: Advantages and challenges. *Asian Journal of Pharmaceutical Sciences*, 10(6), 481-489.

[502] Boegh, M. and Nielsen, H.M., 2015. Mucus as a barrier to drug delivery–understanding and mimicking the barrier properties. *Basic and Clinical Pharmacology and Toxicology*, 116(3), 179-186.

[503] Moribe, K., Limwikrant, W., Higashi, K. and Yamamoto, K., 2011. Drug nanoparticle formulation using ascorbic acid derivatives. *Journal of Drug Delivery*, 2011, 138929, 9 pages.

[504] Palma, S., Manzo, R.H., Allemandi, D., Fratoni, L. and Nostro, P.L., 2003. Drugs solubilization in ascorbyl–decanoate micellar solutions. *Colloids and Surfaces A: Physicochemical and Engineering Aspects*, 212(2), 163-173.

[505] Palma, S., Manzo, R.H., Allemandi, D., Fratoni, L. and Lo Nostro, P., 2002. Solubilization of hydrophobic drugs in octanoyl-6-O-ascorbic acid micellar dispersions. *Journal of Pharmaceutical Sciences*, 91(8), 1810-1816.

[506] Jong, T., Li, J., Morton, D.A., Zhou, Q.T. and Larson, I., 2016. Investigation of the changes in aerosolization behavior between the jet-milled and spray-dried colistin powders through surface energy characterization. *Journal of Pharmaceutical Sciences*, 105(3), 1156-1163.

[507] Sou, T., Orlando, L., McIntosh, M.P., Kaminskas, L.M. and Morton, D.A., 2011. Investigating the interactions of amino acid components on a mannitol-based spray-dried powder formulation for pulmonary delivery: a design of experiment approach. *International Journal of Pharmaceutics*, 421(2), 220-229.

[508] Hata, R.I. and Senoo, H., 1989. L-ascorbic acid 2-phosphate stimulates collagen accumulation, cell proliferation, and formation of a three-dimensional tissuelike substance by skin fibroblasts. *Journal of Cellular Physiology*, 138(1), 8-16.

[509] Humbert, P.G., Haftek, M., Creidi, P., Lapière, C., Nusgens, B., Richard, A., Schmitt, D., Rougier, A. and Zahouani, H., 2003. Topical ascorbic acid on photoaged skin. Clinical, topographical and ultrastructural evaluation: double-blind study vs. placebo. *Experimental Dermatology*, 12(3), 237-244.

[510] Dunphy, J.E., Udupa, K.N. and Edwards, L.C., 1956. Wound healing a new perspective with particular reference to ascorbic acid deficiency. *Annals of Surgery*, 144(3), 304-317.

[511] Alsaadi, M., Italia, J.L., Mullen, A.B., Kumar, M.R., Candlish, A.A., Williams, R.A.M., Shaw, C.D., Al Gawhari, F., Coombs, G.H., Wiese, M. and Thomson, A.H., 2012. The efficacy of aerosol treatment with non-ionic surfactant vesicles containing amphotericin B in rodent models of leishmaniasis and pulmonary aspergillosis infection. *Journal of Controlled Release*, 160(3), 685-691.

[512] Niki, Y., Bernard, E.M., Schmitt, H.J., Tong, W.P., Edwards, F.F. and Armstrong, D., 1990. Pharmacokinetics of aerosol amphotericin B in rats. *Antimicrobial Agents and Chemotherapy*, 34(1), 29-32.

[513] Lambros, M.P., Bourne, D.W., Abbas, S.A. and Johnson, D.L., 1997. Disposition of aerosolized liposomal amphotericin B. *Journal of Pharmaceutical Sciences*, 86(9), 1066-1069.

[514] Schmitt, H.J., Bernard, E.M., Häuser, M. and Armstrong, D., 1988. Aerosol amphotericin B is effective for prophylaxis and therapy in a rat model of pulmonary aspergillosis. *Antimicrobial Agents and Chemotherapy*, 32(11), 1676-1679.

[515] Ruijgrok, E.J., Vulto, A.G. and Van Etten, E.W., 2001. Efficacy of aerosolized amphotericin B desoxycholate and liposomal amphotericin B in the treatment of invasive pulmonary aspergillosis in severely immunocompromised rats. *Journal of Antimicrobial Chemotherapy*, 48(1), 89-95.

[516] Mesa-Arango, A.C., Scorzoni, L. and Zaragoza, O., 2012. It only takes one to do many jobs: Amphotericin B as antifungal and immunomodulatory drug. *Frontiers in Microbiology*, 3, 286.

[517] Sangalli-Leite, F., Scorzoni, L., Mesa-Arango, A.C., Casas, C., Herrero, E., Gianinni, M.J.S.M., Rodríguez-Tudela, J.L., Cuenca-Estrella, M. and Zaragoza, O., 2011. Amphotericin B mediates killing in Cryptococcus neoformans through the induction of a strong oxidative burst. *Microbes and Infection*, 13(5), 457-467.

[518] Ferreira, G.F., de Matos Baltazar, L., Santos, J.R.A., Monteiro, A.S., de Oliveira Fraga, L.A., Resende-Stoianoff, M.A. and Santos, D.A., 2013. The role of oxidative and nitrosative bursts caused by azoles and amphotericin B against the fungal pathogen Cryptococcus gattii. *Journal of Antimicrobial Chemotherapy*, 68(8), 1801-1811.

[519] Iman, M., Huang, Z., Szoka, F.C. and Jaafari, M.R., 2011. Characterization of the colloidal properties, in vitro antifungal activity, antileishmanial activity and toxicity in mice of a distigmasterylhemisuccinoyl-glycero-phosphocholine liposome-intercalated amphotericin B. *International Journal of Pharmaceutics*, 408(1), 163-172.

[520] Torrado, J.J., Espada, R., Ballesteros, M.P. and Torrado-Santiago, S., 2008. Amphotericin B formulations and drug targeting. *Journal of Pharmaceutical Sciences*, 97(7), 2405-2425.

[521] Chaubey, P., Patel, R.R. and Mishra, B., 2014. Development and optimization of curcumin-loaded mannosylated chitosan nanoparticles using response surface methodology in the treatment of visceral leishmaniasis. *Expert Opinion on Drug Delivery*, 11(8), 1163-1181.

[522] Crowe, L.M. and Crowe, J.H., 1988. Trehalose and dry dipalmitoylphosphatidylcholine revisited. *Biochimica et Biophysica Acta (BBA)-Biomembranes*, 946(2), 193-201.

[523] Tsvetkova, N., Tenchov, B., Tsonev, L. and Tsvetkov, T., 1988. Dependence of trehalose protective action on the initial phase state of dipalmitoylphosphatidylcholine bilayers. *Cryobiology*, 25(3), 256-263.

[524] Huang, G., Zang, B., Wang, X., Liu, G. and Zhao, J., 2015. Encapsulated paclitaxel nanoparticles exhibit enhanced anti-tumour efficacy in A549 non-small lung cancer cells. *Acta Biochimica et Biophysica Sinica*, 47(12), 981-987.

[525] Zhang, Q., Jiang, X., Jiang, W., Lu, W., Su, L. and Shi, Z., 2004. Preparation of nimodipine-loaded microemulsion for intranasal delivery and evaluation on the targeting efficiency to the brain. *International Journal of Pharmaceutics*, 275(1), 85-96.

[526] Kumar, M., Misra, A., Babbar, A.K., Mishra, A.K., Mishra, P. and Pathak, K., 2008. Intranasal nanoemulsion based brain targeting drug delivery system of risperidone. *International Journal of Pharmaceutics*, 358(1), 285-291.

[527] Lapchak, P.A. and McKim, J.M., 2011. CeeTox™ analysis of CNB-001 a novel curcumin-based neurotrophic/neuroprotective lead compound to treat stroke: comparison with NXY-059 and Radicut. *Translational Stroke Research*, 2(1), 51-59.

[528] Jayachandra Babu, R., Dayal, P.P., Pawar, K. and Singh, M., 2011. Nose-to-brain transport of melatonin from polymer gel suspensions: a microdialysis study in rats. *Journal of Drug Targeting*, 19(9), 731-740.

[529] Chemuturi, N.V., Hayden, P., Klausner, M. and Donovan, M.D., 2005. Comparison of human tracheal/bronchial epithelial cell culture and bovine nasal respiratory explants for nasal drug transport studies. *Journal of Pharmaceutical Sciences*, 94(9), 1976-1985.

[530] Hansen, J.T., Koeppen, B.M. and Koeppen, B.M., 2002. Netter's Atlas of Human Physiology, Icon Learning Systems, Elsevier Inc, New Jersey.

[531] A.A. Peters, S.L. Palay, H.D. Webster, 1991. The Fine Structure of the Nervous System: Neurons and their Supporting Cells, Oxford University Press, New York.

8

CHAPTER 8

Appendix

Appendix 1 | HPLC validation for the analytical methods developed

A1.1 Amphotericin B

Accuracy: The accuracy of analytical method is expressed as % bias or the % relative error. Tolerance limits obtained from the accuracy determination of each concentration under study is as tabulated in Table A1.1 and Table A1.2 for both intraday and inter-day analysis. No significant difference ($p > 0.05$) was found between the amount of amphotericin B added (true/actual) and concentration observed at all the concentrations tested under the linearity range for amphotericin B, indicative of the accuracy of the developed HPLC method.

Precision: Precision of the analytical method was analyzed by determination of amphotericin B at different concentrations of 2, 7 and 12 µg/mL that was within the linearity range of the method for the drug as per Beer-Lambert law. Three replicate readings of each of the concentrations were analyzed and results expressed as relative standard deviation (RSD) was assessed for both inter-day and intraday evaluation. These are as tabulated in Table A1.1 and Table A1.2. A low % RSD (or %CV) is indicative of the precision of the method for analysis of amphotericin B.

Table A1.1: Intraday precision and accuracy observed for the HPLC analysis method of amphotericin B

Standard concentration (µg/mL)		Accuracy[a] (%)	Precision[b] (%)
Actual	Observed		
2	2.15±0.038	107.55	1.76
7	7.00±0.180	100.03	2.57
12	12.1±0.012	101.275	0.10

[a] Accuracy expressed as % i.e. (mean observed concentration/actual concentration) x100
[b] Precision expressed as RSD (relative standard deviation) = (standard deviation/mean) x100

Table A1.2: Interday precision and accuracy observed for the HPLC analysis method of amphotericin B

Standard concentration (µg/mL)		Accuracy[a] (%)	Precision[b] (%)
Actual	Observed		
2	1.91±0.064	95.25	3.34
7	7.03±0.180	100.53	2.57
12	12.06±0.019	100.52	0.16

[a] Accuracy expressed as % i.e. (mean observed concentration/actual concentration) x100
[b] Precision expressed as RSD (relative standard deviation) = (standard deviation/mean) x100

Representative HPLC chromatogram of amphotericin B is as shown in Figure A1.1

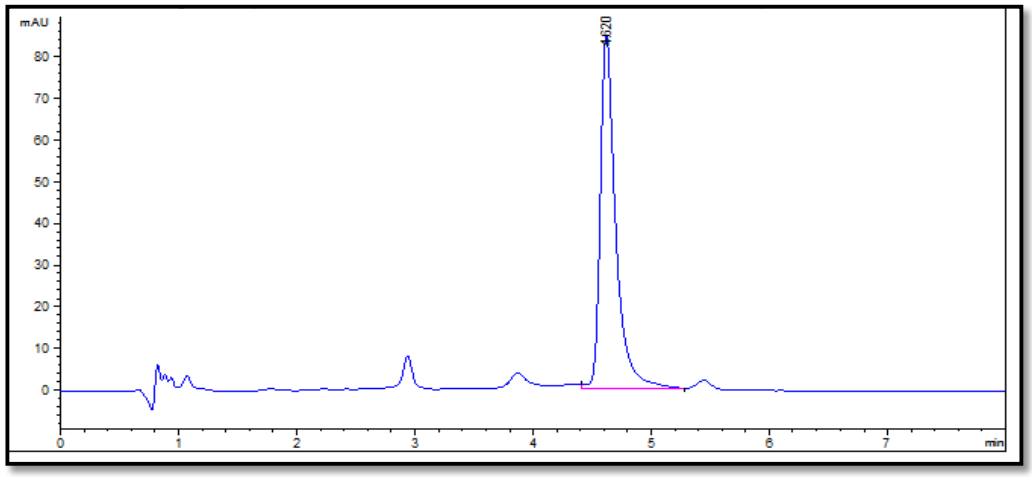

Figure A1.1: Representative HPLC chromatogram of amphotericin B

A1.2 Rifampicin and ibuprofen

Accuracy: The accuracy of analytical method is expressed as % bias or the % relative error. Tolerance limits obtained from the accuracy determination of each concentration under study is as tabulated in Table A1.3, Table A1.4, Table A1.5 and Table A1.6 for both intraday and inter-day analysis. No significant difference ($p > 0.05$) was found between the amount of rifampicin and ibuprofen added (true/actual) and concentration observed at all the concentrations tested under the linearity range for these drugs, indicative of the accuracy of the developed HPLC method.

Precision: Precision of the analytical method was analyzed by determination of rifampicin and ibuprofen at different concentrations of 10, 50 and 100 µg/mL. These are as tabulated in Table A1.3, Table A1.4, Table A1.5 and Table A1.6. A low % RSD (or %CV) is indicative of the precision of the HPLC method for analysis of the antitubercular drugs.

Table A1.3: Intraday precision and accuracy observed for the HPLC analysis method of ibuprofen

Standard concentration (µg/mL)		Accuracy [a] (%)	Precision [b] (%)
Actual	Observed		
10	10.1945 ± 1.212	101.94	1.8930
50	50.9386 ± 1.762	101.88	3.4583
100	102.3630 ± 0.543	102.36	5.3054

[a] Accuracy expressed as % i.e. (mean observed concentration/actual concentration) x100
[b] Precision expressed as RSD (relative standard deviation) = (standard deviation/mean) x100

Table A1.4: Intraday precision and accuracy observed for the HPLC analysis method of rifampicin

Standard concentration (µg/mL)		Accuracy [a] (%)	Precision [b] (%)
Actual	Observed		
10	10.4306 ± 0.190	104.31	1.8219
50	50.7646 ± 2.276	101.53	4.4834
100	101.2127 ± 2.485	101.21	2.4554

[a] Accuracy expressed as % i.e. (mean observed concentration/actual concentration) x100
[b] Precision expressed as RSD (relative standard deviation) = (standard deviation/mean) x100

Table A1.5: Interday precision and accuracy observed for the HPLC analysis method of ibuprofen

Standard concentration (µg/mL)		Accuracy [a] (%)	Precision [b] (%)
Actual	Observed		
10	11.0573 ± 0.611	110.57	5.5258
50	52.2795 ± 0.349	104.56	6.5449
100	104.3380 ± 0.413	104.34	3.8516

[a] Accuracy expressed as % i.e. (mean observed concentration/actual concentration) x100
[b] Precision expressed as RSD (relative standard deviation) = (standard deviation/mean) x100

Table A1.6: Interday precision and accuracy observed for the HPLC analysis method of rifampicin

Standard concentration (µg/mL)		Accuracy [a] (%)	Precision [b] (%)
Actual	Observed		
10	9.9487 ± 0.924	99.49	9.2916
50	48.9868 ± 3.056	97.97	6.2382
100	98.9743 ± 2.743	98.97	2.8282

[a] Accuracy expressed as % i.e. (mean observed concentration/actual concentration) x100
[b] Precision expressed as RSD (relative standard deviation) = (standard deviation/mean) x100

Representative HPLC chromatogram of simultaneous determination of rifampicin and ibuprofen is as shown in Figure A1.2.

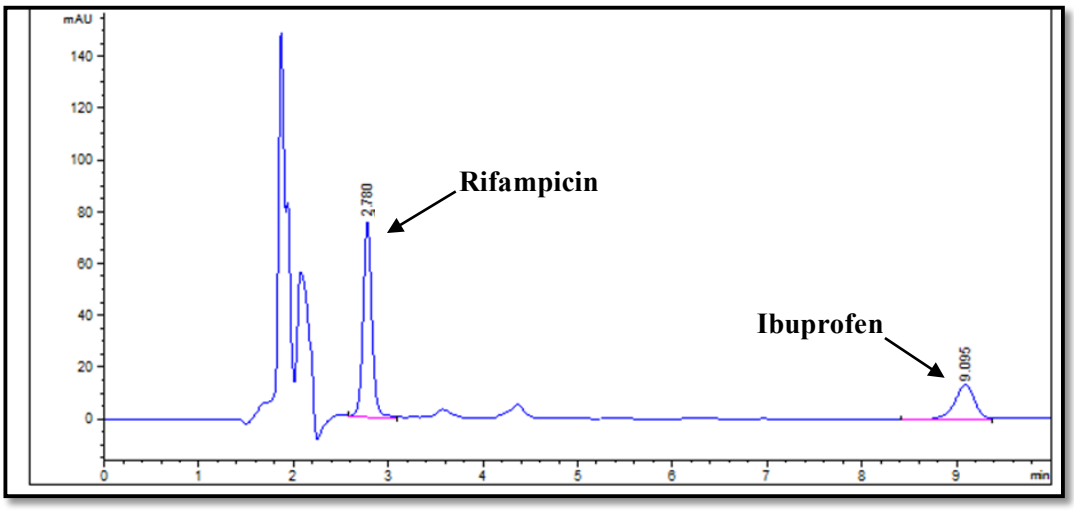

Figure A1.2: Representative HPLC chromatogram of rifampicin and ibuprofen simultaneously eluted

A1.3 CNB001 and curcumin

Accuracy: The accuracy of analytical method is expressed as % bias or the % relative error. Tolerance limits obtained from the accuracy determination of each concentration under study is as tabulated in Table A1.7, Table A1.8, Table A1.9 and Table A1.10 and for both intraday and inter-day analysis. No significant difference ($p > 0.05$) was found between the amount of curcumin and CNB001 added (true/actual) and concentration observed at all the concentrations tested under the linearity range for these drugs, indicative of the accuracy of the developed HPLC method.

Precision: Precision of the analytical method was analyzed by determination of curcumin and CNB001 at different concentrations (as indicated in the tables for each drug). These are as tabulated in Table A1.7, Table A1.8, Table A1.9 and Table A1.10. A low % RSD (or %CV) is indicative of the precision of the HPLC method for analysis of the drugs.

Table A1.7: Intraday precision and accuracy observed for the HPLC analysis method of curcumin

Standard concentration (µg/mL)		Accuracy [a] (%)	Precision [b] (%)
Actual	Observed		
2	2.1224 ± 0.22	106.12	1.0251
20	20.9096 ± 0.835	104.55	2.9941
50	51.5808 ± 0.861	103.16	1.6695

[a] Accuracy expressed as % i.e. (mean observed concentration/actual concentration) x100
[b] Precision expressed as RSD (relative standard deviation) = (standard deviation/mean) x100

Table A1.8: Intraday precision and accuracy observed for the HPLC analysis method of CNB001

Standard concentration (µg/mL)		Accuracy [a] (%)	Precision [b] (%)
Actual	Observed		
5	4.9343 ± 0.044	98.69	0.8957
20	20.1382 ± 0.526	100.69	2.6142
50	48.8942 ± 0.5214	97.78	1.0665

[a] Accuracy expressed as % i.e. (mean observed concentration/actual concentration) x100
[b] Precision expressed as RSD (relative standard deviation) = (standard deviation/mean) x100

Table A1.9: Interday precision and accuracy observed for the HPLC analysis method of curcumin

Standard concentration (µg/mL)		Accuracy [a] (%)	Precision [b] (%)
Actual	Observed		
2	2.0214 ± 0.0741	101.07	3.6657
20	20.7320 ± 0.112	103.66	0.5402
50	49.9564 ± 0.415	99.92	0.8307

[a] Accuracy expressed as % i.e. (mean observed concentration/actual concentration) x100
[b] Precision expressed as RSD (relative standard deviation) = (standard deviation/mean) x100

Table A1.10: Interday precision and accuracy observed for the HPLC analysis method of CNB001

Standard concentration (µg/mL)		Accuracy [a] (%)	Precision [b] (%)
Actual	Observed		
5	4.9541 ± 0.124	99.08	2.5029
20	21.0041 ± 0.457	105.02	2.1758
50	49.1156 ± 0.874	98.23	1.7795

[a] Accuracy expressed as % i.e. (mean observed concentration/actual concentration) x100
[b] Precision expressed as RSD (relative standard deviation) = (standard deviation/mean) x100

Representative HPLC chromatogram of CNB001 and curcumin is as shown in Figure A1.3 and Figure A1.4 respectively.

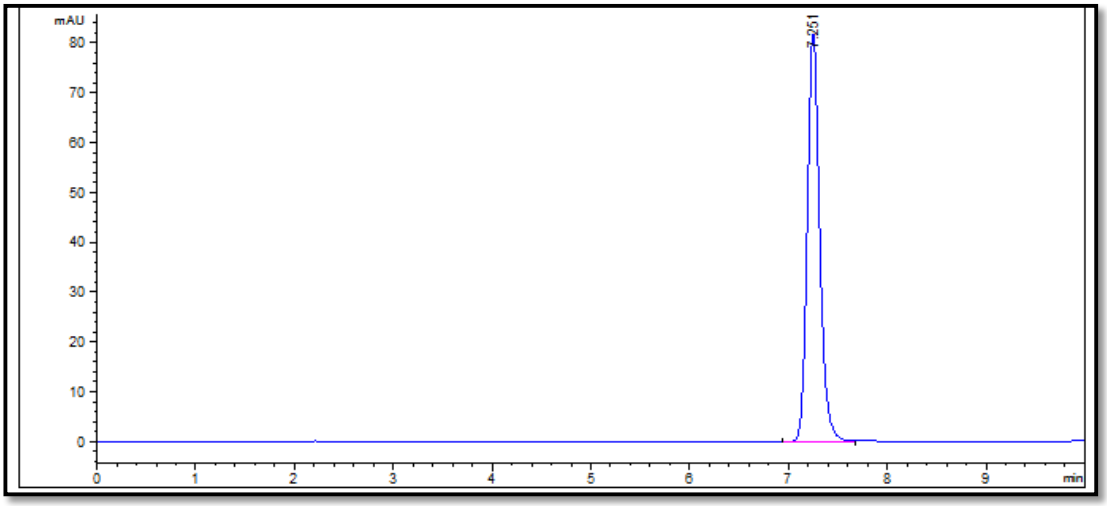

Figure A1.3: Representative HPLC chromatogram of CNB001

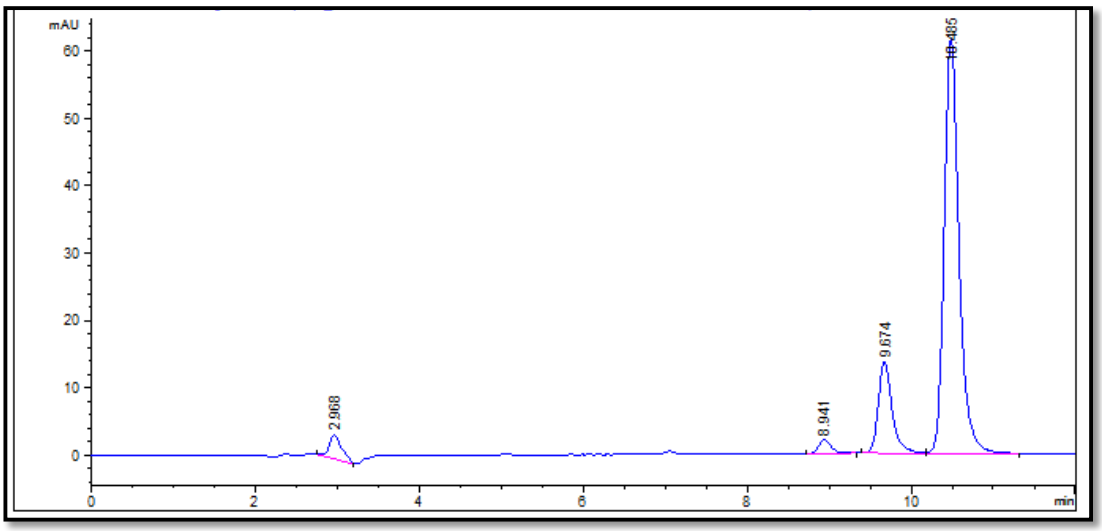

Figure A1.4: Representative HPLC chromatogram of curcumin

Appendix 2 | Design of Experiment (DoE) model validation

Diagnostic plot of normal percentage probability of studentized residuals were used to validate the Design of Experiment model statistics. In the normal percentage probability plot the spread of data points was approximately along a straight line depictive of a good correlation between the model predicted and model fitted, confirming that the model fitted was normal and could be used to study the effect of the different factors on the various responses [428]. The normal percentage probability plots for DoE1 (choice of lipids) and DoE 2 (ratio of drugs) is as shown in Figure A2.1 and Figure A2.2 respectively.

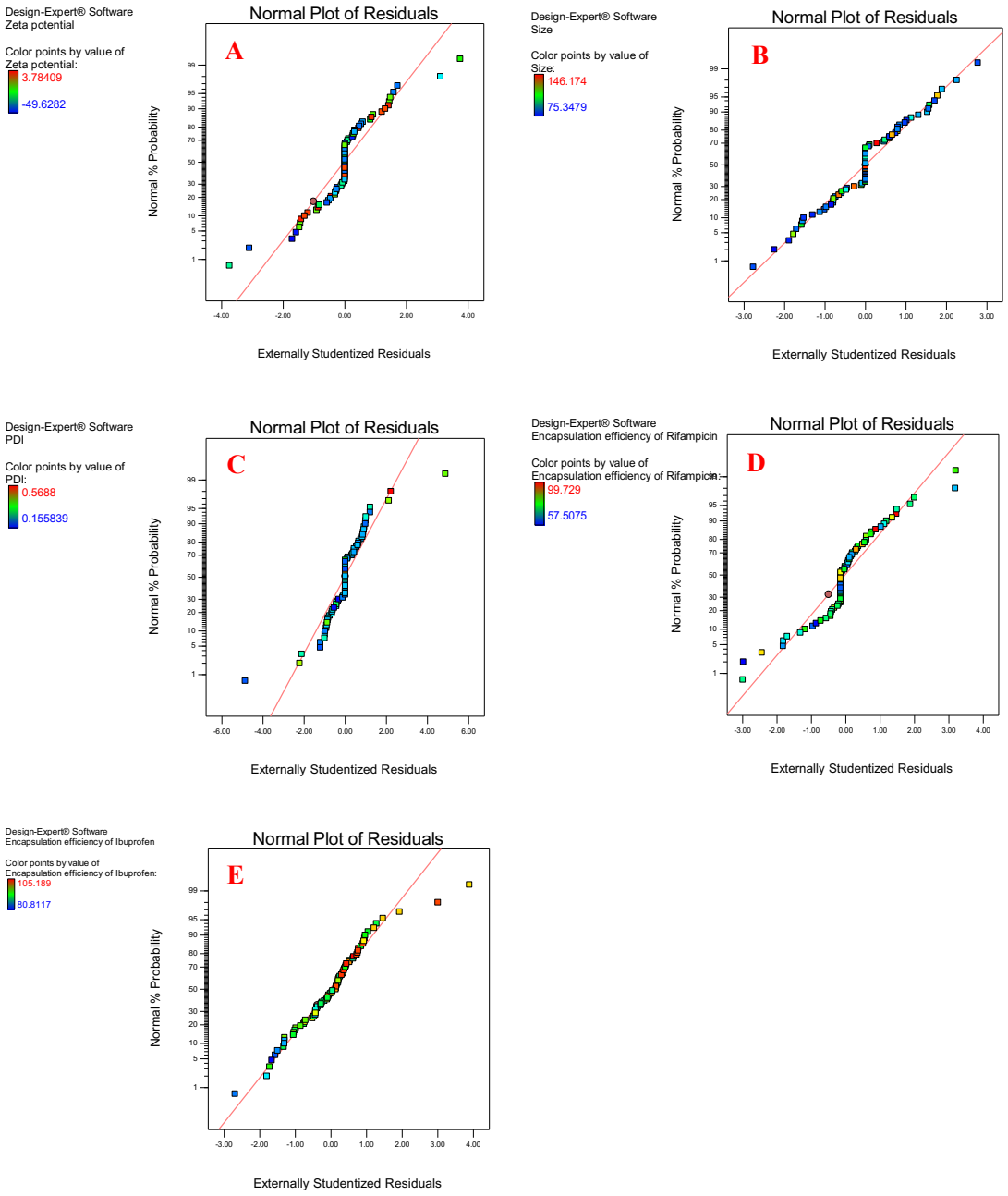

Figure A2.1: DoE 1- Choice of lipids, normal percentage probability plot for zeta potential (A), mean size (B), PDI (C), encapsulation efficiency of rifampicin (D) and encapsulation efficiency of ibuprofen (E) (mean±SD, n=3, Design-Expert® 10 (Stat-Ease, Inc.))

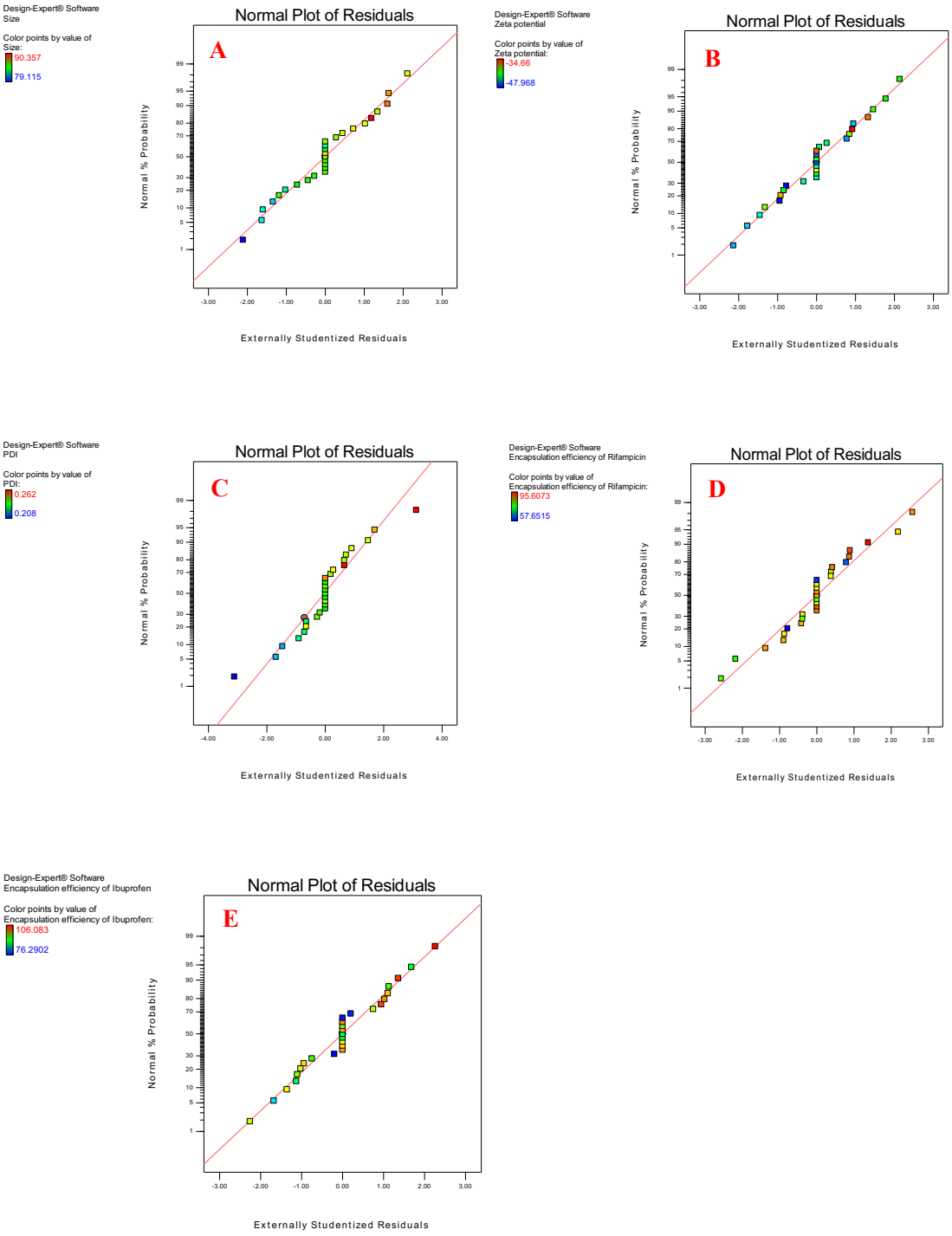

Figure A2.2: DoE 2- Ratio of drugs, normal percentage probability plot for zeta potential (A), mean size (B), PDI (C), encapsulation efficiency of rifampicin (D) and encapsulation efficiency of ibuprofen (E) (mean±SD, n=3, Design-Expert® 10 (Stat-Ease, Inc.))

Appendix 3 | *In vitro* drug release kinetics

Release kinetics of the drugs CNB001 or curcumin from the different surfactants namely Kolliphor® TPGS or Solutol® HS 15, were fitted into various kinetic models and the regression coefficient R^2 used to ascertain the best fit model.

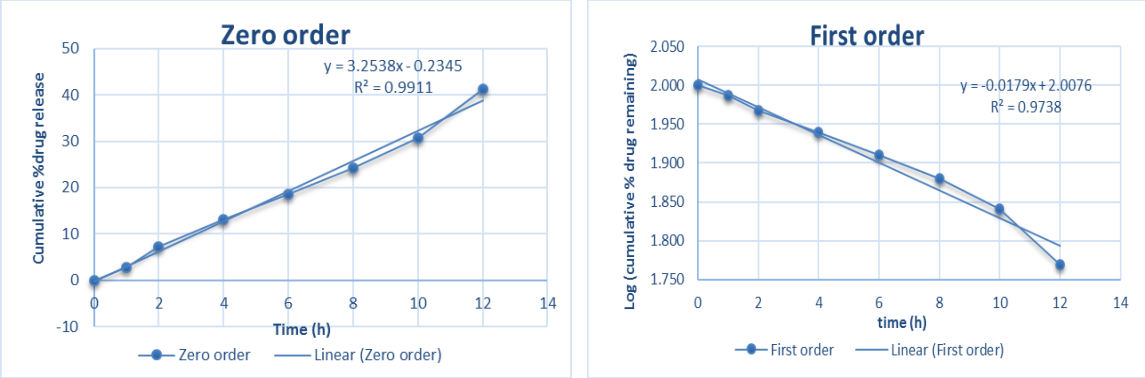

Figure A3.1: Drug release of CNB001: Solutol® HS 15:0% mole cholesterol fitted into zero-order (left) and first-order (right) kinetic models

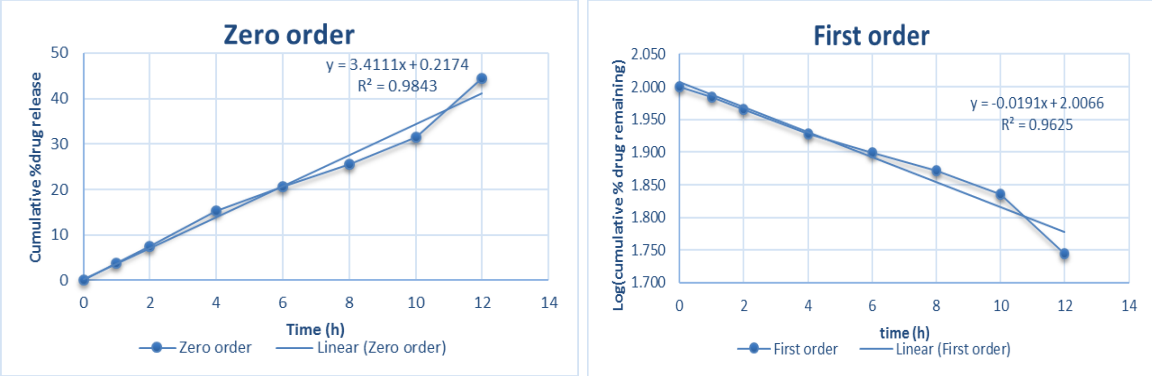

Figure A3.2: Drug release of CNB001: Solutol® HS 15:15% mole cholesterol fitted into zero-order (left) and first-order (right) kinetic models

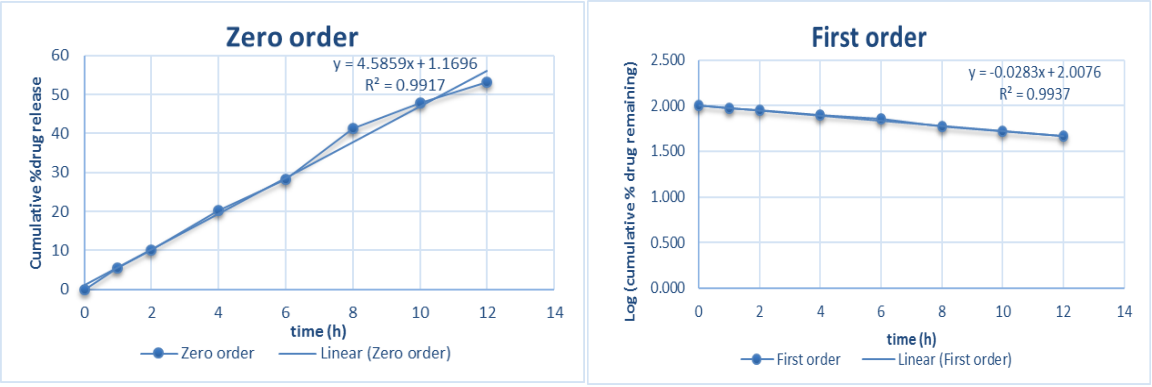

Figure A3.3: Drug release of CNB001: Solutol® HS 15:30% mole cholesterol fitted into zero-order (left) and first-order (right) kinetic models

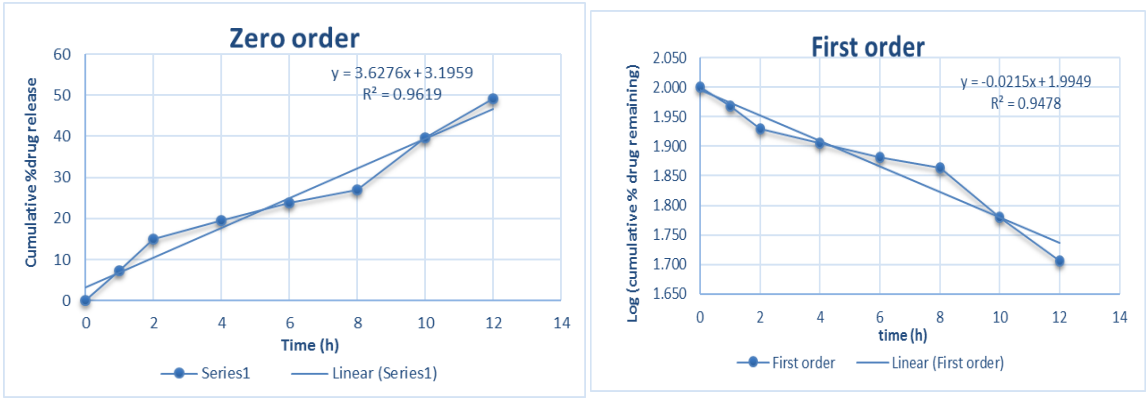

Figure A3.4: Drug release of curcumin: Solutol® HS 15:0% mole cholesterol fitted into zero-order (left) and first-order (right) kinetic models

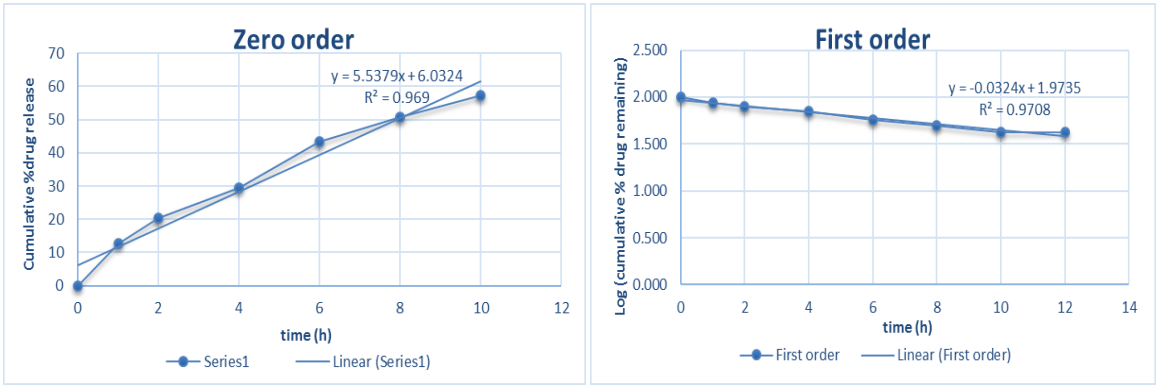

Figure A3.5: Drug release of curcumin: Solutol® HS 15:15% mole cholesterol fitted into zero-order (left) and first-order (right) kinetic models

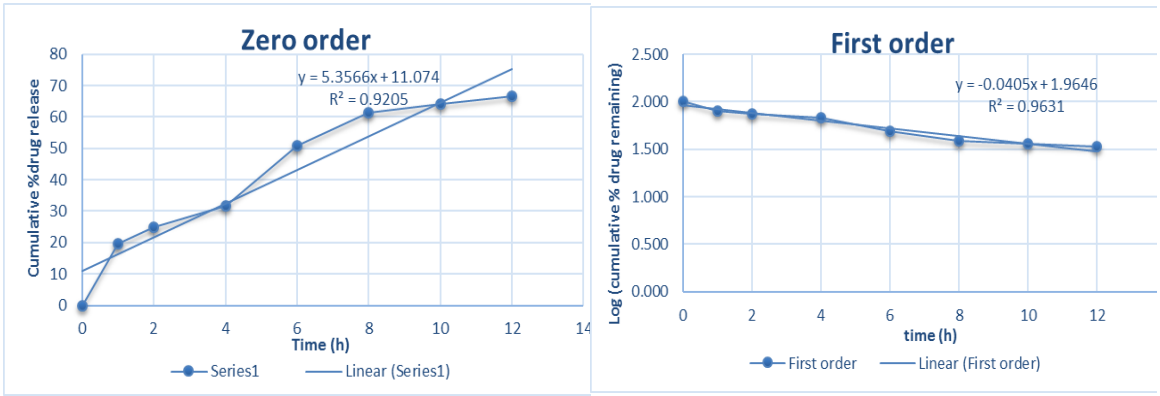

Figure A3.6: Drug release of curcumin: Solutol® HS 15:30% mole cholesterol fitted into zero-order (left) and first-order (right) kinetic models

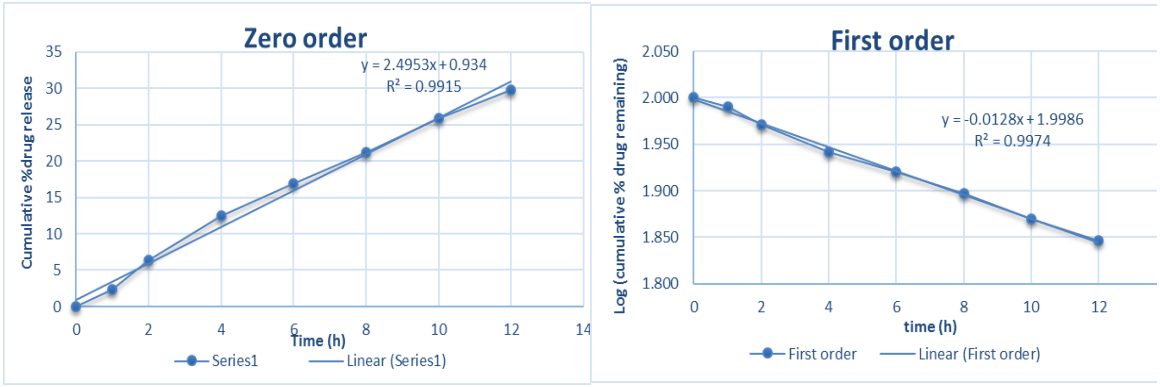

Figure A3.7: Drug release of curcumin: Kolliphor® TPGS:0% mole dequalinium fitted into zero-order (left) and first-order (right) kinetic models

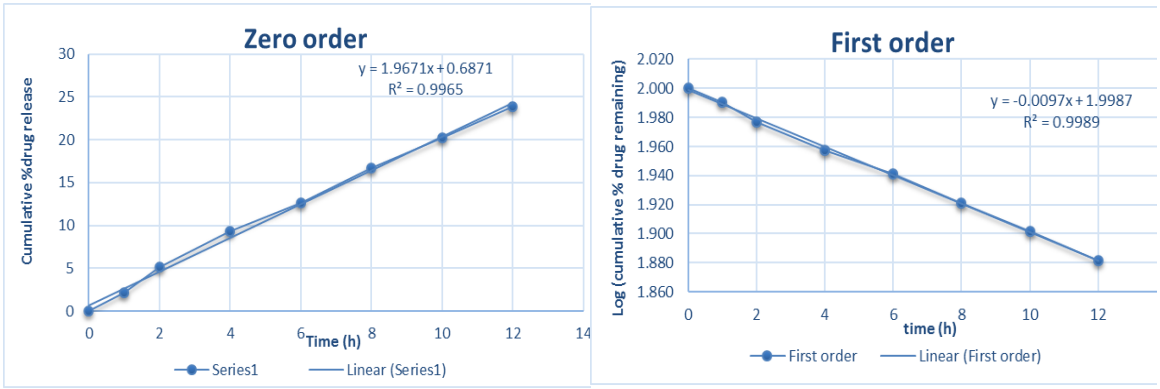

Figure A3.8: Drug release of curcumin: Kolliphor® TPGS:30% mole dequalinium fitted into zero-order (left) and first-order (right) kinetic models